THE HUNGA VOLCANIC ERUPTION ATMOSPHERIC IMPACTS REPORT 2025

APARC Report No. 11
WCRP Report No. 10/2025

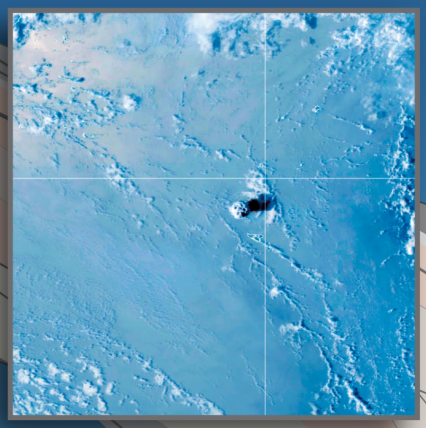
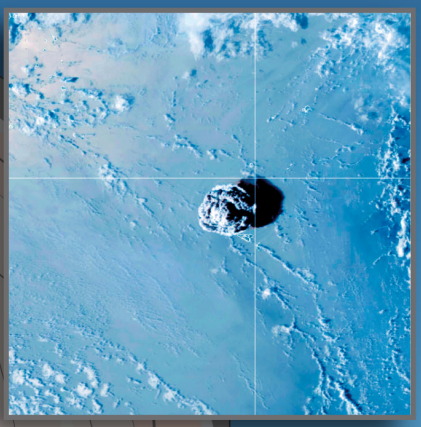
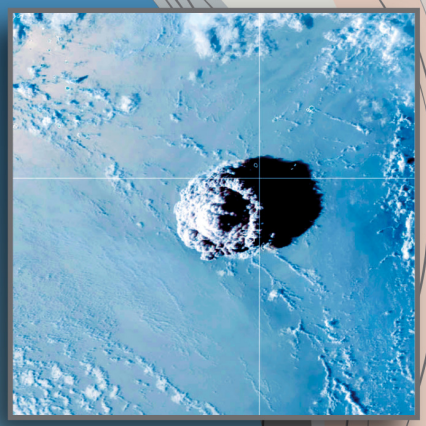
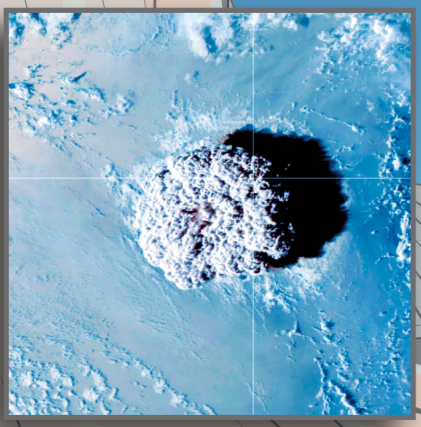
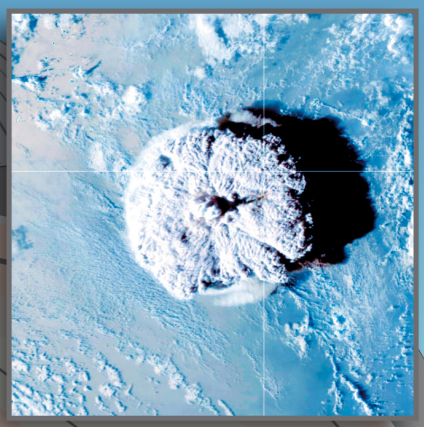
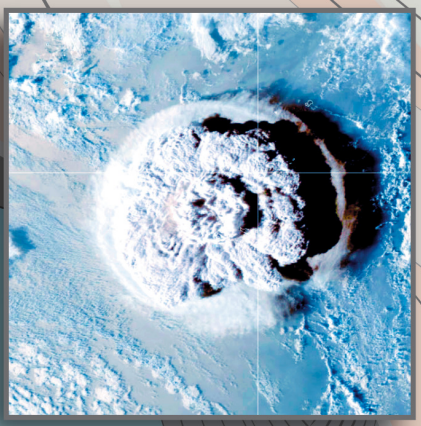
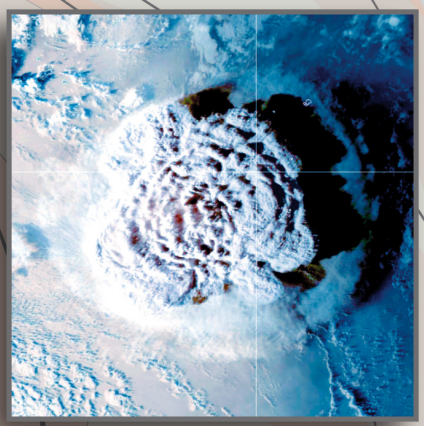

Hunga Impact
APARC 2022–2025

APARC
Atmospheric Processes And their Role in Climate

WCRP
World Climate Research Programme

NOAA NASA WMO unesco Intergovernmental Oceanographic Commission IPSL cnrs LMD ENS

CIRES UNIVERSITY OF LEEDS JÜLICH Forschungszentrum

NSF NCAR National Centre for Atmospheric Science NATURAL ENVIRONMENT RESEARCH COUNCIL International Science Council

The Hunga Volcanic Eruption Atmospheric Impacts Report

APARC Report No. 11, WCRP Report No. 10/2025

Yunqian Zhu, Graham Mann, Paul A. Newman, William Randel (Eds.)

December 2025

Citation

APARC, 2025: The Hunga Volcanic Eruption Atmospheric Impacts Report. Yunqian Zhu, Graham Mann, Paul A. Newman, William Randel (Eds.), APARC Report No. 11, WCRP Report No. 10/2025, DOI: 10.34734/FZJ-2025-05237, available at https://aparc-climate.org/publications/aparc-report-no-11/.

This work is licensed under a
Creative Commons Attribution 4.0 International License (CC BY-NC 4.0).

Electronic version available at https://aparc-climate.org/publications/aparc-report-no-11/.

ISSN (Print) 3054-1549
ISSN (Online) 3054-1530

Editing, Design, and Layout: Ines Tritscher, Lars Hoffmann, Rolf Müller, Olaf Stein

Authors, contributors and reviewers

Co-chairs

Yunqian Zhu	University of Colorado Boulder, Cooperative Institute for Research in Environmental Science (CIRES) at NOAA Chemical Sciences Laboratory, USA
Graham Mann	School of Earth and Environment, University of Leeds, Leeds, UK National Centre for Atmospheric Science, University of Leeds, Leeds, UK
Paul A. Newman	University of Maryland Baltimore County at NASA Goddard Space Flight Center, USA
William Randel	NSF National Center for Atmospheric Research (NCAR), USA

Assessment coordinator

Ines Tritscher	APARC International Project Office, Forschungszentrum Jülich, Germany

Graphic and layout coordinator

Chelsea R. Thompson	National Oceanic and Atmospheric Administration (NOAA) Chemical Sciences Laboratory, USA

Chapter 1

Lead authors

Simon Carn	Michigan Technological University, USA
Anja Schmidt	Deutsches Zentrum für Luft- und Raumfahrt (DLR) German Aerospace Center Institute of Atmospheric Physics (IPA), Germany

Co-authors

Kristen Fauria	Vanderbilt University, USA
Corinna Kloss	Forschungszentrum Jülich, Germany
Isobel Yeo	National Oceanography Centre, UK

Contributing authors

Larry Mastin	USGS Cascades Volcano Observatory, USA
Tjarda Roberts	Centre national de la recherche scientifique (CNRS), France

Reviewer editor

Owen Brian Toon	University of Colorado Boulder, USA

Chapter 2

Lead authors

Elizabeth Asher	University of Colorado Boulder, Cooperative Institute for Research in Environmental Sciences (CIRES) at NOAA Global Monitoring Laboratory, USA
Bernard Legras	Laboratoire de Météorologie Dynamique, Institut Pierre-Simon-Laplace (LMD-IPSL), France

Co-authors

Marie Boichu	CNRS/University of Lille, Laboratoire d'Optique Atmosphérique, Lille, France
Julia Bruckert	Institute of Meteorology and Climate Research Tropospheric Research (IMKTRO), Karlsruhe Institute of Technology (KIT), Karlsruhe, Germany
Aurélien Podglajen	Laboratoire de Météorologie Dynamique, Paris, France
Ghassan Taha	Morgan State University, Baltimore, USA NASA Goddard Space Flight Center, USA

Contributing authors

Alexandre Baron	University of Colorado Boulder, Cooperative Institute for Research in Environmental Science (CIRES) at NOAA Chemical Sciences Laboratory, USA
Simran Chopra	Institute of Meteorology and Climate Research Tropospheric Research (IMKTRO), Karlsruhe Institute of Technology (KIT), Karlsruhe, Germany
Stéphanie Evan	Laboratoire de l'Atmosphère et des Cyclones, La Réunion (LACy, UMR 8105, CNRS, Université de La Réunion, Météo-France), France
Neil Hindley	Natural Environmental Research Council (NERC) Fellow, University of Bath, UK
Ákos Horváth	Meteorological Institute, University of Hamburg, Hamburg, Germany
Ali Hoshyaripour	Institute of Meteorology and Climate Research Tropospheric Research (IMKTRO), Karlsruhe Institute of Technology (KIT), Karlsruhe, Germany
Michelle L. Santee	Jet Propulsion Laboratory (JPL), California Institute of Technology, USA
Paul Walter	St. Edward's University, Austin, USA
Pengfei Yu	Jinan University, China
Yunqian Zhu	University of Colorado Boulder, Cooperative Institute for Research in Environmental Science (CIRES) at NOAA Chemical Sciences Laboratory, USA

Reviewer editor

Thomas J. Aubry	Department of Earth Sciences, University of Oxford, UK

Chapter 3

Lead authors

Sergey Khaykin	Laboratoire Atmosphère Observations Spatiales (LATMOS), IPSL, Sorbonne University, UVSQ, France
Adam Bourassa	Institute of Space and Atmospheric Studies, University of Saskatchewan, Canada

Co-authors

Valentina Aquila	Department of Environmental Science, American University, Washington DC, USA
Alexandre Baron	University of Colorado Boulder, Cooperative Institute for Research in Environmental Science (CIRES) at NOAA Chemical Sciences Laboratory, USA
Landon Rieger	Environment and Climate Change Canada, Canada
Alexei Rozanov	Institute of Environmental Physics (IUP), University of Bremen, Germany
Rei Ueyama	NASA Ames Research Center, USA

Contributing authors

Elizabeth Asher	University of Colorado Boulder, Cooperative Institute for Research in Environmental Science (CIRES) at NOAA Global Monitoring Laboratory, USA
Nelson Begue	Laboratoire de l'Atmosphère et des Cyclones, UMR 8105 CNRS, Université de La Réunion, Météo-France, Réunion Island, France
Slimane Bekki	LATMOS - Laboratoire Atmosphère Observations Spatiales, UVSQ, CNRS, Sorbonne University, Guyancourt, France
Ewa M. Bednarz	University of Colorado Boulder, Cooperative Institute for Research in Environmental Science (CIRES) at NOAA Chemical Sciences Laboratory, USA
Marie Boichu	CNRS/University of Lille, Laboratoire d'Optique Atmosphérique, Lille, France
Christoph Brühl	Max Planck Institute for Chemistry, Mainz, Germany
Parker Case	Earth System Science Interdisciplinary Center, University of Maryland, College Park, MD, USA
Simon Chabrillat	Royal Belgian Institute for Space Aeronomy, BIRA-IASB, 1180 Brussels, Belgium
Margot Clyne	Laboratory for Atmospheric and Space Physics, University of Colorado Boulder, USA; Department of Atmospheric Science, Colorado State University, Fort Collins, CO, USA
Peter Colarco	NASA Goddard Space Flight Center, Code 614, Greenbelt, MD, USA
Kimberlee Dube	University of Saskatchewan, Canada
Lola Falletti	LATMOS - Laboratoire Atmosphère Observations Spatiales, UVSQ, CNRS, Sorbonne University, Guyancourt, France
David Flittner	NASA Langley Research Center, USA
Raphael Grandin	Université Paris Cité, Institut de Physique du Globe de Paris
Eilidh Hlady	University of Saskatchewan, Canada
Julien Jumelet	Laboratoire Atmosphère Observations Spatiales (LATMOS), IPSL, Sorbonne University, UVSQ, France
Mahesh Kovilakam	NASA Langley Research Center, VA, USA
Nicolas Lebas	LOCEAN/IPSL, Sorbonne Université, CNRS, IRD, MNHN, Paris, France
Cheng-Cheng Liu	Laboratory for Atmospheric and Space Physics, University of Colorado Boulder, Boulder, CO, USA
Gloria L. Manney	NorthWest Research Associates, Socorro, NM, USA; New Mexico Institute of Mining and Technology, Socorro, NM, USA
Marion Marchand	LATMOS - Laboratoire Atmosphère Observations Spatiales, UVSQ, CNRS, Sorbonne University, Guyancourt, France
Luis F. Millán	Jet Propulsion Laboratory (JPL), California Institute of Technology, USA
Yifeng Peng	College of Atmospheric Science, Lanzhou University, Lanzhou, China
Richard Querel	National Institute of Water and Atmospheric Research (NIWA), New Zealand
Samuel Remy	HYGEOS, Lille, France
Tetsu Sakai	Meteorological Research Institute (MRI-JMA), Japan
Michelle L. Santee	Jet Propulsion Laboratory (JPL), California Institute of Technology, USA
Takashi Sekiya	Japan Agency for Marine-Earth Science and Technology (JAMSTEC), Yokohama, Japan

Florent Tence	Laboratoire Atmosphère Observations Spatiales (LATMOS), IPSL, Sorbonne University, UVSQ, France
Simone Tilmes	NSF National Center for Atmospheric Research (NCAR), USA
Xinyue Wang	Department of Atmospheric and Oceanic Sciences, University of Colorado Boulder, Boulder, USA
Shingo Watanabe	Japan Agency for Marine-Earth Science and Technology (JAMSTEC), Yokohama, Japan; Advanced Institute for Marine Ecosystem Change (WPI-AIMEC), Tohoku University, Sendai, Japan
Pengfei Yu	College of Environment and Climate, Jinan University, Guangzhou, China
Wandi Yu	Lawrence Livermore National Laboratory (Research prepared under Contract DE-AC52-07NA27344), USA
Jun Zhang	NSF National Center for Atmospheric Research (NCAR), USA
Yunqian Zhu	University of Colorado Boulder, Cooperative Institute for Research in Environmental Science (CIRES) at NOAA Chemical Sciences Laboratory, USA
Zhihong Zhuo	Department of Earth and Atmospheric Sciences, University of Quebec in Montreal, Montreal (Quebec), Canada

Reviewer editor

Kostas Tsigaridis	Columbia University, USA; NASA Goddard Institute for Space Studies, USA

Chapter 4

Lead authors

Xinyue Wang	Department of Atmospheric and Oceanic Sciences, University of Colorado Boulder, USA
Lawrence Coy	NASA Goddard Space Flight Center, USA; Science Systems and Applications, Inc. (SSAI), USA

Co-authors

Masatomo Fujiwara	Faculty of Environmental Earth Science, Hokkaido University, Japan
Pu Lin	National Oceanic and Atmospheric Administration (NOAA) Geophysical Fluid Dynamics Laboratory, USA
Alison Ming	University of Cambridge, UK
Feng Li	NASA Goddard Space Flight Center, USA; University of Maryland, Baltimore County, USA
Ewa M. Bednarz	University of Colorado Boulder, Cooperative Institute for Research in Environmental Science (CIRES) at NOAA Chemical Sciences Laboratory, USA
Zhihong Zhuo	Department of Earth and Atmospheric Sciences, University of Quebec in Montreal, Montreal (Quebec), Canada
Kirstin Krüger	University of Oslo, Norway

Contributing authors

William Randel	NSF National Center for Atmospheric Research (NCAR), USA
Jon Starr	NSF National Center for Atmospheric Research (NCAR), USA
Wandi Yu	Lawrence Livermore National Laboratory (Research prepared under Contract DE-AC52-07NA27344), USA
Simone Tilmes	NSF National Center for Atmospheric Research (NCAR), USA
Chengyun Yang	University of Science and Technology of China, China

Yunqian Zhu	University of Colorado Boulder, Cooperative Institute for Research in Environmental Science (CIRES) at NOAA Chemical Sciences Laboratory, USA
Jun Zhang	NSF National Center for Atmospheric Research (NCAR), USA
Simchan Yook	Massachusetts Institute of Technology, Massachusetts, USA
Eric Fleming	NASA Goddard Space Flight Center, USA; Science Systems and Applications, Inc. (SSAI), USA
Peter Colarco	NASA Goddard Space Flight Center, USA
Shingo Watanabe	Japan Agency for Marine-Earth Science and Technology (JAMSTEC), Yokohama, Japan; Advanced Institute for Marine Ecosystem Change (WPI-AIMEC), Tohoku University, Sendai, Japan
Mijeong Park	NSF National Center for Atmospheric Research (NCAR), USA
Martin Jucker	University of New South Wales, New South Wales, Australia

Reviewer editor

Alexey Yu. Karpechko	Finnish Meteorological Institute, Finland

Chapter 5

Lead authors

Freja F. Østerstrøm	Department of Environmental Science, Aarhus University, Denmark Harvard John A. Paulson School of Engineering and Applied Sciences, Harvard University, USA
Michelle L. Santee	Jet Propulsion Laboratory (JPL), California Institute of Technology, USA

Co-authors

Martyn P. Chipperfield	School of Earth and Environment, University of Leeds, UK
Stéphanie Evan	Laboratoire de l'Atmosphère et des Cyclones (LACy, UMR8105, CNRS, Université de La Réunion, Météo-France), France
Dan Smale	National Institute of Water and Atmospheric Research, New Zealand
Krzysztof Wargan	Science Systems and Applications Inc. (SSAI) at NASA Goddard Space Flight Center, USA
David M. Wilmouth	Harvard John A. Paulson School of Engineering and Applied Sciences, Harvard University, USA
Ingo Wohltmann	Alfred Wegener Institute for Polar and Marine Research, Potsdam, Germany

Contributing authors

Ewa M. Bednarz	University of Colorado Boulder, Cooperative Institute for Research in Environmental Science (CIRES) at NOAA Chemical Sciences Laboratory, USA
Sandip Dhomse	School of Earth and Environment, University of Leeds, Leeds, UK National Centre for Earth Observation, University of Leeds, Leeds, UK National Centre for Atmospheric Science, University of Leeds, Leeds, UK
Eric L. Fleming	NASA Goddard Space Flight Center, USA
Stacey M. Frith	Science Systems and Applications, Inc., USA; NASA Goddard Space Flight Center, USA
Gloria L. Manney	NorthWest Research Associates, Socorro, NM, USA; New Mexico Institute of Mining and Technology, Socorro, NM, USA
Luis F. Millán	Jet Propulsion Laboratory (JPL), California Institute of Technology, USA
Jun Zhang	NSF National Center for Atmospheric Research (NCAR), USA

Xin Zhou	School of Atmospheric Sciences, Chengdu University of Information Technology, China; School of Earth and Environment, University of Leeds, UK

Reviewer editor

Olaf Morgenstern	Deutscher Wetterdienst (DWD), Offenbach, Germany; University of Canterbury, Christchurch, New Zealand

Chapter 6

Lead authors

Corwin Wright	Center for Climate Adaptation and Environment Research, University of Bath, UK
Jia Yue	NASA Goddard Space Flight Center, USA

Co-authors

Neil Hindley	University of Bath, UK
Jinhou Lei	University of Science and Technology of China, China
Luis F. Millán	Jet Propulsion Laboratory (JPL), California Institute of Technology, USA
David Themens	University of Birmingham, UK
Sandra Wallis	University of Greifswald, Germany
Wandi Yu	Lawrence Livermore National Laboratory (Research prepared under Contract DE-AC52-07NA27344), USA

Contributing authors

Ewa M. Bednarz	University of Colorado Boulder, Cooperative Institute for Research in Environmental Science (CIRES) at NOAA Chemical Sciences Laboratory, USA
Eric Fleming	NASA Goddard Space Flight Center, USA; Science Systems and Applications, Inc. (SSAI), USA
Ruoxi Li	University of Science and Technology of China, China
David Plummer	Climate Research Division, Environment and Climate Change Canada, Canada
Simone Tilmes	NSF National Center for Atmospheric Research (NCAR), USA
Xinyue Wang	Department of Atmospheric and Oceanic Sciences, University of Colorado Boulder, USA
Jun Zhang	NSF National Center for Atmospheric Research (NCAR), USA
Yunqian Zhu	University of Colorado Boulder, Cooperative Institute for Research in Environmental Science (CIRES) at NOAA Chemical Sciences Laboratory, USA
Zhihong Zhuo	Department of Earth and Atmospheric Sciences, University of Quebec in Montreal, Montreal (Quebec), Canada

Reviewer editor

Hanli Liu	NSF National Center for Atmospheric Research (NCAR), USA

Chapter 7

Lead authors

Georgiy Stenchikov	King Abdullah University of Science and Technology, Saudi Arabia
Mark R. Schoeberl	Science and Technology Corporation (STC), Columbia, Maryland, USA

Co-authors

Ewa M. Bednarz	University of Colorado Boulder, Cooperative Institute for Research in Environmental Science (CIRES) at NOAA Chemical Sciences Laboratory, USA
Eric Fleming	NASA Goddard Space Flight Center, USA; Science Systems and Applications, Inc. (SSAI), USA
Yi Huang	McGill University, Canada
Ilaria Quaglia	NSF National Center for Atmospheric Research (NCAR), USA
Pasquale Sellitto	Laboratoire Interuniversitaire des Systèmes Atmosphériques, Institut Pierre-Simon-Laplace (LISA-IPSL), France
Claudia Timmreck	Max-Planck-Institut für Meteorologie, Germany
Matthew Toohey	University of Saskatchewan, Canada
Jun Wang	University of Iowa, USA
Zhihong Zhuo	Department of Earth and Atmospheric Sciences, University of Quebec in Montreal, Montreal (Quebec), Canada

Contributing authors

Peter Colarco	NASA Goddard Space Flight Center, USA
David Plummer	Climate Research Division, Environment and Climate Change Canada, Canada
Takashi Sekiya	Japan Agency for Marine-Earth Science and Technology (JAMSTEC), Yokohama, Japan
Simone Tilmes	NSF National Center for Atmospheric Research (NCAR), USA
Xinyue Wang	Department of Atmospheric and Oceanic Sciences, University of Colorado Boulder, USA
Shingo Watanabe	Japan Agency for Marine-Earth Science and Technology (JAMSTEC), Yokohama, Japan; Advanced Institute for Marine Ecosystem Change (WPI-AIMEC), Tohoku University, Sendai, Japan
Wandi Yu	Lawrence Livermore National Laboratory (Research prepared under Contract DE-AC52-07NA27344), USA
Jun Zhang	NSF National Center for Atmospheric Research (NCAR), USA

Reviewer editor

Amanda C. Maycock	School of Earth and Environment, University of Leeds, UK

Supplementary I, II, III and V: HTHH-MOC, Observations and Tonga-MIP

First authors

Yunqian Zhu	University of Colorado Boulder, Cooperative Institute for Research in Environmental Science (CIRES) at NOAA Chemical Sciences Laboratory, USA
William Randel	NSF National Center for Atmospheric Research (NCAR), USA
Valentina Aquila	Department of Environmental Science, American University, Washington DC, USA

Zhihong Zhuo	Department of Earth and Atmospheric Sciences, University of Quebec in Montreal, Montreal (Quebec), Canada
Ewa M. Bednarz	University of Colorado Boulder, Cooperative Institute for Research in Environmental Science (CIRES) at NOAA Chemical Sciences Laboratory, USA
Ilaria Quaglia	NSF National Center for Atmospheric Research (NCAR), USA
Wandi Yu	Lawrence Livermore National Laboratory (Research prepared under Contract DE-AC52-07NA27344), USA
Margot Clyne	Laboratory for Atmospheric and Space Physics, University of Colorado Boulder, USA; Department of Atmospheric Science, Colorado State University, Fort Collins, CO, USA
Owen Brian Toon	University of Colorado Boulder, USA

Contributing authors

Hideharu Akiyoshi	National Institute for Environmental Studies (NIES), Tsukuba, Japan
Valentina Aquila	Department of Environmental Science, American University, Washington DC, USA
Elizabeth Asher	University of Colorado Boulder, Cooperative Institute for Research in Environmental Science (CIRES) at NOAA Global Monitoring Laboratory, USA
Slimane Bekki	Laboratoire Atmosphère Observations Spatiales (LATMOS), IPSL, Sorbonne University, UVSQ, France
Adam Bourassa	University of Saskatchewan, Canada
Ewa M. Bednarz	University of Colorado Boulder, Cooperative Institute for Research in Environmental Science (CIRES) at NOAA Chemical Sciences Laboratory, USA
Christoph Brühl	Max Planck Institute for Chemistry, Mainz, Germany
Amy H. Butler	National Oceanic and Atmospheric Administration (NOAA) Chemical Sciences Laboratory, USA
Parker Case	Earth System Science Interdisciplinary Center, University of Maryland, College Park, MD, USA
Simon Chabrillat	Royal Belgian Institute for Space Aeronomy (BIRA-IASB), Belgium
Gabriel Chiodo	ETH Zurich, Switzerland; Instituto de Geociencias, Spanish National Research Council (IGEO-CSIC-UCM), Spain
Margot Clyne	Laboratory for Atmospheric and Space Physics, University of Colorado Boulder, USA; Department of Atmospheric Science, Colorado State University, Fort Collins, CO, USA
Peter R. Colarco	NASA Goddard Space Flight Center, Greenbelt, MD, USA
Sandip Dhomse	School of Earth and Environment, University of Leeds, Leeds, UK National Centre for Earth Observation, University of Leeds, Leeds, UK National Centre for Atmospheric Science, University of Leeds, Leeds, UK
Lola Falletti	Laboratoire Atmosphère Observations Spatiales (LATMOS), IPSL, Sorbonne University, UVSQ, France
Eric Fleming	NASA Goddard Space Flight Center, USA; Science Systems and Applications, Inc. (SSAI), USA
Ben Johnson	Met Office Hadley Centre, Exeter, UK
Andrin Jörimann	ETH Zurich, Switzerland; Instituto de Geociencias, Spanish National Research Council (IGEO-CSIC-UCM), Spain; Physikalisch-Meteorologisches Observatorium Davos and World Radiation Center, Switzerland
Mahesh Kovilakam	NASA Langley Research Center, VA, USA
Gerbrand Koren	Utrecht University, Netherlands
Ales Kuchar	BOKU University, Vienna, Austria
Paul J. Kushner	Department of Physics, University of Toronto, Canada

Nicolas Lebas	LOCEAN/IPSL, Sorbonne Université, CNRS, IRD, MNHN, Paris, France
Qing Liang	NASA Goddard Space Flight Center, USA
Nathaniel Livesey	Jet Propulsion Laboratory (JPL), California Institute of Technology, USA
Cheng-Cheng Liu	Laboratory for Atmospheric and Space Physics, University of Colorado Boulder, Boulder, CO, USA
Graham Mann	School of Earth and Environment, University of Leeds, Leeds, UK National Centre for Atmospheric Science, University of Leeds, Leeds, UK
Michael Manyin	NASA Goddard Space Flight Center, USA; Science Systems and Applications, Inc., USA
Marion Marchand	LATMOS - Laboratoire Atmosphère Observations Spatiales, UVSQ, CNRS, Sorbonne University, Guyancourt, France
Olaf Morgenstern	Deutscher Wetterdienst (DWD), Offenbach, Germany; University of Canterbury, Christchurch, New Zealand
Tatsuya Nagashima	National Institute for Environmental Studies (NIES), Tsukuba, Japan
Paul A. Newman	University of Maryland Baltimore County at NASA Goddard Space Flight Center, USA
Luke D. Oman	NASA Goddard Space Flight Center, USA
Freja F. Østerstrøm	Department of Environmental Science, Aarhus University, Denmark Harvard John A. Paulson School of Engineering and Applied Sciences, Harvard University, USA
Francesco S. R. Pausata	Department of Earth and Atmospheric Sciences, University of Quebec in Montreal, Montreal (Quebec), Canada
Yifeng Peng	College of Atmospheric Science, Lanzhou University, Lanzhou, China
David Plummer	Climate Research Division, Environment and Climate Change Canada, Canada
William Randel	NSF National Center for Atmospheric Research (NCAR), Boulder, CO, USA
Samuel Rémy	HYGEOS, Lille, France
Mark R. Schoeberl	Science and Technology Corporation, Columbia, MD, USA
Takashi Sekiya	Japan Agency for Marine-Earth Science and Technology (JAMSTEC), Yokohama, Japan
Stephen Steenrod	University of Maryland-Baltimore County, USA
Georgiy Stenchikov	King Abdullah University of Science and Technology, Saudi Arabia
Kengo Sudo	Japan Agency for Marine-Earth Science and Technology (JAMSTEC), Yokohama, Japan; Graduate School of Environmental Studies, Nagoya University, Nagoya, Japan
Timofei Sukhodolov	Physikalisch-Meteorologisches Observatorium Davos and World Radiation Center, Davos, Switzerland
Simone Tilmes	NSF National Center for Atmospheric Research (NCAR), USA
Kostas Tsigaridis	Columbia University, USA; NASA Goddard Institute for Space Studies, USA
Matthew Toohey	University of Saskatchewan, Canada
Rei Ueyama	NASA Ames Research Center, USA
Daniele Visioni	Cornell University, USA
Xinyue Wang	Department of Atmospheric and Oceanic Sciences, University of Colorado Boulder, Boulder, USA
Shingo Watanabe	Japan Agency for Marine-Earth Science and Technology (JAMSTEC), Yokohama, Japan; Advanced Institute for Marine Ecosystem Change (WPI-AIMEC), Tohoku University, Sendai, Japan
Yousuke Yamashita	National Institute for Environmental Studies (NIES), Tsukuba, Japan
Pengfei Yu	College of Environment and Climate, Jinan University, Guangzhou, China
Wandi Yu	Lawrence Livermore National Laboratory (Research prepared under Contract DE-AC52-07NA27344), USA
Jia Yue	NASA Goddard Space Flight Center, USA

Jun Zhang	NSF National Center for Atmospheric Research (NCAR), USA
Yunqian Zhu	University of Colorado Boulder, Cooperative Institute for Research in Environmental Science (CIRES) at NOAA Chemical Sciences Laboratory, USA
Zhihong Zhuo	Department of Earth and Atmospheric Sciences, University of Quebec in Montreal, Montreal (Quebec), Canada

Reviewers

Slimane Bekki	Laboratoire Atmosphère Observations Spatiales (LATMOS), IPSL, Sorbonne University, UVSQ, France
Amy H. Butler	National Oceanic and Atmospheric Administration (NOAA) Chemical Sciences Laboratory, USA
Martina Bramberger	NSF National Center for Atmospheric Research (NCAR), USA
Natalia Calvo	Departamento Física de la Tierra y Astrofísica (Earth Physics and Astrophysics), Facultad Ciencias Físicas, Universidad Complutense de Madrid, Spain
Parker Case	University of Maryland College Park; NASA Goddard Space Flight Center, USA
Gabriel Chiodo	ETH Zurich, Switzerland; Instituto de Geociencias, Spanish National Research Council (IGEO-CSIC-UCM), Madrid, Spain
Margot Clyne	Department of Atmospheric Science, Colorado State University, USA
Peter R. Colarco	NASA Goddard Space Flight Center, USA
Mohamadou A. Diallo	Institute of Climate and Energy Systems – Stratosphere (ICE-4), Forschungszentrum Jülich, Germany
Alexa Van Eaton	U.S. Geological Survey, USA
Hella Garny	Institut für Physik der Atmosphäre, Deutsches Zentrum für Luft und Raumfahrt (DLR), Germany
Edwin P. Gerber	Courant Institute of Mathematical Sciences, New York University, USA
Sophie Godin-Beekmann	LATMOS-IPSL, CNRS, France
Pavel Inchin	Computational Physics, Inc., USA
Eric Jensen	University of Colorado Boulder, Cooperative Institute for Research in Environmental Science (CIRES) at NOAA Chemical Sciences Laboratory, USA
Manoj M. Joshi	Climatic Research Unit, School of Environmental Sciences, University of East Anglia, UK
James Keeble	Lancaster Environment Centre, Lancaster University, Lancaster, UK
Eun-Pa Lim	The Bureau of Meteorology, Australia
Graham Mann	School of Earth and Environment, University of Leeds, Leeds, UK National Centre for Atmospheric Science, University of Leeds, Leeds, UK
Zachary McGraw	Columbia University, USA; NASA Goddard Institute for Space Studies, USA
Stergios Misios	Academy of Athens, Greece
Paul A. Newman	University of Maryland Baltimore County at NASA Goddard Space Flight Center, USA
Shigenori Otsuka	RIKEN, Japan
Felix Plöger	Institute of Climate and Energy Systems, Stratosphere (ICE-4), Research Centre Jülich, Wilhelm-Johnen-Strasse, Jülich, Germany
Facundo L. Poblet	Leibniz Institute of Atmospheric Physics at the University of Rostock, Germany
Andrew Prata	Commonwealth Scientific and Industrial Research Organisation (CSIRO), Australia
Karen H. Rosenlof	National Oceanic and Atmospheric Administration (NOAA) Chemical Sciences Laboratory, USA
William Randel	NSF National Center for Atmospheric Research (NCAR), USA
Christian von Savigny	University of Greifswald, Germany
Atsuki Shinbori	Institute for Space-Earth Environmental Research, Nagoya University, Japan

Keith P. Shine	Department of Meteorology, University of Reading, UK
Kane Stone	Department of Earth, Atmospheric and Planetary Sciences, Massachusetts Institute of Technology, USA
Isabelle A. Taylor	Atmospheric, Oceanic and Planetary Physics (AOPP), University of Oxford, UK
Simone Tilmes	NSF National Center for Atmospheric Research (NCAR), USA
Davide Zanchettin	Department of Environmental Sciences, Informatics and Statistics, University Ca' Foscari of Venice, Italy
Yunqian Zhu	University of Colorado Boulder, Cooperative Institute for Research in Environmental Science (CIRES) at NOAA Chemical Sciences Laboratory, USA

Editorial team, admin and technical support

Ines Tritscher	APARC International Project Office, Forschungszentrum Jülich, Germany
Lars Hoffmann	APARC International Project Office, Forschungszentrum Jülich, Germany
Rolf Müller	APARC International Project Office, Forschungszentrum Jülich, Germany
Olaf Stein	APARC International Project Office, Forschungszentrum Jülich, Germany
Catherine Burgdorf Rasco	University of Colorado Boulder, Cooperative Institute for Research in Environmental Science (CIRES) at NOAA Chemical Sciences Laboratory, USA

Final author meeting
Executive summary and Highlights
Boulder, Colorado, USA — 12–14 June 2025

Yunqian Zhu	University of Colorado Boulder, Cooperative Institute for Research in Environmental Science (CIRES) at NOAA Chemical Sciences Laboratory, USA
Graham Mann	School of Earth and Environment, University of Leeds, Leeds, UK National Centre for Atmospheric Science, University of Leeds, Leeds, UK
Paul A. Newman	NASA Goddard Space Flight Center, USA; University of Maryland Baltimore County, USA
William Randel	NSF National Center for Atmospheric Research (NCAR), USA
Valentina Aquila	Department of Environmental Science, American University, Washington DC, USA
Elizabeth Asher	University of Colorado Boulder, Cooperative Institute for Research in Environmental Sciences (CIRES) at NOAA Global Monitoring Laboratory, USA
Thomas J. Aubry	Department of Earth Sciences, University of Oxford, UK
Ewa M. Bednarz	University of Colorado Boulder, Cooperative Institute for Research in Environmental Science (CIRES) at NOAA Chemical Sciences Laboratory, USA
Adam Bourassa	University of Saskatchewan, Canada
Martina Bramberger	NSF National Center for Atmospheric Research (NCAR), USA
Amy H. Butler	National Oceanic and Atmospheric Administration (NOAA) Chemical Sciences Laboratory, USA
Simon Carn	Michigan Technological University, USA
Margot Clyne	Laboratory for Atmospheric and Space Physics, University of Colorado Boulder, USA; Department of Atmospheric Science, Colorado State University, Fort Collins, CO, USA
Lawrence Coy	Science Systems and Applications, Inc. (SSAI) at NASA Goddard Space Flight Center, USA
Edwin P. Gerber	Courant Institute of Mathematical Sciences, New York University, USA
Pavel Inchin	Computational Physics, Inc., USA
Alexey Yu. Karpechko	Finnish Meteorological Institute, Finland
Sergey Khaykin	Laboratoire Atmosphère Observations Spatiales, Institut Pierre-Simon-Laplace (LATMOS-IPSL), France

Bernard Legras	Laboratoire de Météorologie Dynamique, Institut Pierre-Simon-Laplace (LMD-IPSL), France
Hanli Liu	NSF National Center for Atmospheric Research (NCAR), USA
Amanda C. Maycock	School of Earth and Environment, University of Leeds, UK
Olaf Morgenstern	Deutscher Wetterdienst (DWD), Offenbach, Germany; University of Canterbury, Christchurch, New Zealand
Freja F. Østerstrøm	Department of Environmental Science, Aarhus University, Denmark Harvard John A. Paulson School of Engineering and Applied Sciences, Harvard University, USA
Ilaria Quaglia	NSF National Center for Atmospheric Research (NCAR), USA
Karen H. Rosenlof	National Oceanic and Atmospheric Administration (NOAA) Chemical Sciences Laboratory, USA
Michelle L. Santee	Jet Propulsion Laboratory (JPL), California Institute of Technology, USA
Mark R. Schoeberl	Science and Technology Corporation (STC), Columbia, Maryland, USA
Georgiy Stenchikov	King Abdullah University of Science and Technology, Saudi Arabia
Kane Stone	Department of Earth, Atmospheric and Planetary Sciences, Massachusetts Institute of Technology, USA
Ghassan Taha	NASA Goddard Space Flight Center, USA
Chelsea R. Thompson	National Oceanic and Atmospheric Administration (NOAA) Chemical Sciences Laboratory, USA
Owen Brian Toon	University of Colorado Boulder, USA
Kostas Tsigaridis	Columbia University, USA; NASA Goddard Institute for Space Studies, USA
Xinyue Wang	Department of Atmospheric and Oceanic Sciences, University of Colorado Boulder, USA
Krzysztof Wargan	Science Systems and Applications, Inc. (SSAI) at NASA Goddard Space Flight Center, USA
David M. Wilmouth	Harvard John A. Paulson School of Engineering and Applied Sciences, Harvard University, USA
Corwin J. Wright	University of Bath, UK
Wandi Yu	Lawrence Livermore National Laboratory (Research prepared under Contract DE-AC52-07NA27344), USA
Jia Yue	NASA Goddard Space Flight Center, USA
Zhihong Zhuo	Department of Earth and Atmospheric Sciences, University of Quebec in Montreal, Montreal (Quebec), Canada

Participating countries

Australia, Austria, Belgium, Canada, China, Denmark, Finland, France, Germany, Greece, Italy, Japan, Netherlands, New Zealand, Norway, Russia, Saudi Arabia, Spain, Switzerland, United Kingdom, United States

Front cover figure origin

Chelsea R. Thompson	National Oceanic and Atmospheric Administration (NOAA) Chemical Sciences Laboratory, USA

Imagery is from the US government NOAA Advanced Baseline Imager on the GOES-17 satellite.
`https://www.goes-r.gov`

Back cover figure origin

Yunqian Zhu	University of Colorado Boulder, Cooperative Institute for Research in Environmental Science (CIRES) at NOAA Chemical Sciences Laboratory, USA

Acknowledgements

We acknowledge the scientific coordination and sponsorship of the World Climate Research Programme (WCRP), within the framework of the WCRP activity Atmospheric Processes And their Role in Climate (APARC). We thank the APARC co-chairs Amanda Maycock, Karen Rosenlof, Seok-Woo Son and Olaf Morgenstern, for their guidance and advice during the proposal phase of the project, and their continuing support through the Hunga cross-activity project. We are grateful to the chapter lead authors, co- and contributing authors and review editors (over 150 scientists) for their leadership, and for generously giving their time for the volunteer roles.

We acknowledge the key role satellite observational programs funded by US, European, Canadian, Japanese, and other atmospheric and space science agencies played, enabling global monitoring of the evolving Hunga volcanic cloud. In particular, the MLS instrument on the Aura satellite, the SAGE-III instrument on the International Space Station, and many others (e.g., ACE-FTS, OMPS, OSIRIS, MISR, MODIS, GPS-RO, DSCOVR/EPIC, N20/NPP NM), provided benchmark measurement datasets for the Hunga-excess water vapour and volcanic aerosol in the stratosphere. We note Hunga is the first time lidar measurements from satellite have monitored a deep-stratosphere injecting volcanic eruption cloud. And we acknowledge the joint public investment from NASA and the French space agency (CNES) that enabled this, to measure the vertical structure of the full extent of the dispersing Hunga volcanic cloud, from the CALIOP lidar on the CALIPSO satellite.

In the initial hours and days after the Hunga eruption, the geostationary GOES and Himawari satellite instruments measured the atmospheric waves and properties of the umbrella cloud of ice, ash and sulfate aerosol, these capabilities funded by NOAA and NASA, and the Japanese meteorological agency (JMA) respectively. A key element of the early-phase post-eruption satellite monitoring of such an explosive event requires quantifying the sulfur released to the stratosphere, for potential climate and ozone impacts. In this regard, the Aura, Sentinel-5 and MetOp-B satellite hosting the OMI, TROPOMI and IASI instruments, were key to establishing a reliable consensus on the emitted sulfur.

We acknowledge also the value of in-situ measurements and ground-based remote sensing networks (e.g. TAC/BUFR radiosonde, NDACC, NOAA B2SAP, AERONET, WMO GAW, GNSS, and other ground-based balloon and lidar systems hosted by different countries) in providing ground-truth information to validate satellite assessments and to ensure reliable model predictions. We are grateful for the international collaborations that led to two field campaigns specifically to measure the progressing global dispersion of the Hunga cloud: the balloon and lidar monitoring in the TR2Ex rapid response campaign from Reunion Island, and the BraVo field campaigns from Sao Paulo. We recognise also the value of prior co-ordination via the NASA VolRes coordination activity to prepare for future major eruption (see Carn et al., 2021).

We acknowledge also the investment leading to the long-term record of air temperatures in the stratosphere from the SSU (1978-2006) and AMSU (2001-present) sounders on the NOAA series of satellites. The long-term records provide important datasets to understand the opposite-sign post-volcanic cooling of the stratosphere after Hunga, compared to the warming after El Chichón and Pinatubo (see Figure ES-3). We also acknowledge other valuable atmospheric data for monitoring the gravity wave propagation into the upper atmosphere, and the atmospheric waves and ionospheric perturbations from the initial Hunga explosions.

This report has aligned closely with two of APARC's activities, the Stratospheric Sulfur and its Role in Climate (SSiRC) and Chemistry Climate Model Initiative (CCMI). We thank the support of University of Leeds and Ecole Normale Superieure, Paris, for hosting the Hunga activity open science workshops in 2022 and 2024, and NSF NCAR Boulder for hosting the Hunga assessment meeting in 2025. Funding from NASA and APARC provided travel support for early career and scientists from the global south to attend the meetings in person.

We thank the reanalysis centres for providing their support and data products, key input datasets for the HTHH-MOC co-ordinated modelling and other analysis. We acknowledge all the participating models (detailed in Supplementary S1, S4 and S5). In particular, we are grateful to the UK Centre for Environmental Data Analysis (CEDA) for hosting the group workspace for the Hunga modelling activities, within the UK collaborative Joint Analysis System Meeting Infrastructure Needs system (JASMIN, Lawrence et al., 2012). We also thank the APARC International Project Office at Forschungszentrum Jülich (Rolf Müller, Ines Tritscher, Lars Hoffmann and Olaf Stein), for their support, and in particular for organising the typesetting and printing of the report.

Contents

Highlights xxi

Executive summary xxiii

Preface xxxi

1 Volcanological context of the 2022 Hunga eruption 1
1.1 Introduction to submarine volcanism and Hunga volcano . . . 5
1.1.1 Submarine volcanism and submarine eruptions . . . 5
1.1.2 Introduction to the Tonga (Tofua) arc . . . 7
1.1.3 Physical description of Hunga volcano . . . 8
1.1.4 Historic activity of Hunga volcano . . . 9
1.2 The 2022 Hunga eruption . . . 9
1.2.1 Short-term precursors to the 2022 Hunga eruption . . . 9
1.2.2 Description and timeline of the 15 January 2022 Hunga eruption . . . 11
1.2.3 Eruption magnitude assessment . . . 13
1.2.4 Response to the 2022 Hunga eruption . . . 17
1.3 The 2022 Hunga eruption in the context of other historic eruptions . . . 19
1.3.1 Comparison with the 1883 Krakatau eruption . . . 19
1.3.2 Summary of recent eruptions and large wildfires with radiative impacts . . . 22
1.4 Summary and conclusions . . . 24

2 The 2022 Hunga plume – first month post-eruption 35
2.1 Initial eruption sequence . . . 38
2.2 Volcano-generated GW (and Lamb waves) . . . 39
2.2.1 Types of waves and early observations . . . 40
2.2.2 Wave generation mechanisms, and what we can learn from the waves . . . 41
2.3 Water vapour injection . . . 42
2.4 Plume altitude and dispersion during the first month . . . 44
2.5 Rapid formation of sulfate aerosol layer . . . 47
2.6 Microphysical and optical aerosol properties . . . 49
2.7 Other plume chemical composition: minor injections of gas phase compounds and primary aerosols . . . 51
2.7.1 Halogens . . . 51
2.7.2 Lightning nitrogen oxide (NO) . . . 52
2.7.3 Ash and sea salt . . . 52
2.7.4 Ozone anomalies and the role of tropospheric transport . . . 52
2.8 Sources of uncertainty . . . 52
2.9 The value of observations . . . 53

3 Atmospheric transport and evolution of Hunga water vapour and aerosols 61
3.1 Meridional dispersion of water vapour and aerosol . . . 65
3.2 Evolution of sulfate aerosols . . . 68
3.2.1 Aerosol growth and changes in the size distribution . . . 68
3.2.2 Sedimentation of aerosol particles . . . 69
3.2.3 Hunga aerosol in the long-term record . . . 70

3.3 Transport of volcanic material into the polar regions . . . 71
3.3.1 Water vapour . . . 71
3.3.2 Aerosol . . . 72
3.4 Uncertainty of observations . . . 74
3.4.1 Aerosol optical depth and extinction . . . 74
3.4.2 Water vapour . . . 77
3.5 Modelling of the Hunga plume evolution . . . 78
3.5.1 Meridional dispersion of the volcanic aerosol and water vapour . . . 78
3.5.2 Vertical separation of the volcanic aerosol and water vapour and evolution of the aerosol radius . . . 80
3.5.3 Longevity and decay of the water-vapour and aerosol perturbations . . . 82
3.5.4 Summary of model performances . . . 83

4 Hunga effects on stratospheric temperatures and circulation 89
4.1 The large-scale evolution of the Hunga H_2O cloud . . . 92
4.2 Stratospheric transport, temperatures and zonal winds . . . 92
4.2.1 Observations of temperature anomalies following the eruption of Hunga . . . 92
4.2.2 Assimilated temperature and wind anomalies following the Hunga eruption . . . 94
4.2.3 Hunga induced temperature and circulation anomalies in models . . . 96
4.3 Residual mean meridional circulation and Eliassen-Palm flux . . . 98
4.3.1 Residual mean meridional circulation and EP flux in the global data assimilation systems 98
4.3.2 Residual mean circulation and EP flux changes in models . . . 99
4.4 Interaction of Hunga with the Quasi-Biennial Oscillation (QBO) . . . 101
4.5 Summary . . . 102

5 Effects of the Hunga eruption on stratospheric ozone and related trace gases 107
5.1 Overview of Hunga effects on total column ozone . . . 112
5.2 Initial chemical processing and ozone loss in the fresh plume . . . 112
5.3 Longer-term impacts on stratospheric composition . . . 116
5.3.1 Midlatitudes . . . 116
5.3.2 Tropics . . . 121
5.3.3 Antarctic winters/springs of 2022, 2023, and 2024 . . . 124
5.3.4 Arctic winters/springs of 2021/2022, 2022/2023, and 2023/2024 . . . 131
5.4 Predictions of the future impacts on the stratospheric ozone layer . . . 132
5.4.1 Future evolution of stratospheric water vapour . . . 132
5.4.2 Future Hunga-related changes in stratospheric composition . . . 133

6 Upper stratosphere to thermosphere effects and H_2O transport in the deep Brewer-Dobson branch 137
6.1 Introduction . . . 140
6.2 Short-term dynamical impacts on the middle atmosphere . . . 140
6.2.1 Stratosphere and mesosphere . . . 140
6.2.2 Impacts on the thermosphere . . . 142
6.3 Impacts on the ionosphere . . . 143
6.4 Water vapour transport in the middle and upper atmosphere . . . 144
6.5 Modelling of long-term middle-atmospheric impacts . . . 145
6.5.1 Overview . . . 145
6.5.2 Water vapour plume in the mesosphere . . . 145
6.5.3 Mesospheric cooling in 2023 . . . 147
6.5.4 Mesospheric circulation and temperature response in 2022 . . . 148
6.6 Summary . . . 149

7 Radiative forcing and climate impacts caused by the 2022 Hunga volcano eruption 157
7.1 Mechanisms of volcanic climate impacts . . . 160
7.1.1 Impacts of volcanic sulfate aerosols . . . 160
7.1.2 Impact of volcanic water vapour . . . 161
7.1.3 Stratospheric chemistry and dynamics feedbacks . . . 161
7.1.4 The 2022 Hunga eruption . . . 161
7.2 Hunga's radiative forcing agents . . . 162
7.2.1 Hunga's sulfate aerosol perturbation . . . 162
7.2.2 Hunga's water vapour perturbation . . . 163
7.2.3 Hunga's ozone perturbation . . . 164
7.3 Hunga's radiative forcing . . . 164
7.3.1 IRF, ERF, and SARF . . . 164
7.3.2 Clear sky and all sky RF . . . 165
7.3.3 Hunga's sulfate aerosol and water vapour IRF . . . 166
7.3.4 Empirically calculated ERF . . . 167
7.3.5 Model calculated ERF . . . 167
7.3.6 Uncertainty in radiative forcing . . . 170
7.4 Hunga's climate impact . . . 171
7.4.1 SA-dominated climate response (2022-2023) . . . 171
7.4.2 WV-dominated climate response (2024-2030) . . . 173
7.4.3 Indirect atmospheric effects . . . 174
7.4.4 Uncertainties in climate response . . . 176
7.5 Discussion and conclusions . . . 176

Appendices 193

Acronym dictionary 193

Chemical acronyms 199

Supplements 203

S1 HTHH-MOC: experiment protocol and model description 203
S1.1 Introduction and motivations of this project . . . 204
S1.2 Experiment design . . . 205
S1.3 Model output . . . 207
S1.4 Model descriptions and the Hunga volcanic injection specification . . . 209
S1.5 Preliminary results . . . 221
S1.6 Summary . . . 221

S2 Hunga impacts report observational data supplement 231
S2.1 Satellite remote sensing data . . . 232
S2.2 Ground-based and balloon measurements . . . 239

S3 HTHH-MOC model validation and analysis results 253
S3.1 Evolution of water and aerosol plumes (Exp2) . . . 253
S3.2 Hunga plumes evolution and stratospheric responses (based on EXP1 10-year output analysis) 260
S3.2.1 Stratospheric aerosol optical depth (SAOD) anomaly . . . 261
S3.2.2 Water vapour variation . . . 261
S3.2.3 Global-mean air temperature evolution . . . 263
S3.2.4 Global-mean ozone variation . . . 264

S3.2.5 Summary and conclusions . . . 265
S3.3 Hunga impact on radiative forcing . . . 270
S3.4 Indirect climate impacts of the Hunga eruption . . . 275
S3.4.1 Simulated changes in near-surface air temperatures following the eruption . . . 276
S3.4.2 Seasonal changes in the NH polar vortex and impacts on the extratropical surface climate 279
S3.4.3 Seasonal changes in the SH polar vortex and impacts on the extratropical surface climate 283
S3.5 Upper stratosphere to thermosphere effects and H_2O transport in the deep Brewer–Dobson branch: modelling of long-term middle-atmospheric impacts . . . 286
S3.6 Simulated effects on total column ozone and halogen repartitioning in the Southern Hemisphere lower stratosphere . . . 289

S4 Other chapter supplementaries 295
S4.1 Stratospheric anomalies following the Hunga eruption for Chapter 4 . . . 296
S4.2 Models used in Chapter 5 but not included in HTHH-MOC or Tonga-MIP . . . 297
S4.2.1 ATLAS . . . 297
S4.2.2 SOCOL-AERv2-Volc . . . 297
S4.2.3 TOMCAT . . . 297

S5 Tonga-MIP: experiment protocol, model descriptions and result preview 301
S5.1 Experiment protocol and model descriptions . . . 302
S5.2 Result preview . . . 302

Overall references 309

Highlights

- **The 15th January 2022 eruption of Hunga volcano was a high-magnitude (Volcanic Explosivity Index 6) submarine explosive eruption unique in the era of satellite observations.** The shallow underwater setting led to interaction of volcanic magma and seawater, making this event distinct from large subaerial eruptions of recent decades (e.g., Mt. Pinatubo in 1991). The Hunga eruption increased the global stratospheric water burden by ~10%, and most of this water vapour remains in the stratosphere through 2025. The shallow underwater setting removed most of the volcanic sulfur released, and a modest amount of sulfur dioxide (SO_2, 0.5–1 Tg) was transported into the stratosphere.

- **Hunga water vapour led to a cooling of 0.5–1 K in the global mid-to-upper stratosphere over the first two years after the eruption and $>$ 1 K in the mesosphere afterwards.** This contrasts with previous major volcanic eruptions where aerosols led to stratospheric warming.

- **In the months following the eruption, substantial perturbations in stratospheric ozone and related trace gases were observed throughout the Southern Hemisphere.** The changes in 2022, while partly driven by anomalous heterogeneous chemistry on volcanic aerosol, were dominated by transport. The extent to which transport anomalies were causally connected to the eruption is not clear. Low ozone abundances observed in the SH midlatitude lower stratosphere had minor impacts on total column ozone.

- **The Hunga eruption had no significant impact on the Antarctic ozone hole or ozone in the Arctic stratosphere.**

- **The record-high global surface temperatures in 2023/2024 were not due to the Hunga eruption.** The Hunga global-mean tropopause radiative forcing was about -0.4 W m^{-2} averaged over the first two years; this cooling was mainly caused by aerosol attenuation of solar radiation. The maximum Hunga-induced cooling in global surface air temperature was estimated to be 0.05 K (with about 50% uncertainty), but this cooling is indistinguishable from background variability in the current climate. Surface climate impacts of the eruption—driven either directly by radiation or indirectly by Hunga-induced changes in atmospheric circulation and stratosphere–troposphere coupling—are relatively small and not distinguishable from the background internal variability of the Earth system.

- **After 2024, the Hunga aerosol loading largely disappeared. The remaining Hunga stratospheric water vapour positive radiative forcing is expected to be negligible.**

- **The Hunga eruption and its aftermath provided a unique opportunity to assess the impacts of a water-rich volcanic eruption, where sulfate aerosol formed unusually fast.**

- **Global chemistry–climate models consistently reproduce key aspects of the observed middle-atmospheric transport, temperature change, and mesospheric ozone response after the Hunga eruption.** Models are critical tools to elucidate the detailed chemical, radiative, and dynamical impacts on the Earth system from volcanic events, especially in the context of interannual variability. Models differ in their simulations of Hunga aerosol microphysical properties, indicating that simulating aerosol microphysics remains a challenge for model development.

- **Comprehensive observations of the Hunga eruption and its aftermath were produced by satellites, balloons, and ground observation networks developed over the last few decades by many countries.** These observations were critical for understanding the Hunga atmospheric impacts. Geostationary satellite measurements yielded minute-by-minute observations of the eruption cloud evolution and spread. The NASA Aura Microwave Limb Sounder (MLS) provided global observations of the high water vapour from Hunga. Additional observations from MLS and NASA/NOAA ozone instruments characterised stratospheric chemistry changes following the eruption. Observations from the Stratospheric Aerosol and Gas Experiment III on the International Space Station, the joint NASA/CNES Cloud-Aerosol Lidar with Orthogonal Polarization, and NOAA/NASA Ozone Mapping and Profiler Suite documented the evolution of the sulfate aerosol layer. The rapid-response balloon deployment to La Réunion in the Indian Ocean within the first week after the Hunga eruption quantified early development of aerosols and sulfur dioxide in the Hunga stratospheric plume. The Network for the Detection of Atmospheric Composition Change and the AErosol RObotic NETwork of ground-based instruments provided observations of composition and aerosol spread. Other satellites and instruments, unnamed here, contributed to understanding of the Hunga impacts.
- **Loss of observational capabilities will severely hinder our ability to observe future volcanic eruptions and other stratospheric aerosol injections and to understand their impacts.** Hunga research illustrates the importance of global satellite measurements of chemical constituents, temperature, and aerosols. Gaps due to asset cancellation and lack of new instrument deployments will result in far fewer key observations (in particular, vertically resolved water vapour measurements) that were critical for understanding the Hunga impacts. Gaps could be covered with high-altitude aircraft missions to sample stratospheric plumes, expanded research-quality balloon sampling, and additional ground-based network observations.

Executive summary

Introduction

On 15 January 2022 a highly explosive eruption of the Hunga volcano occurred in the Kingdom of Tonga in the South Pacific Ocean (175°24' W, 20°33' S). The Volcanic Explosivity Index (VEI) 6 eruption originated from a shallow submarine vent, making it distinct from large subaerial eruptions of recent decades (e.g., 1982 El Chichón, 1991 Mt. Pinatubo). In particular, seawater enhanced explosivity and dampened sulfur dioxide (SO_2) emissions. The eruption was the culmination of ~1 month of precursory activity; however, the timing and size of the eruption were unexpected, partly due to the challenges of monitoring submarine volcanoes. The stratospheric hydration caused by the eruption was unprecedented in magnitude, altitude, and duration in the satellite record.

This Executive Summary reflects the current assessment of the Hunga eruption and its impact on the climate system. We report key observations of the eruption and its aftermath, as well as simulations of its impact by global chemistry-climate models. The Hunga eruption had an unprecedented impact on the stratosphere and mesosphere due to the plume height and large water content, which increased the global stratospheric water vapour burden by 10%. Most of this water has remained in the atmosphere into 2025. However, Hunga's net impact on surface climate was small compared to that of earlier large-magnitude volcanic eruptions, due to limited sulfate aerosol loading in the stratosphere and the high altitude of the water vapour injection.

The eruption and its emissions

- The paroxysmal plume appeared at around 04 UTC on 15 January 2022, with geophysical signals subsiding by approximately 15 UTC.
- Post-eruption bathymetric observations suggest that the Hunga eruption, with a VEI of 6, was similar in magnitude to the 1991 Mt. Pinatubo eruption.
- The highest plume overshoot reached 58 km altitude in the lower mesosphere. The main volcanic plume detrained at 30-35 km, with rapid descent over a few days to a layer at 26-30 km altitude.
- The umbrella cloud expanded to a diameter of 400 km within an hour and was blown westward by stratospheric winds. The Hunga ash cloud disappeared within 15 hours of forming, probably washed out by massive precipitation of ice and water, scavenging the ash.
- The Hunga eruption is estimated to have emitted ~20 Tg of SO_2, but ~95% was removed in the seawater, such that only ~0.5-1 Tg reached the stratosphere. This is at least an order of magnitude less than Mt. Pinatubo's stratospheric injection of SO_2.
- Hunga injected an exceptional amount of water into the stratosphere, causing a ~10% (~150 Tg) increase in the global stratospheric water vapour burden.
- The eruption injected very minor amounts of halogens into the stratosphere.
- The stratospheric injection of salt from seawater is subject to ongoing research. Based on all available measurements the presence of salt in the Hunga aerosol that remained in the atmosphere was likely minor.
- Hunga generated the most intense lightning (peak intensity >2,615 flashes min^{-1}) ever observed in Earth's atmosphere. However, the lightning-generated perturbations in nitrogen oxides (NO_x) and related stratospheric chemistry were not observed.

Transport of the volcanic water and aerosol cloud

- The infrared cooling due to Hunga water vapour caused the initial cloud to descend to around 23-27 km altitude by the middle of February 2022, where it resided for the following few months. (See A on Figures ES-1c and ES-1d)
- Easterly stratospheric winds moved the volcanic cloud westward; several downwind ground-based observations and a rapid response campaign successfully measured the fresh volcanic cloud in the weeks following the eruption.
- Within a month after the eruption, the volcanic cloud had spread across the tropics between 30°S and 10°N latitude. (See B on Figures ES-1a and ES-1b)
- The Hunga water vapour and aerosol were initially co-located but began to separate in altitude in the first months after the eruption as the aerosol particles grew and sedimented toward the lower stratosphere. This separation resulted in different long-term transport of the water vapour and aerosol. (compare C between Figures ES-1c and ES-1d)
- After initially covering the lower-stratospheric tropics in February 2022, both water vapour and aerosol spread into the southern midlatitudes during the austral fall (April-June 2022) as the stratospheric flow reversed from westward to eastward (See D on Figures ES-1a and ES-1b).
- Hunga water vapour had spread to the Northern Hemisphere (NH) midlatitudes about one year after the eruption in January-March 2023. (see E on Figures ES-1a and ES-1b)
- The excess water vapour remained at 20-32 km altitude until October 2022. After November 2022, the Hunga water vapour was carried upward by the tropical stratospheric circulation and reached the mesosphere by early 2023 (see F on Figure ES-1c). By mid-2023, the Hunga water vapour was meridionally well mixed across both hemispheres in the mesosphere (50-80 km).
- The water vapour reached both polar regions after the breakdown of the Southern Hemisphere (SH) and NH polar vortices in December 2022 and April 2023, respectively. Enhanced water vapour from Hunga was also observed in subsequent years and continues to persist in the stratosphere up through the present (mid-2025). See G in both hemispheres on Figure ES-1a.
- Volcanic aerosol remained mostly in the tropics and SH lower stratosphere through 2024. While the bulk of the aerosol and water vapour did not penetrate the Antarctic vortex in 2022, observations suggest that there was some aerosol transport to high southern latitudes in the lowermost stratosphere in June 2022.
- Global chemistry-climate models simulate key aspects of the southward transport and vertical separation of the volcanic aerosol from the water vapour, indicating satisfactory representation of the large-scale circulation and particle sedimentation. The cross-equatorial transport of the aerosol from the SH to the NH is underestimated. (Figure ES-2)
- Aura Microwave Limb Sounder (MLS) measurements and model simulations suggest that the excess Hunga stratospheric water vapour will persist through the end of this decade. (Figure ES-2)

Aerosol cloud evolution

- Hunga produced the largest global stratospheric aerosol optical depth (SAOD) since Mt. Pinatubo in 1991. (Figures ES-1b and ES-1d)
- The aerosol particles grew to an effective radius of 0.4 μm in the densest part of the volcanic cloud within a couple of weeks, and the size was roughly maintained through the first two years. The rapid growth occurred through fast conversion of the SO_2 to sulfate aerosol due to the high water vapour providing abundant OH for SO_2 oxidation. The aerosol sedimented gradually toward the tropopause.
- Models simulate a rapid growth in aerosol effective radius, up to 0.3-0.5 um (depending on the model), then the simulated effective radius decreases faster than is observed.
- The first significant post-Hunga SAOD perturbation, caused by the Ruang volcanic eruption in April 2024, ended the period of Hunga-driven stratospheric aerosol perturbation. (see R in Figures ES-1b and ES-1d)
- The Hunga eruption highlighted challenges in limb scattering satellite aerosol retrieval algorithms. Solar occultation measurements provide an accurate measurement, but with sparse sampling.

Impacts on stratospheric and mesospheric ozone and related constituents

- The Hunga eruption initially caused a rapid 5% reduction in ozone in the 25–29 km layer over the tropical southwestern Pacific and Indian Ocean region within the first two weeks after the eruption. The ozone loss was driven by the Hunga excess water vapour intensifying both gas-phase and heterogeneous chemistry on aerosol.
- Starting in mid-2022, heterogeneous chemical processing led to widespread perturbations in stratospheric chlorine and nitrogen partitioning of unprecedented magnitude and duration in the southern tropics and midlatitudes. Although the observed chlorine activation was exceptional for those latitudes, the chlorine radical concentration was still an order of magnitude less than that observed in a typical polar winter.
- Record-low abundances of stratospheric ozone were observed in the southern midlatitudes in the months following the eruption. However, the degree of ozone destruction due to heterogeneous chemistry on volcanic sulfate aerosol was relatively minor, and the observed ozone changes in the tropics and southern midlatitudes were largely produced by transport.
- Hunga has not substantially perturbed the Antarctic ozone hole.
  - In 2022 the Hunga water vapour was excluded from the Antarctic polar vortex by the strong transport barrier at the vortex edge, and consequently the heterogeneous chemical processing and springtime ozone loss that took place within it were unremarkable.
  - In 2023 the enhanced water vapour prompted unusually early and vertically extensive polar stratospheric cloud (PSC) formation and chlorine activation. Dehydration subsequently removed the enhanced water vapour. By August, lower stratospheric chemical processing had essentially run to completion, as is typical in the Antarctic, preventing an exceptionally severe ozone hole.
  - In 2024 the Antarctic vortex also had enhanced water vapour from Hunga, but warm and dynamically disturbed conditions led to near- or slightly above-average ozone amounts.
- Hunga has not substantially perturbed Arctic ozone abundances. The Hunga water vapour reached the Arctic in spring 2023 after the ozone loss season. Although high water vapour abundances were present inside the 2023/2024 vortex, warm and dynamically disturbed conditions were unfavorable for substantial chemical ozone loss.
- Mesospheric water vapour increased by ~3-4 Tg in 2023 via upward transport from the stratosphere. (Figsures ES-1a and ES-1c) The water vapour increases led to ~5% loss of mesospheric ozone, because of enhanced HO_x chemistry.
- Global chemistry-climate models reproduce the water vapour transport (Figures ES-2a and ES-2b) and ozone anomalies in the stratosphere and mesosphere observed by MLS. The models predict that perturbations to mesospheric water vapour will persist until at least 2026.

Middle and upper atmospheric radiative and dynamical impacts

- The Hunga eruption produced short-term gravity wave and Lamb wave responses that were unprecedented in the observational record; these perturbations traversed the globe several times and extended up to the top of the atmosphere (including the thermosphere and ionosphere).
- The Hunga water vapour led to a cooling of 0.5-1 K in the global stratosphere (50-1 hPa) through the first two years, and a 1-2 K cooling in the mesosphere after 2023. The stratospheric cooling is in contrast to the warming associated with large amounts of volcanic aerosol in other previous major volcanic eruptions. (Figure ES-3)
- Global chemistry-climate models reproduce the observed Hunga global-mean temperature perturbations throughout the middle atmosphere.
- The 2022 SH winter stratosphere was characterized by extremely low midlatitude temperatures, an unusually strengthened and equatorward-shifted upper stratospheric polar vortex, a weakened mean meridional circulation, and reduced planetary wave forcing. Model simulations suggest some aspects of these circulation anomalies may have been forced by Hunga.
- In the NH, observed stratospheric meteorological conditions following the Hunga eruption were within the range of interannual variability, and model simulations show no consistent circulation response.

- Current evidence is insufficient to say whether the Hunga eruption affected the quasi-biennial oscillation, the major source of interannual tropical stratospheric variability.

Radiative forcing and surface climate effects

- The net globally averaged top-of-atmosphere radiative forcing (TOA RF) due to the Hunga eruption is estimated to be around -0.4 Wm^{-2} over 2022-2023.
- The TOA RF due to the Hunga eruption is the result of a negative radiative forcing from the increased stratospheric aerosol loading, which is slightly offset by a small positive radiative forcing from the increased stratospheric water vapour. Changes in stratospheric ozone and mesospheric composition due to the eruption did not significantly modify the TOA RF.
- As a consequence of the negative TOA RF, the Hunga eruption is estimated to have decreased global surface air temperature by about 0.05 K during 2022-2023; due to larger interannual variability, this temperature change cannot be observed.
- The climatic influence of the Hunga eruption cannot explain the record global average surface temperature increase in 2023-2024.
- After 2024, the TOA RF due to the remaining water vapour is estimated to be negligible (TOA RF < 0.005 Wm^{-2}) and is too small to cause a significant long-term climate response.
- The Hunga-induced stratospheric temperature changes due to aerosol, water vapour, and ozone could have impacted regional surface climate through stratosphere-troposphere dynamic coupling. However, global chemistry-climate model results suggest that the impact is likely smaller than interannual variability.

Authors

Yunqian Zhu, Graham Mann, William Randel, Paul A. Newman, Valentina Aquila, Elizabeth Asher, Thomas J. Aubry, Ewa M. Bednarz, Adam Bourassa, Martina Bramberger, Amy H. Butler, Simon Carn, Margot Clyne, Lawrence Coy, Ed Gerber, Pavel Inchin, Alexey Yu. Karpechko, Sergey Khaykin, Bernard Legras, Hanli Liu, Amanda C. Maycock, Olaf Morgenstern, Freja F. Østerstrøm, Ilaria Quaglia, Karen Rosenlof, Michelle L. Santee, Mark R. Schoeberl, Georgiy Stenchikov, Kane Stone, Ghassan Taha, Chelsea Thompson, Owen B. Toon, Kostas Tsigaridis, Xinyue Wang, Krzysztof Wargan, David M. Wilmouth, Corwin J. Wright, Wandi Yu, Jia Yue, Zhihong Zhuo

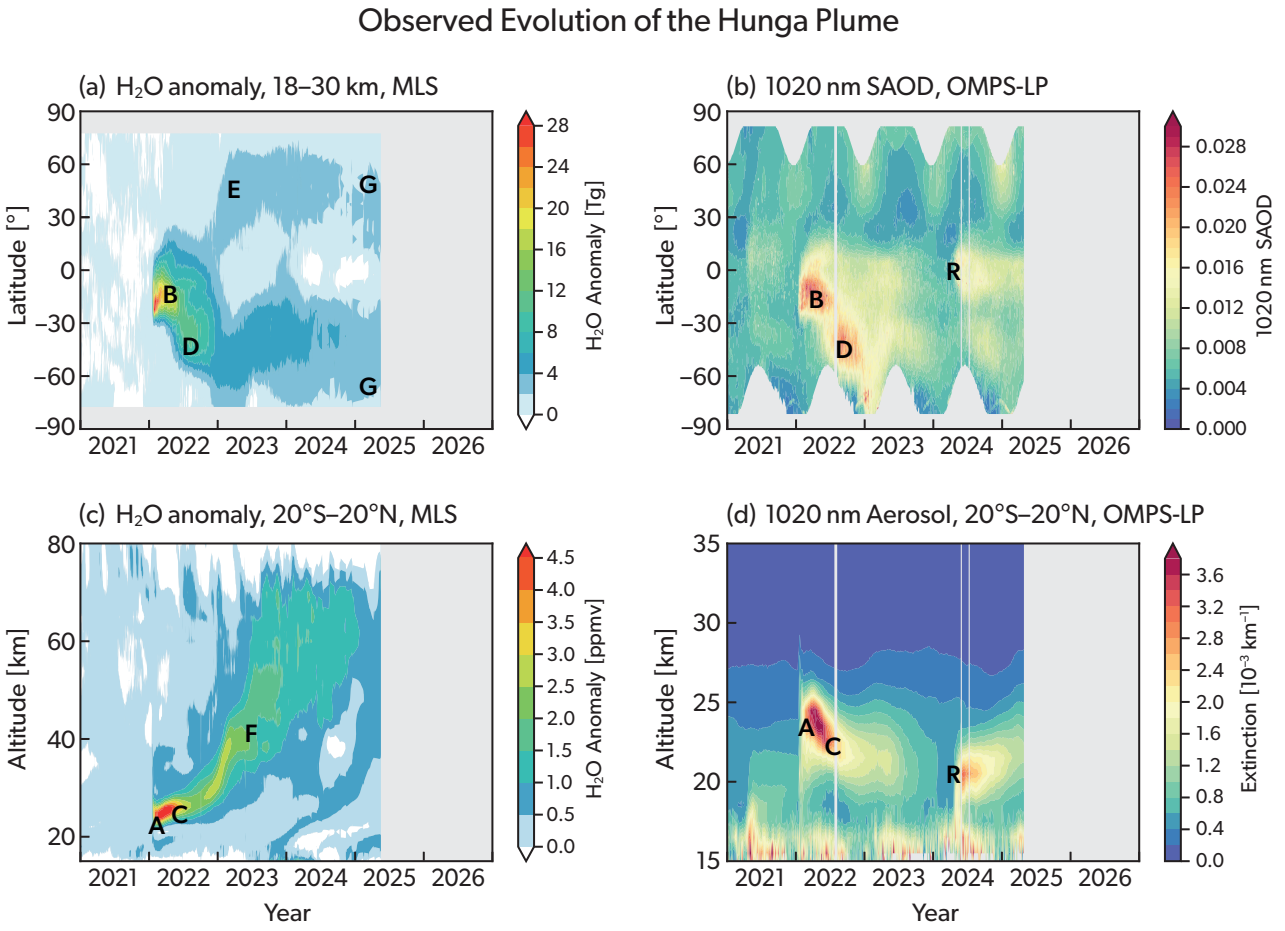

Figure ES-1: Observed evolution of the Hunga water vapour and aerosol perturbations through early 2025. *(Panel a) Water vapour anomalies (terragrams compared to background) in the lower-middle stratosphere as a function of latitude, and (Panel c) water vapour anomalies (parts per million by volume) over 20° N-S as a function of altitude. (Panel b) Stratospheric aerosol optical depth (SAOD) at 1020 nm as a function of latitude, and (Panel d) 1020 nm aerosol extinction over 20° N-S as a function of altitude; note the vertical axis only covers 15-35 km, as the aerosols did not extend above the lower stratosphere. Capital letters on the individual panels refer to specific features discussed in the Executive Summary: A = initial Hunga cloud, B = latitudinal spread over 30° S to 10° N, C = separation of water and aerosol clouds, D = transport to southern hemisphere mid-latitudes, E = water vapour transport to northern hemisphere, F = water vapour transport to mesosphere, G = persistence of water vapour anomalies in both hemispheres, R = eruption of Ruang volcano in April 2024.*

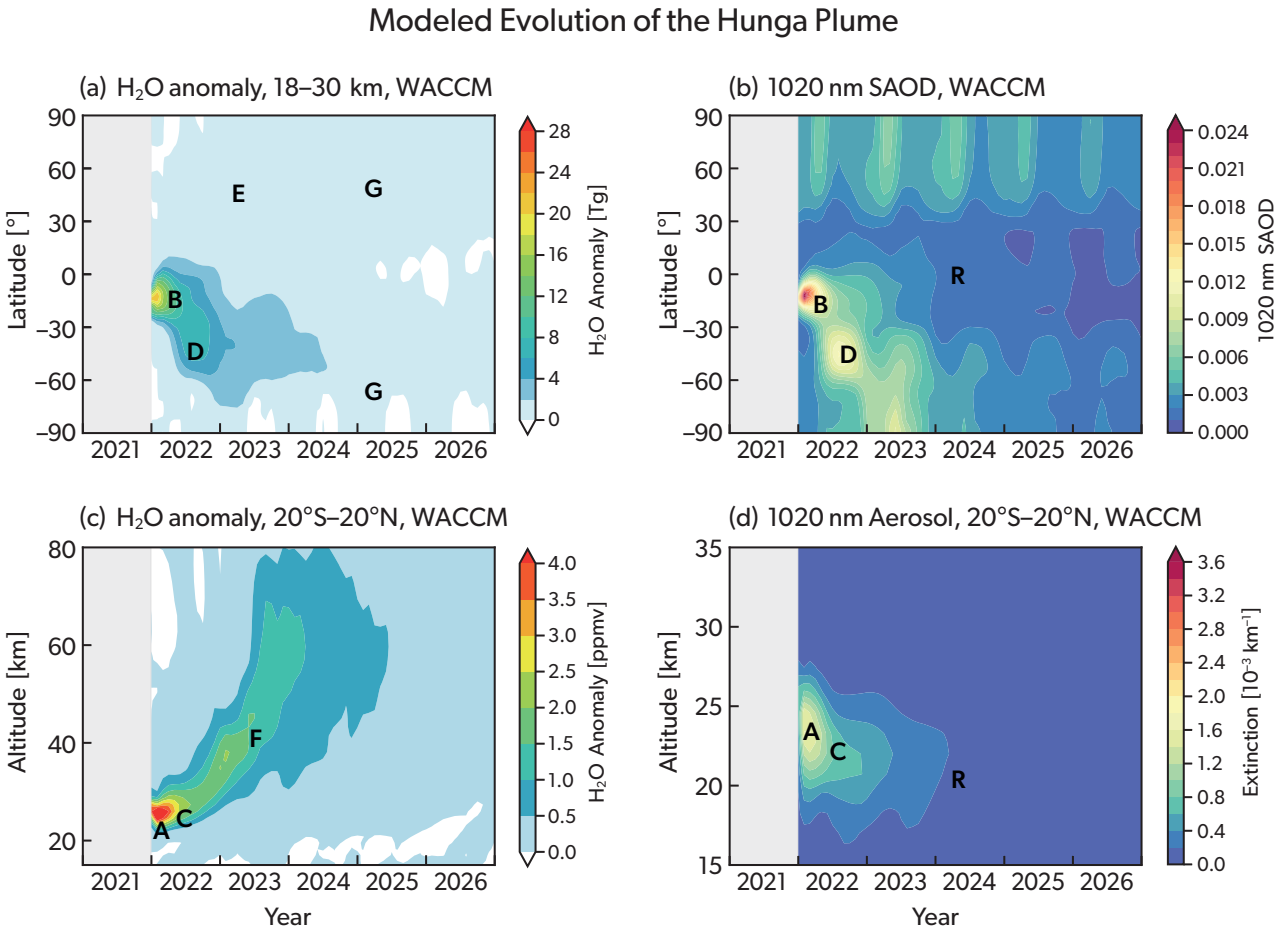

Figure ES-2: Evolution of the Hunga water vapour and aerosol perturbations simulated in a chemistry-climate model. *Panels show modeled evolution of Hunga water vapour and aerosol using the same diagnostics as the observations in Figure ES-1. Results are from the Whole Atmosphere Chemistry-Climate Model, but similar evolution is found in other global model simulations. The 2024 Ruang eruption (see R in Figure ES-1 panels b and d) is not included in the model simulations. Capital letters on the individual panels refer to specific features discussed in the Executive Summary: A = initial Hunga cloud, B = latitudinal spread over 30° S to 10° N, C = separation of water and aerosol clouds, D = transport to southern hemisphere mid-latitudes, E = water vapour transport to northern hemisphere, F = water vapour transport to mesosphere, G = persistence of water vapour anomalies in both hemispheres, R = eruption of Ruang volcano in April 2024.*

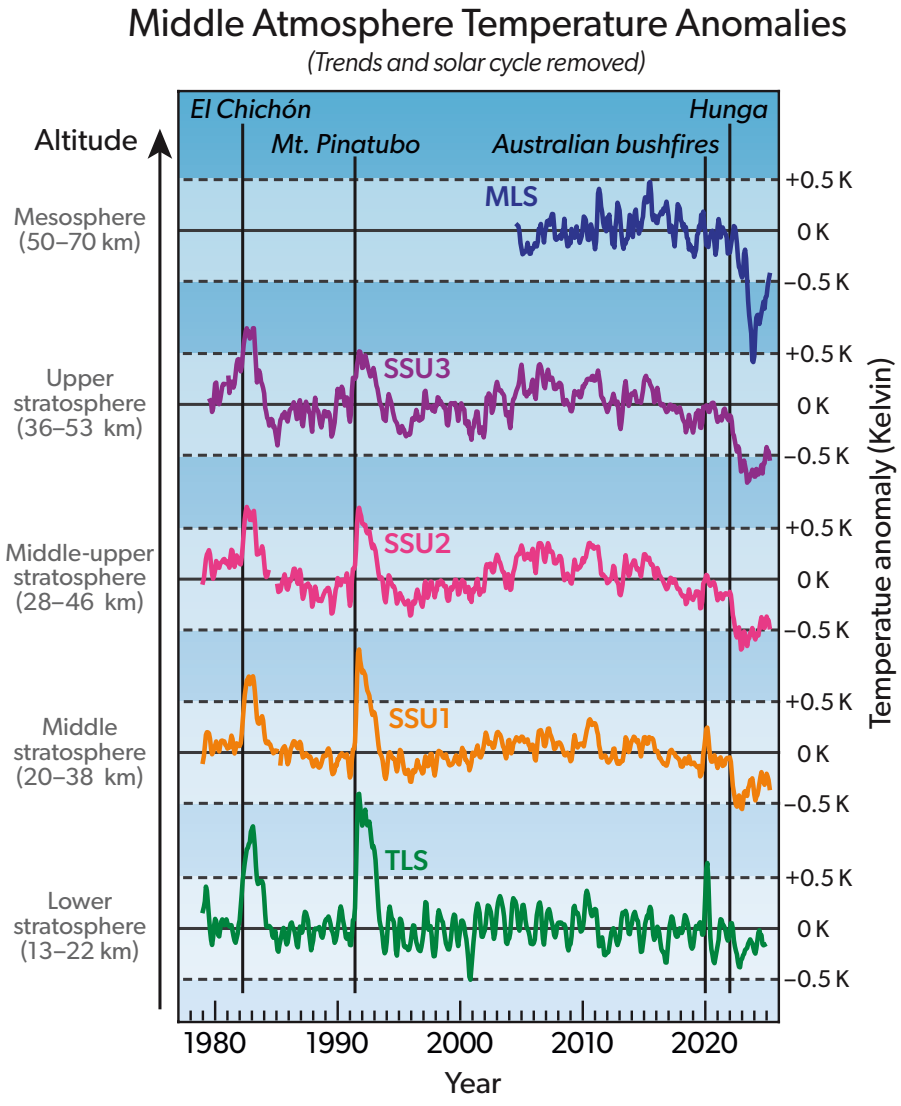

Figure ES-3: Anomalous cooling of the middle atmosphere due to Hunga. *Time series of monthly global average temperature anomalies for thick-layer average satellite measurements spanning the lower to upper stratosphere and mesosphere (bottom to top). Data for each level have been deseasonalized, and linear trends and solar cycle fits have been subtracted. These data are described in Chapter 4 (Figure 4.2). The four black vertical lines mark the timing of major events linked to stratospheric temperature anomalies: the eruptions of El Chichón (1982) and Mount Pinatubo (1991), the 2019–2020 Australian wildfires, and the 2022 Hunga eruption.*

Preface

The 15 January 2022 eruption of the Hunga volcano was the most explosive eruption in the satellite era, and within hours of the eruption information on the unprecedented altitude of the initial plume burst across the scientific community and social media. Scientists immediately began organising observational campaigns and analysing satellite information and ground observations to measure and understand the deep impact that the eruption would cause.

Activity towards a Hunga assessment report began in October 2022 at the General Assembly for the Stratosphere-troposphere Processes And their Role in Climate (SPARC) (SPARC is now the Atmospheric Processes And their Role in Climate, APARC). The Assembly included many presentations related to the Hunga eruption, and final-day discussions precipitated an effort to scope a potential community assessment of the eruption and its impacts. Key scientists were then invited to join a special meeting to discuss the idea, at which Drs. Yunqian Zhu (CIRES/NOAA CSL), William Randel (NCAR), Graham Mann (U. Leeds), and Paul A. Newman (NASA) volunteered to co-ordinate a potential outline for the report.

This initial Hunga report team co-wrote a proposal to APARC outlining a "Hunga Impacts" activity, and guidance from the APARC leadership saw a proposal submitted in January 2023 for a 3-year activity to co-ordinate an assessment report for publication in December 2025. The proposal outlined a 7-chapter document that both described the eruption, analysed the eruption's impacts and modelled its atmospheric effects. APARC leadership approved this proposal in late-January 2023 as a formal APARC "limited-term cross-activity focus" project defined to run from February 2023 to January 2026.

The new APARC activity enabled co-ordination across the inherently cross-cutting nature of the eruption's impacts, but an overarching focus of the report was to provide a definitive source ahead of the upcoming 2026 UNEP/WMO Scientific Assessment of Ozone Depletion Report. In addition to the report providing a comprehensive synthesis of observational studies on the volcanic cloud evolution and impacts, the Activity was also given a remit to co-ordinate multi-model activities building upon initial studies which predicted significant impacts on climate and the ozone layer.

On 2 February 2023 an email announcing the Activity was sent to over 100 members of the atmospheric sciences community, seeking feedback on the proposed structure and volunteer report contributors (lead authors, co-authors, reviewer). The community's responses revised the initial report structure, and provided a traceable basis for the subsequent recruitment of chapter co-author teams and review editors.

Announcements of the APARC Hunga activity were also sent to community mailing lists including SSiRC, S-RIP, CCMI, VolRes and CMIP-VolMIP activities. The timeline for the report's formal peer-review stages was devised, and also included two open science workshops, for further input from the scientific community, with 160 scientists attending the May 2023 online workshop and 56 abstracts presenting at the in-person May 2024 workshop. In September 2023, the report's lead authors were selected, and review editors for each chapter were also selected.

Multi-modelling activity began April 2023, and was termed the Hunga Tonga–Hunga Ha'apai Model Observation Comparison (HTHH-MOC), to emphasise a focus on simulations of the eruption's impacts. More than 50 scientists participated in writing the HTHH-MOC protocols (see Supplementary S1), over 10 global model groups signed up to run the simulations, and a data analysis team volunteered to perform multi-model analysis on different sub-topics.

Monthly online HTHH-MOC meetings involved discussion of emerging findings and also helped provide support and feedback to participating modelling groups. For the multi-model analysis, a group workspace area was set-up on the JASMIN (Joint Analysis System Meeting Infrastructure Needs) data analysis facility. This allowed the data analysis team to conduct initial data inspection and evaluation ahead of the initial multi-model papers being written (see Supplementary S3). The model simulations fed into the second, third, and the final drafts of the assessment. In autumn 2025, the datasets will be migrated from JASMIN to Centre for Environmental Data Analysis (CEDA) as a public release of the HTHH-MOC datasets.

Details of the various observational data sets (satellites, ground-based and balloon) used throughout the report are included in the Observational Data Supplement. These were compiled with input from recruited data experts and teams with extensive knowledge of the different data sets. At the December 2023 and December 2025 AGU fall meetings, the author team convened dedicated sessions, the former focused on observations and the latter on model findings from HTHH-MOC and other studies. In addition to the event meetings, the co-chairs held weekly meetings and hosted monthly “lead-author meetings" to facilitate team communications.

The report underwent three review cycles. The first report draft was completed by 15 September 2024 and was sent to anonymous reviewers by the Review Editors. Reviews were returned by 31 October 2024 and authors began chapter revisions in conjunction with the Review Editors. The 2nd draft was completed by 10 March 2025 and sent out for a 2nd review. Reviews were returned by April 10, and the 3rd report draft was completed by 10 May 2025. This 3rd draft was sent out to reviewers for final comments.

The final meeting of the report team was held in Boulder, CO, USA 10-12 June 2025. At this meeting the individual final chapter drafts were discussed in an open review forum as moderated by the Review Editors. Meeting attendees included the Co-chairs, Lead Authors, 1-2 selected co-authors from each chapter, the Review Editors, and a few specific reviewers selected by the Review Editors. Final chapter changes were discussed in an open plenary session and agreed upon. The final chapter revisions and write-ups were approved by the Review Editors in July 2025.

This final 10-12 June 2025 report team meeting was also set-up for the writing of the Executive Summary (ES). This ES was initially drafted by the report co-chairs from the detailed chapter bullets. The ES was edited and adjusted during the meeting by the attendees. The ES text was line-by-line agreed to in plenary session by all participants (both in-person and virtually on-line).

The 4th and final chapters drafts were submitted for detailed technical editing in August 2025, and this report was released in December 2025.

1 Volcanological context of the 2022 Hunga eruption

Lead authors	Simon Carn Anja Schmidt
Co-authors	Kristen Fauria Corinna Kloss Isobel Yeo
Contributing authors	Larry Mastin Tjarda Roberts

Cite this as:

Carn, S., A. Schmidt et al. (2025): Volcanological context of the 2022 Hunga eruption. In APARC, 2025: The Hunga Eruption Atmospheric Impacts Report [Yunqian Zhu, Graham Mann, Paul A. Newman, William Randel (Eds.)]. APARC Report No. 11, WCRP Report No. 10/2025, DOI: 10.34734/FZJ-2025-05238, available at `https://aparc-climate.org/publications/aparc-report-no-11/`.

Key points

- **The 15 January 2022 eruption of Hunga volcano (Kingdom of Tonga) was a submarine explosive eruption that may represent the first geophysically-observed example of a 'phreatoplinian' event.** A phreatoplinian event is a high-magnitude explosive volcanic eruption involving the interaction of magma and external water. This renders the Hunga eruption unique in the era of satellite observations and distinct from large eruptions of recent decades that were subaerial (e.g., 1982 El Chichón, 1991 Pinatubo).

- **Hunga provides the first direct observations of substantial stratospheric hydration by a submarine eruption.** Stratospheric injection of large quantities of water vapour by volcanic eruptions has been hypothesised in the past, but never directly observed. The Hunga eruption also provides evidence for atmospheric injection of sea salt derived from evaporated seawater.

- **Hunga volcano was persistently active in the century prior to the 2022 eruption.** This is unusual for volcanoes that produce major eruptions, which are usually dormant for decades to centuries prior.

- **The 15 January 2022 Hunga eruption was preceded by a month of precursory unrest.** This included two other significant explosive eruptions on 19 December 2021 and 13 January 2022. Weeks to months of precursory unrest is typical of major volcanic eruptions.

- **The 15 January 2022 eruption of Hunga provided a wealth of correlated, geophysical observations of a high-magnitude, phreatomagmatic eruption.** Satellite measurements of umbrella cloud growth rates, lightning detection, explosion and atmospheric wave detection, tsunami inundation records, and bathymetric mapping of deposits combine to yield an unprecedented dataset for a potentially phreatoplinian eruption.

- **The 2022 Hunga eruption had a Volcanic Explosivity Index (VEI) of 6, equal to the 1991 Pinatubo eruption.** Most of the Hunga eruption products were emplaced underwater by submarine volcaniclastic density currents, complicating assessments of eruption magnitude. Future refinements of eruption magnitude are likely as bathymetric investigations continue at Hunga.

- **Hunga's sulfur dioxide (SO_2) emissions (~0.5-1 Tg) were at least an order of magnitude less than Pinatubo.** This is well below the ~5 Tg SO_2 threshold required for significant climate impacts due to sulfate aerosols. The Hunga magma may have degassed up to ~20 Tg SO_2 during the eruption, but the majority did not reach the atmosphere.

- **Rapid response to the Hunga eruption from the volcanological and atmospheric science communities collected critical data.** Rapid tephra sampling enabled characterisation of the magma composition and volatile budget. Balloon sondes were able to sample the stratospheric Hunga plume downwind 7-10 days after the eruption. Rapid response cruises to collect bathymetric data provided critical observations of submarine deposits for eruption magnitude assessment.

- **Stratospheric aerosol perturbations by volcanic eruptions and extreme wildfires were frequent in the decade prior to the 2022 Hunga eruption.** At the time of the Hunga eruption in January 2022, the stratospheric aerosol optical depth was approximately double the baseline value.

- **Although the 15 January 2022 Hunga eruption was strongly influenced by the interaction of magma and seawater, the precise role of seawater in driving the eruption is a fundamental question yet to be resolved.** Future, detailed analysis of predominantly submarine tephra samples (challenging to access) will provide further insight into volcanic processes.

- **The 2022 Hunga eruption is by far the largest of several recent explosive eruptions that also produced water-rich, upper tropospheric and stratospheric plumes.** If modest SO_2 emissions are characteristic of these events, they may be poorly preserved in ice core proxy records of prehistoric eruptions.

- **The closest historical analog to the 2022 Hunga eruption is the August 1883 Krakatau eruption (Indonesia).** The Hunga and Krakatau eruptions both produced multiple paroxysmal explosions, globally detected atmospheric waves and tsunamis, submarine calderas and extensive submarine pyroclastic density current deposits. Comparisons of the Hunga and Krakatau eruptions should improve our understanding of the 1883 event.

- **The frequency of explosive submarine eruptions similar to or larger than the 2022 Hunga eruption prior to the instrumental era is unknown.** However, emerging research on submarine volcanism in Tonga and elsewhere suggests that submarine eruptions of a similar magnitude to Hunga may be more common in the geological record than previously recognised. More extensive and detailed seafloor bathymetry and geological studies are needed to elucidate the frequency and potential hazards of future Hunga-like eruptions.

Contents

1.1 Introduction to submarine volcanism and Hunga volcano 5
1.1.1 Submarine volcanism and submarine eruptions 5
1.1.2 Introduction to the Tonga (Tofua) arc 7
1.1.3 Physical description of Hunga volcano 8
1.1.4 Historic activity of Hunga volcano 9
1.2 The 2022 Hunga eruption 9
1.2.1 Short-term precursors to the 2022 Hunga eruption 9
1.2.2 Description and timeline of the 15 January 2022 Hunga eruption 11
1.2.3 Eruption magnitude assessment 13
1.2.4 Response to the 2022 Hunga eruption 17
1.3 The 2022 Hunga eruption in the context of other historic eruptions 19
1.3.1 Comparison with the 1883 Krakatau eruption 19
1.3.2 Summary of recent eruptions and large wildfires with radiative impacts 22
1.4 Summary and conclusions 24

Preamble

Large volcanic eruptions that inject material into the stratosphere are of major scientific interest. The atmospheric science community is concerned with potential impacts on atmospheric chemistry (including stratospheric ozone) and climate, and uses large eruptions to test climate and global circulation models. Large eruptions are of great interest to volcanologists as they provide insight into the volcanic processes and hazards associated with these rare, high-magnitude events and their frequency on geological timescales. The eruption of the submarine Hunga volcano (Kingdom of Tonga) on 15 January 2022 was among the largest eruptions of any type of the past century, and the largest known historical submarine explosive eruption. The Hunga eruption was similar in magnitude (erupted volume) to the 1991 Pinatubo eruption (Philippines), but distinct in terms of emissions and impacts because Hunga is a submarine volcano, yielding emissions dominated by evaporated seawater and including exotic particles such as sea salts (Chapters 2, 3). This has important implications for the atmospheric and climate impacts of submarine eruptions (Chapters 4, 5, 7). Hunga produced the most energetic volcanic explosion recorded on Earth since the 1883 Krakatau eruption (Indonesia), injecting a volcanic plume into the lower mesosphere (Chapter 6), and the 2022 paroxysm may represent the first example of a well-observed phreatoplinian style eruption. It produced the third-largest stratospheric aerosol perturbation observed in the satellite era (since 1978), after the 1991 Pinatubo and 1982 El Chichón eruptions (Chapter 3).

Chapter 1 provides the volcanological context of the 2022 Hunga eruption. It includes a brief review of explosive submarine volcanism (Section 1.1), some background on Hunga volcano and its tectonic setting in the Tonga-Kermadec volcanic arc (Section 1.1.3), a summary of the main characteristics of the 2022 eruption (sequence of events, eruption magnitude, and potential analogs; Sections 1.2–1.3), and describes the state of the stratosphere prior to the 2022 eruption (Section 1.3). Chapter 2 provides a more detailed account of satellite observations of the 2022 eruption products and the first month of atmospheric residence; this chapter focuses on the volcanological aspects. Chapters 3–7 focus on the later evolution of the stratospheric perturbation by the Hunga eruption and its impacts on atmospheric circulation, chemistry, and climate.

1.1 Introduction to submarine volcanism and Hunga volcano

1.1.1 Submarine volcanism and submarine eruptions

Volcanism on Earth is broadly categorised as either subaerial or subaqueous, according to the realm in which it occurs. Subaqueous volcanism includes any volcanic activity beneath surface water – i.e., the oceans, lakes, and glaciers – and is dominated by submarine volcanism beneath the ocean surface. Subaerial volcanism occurs above the surface of any water body and vents material directly into the atmosphere. Based on total erupted volume, it has been estimated that 85% of volcanism on Earth is subaqueous (~3.5 km^3 erupted magma per year; White et al., 2015). This is due to the prevalence of submarine, mid-oceanic ridge (MOR) spreading centres (which contribute at least ~3 km^3 erupted magma per year), where the majority of Earth's volcanic output occurs (e.g., Deligne and Sigurdsson, 2015). Other submarine volcanism occurs at oceanic islands (or hot spots; e.g., Hawai'i, USA) and in volcanic arcs (e.g., the Tofua arc, Tonga). Volcanic arcs form above subduction zones or convergent plate margins and produce arcuate chains of stratovolcanoes or volcanic islands (Deligne and Sigurdsson, 2015). Although submarine arc volcanism is relatively minor in volumetric terms, it is distinct from the majority of other (mostly effusive) submarine volcanism due to the potential for explosive eruptions and impacts on the atmosphere and climate. Regardless of tectonic setting, the vast majority of submarine volcanic activity is very poorly observed relative to subaerial volcanism due to the challenges of instrumenting and mapping the seafloor, directly observing eruptions beneath the ocean, and accessing submarine volcanic deposits (Abbott and Rubenstone, 2024; Carey et al., 2018). Our limited knowledge of submarine volcanism was highlighted in a National Academies report (NASEM, 2017).

Our understanding of the physical processes controlling the dynamics, style, intensity, and impacts of explosive volcanic eruptions is largely derived from observations of high-magnitude subaerial eruptions in the post-1979 satellite era (e.g., 1980 Mt St Helens, 1982 El Chichón, 1991 Mt Pinatubo) and from analysis of well-preserved deposits of older subaerial volcanic eruptions. Explosive volcanic eruptions are driven by the exsolution of dissolved gases (mostly water [H_2O] and carbon dioxide [CO_2]) and subsequent expansion of gas bubbles as magmas decompress towards atmospheric pressure (0.1 MPa), which ultimately leads

to magma fragmentation and atmospheric injection of gases and ash in a volcanic plume. In the submarine realm (including MOR systems, intraplate hotspots/seamounts, oceanic plateaus, and oceanic volcanic arcs), the high hydrostatic pressure (~1 MPa per 100 m of water depth) can suppress explosive volcanism (e.g., Cas and Simmons, 2018) – except within a few hundred meters of the ocean surface. Hence, perhaps as much as 95% of submarine eruptions are effusive (non-explosive), with explosive submarine eruptions (~5% of submarine eruptions; White et al., 2015) commonly thought to be restricted to water depths of less than a few hundred meters. In shallow subaqueous environments the interaction between hot magma (800–1200°C) and external water (<20°C) can be highly explosive, due to instantaneous superheating and explosive boiling and expansion of liquid water in contact with magma (Molten Fuel-Coolant Interaction or MFCI processes; Cas and Simmons, 2018; Zimanowski et al., 2015; Sparks et al., 1997). Volcanic activity involving external water is called 'phreatomagmatic' (also termed hydrovolcanic or hydromagmatic), one key characteristic of which is the generation of fine ash particles (with diameters <1000 μm or 0.1 mm) via MFCI processes that fragment erupting magma more efficiently than magmatic fragmentation (e.g., Zimanowski et al., 2015).

Individual subaerial and subaqueous (phreatomagmatic) eruptions span orders of magnitude of erupted magma volume, mass flow rate, tephra dispersal (determined by plume height), and energy release. Early classification schemes for volcanic eruptions were based on measurements of the area of dispersal (D, km^2) and degree of fragmentation (F, %) of the resulting pyroclastic fall (tephra) deposits (Walker, 1973). The F parameter represents the percentage of tephra particles in the deposit with diameter of <1 mm, and varies from less than 20 for deposits generated by magmatic fragmentation (via exsolution of volcanic gases), to over 80 for phreatomagmatic eruption deposits (fragmented via MFCI processes). Based on their D and F values, Walker (1973) identified three kinds of pyroclastic fall deposit: Hawaiian/Strombolian (magmatic; low D and low F); Surtseyan (phreatomagmatic; low D and high F); and Plinian (magmatic; high D and low/moderate F). The Walker (1973) classification omitted the phreatomagmatic equivalent of a Plinian eruption. However, some tephra deposits were observed to have widespread dispersal (high D), similar to Plinian tephra, but with a much finer grain size (high F). Self and Sparks (1978) argued that such deposits are the phreatomagmatic analog of Plinian deposits and proposed the term 'phreatoplinian'. Well-preserved phreatoplinian deposits are rare, but archetypal examples include the Oruanui Formation, Taupo volcano, New Zealand (produced by the ~26 ka Oruanui eruption of Taupo, the largest known phreatomagmatic eruption) and the 1875 Askja (Iceland) eruption deposit (e.g., Van Eaton et al., 2012; Houghton et al., 2015). The 1875 Askja eruption is often cited as the only phreatoplinian eruption documented by eye-witness records, but the phreatoplinian phase of the eruption was brief (~1 hr) due to a limited supply of external water from ice melt runoff and groundwater (Houghton et al., 2015). Delos Reyes et al. (2018) assert that the January 1911 eruption of Taal volcano (Philippines), which was well observed, should also be classified as phreatoplinian, but this remains contentious. As discussed later, a significant volcanological aspect of the 2022 Hunga eruption is that it likely represents the first phreatoplinian eruption in the modern instrumental era, although it has yet to be officially classified in this category.

In its Volcanoes of the World (VOTW) database, the Smithsonian Institution's Global Volcanism Program (GVP) lists 120 active Holocene submarine volcanoes, of which 80 have reported eruption dates and 40 have erupted since 1978 (Global Volcanism Program, 2024). Although 70% of the Earth is submarine, only 15% of Holocene arc volcanoes in the VOTW database are submarine (Abbott and Rubenstone, 2024). Most historically active submarine volcanoes are located in the following regions: Japan, Taiwan and the Mariana Islands (Izu–Bonin–Mariana arc); Melanesia (Solomon Islands, Vanuatu, Papua New Guinea); the Tonga–Kermadec Islands; and the Mediterranean Sea (Italy, Greece). Several submarine volcanoes (e.g., Hunga, Home Reef and Lateiki in Tonga, Fukutoku-Oka-no-Ba in Japan) have multiple reported eruptions since 1978; these are also among the shallowest and hence more likely to produce plumes that breach the ocean surface. Abbott and Rubenstone (2024) argue that, due to observational challenges, the VOTW database significantly underestimates the actual number of submarine volcanoes, proposing that >32% of Holocene arc volcanoes are submarine.

One of the key observations arising from the 2022 Hunga eruption is the potential for stratospheric hydration by water vapor emitted by submarine volcanic eruptions (Chapters 2, 3). Water is by far the most abundant volcanic gas species in magmas (typically >90 mol%; e.g., Oppenheimer et al., 2014), but

volcanic emissions of water vapor (WV) are very difficult to quantify (e.g., Millán et al., 2022; Sioris et al., 2016; Murcray et al., 1981), and direct observations of volcanic WV emissions are rare, even after major eruptions. There are three potential sources of WV in emissions from explosive volcanic eruptions: degassing of water from the erupting magma (i.e., "volcanic" water), entrainment of tropospheric WV into the volcanic plume (e.g., Glaze et al., 1997), and, in phreatomagmatic eruptions, the incorporation of external water at the vent (e.g., Rowell et al., 2022). The main factor limiting direct stratospheric WV injection by volcanic eruptions is condensation of water (or deposition of ice) in rising volcanic plumes (e.g., Pitari and Mancini, 2002). Prior to the 2022 Hunga eruption, the potential atmospheric and climate impacts of explosive submarine volcanic eruptions and associated WV emissions had received little attention. Cronin (1971) speculated that submarine and phreatomagmatic volcanic eruptions in the 1960s (e.g., Surtsey, Iceland in 1964; Taal, Philippines in 1965) may have been partly responsible for increases in stratospheric WV observed in that decade. Valentine (1993) suggested that phreatoplinian eruptions could theoretically inject large quantities of WV into the stratosphere, along with very fine ash particles. Joshi and Jones (2009) considered the potential effects of stratospheric WV injection by volcanic eruptions in the context of the 1883 Krakatau (Indonesia) eruption. The 1883 Krakatau eruption generated "co-ignimbrite" clouds rising above pyroclastic density currents (PDCs) that partially flowed over open water (Self and Rampino, 1981; Self, 1992), potentially entraining large amounts of WV that could ascend to stratospheric altitudes in the co-ignimbrite plume (Dartevelle et al., 2002). Joshi and Jones (2009) hypothesised that tropospheric warming due to the stratospheric WV injected via this process could partially offset surface cooling induced by sulfate aerosols.

Satellite observations of recent submarine eruptions and modelling of water-rich plumes have suggested limited potential for climate impacts due to the suppression of eruption column height and low SO_2 emissions due to scavenging by seawater (e.g., Rowell et al., 2022). In the era of satellite measurements (since 1978), only ~13 submarine eruptions (not including the 2021–2022 Hunga eruptions) have been sufficiently energetic to generate plumes that breached the ocean surface and produce potentially detectable SO_2 emissions (Carn et al., 2022). The May 2010 eruption of South Sarigan seamount (CNMI), which produced a subaerial eruption column that rose to ~12 km from an eruption vent at ~200 m water depth (Green et al., 2013; Embley et al., 2014), appears to be the deepest submarine eruption to have produced SO_2 emissions detectable from space to date, although the measured SO_2 mass was low (~1 kiloton, kt). Mastin and Witter (2000) list only two other submarine volcanoes reported to have produced surface breaching from depths of >100 m: at Kick'em Jenny (West Indies) in 1939, 1974 and 1988; and Ritter Island (Papua New Guinea) in 1972 and 1974. In these cases, the subaerial eruption columns extended only a few hundred meters above the ocean surface (Mastin and Witter, 2000). The 2012 eruption of Havre Volcano in the Kermadec Arc is the only deep-sea eruption (~900 mbsl vent) known to have produced an atmospheric plume (Jutzeler et al., 2014; Carey et al., 2018). However, it is debated whether the Havre gas jet extended throughout the water column versus generation of the atmospheric plume by clast–water interactions close to the sea surface (Manga et al., 2018; Knafelc et al., 2022). Modelling of condensable submarine volcanic gas jets suggests that surface breaching is possible from vents as deep as 500 m below sea level (Cahalan and Dufek, 2021).

1.1.2 Introduction to the Tonga (Tofua) arc

Hunga volcano (20.553°S, 175.38°W) is located in the ~800 km-long Tofua volcanic arc, at the northern end of the larger Tonga–Kermadec volcanic arc, which extends north-east of New Zealand into the Pacific Ocean (Figure 1.1). The Tonga–Kermadec arc is the result of westward subduction of the Pacific Plate beneath the Indo-Australian Plate and is one of the most volcanically active island arcs on Earth. Even so, records of volcanic activity are incomplete because most volcanoes in the region are fully or partially submerged, remote, and poorly monitored; hence many eruptions likely go undetected (Yeo et al., 2024). Hunga is one of 14 Holocene volcanoes in the Tofua arc, of which nine are submarine and seven (including Hunga) have been active since 1960 (Global Volcanism Program, 2024). Characterisation of eruption size in the region is challenging, but it is thought that most historic eruptions in the Tofua arc have been relatively small: of the 65 eruptions recorded in the region before 2021, 64 had a Volcanic Explosivity Index (VEI; Newhall and Self, 1982) of 3 or less (Global Volcanism Program, 2024). Prior to the 2022 Hunga eruption, the largest known historic eruption in the Tofua arc was a VEI 4 eruption of Fonualei (Tonga) in

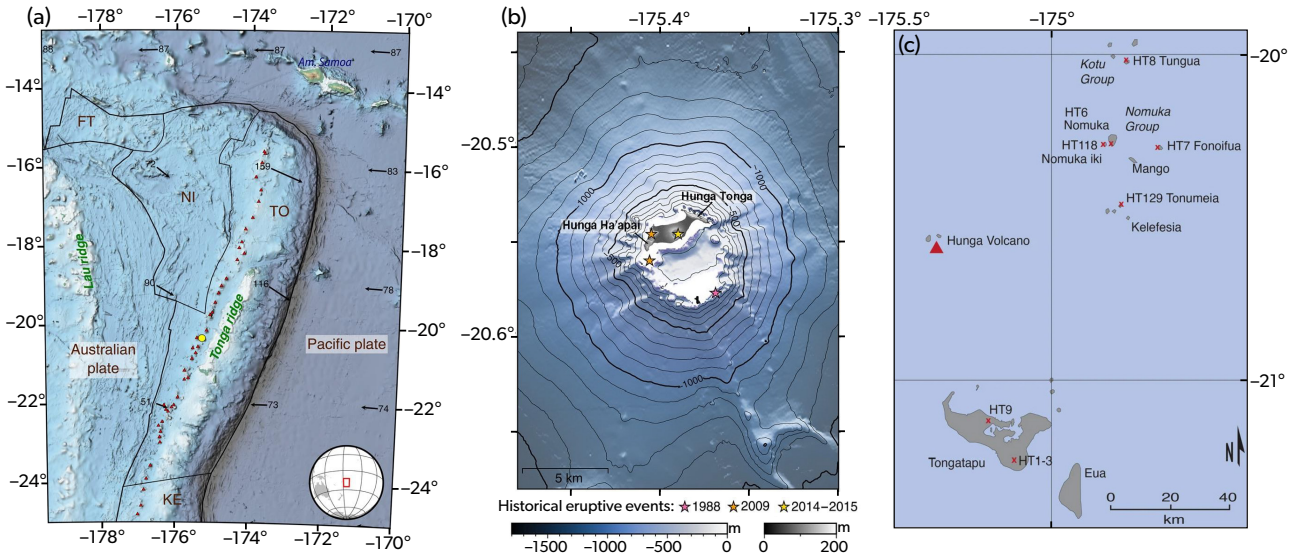

Figure 1.1: *Location map of the Tonga-Kermadec arc and Hunga volcano. (a) Tectonic setting of the Tofua volcanic arc (~21.5°S to 15.5°S), in the northern Tonga-Kermadec subduction zone. The map shows known volcanoes (*red triangles*; includes volcanoes with Holocene eruptions and older volcanoes with no eruptive history), Hunga volcano (*yellow circle*), tectonic plate boundaries (*black lines*), and plate velocities relative to the Australian plate (*black arrows, millimeters per year*). FT, Futuna; NI, Niuafo'ou; TO, Tonga; KE, Kermadec microplates. (b) Pre-2022 multibeam bathymetry of Hunga volcano and topography of Hunga-Tonga and Hunga-Ha'apai islands in September 2017. (c) Location of Hunga (*red triangle*) in relation to other Tongan islands.* Red crosses *show tephra sampling locations after the 15 January 2022 Hunga eruption. Figure taken from Le Mével et al. (2023) and Colombier et al. (2023).*

1846 (although the magnitude is uncertain). Although major explosive eruptions are largely absent from the recent eruptive record, at least eight Tofua arc volcanoes mapped or partially mapped to date have wide (>1 km diameter), flat-bottomed central craters that may be interpreted as calderas produced by large volume, prehistoric eruptions (Yeo et al., 2024). All of them have shallow vents, where the overlying water column would be unlikely to suppress a future explosive eruption, and four of these caldera systems appear to erupt regularly (Curacoa, Volcano-F, Tofua and Hunga), although the 2022 Hunga eruption is the only 'caldera-forming' event in historic times (Yeo et al., 2024). More seafloor surveys, high-resolution bathymetry, seismic surveys, and sediment coring are needed to further characterise the morphology and eruptive history of submarine volcanoes in the Tofua arc.

Due to its oceanic setting, explosive volcanic eruptions in the Tofua arc have the potential to generate a range of volcanic hazards, including:

I. tsunamis (Carvajal et al., 2022; Lynett et al., 2022; Borrero et al., 2023);
II. pyroclastic density currents that travel over the ocean surface (Carey et al., 1996);
III. submarine volcaniclastic density currents (Seabrook et al., 2023; Clare et al., 2023);
IV. pumice rafts (Bryan et al., 2004; Jutzeler et al., 2014; Brandl et al., 2020).

1.1.3 Physical description of Hunga volcano

Hunga volcano is a massive, almost entirely submerged andesitic stratovolcano that rises more than 2 km from the surrounding seafloor, breaching the ocean surface to form the islands of Hunga-Tonga and Hunga-Ha'apai (HTHH; Cronin et al., 2017, Figure 1.1). The latter are the emergent remnants of the rim of a submarine caldera ~6 km in diameter, which formed during a caldera-forming eruption dated to 1040–1180 CE (Cronin et al., 2017; Brenna et al., 2022). Prior to the 2022 Hunga eruption, the caldera depression was up to ~150 meters deep (Figure 1.1), and ignimbrite units emplaced by the 1040–1180 CE caldera-forming eruption formed the topmost deposits on HTHH. At least two additional ignimbrite units and pyroclastic flow deposits preserved on HTHH (as yet undated) are evidence of other, high-magnitude eruptions of Hunga prior to 1040–1180 CE (Cronin et al., 2017; Brenna et al., 2022). The 1040–1180 CE Hunga caldera- forming event has been tentatively proposed (within error bounds) as the source of an unknown

tropical eruption in 1108 CE that produced a sulfate anomaly in ice cores and significant (>1°C) global cooling (Cronin et al., 2017; Sigl et al., 2015).

1.1.4 Historic activity of Hunga volcano

Hunga volcano was relatively active in the century prior to the 2022 eruption, with 5 confirmed eruptions. This contrasts with volcanoes that have produced major (VEI 5+), climate-forcing subaerial eruptions, which typically show centuries of pre-eruptive quiescence (e.g., Pinatubo, El Chichón). Activity at Hunga was first recorded in 1912, but little is known about its earlier eruptive history (Cronin et al., 2017). Shallow submarine eruptions were observed in 1912 (VEI 2), 1937 (VEI 2), and 1988 (VEI 0). These eruptions were all located near a group of shallow reefs about 3 km south of Hunga-Tonga island, on the SE rim of Hunga caldera (Global Volcanism Program, 2022b). Monitoring of more recent eruptions from this remote, largely submarine volcano has benefited from the availability of satellite remote sensing and hydroacoustic monitoring (e.g., Vaughan and Webley, 2010; Bohnenstiehl et al., 2013; Garvin et al., 2018). An eruption in March 2009 (VEI 2) began as a submarine event, progressing to a subaerial eruption as tephra deposits enlarged Hunga-Ha'apai island, although these deposits eroded away within ~6 months (Global Volcanism Program, 2009; Vaughan and Webley, 2010; Bohnenstiehl et al., 2013). Surtseyan eruptions in December 2014 – January 2015 (VEI 2) were also initially submarine prior to subaerial tephra deposition that formed a subaerial tombolo between the two islands of HTHH (Cronin et al., 2017; Garvin et al., 2018; Colombier et al., 2018); this tombolo persisted until the 2022 eruptions (Figure 1.2). After the 2014–15 eruption ended in January 2015, no further activity was reported at Hunga until December 2021 (Global Volcanism Program, 2022b).

1.2 The 2022 Hunga eruption

1.2.1 Short-term precursors to the 2022 Hunga eruption

High-magnitude (VEI 5+) eruptions are often preceded by weeks to months of precursory activity prior to the paroxysmal event (e.g., 1980 Mount St Helens, 1991 Pinatubo), and the 2022 Hunga eruption also followed this pattern. The 2021–2022 Hunga eruptive episode began around 09:35 local time on 20 December 2021 (20:35 UTC on 19 December 2021) with the generation of a ~16–20 km tall plume and a circular umbrella cloud (a density-driven, horizontal intrusion) with a maximum radius of ~130 km from a vent adjacent to the 2014–2015 eruption vent on HTHH (Figure 1.2c; Prata et al., 2025; Gupta et al., 2022; Global Volcanism Program, 2022b). The umbrella cloud persisted for ~5–6 hours (Prata et al., 2025; Gupta et al., 2022). The 19 December 2021 eruption plume was water-ice rich, contained ~10 kt of SO_2, and dusted islands in the Kingdom of Tonga with ash (Gupta et al., 2022; Carn et al., 2022). Although the location of the 19 December 2021 eruption vent (orange line in Figure 1.2c) is subaerial in prior satellite observations on 10 December 2021, it is likely that seawater gained access to the vent early in the eruption to produce the observed water-ice rich plume, with subsequent tephra deposition during the eruption then enlarging the island (Figure 1.2c,d). Following the 19 December 2021 eruption, Surtseyan-style explosions, the creation of steam-rich plumes rising several kilometres, and horizontal steam bursts continued throughout late December 2021 and early January 2022 (Global Volcanism Program, 2022b). These intermittent eruptions also released daily plumes containing up to 15 kilotons of SO_2 (Carn et al., 2022). Occasional strands of floating pumice were found within several kilometres of Hunga in late December 2021, and some drifted to beaches in the Kingdom of Tonga (Global Volcanism Program, 2022b). During this period, HTHH island increased in size from 2 km^2 on 10 December 2021 to 3.6 km^2 on 2 January 2022 by expanding its tephra apron (Global Volcanism Program, 2022b); Figure 1.2d). Several additional small plumes were observed between 1 and 13 January 2022 (e.g., Carn et al., 2022; Gupta et al., 2022).

A major eruptive event occurred on 13 January 2022 at ~15:20 UTC, generating a plume that rose to an altitude of 18–19 km (just above the tropopause at ~18 km) and a 250-km wide ice-rich umbrella cloud containing 60 kt of SO_2 (Prata et al., 2025; Carn et al., 2022; Gupta et al., 2022; Global Volcanism Program, 2022a). The plume was sustained for almost a full day (~22 hours), making this the longest-duration eruptive event of the entire 2021–2022 eruption sequence (Gupta et al., 2022). Ground-based images from the Tonga Geological Survey show Surtseyan-style pulses ejecting dark volcaniclastic material into the air and pyroclastic currents extending into the ocean (Global Volcanism Program, 2022a). Minor ashfall was detected in the Kingdom of Tonga and the Tonga Meteorological Survey issued tsunami warnings from this event (Global Volcanism Program, 2022b). The central section of HTHH island was destroyed by this event, such that the vent from which the eruption had oc-

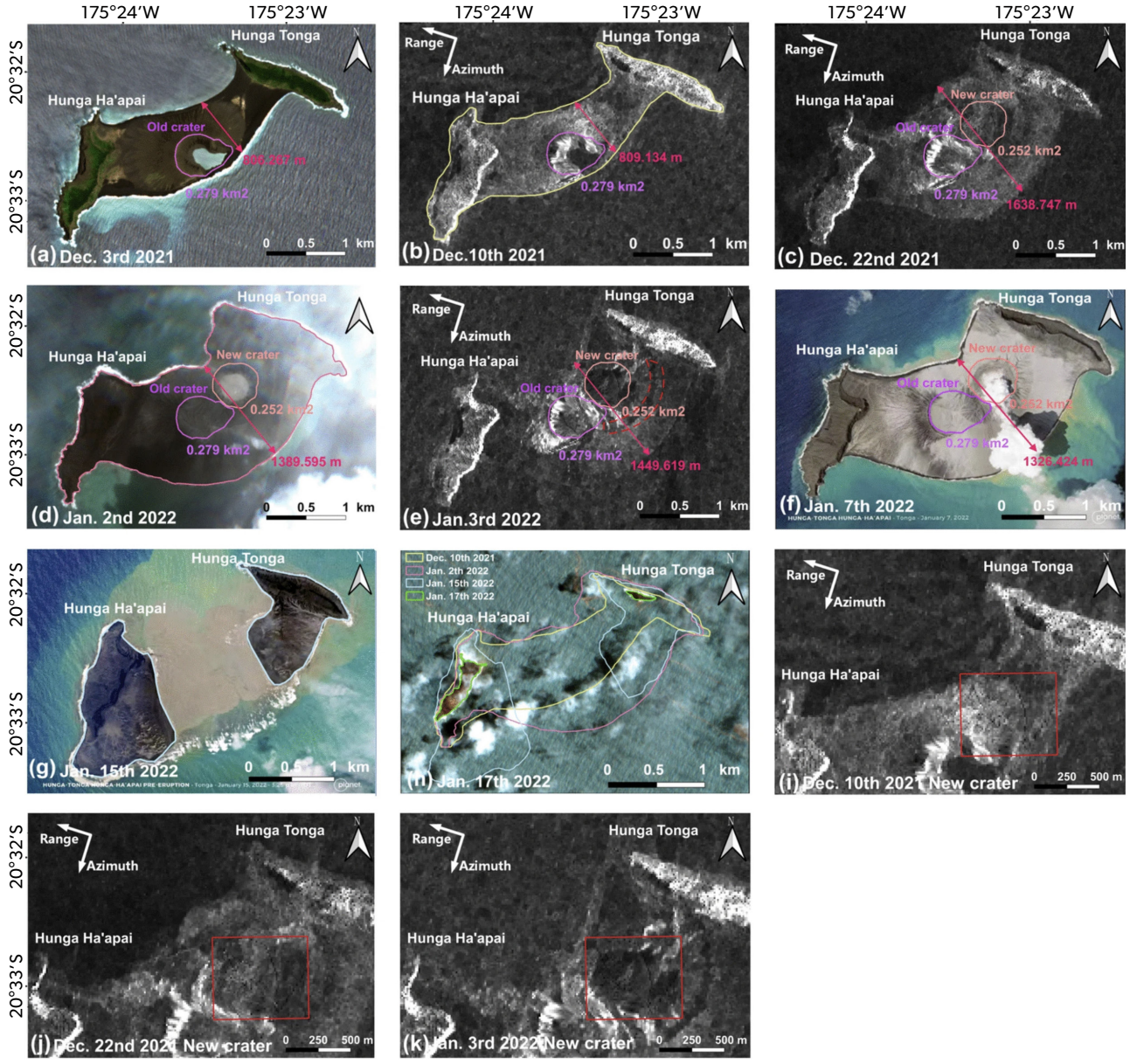

Figure 1.2: *Satellite imagery showing the changing morphology of Hunga-Tonga and Hunga-Ha'apai (HTHH) islands during the 2021-2022 Hunga eruption sequence from December 2021 to January 2022. (a, d, h) Sentinel-2A visible imagery; (b, c, e) Amplitude imagery from the Sentinel-1A radar satellite; (f, g) Planet Labs SkySat imagery (Image © 2022 Planet Labs PBC); (i, j, k) Enlarged regions of Sentinel-1A images on 10 December 2021 (b), 22 December 2021 (c), and 3 January 2022 (e), respectively. Figure taken from Wei et al. (2025).*

curred up to this point was fully submerged below sea level by 15 January 2022 (Figure 1.2).

1.2.2 Description and timeline of the 15 January 2022 Hunga eruption

Following the 13–14 January 2022 eruption, Hunga emitted several short-lived plumes (or puffs) that were visible in satellite imagery rising to the mid- to upper troposphere (Carn et al., 2022; Van Eaton et al., 2023). These plumes contributed negligible mass flux relative to subsequent events, but indicate that the volcanic system remained open immediately prior to the climactic eruption. An eruption start time of ~04:00 UTC (~17:00 local time) on 15 January 2022 is often reported in the literature (Gupta et al., 2022; Matoza et al., 2022) and reflects the sudden onset of plume development (Figures 1.3 and 1.4), audible explosions on Tongatapu (Purkis et al., 2023), geophysical signals such as long-range infrasound (Vergoz et al., 2022; Matoza et al., 2022), and the highest flux phase of the eruption (Gupta et al., 2022; Van Eaton et al., 2023). Loud explosions were heard on Tongatapu at 04:06 and 04:18 UTC, and tsunami waves reached the port of Nuku'alofa (Tongatapu) by 04:26 UTC (Purkis et al., 2023). The timing of these explosions precisely matches explosion onset times estimated from disturbances in ionospheric total electron content, with the strongest explosion occurring at 04:18 UTC (Astafyeva et al., 2022). By 04:36 UTC, the eruption column reached its maximum overshoot height of 57–58 km, in the lower mesosphere (Figure 1.3; Proud et al., 2022; Carr et al., 2022). The umbrella cloud expanded to a diameter of 400 km over the next ~1 hour, coincident with observations of the most intense lightning rates ever documented in Earth's atmosphere (>2,615 flashes min^{-1} at peak intensity (Figure 1.3; Van Eaton et al., 2023). Lateral spread of the volcanic column occurred at two altitudes: 30–40 km for the upper umbrella and 17–20 km (coincident with the tropopause) for the lower umbrella (Figure 1.3; Carr et al., 2022; Gupta et al., 2022). Lapilli (tephra particles with diameters of 2–64 mm) began falling on Tongatapu by ~04:50 UTC, followed by ash (tephra particles with diameters of <2 mm) at ~05:00 UTC (Wu et al., 2025). A blast at 04:56 UTC broke windows in Nuku'alofa, and the largest tsunami reached the port at 05:15 UTC (Figure 1.3; Purkis et al., 2023). Over the next hours the altitude of the upper umbrella cloud declined as the cloud was blown westward by stratospheric winds (Figure 1.3). A brief eruptive pulse occurred close to 08:30 UTC which produced infrasound signals, an overshooting top to 39 km, and renewed lightning (Figure 1.3; Matoza et al., 2022; Gupta et al., 2022; Van Eaton et al., 2023). The umbrella clouds from the Hunga eruption spread over the Kingdom of Tonga (Figures 1.3 and 1.4) and ash fallout produced deposits up to 3.5 cm thick (Figure 1.5; Kelly et al., 2024). Plume heights and volcanic lightning subsided by 15:12 UTC, indicating an end to the eruption (Figure 1.3; Van Eaton et al., 2023).

The impacts of the 15 January 2022 Hunga eruption in the ocean and on the seafloor were significant and widespread. Local tsunamis produced by the 15 January 2022 eruption reached Tongatapu, the largest island in the Kingdom of Tonga, with wave heights over 6 meters (Borrero et al., 2023; Purkis et al., 2023). Photographs taken from a vessel tens of kilometres from Hunga show evidence for a partially collapsing eruption column producing pyroclastic currents that entered the sea (Clare et al., 2023, Figure 1.4). Tonga's domestic and international seafloor communication cables stopped working at 04:30 and 05:44 UTC, indicating the timing of major seafloor disturbances 16–18 km and 47–70 km from the vent, respectively (Figure 1.3; Clare et al., 2023). Comparisons of bathymetry before and after the 2022 eruption revealed that Hunga's caldera floor dropped by ~800 m (Figure 1.6), up to 30 m of scour occurred along the caldera rim, and deposits up to 40 m thick were present outside of the caldera (Seabrook et al., 2023). Together, the bathymetry changes and the timing of cable breakage have been interpreted to indicate that the 15 January eruption produced fast-moving volcaniclastic density currents along the seafloor (Seabrook et al., 2023; Clare et al., 2023). Serendipitous remotely operated vehicle (ROV) dives in the Lau Basin in March/April 2022 demonstrate that Hunga's submarine volcaniclastic currents travelled at least 80 km west of the vent and buried benthic communities as they travelled (Beinart et al., 2024; Seabrook et al., 2023; Chaknova et al., 2025).

The 15 January 2022 Hunga eruption was highly explosive, and certainly driven at least in part by phreatomagmatic processes. It is likely to meet the criteria for a phreatoplinian eruption (e.g., wide dispersal of fine ash; pulsating eruption column behavior; Van Eaton et al., 2012), in which case it would be the first such event in the modern era. However, work is ongoing to fully characterise the products of the 2022 eruption and elucidate the role of external water versus internal magmatic processes in triggering the event.

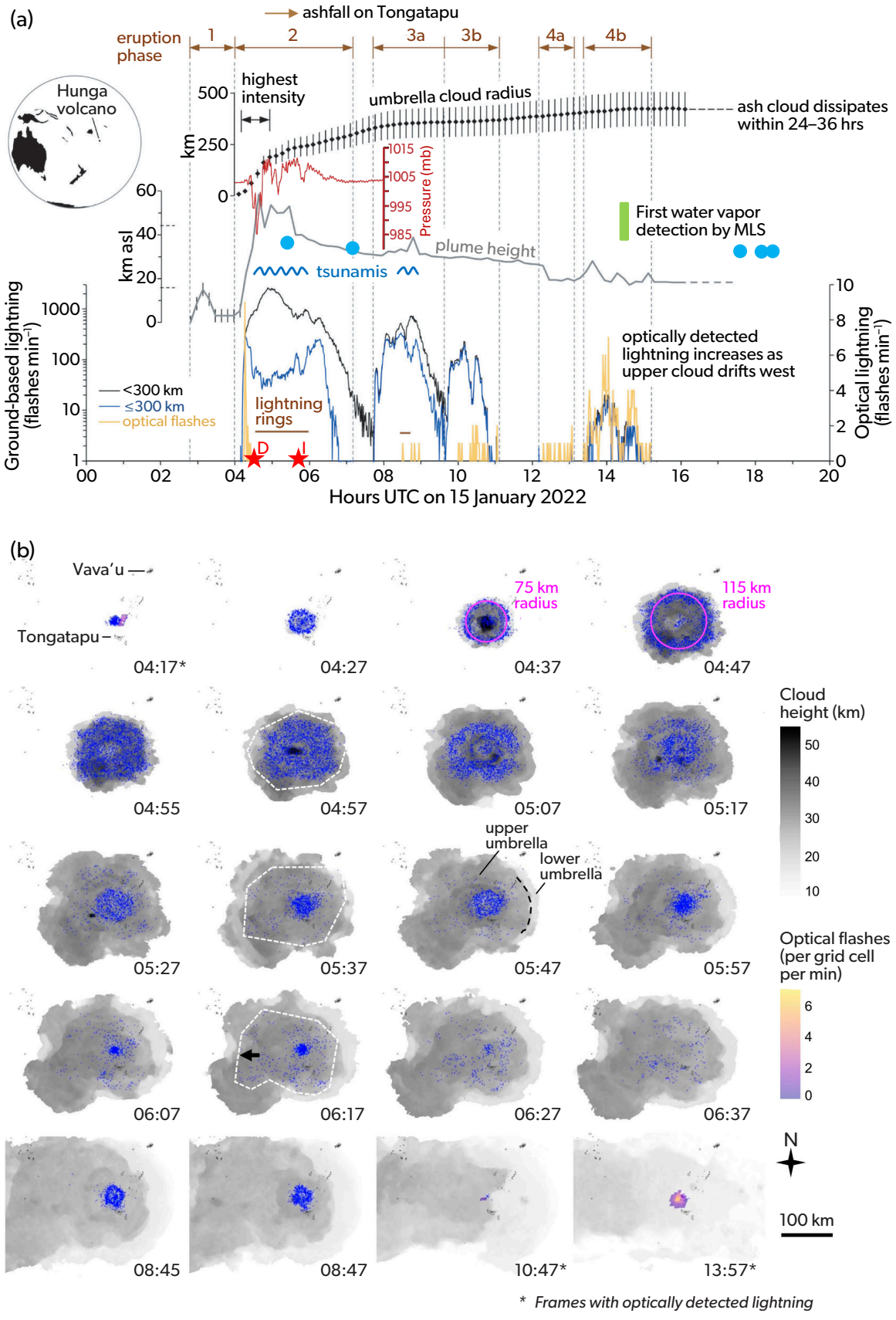
(a)
ashfall on Tongatapu
eruption phase
1
2
3a
3b
4a
4b
Hunga volcano
highest intensity
umbrella cloud radius
ash cloud dissipates within 24–36 hrs
km
500
250
0
1015
1005
995
985
Pressure (mb)
First water vapor detection by MLS
km asl
60
40
20
0
plume height
tsunamis
optically detected lightning increases as upper cloud drifts west
Ground-based lightning (flashes min⁻¹)
1000
100
10
1
<300 km
≤300 km
optical flashes
lightning rings
D
I
Optical lightning (flashes min⁻¹)
10
8
6
4
2
0
00
02
04
06
08
10
12
14
16
18
20
Hours UTC on 15 January 2022
(b)
Vava'u
Tongatapu
75 km radius
115 km radius
04:17*
04:27
04:37
04:47
04:55
04:57
05:07
05:17
upper umbrella
lower umbrella
05:27
05:37
05:47
05:57
06:07
06:17
06:27
06:37
08:45
08:47
10:47*
13:57*
Cloud height (km)
50
40
30
20
10
Optical flashes (per grid cell per min)
6
4
2
0
N
100 km
* Frames with optically detected lightning

Figure 1.3: *(a) Satellite, volcanic lightning and surface pressure chronology of the 15 January 2022 Hunga eruption. Four phases of eruptive activity can be distinguished using umbrella cloud growth, maximum plume heights over Hunga volcano, and lightning rates (with phases 3 and 4 subdivided based on variable lightning rates). Lightning detected by ground-based networks is shown on the left axis (log scale) in terms of flashes min^{-1} occurring within 300 km (*black line*) and 20 km of Hunga (*blue line*). Optically detected flash rates from the GOES-17 satellite (*yellow bars*) are shown on the right axis (linear scale) and include lightning detected within 250 km of the volcano. The timing of lightning rings described by Van Eaton et al. (2023) is indicated by two horizontal lines. Heights of the tropopause (~17 km) and stratopause (~43 km) are shown as dashed lines on the plume height axis, given in km above sea level (asl).* Red line *shows barometric pressure (millibars, mb) recorded at Nuku'alofa (Tongatapu) from 04:00-08:00 UTC (Purkis et al., 2023), with pressure drops indicating major explosions at Hunga.* Blue wave *indicates the timing of tsunamis on Tongatapu (Purkis et al., 2023; Wu et al., 2025).* Green bar *indicates the timing (~14:30 UTC) and vertical extent (~38–54 km) of the first Hunga water vapor detection by the Aura/Microwave Limb Sounder (MLS).* Blue circles *indicate Hunga plume heights determined from Constellation Observing System for Meteorology, Ionosphere, and Climate (COSMIC)-2 radio occultation (RO) measurements, which are sensitive to atmospheric moisture (Babu and Lin, 2023).* Red stars *on the time axis indicate the inferred times that the domestic (D) and international (I) seafloor telecommunications cables in Tonga were broken by submarine volcaniclastic density currents (Clare et al., 2023); (b) Satellite observations of volcanic plume and lightning development during the 15 January 2022 Hunga eruption, with times shown in UTC.* Grayscale *gives stereoscopic cloud heights derived from geostationary satellite imagery (NOAA/GOES-17 and JMA/Himawari-8),* blue dots *show lightning flashes detected by ground-based radio frequency networks over the following minute, and* purple-yellow color scale *shows optically detected lightning from the Geostationary Lightning Mapper (GLM) sensor on GOES-17. (*) indicates frames with optically detected lightning.* Pink circles *outline a distinctive lightning ring in two frames, showing an (average) expansion rate exceeding 60 m s^{-1}. Westward advection of the upper umbrella cloud starts to reveal a lower level cloud by 05:37 UTC.* White dashed polygons *outline the lightning locations, showing their westward movement with the stratospheric umbrella cloud. Local islands are outlined in black. Figure modified from Van Eaton et al. (2023).*

Analysis of gravity data derived from satellite altimetry before and after the 2022 eruption suggests that the Hunga magmatic system consisted of multiple magmatic reservoirs that were tapped and reorganised during the 2021–2022 events, and that eruptible magma remains below Hunga post-2022 (Le Mével et al., 2023). International research cruises are planned in the coming years to further map and sample the extensive submarine deposits from the 2022 Hunga eruption, in order to elucidate the dominant volcanic processes during the eruption and refine estimates of eruption magnitude (Section 1.2.3).

1.2.3 Eruption magnitude assessment

Assessment of the size or magnitude of a volcanic eruption is a critical step that permits comparison with other historic and prehistoric events and analysis of the relationship between eruption magnitude and frequency on various timescales. Two quantities that are commonly used to define the scale of an eruption are magnitude (the total mass or volume of material erupted) and intensity (the mass eruption rate, MER [kg s^{-1}]), both of which can be estimated for modern and ancient eruptions (Pyle, 2015). The most widely used eruption magnitude scale is the VEI, which is an integer scale from 0 to 8 that is assigned based on the erupted volume of juvenile material (tephra) or the eruption column height (Newhall and Self, 1982). Measurement of erupted mass or volume (e.g., based on mapping of deposits in the field or inferred from caldera volume) provides the most robust indication of VEI and is the technique primarily used to assign VEIs to eruptions prior to the era of satellite observations. For modern eruptions, a common approach is to use a well-established relationship between eruption column height in the atmosphere and intensity or MER (Mastin et al., 2009); satellite observations of column height are integrated over the duration of an eruption to estimate the total erupted mass. Due to the complexities of magma–water interaction, which can modify eruption dynamics and plume rise heights (Mastin et al., 2024; Rowell et al., 2022), it can be challenging to rely solely on atmospheric column height to estimate the VEI of submarine eruptions. One limitation of the VEI scale is that it is discrete; continuous scales of magnitude and intensity have been defined based on the logarithm of erupted mass and mass eruption rate, respectively (Pyle, 2015). For reference, the 1991 Pinatubo eruption erupted a total bulk volume of 8.4–10.4 km^3 (3.7–5.3 km^3 dense rock equivalent, DRE), resulting in a VEI of 6 and a magnitude of 6.1.

Assessment of magnitude for submarine volcanic eruptions is inherently more challenging than for

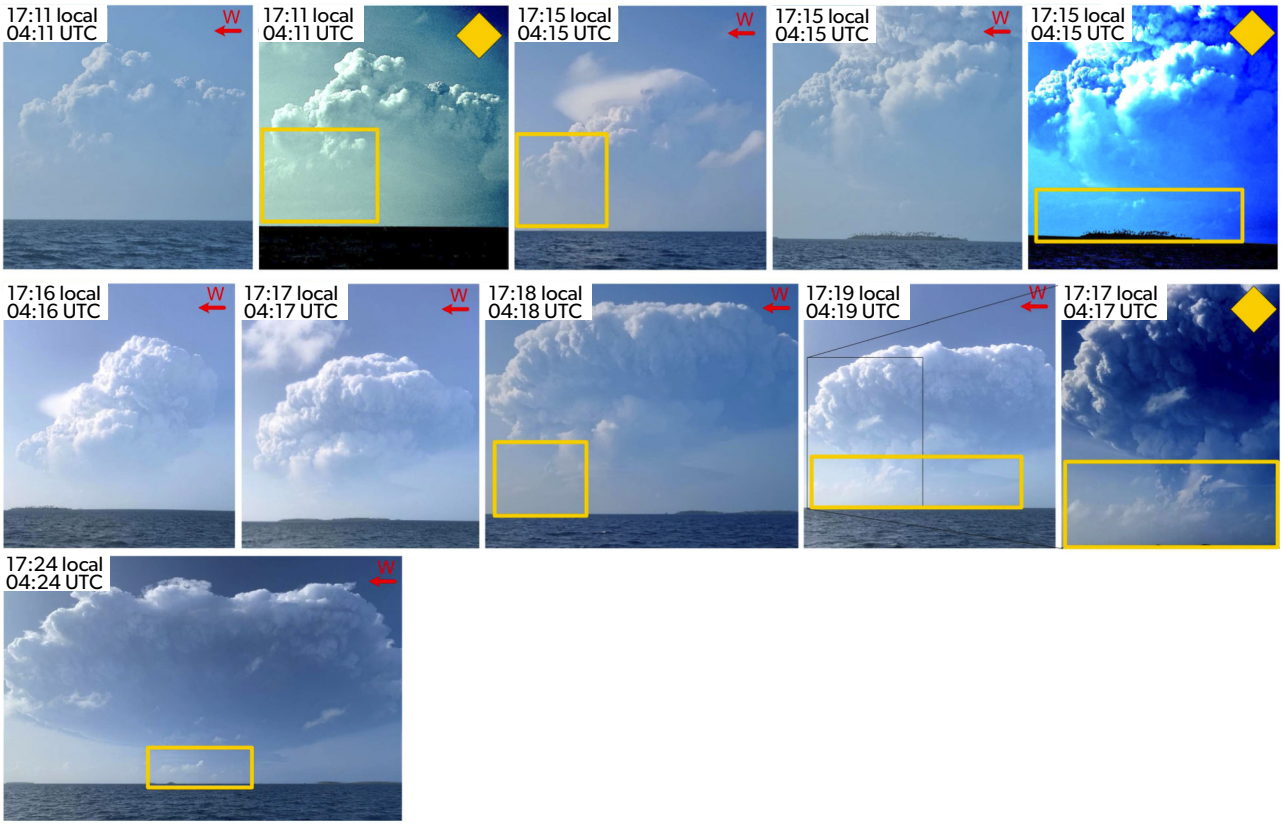

Figure 1.4: *Photographs of the 15 January 2022 Hunga eruption plume (taken by Branko Sugar, South Sea Charters, Nuku'alofa, using a mobile phone). Images marked with a yellow diamond have had contrast or colors enhanced to clarify features in the eruption plume. Red arrows point westward. Images at 04:11 UTC show the initial explosive event and the possible onset of column collapse on the western side of the plume (*yellow boxes*). After the larger explosion at 04:15 UTC the eruption column grows substantially, with skirt clouds at the base of the column indicating column collapse from the plume margins into the ocean and/or steam clouds rising from submarine pyroclastic flows (*yellow boxes*). Similar skirt clouds are also observed in images taken at 04:18, 04:19 and 04:24 UTC. Figure taken from Clare et al. (2023).*

subaerial eruptions. This is due to the difficulty of quantifying the mass or volume of erupted material emplaced underwater and the volume of ashfall deposited over the open ocean. Initial estimates of the magnitude of the Hunga eruption were thus based on satellite observations of eruption column height and inferred from the seismic energy released by the paroxysmal explosions (Table 1.1). Although the 2021–2022 Hunga eruptions comprised several discrete explosive events (19 December 2021, 13–14 January 2022, and 15 January 2022), the eruption magnitude is assigned based on the paroxysmal event that began at 04:14:45 UTC on 15 January 2022 (Matoza et al., 2022). This event generated both the highest volcanic plume (~57–58 km altitude) and the fastest-growing umbrella cloud (reaching 450 km diameter within 50 min) observed in the satellite era (Figure 1.3; Proud et al., 2022; Mastin et al., 2024; Prata et al., 2025). The maximum Hunga plume height and umbrella cloud growth rate exceeded the climactic 1991 Pinatubo plume by 10–20 km and 60%, respectively (Mastin et al., 2024; Prata et al., 2025). Based on conventional relationships between umbrella-growth rate and MER (which, notably, were not calibrated using any large submarine volcanic eruptions or plume heights over 35–40 km), the estimated paroxysmal Hunga MER was ~5–6 × 10^9 kg s^{-1}, which would theoretically have injected 7.2–8.6 km^3 of tephra (DRE) in 1 hour, exceeding the ~5 km^3 (DRE) erupted by Pinatubo in 1991 (Van Eaton et al., 2023; Mastin et al., 2024). However, mapping of tephra fall deposits on islands in Tonga and analysis of ocean discoloration by ashfall yielded a minimum bulk airfall volume of only 1.8 km^3 (0.36–0.75 km^3 DRE; Figure 1.5; Kelly et al., 2024).

Subsequent bathymetric mapping of Hunga volcano revealed a large crater or caldera-collapse structure ~850 m deep (~700 m deeper than the pre-eruption

Table 1.1: *Estimates of magnitude, energy release and volume for the 2022 Hunga eruption.*

Magnitude/VEI/Energy	Volume (km^3)	Technique	Reference
M_s 5.8		Surface seismic waves	USGS NEIC (real-time)
VEI 6		Seismic explosion impulse	Poli and Shapiro (2022)
M_w 5.7–5.8		Seismic data inversion	International Seismological Centre (2022)
M_w 6.34		Seismic data inversion	Thurin et al. (2022)
10–28 EJ		Surface pressure inversion	Wright et al. (2022)
	10	Submarine deposits (total, bathymetry)	Seabrook et al. (2023)
	6.3	Submarine deposits (uncompacted)	Seabrook et al. (2023)
	6.0	Caldera volume (DRE)	Seabrook et al. (2023)
	3.5	Loss from outer flanks (uncompacted)	Seabrook et al. (2023)
	0.4–0.8	Airfall volume estimate (DRE)	Kelly et al. (2024)
	0.03–0.6	Airfall volume (based on sea salt deposits, DRE)	Colombier et al. (2023)

VEI = volcanic explosivity index; M_s = surface wave magnitude; M_w = moment magnitude; EJ = exajoules (1 EJ = 10^{18} J); DRE = dense rock equivalent.

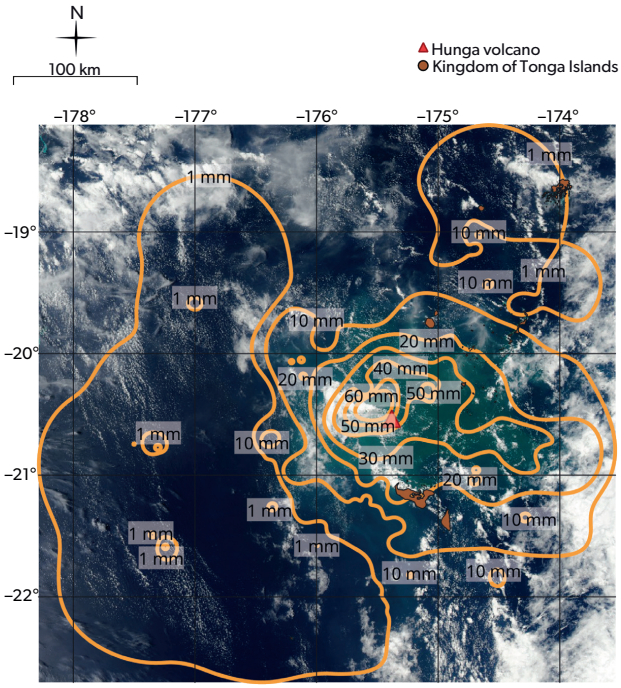

Figure 1.5: *Contour (isopach) map of Hunga ashfall (thickness in millimeters, mm) overlain on a true-color image from NASA's Aqua/Moderate Resolution Imaging Spectroradiometer (MODIS) on 17 January 2022 at 01:42 UTC. Aqua/MODIS image shows ocean discoloration around Hunga volcano (*red triangle*) due to suspended volcanic ash in the water column. Tephra thicknesses are derived from direct measurements on islands, and inferred from MODIS satellite observations of ocean discoloration over the open ocean. Figure from Kelly et al. (2024).*

seafloor), 4 km in diameter and ~6.85 km^3 in volume (Figure 1.6), with 6.3 km^3 of uncompacted deposits emplaced on the volcano's flanks by submarine density currents (Wu et al., 2025; Clare et al., 2023; Seabrook et al., 2023, Table 1.1). Note that it remains uncertain whether the submarine void produced by the eruption is a caldera (implying structural collapse after magma removal) or an explosion crater (excavated by phreatomagmatic activity), or if it was formed by a combination of processes (Walker and de Ronde, 2024). This interpretation also impacts estimates of the relative volume of juvenile (i.e., fresh magma) and pre-existing material discharged by the eruption. Combining the airfall tephra and submarine deposit volumes yields a total bulk erupted volume of ~8 km^3 for the 15 January 2022 Hunga eruption, with most (~75%) of the deposits emplaced by submarine gravity currents. A bulk volume of ~8 km^3 suggests that the 2022 Hunga eruption was a high-end VEI 5 event, as currently listed in (Global Volcanism Program, 2024). Alternatively, assuming that the caldera collapse volume (~6.85 km^3) represents the DRE eruption volume yields a VEI of 6 (Wu et al., 2025). Given the uncertainties on eruption volumes, it is therefore likely that the 2022 Hunga eruption was a similar magnitude to the 1991 Pinatubo eruption (VEI 6), and certainly larger than other VEI 5 eruptions since 1979 (Table 1.2). Estimates of juvenile magma discharge into the atmosphere based on sea salt deposition on tephra (~0.03–0.6 km^3; Colombier et al., 2023) are broadly consistent with the estimated airfall tephra volume (Kelly et al., 2024, Table 1.2).

Seismic energy released by the paroxysmal explosive phase of the 15 January 2022 Hunga eruption was also used to provide rapid (near real-time) estimates of earthquake magnitude, which were an early indic-

Table 1.2: *Major (VEI 5+) volcanic eruptions since 1979.*

Eruption	Date	VEI	Volume (bulk, km^3)	Volume (DRE*, km^3)	Reference
Hunga (Tonga)	Jan 15, 2022	5–6	8	6?	Seabrook et al. (2023)
Cordon Caulle (Chile)	Jun 2011	4–5	2.4	–	Delgado et al. (2019)
Cerro Hudson (Chile)	Aug 1991	5	4.3	2.7	Kratzmann et al. (2009)
Pinatubo (Philippines)	Jun 1991	6	8.4–10.4	3.7–5.3	Scott et al. (1996)
El Chichón (Mexico)	Mar–Apr 1982	5	2.2	1.1	Carey and Sigurdsson (1986)
Mt St Helens (USA)	May 1980	5	1.3	–	Tilling et al. (1990)

*DRE: dense rock equivalent (i.e., void-free).

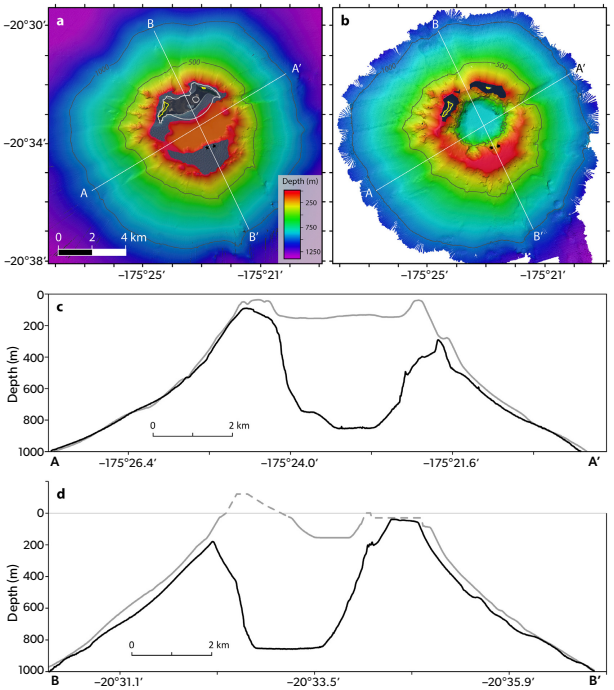

Figure 1.6: *Changes to the seafloor due to the 15 January 2022 Hunga eruption: (a) pre-eruption bathymetry from 2016. White polygon outlines HTHH island in early January 2022, including its crater lake (Figure 1.2d). Depth color scale and scale bar are the same for (b). Transects A-A' and B-B' (*white lines*) show locations of depth profiles shown in (c) and (d), respectively. (b) Post-eruption bathymetry mapped by USV Maxlimer in July/August 2022 (NIWA-Nippon Foundation TESMaP project, 2023) (c) depth profiles along line A-A' from 2016 (gray) and 2022 (black); (d) depth profiles along line B-B' from 2016 (gray, dashed line estimates height of HTHH island built during 2015 eruption and south rim shoal that was too shallow to map in 2016) and 2022 (black). Yellow polygons in (a) and (b) show remaining above-sea-level extent of the HTHH islands, post-eruption. Figure taken from Henley et al. (2024).*

ation of the size of the event (Table 1.1). Although earthquake magnitudes are not appropriate for scaling volcanic eruptions (Ringler et al., 2023), Poli and Shapiro (2022) used broadband seismic data to measure the paroxysmal explosion impulse and derive a magnitude of 5.8 (VEI 6) for the Hunga eruption (Table 1.1). Magnitudes derived from seismic data are thus consistent with the VEI derived from measurements of erupted volume.

Although, in volumetric terms, the Hunga eruption was not exceptional relative to other major volcanic eruptions of recent decades, it is the size of the paroxysmal explosion on 15 January 2022 that sets it apart from other events in the modern geophysical record. Wright et al. (2022) estimated a single-event energy release from the initial explosion on 15 January 2022 of 10–28 exajoules (EJ; 1 EJ = 10^{18} J), likely larger than the 1991 Pinatubo eruption (~10 EJ), and possibly comparable to the 27 August 1883 Krakatau explosion (~30 EJ). The 2022 Hunga eruption generated a broad range of atmospheric waves, including external Lamb waves, acoustic waves and internal gravity waves (see Chapter 6). The 1883 Krakatau and 1991 Pinatubo eruptions also produced strong Lamb waves visible in surface pressure observations. Global propagation of infrasound and Lamb waves were also reported for VEI ≥ 5 eruptions at Bezymianny (Russia) in 1956, Mt. St. Helens (USA) in 1980, and El Chichón (Mexico) in 1982 (Vergoz et al., 2022). The surface-guided Lamb wave generated by the 15 January 2022 Hunga eruption was observed propagating for four passages around the Earth over six days, approximately the same as observed for the 1883 Krakatau eruption (Matoza et al., 2022). The atmospheric pressure pulse generated by the Hunga eruption was found to be comparable to that of the 1883 Krakatau eruption, although the Krakatau pulse was approximately 30% longer in duration at comparable stations (Matoza et al., 2022). Accounts of audible sound were reported at distances of up to ~17,000 km from Hunga (Matoza et al., 2022; Kraft et al., 2023), compared to ~4,800 km for Krakatau in 1883.

The driving mechanism responsible for the par-

oxysmal Hunga explosion and exceptional plume height remains a subject of debate. Mastin et al. (2024) propose that steam (i.e., evaporated seawater) rising from intense phreatomagmatic jets and/or submarine pyroclastic density currents was the principal source of heat that boosted the height of the Hunga eruption plume (as opposed to hot tephra that supplies heat in subaerial eruptions). Such a process would be consistent with the relatively modest tephra-fall deposits, and with the presence of high concentrations of sea salts in Hunga tephra collected shortly after deposition, which is attributed to significant seawater evaporation during the eruption (Colombier et al., 2023). It would also provide a mechanism for the stratospheric injection of sea salt (Colombier et al., 2023; Vernier et al., 2025). Henley et al. (2024) invoke a non-phreatomagmatic eruption trigger whereby the eruption was driven by the explosive release of pressurized magmatic gases trapped beneath a sealed carapace. However, this theory is difficult to reconcile with the persistent activity at Hunga in the month prior to the 15 January 2022 eruption, including the large eruption on 13–14 January, which indicate a more open volcanic system.

The Mastin et al. (2024) model requires input of ~2900 Tg of steam during the first hour of the 15 January 2022 eruption to propel the Hunga plume to the observed altitude (Figure 1.3; Wu et al., 2025). Petrological analyses of Hunga tephra suggest that a maximum of 319 Tg of water would have degassed from the magma during the eruption (Figure 1.7; Wu et al., 2025), i.e., an order of magnitude less than the required mass of steam, confirming that evaporated seawater was the dominant source of WV in the Hunga plume. Petrological data also elucidate the sulfur budget of the Hunga eruption (Wu et al., 2025). Measurements of sulfur concentrations in Hunga tephra indicate that the magma degassed up to ~19 Tg of SO_2 during the eruption, but only ~7% of this SO_2 (1.3 Tg) entered the atmosphere, with the rest likely absorbed by the ocean or sequestered on ash deposits (Figure 1.7; Wu et al., 2025). The implication is that, had the 2022 Hunga eruption been subaerial rather than submarine, the stratospheric SO_2 injection might have been comparable to the 1991 Pinatubo eruption.

1.2.4 Response to the 2022 Hunga eruption

Rapid responses to collect in-situ observations after major volcanic eruptions enable timely, initial estimates of potential climate impacts and also provide critical opportunities to advance volcano science

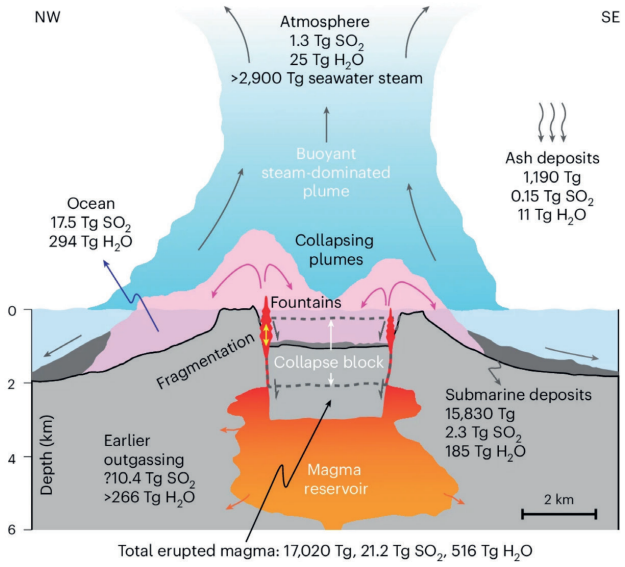

Figure 1.7: *Conceptual model of the 15 January 2022 Hunga eruption showing the initial mass of sulfur dioxide (SO_2) and water (H_2O) in the erupted magma and its final partitioning into pre-eruption outgassing, elements trapped within volcanic deposits, and gas released into the atmosphere and ocean. These values are based on a magma volume of 6.75 km^3 and concentrations of volatiles in the magma preceding the eruption estimated by analysis of melt inclusions. The calculated atmospheric injection of 1.3 Tg SO_2 is close to the upper limit of SO_2 emission estimated from satellite measurements (Carn et al., 2022; Sellitto et al., 2022; Sellitto et al., 2024). Magma fragmentation mainly occurred 400–1,000 m below sea level. The position of the pre-eruption caldera floor is shown by a* dotted line*, with the final position indicating that a 1-km block collapse occurred onto the emptying magma reservoir. Figure from Wu et al. (2025).*

(NASEM, 2017). NASA has developed a volcanic eruption response plan to maximize the quantity and quality of observations it makes following major eruptions (Carn et al., 2021). Activation of an eruption response is primarily contingent on the magnitude and altitude of volcanic SO_2 emissions measured by satellites. On the basis of prior eruptions, NASA considers that an injection of ~5 teragrams (5 Tg; 5 million metric tons) of SO_2 or more into the stratosphere has sufficient potential for climate forcing of -1 W m^{-2} and warrants the deployment of substantial observational assets, including rapid response balloons and high-altitude aircraft (Carn et al., 2021). Although the 2022 Hunga eruption was undoubtedly a major event, early satellite measurements of SO_2 loading well below the ~5 Tg threshold (~0.5–1 Tg; Carn et al., 2022; Sellitto et al., 2022; Sellitto et al., 2024) suggested that significant climate impacts were unlikely, precluding an imme-

diate NASA response. Additional complications were the exceptional plume height (~30–58 km), which is above the ceiling of high-altitude research aircraft, and the southern hemisphere location of the eruption, limiting available sites for ground-based observations of the Hunga eruption plume.

The principal rapid response to the 2022 Hunga eruption from the atmospheric sciences community involved balloon sonde flights and lidar measurements from the high-altitude Maïdo Atmospheric Observatory on La Réunion (21.1°S, 55.3°E), ~8000 miles west of Tonga (Kloss et al., 2022; Asher et al., 2023; Baron et al., 2023). These observations sampled the stratospheric Hunga SO_2 and aerosol plume as it drifted west from the volcano, 7–10 days after the 15 January 2022 eruption. The U.S. National Oceanic and Atmospheric Administration (NOAA) Earth Radiation Budget program's Baseline Balloon Stratospheric Aerosol Profiles (B^2SAP) project supported the Tonga volcano Rapid Response Experiment (TR^2Ex) on Réunion (Asher et al., 2023), which was coordinated with additional sonde and lidar measurements at the Maïdo Observatory (Kloss et al., 2022; Baron et al., 2023). TR^2Ex deployed a suite of balloon-borne instrumentation to collect high-resolution vertical profiles of SO_2, H_2O and ozone to ~30 km altitude and information on the aerosol size distribution in the plume (Asher et al., 2023). TR^2Ex instruments were unable to measure components of the volcanic plume detected above 30 km by satellite and ground-based remote sensing (Taha et al., 2022; Baron et al., 2023) as these were above the operational ceiling of balloon sondes. Later in 2022, further balloon sonde measurements of the Hunga aerosol plume as it descended in altitude were made from Bauru, Brazil (22.36°S, 49.03°W) during the NASA-supported Brazil Volcano (BraVo) project in May–August 2022 (Souza et al., 2025; Vernier et al., 2025).

The extent of airfall tephra deposits available for direct sampling was limited by land area (Figures 1.1 and 1.5), but concerted efforts were made to sample Hunga tephra as soon as possible after the 15 January 2022 eruption. Samples of Hunga ashfall were collected on islands in Tonga (including Tongatapu and islands E–NE of Hunga; Figure 1.1) between one day and two weeks after the eruption (Wu et al., 2025; Chaknova et al., 2025; Colombier et al., 2023). Airfall tephra thickness and surface density measurements were also made throughout Tonga between a few days and ~5 months after 15 January (Kelly et al., 2024). In April 2022, submarine tephra samples were collected ~100–200 km west of Hunga at depths of ~1.8–2.8 km below sea level in the Lau back-arc basin, using the ROV *Jason* (National Deep Submergence Facility, Woods Hole Oceanographic Institution; Chaknova et al., 2025). Sediment cores containing Hunga tephra were also collected from the flanks of the volcano during phase 1 of the National Institute for Water and Atmospheric Research (NIWA) – Nippon Foundation's Tonga Eruption Seabed Mapping Project (TESMaP-1) in April–May 2022 (Seabrook et al., 2023). Analyses of major elements in subaerial and submarine samples of juvenile Hunga tephra showed consistent silica (SiO_2) contents of 55–60 wt%, corresponding to basaltic andesite or andesite composition (Chaknova et al., 2025; Wu et al., 2025; Seabrook et al., 2023). This is similar to the 2009 and 2014–15 Hunga eruptions, and within the known compositional range of all historic and prehistoric Hunga eruptions and other Tofua arc magmas (~50–62 wt% SiO_2; Brenna et al., 2022). The bulk and skeletal (void-free) densities of airfall tephra were determined to be 1.12 g cm^{-3} and 2.68 g cm^{-3}, respectively (Kelly et al., 2024), the latter consistent with the density of andesite magma. A notable characteristic of all Hunga tephra samples is the dominance of fine and very fine ash particles (<100–300 μm diameter; Chaknova et al., 2025; Wu et al., 2025; Seabrook et al., 2023; Colombier et al., 2023). The predominance of fine ash, coupled with evidence of phreatomagmatic fragmentation (via MFCI) and rapid quenching below sea level (Wu et al., 2025), is indicative of a high-intensity, phreatomagmatic (i.e., phreatoplinian) eruption.

Given the submarine nature of the event, a critical component of the Hunga eruption response involved research cruises to collect bathymetric data and assess impacts to the seafloor and the status of any ongoing submarine volcanic and/or hydrothermal activity (Walker and de Ronde, 2024). Ships equipped for such a response are a limited resource, and rapid response cruises can be difficult to mobilise in remote locations (Walker and de Ronde, 2024). There are also safety concerns for vessels sailing over an active submarine volcano, and response to the Hunga eruption was further complicated by restrictions in place at the time due to the COVID-19 pandemic (Walker and de Ronde, 2024). GNS Science (New Zealand) organised the first post-eruption expedition to collect bathymetric data at Hunga volcano in April 2022 (~2.5 months after the eruption) but was forced to turn back when the multibeam sonar unit was damaged en route (Walker and de Ronde, 2024). In April–May 2022, TESMaP-1

mapped the seafloor surrounding Hunga volcano to a distance of 20 km, and collected sediment cores and seawater samples, but did not sail directly over the 2022 eruption crater due to safety concerns (Seabrook et al., 2023). The first bathymetric map revealing the large ~850 m deep crater structure formed by the Hunga eruption was produced in late May 2022 by a team from the University of Auckland (New Zealand) and Tonga Geological Services (Walker and de Ronde, 2024). In July–August 2022, TESMaP phase 2 (TESMaP-2) utilised the uncrewed surface vessel (USV) Maxlimer (SEA-KIT International) to investigate any ongoing hydrothermal or eruptive activity within the crater and map the bathymetry of the post-eruption edifice at higher spatial resolution (Figure 1.6; Walker and de Ronde, 2024).

1.3 The 2022 Hunga eruption in the context of other historic eruptions

In terms of explosivity, maximum plume height and stratospheric impact (dominated by water vapor injection) there is no analog of the 2022 Hunga eruption in the modern geophysical or instrumental era. As such, it provides the first detailed observational record for a high-intensity, explosive submarine (potentially phreatoplinian) volcanic eruption and greatly improves our understanding of the potential hazards and impacts of these events.

There are other examples of smaller submarine (or partly submarine) eruptions that show some similarities to Hunga. The 1994 eruption of Rabaul (Papua New Guinea; VEI 4) provided the first satellite measurements of an ice-dominated, stratospheric volcanic cloud with modest SO_2 loading (~0.2 Tg), attributed to the entry of seawater into the eruption vent (Rose et al., 1995). Shallow, submarine explosions at Bogoslof volcano (Alaska, USA) in 2016–17 produced ash-poor, water-rich plumes with SO_2 emissions possibly affected by scrubbing of soluble SO_2 by seawater (Lyons et al., 2019; Lopez et al., 2020). In December 2018, phreatomagmatic activity at Anak Krakatau (Indonesia) generated a sustained, lower stratospheric plume that was ice-rich and ash-poor, also with relatively low SO_2 content (~0.06 Tg; Prata et al., 2020). The January 2020 phreatomagmatic eruption of Taal volcano (Philippines) erupted through a pre-existing crater lake and produced a water-rich plume (containing ~0.2 Tg SO_2) and abundant lightning (Van Eaton et al., 2022; Perttu et al., 2023). The August 2021 eruption of Fukutoku-Oka-no-ba (Japan) produced another tephra-poor, water-rich plume from a shallow submarine vent, along with a pumice raft and new islands (~0.02 Tg SO_2; Fauria et al., 2023; Maeno et al., 2022). Despite its low tephra content, the eruption plume reached a relatively high altitude (16 km), attributed to vaporisation of seawater in the shallow submarine environment (Maeno et al., 2022). Along with Hunga, these events demonstrate the potential for shallow subaqueous eruptions to produce water- or ice-rich, but tephra- and sulfur-poor upper tropospheric or stratospheric plumes.

Given the predominance of submarine volcanism on Earth, it is certain that many explosive submarine eruptions of similar or higher magnitude to the Hunga eruption must have occurred in prehistoric times. However, if low SO_2 output is a pervasive feature of these events, then they may be poorly preserved in ice core proxy records (Wu et al., 2025), unless they also involve a significant subaerial (magmatic) component. The Santorini-Kolumbo complex (Aegean Sea, Greece) is one example of a shallow, submarine volcanic system that has been investigated in some detail. Deposits of the Late Bronze-Age (~1610 BCE) Minoan, caldera-forming eruption of Santorini (VEI 7) include Surtseyan ashfall, indicating phreatomagmatic activity when seawater gained access to the vent (Bond and Sparks, 1976). The 1650 CE submarine eruption of Kolumbo (7 km north-east of Santorini) was a VEI 5 event that generated a destructive tsunami (Cantner et al., 2014; Ulvrova et al., 2016). More recent investigations at Santorini have found evidence for a VEI 5 explosive submarine eruption in 726 CE (Preine et al., 2024), indicating that such events may be more common than previously recognised.

1.3.1 Comparison with the 1883 Krakatau eruption

Several studies have proposed the August 1883 eruption of Krakatau as a close analog of the 15 January 2022 Hunga eruption. This is based primarily on the striking similarity between the atmospheric Lamb waves and audible sounds generated by the paroxysmal Hunga explosion (~04:15 UTC on 15 January 2022) and the climactic caldera-forming event at Krakatau on 27 August 1883 (Wright et al., 2022; Matoza et al., 2022; Vergoz et al., 2022), supporting a similar eruptive process. During their climactic phases, the Hunga and Krakatau eruptions both produced at least 4 or 5 discrete, loud and energetic explosions (Self and Rampino, 1981; Self, 1992; Madden-Nadeau et al., 2021; Astafyeva et al., 2022; Purkis et al., 2023), intense lightning (Verbeek, 1885; Van Eaton et al.,

2023), maximum plume altitudes exceeding 40 km (Verbeek, 1884; Self, 1992; Proud et al., 2022), and globally observed tsunami waves (Lynett et al., 2022).

The final phase of the Krakatau eruption on 26–27 August involved at least four powerful explosions, and ejected a total of 18–21 km^3 (9–10 km^3 DRE; VEI 6) of rhyodacite ejecta (Verbeek, 1884; Self and Rampino, 1981), roughly twice the volume of the 2022 Hunga (and 1991 Pinatubo) eruption deposits and more silicic in composition than 2022 Hunga andesite. Most of the Krakatau deposits were emplaced as PDCs that entered the ocean (Verbeek, 1884), causing destructive tsunamis responsible for most of the ~36,000 fatalities around the Sunda Straits, and hot ash-cloud surges that decoupled from the PDCs and moved 40 km across the ocean surface to Sumatra (Self and Rampino, 1981; Sigurdsson et al., 1991; Self, 1992; Carey et al., 1996). Similar voluminous PDCs entering the ocean may have caused the tsunamis observed during the Hunga eruption (Seabrook et al., 2023; Clare et al., 2023; Purkis et al., 2023).

At Krakatau and Hunga, it has been proposed that the likely origin of the PDCs was collapse of the eruption column during phases of high mass flux, most likely coincident with caldera collapse (Figure 1-6; Self, 1992; Clare et al., 2023). The relatively coarse-grained nature of the Krakatau PDC deposits (ignimbrites) and paleomagnetic evidence for high emplacement temperature argue against significant magma-seawater interaction during the climactic phase of the 1883 eruption, indicating that the eruption was not phreatoplinian (Self and Rampino, 1981; Mandeville et al., 1994; Mandeville et al., 1996b). Rather, it is thought that the Krakatau PDCs were generated by a subaerial vent (via column collapse) and then entered the ocean (Sigurdsson et al., 1991), in contrast to the Hunga PDCs that were formed via collapse of an eruption column issuing from a submarine vent (Seabrook et al., 2023; Clare et al., 2023).

At Krakatau, maximum eruption column heights (estimated to be ~40–50 km) occurred during the ignimbrite phase in the morning of 27 August, and were probably supplied by co-ignimbrite plumes rising above PDCs and ash-cloud surges as they swept across (and into) the ocean (Self and Rampino, 1981; Self, 1992). These co-ignimbrite plumes would have been humidified through entrainment of moist tropospheric air and (presumably) some evaporated seawater (Carey et al., 1996; Dartevelle et al., 2002). Textural evidence suggests that the Krakatau PDCs did not significantly mix with seawater (Sigurdsson et al., 1991), so the role of seawater evaporation is debatable, although some steam was likely produced at the seawater-flow interface (Carey et al., 1996). Had the PDCs mixed with seawater, Mandeville et al. (1996b) estimated that this could have yielded ~4200 Tg of steam (and ~7.6 Tg SO_2 from seawater sulfate).

At Hunga, in contrast, evaporated seawater rising above submarine PDCs or phreatomagmatic jets has been postulated as the main source of heat that drove the plume to an altitude of 58 km, requiring ~2900 Tg of steam (Mastin et al., 2024). Hence, during both the 2022 Hunga and 1883 Krakatau eruptions, PDCs likely played a role in the generation of stratospheric plumes, but the submarine vent at Hunga would have favored a phreatoplinian eruption style without significant subaerial co-ignimbrite plumes as invoked at Krakatau. Stratospheric injection via large co-ignimbrite plumes is a hallmark of the highest magnitude subaerial explosive eruptions (VEI 6+), with direct injection via Plinian eruption columns dominant in smaller eruptions (Rampino and Self, 1982; Dartevelle et al., 2002). At Hunga, one could envisage a process whereby submarine eruption of hot magma mixing with seawater generated large quantities of steam, but rapid burial by freshly erupted material delayed the explosive expansion until sufficient overpressure was achieved, producing repetitive strong explosions via a process originally proposed by Walker (1979) for explosions generated by ocean-entering PDCs.

The 1883 Krakatau eruption destroyed most of the pre-existing island (including the Danan and Perbuwatan cones that were the main eruption vents) and formed a ~250 m deep submarine caldera (Deplus et al., 1995); shallower than the ~850 m deep 2022 Hunga caldera formed by ~700 m of subsidence (Figure 1.6). However, taking into account the pre-eruption elevation of the Krakatau edifice (~1500 ft or 500 m asl at Danan; Symons et al., 1888), the vertical change in height due to caldera collapse at Hunga and Krakatau was similar. As noted above, it remains unclear whether the void excavated by the Hunga eruption was formed entirely by caldera collapse or phreatomagmatic explosive activity or a combination of processes. Nevertheless, the similarity between the geophysical signals produced by the paroxysmal Hunga and Krakatau explosions, coupled with the suite of observations available for Hunga, may improve our understanding of the Krakatau eruption.

The atmospheric and climate impacts of the 1883 Krakatau eruption were notably different from the

2022 Hunga eruption, apparently due to a major difference in stratospheric SO_2 loading. The Krakatau eruption famously produced vivid sunsets and other atmospheric optical effects that were observed at various locations around the world up to a year after the eruption (Symons et al., 1888), whereas the Hunga eruption was unremarkable in this regard (Carn et al., 2022). This can be attributed to the much higher stratospheric sulfur loading by the 1883 Krakatau eruption, which produced clear bipolar sulfate anomalies in Greenland and Antarctic ice cores. Based on the Greenland Ice Sheet Project 2 (GISP2) ice core sulfate anomaly, Zielinski (1995) estimated a maximum stratospheric sulfate aerosol loading of 46 Tg for Krakatau, equivalent to ~30 Tg SO_2. Although such estimates are subject to significant uncertainty, this suggests a stratospheric sulfur loading of a similar order of magnitude to the 1991 Pinatubo eruption. Using petrological data, Mandeville et al. (1996b) estimated a significantly lower eruptive SO_2 yield of ~6 Tg; they suggested that ~8 Tg SO_2 potentially derived from evaporated seawater and degassing of unerupted magma would resolve some of the discrepancy. However, if the potential contribution of a sulfur-rich pre-eruptive gas phase in the Krakatau magma is considered, SO_2 yields of up to 160 Tg are possible (Scaillet et al., 2003).

Global mean stratospheric aerosol optical depth (SAOD) values reconstructed from sulfate anomalies in ice cores reach a maximum of about 0.12 after the Krakatau eruption (Toohey and Sigl, 2017), similar to the post-Pinatubo SAOD. In contrast, the relatively low SO_2 emissions from the 2022 Hunga eruption suggest that the frequency of high-magnitude explosive submarine (i.e., phreatoplinian) eruptions may be poorly represented in the ice core record (Wu et al., 2025). As noted earlier (Section 1.1.3), the 1040–1180 CE Hunga caldera-forming event has been tentatively linked to a 1108 CE sulfate anomaly in ice cores and significant (>1°C) global cooling (Cronin et al., 2017; Sigl et al., 2015); if this match is confirmed, it would suggest that the previous caldera- forming event at Hunga may have been more subaerial in character than the 2022 eruption, i.e., more similar to the 1883 Krakatau eruption.

The 2022 Hunga eruption emitted ~0.5–1 Tg of SO_2 (Carn et al., 2022; Sellitto et al., 2022; Sellitto et al., 2024), which yielded 1.6 ± 0.5 Tg of stratospheric sulfate aerosol (Sellitto et al., 2024). Whilst the timing and magnitude of SO_2 emissions from Hunga is well-constrained by satellite observations, the ice core record can only provide a reasonable estimate of the total SO_2 loading for the 1883 Krakatau eruption, and cannot resolve SO_2 emissions by individual events in the ~4 month-long eruption sequence (May–August 1883), including the multiple major explosions during the 22–24 hour climactic phase on 26–27 August (Self and Rampino, 1981; Self, 1992; Madden-Nadeau et al., 2021). Hence, the specific SO_2 loading associated with the paroxysmal Krakatau explosion at ~10:00 am (local time) on 27 August 1883 (the Hunga analog) is unknown. Self (1992) notes that atmospheric optical effects indicative of stratospheric aerosols (solar haloes and blue moons) were reported as early as July 1883 from almost 3000 km away, and were most likely sourced from Krakatau. Further optical effects were observed in South Africa in mid-August 1883, prior to the climactic phase of the eruption (Self, 1992). This suggests that significant stratospheric SO_2 injection had likely already occurred prior to 26–27 August 1883.

The main, lasting impact of the 2022 Hunga eruption was hydration of the tropical stratosphere due to the direct injection of ~150 Tg of WV (Millán et al., 2022). This is likely only a small fraction of the total amount of WV initially present in the volcanic plume (estimated to be ~2900 Tg during the first hour; Mastin et al., 2024; Wu et al., 2025), most of which was lost by freezing and ice fallout during plume ascent. Based on petrological data, total magmatic water emissions during the 1883 Krakatau eruption have been estimated at ~920 Tg (Mandeville et al., 1996a), compared to ~320 Tg magmatic water degassed from Hunga (Wu et al., 2025).

In their modelling study of the potential climate impact of stratospheric WV injection, Joshi and Jones (2009) assumed a WV injection of 500 Tg by the 1883 Krakatau eruption with a constant mixing ratio between 0 and 40 km altitude (i.e., not all the injected WV was stratospheric); the injected mass was based solely on estimates of water emissions by the 1991 Pinatubo eruption (minimum ~500 Tg magmatic water; Gerlach et al., 1996). Hence, the total stratospheric WV injection by the 1883 Krakatau eruption remains poorly constrained, but given the higher magmatic water emissions than Hunga, plus potential contributions from WV entrained into co-ignimbrite plumes (estimated to be ~2500 Tg for Pinatubo; Dartevelle et al., 2002) and seawater evaporated by PDCs (potentially up to 4200 Tg; Mandeville et al., 1996a), a stratospheric WV injection similar to or larger than Hunga seems plausible.

Further evidence for similarities in the evolution of the Hunga and Krakatau stratospheric aerosols stems from widespread purple twilight observations in the tropics after the 1883 Krakatau eruption, indicating that the aerosol descended from 32 km to 24 km in the first weeks post-eruption (Symons et al., 1888; Pernter, 1889; Wexler, 1951). The Hunga plume descent rate was remarkably similar (Sellitto et al., 2022; Legras et al., 2022), consistent with strong radiative cooling induced by stratospheric WV. Estimates of stratospheric WV injection are important in the context of discrepancies between the observed and modelled cooling following the 1883 Krakatau eruption (Knutson et al., 2006), whereby warming due to injected WV would partially offset surface cooling due to sulfate aerosols (Joshi and Jones, 2009). A similar interaction between the effects of WV and sulfate aerosols has been proposed for the 2022 Hunga eruption (Chapter 7; e.g., Sellitto et al., 2022; Schoeberl et al., 2024).

1.3.2 Summary of recent eruptions and large wildfires with radiative impacts

In the decade prior to the 2022 Hunga eruption, multiple stratospheric events—including extreme wildfires and explosive volcanic eruptions—significantly influenced the stratospheric aerosol layer and SAOD. Figure 1.8 and Table 1.3 show that between 2012 and 2022, the stratosphere was frequently impacted by either volcanic eruptions or strong wildfire events, primarily injected into the Upper Troposphere and Lower Stratosphere (UTLS) via pyro-cumulonimbus clouds (pyro-Cbs) forming above intense wildfires (Fromm et al., 2010).

Large wildfire events inject aerosols with a different composition compared to volcanic eruptions. These fire-derived aerosols typically enter the UTLS through intense pyro-convection (Fromm et al., 2010). Whereas volcanic aerosols vary in sulfur and ash content (Muser et al., 2020) and can be influenced by water content (as for the Hunga eruption), wildfire plumes are dominated by carbonaceous particles, such as black carbon. Radiative heating of these particles can lead to further lofting, enhancing their atmospheric lifetime and climatic influence (Yu et al., 2019; Ohneiser et al., 2023).

The main events in 2012–2022 with significant stratospheric impact are summarised below.

Kelut 2014 (Java, Indonesia): In February 2014, the tropical Kelut volcano (8°S, 112°E) erupted, injecting ~0.2 Tg SO_2 to altitudes above 20 km and generating an estimated global, stratospheric radiative forcing of -0.2 W/m^2. Part of the aerosol plume was entrained in the tropical pipe, impacting the stratosphere for several years (Friberg et al., 2018). Volcanic ash played a significant role for approximately three months after the injection (Vernier et al., 2016), impacting the stratospheric SO_2 lifetime and aerosol optical properties (Zhu et al., 2020).

Calbuco 2015 (Chile): Calbuco (41°S, 73°W) erupted in April 2015, emitting approximately 0.4 Tg of SO_2. sulfate aerosols were transported southwards, enhancing polar ozone depletion (Stone et al., 2017; Zhu et al., 2018). Reactive field campaigns, including airborne aerosol observations on small balloons, took place on Réunion Island within a month of the Calbuco eruption (Bègue et al., 2017), similar to the subsequent response activated after the 2022 Hunga eruption. Réunion was more favorably located for the Hunga eruption response, being directly downwind of the volcano at a similar latitude (~20°S).

British Columbia Fires 2017 (Canada): Intense wildfires in British Columbia, Canada, injected significant amounts of smoke into the lower stratosphere through pyro-convection in August 2017 (Khaykin et al., 2018). The plume circled the Earth in the northern hemisphere, with record-breaking aerosol perturbations 2–5 km above the tropopause observed over Europe in August 2017 (Ansmann et al., 2018). The aerosol plume was lofted by radiative heating to an altitude of 23 km (Yu et al., 2019). Das et al. (2021) estimated a clear-sky, global top-of-the-atmosphere (TOA) radiative forcing of -0.03 W/m² due to the stratospheric smoke aerosols.

Ambae 2018 (Vanuatu): Two eruptions at Ambae volcano (15°S, 168°E) in April and July 2018 injected ~0.4 Tg SO_2 into the lower stratosphere with injection altitudes of up to 18 km, impacting both hemispheres with elevated aerosol concentrations (Kloss et al., 2020). The respective tropical (20°N to 20°S) radiative forcing is estimated at approximately -0.13 W/m² (Malinina et al., 2021). Although the SO_2 injected was only slightly lower than that of the Hunga eruption (~0.6–1 Tg; Carn et al., 2022; Sellitto et al., 2024), Figure 1.8 shows that the Ambae eruptions had the least impact on SAOD over the past decade. Two factors likely explain this: (1) the significantly lower injection altitude at Ambae, which allowed aerosols to settle into the troposphere more quickly, and (2) the co-injection of water during the Hunga eruption, which contributed to rapid formation of sulfate aero-

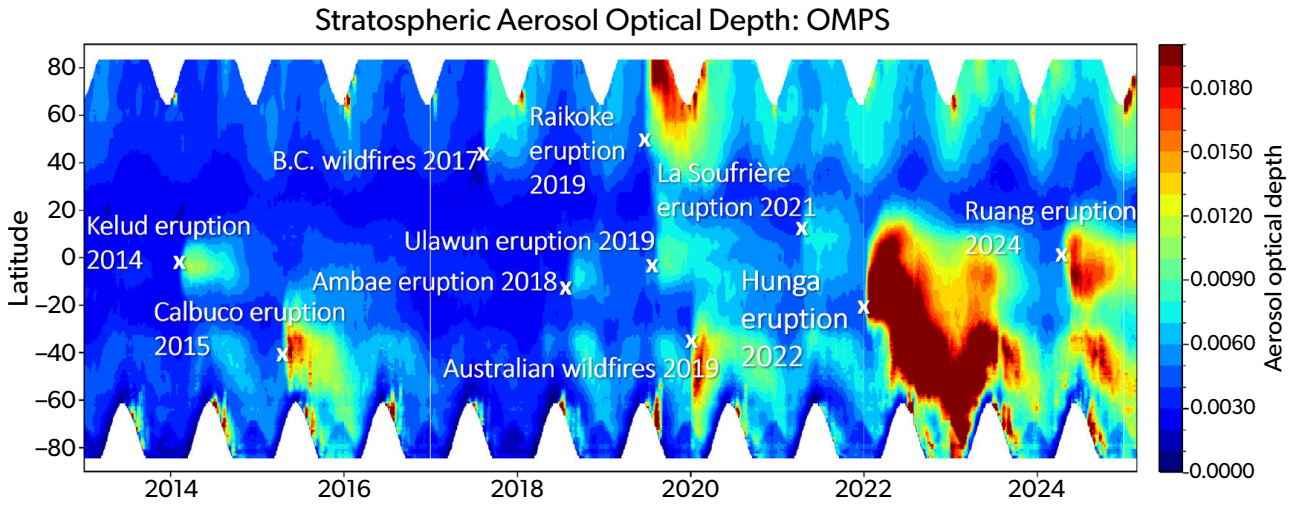

Figure 1.8: *Stratospheric Aerosol Optical Depth (SAOD) at 675 nm from Suomi National Polar-orbiting Partnership/Ozone Mapping and Profiler Suite (SNPP/OMPS) Limb-profiler (LP) version 2.0 (Taha et al., 2021) aerosol extinction observations (2012–2025). Periods of major stratospheric aerosol events, including extreme wildfires and volcanic eruptions, are indicated.*

Table 1.3: *Significant stratospheric aerosol optical depth (SAOD) perturbations in the decade preceding the 2022 Hunga eruption.*

Eruption/Wildfire	Date	Latitude	SO_2 loading (Tg)	Peak SAOD[1]
Kelut (Indonesia)	Feb 2014	8°S	0.2	0.007
Calbuco (Chile)	Apr 2015	41°S	0.4	0.01
BC Fires (Canada)	Aug 2017	42°N	–	0.006
Ambae/Aoba (Vanuatu)	Apr–Jul 2018	15°S	0.4	0.009
Raikoke (Russia)	Jun 2019	48°N	1.4	0.015
Ulawun (Papua New Guinea)	Jun–Aug 2019	5°S	0.4	0.015*
Australian Fires	Dec 2019	27–38°S	–	0.016*
Taal (Philippines)	Jan 2020	14°N	0.2	0.016*
La Soufrière (St. Vincent)	Apr 2021	13°N	0.6	0.01

[1]Monthly mean SAOD in the 60°S–60°N latitude band from the GloSSAC database (Kovilakam et al., 2020).

* The Ulawun, Australian Fire, and Taal SAOD signals merge with the earlier Raikoke anomaly.

sols (Zhu et al., 2022; Sellitto et al., 2024; Asher et al., 2023).

Raikoke (Kuril Islands, Russia) and Ulawun (Papua New Guinea) 2019: The Raikoke (48°N, 153°E) and Ulawun (5°S, 151°E) volcanoes produced near-coincident eruptions in the northern hemisphere summer of 2019. The Raikoke eruption injected around 1.5 Tg of SO_2 and 0.7 Tg of fine ash, leading to a global monthly mean radiative forcing of -0.17 W/m² (Prata et al., 2022; Vernier et al., 2024). During two Ulawun eruptions (June and August 2019), a total of ~0.4 Tg SO_2 was injected (Carn, 2024), resulting in an all-sky global radiative forcing estimate of -0.05 W/m² (Kloss et al., 2021). While the Raikoke plume was primarily distributed in the northern hemisphere, the tropical Ulawun eruptions affected the tropical stratosphere and southern mid-latitudes. A large phreatomagmatic eruption of Taal volcano (Philippines) in January 2020 (Van Eaton et al., 2022; Perttu et al., 2023) injected an additional ~0.2 Tg SO_2 into the stratosphere, overprinting the SAOD signals from the 2019 Raikoke and Ulawun eruptions and the 2019–2020 Australian Fires.

Australian Fires 2019/2020, the Black Summer': During the wildfire season in Australia, a series of pyro-Cb events injected gases and aerosols into the UTLS around New Year 2019/2020. The resulting aerosol plume caused abrupt lower stratospheric warming, not observed since Pinatubo, and led to extended recovery of the Antarctic ozone layer (Yu et al., 2021; Damany-Pearce et al., 2022; Solomon et al., 2022; Ohneiser et al., 2022). Peak TOA radiative forcing values are estimated at ~-0.3 W/m² based on satellite observations and microphysical properties (Sellitto

et al., 2022). During the Australian fires, self-induced smoke vortices' were observed, which carried ozone holes and persisted for several months (Khaykin et al., 2020; Kablick et al., 2020). Similar features may also result from volcanic eruptions with ash injections, as seen after the Raikoke eruption (Lestrelin et al., 2021; Khaykin et al., 2022). Both the 2017 British Columbia fires and the 2019–2020 Australian fires are among the strongest recorded wildfires with global stratospheric impact, comparable to moderate volcanic eruptions.

La Soufrière 2021 (St. Vincent and the Grenadines): The eruption at La Soufrière (13.3°N, 61.2°W) occurred ~9 months before the 2022 Hunga eruption, providing context for the pre-Hunga stratospheric state. The 2021 La Soufrière eruption injected an estimated 0.6 Tg SO_2 (Taylor et al., 2023), reaching altitudes between 18 and 20 km (Horváth et al., 2022). The aerosol plume contributed to an increase in smaller particles (<400 nm). The global 1-year average radiative forcing was calculated at -0.08 W/m² for clear-sky conditions and -0.04 W/m² for all-sky conditions, affecting both the tropics and northern mid-latitudes (Li et al., 2023). As shown in Figure 1.8 using OMPS-LP measurements, SAOD enhancements following the La Soufrière eruption had not entirely returned to background levels at the time of the Hunga eruption in January 2022. Compared to the background SAOD in the tropics in 2017/2018 (~0.003), the stratospheric aerosol layer remained elevated at ~0.005, roughly double the baseline value.

1.4 Summary and conclusions

As the first high-magnitude, explosive submarine eruption in the modern instrumental or satellite eras, the 15 January 2022 Hunga eruption has provided a wealth of new observations of such events that will inform responses to, and modelling of, future analogous eruptions. The Hunga eruption may yet be categorised as a phreatoplinian eruption, although we note that past eruptions in this category have been classified based solely on the eruption deposits (e.g., high proportions of fine ash particles). The Hunga eruption, where subaerial tephra deposits were limited, provides a new set of geophysical observations that may be used to further refine the criteria for a phreatoplinian event, and classify future phreatomagmatic eruptions in this category.

On the basis of observations made during the 2022 Hunga eruption, we can draw the following preliminary conclusions:

- Future phreatoplinian eruptions may not produce climatically significant SO_2 loading detectable by satellites (>5 Tg), yet may still have significant impacts on atmospheric chemistry, circulation, and climate. Volcanic eruption response plans used by NASA and others may need to be updated to account for such events, e.g., by using umbrella cloud growth rates or mass eruption rates (which are easily determined using geostationary satellite data) as additional criteria for eruption response.
- Based on observations of Hunga and other recent phreatomagmatic eruptions, phreatoplinian eruption clouds are likely to be ash-poor, although the presence of very fine ash particles produced by phreatomagmatic fragmentation remains possible. In water-rich eruptions, ash particles are rapidly stripped from the plume by hydrometeors.
- Phreatoplinian eruptions may inject water vapor, SO_2, volcanic ash, and other constituents (e.g., HCl, sea salt) into the stratosphere, potentially to very high altitudes (>50 km). The injection heights and vertical profiles of these constituents may differ temporally and spatially due to complex eruption processes (e.g., if water vapor is derived from seawater evaporation above submarine PDCs, which releases little SO_2).
- Regardless of their initial vertical profiles, constituent profiles are expected to rapidly evolve in a water-rich, phreatoplinian eruption (more rapidly than a magmatic eruption) as water freezes and/or condenses (which is dependent on plume altitude, determining temperature and water saturation). Liquid water and ice would rapidly remove volcanic ash, leaving some water vapor and SO_2. The remaining SO_2 would begin rapidly converting to sulfate aerosol in water-rich layers.
- The injection of sea salt derived from evaporated seawater may lead to enhanced concentrations of halogens (Cl, Br), with consequences for atmospheric chemistry.

References

Abbott, D. and J. L. Rubenstone (2024). 'The abundance of submarine volcanism in arcs'. *Volcanica*, 7, pp. 447–459. DOI: 10.30909/vol.07.02.447459.

Ansmann, A., H. Baars, A. Chudnovsky, I. Mattis, I. Veselovskii, M. Haarig, P. Seifert, R. Engelmann and U. Wandinger (2018). 'Extreme levels of Canadian wildfire smoke in the stratosphere over central Europe on 21–22 August 2017'. *Atmos. Chem. Phys.*, 18, pp. 11831–11845. DOI: 10.5194/acp-18-11831-2018.

Asher, E., M. Todt, K. Rosenlof, T. Thornberry, R.-S. Gao, G. Taha, P. Walter, S. Alvarez, J. Flynn, S. M. Davis et al. (2023). 'Unexpectedly rapid aerosol formation in the Hunga Tonga plume'. *Proc. Natl. Acad. Sci.*, 120, e2219547120. DOI: 10.1073/pnas.2219547120.

Astafyeva, E., B. Maletckii, T. D. Mikesell, E. Munaibari, M. Ravanelli, P. Coisson, F. Manta and L. Rolland (2022). 'The 15 January 2022 Hunga Tonga Eruption History as Inferred From Ionospheric Observations'. *Geophys. Res. Lett.*, 49, e2022GL098827. DOI: 10.1029/2022GL098827.

Babu, S. R. and N.-H. Lin (2023). 'Extreme Heights of 15 January 2022 Tonga Volcanic Plume and Its Initial Evolution Inferred from COSMIC-2 RO Measurements'. *Atmosphere*, 14, 121. DOI: 10.3390/atmos14010121.

Baron, A., P. Chazette, S. Khaykin, G. Payen, N. Marquestaut, N. Bègue and V. Duflot (2023). 'Early Evolution of the Stratospheric Aerosol Plume Following the 2022 Hunga Tonga-Hunga Ha'apai Eruption: Lidar Observations From Reunion (21°S, 55°E)'. *Geophys. Res. Lett.*, 50, e2022GL101751. DOI: 10.1029/2022gl101751.

Bègue, N., D. Vignelles, G. Berthet, T. Portafaix, G. Payen, F. Jégou, H. Benchérif, J. Jumelet, J.-P. Vernier, T. Lurton et al. (2017). 'Long-range transport of stratospheric aerosols in the Southern Hemisphere following the 2015 Calbuco eruption'. *Atmos. Chem. Phys.*, 17, pp. 15019–15036. DOI: 10.5194/acp-17-15019-2017.

Beinart, R. A., S. M. Arellano, M. Chaknova, J. Meagher, A. J. Davies, J. Lopresti, E. J. Cowell, M. Betters, T. M. Ladd, C. Q. Plowman et al. (2024). 'Deep seafloor hydrothermal vent communities buried by volcanic ash from the 2022 Hunga eruption'. *Commun. Earth Environ.*, 5, 254. DOI: 10.1038/s43247-024-01411-w.

Bohnenstiehl, D. R., R. P. Dziak, H. Matsumoto and T.-K. Lau (2013). 'Underwater acoustic records from the March 2009 eruption of Hunga Ha'apai–Hunga Tonga volcano in the Kingdom of Tonga'. *J. Volcanol. Geotherm. Res.*, 249, pp. 12–24. DOI: 10.1016/j.jvolgeores.2012.08.014.

Bond, A. and R. S. J. Sparks (1976). 'The Minoan eruption of Santorini, Greece'. *J. Geol. Soc.*, 132, pp. 1–16. DOI: 10.1144/gsjgs.132.1.0001.

Borrero, J. C., S. J. Cronin, F. H. Latu'ila, P. Tukuafu, N. Heni, A. M. Tupou, T. Kula, O. Fa'anunu, C. Bosserelle, E. Lane et al. (2023). 'Tsunami Runup and Inundation in Tonga from the January 2022 Eruption of Hunga Volcano'. *Pure Appl. Geophys.*, 180, pp. 1–22. DOI: 10.1007/s00024-022-03215-5.

Brandl, P. A., F. Schmid, N. Augustin, I. Grevemeyer, R. J. Arculus, C. W. Devey, S. Petersen, M. Stewart, H. Kopp and M. D. Hannington (2020). 'The 6–8 Aug 2019 eruption of 'Volcano F' in the Tofua Arc, Tonga'. *J. Volcanol. Geotherm. Res.*, 390, 106695. DOI: 10.1016/j.jvolgeores.2019.106695.

Brenna, M., S. J. Cronin, I. E. M. Smith, A. Pontesilli, M. Tost, S. Barker, S. Tonga'onevai, T. Kula and R. Vaiomounga (2022). 'Post-caldera volcanism reveals shallow priming of an intra-ocean arc andesitic caldera: Hunga volcano, Tonga, SW Pacific'. *Lithos*, 412-413, 106614. DOI: 10.1016/j.lithos.2022.106614.

Bryan, S. E., A. Cook, J. P. Evans, P. W. Colls, M. G. Wells, M. G. Lawrence, J. S. Jell, A. Greig and R. Leslie (2004). 'Pumice rafting and faunal dispersion during 2001–2002 in the Southwest Pacific: record of a dacitic submarine explosive eruption from Tonga'. *Earth Planet. Sci. Lett.*, 227, pp. 135–154. DOI: 10.1016/j.epsl.2004.08.009.

Cahalan, R. and J. Dufek (2021). 'Explosive submarine eruptions: The role of condensable gas jets in underwater eruptions'. *J. Geophys. Res.*, 126, e2020JB020969. DOI: 10.1029/2020JB020969.

Cantner, K., S. Carey and P. Nomikou (2014). 'Integrated volcanologic and petrologic analysis of the 1650 AD eruption of Kolumbo submarine volcano, Greece'. *J. Volcanol. Geotherm. Res.*, 269, pp. 28–43. DOI: 10.1016/j.jvolgeores.2013.10.004.

Carey, R., S. A. Soule, M. Manga, J. D. L. White, J. McPhie, R. Wysoczanski, M. Jutzeler, K. Tani, D. Yoerger, D. Fornari et al. (2018). 'The largest deep-ocean silicic volcanic eruption of the past century'. *Sci. Adv.*, 4, e1701121. DOI: 10.1126/sciadv.1701121.

Carey, S. and H. Sigurdsson (1986). 'The 1982 eruptions of El Chichon volcano, Mexico (2): Observations and numerical modelling of tephra-fall distri-

bution'. *Bull. Volcanol.*, 48, pp. 127–141. DOI: 10.1007/BF01046547.

Carey, S., H. Sigurdsson, C. Mandeville and S. Bronto (1996). 'Pyroclastic flows and surges over water: an example from the 1883 Krakatau eruption'. *Bull. Volcanol.*, 57, pp. 493–511. DOI: 10.1007/BF00304435.

Carn, S. A., N. A. Krotkov, B. L. Fisher and C. Li (2022). 'Out of the blue: volcanic SO_2 emissions during the 2021-2022 Hunga Tonga-Hunga Ha'apai eruptions'. *Front. Earth Sci.*, 13. DOI: 10.3389/feart.2022.976962.

Carn, S. (2024). *Multi-Satellite Volcanic Sulfur Dioxide L4 Long-Term Global Database V4*. Goddard Earth Science Data and Information Services Center (GES DISC), Greenbelt, MD, USA. Last access: 20 March 2025. DOI: 10.5067/MEASURES/SO2/DATA405.

Carn, S. A., P. A. Newman, V. Aquila, H. Gonnermann and J. Dufek (2021). 'Anticipating climate impacts of major volcanic eruptions'. *Eos*, 102. DOI: 10.1029/2021EO162730.

Carr, J. L., Á. Horváth, D. L. Wu and M. D. Friberg (2022). 'Stereo Plume Height and Motion Retrievals for the Record-Setting Hunga Tonga-Hunga Ha'apai Eruption of 15 January 2022'. *Geophys. Res. Lett.*, 49, e2022GL098131. DOI: 10.1029/2022gl098131.

Carvajal, M., I. Sepúlveda, A. Gubler and R. Garreaud (2022). 'Worldwide signature of the 2022 Tonga volcanic tsunami'. *Geophys. Res. Lett.*, 49, e2022GL098153. DOI: 10.1029/2022gl098153.

Cas, R. A. F. and J. M. Simmons (2018). 'Why deep-water eruptions are so different from subaerial eruptions'. *Front. Earth Sci.*, 6, 198. DOI: 10.3389/feart.2018.00198.

Chaknova, M., T. Giachetti, J. Paredes-Mariño, A. Soule, A. R. Van Eaton, R. Beinart, M. Crundwell, S. J. Cronin, M. Jutzeler, K. E. Fauria et al. (2025). 'How did westward volcaniclastic deposits accumulate in the deep sea following the January 2022 eruption of Hunga volcano?' *Geochem. Geophys. Geosyst.*, 26, e2024GC011629. DOI: 10.1029/2024GC011629.

Clare, M. A., I. A. Yeo, S. Watson, R. Wysoczanski, S. Seabrook, K. Mackay, J. E. Hunt, E. Lane, P. J. Talling, E. Pope et al. (2023). 'Fast and destructive density currents created by ocean-entering volcanic eruptions'. *Science*, 381, pp. 1085–1092. DOI: 10.1126/science.adi3038.

Colombier, M., B. Scheu, F. B. Wadsworth, S. Cronin, J. Vasseur, K. J. Dobson, K.-U. Hess, M. Tost, T. I. Yilmaz, C. Cimarelli et al. (2018). 'Vesiculation and quenching during Surtseyan eruptions at Hunga Tonga-Hunga Ha'apai Volcano, Tonga'. *J. Geophys Res.*, 123, pp. 3762–3779. DOI: 10.1029/2017JB015357.

Colombier, M., I. A. Ukstins, S. Tegtmeier, B. Scheu, S. J. Cronin, S. Thivet, J. Paredes-Mariño, C. Cimarelli, K.-U. Hess, T. Kula et al. (2023). 'Atmosphere injection of sea salts during large explosive submarine volcanic eruptions'. *Sci. Rep.*, 13, 14435. DOI: 10.1038/s41598-023-41639-8.

Cronin, J. F. (1971). 'Recent volcanism and the stratosphere'. *Science*, 172, pp. 847–849. DOI: 10.1126/science.172.3985.847.

Cronin, S., M. Brenna, I. Smith, S. Barker, M. Tost, M. Ford, S. Tonga'onevai, T. Kula and R. Vaiomounga (2017). 'New volcanic island unveils explosive past'. *Eos*, 98. DOI: 10.1029/2017EO076589.

Damany-Pearce, L., B. Johnson, A. Wells, M. Osborne, J. Allan, C. Belcher, A. Jones and J. Haywood (2022). 'Australian wildfires cause the largest stratospheric warming since Pinatubo and extend the lifetime of the Antarctic ozone hole'. *Sci. Rep.*, 12, 12665. DOI: 10.1038/s41598-022-15794-3.

Dartevelle, S., G. G. J. Ernst, J. Stix and A. Bernard (2002). 'Origin of the Mount Pinatubo climactic eruption cloud: Implications for volcanic hazards and atmospheric impacts'. *Geology*, 30, pp. 663–666. DOI: 10.1130/0091-7613(2002)030<0663:ootmpc>2.0.co;2.

Das, S., P. R. Colarco, L. D. Oman, G. Taha and O. Torres (2021). 'The long-term transport and radiative impacts of the 2017 British Columbia pyrocumulonimbus smoke aerosols in the stratosphere'. *Atmos. Chem. Phys.*, 21, pp. 12069–12090. DOI: 10.5194/acp-21-12069-2021.

Delgado, F., J. Kubanek, K. Anderson, P. Lundgren and M. Pritchard (2019). 'Physicochemical models of effusive rhyolitic eruptions constrained with InSAR and DEM data: A case study of the 2011-2012 Cordón Caulle eruption'. *Earth Planet. Sci. Lett.*, 524, 115736. DOI: 10.1016/j.epsl.2019.115736.

Deligne, N. I. and H. Sigurdsson (2015). 'Global Rates of Volcanism and Volcanic Episodes'. *Encyclopedia of Volcanoes, 2nd Ed.* Pp. 265–272. DOI: 10.1016/B978-0-12-385938-9.00014-6.

Delos Reyes, P. J., M. A. V. Bornas, D. Dominey-Howes, A. C. Pidlaoan, C. R. Magill and R. U. Solidum, Jr. (2018). 'A synthesis and review of historical eruptions at Taal Volcano, Southern Luzon, Philippines'.

Earth Sci. Rev., 177, pp. 565–588. DOI: 10.1016/j.Earscirev.2017.11.014.

Deplus, C., S. Bonvalot, D. Dahrin, M. Diament, H. Harjono and J. Dubois (1995). 'Inner structure of the Krakatau volcanic complex (Indonesia) from gravity and bathymetry data'. *J. Volcanol. Geotherm. Res.*, 64, pp. 23–52. DOI: 10.1016/0377-0273(94)00038-i.

Embley, R., Y. Tamura, S. Merle, T. Sato, O. Ishizuka, W. Chadwick, D. Wiens, P. Shore and R. Stern (2014). 'Eruption of South Sarigan seamount, Northern Mariana Islands: Insights into hazards from submarine volcanic eruptions'. *Oceanography*, 27, pp. 24–31. DOI: 10.5670/oceanog.2014.37.

Fauria, K. E., M. Jutzeler, T. Mittal, A. K. Gupta, L. J. Kelly, J. Rausch, R. Bennartz, B. Delbridge and L. Retailleau (2023). 'Simultaneous creation of a large vapor plume and pumice raft by a shallow submarine eruption'. *Earth Planet. Sci. Lett.*, 609, 118076. DOI: 10.1016/j.epsl.2023.118076.

Friberg, J., B. Martinsson, S. Andersson and O. Sandvik (2018). 'Volcanic impact on the climate – the stratospheric aerosol load in the period 2006–2015'. *Atmos. Chem. Phys.*, 18, pp. 11149–11169. DOI: 10.5194/acp-18-11149-2018.

Fromm, M., D. T. Lindsey, R. Servranckx, G. Yue, T. Trickl, R. Sica, P. Doucet and S. Godin-Beekmann (2010). 'The untold story of pyrocumulonimbus'. *Bull. Am. Meteorol. Soc.*, 91, pp. 1193–1209. DOI: 10.1175/2010bams3004.1.

Garvin, J. B., D. A. Slayback, V. Ferrini, J. Frawley, C. Giguere, G. R. Asrar and K. Andersen (2018). 'Monitoring and modeling the rapid evolution of Earth's newest volcanic island: Hunga Tonga Hunga Ha'apai (Tonga) using high spatial resolution satellite observations'. *Geophys. Res. Lett.*, 45, pp. 3445–3452. DOI: 10.1002/2017GL076621.

Gerlach, T. M., H. R. Westrich and R. B. Symonds (1996). 'Preeruption Vapor in Magma of the Climactic Mount Pinatubo Eruption: Source of the Giant Stratospheric Sulfur Dioxide Cloud'. *Fire and Mud: Eruptions and Lahars of Mount Pinatubo, Philippines*. Ed. by C. Newhall and R. Punongbayan. University of Washington Press, Seattle, USA.

Glaze, L. S., S. M. Baloga and L. Wilson (1997). 'Transport of atmospheric water vapor by volcanic eruption columns'. *J. Geophys. Res.*, 102, pp. 6099–6108. DOI: 10.1029/96JD03125.

Global Volcanism Program (2009). *Report on Hunga Tonga-Hunga Ha'apai (Tonga) (Venzke, E. A., and Wunderman, R., eds.)* Bulletin of the Global Volcanism Network, 34:2. Smithsonian Institution. DOI: 10.5479/si.GVP.BGVN200902-243040.

Global Volcanism Program (2022a). *Report on Hunga Tonga-Hunga Ha'apai (Tonga) (Bennis, K. L., and Venzke, E., eds.)* Bulletin of the Global Volcanism Network, 47:3. Smithsonian Institution. DOI: 10.5479/si.GVP.BGVN202203-243040.

Global Volcanism Program (2022b). *Report on Hunga Tonga-Hunga Ha'apai (Tonga) (Crafford, A. E., and Venzke, E., eds.)* Bulletin of the Global Volcanism Network, 47:2. Smithsonian Institution. DOI: 10.5479/si.GVP.BGVN202202-243040.

Global Volcanism Program (2024). *Volcanoes of the World (v. 5.2.8; 6 May 2025).* Distributed by Smithsonian Institution, compiled by Venzke, E. DOI: 10.5479/si.GVP.VOTW5-2024.5.2.

Green, D. N., L. G. Evers, D. Fee, R. S. Matoza, M. Snellen, P. Smets and D. Simons (2013). 'Hydroacoustic, infrasonic and seismic monitoring of the submarine eruptive activity and sub-aerial plume generation at South Sarigan, May 2010'. *J. Volcanol. Geotherm. Res.*, 257, pp. 31–43. DOI: 10.1016/j.jvolgeores.2013.03.006.

Gupta, A. K., R. Bennartz, K. E. Fauria and T. Mittal (2022). 'Eruption chronology of the December 2021 to January 2022 Hunga Tonga-Hunga Ha'apai eruption sequence'. *Commun. Earth Environ.*, 3, 314. DOI: 10.1038/s43247-022-00606-3.

Henley, R. W., C. E. J. de Ronde, R. J. Arculus, G. Hughes, T.-S. Pham, A. S. Casas, V. Titov and S. L. Walker (2024). 'The 15 January 2022 Hunga (Tonga) eruption: A gas-driven climactic explosion'. *J. Volcanol. Geotherm. Res.*, 451, 108077. DOI: 10.1016/j.jvolgeores.2024.108077.

Horváth, Á., J. L. Carr, D. L. Wu, J. Bruckert, G. A. Hoshyaripour and S. A. Buehler (2022). 'Measurement report: Plume heights of the April 2021 La Soufrière eruptions from GOES-17 side views and GOES-16–MODIS stereo views'. *Atmos. Chem. Phys.*, 22, pp. 12311–12330. DOI: 10.5194/acp-22-12311-2022.

Houghton, B., J. White and A. Van Eaton (2015). 'Phreatomagmatic and Related Eruption Styles'. *Encyclopedia of Volcanoes, 2nd Ed.* Pp. 537–552. DOI: 10.1016/B978-0-12-385938-9.00030-4.

International Seismological Centre (2022). *On-line Bulletin.* DOI: 10.31905/D808B830.

Joshi, M. M. and G. S. Jones (2009). 'The climatic effects of the direct injection of water vapour into the stratosphere by large volcanic eruptions'. *Atmos.*

Chem. Phys., 9, pp. 6109–6118. DOI: 10.5194/acp-9-6109-2009.

Jutzeler, M., R. Marsh, R. J. Carey, J. D. L. White, P. J. Talling and L. Karlstrom (2014). 'On the fate of pumice rafts formed during the 2012 Havre submarine eruption'. *Nat. Commun.*, 5, 3660. DOI: 10.1038/ncomms4660.

Kablick, G. P. I., D. R. Allen, M. D. Fromm and G. E. Nedoluha (2020). 'Australian pyroCb smoke generates synoptic-scale stratospheric anticyclones'. *Geophys. Res. Lett.*, 47, e2020GL088101. DOI: 10.1029/2020GL088101.

Kelly, L. J., K. E. Fauria, M. Manga, S. J. Cronin, F. H. Latu'ila, J. Paredes-Mariño, T. Mittal and R. Bennartz (2024). 'Airfall volume of the 15 January 2022 eruption of Hunga volcano estimated from ocean color changes'. *Bull. Volcanol.*, 86, 59. DOI: 10.1007/s00445-024-01744-6.

Khaykin, S. M., S. Godin-Beekmann, A. Hauchecorne, J. Pelon, F. Ravetta and P. Keckhut (2018). 'Stratospheric smoke with unprecedentedly high backscatter observed by lidars above southern France'. *Geophys. Res. Lett.*, 45, pp. 1639–1646. DOI: 10.1002/2017GL076763.

Khaykin, S., B. Legras, S. Bucci, P. Sellitto, L. Isaksen, F. Tencé, S. Bekki, A. Bourassa, L. Rieger, D. Zawada et al. (2020). 'The 2019/20 Australian wildfires generated a persistent smoke-charged vortex rising up to 35 km altitude'. *Commun. Earth Environ.*, 1, 22. DOI: 10.1038/s43247-020-00022-5.

Khaykin, S., A. Podglajen, F. Ploeger, J.-U. Grooß, F. Tence, S. Bekki, K. Khlopenkov, K. Bedka, L. Rieger, A. Baron et al. (2022). 'Global perturbation of stratospheric water and aerosol burden by Hunga eruption'. *Commun. Earth Environ.*, 3, 316. DOI: 10.1038/s43247-022-00652-x.

Kloss, C., G. Berthet, P. Sellitto, F. Ploeger, G. Taha, M. Tidiga, M. Eremenko, A. Bossolasco, F. Jégou, J.-B. Renard et al. (2021). 'Stratospheric aerosol layer perturbation caused by the 2019 Raikoke and Ulawun eruptions and their radiative forcing'. *Atmos. Chem. Phys.*, 21, pp. 535–560. DOI: 10.5194/acp-21-535-2021.

Kloss, C., P. Sellitto, B. Legras, J.-P. Vernier, F. Jégou, M. Venkat Ratnam, B. Suneel Kumar, B. Lakshmi Madhavan and G. Berthet (2020). 'Impact of the 2018 Ambae eruption on the global stratospheric aerosol layer and climate'. *J. Geophys. Res.*, 125, e2020JD032410. DOI: 10.1029/2020JD032410.

Kloss, C., P. Sellitto, J.-B. Renard, A. Baron, N. Bègue, B. Legras, G. Berthet, E. Briaud, E. Carboni, C. Duchamp et al. (2022). 'Aerosol characterization of the stratospheric plume from the volcanic eruption at Hunga Tonga 15 January 2022'. *Geophys. Res. Lett.*, 49, e2022GL099394. DOI: 10.1029/2022GL099394.

Knafelc, J., S. E. Bryan, M. W. M. Jones, D. Gust, G. Mallmann, H. E. Cathey, A. J. Berry, E. C. Ferré and D. L. Howard (2022). 'Havre 2012 pink pumice is evidence of a short-lived, deep-sea, magnetite nanolite-driven explosive eruption'. *Commun. Earth Environ.*, 3, 19. DOI: 10.1038/s43247-022-00355-3.

Knutson, T. R., T. L. Delworth, K. W. Dixon, I. M. Held, J. Lu, V. Ramaswamy, M. D. Schwarzkopf, G. Stenchikov and R. J. Stouffer (2006). 'Assessment of twentieth-century regional surface temperature trends using the GFDL CM2 coupled models'. *J. Climate*, 19, pp. 1624–1651. DOI: 10.1175/jcli3709.1.

Kovilakam, M., L. W. Thomason, N. Ernest, L. Rieger, A. Bourassa and L. Millán (2020). 'The Global Space-based Stratospheric Aerosol Climatology (version 2.0): 1979–2018'. *Earth Syst. Sci. Data*, 12, pp. 2607–2634. DOI: 10.5194/essd-12-2607-2020.

Kraft, T., O. K. A. Ling, T. Toledo, B. Scheu, S. C. Stähler, J. Clinton and S. Stange (2023). 'An Antipodal Seismic and (Infra)acoustic View from Central Europe on the 15 January 2022 Hunga–Tonga–Hunga–Ha'apai Eruption'. *Seismol. Res. Lett.*, DOI: 10.1785/0220220254.

Kratzmann, D. J., S. Carey, R. Scasso and J.-A. Naranjo (2009). 'Compositional variations and magma mixing in the 1991 eruptions of Hudson volcano, Chile'. *Bull. Volcanol.*, 71, pp. 419–439. DOI: 10.1007/s00445-008-0234-x.

Le Mével, H., C. A. Miller, M. Ribó, S. Cronin and T. Kula (2023). 'The magmatic system under Hunga volcano before and after the 15 January 2022 eruption'. *Sci. Adv.*, 9. DOI: 10.1126/sciadv.adh3156.

Legras, B., C. Duchamp, P. Sellitto, A. Podglajen, E. Carboni, R. Siddans, J.-U. Grooß, S. Khaykin and F. Ploeger (2022). 'The evolution and dynamics of the Hunga Tonga–Hunga Ha'apai sulfate aerosol plume in the stratosphere'. *Atmos. Chem. Phys.*, 22, pp. 14957–14970. DOI: 10.5194/acp-22-14957-2022.

Lestrelin, H., B. Legras, A. Podglajen and M. Salihoglu (2021). 'Smoke-charged vortices in the stratosphere generated by wildfires and their behaviour in both hemispheres: comparing Australia 2020 to Canada 2017'. *Atmos. Chem. Phys.*, 21, pp. 7113–7134. DOI: 10.5194/acp-21-7113-2021.

Li, Y., C. Pedersen, J. Dykema, J.-P. Vernier, S. Vattioni, A. K. Pandit, A. Stenke, E. Asher, T. Thornberry, M. A. Todt et al. (2023). 'In situ measurements of perturbations to stratospheric aerosol and modeled ozone and radiative impacts following the 2021 La Soufrière eruption'. *Atmos. Chem. Phys.*, 23, pp. 15351–15364. DOI: 10.5194/acp-23-15351-2023.

Lopez, T., L. Clarisse, H. Schwaiger, A. Van Eaton, M. Loewen, D. Fee, J. Lyons, K. Wallace, C. Searcy, A. Wech et al. (2020). 'Constraints on eruption processes and event masses for the 2016–2017 eruption of Bogoslof volcano, Alaska, through evaluation of IASI satellite SO_2 masses and complementary datasets'. *Bull. Volcanol.*, 82, 17. DOI: 10.1007/s00445-019-1348-z.

Lynett, P., M. McCann, Z. Zhou, W. Renteria, J. Borrero, D. Greer, O. Fa'anunu, C. Bosserelle, B. Jaffe, S. La Selle et al. (2022). 'Diverse tsunamigenesis triggered by the Hunga Tonga-Hunga Ha'apai eruption'. *Nature*, 609, pp. 728–733. DOI: 10.1038/s41586-022-05170-6.

Lyons, J. J., M. M. Haney, D. Fee, A. G. Wech and C. F. Waythomas (2019). 'Infrasound from giant bubbles during explosive submarine eruptions'. *Nat. Geosci.*, 12, pp. 952–958. DOI: 10.1038/s41561-019-0461-0.

Madden-Nadeau, A. L., M. Cassidy, D. M. Pyle, T. A. Mather, S. F. L. Watt, S. L. Engwell, M. Abdurrachman, M. E. M. Nurshal, D. R. Tappin and T. Ismail (2021). 'The magmatic and eruptive evolution of the 1883 caldera-forming eruption of Krakatau: Integrating field- to crystal-scale observations'. *J. Volcanol. Geotherm. Res.*, 411, 107176. DOI: 10.1016/j.jvolgeores.2021.107176.

Maeno, F., T. Kaneko, M. Ichihara, Y. J. Suzuki, A. Yasuda, K. Nishida and T. Ohminato (2022). 'Seawater-magma interactions sustained the high column during the 2021 phreatomagmatic eruption of Fukutoku-Oka-no-Ba'. *Commun. Earth Environ.*, 3, 260. DOI: 10.1038/s43247-022-00594-4.

Malinina, E., A. Rozanov, U. Niemeier, S. Wallis, C. Arosio, F. Wrana, C. Timmreck, C. von Savigny and J. P. Burrows (2021). 'Changes in stratospheric aerosol extinction coefficient after the 2018 Ambae eruption as seen by OMPS-LP and MAECHAM5-HAM'. *Atmos. Chem. Phys.*, 21, pp. 14871–14891. DOI: 10.5194/acp-21-14871-2021.

Mandeville, C. W., S. Carey and H. Sigurdsson (1996a). 'Magma mixing, fractional crystallization and volatile degassing during the 1883 eruption of Krakatau volcano, Indonesia'. *J. Volcanol. Geotherm. Res.*, 74, pp. 243–274. DOI: 10.1016/s0377-0273(96)00060-1.

Mandeville, C. W., S. Carey and H. Sigurdsson (1996b). 'Sedimentology of the Krakatau 1883 submarine pyroclastic deposits'. *Bull. Volcanol.*, 57, pp. 512–529. DOI: 10.1007/BF00304436.

Mandeville, C. W., S. Carey, H. Sigurdsson and J. King (1994). 'Paleomagnetic evidence for high-temperature emplacement of the 1883 subaqueous pyroclastic flows from Krakatau Volcano, Indonesia'. *J. Geophys. Res.*, 99, pp. 9487–9504. DOI: 10.1029/94JB00239.

Manga, M., K. E. Fauria, C. Lin, S. J. Mitchell, M. P. Jones, C. E. Conway, W. Degruyter, B. Hosseini, R. Carey, R. Cahalan et al. (2018). 'The pumice raft-forming 2012 Havre submarine eruption was effusive'. *Earth Planet. Sci. Lett.*, 489, pp. 49–58. DOI: 10.1016/j.epsl.2018.02.025.

Mastin, L. G., M. Guffanti, R. Servranckx, P. Webley, S. Barsotti, K. Dean, A. Durant, J. W. Ewert, A. Neri, W. I. Rose et al. (2009). 'A multidisciplinary effort to assign realistic source parameters to models of volcanic ash-cloud transport and dispersion during eruptions'. *J. Volcanol. Geotherm. Res.*, 186, pp. 10–21. DOI: 10.1016/j.jvolgeores.2009.01.008.

Mastin, L. G. and J. B. Witter (2000). 'The hazards of eruptions through lakes and seawater'. *J. Volcanol. Geotherm. Res.*, 97, pp. 195–214. DOI: 10.1016/s0377-0273(99)00174-2.

Mastin, L. G., A. R. Van Eaton and S. J. Cronin (2024). 'Did steam boost the height and growth rate of the giant Hunga eruption plume?' *Bull. Volcanol.*, 86, 64. DOI: 10.1007/s00445-024-01749-1.

Matoza, R. S., D. Fee, J. D. Assink, A. M. Iezzi, D. N. Green, K. Kim, L. Toney, T. Lecocq, S. Krishnamoorthy, J.-M. Lalande et al. (2022). 'Atmospheric waves and global seismoacoustic observations of the January 2022 Hunga eruption, Tonga'. *Science*, 377, pp. 95–100. DOI: 10.1126/science.abo7063.

Millán, L., M. L. Santee, A. Lambert, N. J. Livesey, F. Werner, M. J. Schwartz, H. C. Pumphrey, G. L. Manney, Y. Wang, H. Su et al. (2022). 'The Hunga Tonga-Hunga Ha'apai Hydration of the Stratosphere'. *Geophys. Res. Lett.*, 49, e2022GL099381. DOI: 10.1029/2022gl099381.

Murcray, D. G., F. J. Murcray, D. B. Barker and H. J. Mastenbrook (1981). 'Changes in stratospheric water vapor associated with the Mount St. Helens

eruption'. *Science*, 211, pp. 823–824. DOI: 10.1126/science.211.4484.823.

Muser, L. O., G. A. Hoshyaripour, J. Bruckert, Á. Horváth, E. Malinina, S. Wallis, F. J. Prata, A. Rozanov, C. von Savigny, H. Vogel et al. (2020). 'Particle aging and aerosol–radiation interaction affect volcanic plume dispersion: evidence from the Raikoke 2019 eruption'. *Atmos. Chem. Phys.*, 20, pp. 15015–15036. DOI: 10.5194/acp-20-15015-2020.

NASEM (2017). *Volcanic Eruptions and Their Repose, Unrest, Precursors, and Timing*. National Academies Press. DOI: 10.17226/24650.

Newhall, C. and S. Self (1982). 'The volcanic explosivity index (VEI) an estimate of explosive magnitude for historical volcanism'. *J. Geophys. Res.*, 87, pp. 1231–1238. DOI: 10.1029/hg002p0143.

Ohneiser, K., A. Ansmann, B. Kaifler, A. Chudnovsky, B. Barja, D. A. Knopf, N. Kaifler, H. Baars, P. Seifert, D. Villanueva et al. (2022). 'Australian wildfire smoke in the stratosphere: the decay phase in 2020/2021 and impact on ozone depletion'. *Atmos. Chem. Phys.*, 22, pp. 7417–7442. DOI: 10.5194/acp-22-7417-2022.

Ohneiser, K., A. Ansmann, J. Witthuhn, H. Deneke, A. Chudnovsky, G. Walter and F. Senf (2023). 'Self-lofting of wildfire smoke in the troposphere and stratosphere: simulations and space lidar observations'. *Atmos. Chem. Phys.*, 23, pp. 2901–2925. DOI: 10.5194/acp-23-2901-2023.

Oppenheimer, C., T. P. Fischer and B. Scaillet (2014). 'Volcanic Degassing: Process and Impact'. *Treatise on Geochemistry*. Vol. 4. Elsevier, pp. 111–179. DOI: 10.1016/b978-0-08-095975-7.00304-1.

Pernter, J. (1889). 'Der Krakatau-Ausbruch und seine Folge-Erscheinungen'. *Meteorol. Z.*, 6, 457. https://homepages.see.leeds.ac.uk/~amtgwm/Pernter_1889_Pg457.pdf.

Perttu, A., J. Assink, A. R. Van Eaton, C. Caudron, C. Vagasky, J. Krippner, K. McKee, S. De Angelis, B. Perttu, B. Taisne et al. (2023). 'Remote Characterization of the 12 January 2020 Eruption of Taal Volcano, Philippines, Using Seismo-Acoustic, Volcanic Lightning, and Satellite Observations'. *Bull. Seismol. Soc. Am.*, 113, pp. 1471–1492. DOI: 10.1785/0120220223.

Pitari, G. and E. Mancini (2002). 'Short-term climatic impact of the 1991 volcanic eruption of Mt. Pinatubo and effects on atmospheric tracers'. *Nat. Hazards Earth Syst. Sci.*, DOI: 10.5194/nhess-2-91-2002.

Poli, P. and N. M. Shapiro (2022). 'Rapid Characterization of Large Volcanic Eruptions: Measuring the Impulse of the Hunga Tonga Ha'apai Explosion From Teleseismic Waves'. *Geophys. Res. Lett.*, 49, e2022GL098123. DOI: 10.1029/2022GL098123.

Prata, A. T., A. Folch, A. J. Prata, R. Biondi, H. Brenot, C. Cimarelli, S. Corradini, J. Lapierre and A. Costa (2020). 'Anak Krakatau triggers volcanic freezer in the upper troposphere'. *Sci. Rep.*, 10, pp. 1–13. DOI: 10.1038/s41598-020-60465-w.

Prata, A. T., R. G. Grainger, I. A. Taylor, A. C. Povey, S. R. Proud and C. A. Poulsen (2022). 'Uncertainty-bounded estimates of ash cloud properties using the ORAC algorithm: application to the 2019 Raikoke eruption'. *Atmos. Meas. Tech.*, 15, pp. 5985–6010. DOI: 10.5194/amt-15-5985-2022.

Prata, F., A. T. Prata, R. Tanner, R. G. Grainger, M. Borgas and T. J. Aubry (2025). 'The radial spreading of volcanic umbrella clouds deduced from satellite measurements'. *Volcanica*, 8, pp. 1–29. DOI: 10.30909/vol.08.01.0129.

Preine, J., J. Karstens, C. Hübscher, T. Druitt, S. Kutterolf, P. Nomikou, M. Manga, R. Gertisser, K. Pank, S. Beethe et al. (2024). 'Hazardous explosive eruptions of a recharging multi-cyclic island arc caldera'. *Nat. Geosci.*, 17, pp. 323–331. DOI: 10.1038/s41561-024-01392-7.

Proud, S. R., A. T. Prata and S. Schmauß (2022). 'The January 2022 eruption of Hunga Tonga-Hunga Ha'apai volcano reached the mesosphere'. *Science*, 378, pp. 554–557. DOI: 10.1126/science.abo4076.

Purkis, S. J., S. N. Ward, N. M. Fitzpatrick, J. B. Garvin, D. Slayback, S. J. Cronin, M. Palaseanu-Lovejoy and A. Dempsey (2023). 'The 2022 Hunga-Tonga megatsunami: Near-field simulation of a once-in-a-century event'. *Sci. Adv.*, 9, eadf5493. DOI: 10.1126/sciadv.adf5493.

Pyle, D. M. (2015). 'Sizes of Volcanic Eruptions'. *The Encyclopedia of Volcanoes*. Ed. by H. Sigurdsson et al. 2nd. Elsevier, pp. 257–264. DOI: 10.1016/b978-0-12-385938-9.00013-4.

Rampino, M. R. and S. Self (1982). 'Historic Eruptions of Tambora (1815), Krakatau (1883), and Agung (1963), Their Stratospheric Aerosols, and Climatic Impact'. *Quat. Res.*, 18, pp. 127–143. DOI: 10.1016/0033-5894(82)90065-5.

Ringler, A. T., R. E. Anthony, R. C. Aster, T. Taira, B. R. Shiro, D. C. Wilson, S. De Angelis, C. Ebeling, M. Haney, R. S. Matoza et al. (2023). 'The global seismographic network reveals atmospherically coupled

normal modes excited by the 2022 Hunga Tonga eruption'. *Geophys. J. Int.*, 232, pp. 2160–2174. DOI: 10.1093/gji/ggac284.

Rose, W. I., D. J. Delene, D. J. Schneider, G. J. S. Bluth, A. J. Krueger, I. Sprod, C. McKee, H. L. Davies and G. G. J. Ernst (1995). 'Ice in the 1994 Rabaul eruption cloud: implications for volcano hazard and atmospheric effects'. *Nature*, 375, pp. 477–479. DOI: 10.1038/375477a0.

Rowell, C. R., A. M. Jellinek, S. Hajimirza and T. J. Aubry (2022). 'External Surface Water Influence on Explosive Eruption Dynamics, With Implications for Stratospheric Sulfur Delivery and Volcano-Climate Feedback'. *Front. Earth Sci.*, 10, 788294. DOI: 10.3389/feart.2022.788294.

Scaillet, B., J. F. Luhr and M. R. Carroll (2003). 'Petrological and Volcanological Constraints on Volcanic Sulfur Emissions to the Atmosphere'. *Volcanism and the Earth's Atmosphere*. Vol. 139. Geophysical Monograph. American Geophysical Union, pp. 11–40. DOI: 10.1029/139GM02.

Schoeberl, M. R., Y. Wang, G. Taha, D. J. Zawada, R. Ueyama and A. Dessler (2024). 'Evolution of the Climate Forcing During the Two Years After the Hunga Tonga-Hunga Ha'apai Eruption'. *J. Geophys. Res.*, 129, e2024JD041296. DOI: 10.1029/2024jd041296.

Scott, W. E. et al. (1996). 'Pyroclastic Flows of the June 15, 1991, Climactic Eruption of Mount Pinatubo'. *Fire and Mud: Eruptions and Lahars of Mount Pinatubo, Philippines*. Ed. by C. Newhall and R. Punongbayan. https://pubs.usgs.gov/pinatubo/index.html. Seattle, USA: University of Washington Press.

Seabrook, S., K. Mackay, S. J. Watson, M. A. Clare, J. E. Hunt, I. A. Yeo, E. M. Lane, M. R. Clark, R. Wysoczanski, A. A. Rowden et al. (2023). 'Volcaniclastic density currents explain widespread and diverse seafloor impacts of the 2022 Hunga Volcano eruption'. *Nat. Commun.*, 14, 7881. DOI: 10.1038/s41467-023-43607-2.

Self, S. (1992). 'Krakatau revisited: the course of events and interpretation of the 1883 eruption'. *GeoJournal*, 28, pp. 109–121. DOI: 10.1007/BF00177223.

Self, S. and M. R. Rampino (1981). 'The 1883 eruption of Krakatau'. *Nature*, 294, pp. 699–704. DOI: 10.1038/294699a0.

Self, S. and R. S. J. Sparks (1978). 'Characteristics of widespread pyroclastic deposits formed by the interaction of silicic magma and water'. *Bull. Volcanol.*, 41, pp. 196–212. DOI: 10.1007/bf02597223.

Sellitto, P., A. Podglajen, R. Belhadji, M. Boichu, E. Carboni, J. Cuesta, C. Duchamp, C. Kloss, R. Siddans, N. Bègue et al. (2022). 'The unexpected radiative impact of the Hunga Tonga eruption of 15th January 2022'. *Commun. Earth Environ.*, 3, 288. DOI: 10.1038/s43247-022-00618-z.

Sellitto, P., R. Siddans, R. Belhadji, E. Carboni, B. Legras, A. Podglajen and et al. (2024). 'Observing the SO_2 and sulfate aerosol plumes from the 2022 Hunga eruption with the Infrared Atmospheric Sounding Interferometer (IASI)'. *Geophys. Res. Lett.*, 51, e2023GL105565. DOI: 10.1029/2023GL105565.

Sigl, M., M. Winstrup, J. R. McConnell, K. C. Welten, G. Plunkett, F. Ludlow, U. Büntgen, M. Caffee, N. Chellman, D. Dahl-Jensen et al. (2015). 'Timing and climate forcing of volcanic eruptions for the past 2,500 years'. *Nature*, 523, pp. 543–549. DOI: 10.1038/nature14565.

Sigurdsson, H., S. Carey, C. W. Mandeville and S. Bronto (1991). 'Pyroclastic Flows of the 1883 Krakatau Eruption'. *Eos*, 72. DOI: 10.1029/90EO00286.

Sioris, C. E., A. Malo, C. A. McLinden and R. D'Amours (2016). 'Direct injection of water vapor into the stratosphere by volcanic eruptions'. *Geophys. Res. Lett.*, 43, pp. 7694–7700. DOI: 10.1002/2016GL069918.

Solomon, S., K. Dube, K. Stone, P. Yu, D. Kinnison, O. B. Toon, S. E. Strahan, K. H. Rosenlof, R. Portmann, S. Davis et al. (2022). 'On the stratospheric chemistry of midlatitude wildfire smoke'. *Proc. Natl. Acad. Sci.*, 119, e2117325119. DOI: 10.1073/pnas.2117325119.

Souza, G., J.-P. Vernier, D. Quintão, B. Biazon, F. Lopes, J. Ricardo, A. K. Pandit, R. C. Das, H. Liu, T. N. N. Knepp et al. (2025). 'Sedimentation and growth of volcanic aerosols within the Hunga plume: Insights from unique tropical in situ and satellite measurements'. *ESS Open Archive*, DOI: 10.22541/essoar.174241613.36494891/v1.

Sparks, R. S. J. et al. (1997). *Volcanic Plumes (Chapter 8: Submarine volcanism and hydrovolcanism)*. John Wiley & Sons, Inc., p. 557.

Stone, K. A., S. Solomon, D. E. Kinnison, M. C. Pitts, L. R. Poole, M. J. Mills, A. Schmidt, R. R. Neely, D. Ivy, M. J. Schwartz et al. (2017). 'Observing the impact of Calbuco volcanic aerosols on south polar ozone depletion in 2015'. *J. Geophys. Res.*, 122, pp. 11862–11879. DOI: 10.1002/2017JD026987.

Symons, G. J. et al., eds. (1888). *The Eruption of Krakatoa and Subsequent Phenomena: report of the Krakatoa committee of the Royal Society*. UK: Trübner & Company, p. 494.

Taha, G., R. Loughman, P. R. Colarco, T. Zhu, L. W. Thomason and G. Jaross (2022). 'Tracking the 2022 Hunga Tonga-Hunga Ha'apai Aerosol Cloud in the Upper and Middle Stratosphere Using Space-Based Observations'. *Geophys. Res. Lett.*, 49, e2022GL100091. DOI: 10.1029/2022gl100091.

Taha, G., R. Loughman, T. Zhu, L. Thomason, J. Kar, L. Rieger and A. Bourassa (2021). 'OMPS LP Version 2.0 multi-wavelength aerosol extinction coefficient retrieval algorithm'. *Atmos. Meas. Tech.*, 14, pp. 1015–1036. DOI: 10.5194/amt-14-1015-2021.

Taylor, I. A., R. G. Grainger, A. T. Prata, S. R. Proud, T. A. Mather and D. M. Pyle (2023). 'A satellite chronology of plumes from the April 2021 eruption of La Soufrière, St Vincent'. *Atmos. Chem. Phys.*, 23, pp. 15209–15234. DOI: 10.5194/acp-23-15209-2023.

Thurin, J., C. Tape and R. Modrak (2022). 'Multi-Event Explosive Seismic Source for the 2022 Mw 6.3 Hunga Tonga Submarine Volcanic Eruption'. *The Seismic Record*, 2, pp. 217–226. DOI: 10.1785/0320220027.

Tilling, R. I., L. Topinka and D. A. Swanson, eds. (1990). *Eruptions of Mount St. Helens: Past, Present, and Future*. Denver, CO: U.S. Geological Survey. DOI: 10.3133/7000008.

Toohey, M. and M. Sigl (2017). 'Volcanic stratospheric sulfur injections and aerosol optical depth from 500 BCE to 1900 CE'. *Earth Syst. Sci. Data*, 9, pp. 809–831. DOI: 10.5194/essd-9-809-2017.

Ulvrova, M., R. Paris, P. Nomikou, K. Kelfoun, S. Leibrandt, D. Tappin and F. McCoy (2016). 'Source of the tsunami generated by the 1650 AD eruption of Kolumbo submarine volcano (Aegean Sea, Greece)'. *J. Volcanol. Geotherm. Res.*, 321, pp. 125–139. DOI: 10.1016/j.jvolgeores.2016.04.034.

Valentine, G. (1993). 'Role of magma-water interaction in very large explosive eruptions'. *International Seminar on Physics of Vapor Explosion (Proceedings)*. https://www.osti.gov/biblio/144909. Tomakomai, Hokkaido, Japan, pp. 210–216.

Van Eaton, A. R., M. Herzog, C. J. N. Wilson and J. McGregor (2012). 'Ascent dynamics of large phreatomagmatic eruption clouds: The role of microphysics'. *J. Geophys. Res.*, 117, B03203. DOI: 10.1029/2011jb008892.

Van Eaton, A. R., J. Lapierre, S. A. Behnke, C. Vagasky, C. J. Schultz, M. Pavolonis, K. Bedka and K. Khlopenkov (2023). 'Lightning Rings and Gravity Waves: Insights Into the Giant Eruption Plume From Tonga's Hunga Volcano on 15 January 2022'. *Geophys. Res. Lett.*, 50, e2022GL102341. DOI: 10.1029/2022gl102341.

Van Eaton, A. R., C. M. Smith, M. Pavolonis and R. Said (2022). 'Eruption dynamics leading to a volcanic thunderstorm—The January 2020 eruption of Taal volcano, Philippines'. *Geology*, 50, pp. 491–495. DOI: 10.1130/g49490.1.

Vaughan, R. G. and P. W. Webley (2010). 'Satellite observations of a surtseyan eruption: Hunga Ha'apai, Tonga'. *J. Volcanol. Geotherm. Res.*, 198, pp. 177–186. DOI: 10.1016/j.jvolgeores.2010.08.017.

Verbeek, R. D. M. (1884). 'The Krakatoa Eruption'. *Nature*, 30, pp. 10–15. DOI: 10.1038/030010a0.

Verbeek, R. D. M. (1885). *Krakatau*. Batavia, p. 614. DOI: 10.2307/196734.

Vergoz, J., P. Hupe, C. Listowski, A. Le Pichon, M. A. Garcés, E. Marchetti, P. Labazuy, L. Ceranna, C. Pilger, P. Gaebler et al. (2022). 'IMS observations of infrasound and acoustic-gravity waves produced by the January 2022 volcanic eruption of Hunga, Tonga: A global analysis'. *Earth Planet. Sci. Lett.*, 591, 117639. DOI: 10.1016/j.epsl.2022.117639.

Vernier, H., D. Quintão, B. Biazon, E. Landulfo, G. Souza, V. A. Santos, J. S. F. Lopes, C. P. A. Mendes, A. S. J. D. Matta, K. P. Damaris et al. (2025). 'Balloon Observations Suggesting Sea Salt Injection into the Stratosphere from Hunga Tonga-Hunga Ha'apai'. DOI: 10.5194/egusphere-2025-924.

Vernier, J.-P., T. J. Aubry, C. Timmreck, A. Schmidt, L. Clarisse, F. Prata, N. Theys, A. T. Prata, G. Mann, H. Choi et al. (2024). 'The 2019 Raikoke eruption as a testbed used by the Volcano Response group for rapid assessment of volcanic atmospheric impacts'. *Atmos. Chem. Phys.*, 24, pp. 5765–5782. DOI: 10.5194/acp-24-5765-2024.

Vernier, J.-P., T. D. Fairlie, T. Deshler, M. Natarajan, T. Knepp, K. Foster, F. G. Wienhold, K. M. Bedka, L. Thomason and C. Trepte (2016). 'In situ and space-based observations of the Kelud volcanic plume: the persistence of ash in the lower stratosphere'. *J. Geophys. Res.*, 121, pp. 11104–11118. DOI: 10.1002/2016jd025344.

Walker, G. P. L. (1973). 'Explosive volcanic eruptions — a new classification scheme'. *Geol. Rundschau*, 62, pp. 431–446. DOI: 10.1007/bf01840108.

Walker, G. P. L. (1979). 'A volcanic ash generated by explosions where ignimbrite entered the sea'. *Nature*, 281, pp. 642–646. DOI: 10.1038/281642a0.

Walker, S. L. and C. E. J. de Ronde (2024). 'Ongoing activity at Hunga submarine volcano, Tonga: The case for better monitoring of submarine volcanoes worldwide'. *Geochem. Geophys. Geosyst.*, 25, e2024GC011685. DOI: 10.1029/2024GC011685.

Wei, L., X. Pan, E. Trasatti, M. Ao, S. Liu, C. Tolomei, G. Liu and G. Ventura (2025). 'Deformation and morphological changes before the 2021–2022 explosive eruption at Hunga Tonga-Hunga Ha'apai submarine caldera revealed by satellite remote sensing'. *Bull. Volcanol.*, 87, 17. DOI: 10.1007/s00445-025-01804-5.

Wexler, H. (1951). 'Spread of the Krakatoa volcanic dust cloud as related to the high-level circulation'. *Bull. Am. Meteorol. Soc.*, 32, pp. 48–51. DOI: 10.1175/1520-0477-32.2.48.

White, J. D. L., C. I. Schipper and K. Kano (2015). 'Submarine Explosive Eruptions'. *Encyclopedia of Volcanoes, 2nd Ed.* Pp. 553–570. DOI: 10.1016/b978-0-12-385938-9.00031-6.

Wright, C. J., N. P. Hindley, M. J. Alexander, M. Barlow, L. Hoffmann, C. N. Mitchell, F. Prata, M. Bouillon, J. Carstens, C. Clerbaux et al. (2022). 'Surface-to-space atmospheric waves from Hunga Tonga-Hunga Ha'apai eruption'. *Nature*, 609, pp. 741–746. DOI: 10.1038/s41586-022-05012-5.

Wu, J., S. J. Cronin, M. Brenna, S.-H. Park, A. Pontesilli, I. A. Ukstins, D. Adams, J. Paredes-Mariño, K. Hamilton, M. Huebsch et al. (2025). 'Low sulfur emissions from 2022 Hunga eruption due to seawater–magma interactions'. *Nat. Geosci.*, 18, pp. 518–524. DOI: 10.1038/s41561-025-01691-7.

Yeo, I. A., I. M. McIntosh, S. E. Bryan, K. Tani, M. Dunbabin, K. J. Dobson, S. J. Mitchell, P. C. Collins, M. A. Clare, H. Cathey et al. (2024). 'The 2019 pumice raft forming eruption of Volcano-F (Volcano 0403–091) and implications for hazards posed by submerged calderas'. *J. Volcanol. Geotherm. Res.*, 454, 108160. DOI: 10.1016/j.jvolgeores.2024.108160.

Yu, P., S. M. Davis, O. B. Toon, R. W. Portmann, C. G. Bardeen, J. E. Barnes, H. Telg, C. Maloney and K. H. Rosenlof (2021). 'Persistent stratospheric warming due to 2019–2020 Australian wildfire smoke'. *Geophys. Res. Lett.*, 48, e2021GL092609. DOI: 10.1029/2021GL092609.

Yu, P., O. B. Toon, C. G. Bardeen, Y. Zhu, K. H. Rosenlof, R. W. Portmann, T. D. Thornberry, R.-S. Gao, S. M. Davis, E. T. Wolf et al. (2019). 'Black carbon lofts wildfire smoke high into the stratosphere to form a persistent plume'. *Science*, 365, pp. 587–590. DOI: 10.1126/science.aax1748.

Zhu, Y., C. G. Bardeen, S. Tilmes, M. J. Mills, X. Wang, V. L. Harvey, G. Taha, D. Kinnison, R. W. Portmann, P. Yu et al. (2022). 'Perturbations in stratospheric aerosol evolution due to the water-rich plume of the 2022 Hunga-Tonga eruption'. *Commun. Earth Environ.*, 3, 248. DOI: 10.1038/s43247-022-00580-w.

Zhu, Y., O. B. Toon, E. J. Jensen, C. G. Bardeen, M. J. Mills, M. A. Tolbert, P. Yu and S. Woods (2020). 'Persisting volcanic ash particles impact stratospheric SO2 lifetime and aerosol optical properties'. *Nat. Commun.*, 11, 4526. DOI: 10.1038/s41467-020-18352-5.

Zhu, Y., O. B. Toon, D. Kinnison, V. L. Harvey, M. J. Mills, C. G. Bardeen, M. Pitts, N. Bègue, J.-B. Renard, G. Berthet et al. (2018). 'Stratospheric aerosols, polar stratospheric clouds, and polar ozone depletion after the Mount Calbuco eruption in 2015'. *J. Geophys. Res.*, 123, pp. 12308–12331. DOI: 10.1029/2018JD028974.

Zielinski, G. A. (1995). 'Stratospheric loading and optical depth estimates of explosive volcanism over the last 2100 years derived from the Greenland Ice Sheet Project 2 ice core'. *J. Geophys. Res.*, 100, pp. 20937–20955. DOI: 10.1029/95jd01751.

Zimanowski, B., R. Büttner, P. Dellino, J. D. L. White and K. H. Wohletz (2015). 'Magma-Water Interaction and Phreatomagmatic Fragmentation'. *Encyclopedia of Volcanoes, 2nd Ed.* Pp. 473–484. DOI: 10.1016/B978-0-12-385938-9.00026-2.

2 The 2022 Hunga plume – first month post-eruption

Lead authors	Elizabeth Asher Bernard Legras
Co-authors	Marie Boichu Julia Bruckert Aurélien Podglajen Ghassan Taha
Contributing authors	Alexandre Baron Simran Chopra Stéphanie Evan Neil Hindley Ákos Horváth Ali Hoshyaripour Michelle L. Santee Paul Walter Pengfei Yu Yunqian Zhu

Cite this as:

Asher, E., B. Legras et al. (2025): The 2022 Hunga plume – first month post-eruption. In APARC, 2025: The Hunga Eruption Atmospheric Impacts Report [Yunqian Zhu, Graham Mann, Paul A. Newman, William Randel (Eds.)]. APARC Report No. 11, WCRP Report No. 10/2025, DOI: 10.34734/FZJ-2025-05239, available at `https://aparc-climate.org/publications/aparc-report-no-11/`.

Key points

- A very explosive eruption (minutes to hours)
  - The plume rose rapidly through the atmosphere, overshooting to approximately 57 km altitude within the first half hour of the eruption, which occurred at approximately 4:00 UTC 15 January, 2022. The initial conditions that might explain such a high altitude are a mass proportion of 90% steam water based on simulations of the plume but this remains an open research question.
  - An unprecedented number of lightning flashes (>300,000) and lightning rate (>2,600 flashes per minute) were detected in the stratosphere over a 2-h period during the eruption, forming several rings up to a radius of 140 km.
  - Large-amplitude gravity and Lamb waves were generated by the Hunga eruption. The main Lamb waves were observed circling the globe at least four times and put this eruption in the same class as the Krakatau eruption of 1883.
- Injection of water vapour and minor components (presumably minutes; first observations within hours)
  - A remarkable feature of the Hunga eruption was the massive injection of water. The initial injection of water vapour is uncertain but is estimated to be thousands of Tg. Approximately 150 Tg of water vapour remained in the stratosphere after one day, representing an almost instantaneous increase of approximately 10% of the total mass of water in the stratosphere, which was very localised for the first weeks. The atmosphere was saturated up to at least 35 km in the immediate aftermath. These extraordinary circumstances were hypothesised but never before observed.
  - The eruption injected very minor amounts of halogens into the stratosphere and volcanic lightning, discussed above, produced nitrogen oxides (NO_x) that played a role in subsequent chemistry. The injection of halites from seawater salt remains an open research question.
- Dispersion (presumably minutes to months; first observations within hours)
  - The initial umbrella cloud dissipated entirely within 15 hours of forming, probably washed out by precipitation of ice and water, entraining the ash. The remaining plume divided into several components shortly after the eruption, with the bulk located between 24 and 32 km altitude, and with some more minor components above and below this. During the first 10 days, the main part of the plume descended as much as 4 km due to the fast cooling produced by water infrared emission, with moister parts experiencing faster descents. This cooling might also be responsible for the rapid dispersion across the equator during the first week. After two weeks (by the beginning of February and a few months thereafter), the main persistent aerosol plume stayed mostly confined to the Southern Hemisphere.
- Fast conversion to sulfates (days instead of weeks)
  - The fast conversion of SO_2 into sulfate occurred within days instead of weeks, as is usually the case in the stratosphere, due to an abundance of water vapour producing OH that accelerated the conversion. SO_2 in the moistest parts of the plume was converted faster, and the formation of the sulfate aerosol appeared complete within approximately three weeks. Except for the first two days after the eruption, satellite retrievals indicate spherical non-depolarising and non-absorbing particles and suggest a main plume composed of sulfates. The total amount of emitted SO_2 was moderate (estimated between 0.45 Tg and 1.0 Tg). The smaller SO_2 estimate (0.45 Tg) is in line with the estimated mass of the aerosol burden, based on remote sensing and in situ measurements.
- Aerosol microphysical properties (first observations within one day)
  - A consequence of the fast conversion to sulfates was fast nucleation of sulfuric acid particles, and when combined with the narrow geographic dispersion, fast growth in aerosol radius due to coagulation, reaching 0.4 μm in the main plume in a couple of weeks, instead of in four months as recorded after Pinatubo. This large particle size scatters light efficiently and produced a high AOD in the plume. After one week, water vapour enhancements had a small effect on the percent weight of sulfuric acid in the aerosol and particle radius.

Contents

2.1 Initial eruption sequence . . . 38
2.2 Volcano-generated GW (and Lamb waves) . . . 39
2.2.1 Types of waves and early observations . . . 40
2.2.2 Wave generation mechanisms, and what we can learn from the waves . . . 41
2.3 Water vapour injection . . . 42
2.4 Plume altitude and dispersion during the first month . . . 44
2.5 Rapid formation of sulfate aerosol layer . . . 47
2.6 Microphysical and optical aerosol properties . . . 49
2.7 Other plume chemical composition: minor injections of gas phase compounds and primary aerosols . . . 51
2.7.1 Halogens . . . 51
2.7.2 Lightning nitrogen oxide (NO) . . . 52
2.7.3 Ash and sea salt . . . 52
2.7.4 Ozone anomalies and the role of tropospheric transport . . . 52
2.8 Sources of uncertainty . . . 52
2.9 The value of observations . . . 53

Preamble

This chapter is devoted to the formation of the stratospheric plume and the sequence of events during the first month after the Hunga eruption, in particular the long-range wave propagation, the dispersion of the plume and the formation of sulfate aerosols. Section 2.1 describes the sequence of atmospheric events during the eruption and the first hours thereafter. Section 2.2 describes the waves that were generated and their long-range propagation around the Earth. Section 2.3 describes the exceptional injection of water vapour in the stratosphere. Section 2.4 describes the initial vertical and horizontal structure of the plume, its initial descent due to radiative cooling and its dispersion during the first month. Section 2.5 describes the unusually fast formation of sulfate aerosols in the plume. Section 2.6 describes the microphysical and optical properties of the aerosols. Section 2.7 describes the injection of other compounds, in particular halogens and ash. Section 2.8 discusses the sources of uncertainties and Section 2.9 fosters the value of systematic observations during such abrupt and intense events.

2.1 Initial eruption sequence

The climactic eruption of the Hunga Volcano occurred on 15 January 2022. A complex eruption sequence was detected by several methods and instruments between 04:00 and 05:00 UTC and a final eruption detected at around 08:30 to 08:40 UTC. The timing of the eruptions was initially derived from satellite observations of the plume development (Carr et al., 2022). However, the Hunga eruption also triggered different types of atmospheric waves (more details in Section 2.2) and produced both seismic and meteorological tsunamis. Backward ray-tracing of these waves helps constrain the precise timing of the eruption sequence. There were at least 4–5 constituent eruptive pulses during the main climactic eruption sequence. A summary of individual eruptive events of the main eruption identified from various observations is given in Table 2.1. Prior to the climactic eruption, the Hunga Volcano erupted intermittently between 19 December 2021 and 13–14 January 2022, with plume heights reaching between 15 and 18 km and producing ice-rich plumes (Gupta et al., 2022).

According to geostationary satellite observations, the plume appeared at about 04:10 UTC (Gupta et al., 2022) and ascended rapidly, reaching 25 km within 15 min and 40 km within 25 min (Proud et al., 2022). It formed an upper umbrella layer at about 34 km altitude (Figures 2.1a and 2.1b taken from Carr et al., 2022; Gupta et al., 2022; Proud et al., 2022) and a lower umbrella layer near 20 km (Proud et al., 2022). In-depth analysis of both visible and infrared satellite imagery, our own in Legras (2025) and that of Prata et al. (2025), undermine a claim that the plume was first observed at 02:57 UTC (Van Eaton et al., 2023). About half an hour after the start of the eruption (by 04:36 UTC), an overshooting dome formed, extending from 34 km up to at least 57 km (Figures 2.1a and b, Carr et al., 2022; Proud et al., 2022) with some small tendrils reaching 58 km. A plume injection at such altitudes is unprecedented in the satellite era. The corresponding volume injection rate into the umbrella exceeded 330 $km^3\ s^{-1}$ (Van Eaton et al., 2023; Mastin et al., 2024; Prata et al., 2025).

The overshooting top dropped to about 35 km over the next 10 min (Van Eaton et al., 2023). During the eruption, the umbrella cloud expanded horizontally with the radius increasing from 20 to 80 km within 20 min (Carr et al., 2022), and further increasing to a 200–250 km within 50 min (Gupta et al., 2022; Van Eaton et al., 2023). At 04:57 UTC, Himawari-8 images show a decrease in the expansion rate of the umbrella, which suggests a lower eruption rate overall or a total collapse of the eruption column (Proud et al., 2022; Jarvis et al., 2024).

During its 15 January eruption, Hunga was the dominant lightning source on Earth for at least the first hour of the event and impulsively charged the direct current global electric circuit twice (Bór et al., 2023). Lightning networks recorded up to 2615 flashes per minute in a combined dataset of the Global Lightning Detection Network (GLD360), the Earth Networks Total Lightning Location Network (ENTLN), and the World Wide Lightning Location Network (WWLLN, Van Eaton et al., 2023). There were 5000 strokes per minute detected from the GLD360 network alone (Bór et al., 2023) at its peak intensity at about 05:00 UTC. An unprecedented number of more than $3{\times}10^5$ flashes over a 2-h period was counted during the eruption, which decreased after 04:53 (Jarvis et al., 2024). The lightning appeared in a ring structure with the largest ring up to 140 km radius and at least four distinct lightning rings from 04:16–05:51 UTC, followed by a ring from 08:38–08:48 UTC with lightning pulses that persisted until 15:15 UTC (Van Eaton et al., 2023). The position of the initial rings are co-located with the phase front of outward-propagating gravity waves (GW) observed in stereoscopic cloud heights from Geostationary Operational Environment Satellite (GOES)-17 and Himawari-8. Lightning was observed between

Table 2.1: *Timing of the eruption events derived from a variety of observations and simulations.*

Timing in UTC	Method	Publication
04:08, 04:20, 04:28, 04:48, 04:55	Variations in ionospheric total electron content	Astafyeva et al. (2022)
~04:00 07:56, 08:06, 08:26, 08:36, 08:46 (final pulse)	Visible satellite channel Divergence in stereo plume-top motion vectors (1 min resolution)	Carr et al. (2022)
~04:00; ~08:40	Satellite brightness temperature (10 min resolution)	Gupta et al. (2022)
04:00–07:11 (main plume), 07:46–09:38 (2nd phase), 09:40–11:03, 12:11–13:07, (additional eruption activity)	Processed visible and infrared satellite channels, lightning detection from satellite and ground-based networks	Van Eaton et al. (2023)
04:07, 04:15, 04:22, 04:29 (main pulse), 08:40–08:45 (final pulse)	Pago Pago surface pressure, Lamb wave formation in satellite images	Horváth et al. (2024)
Complex timing of eruption events between 04:00 and 04:30; final major eruption at ~08:31	Infrasound and hydroacoustic stations. Seismic detection.	Matoza et al. (2022) Vergoz et al. (2022) Donner et al. (2023)
04:16	Seismic detection.	Poli and Shapiro (2022)
Pulses of emissions around 04:14, 04:53, 08:27	Stratospheric balloon observations of infrasound waves	Podglajen et al. (2022)
04:06, 04:18, 04:56	Tsunami simulations	Purkis et al. (2023)
Eruption peak at ~04:28	Peak of Lamb wave pulse in surface pressure stations	Wright et al. (2022)

20 and 30 km (Van Eaton et al., 2023). As lightning intensifies within mixed-phase clouds, these observations of high-altitude lightning suggest the eruption sustained for several hours an abundance of liquid water between 20 and 30 km altitude (Van Eaton et al., 2023).

The submarine nature of the eruption made the composition of the plume very unusual with respect to other recent documented eruptions. The minimum volume of tephra estimated from ocean-discoloration was about $1.8\,km^3 \pm 0.4\,km^3$, which is on the order of only ~12% of the caldera volume change (Kelly et al., 2024). Thus, the majority of the erupted material remained under the ocean surface and deposited on the seafloor by density currents (Clare et al., 2023; Seabrook et al., 2023), which resulted in an ash-poor plume compared to eruptions of similar magnitude. In contrast, a huge amount of ocean water was turned into steam and transported upwards in the plume and significantly affected the plume dynamics. One-dimensional eruption column modelling suggests that the plume was dominated by steam, see Figure 2.1c taken from Mastin et al. (2024) and Wu et al. (2025). A plausible mechanism to form such a huge amount of water vapour involves a partially collapsing eruption plume that produces large-volume pyroclastic density currents. When these hot currents entered the ocean, they transferred their thermal energy to the water, which vaporised and rose buoyantly and vigorously in the upper atmosphere (Mastin et al., 2024; Wu et al., 2025). Sea salt on ash particles collected from the islands of Tonga further highlights the unusual composition of the plume and establishes the ocean, as opposed to the magma, as the source of the water vapour in the plume (Colombier et al., 2023).

2.2 Volcano-generated GW (and Lamb waves)

Due to its exceptional explosivity (Volcanic Explosivity Index (VEI) of 5.7; Poli and Shapiro, 2022), rapid development (less than a few hours), and the deep penetration of the plume up to the mesosphere, the climactic 15 January Hunga eruption triggered the generation of a broad spectrum of atmospheric waves. These include infrasound, Lamb waves, and stratospheric GW (Matoza et al., 2022; Vergoz et al., 2022; Wright et al., 2022). In the vertical, some of these waves were detected in every atmospheric layer from the surface to the edge of space, including from the mesosphere and lower thermosphere. These waves were either excited directly by the eruption or through multi-step vertical coupling and the generation of secondary wave modes (e.g., Vadas et al., 2023, see Chapter 6). The amplitudes of the wave trains from the Hunga eruption, as well as their propagation distances (several round-the-world journeys) are unprecedented in the satellite record.

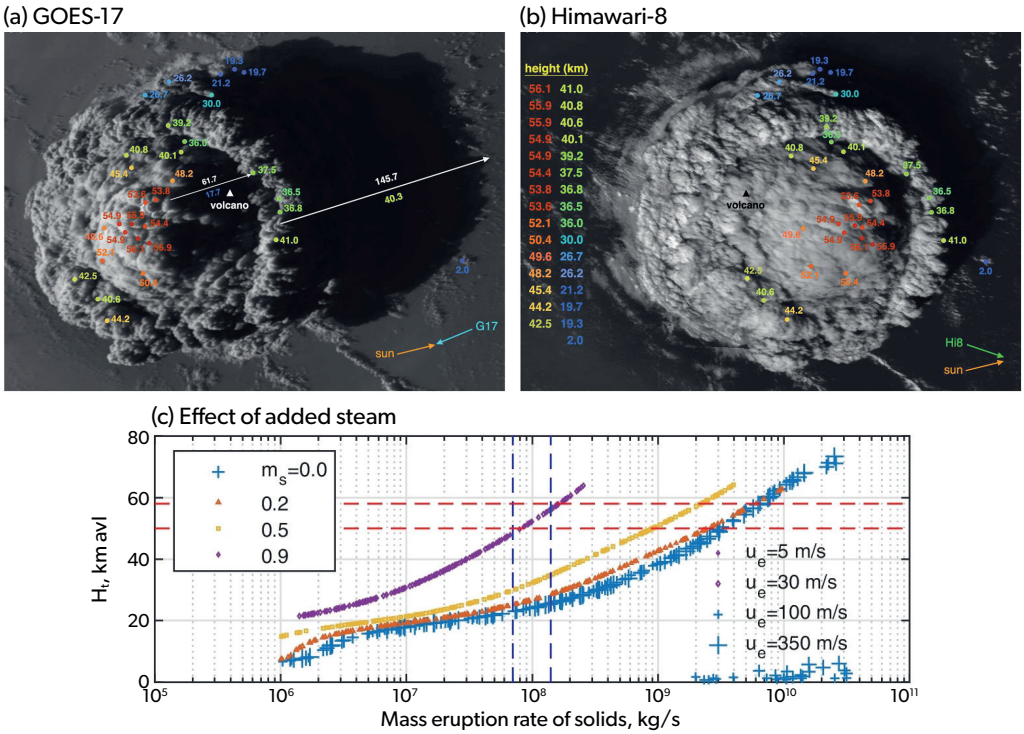

Figure 2.1: *Top row: Satellite images of the plume from (a) GOES-17 and (b) Himawari-8 on 15 January 2022 at 04:30 UTC. Coloured dots indicate stereo height estimates (in km), and the white/black triangles mark the position of the volcano. The white arrows in (a) indicate the shadow of a plume edge feature and a dome feature, with the shadow length above and the derived height below the arrow. The arrows in the lower right corners of the panels show the sun-to-pixel and satellite-to-pixel azimuths (taken from Carr et al., 2022). c) Relationship between plume top height and mass eruption rate (MER) of solids found by Monte-Carlo simulation using the 1-D volcanic plume rise model Plumeria. The different colours refer to the mass fraction of added steam (0, 0.2, 0.5, and 0.9). The red dashed lines indicate the range of plume top heights found in satellite observations. The blue dashed lines show the estimated range of the mass eruption rate derived from a comparison of fall deposit measurements with Ash3d simulations (taken from Mastin et al., 2024)*

2.2.1 Types of waves and early observations

The mesoscale patterns of atmospheric waves (excluding smaller-scale acoustic waves) can best be grasped by looking at successive maps of brightness temperature anomalies in the hours following the eruption, as shown in Figure 2.2a for the geostationary satellite Himawari (available at 10 min resolution). Concentric rings at the scale of the entire Pacific region can be clearly identified, corresponding to wave packets radiating away from the point-source volcano at different speeds. The image brings to mind the ripples that form on the surface of a pond after throwing a pebble into it, though at a very different scale. These rings have been observed in all terrestrial IR channels of geostationary satellite imagery, as well as dedicated imagers (Wright et al., 2022). According to their propagation speed, different wave types can be distinguished:

- First, Lamb wave pulses propagating at about 310 m/s. The Lamb wave is an external mode (edge wave), which can also be identified by its surface pressure signature. Global propagation of a Lamb wave was already documented from surface pressure observations after the eruption of Krakatau (VEI of 6) in 1883 (Symons et al., 1888). Fastest among the wave modes, the Lamb wave has the slowest decay time (Salby, 1979): after the Hunga eruption, the main Lamb wave pulse could be detected circling the globe at least four times (Matoza et al., 2022) and up to five times in satellite observations (Otsuka, 2022), i.e., travelling more than 100,000 km. It had a period of about 20–30 minutes (corresponding to a wavelength of about 500 km). The Lamb wave is weakly dispersive and the wave train propagation remains relatively isotropic for about half of the first transit to the antipodes, while variations in the wind, temperature and topography distort the phase lines for larger distances (Taylor, 1929; Garrett, 1969; Sepúlveda et al., 2023).

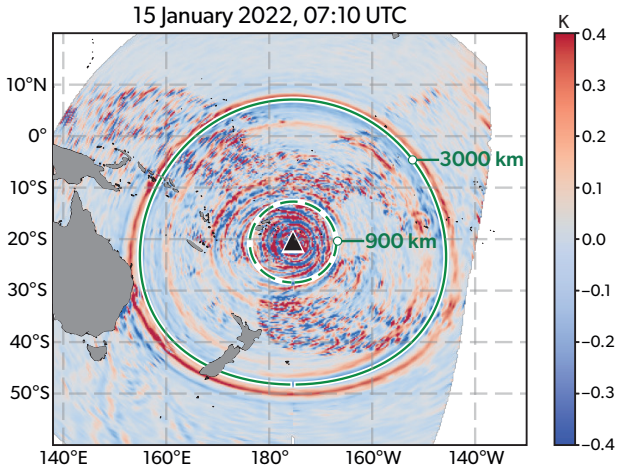

Figure 2.2: *Himawari brightness temperature second-order difference at 07:10 UTC on 15 January 2022 (channel 8), adapted after Matoza et al. (2022). Wave fronts associated with the leading Lamb wave and slower GW packets triggered by the eruption are clearly visible. Green circles are drawn to indicate equal distances from Hunga (dashed: 900 km; solid: 3,000 km).*

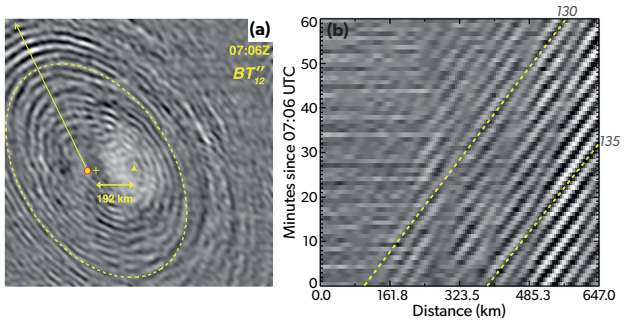

Figure 2.3: *Taken from Horváth et al. (2024), Figure 15. (a) Second-order derivative in time of the brightness temperature from GOES 17 channel 12 at 07:06 UTC filtered to emphasise the wave field and (b) time–distance plot for the period 07:06–08:06 UTC along the yellow arrow in panel (a). The interval used to calculate time derivatives is Δt = 1 min. The yellow dashed curve is an ellipse fitted to one of the concentric rings with its centre marked by the plus sign. The distance between the ellipse centre and Hunga (yellow triangle) is also indicated. The observed 192 km shift is due to advection of the wave field by the mean flow (see Horváth et al., 2024).*

- A train of slower GW with propagation speed up to 240 m/s. A noticeable feature in long-range propagation is the ~70 m/s gap in propagation speed between the Lamb wave and the fastest GW.

The leading GW packet, propagating at 240 m/s (i.e., Pekeris mode; Watanabe et al., 2022), was detected up to 10,000 km away from Hunga (Wright et al., 2022). Its decay is thus more than 10 times faster than that of the Lamb wave, in agreement with theoretical predictions (Salby, 1979). This mode is also more anisotropic than the Lamb wave, and its travel speed and dispersion depend on the propagation direction. While its signal is clearest in stratospheric temperatures, it has also been identified in surface pressure measurements (Watanabe et al., 2022).

The faster waves (Lamb wave and leading GW) are the only ones which were observed in the far field (>5,000 km away from the source). Other, slower GW are found closer to the volcano, but they cannot be traced further than 2,000 km away from Hunga. Dispersion is evident in those GW packets, with a slower and shorter-range propagation of the shorter horizontal wavelength waves. Due to their slower phase speed, shorter waves are more sensitive to the background wind, with dynamical processes such as Doppler shift or critical level filtering coming into play. Consistently, high-frequency (1 min) GOES brightness temperature imagery in the 9.6-micron band collected about three hours after the eruption reveal a rich small-scale wave field (Figure 2.2b): 50 m/s, ~5-minute period waves are observed. The distortion of the rings with a centre shifted West of Hunga is likely related to Doppler-shift by the background Westerlies (Horváth et al., 2024). Small to mesoscale GW persisted in the area of Hunga for more than 10 hours after the eruption peak, suggesting continuous generation during that period (e.g. Wright et al., 2022; Horváth et al., 2024).

2.2.2 Wave generation mechanisms, and what we can learn from the waves

The exact processes forcing the waves during the eruption and their relative importance are not entirely understood. Likely candidates include the explosions, volcanic jets and plume dynamics, as well as diabatic heating through heat exchange between the volcanic materials and surrounding air or latent heat release (i.e., through the condensation of steam water into ice). Despite remaining gaps in our understanding, gravity wave observations already provide key constraints on the eruption scenario. Precise records of the amplitude of the Lamb wave (5 hPa, 2,000 km away from the volcano) enabled estimations of the energy released by the eruption (Posey and Pierce, 1971; Matoza et al., 2022), at least relative to previous events, and showed it to be equivalent to the historical eruption of Krakatau in 1883. The waves also provide precious information on the eruption chronology, which can be most easily inferred from the

quasi-nondispersive Lamb wave. Back tracing the pressure maximum of the main Lamb pulse to the location of Hunga, it is possible to recover a time for the climax of the eruption (04:30 ± 5 min UTC, Wright et al., 2022) which falls within 5 minutes of the rising plume reaching its peak altitude (Carr et al., 2022). Besides the main Lamb waveform, earlier and later pulses of Lamb waves also bear the imprint of the complex eruption sequence, from its start between 04:00 and 04:15 UTC to a significant later explosion and plume around 08:40 UTC (Horváth et al., 2024). In general, notwithstanding time shifts related to the diversity of generation processes, there is a good correspondence between pulses of atmospheric waves and the plume dynamics inferred from geostationary satellites (Podglajen et al., 2022), or seismic activity (Vergoz et al., 2022). Further exploiting the waves to better constrain eruptive processes will require an interdisciplinary effort between volcanologists and atmospheric GW scientists.

2.3 Water vapour injection

A defining characteristic of the energetic underwater Hunga eruption was the amount of water vapour injected to high altitudes in the stratosphere (Table 2.2; Millán et al., 2022; Sellitto et al., 2022; Vömel et al., 2022; Khaykin et al., 2022; Randel et al., 2023). Steam (estimated to be more than 2900 Tg) likely accounted for 90% of the total injected material in mass (Van Eaton et al., 2023; Mastin et al., 2024; Wu et al., 2025).

During the climactic eruption on 15 January, the injection reached the mesosphere (~53 km), and water vapour saturated the stratospheric column up to about 35 km altitude within approximately one hour (Khaykin et al., 2022). Excess water condensed into hydrometeors (Vömel et al., 2022). Large anomalies in stratospheric water vapour concentrations of >7,000 ppmv up to 40 km altitude were recorded by GPS radio occultation (RO) measurements on the first day and of >1000 ppmv up to 30 km altitude by radiosonde measurements between days one and four (Figure 2.4; Vömel et al., 2022; Khaykin et al., 2022; Randel et al., 2023). The water vapour mixing ratio at ice saturation increased rapidly with altitude in the stratosphere, from approximately 10 ppmv at 17 km, to 100 ppmv at 21 km altitude, and to 1000 ppmv at 26 km (Vömel et al., 2022). The Aura Microwave Limb Sounder (MLS) retrievals of water vapour in the plume in the first four days are in agreement with these values, considering the coarse vertical resolution of the satellite retrievals (Millán et al., 2022). MLS

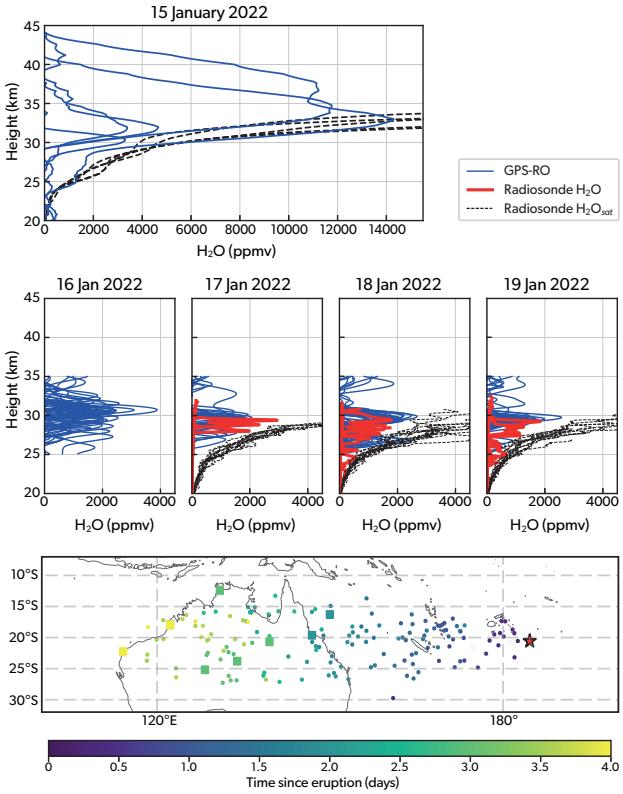

Figure 2.4: *(First two rows) Water vapour mixing ratio profiles (solid lines) in the Hunga plume, from GPS-RO and Australian radiosondes over January 15-19, 2022. Dashed lines are profiles of saturation mixing ratio. (Third row): Map of the soundings (GPS-RO as dots, radiosondes as squares; colour: time since main eruption). Data shown in Khaykin et al. (2022), Vömel et al. (2022) and Randel et al. (2023)*

first measured enhanced water vapour on 14 January near 18 km, injected by the 13–14 January smaller eruption (Millán et al., 2022).

The total water amount initially present in the plume is uncertain, but may have reached several thousands of Tg based on a 1-D steady plume model and observations of the umbrella growth-rate, the plume height, and the volume of tephra-fall deposits (Mastin et al., 2024; Wu et al., 2025). Most of it froze, and a fraction of the ice evaporated as it settled, thereby hydrating dry, stratospheric air at lower altitudes. The ice fallout likely contributed to the scavenging of ash and soluble gases, such as hydrogen chloride (HCl) (see Section 2.4 for details). The remaining 146 ± 5 Tg increased the global abundance of stratospheric water vapour by ~15%, representing an unprecedented jump in the observational record (see Figure 2.5a and Millán et al., 2022, for details). For comparison, the Calbuco eruption in 2015 reached an altitude of 21 km, directly injecting approximately

Table 2.2: *Injections from the eruption, including altitude, stratospheric injection amount, observing instruments (and simulations when applicable), and their publications.*

Volcanic aerosol/gas	Injection Altitude (km)	Stratospheric Injection (Gg)	Observing Instruments	Publication
H_2O (gas)	~27–35	146,000 ± 5,000	MLS	Millán et al. (2022)
			GPS-RO	Randel et al. (2023)
			RS41-RS	Vömel et al. (2022)
SO_2 (gas)	18–19 (13 Jan.)	60	OMPS, OMI, TROPOMI	Carn et al. (2022)
	>30 (15 Jan.)	400–480	MLS	Millán et al. (2022)
	Total Column	1000	EMI-2	Li et al. (2023)
			IASI	Legras et al. (2022)
				Sellitto et al. (2024)
HCl (gas)	20–25 (16–17 Jan.)	<1	MLS	Millán et al. (2022)
				Zhu et al. (2023)
BrO (gas)	8–15 (16–18 Jan.)	Negligible	EMI-2	Li et al. (2023)
				Zhu et al. (2023)
NO	~15–30	1.4–3.6*	GLD360	Zhu et al. (2023)
			WWLLN	
			ENTLN	
Primary solid aerosol (Ash or possibly sea salt)	>33–40	Likely small	AERONET	Boichu et al. (2023)
			Lidar	Baron et al. (2023)
			TROPOMI	
			Ash samples	Colombier et al. (2023)

*based on NO produced by each lightning flash from a global climate model

2 Tg water vapour into the lower stratosphere (Sioris et al., 2016). The MLS record shows numerous short-lived enhancements of approximately 10 ppmv below 20 km (at 68 hPa) following the Kasatochi eruption in 2008 and the Raikoke eruption in 2019, as well as the Calbuco eruption, due to the entrainment of water vapour from the troposphere into the stratosphere due to volcanic eruption columns (Glaze et al., 1997), and slightly larger, longer-lived enhancements following pyrocumulonimbus (see Figure 2.5a and Millán et al., 2022, for details). The hydration of the stratosphere on the scale of Hunga from a volcanic eruption had been proposed (Glaze et al., 1997), but never before observed. Typical volcanic eruptions reaching the stratosphere impact stratospheric water vapour, not through direct injection, but by increasing the tropical cold point temperatures and thereby increasing the entry of water vapour into the stratosphere as a result of aerosol radiative heating months after the eruption (Joshi and Shine, 2003).

Within two days of the eruption, the evaporation of sedimenting ice particles and strong horizontal and vertical wind shear, as may be expected during the SH summer circulation and Quasi-Biennial Oscillation (QBO) easterly phase, contributed to the appearance of thin slanted layers, with very high water vapour concentrations (see Figure 2.4a and Vömel et al., 2022, for details). The water vapour plume descended rapidly during the first two days after the eruption, at a rate of at least 1 km d^{-1}, due to a strong radiative cooling of the order of 10 K d^{-1} in potential temperature associated with the large water vapour enhancements, according to RO measurements (Randel et al., 2023). Thereafter, although still driven by radiative cooling, the descent rate slowed to approximately 0.2 km d^{-1}, with the water vapour enhancement observed above 29.5 km in January and below 26.5 km altitude by the first week of February (Sellitto et al., 2022; Legras et al., 2022). From the first week of February onward, the altitude of the water vapour plume levelled off (see Section 2.4 for details).

MLS shows water vapour anomalies of 1–2 ppmv persisting in the upper stratosphere between 35–50 km until the first week of February (Millán et al., 2022). Stratospheric water vapour concentrations in the plume decreased from <700 ppmv on the 19 January to <100 ppmv by mid-February as the plume spread,

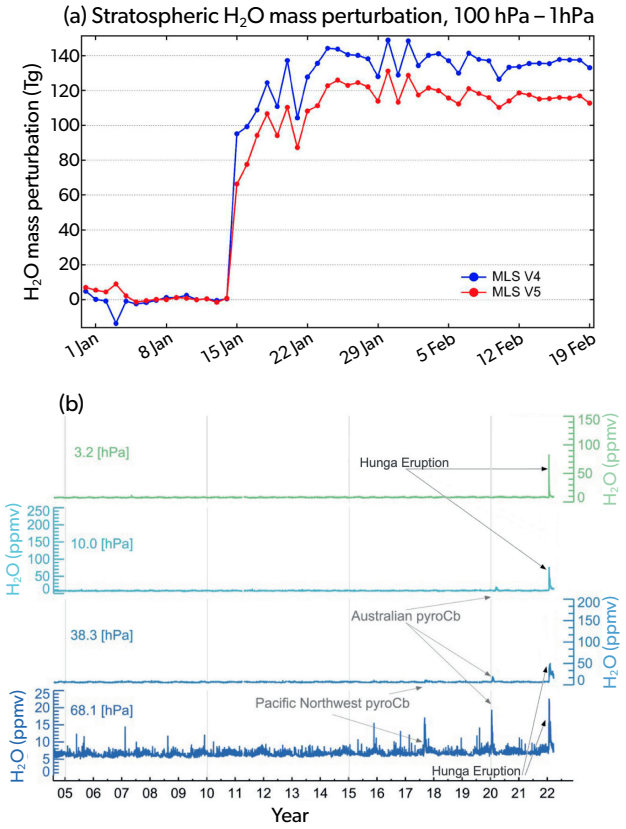

Figure 2.5: *a) Hunga-induced change in the total mass of stratospheric water vapour between 100–1 hPa pressure levels (16-50 km) using MLS V4 and MLS V5 data. Adapted from Khaykin et al. (2022). b) Time series of H_2O (MLS V4 data) mixing ratios at different pressure levels. Adapted from Millán et al. (2022).*

having circumnavigated the globe one and a half times (Vömel et al., 2022). MLS then showed the main water vapour plume had meridional (30°S–5°N) anomalies between 20–50 ppmv at altitudes between 17–26 km (Millán et al., 2022). Maximum water vapour concentrations were observed between 23–26.5 km by radiosondes, RO, and MLS (see Chapter 3 for a full discussion of the water vapour plume transport and dispersion after mid-February). A temperature pattern with negative temperature anomalies above the plume and positive temperature anomalies below the plume developed and lasted for weeks (Stocker et al., 2024), explained in part because water vapour effectively absorbs outgoing radiation (see Chapter 7 for details).

The large water vapour enhancements also accelerated the production of the hydroxyl radical (OH) in the plume above 25 km, likely doubling the availability of OH (Zhu et al., 2022) and hastening the conversion of sulfur dioxide (SO_2) to sulfate aerosol (see Section 2.5 for details). The change in OH concentration also led to rapid hydrogen oxide radicals (HO_x) cycling and the catalytic destruction of ozone (see Chapter 5 and Zhu et al., 2023, for details).

This large, quasi-instantaneous addition of water vapour to the stratosphere and the anomalies it produced in the first month remain exceptional in the observational record. Typical background stratospheric water vapour concentrations are 5 ppmv at 28 km, ranging from approximately 3 ppmv at the tropical tropopause to 7 ppmv in the upper stratosphere (Davis et al., 2016). The annual cycle in the lower stratosphere has an amplitude of approximately 3 ppmv amplitude. Observed trends in stratospheric water vapour from balloon-borne frost point measurements between 1980–2022 were largely positive ($\leq$1.2 ppmv decade^{-1} Hurst et al., 2011), but the anticipated increase in the tropical lower stratosphere related to greenhouse gas forcing is modest 0.31 ± 0.39 ppmv K^{-1} (Nowack et al., 2023). Removal of stratospheric water vapour occurs primarily through mean overturning Brewer-Dobson circulation, dehydration in the Antarctic polar vortex and Lyman-alpha photodissociation in the upper stratosphere, yielding an expected residence time of several years (see Chapter 7 for details). Enhancements in stratospheric water have radiative impacts (see Chapter 7), alter aerosol microphysical and radiative properties (see Section 2.6), and influence atmospheric chemistry (see Chapter 5) and atmospheric circulation (see Chapter 3).

2.4 Plume altitude and dispersion during the first month

Within the 10 hours following the initial eruption and after damping of the overshoot oscillations described in Section 2.1, GOES-17 observed the umbrella's descent, estimating a rate of approximately 1.7 km h^{-1} (Carr et al., 2022). Himawari-8 false color imagery confirmed the dissipation of the umbrella, which was attributed to the sedimentation of most large ice and ash particles (Legras et al., 2022).

The fast sedimentation of the condensed part of the volcanic plume, primarily composed of ice and ash, occurred within 15 hours of the eruption by 19:00 UTC on 15 January. The remaining plume led to multiple aerosol layers in the stratosphere from 18 km to >44 km. These layers were detected by multiple instruments in the following days. Two main clouds of aerosols, referred to as C1 and C2, emerged in the Himawari false colour imagery between 170°W and 177.5°W west of the maximum extent of the collapsing umbrella (Figure 2.6a–b; Carn et al., 2022;

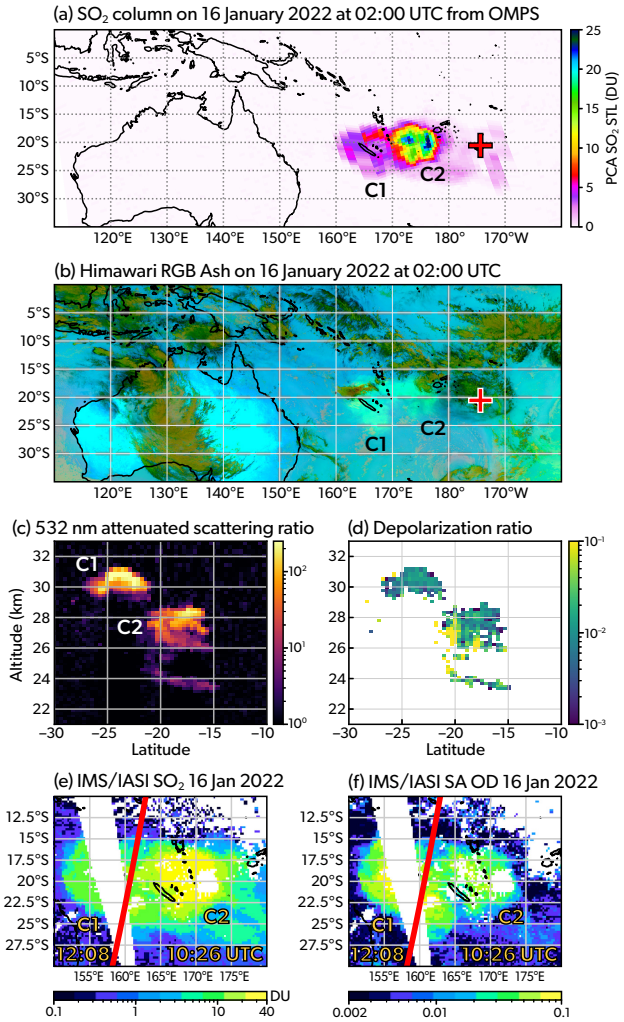

Figure 2.6: *a) SO_2 column for C1 and C2 clouds as seen from OMPS on 16 January 2022 at 2 UTC adapted from Carn et al. (2022) , b) Himawari false colour imagery using channels at 8.5, 10.4 and 12 µm for the same time showing C1 and C2 sulfate aerosols as greenish bright patches; brown patches are clouds and Australia is bright due its high infrared emission, c) 532 nm attenuated scattering ratio from CALIOP on 16 January 2022 at 15:08 UTC intersecting C1 and C2, d) depolarisation ratio in C1 and C2 at the same time, e) SO_2 column from IASI on 16 January 2026 from two swaths spanning C1 and C2, f) sulfate aerosol optical depth on the same swaths (mainly retrieved from 8.5 µm band). The red line in panels e) and f) is the CALIOP track shown in c) and d). b-f are adapted from Legras et al. (2022).*

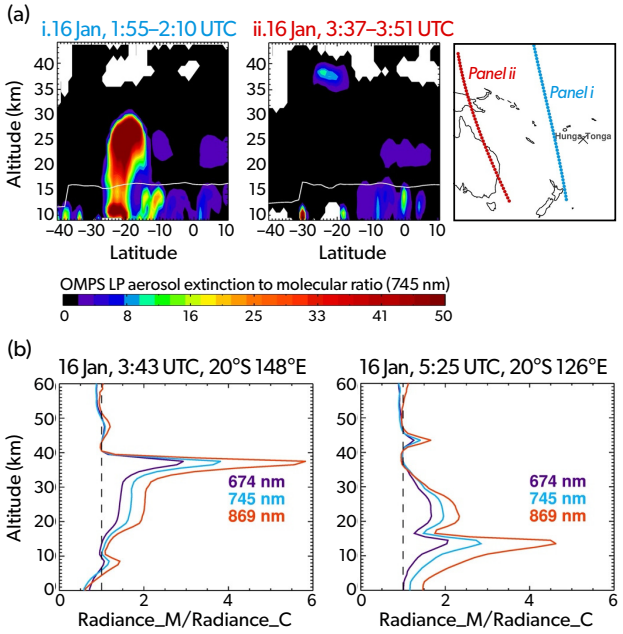

Figure 2.7: *(a) Plot of Ozone Monitoring and Profiler Suite aerosol extinction to molecular ratio profiles measured on 16 January 2022, 1 day after the main volcanic eruption. The right panel is the measurement's location. Blue is for the left panel, and red is for the centre. The white lines in the left and centre panels are the tropopause altitudes derived using the NASA Global modelling and Assimilation Office near-real time atmospheric analyses. (b) Plot of the measured to calculated radiance ratio (assuming aerosol-free atmosphere) profile for three wavelengths measured for two profiles taken on the same day. Taken from Taha et al. (2022).*

Legras et al., 2022). C1 and C2 were detected on 16 January by several instruments moving westward at about 20 m s^{-1}. At 2:45 UTC, the Cloud-Aerosol Lidar with Orthogonal Polarisation (CALIOP) showed C2 as an optically thick cloud, with a backscatter ratio at 532 nm larger than 200 between 26 and 29 km. Both of these clouds were mostly composed of poorly depolarising particles with small depolarising pockets (Sellitto et al., 2022; Legras et al., 2022; Boichu et al., 2023). Below this were optically thinner clouds at or below 20 km, with depolarising properties, which may partly be related to the eruption on 13 January (Zhu et al., 2022). Later at 15 UTC, CALIOP again identifies the C2 cloud between 26 and 28 km and the C1 cloud at 30–32 km with a stratospheric aerosol optical depth (AOD) greater than 0.5 (Figure 2.6c; Sellitto et al., 2022; Legras et al., 2022; Boichu et al., 2023). On the same day, the Ozone Mapping and Profiler Suite Limb Profiler (OMPS-LP), measured aerosols spread between 20–30 km and confirmed that aerosol from the first eruption on 13 January reached 20 km (Figure 2.7; Taha et al., 2022)

The depolarising pockets of the two main clouds were observed only over the first two days following the eruption, suggesting the presence of ice or ash. However, ice could not persist and UV instrument measurements show that absorbing aerosols dissipated in the days that followed, leaving the main volcanic plume composed primarily of SO_2 and rapidly forming sul-

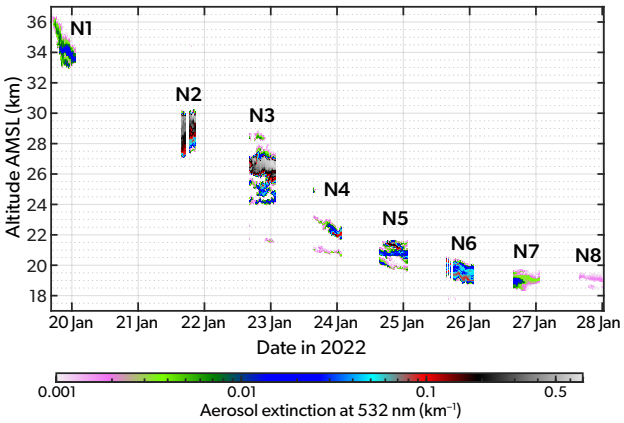

Figure 2.8: *Time-altitude curtain of aerosol extinction coefficient at 532 nm from 19-28 January. Layers are named N1 to N8, corresponding to every night of observations showing a significant aerosol burden. Taken from Baron et al. (2023).*

furic acid particles, hereafter referred to as sulfate aerosol (Sellitto et al., 2022; Taha et al., 2022; Legras et al., 2022). In the following days, the Multi-angle Imaging SpectroRadiometer (MISR) detected primarily spherical, non-absorbing particles, typical of volcanic sulfate aerosols in the stratosphere (Kahn et al., 2024). Ground-based Aerosol Robotic Network (AERONET) data was used to identify an unusual coarse mode that persisted during the first week of the plume's circumnavigation of the globe, attributed to sulfate-coated thin ash particles, though their altitude could not be determined (Boichu et al., 2023). Additionally, ground-based Lidar measurements at Réunion Island showed a negative or very small Ångström exponent on 21–22 January at altitudes of 22–29 km, indicating the presence of some relatively large aerosols (Figure 2.8; Baron et al., 2023). From the same location, Kloss et al. (2022) detected some partially absorbing particles near 22 km on 23 January and 20 km on 26 January.

The presence of ash and ice is not uncommon following volcanic eruptions (Rose et al., 1995; Brown et al., 2012; Romeo et al., 2025). However, the unusually large aerosol extinction and backscatter coefficients measured by OMPS-LP and CALIOP in the days after this eruption were surprising, particularly given the modest amounts of SO_2 injected into the stratosphere (see Section 2.1). The presence of large quantities of water vapour (see Section 2.3) led to an accelerated conversion to sulfate (see Section 2.5).

A smaller portion of the plume above 35 km (from the 15 January eruption), was detected by OMPS-LP (Figure 2.7; Taha et al., 2022) and by CALIOP as strongly depolarising particles on 15 January. This layer was detected where sulfate evaporates (Kremser et al., 2016), suggesting the presence of ultrafine ash (radius $<1\,\mu$m). In fact, OMPS-LP measured aerosols between 40–50 km on the second day after the eruption and continued to measure the volcanic layer above 40 km for two weeks, and above 36 km for the following three months (Khaykin et al., 2022; Taha et al., 2022). Nonetheless, the aerosol loading above 35 km was minimal, and its relevance to climate and atmospheric chemistry is likely negligible.

Another secondary layer that formed at an altitude of 19–22 km moved slowly westward and possibly originated from a combination of the 13 January eruption plume and portions of the 15 January eruption plume, where the SO_2 separated from the water-rich plume at higher altitudes (Taha et al., 2022). As a result, the conversion from SO_2 to sulfates was much slower in that part of the plume than in the higher aerosol clouds. This layer was measured by the Portable Optical Particle Spectrometer (POPS) and SO_2 sondes over La Réunion on 24 and 25 January. These measurements showed that at altitudes of 19–22 km, where the air was drier, the effective radius of the particles was similar to background values of 0.2 μm (Asher et al., 2023); see also Section 2.6). On 25 January, simultaneous measurements of SO_2 and aerosols at 20 km revealed that SO_2 levels exceeded the H_2SO_4 aerosol mass, suggesting that the SO_2 oxidation rate was slower in this layer compared to the main layer, where water vapour was significantly elevated (Figure 2.11b; see also Section 2.5).

During the first two days after the eruption, the aerosol plume was confined in the 15°S–25°S band. Wind shear in the lower stratosphere, typical during the SH circulation and QBO easterly phase resulted in the appearance of a stretched aerosol layer at low altitudes within the first two weeks (Figure 2.8). In the following 10 days, while crossing the Indian Ocean, the plume rapidly dispersed in latitude to a domain extending from 30°S to 10°N (Figure 2.9; Taha et al., 2022; Schoeberl et al., 2023). The plume reached 10°N by 26 January, but then stopped this meridional expansion and remained essentially confined within this domain with a very slow expansion to 40°S–20°N over the following six months (Taha et al., 2022; Legras et al., 2022); see Chapter 3 for details. The same pattern was observed for water vapour (Khaykin et al., 2022).

The vertical motion of the aerosol plume was characterised by a fast initial descent of at least 400 m day^{-1}

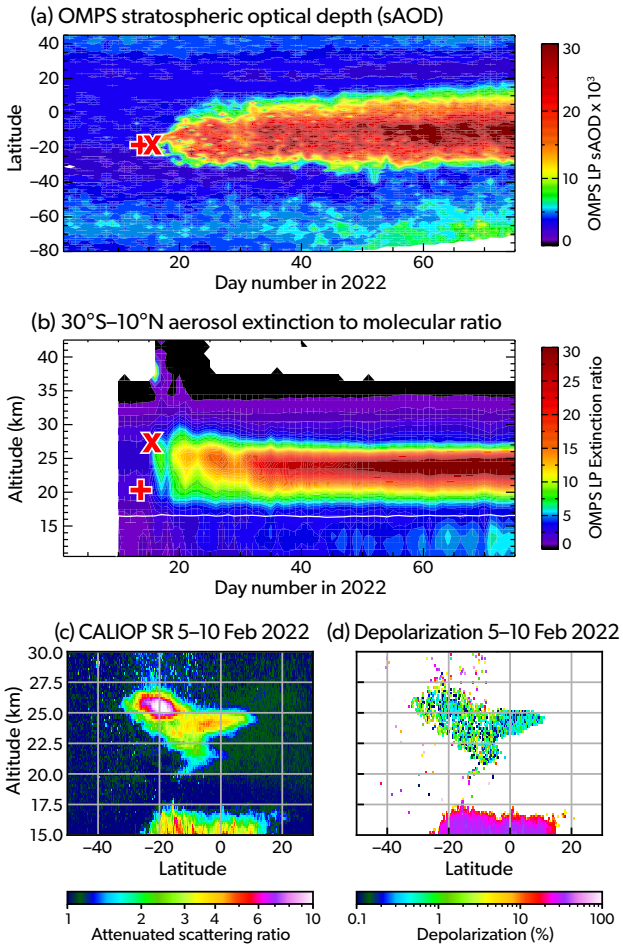

Figure 2.9: *(a) Plot of OMPS stratospheric optical depth (sAOD) x103 zonal mean at 869 nm for early 2022. (b) The extinction to molecular ratio zonal mean profiles between 30°S and 10°N for the same period. The white line is the tropopause altitude. The plus and cross and symbols in both figures are for the time and location of the two eruptions on 13 and 15 January (adapted from Taha et al., 2022). c-d) CALIOP mean scattering ratio and depolarisation averaged over all orbits during 5-10 February 2022. Below 17.5 km are tropical ice clouds (adapted from Legras et al., 2022).*

for the first 10 days within the moister parts of the sulfate layer (Sellitto et al., 2022). This descent corresponded to a cooling of 5 K day^{-1} in potential temperature, compatible with the initial water vapour descent reported in Section 2.3. Sellitto et al. (2022) attributed the descent to the radiative cooling by the water vapour infrared emission. Model simulations of the Hunga eruption also indicated that radiative cooling of water vapour was the primary driver of the rapid descent of the plume observed during the first two weeks of the eruption (Niemeier et al., 2023). After 27 January, the mean zonal MLS water vapour and CALIOP backscatter signals exhibit a descent pattern corresponding to a cooling of 4 K day^{-1} for another couple of weeks (Sellitto et al., 2022). Such intense and localised cooling is expected to induce a dynamical response (Podglajen et al., 2024), which in this case may have taken the form of an equatorial Rossby wave and led to the rapid transport across the equator on 20–23 January (Schoeberl et al., 2023).

After initially crossing the equator, zonal dispersion of the two main components of the plume was observed due to the westerly winds and the strong meridional shear that prevailed for several weeks at the latitude of the eruption and between 23 and 28 km altitude. As a result, the main plume completed its first circumnavigation of the globe in 15 days (Legras et al., 2022; Khaykin et al., 2022) and independent components merged rapidly and could not be distinguished by the beginning of February. Homogenisation of the main plume was slowed by the persistence of numerous compact anticyclonic patches of sulfate aerosols that might have been initially induced by the fast descent inside concentrated regions (Podglajen et al., 2024) and maintained afterwards by the ambient shear (Legras et al., 2022).

During the initial descent, the aerosols and the gas compounds (including water vapour and SO_2) remained well mixed (Sellitto et al., 2022). This phase ended by early February with the dilution of water vapour and the reduction of its radiative effect. Gravitational settling induced a slower but persisting descent of the aerosols (Asher et al., 2023) with respect to the ambient air, while the water vapour stalled and began an ascent due to the large-scale motion consistent with Brewer-Dobson circulation and the phase of the QBO (Schoeberl et al., 2023). As a result, the sulfate and the water plumes started to separate by mid-February at a rate of 16 m day^{-1} (Figure 2.10). Besides the direct impact on the plume altitude, the cooling effect of water persisted at a large scale and altered the circulation (Schoeberl et al., 2022; Coy et al., 2022).

2.5 Rapid formation of sulfate aerosol layer

Episodic volcanic eruptions remain one of the primary sources of SO_2 to the stratosphere (Robock, 2000; Kremser et al., 2016). On 16 January between approximately 23 and more than 33 km altitude, MLS detected SO_2 enhancements of >900 ppbv (Millán et al., 2022). Between 21 and 25 January and 18 and 30 km altitude, balloon instruments observed SO_2 enhancements >50 ppbv over Réunion Island (Figure 2.11a).

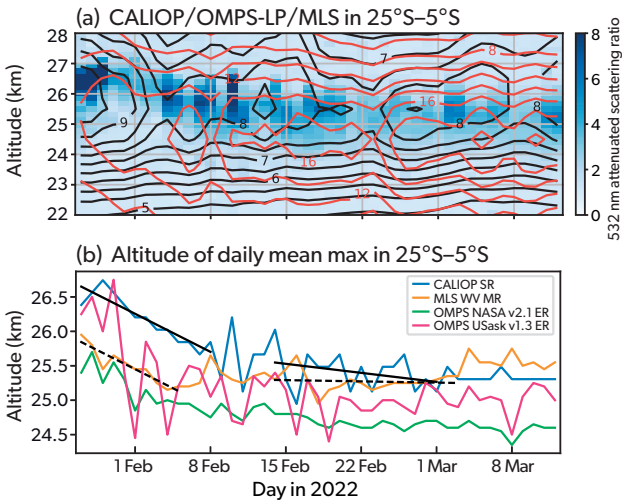

Figure 2.10: *. a) Comparative evolution of CALIOP attenuated scattering ratio (color), MLS water vapour mixing ratio (black contours, ppmv) , OMPS-LP 745 nm extinction ratio (red contours) based on the NASA v2.1 product as in Taha et al. (2022). b) daily mean vertical locations of maximum of aerosols ratios and water mixing ratio. All quantities are zonally averaged in the 25°S-5°S latitude band. Slopes are fitted for CALIOP scattering ratio and MLS water vapour: respectively -79.0 m d-1 and -78.8 m d-1 in the early period before 8 February and -18.8 m d-1 and -2.6 m d-1 in the second half of February. Both panels show common descent of water and aerosols until early February followed by vertical separation.*

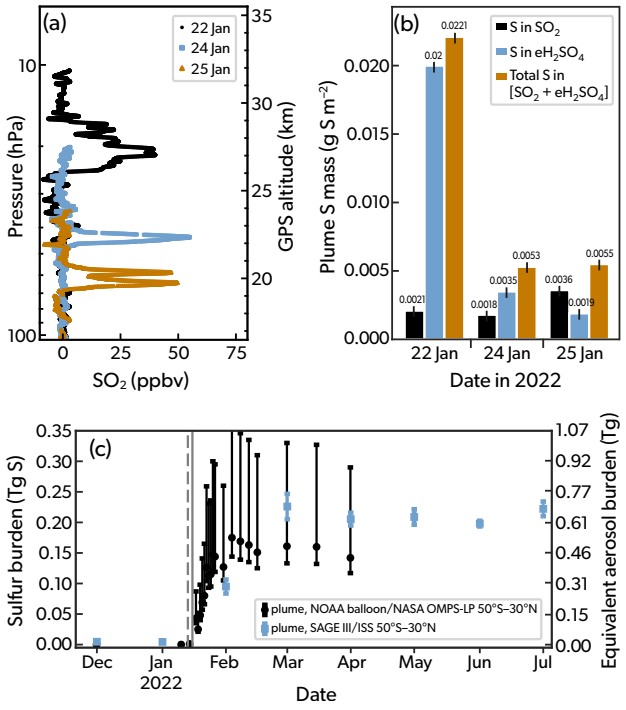

Figure 2.11: *Balloon-borne vertical profiles of SO_2 over the Maïdo in La Réunion. a) and b) adapted from Asher et al. (2023). c) The calculated total sulfur burden (and equivalent aerosol burden) calculated based on a combination of NASA OMPS-LP measurements and balloon-borne measurements, and from SAGE-III /ISS measurements assuming 70 percent weight of sulfuric acid in aerosol. Data in c) from Asher et al. (2023) and Duchamp et al. (2023). Error Bars represent the measurement uncertainty.*

As seen by Infrared Atmospheric Sounding Interferometer (IASI) (Figure 2.6e–f Legras et al., 2022; Sellitto et al., 2024), the conversion of SO_2 to sulfate aerosol was already underway in the C1 cloud at 10 UTC on 16 January due to the large injection of water vapour (see Section 2.3 for details), a few hours after the initial estimate of total SO_2 derived based on a Tropospheric Monitoring Instrument (TROPOMI) overpass at 2 UTC (Carn et al., 2022, see also Figure 2.6a). At this time, SO_2 was mostly concentrated in a horizontal patch corresponding roughly to C2 with no conversion yet to sulfates because of a drier environment. The analysis of subsequent evolution shows that no SO_2 is detected in C1 after 20 January (Legras et al., 2022). Carn et al. (2022) estimated a SO_2 e-folding time of $\tau = 6$ days based on satellite estimates of the SO_2 column and used this to estimate a total emitted mass of about 0.45 Tg of SO_2 from the 15 January eruption. This estimate was lately confirmed by Spurr et al. (2025). Including the contribution of the 13 January eruption (0.03 Tg sulfur or 0.06 Tg SO_2), the Carn et al. (2022) total estimate of sulfur injection is 0.25–0.27 Tg sulfur or 0.49–0.54 Tg SO_2 (Table 2.2). Other estimates from IASI are significantly higher at ~1 Tg SO_2 (Sellitto et al., 2022; Sellitto et al., 2024), a weather and climate model modelling study suggests 1.2 Tg (Bruckert et al., 2025), and one volcanology study proposes 1.3 Tg (Wu et al., 2025, and Table 2.2) (see discussion in Section 2.8). Estimates of the aerosol burden (~ 0.5 - 0.6 Tg) observed in subsequent weeks and months are consistent with the smaller 0.45 Tg SO2 injection (Asher et al., 2023; Duchamp et al., 2023). Estimated totals from the Hunga eruptions correspond to approximately 30% to 80% of the SO_2 emitted during the 2019 Raikoke eruption (1.5 Tg, Leeuw et al., 2021) and 2–5% of the SO_2 released during the 1991 Mt. Pinatubo eruption (20 Tg according to Bluth et al., 1992). Even the smallest estimate is more than double the amount of SO_2 needed to sustain the background stratospheric aerosol sulfur burden for one year (Feinberg et al., 2019).

CALIOP does not detect any significant depolarisation in C1 and C2, except marginally on their periphery on 16–17 January, possibly due to ice (Figure 2.6d). A significant depolarisation is only detected by

CALIOP on the low clouds seen on 16 January (Zhu et al., 2022) and on a high-altitude thin cloud between 34 and 39 km (see Section 2.4). At the same time, the UV instruments (Carn et al., 2022; Taha et al., 2022) do not detect any absorbing aerosol and MISR (Kahn et al., 2024) sees only spherical non-light-absorbing particles in C1 and C2. Ground-based photometric observations on 16 January (around 22:00 UTC) and following days also indicate an excess abundance of fine ($r_{\text{eff}} < 0.5\,\mu$m) poorly absorbing aerosols and also the presence of an unusual coarse mode (a few μm) possibly associated to sulfate coated ash (Boichu et al., 2023). depolarisation or light absorption were also occasionally observed in low clouds below 20 km (Kahn et al., 2024; Baron et al., 2023), possibly associated with the plume of the 13 January eruption. Besides these early features, no depolarisation or visible light absorption are detected by any spaceborne instrument during the subsequent evolution of the plume. We therefore conclude that almost all condensed material emitted during the eruption was scavenged by precipitations during the collapse of the umbrella clouds. As a consequence, it is more than likely that the aerosols were composed almost entirely of liquid sulfate droplets. The possible inclusion of solid nuclei inside these droplets cannot be ruled out but cannot be determined from remote sensing in the absence of optical signature.

On 20 January, the C1 and C2 clouds were located over the Indian ocean with a strong elongation in longitude from Australia to 60°E, due to the strong prevalent meridional shear at the altitudes of the clouds. IASI shows that on this date the conversion of the most western C1 to sulfate is achieved while the conversion of C2 is still in progress (Legras et al., 2022). A third cloud (C3) located to the north of C2, was identified drifting more slowly westward at a height of nearly 20 km and without a significant amount of sulfate aerosols. This cloud is a confirmation of the presence of drier layers in the initial distribution of SO_2 and of the heterogeneity of the plume.

Even if the clouds C1 and C2 were still spatially separated, it is likely that a significant amount of mixing had already occurred between them. The high moisture content implies radiative cooling and a mean descent of the clouds on the order of 350 m d^{-1} (12 K d^{-1} in potential temperature) from 27 January to 10 February, observed using mean aerosol scattering profiles retrieved from CALIOP (Sellitto et al., 2022). Large variation of this descent within the clouds is likely to have occurred according to the water vapour concentration.

As the plume passed over Réunion Island (21°S, 55°E) between 22 and 26 January, its components (the plume experienced significant wind shear as discussed above) passed in sequence from the highest and most humid to the lowest and driest (see Figure 2.8a; Kloss et al., 2022; Baron et al., 2023; Asher et al., 2023). in situ and ground based measurements confirmed the largest SO_2 conversion related to moisture (see Figure 2.11 and Asher et al., 2023), the low visible light absorption (Kloss et al., 2022; Boichu et al., 2023) and provided estimates of the size distribution with largest particles (r_{eff} about 0.4 μm, see Section 2.6 for more details) being consistently observed in the high plume (C1) (Baron et al., 2023; Asher et al., 2023; Boichu et al., 2023) and smaller values (0.2 μm) in the lowest part (C3). AERONET observations (Figure 2.12) document the rapid growth of Hunga aerosols from Australia to Réunion Island, with the column-integrated r_{eff} doubling in the first week after eruption (Boichu et al., 2023).

Mass estimate (based on OMPS-LP and balloon profiles) yields 0.18 Tg of sulfur in sulfate aerosol after 3 weeks (Asher et al., 2023) and stabilises after. This is in rough agreement with the stable estimate of 0.21 Tg found at later times between March and November 2022 (Duchamp et al., 2023) from NASA Stratospheric Aerosol and Gas Experiment onboard the international space station (SAGE III/ISS) and as mentioned above is compatible with the estimated initial injection (Carn et al., 2022).

Due to the large injection of water vapour, the conversion of SO_2 to sulfates, which usually occurs with an e-folding time of one month, occurred three times faster overall (Carn et al., 2022; Zhu et al., 2022; Asher et al., 2023), and SO_2 values returned to background levels by early February.

2.6 Microphysical and optical aerosol properties

The Hunga eruption produced a 4–5 fold global increase of the stratospheric aerosol optical depth (sAOD), according to OMPS-LP and SAGE III/ISS satellite observations (Taha et al., 2022; Khaykin et al., 2022). According to the Global Space-based Stratospheric Aerosol Climatology (GloSSAC), this perturbation represents the largest sAOD anomaly since the 1991 Mt. Pinatubo eruption, which was six times larger (Kovilakam et al., 2020). Total sAOD increased rapidly after the Hunga eruption (Kovilakam et al., 2020), reaching ~0.01 at 869 nm between 30°S and

15°N in less than two weeks according to OMPS-LP (Taha et al., 2022). Water vapour enhancements contributed minimally to ambient particle radius (< 10%) after one week (Asher et al., 2023).

As discussed in Section 2.5, the Hunga plume revealed its sheared plume structure. Between 17 January and mid-February, the aerosol size distribution was obtained from ground-based photometric observations at multiple stations of the worldwide AERONET network (Boichu et al., 2023) and from balloon-borne in situ measurements launched on several occasions over Réunion Island (Asher et al., 2023) (Figures 2.12 and 2.13). in situ balloon-borne measurements indicate that the main Hunga plume, defined as the part with the highest particle concentration, passed over Réunion Island above 25 km altitude between 22 January (parcel #0122 in Figure 2.12b) and 23 January (parcel #0123-a in Figure 2.12c), in agreement with ground-based Lidar observations (Figure 2.12f; Baron et al., 2023). During this first week, the number density in the plume was more than three times greater than in background air masses (Figure 2.13; Asher et al., 2023; Boichu et al., 2023). At that time, the volcanic parcels above 33 km were no longer observed (Taha et al., 2022; Baron et al., 2023). This main part of the plume (clouds C1 and C2) contained particles with $r_{\text{eff}} \geq 0.35\,\mu$m. A lower-altitude plume part (parcel #0123-b in Figure 2.12c below 25 km on 23 January) was populated by smaller particles with r_{eff} of 0.23 μm, a value comparable to the stratospheric baseline (~0.20 μm). On 22 January (11:41 UTC), AERONET recorded a column-integrated r_{eff} of 0.39 μm (Figure 2.13a). On the following days, Hunga aerosols from the plume tail were consistently detected at a much lower altitude, ~22 km on 24 January (Figure 2.12d) and ~20 km on 25 January (Asher et al., 2023), by balloon soundings and associated to lower r_{eff} of 0.19–0.20 μm, in agreement with AERONET observations (Figure 2.13a). According to AERONET observations on Réunion Island, a coarse mode with poorly-absorbing properties may have persisted from one to three weeks (Boichu et al., 2023). Submicron absorbing particles were also reported based on the Light Optical Aerosol Counter (LOAC) balloon soundings, measuring an absorption signal based on scattering from two angles, on 23 January at 23 km altitude and 26 January at 19 km altitude (Kloss et al., 2022).

After the first circumnavigation of the globe, an aerosol layer with a high effective radius (0.35–0.38 μm) was again detected over Réunion Island by AERONET (Figure 2.12a) and above 24 km by balloons

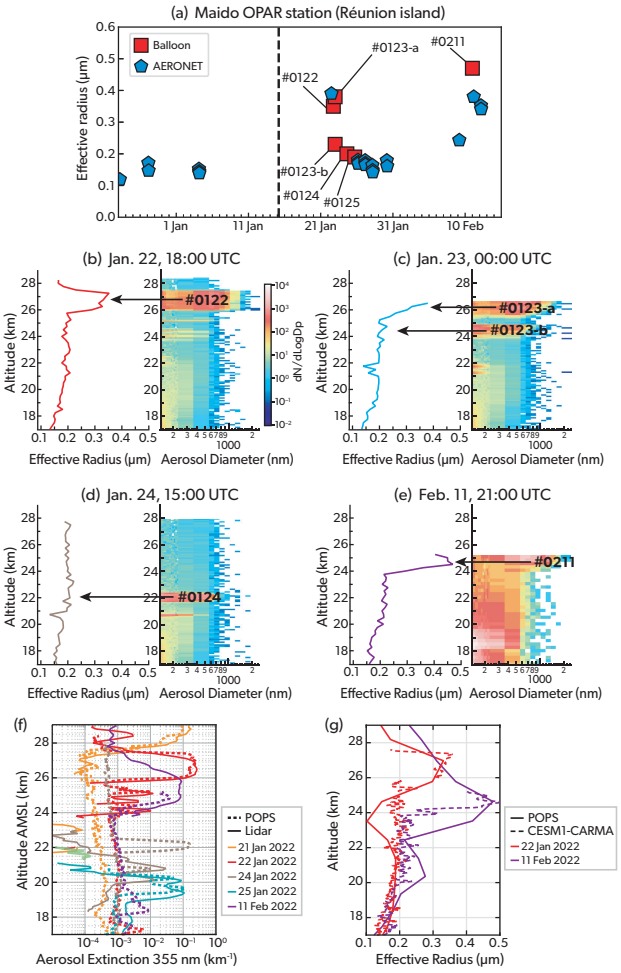

Figure 2.12: *Aerosol size over Maido OPAR station (Réunion Island) in the first month following eruption (until 15 February 2022). (a) Time series of effective radius (r_{eff} in μm) from balloon-borne measurements with POPS (maximum r_{eff}, as a function of altitude, within the Hunga plume) with red squares (from Asher et al., 2023) and from AERONET column-integrated effective radius with blue pentagons (Boichu et al., 2023). Plume parcels (#) are illustrated in panels b-e below. (b-e) Vertical distribution of effective radius (left) and aerosol number size distribution $dN/d\log D_p$ (right) up to an altitude of 30 km on (b) 22 Jan 18:00 UTC, (c) 23 Jan 00:00 UTC, (d) 24 Jan 15:00 UTC, (e) 11 Feb 21:30 UTC, b-e adapted from Asher et al. (2023). (f) Vertical profile of aerosol extinction at 355 nm calculated from POPS size distributions and Lidar backscatter observations (using vertical profiles of lidar ratios, i.e., aerosol extinction to backscatter coefficient ratios, derived from observations on each night). (g) Vertical distribution of aerosol effective radius on 22 January and 11 February from POPS observations (solid lines) and daily mean simulations with the CESM1-CARMA sectional aerosol model (dashed lines), adapted from Li et al. (2024).*

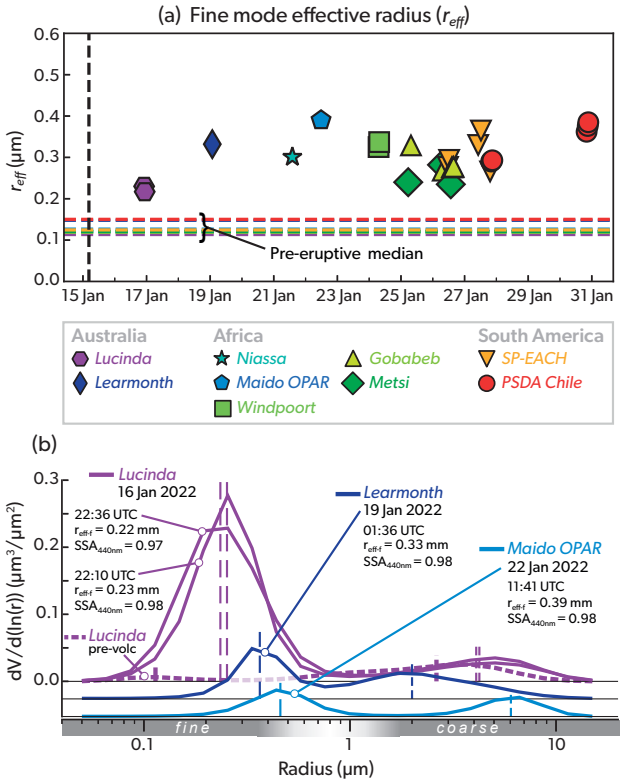

Figure 2.13: *(a) Time series of AERONET fine mode aerosol effective radius in January 2022 at 9 stations along the Hunga plume transport from Australia to South America (Lucinda and Learmonth in eastern/western Australia, Maïdo OPAR in Réunion Island, Niassa in Mozambique, Metsi in South Africa, Windpoort and Gobabeb in Namibia, SP-EACH in Brazil and PSDA Chile in Chile). Horizontal dashed lines indicate the median of fine mode radius values between 1 January 2020 and 15 January 2022 (date of the eruption) for each station. (b) Column-integrated aerosol volume size distribution and absorption properties (SSA_{440nm}) at Lucinda, Learmonth and Maïdo OPAR in the week after eruption, adapted from Boichu et al. (2023).*

on 11 February (Figure 2.12e), coexisting with large water vapour enhancements. Balloon observations show a higher aerosol effective radius on 11 February (0.47 µm) than on 22 January (0.35 µm) or 23 January (≥0.38 µm) (Figure 2.13); however, it is difficult to draw conclusions regarding the growth of particles based on so few in situ samples in a complex plume. On the other hand, AERONET measurements provide an average of the effective radius of aerosols across the atmospheric column that could be influenced by their vertical distribution.

Nevertheless, under the water-rich conditions of the plume, models replicate a similar increase in effective radius up to 0.35 µm in 3 weeks according to Zhu et al. (2022), and up to 0.5 µm by mid-February 2022 according to Li et al. (2024) (Figure 2.12g) due to accelerated SO_2 oxidation, particle nucleation, and heightened coagulation due to high particle number in the plume. Important differences between these studies include the use of a size-sectional aerosol model with a model vertical resolution of 3–4 km near 20 hPa (Li et al., 2024), compared to a modal aerosol model with a model vertical resolution of 1.5–2 km near 20 hPa (Zhu et al., 2022). Hunga particles grew much faster than Pinatubo particles, reaching a radius size of approximately 0.4 µm in one week instead of 4 months (Boichu et al., 2023). Particles from a number of recent eruptions (Kasatochi 2008, Sarychev 2009, Ambae 2018, Raikoke 2019, Ulawun 2019, La Soufrière 2022) did not grow this large (O'Neill et al., 2012; Jégou et al., 2013; Wrana et al., 2023; Boichu et al., 2023; Boone et al., 2024) (see Chapter 3) and stay basically under 0.2 µm.

Thereafter, the size stabilised near 0.4 µm for most of the plume (Khaykin et al., 2022; Asher et al., 2023; Boichu et al., 2023) and persisted over many months (Duchamp et al., 2023; Boichu et al., 2023, see Chapter 3 for details). The large aerosols of 0.4 µm in r_{eff} with narrow distribution (Duchamp et al., 2023) scatter incoming light very efficiently and so nearly maximise optical depth (Murphy et al., 2021). Therefore, despite the modest total mass of injected SO_2, particle sizes produced a relatively large radiative impact per unit mass of sulfate (Zhu et al., 2022).

2.7 Other plume chemical composition: minor injections of gas phase compounds and primary aerosols

2.7.1 Halogens

HCl and hydrogen bromide (HBr) are also emitted from volcanos. An HCl injection in the stratosphere was observed by Aura MLS at approximately 24 km altitude within one day of the eruption (Millán et al., 2022; Table 2.2). This small (likely less than 1 Gg; Zhu et al., 2023) injection, representing < 0.1% of organic chlorine in the stratosphere, resulted in elevated reactive chlorine, contributing to the rapid ozone depletion in the tropical stratosphere observed within one week of the eruption (see Evan et al., 2023, and Chapter 5 for details). Enhancements in reactive bromine (e.g., BrO), expected after rapid photolysis of HBr and/or other bromine reservoir Br species, were observed after the ~ 8 UTC eruption on 15 January between 8 and 15 km altitude, primarily in the troposphere (Li et al., 2023; Table 2.2). BrO emissions occurred after the SO_2 emissions, and <20% of the total BrO injection

was observed in the stratosphere, moving west, in the trailing edge of the SO_2 plume (Li et al., 2023). The Environmental Monitoring Instrument (EMI-2) could not provide information on the duration or the total BrO emission, but it is considered negligible (<0.001% of the inorganic bromine in the stratosphere), and did not appear to contribute to ozone depletion (Zhu et al., 2023). Differences in the altitudes of the SO_2, HCl and Br injections may be related to their solubility in water and scavenging by ice, or possibly the time at which they were released from the magmatic melt, although this topic remains an active area of research.

2.7.2 Lightning nitrogen oxide (NO)

The Hunga volcanic lightning (see Section 2.1) likely produced 1–4 Gg nitric oxide (NO) in situ at altitudes of 20–30 km based on reported lightning rates Zhu et al., 2023; see Chapter 5 for a discussion of its impact on stratospheric chemistry), exceeding previously reported rates in tropical storms and during other volcanic eruptions. For comparison, globally, lightning produces approximately 10 Tg yr^{-1} NO in the troposphere and occasionally overshoots the tropopause.

2.7.3 Ash and sea salt

A relatively small number of UV absorbing particles, indicative of ash, were observed in the high-altitude, leading edge of the plume as it travelled west (see Section 2.4 and Section 2.6 for details). Between 15–17 January, absorbing particles were observed over Eastern Australia between 35 and 40 km using a combination of CALIOP, Himawari-8, and OMPS-LP (e.g., Taha et al., 2022; Legras et al., 2022; Khaykin et al., 2022). Ground-based photometric measurements on 16 January also detected a slightly larger coarse mode over Eastern Australia, consistent with the presence of ash (Boichu et al., 2023). Lidar observations over Réunion Island on 19 January suggest the presence of absorbing particles in this leading edge of the plume (Baron et al., 2023). Based on extinction to backscatter ratios at a wavelength of 355 nm, up to 75% of this layer may have contained absorbing aerosols, such as fine ash. The AOD of this layer was ≤3.5% of that in the main part of the plume. A fraction (approximately 7% on average) of volcanic ash deposits, i.e., ~ 700 μm–2 mm diameter particles, collected from the islands of Tonga within two weeks of the eruption, also contained salts (e.g., NaCl, $CaSO_4$) bound to ash and other ions commonly found in seawater (e.g., Br, Mg, K; Colombier et al., 2023). The mass of sea salt in stratospheric particles is likely to be small compared to the gigantic amount of water vapour that remained in the stratosphere (see Zhu et al., 2023, and Section 2.3 for details), but remains an open question.

2.7.4 Ozone anomalies and the role of tropospheric transport

Anomalously low ozone was observed in the main, water-rich plume at altitudes between 26 and 30 km by balloons and MLS between 16–24 January (Evan et al., 2023; Zhu et al., 2023). The lowest ozone levels near Réunion Island were specifically observed by ozonesondes between 26 and 29 km on 21 and 22 January, with SO_2 interference accounting for approximately 3 to 4% of this decrease (Evan et al., 2023). MLS recorded the lowest O_3 levels at 27 km on 17 January near 20°S, east of Australia, on 20 January near 90°longitude, and on 24 January west of Africa (Zhu et al., 2023).

Climate model simulations, which consider both chemical and transport effects on the low ozone observed in the stratosphere after the eruption, suggest that a significant portion of this low ozone at 27 km (particularly from 15–18 January) may be attributed to the transport of low-ozone tropospheric air (Zhu et al., 2023). This contribution rapidly diminished from an estimated 50% on 16 January to approximately 10% on 22 January, primarily due to the short time required to produce ozone within the plume and the subsequent mixing and dilution of the injected air in the stratosphere (Zhu et al., 2023). Therefore, chemical processes, rather than tropospheric air transport, were the dominant factor in the observed ozone depletion after the initial injection phase (see Chapter 5 for details).

2.8 Sources of uncertainty

Several factors contribute to uncertainties in the initial injections of water, SO_2, ash and sea salt aerosol in the atmosphere, which remain an area of active research. Due to the nature of the energetic underwater eruption, empirical relationships between plume height and the mass eruption rate, used to calculate the emitted ashfall, do not apply (Mastin et al., 2024). Ocean-decolorisation suggests a minimum ashfall volume of 1.8 km^3 ± 0.4 km^3, which is approximately 12% of the caldera volume collapse (Kelly et al., 2024). Upper atmospheric composition observations are unavailable or unreliable within minutes of this eruption, and ground-based observations of tephra fall deposits landed primarily in the ocean, making it challenging to reconstruct their volume and dispersal

characteristics.

Especially during and in the first hours after the eruption, an optically thick plume, most likely consisting mainly of ash and ice made satellite measurements of the gas-phase composition difficult. The initial amount of injected ash and ice is itself very uncertain. The SO_2 burden estimated with four different UV satellite instruments immediately after the main eruption on 15 January was 0.5 Tg (Carn et al., 2022). Such measurements are well suited to measure the SO_2 burden. However, in estimates from infrared and microwave sounders the burden increased to about 1.0 Tg on 18 January, possibly due to the opacity of the early plume or instrumental saturation (Sellitto et al., 2022). Simulations using the ICOsahedral Nonhydrostatic model with Aerosols and Reactive Trace gases (ICON-ART), which is a weather and climate model, indicate that an initial injection of ∼ 1.2 Tg of SO_2 is needed to reproduce observed SO_2 columns and sulfate sAOD (Bruckert et al., 2025). Similarly, sulfur degassing rates estimated from melt inclusions found in pyroclastic deposits are consistent with a larger SO_2 injection (1.3 Tg SO_2; Wu et al., 2025). Closure of the sulfur budget is not achieved given these higher estimations of SO_2 and the observed amount of sulfate aerosol (Asher et al., 2023; Duchamp et al., 2023). However, IASI is a total column measurement of SO_2, and uncertainties in the injection altitude of SO_2 in the stratosphere or in the troposphere could influence its atmospheric lifetime and its propensity to form sulfuric acid particles and grow to accumulation mode sizes that may be detected by balloons and space-based remote sensing instruments.

The amount of SO_2, HCl, HBr, and other halogens reaching the upper part of the plume strongly depends on their dissolution in water and scavenging by ice (e.g., Textor et al., 2003). The Hunga Volcano emitted large amounts of water vapour into the atmosphere, which was mostly converted to liquid water and ice (Van Eaton et al., 2023; Mastin et al., 2024). The role of liquid and solid hydrometeors in scavenging chemical compounds is an active area of research. However, the different injection heights for SO_2 and HCl (Millán et al., 2022) might be due to differences in the solubility in water and scavenging by ice and when compounds were released from the magmatic melt.

Space-borne and ground-based measurements consistently show that relatively few absorbing particles were observed beyond the first two days after the eruption (Taha et al., 2022; Legras et al., 2022; Baron et al., 2023). The presence of persisting ice instead of ash cannot be ruled out as these features rapidly vanish in the following days. These particles were primarily concentrated in the collapsing umbrella (Kahn et al., 2024), and then above 34 km in the leading edge of the plume. in situ balloon measurements of particle number and size and SO_2 in the plume within 7–10 days of the eruption are consistent with a short SO_2 lifetime and the rapid formation of a sulfate aerosol layer (below 30 km; Asher et al., 2023).

However, these measurements do not preclude the existence of sulfate-coated ash and/or sea salt particles within the plume. Additional balloon measurements within 11 days of the eruption suggested the presence of small absorbing particles below 23 km altitude (Kloss et al., 2022). These measurements should be interpreted with caution, however, due to the order of magnitude differences in calculated extinction based on these particle size distributions and simultaneous lidar measurements of extinction (Kloss et al., 2022). This is not the case for POPS measurements, which show good agreement with lidar measurements (see Section 2.6 for details).

A small but variable fraction of the ashfall contained salts and ions common in seawater (Colombier et al., 2023); see Sect 2.7.3 for details. Interestingly, little reactive chlorine (and no reactive bromine or iodine) is needed to explain the observed ozone depletion, and the eruption column was likely steam-driven, which would be poor in sea salt (see Zhu et al., 2023; Mastin et al., 2024, for details).

The inhomogeneity of the initial injection represents a final source of uncertainty because the kinetics of sulfate conversion and chemistry cannot be assumed uniform in the plume. In this respect, the modelling studies have been constrained to more or less arbitrary assumptions which differ from one study to the next. For instance, SO_2 and H_2O injections are not fully correlated in (Zhu et al., 2022) but they are in (Li et al., 2024).

The figures shown in this chapter are using version v2.1 of the OMPS-LP aerosol product like in Taha et al. (2022). It has been checked that using the new version v2.5 does not make a significant difference regarding the features discussed in this chapter.

2.9 The value of observations

The Hunga submarine volcano erupted in a very isolated and poorly monitored area at the surface in the South Pacific. Nevertheless, a tremendous amount of satellite and ground-based observations, in addition to opportunistic in situ measurements, were made

for this volcanic eruption. This is largely due to the number of satellite instruments which were operating at the time of the eruption and the large variety of their capabilities. Geostationary imagers GOES-17 and Himawari-8 covered the whole Southern Hemisphere equator at high frequency and were the first to witness the eruption, and proved particularly useful for determining the unprecedented altitude of the volcanic cloud and its subsequent collapse (Carr et al., 2022). The limb vertical profile measurements of MLS were crucial in showing the large amount of water vapour reaching the upper stratosphere and lower mesosphere (Millán et al., 2022), while a combination of the limb measurements of OMPS-LP and CALIOP Lidar provided an unprecedented view of the vertical and spatial distribution of the volcanic aerosol (Sellitto et al., 2022; Taha et al., 2022; Legras et al., 2022). Furthermore, multiple UV (TROPOMI, DSCOVR/EPIC, OMI, SNPP/OMPS and N20/NPP NM) and IR (IASI) nadir instruments tracked the volcanic plume as it circulated the globe, providing a fairly consistent estimate of the injected SO_2 and an early insight into the rapid SO_2 conversion to sulfate aerosol (Carn et al., 2022; Sellitto et al., 2022). These satellite observations were complemented by ground-based and in situ measurements from an international rapid response campaign on Réunion Island within one week of the eruption (Kloss et al., 2022; Baron et al., 2023; Asher et al., 2023; Evan et al., 2023) and by photometric observations from many AERONET ground stations of the Southern Hemisphere (Boichu et al., 2023). Furthermore, the Vaisala radiosonde (weather balloon) in situ measurements and RO, which are sufficiently sensitive to measure extreme water vapour amounts in the stratosphere, outside their standard operation range, were utilised to track the volcanic cloud, providing high-resolution vertical profiles of the stratospheric water vapour (Vömel et al., 2022; Khaykin et al., 2022). Within hours, information circulated and was exchanged on the Stratospheric sulfur and its Role in Climate (SSiRC) and volcanic group mailing lists, from which a fairly clear consensus on the eruption and its consequences emerged rapidly and was very helpful in the completion of the initial studies and their follow-up that led to this report.

References

Asher, E., M. Todt, K. Rosenlof, T. Thornberry, R.-S. Gao, G. Taha, P. Walter, S. Alvarez, J. Flynn, S. M. Davis et al. (2023). 'Unexpectedly rapid aerosol formation in the Hunga Tonga plume'. *Proc. Natl. Acad. Sci.*, 120, e2219547120. DOI: 10.1073/pnas.2219547120.

Astafyeva, E., B. Maletckii, T. D. Mikesell, E. Munaibari, M. Ravanelli, P. Coisson, F. Manta and L. Rolland (2022). 'The 15 January 2022 Hunga Tonga Eruption History as Inferred From Ionospheric Observations'. *Geophys. Res. Lett.*, 49, e2022GL098827. DOI: 10.1029/2022GL098827.

Baron, A., P. Chazette, S. Khaykin, G. Payen, N. Marquestaut, N. Bègue and V. Duflot (2023). 'Early Evolution of the Stratospheric Aerosol Plume Following the 2022 Hunga Tonga-Hunga Ha'apai Eruption: Lidar Observations From Reunion (21°S, 55°E)'. *Geophys. Res. Lett.*, 50, e2022GL101751. DOI: 10.1029/2022gl101751.

Bluth, G. J. S., S. D. Doiron, C. C. Schnetzler, A. J. Krueger and L. S. Walter (1992). 'Global tracking of the SO_2 clouds from the June, 1991 Mount Pinatubo eruptions'. *Geophys. Res. Lett.*, 19, pp. 151–154. DOI: 10.1029/91GL02792.

Boichu, M., R. Grandin, L. Blarel, B. Torres, Y. Derimian, P. Goloub, C. Brogniez, I. Chiapello, O. Dubovik, T. Mathurin et al. (2023). 'Growth and Global Persistence of Stratospheric Sulfate Aerosols From the 2022 Hunga Tonga–Hunga Ha'apai Volcanic Eruption'. *J. Geophys. Res.*, 128, e2023JD039010. DOI: 10.1029/2023JD039010.

Boone, C. D., P. F. Bernath, A. Pastorek and M. Lecours (2024). 'Sulfate aerosol properties derived from combining coincident ACE-FTS and SAGE III/ISS measurements'. *J. Quant. Spectrosc. Radiat. Transfer*, 312, 108815. DOI: 10.1016/j.jqsrt.2023.108815.

Bór, J., T. Bozóki, G. Sátori, E. Williams, S. A. Behnke, M. J. Rycroft, A. Buzás, H. G. Silva, M. Kubicki, R. Said et al. (2023). 'Responses of the AC/DC Global Electric Circuit to Volcanic Electrical Activity in the Hunga Tonga-Hunga Ha'apai Eruption on 15 January 2022'. *J. Geophys. Res.*, 128, e2022JD038238. DOI: 10.1029/2022JD038238.

Brown, R. J., C. Bonadonna and A. J. Durant (2012). 'A review of volcanic ash aggregation'. *Phys. Chem. Earth*, 45–46, pp. 65–78. DOI: 10.1016/j.pce.2011.11.001.

Bruckert, J., S. Chopra, R. Siddans, C. Wedler and G. A. Hoshyaripour (2025). 'Aerosol dynamic processes in the Hunga plume in January 2022: does water vapor accelerate aerosol aging?' *Atmos. Chem. Phys.*, 25, pp. 9859–9884. DOI: 10.5194/acp-25-9859-2025.

Carn, S. A., N. A. Krotkov, B. L. Fisher and C. Li (2022). 'Out of the blue: volcanic SO_2 emissions during the 2021-2022 Hunga Tonga-Hunga Ha'apai eruptions'. *Front. Earth Sci.*, 13. DOI: 10.3389/feart.2022.976962.

Carr, J. L., Á. Horváth, D. L. Wu and M. D. Friberg (2022). 'Stereo Plume Height and Motion Retrievals for the Record-Setting Hunga Tonga-Hunga Ha'apai Eruption of 15 January 2022'. *Geophys. Res. Lett.*, 49, e2022GL098131. DOI: 10.1029/2022gl098131.

Clare, M. A., I. A. Yeo, S. Watson, R. Wysoczanski, S. Seabrook, K. Mackay, J. E. Hunt, E. Lane, P. J. Talling, E. Pope et al. (2023). 'Fast and destructive density currents created by ocean-entering volcanic eruptions'. *Science*, 381, pp. 1085–1092. DOI: 10.1126/science.adi3038.

Colombier, M., I. A. Ukstins, S. Tegtmeier, B. Scheu, S. J. Cronin, S. Thivet, J. Paredes-Mariño, C. Cimarelli, K.-U. Hess, T. Kula et al. (2023). 'Atmosphere injection of sea salts during large explosive submarine volcanic eruptions'. *Sci. Rep.*, 13, 14435. DOI: 10.1038/s41598-023-41639-8.

Coy, L., P. Newman, K. Wargan, G. Partyka, S. Strahan and S. Pawson (2022). 'Stratospheric Circulation Changes Associated with the Hunga Tonga-Hunga Ha'apai Eruption'. *Geophys. Res. Lett.*, 49, e2022GL100982. DOI: 10.1029/2022GL100982.

Davis, S. M., K. H. Rosenlof, B. Hassler, D. F. Hurst, W. G. Read, H. Vömel, H. Selkirk, M. Fujiwara and R. Damadeo (2016). 'The Stratospheric Water and Ozone Satellite Homogenized (SWOOSH) database:a long-term database for climate studies'. *Earth Syst. Sci. Data*, 8, pp. 461–490. DOI: 10.5194/essd-8-461-2016.

Donner, S., A. Steinberg, J. Lehr, C. Pilger, P. Hupe, P. Gaebler, J. O. Ross, E. P. S. Eibl, S. Heimann, D. Rebscher et al. (2023). 'The January 2022 Hunga Volcano explosive eruption from the multitechnological perspective of CTBT monitoring'. *Geophys. J. Int.*, 235, pp. 48–73. DOI: 10.1093/gji/ggad204.

Duchamp, C., F. Wrana, B. Legras, P. Sellitto, R. Belhadji and C. von Savigny (2023). 'Observation of the aerosol plume from the 2022 Hunga Tonga–Hunga Ha'apai eruption with SAGE III/ISS'. *Geophys. Res. Lett.*, 50, e2023GL105076. DOI: 10.1029/2023GL105076.

Evan, S., J. Brioude, K. H. Rosenlof, R.-S. Gao, R. W. Portmann, Y. Zhu, R. Volkamer, C. F. Lee, J.-M. Metzger, K. Lamy et al. (2023). 'Rapid ozone depletion after humidification of the stratosphere by the Hunga Tonga eruption'. *Science*, 382, eadg2551. DOI: 10.1126/science.adg2551.

Feinberg, A., T. Sukhodolov, B.-P. Luo, E. Rozanov, L. H. E. Winkel, T. Peter and A. Stenke (2019). 'Improved tropospheric and stratospheric sulfur cycle in the aerosol–chemistry–climate model SOCOL-AERv2'. *Geosci. Model Dev.*, 12, pp. 3863–3887. DOI: 10.5194/gmd-12-3863-2019.

Garrett, C. J. R. (1969). 'Atmospheric edge waves'. *Q. J. R. Meteorol. Soc.*, 95, pp. 731–753. DOI: 10.1002/qj.49709540607.

Glaze, L. S., S. M. Baloga and L. Wilson (1997). 'Transport of atmospheric water vapor by volcanic eruption columns'. *J. Geophys. Res.*, 102, pp. 6099–6108. DOI: 10.1029/96JD03125.

Gupta, A. K., R. Bennartz, K. E. Fauria and T. Mittal (2022). 'Eruption chronology of the December 2021 to January 2022 Hunga Tonga-Hunga Ha'apai eruption sequence'. *Commun. Earth Environ.*, 3, 314. DOI: 10.1038/s43247-022-00606-3.

Horváth, Á., S. L. Vadas, C. C. Stephan and S. A. Buehler (2024). 'One-Minute Resolution GOES-R Observations of Lamb and Gravity Waves Triggered by the Hunga Tonga-Hunga Ha'apai Eruptions on 15 January 2022'. *J. Geophys. Res.*, 129, e2023JD039329. DOI: 10.1029/2023JD039329.

Hurst, D. F., S. J. Oltmans, H. Vömel, K. H. Rosenlof, S. M. Davis, E. A. Ray, E. G. Hall and A. F. Jordan (2011). 'Stratospheric water vapor trends over Boulder, Colorado: Analysis of the 30 year Boulder record'. *J. Geophys. Res.*, 116, D02306. DOI: 10.1029/2010JD015065.

Jarvis, P. A., T. G. Caldwell, C. Noble, Y. Ogawa and C. Vagasky (2024). 'Volcanic lightning reveals umbrella cloud dynamics of the 15 January 2022 Hunga volcano eruption, Tonga'. *B. Volcanol.*, 86, 54. DOI: 10.1007/s00445-024-01739-3.

Jégou, F., G. Berthet, C. Brogniez, J.-B. Renard, P. François, J. M. Haywood, A. Jones, Q. Bourgeois, T. Lurton, F. Auriol et al. (2013). 'Stratospheric aerosols from the Sarychev volcano eruption in the 2009 Arctic summer'. *Atmos. Chem. Phys.*, 13, pp. 6533–6552. DOI: 10.5194/acp-13-6533-2013.

Joshi, M. M. and K. P. Shine (2003). 'A GCM Study of Volcanic Eruptions as a Cause of Increased Stratospheric Water Vapor'. *J. Climate*, 16, pp. 3525–3534. DOI: 10.1175/1520-0442(2003)016<3525:AGSOVE>2.0.CO;2.

Kahn, R. A., J. A. Limbacher, K. T. Junghenn Noyes, V. J. B. Flower, L. M. Zamora and K. F. McKee (2024). 'Evolving Particles in the 2022 Hunga Tonga—Hunga Ha'apai Volcano Eruption Plume'. *J. Geophys. Res.*, 129, e2023JD039963. DOI: 10.1029/2023JD039963.

Kelly, L. J., K. E. Fauria, M. Manga, S. J. Cronin, F. H. Latu'ila, J. Paredes-Mariño, T. Mittal and R. Bennartz (2024). 'Airfall volume of the 15 January 2022 eruption of Hunga volcano estimated from ocean color changes'. *Bull. Volcanol.*, 86, 59. DOI: 10.1007/s00445-024-01744-6.

Khaykin, S., A. Podglajen, F. Ploeger, J.-U. Grooß, F. Tence, S. Bekki, K. Khlopenkov, K. Bedka, L. Rieger, A. Baron et al. (2022). 'Global perturbation of stratospheric water and aerosol burden by Hunga eruption'. *Commun. Earth Environ.*, 3, 316. DOI: 10.1038/s43247-022-00652-x.

Kloss, C., P. Sellitto, J.-B. Renard, A. Baron, N. Bègue, B. Legras, G. Berthet, E. Briaud, E. Carboni, C. Duchamp et al. (2022). 'Aerosol characterization of the stratospheric plume from the volcanic eruption at Hunga Tonga 15 January 2022'. *Geophys. Res. Lett.*, 49, e2022GL099394. DOI: 10.1029/2022GL099394.

Kovilakam, M., L. W. Thomason, N. Ernest, L. Rieger, A. Bourassa and L. Millán (2020). 'The Global Space-based Stratospheric Aerosol Climatology (version 2.0): 1979–2018'. *Earth Syst. Sci. Data*, 12, pp. 2607–2634. DOI: 10.5194/essd-12-2607-2020.

Kremser, S., L. W. Thomason, M. Von Hobe, M. Hermann, T. Deshler, C. Timmreck, M. Toohey, A. Stenke, J. P. Schwarz, R. Weigel et al. (2016). 'Stratospheric aerosol-Observations, processes, and impact on climate: Stratospheric Aerosol'. *Rev. Geophys.*, 54, pp. 278–335. DOI: 10.1002/2015RG000511.

Leeuw, J. de, A. Schmidt, C. S. Witham, N. Theys, I. A. Taylor, R. G. Grainger, R. J. Pope, J. Haywood, M. Osborne and N. I. Kristiansen (2021). 'The 2019 Raikoke volcanic eruption – Part 1: Dispersion model simulations and satellite retrievals of volcanic sulfur dioxide'. *Atmos. Chem. Phys.*, 21, pp. 10851–10879. DOI: 10.5194/acp-21-10851-2021.

Legras, B. (2025). 'Hunga eruption on 15 January 2022: was there a precursor plume one hour before the eruption?' EarthArXiV manuscript. DOI: 10.31223/X5DT8F.

Legras, B., C. Duchamp, P. Sellitto, A. Podglajen, E. Carboni, R. Siddans, J.-U. Grooß, S. Khaykin and F. Ploeger (2022). 'The evolution and dynamics of the Hunga Tonga–Hunga Ha'apai sulfate aerosol plume in the stratosphere'. *Atmos. Chem. Phys.*, 22, pp. 14957–14970. DOI: 10.5194/acp-22-14957-2022.

Li, C., Y. Peng, E. Asher, A. A. Baron, M. Todt, T. D. Thornberry, S. Evan, J. Brioude, P. Smale, R. Querel et al. (2024). 'Microphysical Simulation of the 2022 Hunga Volcano Eruption Using a Sectional Aerosol Model'. *Geophys. Res. Lett.*, 51, e2024GL108522. DOI: 10.1029/2024GL108522.

Li, Q., Y. Qian, Y. Luo, L. Cao, H. Zhou, T. Yang, F. Si and W. Liu (2023). 'Diffusion Height and Order of Sulfur Dioxide and Bromine Monoxide Plumes from the Hunga Tonga–Hunga Ha'apai Volcanic Eruption'. *Remote Sens.*, 15, 1534. DOI: 10.3390/rs15061534.

Mastin, L. G., A. R. Van Eaton and S. J. Cronin (2024). 'Did steam boost the height and growth rate of the giant Hunga eruption plume?' *Bull. Volcanol.*, 86, 64. DOI: 10.1007/s00445-024-01749-1.

Matoza, R. S., D. Fee, J. D. Assink, A. M. Iezzi, D. N. Green, K. Kim, L. Toney, T. Lecocq, S. Krishnamoorthy, J.-M. Lalande et al. (2022). 'Atmospheric waves and global seismoacoustic observations of the January 2022 Hunga eruption, Tonga'. *Science*, 377, pp. 95–100. DOI: 10.1126/science.abo7063.

Millán, L., M. L. Santee, A. Lambert, N. J. Livesey, F. Werner, M. J. Schwartz, H. C. Pumphrey, G. L. Manney, Y. Wang, H. Su et al. (2022). 'The Hunga Tonga-Hunga Ha'apai Hydration of the Stratosphere'. *Geophys. Res. Lett.*, 49, e2022GL099381. DOI: 10.1029/2022gl099381.

Murphy, D. M., K. D. Froyd, I. Bourgeois, C. A. Brock, A. Kupc, J. Peischl, G. P. Schill, C. R. Thompson, C. J. Williamson and P. Yu (2021). 'Radiative and chemical implications of the size and composition of aerosol particles in the existing or modified global stratosphere'. *Atmos. Chem. Phys.*, 21, pp. 8915–8932. DOI: 10.5194/acp-21-8915-2021.

Niemeier, U., S. Wallis, C. Timmreck, T. van Pham and C. von Savigny (2023). 'How the Hunga Tonga—Hunga Ha'apai Water Vapor Cloud Impacts Its Transport Through the Stratosphere: Dynamical and Radiative Effects'. *Geophys. Res. Lett.*, 50, e2023GL106482. DOI: 10.1029/2023gl106482.

Nowack, P., P. Ceppi, S. M. Davis, G. Chiodo, W. Ball, M. A. Diallo, B. Hassler, Y. Jia, J. Keeble and M. Joshi (2023). 'Response of stratospheric water vapour to warming constrained by satellite observations'. *Nat. Geosci.*, 16, pp. 577–583. DOI: 10.1038/s41561-023-01183-6.

O'Neill, N. T., C. Perro, A. Saha, G. Lesins, T. J. Duck, E. W. Eloranta, G. J. Nott, A. Hoffman, M. L. Karumudi, C. Ritter et al. (2012). 'Properties of Sarychev sulphate aerosols over the Arctic'. *J. Geophys. Res.*, 117, 2011JD016838. DOI: 10.1029/2011JD016838.

Otsuka, S. (2022). 'Visualizing Lamb Waves From a Volcanic Eruption Using Meteorological Satellite Himawari-8'. *Geophys. Res. Lett.*, 49, e2022GL098324. DOI: 10.1029/2022GL098324.

Podglajen, A., A. Le Pichon, R. F. Garcia, S. Gérier, C. Millet, K. Bedka, K. Khlopenkov, S. Khaykin and A. Hertzog (2022). 'Stratospheric Balloon Observations of Infrasound Waves From the 15 January 2022 Hunga Eruption, Tonga'. *Geophys. Res. Lett.*, 49, e2022GL100833. DOI: 10.1029/2022GL100833.

Podglajen, A., B. Legras, G. Lapeyre, R. Plougonven, V. Zeitlin, V. Brémaud and P. Sellitto (2024). 'Dynamics of diabatically forced anticyclonic plumes in the stratosphere'. *Q. J. R. Meteorol. Soc.*, 150, pp. 1538–1565. DOI: 10.1002/qj.4658.

Poli, P. and N. M. Shapiro (2022). 'Rapid Characterization of Large Volcanic Eruptions: Measuring the Impulse of the Hunga Tonga Ha'apai Explosion From Teleseismic Waves'. *Geophys. Res. Lett.*, 49, e2022GL098123. DOI: 10.1029/2022GL098123.

Posey, J. W. and A. D. Pierce (1971). 'Estimation of Nuclear Explosion Energies from Microbarograph Records'. *Nature*, 232, pp. 253–253. DOI: 10.1038/232253a0.

Prata, F., A. T. Prata, R. Tanner, R. G. Grainger, M. Borgas and T. J. Aubry (2025). 'The radial spreading of volcanic umbrella clouds deduced from satellite measurements'. *Volcanica*, 8, pp. 1–29. DOI: 10.30909/vol.08.01.0129.

Proud, S. R., A. T. Prata and S. Schmauß (2022). 'The January 2022 eruption of Hunga Tonga-Hunga Ha'apai volcano reached the mesosphere'. *Science*, 378, pp. 554–557. DOI: 10.1126/science.abo4076.

Purkis, S. J., S. N. Ward, N. M. Fitzpatrick, J. B. Garvin, D. Slayback, S. J. Cronin, M. Palaseanu-Lovejoy and A. Dempsey (2023). 'The 2022 Hunga-Tonga megatsunami: Near-field simulation of a once-in-a-century event'. *Sci. Adv.*, 9, eadf5493. DOI: 10.1126/sciadv.adf5493.

Randel, W. J., B. R. Johnston, J. J. Braun, S. Sokolovskiy, H. Vömel, A. Podglajen and B. Legras

(2023). 'Stratospheric Water Vapor from the Hunga Tonga–Hunga Ha'apai Volcanic Eruption Deduced from COSMIC-2 Radio Occultation'. *Remote Sens.*, 15, 2167, p. 2167. DOI: 10.3390/rs15082167.

Robock, A. (2000). 'Volcanic eruptions and climate'. *Rev. Geophys.*, 38, pp. 191–219. DOI: 10.1029/1998RG000054.

Romeo, F., L. Mereu and S. Scollo (2025). 'Ash and Ice Aggregation in Satellite Retrieval: The 15 January 2022 Hunga Tonga-Hunga Ha'apai Hydromagmatic Eruption'. *J. Geophys. Res.*, 130, e2024JD041196. DOI: 10.1029/2024JD041196.

Rose, W. I., D. J. Delene, D. J. Schneider, G. J. S. Bluth, A. J. Krueger, I. Sprod, C. McKee, H. L. Davies and G. G. J. Ernst (1995). 'Ice in the 1994 Rabaul eruption cloud: implications for volcano hazard and atmospheric effects'. *Nature*, 375, pp. 477–479. DOI: 10.1038/375477a0.

Salby, M. L. (1979). 'On the Solution of the Homogeneous Vertical Structure Problem for Long-Period Oscillations'. *J. Atmos. Sci.*, 36, pp. 2350–2359. DOI: 10.1175/1520-0469(1979)036<2350:OTSOTH>2.0.CO;2.

Schoeberl, M. R., Y. Wang, R. Ueyama, G. Taha, E. Jensen and W. Yu (2022). 'Analysis and Impact of the Hunga Tonga-Hunga Ha'apai Stratospheric Water Vapor Plume'. *Geophys. Res. Lett.*, 49, e2022GL100248. DOI: 10.1029/2022gl100248.

Schoeberl, M. R., Y. Wang, R. Ueyama, G. Taha and W. Yu (2023). 'The Cross Equatorial Transport of the Hunga Tonga-Hunga Ha'apai Eruption Plume'. *Geophys. Res. Lett.*, 50, e2022GL102443. DOI: 10.1029/2022gl102443.

Seabrook, S., K. Mackay, S. J. Watson, M. A. Clare, J. E. Hunt, I. A. Yeo, E. M. Lane, M. R. Clark, R. Wysoczanski, A. A. Rowden et al. (2023). 'Volcaniclastic density currents explain widespread and diverse seafloor impacts of the 2022 Hunga Volcano eruption'. *Nat. Commun.*, 14, 7881. DOI: 10.1038/s41467-023-43607-2.

Sellitto, P., A. Podglajen, R. Belhadji, M. Boichu, E. Carboni, J. Cuesta, C. Duchamp, C. Kloss, R. Siddans, N. Bègue et al. (2022). 'The unexpected radiative impact of the Hunga Tonga eruption of 15th January 2022'. *Commun. Earth Environ.*, 3, 288. DOI: 10.1038/s43247-022-00618-z.

Sellitto, P., R. Siddans, R. Belhadji, E. Carboni, B. Legras, A. Podglajen and et al. (2024). 'Observing the SO_2 and sulfate aerosol plumes from the 2022 Hunga eruption with the Infrared Atmospheric Sounding Interferometer (IASI)'. *Geophys. Res. Lett.*, 51, e2023GL105565. DOI: 10.1029/2023GL105565.

Sepúlveda, I., M. Carvajal and D. C. Agnew (2023). 'Global Winds Shape Planetary-Scale Lamb Waves'. *Geophys. Res. Lett.*, 50, e2023GL106097. DOI: 10.1029/2023GL106097.

Sioris, C. E., A. Malo, C. A. McLinden and R. D'Amours (2016). 'Direct injection of water vapor into the stratosphere by volcanic eruptions'. *Geophys. Res. Lett.*, 43, pp. 7694–7700. DOI: 10.1002/2016GL069918.

Spurr, R. J. D., M. Christi, N. A. Krotkov, W.-E. Choi, S. Carn, C. Li, N. Kramarova, D. Haffner, E.-S. Yang, N. Gorkavyi et al. (2025). 'Solar Backscatter Ultraviolet (BUV) Retrievals of Mid-Stratospheric Aerosols from the 2022 Hunga Eruption'. *EGUsphere [preprint]*, 2025, pp. 1–43. DOI: 10.5194/egusphere-2025-2938.

Stocker, M., A. K. Steiner, F. Ladstädter, U. Foelsche and W. J. Randel (2024). 'Strong persistent cooling of the stratosphere after the Hunga eruption'. *Commun. Earth Environ.*, 5, 450. DOI: 10.1038/s43247-024-01620-3.

Symons, G. J. et al., eds. (1888). *The Eruption of Krakatoa and Subsequent Phenomena: report of the Krakatoa committee of the Royal Society*. UK: Trübner & Company, p. 494.

Taha, G., R. Loughman, P. R. Colarco, T. Zhu, L. W. Thomason and G. Jaross (2022). 'Tracking the 2022 Hunga Tonga-Hunga Ha'apai Aerosol Cloud in the Upper and Middle Stratosphere Using Space-Based Observations'. *Geophys. Res. Lett.*, 49, e2022GL100091. DOI: 10.1029/2022gl100091.

Taylor, G. I. (1929). 'Waves and tides in the atmosphere'. *Proc. R. Soc. Lond. A*, 126, pp. 169–183. DOI: 10.1098/rspa.1929.0213.

Textor, C., H.-F. Graf, M. Herzog and J. M. Oberhuber (2003). 'Injection of gases into the stratosphere by explosive volcanic eruptions'. *J. Geophys. Res.*, 108, 2002JD002987. DOI: 10.1029/2002JD002987.

Vadas, S. L., E. Becker, C. Figueiredo, K. Bossert, B. J. Harding and L. C. Gasque (2023). 'Primary and secondary gravity waves and large-scale wind changes generated by the Tonga volcanic eruption on 15 January 2022: Modeling and comparison with ICON-MIGHTI winds'. *J. Geophys. Res.*, 128, e2022JA031138. DOI: 10.1029/2022JA031138.

Van Eaton, A. R., J. Lapierre, S. A. Behnke, C. Vagasky, C. J. Schultz, M. Pavolonis, K. Bedka and K. Khlopenkov (2023). 'Lightning Rings and Gravity Waves: Insights Into the Giant Eruption Plume

From Tonga's Hunga Volcano on 15 January 2022'. *Geophys. Res. Lett.*, 50, e2022GL102341. DOI: 10.1029/2022gl102341.

Vergoz, J., P. Hupe, C. Listowski, A. Le Pichon, M. A. Garcés, E. Marchetti, P. Labazuy, L. Ceranna, C. Pilger, P. Gaebler et al. (2022). 'IMS observations of infrasound and acoustic-gravity waves produced by the January 2022 volcanic eruption of Hunga, Tonga: A global analysis'. *Earth Planet. Sci. Lett.*, 591, 117639. DOI: 10.1016/j.epsl.2022.117639.

Vömel, H., S. Evan and M. Tully (2022). 'Water vapor injection into the Stratosphere by Hunga Tonga-Hunga Ha'apai'. *Science*, 377, pp. 1444–1447. DOI: 10.1126/science.abq2299.

Watanabe, S., K. Hamilton, T. Sakazaki and M. Nakano (2022). 'First Detection of the Pekeris Internal Global Atmospheric Resonance: Evidence from the 2022 Tonga Eruption and from Global Reanalysis Data'. *J. Atmos. Sci.*, 79, pp. 3027–3043. DOI: 10.1175/JAS-D-22-0078.1.

Wrana, F., U. Niemeier, L. W. Thomason, S. Wallis and C. Von Savigny (2023). 'Stratospheric aerosol size reduction after volcanic eruptions'. *Atmos. Chem. Phys.*, 23, pp. 9725–9743. DOI: 10.5194/acp-23-9725-2023.

Wright, C. J., N. P. Hindley, M. J. Alexander, M. Barlow, L. Hoffmann, C. N. Mitchell, F. Prata, M. Bouillon, J. Carstens, C. Clerbaux et al. (2022). 'Surface-to-space atmospheric waves from Hunga Tonga-Hunga Ha'apai eruption'. *Nature*, 609, pp. 741–746. DOI: 10.1038/s41586-022-05012-5.

Wu, J., S. J. Cronin, M. Brenna, S.-H. Park, A. Pontesilli, I. A. Ukstins, D. Adams, J. Paredes-Mariño, K. Hamilton, M. Huebsch et al. (2025). 'Low sulfur emissions from 2022 Hunga eruption due to seawater–magma interactions'. *Nat. Geosci.*, 18, pp. 518–524. DOI: 10.1038/s41561-025-01691-7.

Zhu, Y., C. G. Bardeen, S. Tilmes, M. J. Mills, X. Wang, V. L. Harvey, G. Taha, D. Kinnison, R. W. Portmann, P. Yu et al. (2022). 'Perturbations in stratospheric aerosol evolution due to the water-rich plume of the 2022 Hunga-Tonga eruption'. *Commun. Earth Environ.*, 3, 248. DOI: 10.1038/s43247-022-00580-w.

Zhu, Y., R. W. Portmann, D. Kinnison, O. B. Toon, L. Millán, J. Zhang, H. Vömel, S. Tilmes, C. G. Bardeen, X. Wang et al. (2023). 'Stratospheric ozone depletion inside the volcanic plume shortly after the 2022 Hunga Tonga eruption'. *Atmos. Chem. Phys.*, 23, pp. 13355–13367. DOI: 10.5194/acp-23-13355-2023.

3 Atmospheric transport and evolution of Hunga water vapour and aerosols

Lead authors Sergey Khaykin
Adam Bourassa

Co-authors Valentina Aquila
Alexandre Baron
Landon Rieger
Alexei Rozanov
Rei Ueyama

Contributing authors

Elizabeth Asher	Nelson Begue
Slimane Bekki	Ewa M. Bednarz
Marie Boichu	Christoph Brühl
Parker Case	Simon Chabrillat
Margot Clyne	Peter Colarco
Kimberlee Dube	Lola Falletti
David Flittner	Raphael Grandin
Eilidh Hlady	Julien Jumelet
Mahesh Kovilakam	Nicolas Lebas
Cheng-Cheng Liu	Gloria L. Manney
Marion Marchand	Luis F. Millán
Yifeng Peng	Richard Querel
Samuel Remy	Tetsu Sakai
Michelle L. Santee	Takashi Sekiya
Florent Tence	Simone Tilmes
Xinyue Wang	Shingo Watanabe
Pengfei Yu	Wandi Yu
Jun Zhang	Yunqian Zhu
Zhihong Zhuo	

Cite this as:

Khaykin, S., A. Bourassa et al. (2025): Atmospheric transport and evolution of Hunga water vapour and aerosols. In APARC, 2025: The Hunga Eruption Atmospheric Impacts Report [Yunqian Zhu, Graham Mann, Paul A. Newman, William Randel (Eds.)]. APARC Report No. 11, WCRP Report No. 10/2025, DOI: 10.34734/FZJ-2025-05240, available at `https://aparc-climate.org/publications/aparc-report-no-11/`.

Key points

Chapter 3 focuses on the evolution of the Hunga aerosol and water vapour after the first month. By March 2022, the volcanic plume had become zonally distributed in the tropics and over the next two years became dispersed meridionally across the globe.

- The volcanic aerosol was transported globally and the perturbation lasted more than two years.
  - In two months (by March 2022) the aerosol covered essentially all of the tropics, reaching stratospheric aerosol optical depth values greater than 0.02 at 1 μm.
  - In five months (by June 2022) the bulk of Hunga aerosol had been transported to the southern mid-latitude stratosphere due to efficient winter transport; northward transport was much weaker and more sporadic during that season.
  - In six months (by July 2022) the global stratospheric aerosol optical depth, which was still dominated by the aerosol in the southern hemisphere, reached a maximum value of 0.01 at 1 μm, and then decayed with an e-folding time of 20 months. This is the largest aerosol optical depth caused by a volcanic eruption since Mt. Pinatubo in 1991.
  - It took over two years for the stratospheric aerosol optical depth to decay to pre-eruption levels. Throughout this time, the bulk of the aerosol remained below 30 km.
  - The Hunga-driven stratospheric aerosol perturbation era has ended with the eruption of Ruang volcano in April 2024.
- The water vapour was transported globally, rose to the mesosphere, and remained dispersed throughout the atmosphere after more than two years.
  - The global anomaly in stratospheric water vapour mass was more than 15% higher than climatology and 10% higher than immediately before the eruption.
  - Transport over the first year was similar to the aerosol transport pattern, extending across most of the tropics in two months (March 2022), and largely moving to the southern mid-latitudes in five months (June 2022).
  - The water vapour remained between 20–32 km altitude for the first nine months (until October 2022), partly because the H_2O-forced radiative cooling counteracted the upwelling.
  - After this point, the water vapour ascended rapidly and reached the stratopause by early 2023.
  - By 2024, the water vapour anomaly was largely confined to the mesosphere, above approximately 50 km, and mostly at mid- and high latitudes.
- The aerosol particle size grew rapidly over less than a month to an effective radius of 0.4 μm and remained roughly constant over two years.
  - Balloon-borne measurements of the aerosol size distribution across the tropics and mid-latitudes show aerosol effective radius values of 0.4 μm in the Southern Hemisphere concurrent with the transport of the bulk aerosol.
  - Aerosol effective radius values in the Northern Hemisphere only reach 0.2 μm due to weaker transport and mixing with the background distribution.
  - Elevated values of particle size remained roughly constant over two years while gradually sedimenting toward tropopause altitudes.
- Transport of the water vapour and aerosol to the poles was effectively blocked by the polar vortex edges in the first winters in both hemispheres, and entrained in the vortices in the following winters.
  - In the Southern Hemisphere, Hunga water vapour reached the Antarctic vortex edge by mid-June 2022 and was excluded from entering the vortex due to the strong transport barrier at the edge; water vapour was entrained in the developing vortex of 2023.
  - Similarly, in the Northern Hemisphere, Hunga water vapour pervaded mid-latitudes by the second fall after the eruption and was entrained into the 2023/2024 vortex as it developed.

  - While the bulk of the aerosol did not penetrate the Antarctic vortex in 2022, observations suggest the presence of subtle aerosol layers in the lowermost high-latitude stratosphere before the vortex onset.

- Satellite observations show remarkable agreement between available measurements of stratospheric water vapour, and unusually large differences in aerosol extinction.
  - Available satellite observations of stratospheric water vapour use widely different measurement techniques yet agree in derived values of stratospheric mass anomaly to a remarkable degree of accuracy (less than 10% difference) throughout the two-year dispersion of the plume.
  - Large differences are observed in comparisons between aerosol measurements from satellites. The SAGE III/ISS measurements are the most accurate. Differences with other observations are often 50% and sometimes up to 100%. A main driver of these differences is systematic effects of the assumed particle size distribution in the limb scatter retrieval algorithms.

- Models simulate the global and vertical transport patterns of aerosols and water vapour reasonably well.
  - Models simulate the southward transport and vertical separation of the volcanic aerosol and water vapour quite well, indicating reasonably good representation of the large-scale circulation, polar vortex dynamics, and aerosol gravitational settling.
  - All models simulate smaller values of the Hunga perturbations in global stratospheric aerosol optical depth and water vapour compared to observations, but the decay rates of the perturbations are generally well simulated.
  - The cross-equatorial transport of the aerosol and water vapour perturbations from the Southern Hemisphere to the Northern Hemisphere is underestimated in all models.
  - All models simulate a rapid increase in effective radius after the eruption followed by a decrease as the largest particles differentially settle out of the atmosphere. The peak radius varies across models, but all models agree on a simulated radius of 0.2–0.3 μm two years after the eruption.

Contents

3.1 Meridional dispersion of water vapour and aerosol . . . 65
3.2 Evolution of sulfate aerosols . . . 68
3.2.1 Aerosol growth and changes in the size distribution . . . 68
3.2.2 Sedimentation of aerosol particles . . . 69
3.2.3 Hunga aerosol in the long-term record . . . 70
3.3 Transport of volcanic material into the polar regions . . . 71
3.3.1 Water vapour . . . 71
3.3.2 Aerosol . . . 72
3.4 Uncertainty of observations . . . 74
3.4.1 Aerosol optical depth and extinction . . . 74
3.4.2 Water vapour . . . 77
3.5 Modelling of the Hunga plume evolution . . . 78
3.5.1 Meridional dispersion of the volcanic aerosol and water vapour . . . 78
3.5.2 Vertical separation of the volcanic aerosol and water vapour and evolution of the aerosol radius . . . 80
3.5.3 Longevity and decay of the water-vapour and aerosol perturbations . . . 82
3.5.4 Summary of model performances . . . 83

Preamble

Chapter 3 describes the global meridional and vertical evolution of the Hunga sulfate aerosols and water vapour after the full zonal dispersion of the plume, which occurred about one month after the eruption. Section 3.1 documents the dispersion of water vapour and aerosol, and Section 3.2 describes the global evolution of aerosol size derived from satellite, balloon-borne, and ground-based observations. Section 3.3 focuses on the transport of Hunga materials to the polar regions, including the Arctic and Antarctic polar vortices. The uncertainties of satellite observations of the Hunga aerosols and water vapour are assessed in Section 3.4, which provides a detailed intercomparison between various satellite data sets. Finally, results from dedicated climate model simulations of the global transport and evolution of Hunga aerosol and water vapour, in comparison with the observations, are provided in Section 3.5.

3.1 Meridional dispersion of water vapour and aerosol

By mid-February 2022, approximately one month after the eruption, the Hunga water vapour and sulfate aerosols were spread zonally across the southern tropics (Khaykin et al. (2022) and Chapter 2 of this assessment). The subsequent meridional dispersion of sulfate aerosols can be seen in Figure 3.1a, which shows the daily zonal average of stratospheric aerosol optical depth (SAOD) as observed by the OMPS-LP satellite instrument. Two months after the eruption, the bulk of the aerosol extended between 25°S–10°N, with zonal-mean SAOD values greater than 0.02 at 997 nm. At that time, there was a measurable SAOD enhancement covering almost the entire tropics (30°S–20°N). While the first detections of Hunga aerosol plumes at southern mid-latitudes were reported at Lauder station, New Zealand (45°S) and Dumont d'Urville (DDU) French Antarctic station (67°S) three and four weeks after the eruption, respectively (Khaykin et al., 2022), the Hunga aerosol largely shifted towards southern mid-latitudes three months after the eruption, in mid-April. At this time, the southern stratosphere started to turn to the winter regime, enabling a more efficient transport from the tropical belt towards the extratropics across the stratospheric "surf zone" around 30°S (Polvani et al., 1995). By June (five months after the eruption), the bulk of Hunga aerosol had migrated to the southern mid-latitudes.

The transport of the Hunga aerosols to northern mid-latitudes was more gradual. Figure 3.1a shows that the enhanced SAOD progressed towards the northern edge of the tropics within three months following the eruption. This was followed by several episodes of in-mixing into the northern extratropics in April 2022 and during November 2022 to January 2023 (Khaykin et al., 2024). These processes were reflected in the slow increase of Northern Hemisphere SAOD, peaking in mid-April 2022 and again in late 2022 (red curve in Figure 3.1c). The northbound dispersion of thin aerosol plumes between 22–25 km was captured by lidar observations across the northern extratropics (38°N–69°N) (Khaykin et al., 2020), whereas the larger-scale increase in the northern extratropical SAOD was not observed before early 2023 (Figure 3.1a). However, by far, the bulk of Hunga aerosol remained in the Southern Hemisphere.

The global SAOD perturbation reached its maximum value six months after the eruption, in July 2022, and subsequently entered a decay phase. During the second half of 2022, the SAOD decay rate in the Southern Hemisphere was faster than the global decay due to interhemispheric northbound transport (Figure 3.1c). One year after the eruption, in early 2023, the Hunga aerosol was spread across the entire Southern Hemisphere, and the SAOD decay rate in the Southern Hemisphere slowed and followed the global decay. By March 2024, more than two years post-eruption, the global and hemispheric SAOD time series converged and approached pre-eruption levels by mid-April 2024. The first significant post-Hunga SAOD perturbation, caused by the eruption of the Ruang stratovolcano in Indonesia on 16 April 2024 (Global Volcanism Program, 2024), ended the era of Hunga-driven stratospheric aerosol perturbation. Extrapolation of the stable decay of Hunga southern-hemispheric SAOD during early 2024 leads to an inferred total lifetime of the Hunga-induced stratospheric aerosol load of about 2.5 years, spanning from mid-January 2022 to mid-July 2024. The e-folding time of the global Hunga SAOD, taken from the peak in Figure 3.1c, is approximately 20 months. For comparison, the e-folding time of the extra-polar (polar regions excluded) SAOD perturbation caused by the Pinatubo eruption was 21 months, as inferred from the GloSSAC merged satellite dataset.

The meridional dispersion of the stratospheric columnar water vapour (SCWV) anomaly, derived from MLS measurements, is shown in Figure 3.1b as a daily zonal average, with the global anomaly reaching above 15% (Figure 3.1d). The observed transport was largely similar to that of the SAOD perturba-

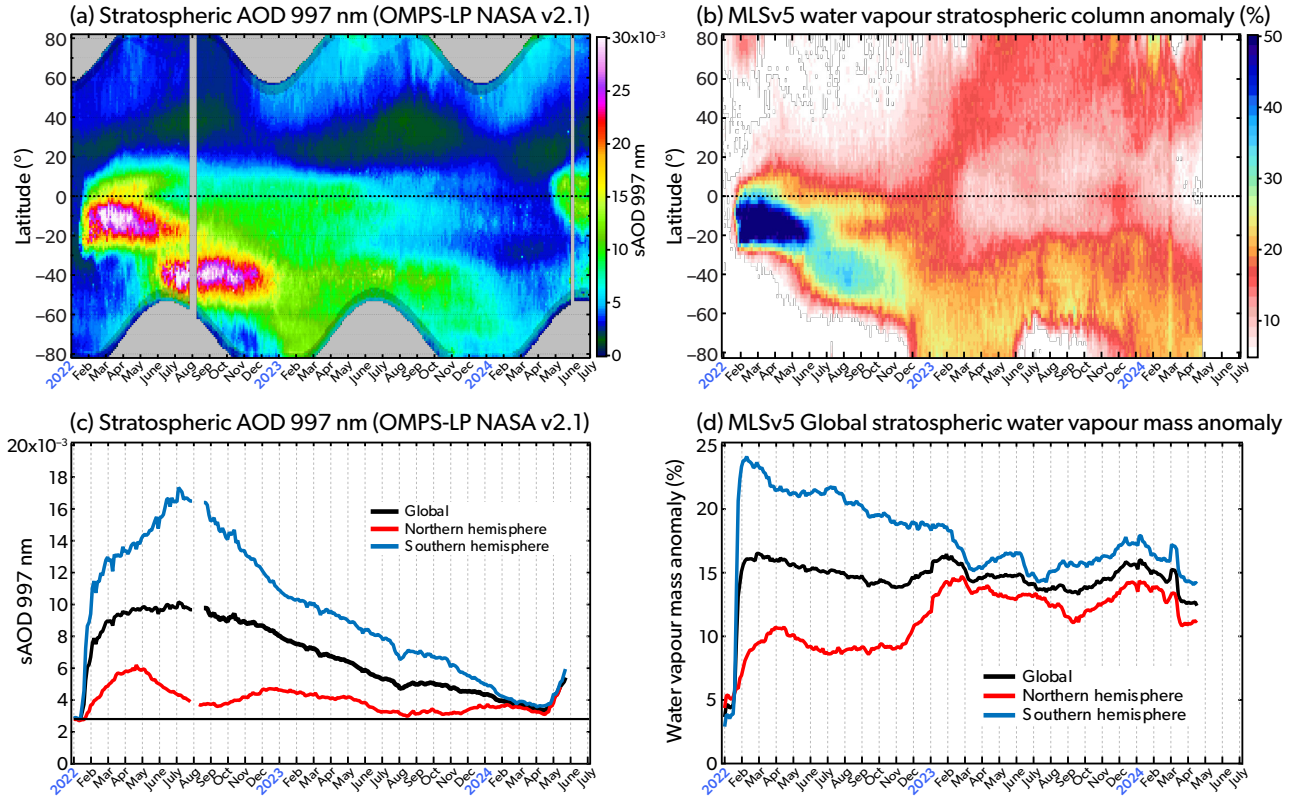

Figure 3.1: *Meridional dispersion and evolution of Hunga aerosol and water vapour perturbation. (a) Stratospheric aerosol optical depth (SAOD) as a function of time and latitude from OMPS-LP NASA at 997 nm. (b) Water vapour anomaly as a function of time and latitude from MLS. (c) OMPS-LP NASA SAOD time series for global average, Northern Hemisphere, and Southern Hemisphere. (d) MLS water vapour anomaly time series for global average, Northern hemisphere, and Southern hemisphere. The anomaly is computed from deseasonalised MLS data prior to 2022.*

tion during the first four months, extending over 30°S–10°N by mid-May 2022. Small in-mixing events of Hunga moisture into the northern extratropics during March–April 2022 observed by MLS were confirmed by balloon soundings in China at 26.7°N (Xu et al., 2022).

A striking difference between the evolutions of the aerosol and water vapour distributions is that, while the Hunga sulfate aerosols experienced descent due to gravitational settling, the water vapour rose in altitude in the tropics within the deep branch of the Brewer–Dobson circulation. This led to vertical separation of the particulate and gaseous Hunga material (detailed below) and substantially modified their meridional transport pattern beginning in late 2022. While the aerosol perturbation remained largely restricted to the Southern Hemisphere, Figure 3.1b shows that in January 2023 the Hunga stratospheric moisture experienced a major episode of northward transport from the tropical pipe to the northern high latitudes. This striking transport can be linked to the seasonal dynamics of the Arctic stratospheric vortex, which was subject to a sudden stratospheric warming event in early 2023 (Newman et al., 2024). By the end of boreal winter 2023, the Hunga water vapour reached full planetary extent; however, at this point, most of the excess moisture was outside the tropics (Figure 3.1b). In the tropics, the anomaly remained mostly below 10% after March 2023 but experienced two measurable enhancements around June 2023 and November 2023, which can both be linked to distinct tropical tropopause temperature variations (not shown).

As with the stratospheric aerosol, the Hunga SCWV perturbation was predominantly in the Southern Hemisphere, where the anomaly from the climatological levels reached 24% shortly after the eruption and decreased to 22% by May 2022 due to cross-equatorial transport (Figure 3.1d). By March 2023, 14 months after the eruption, the hemispheric SCWV anomalies converged to the global anomaly of 15% to within 1%, indicating quasi-uniform global meridional dispersion of Hunga water vapour. This timeframe of 14 months is an indication of the global stratospheric mixing timescale, which has been uniquely provided

by the Hunga eruption as a natural experiment on stratospheric composition.

The further evolution of the SCWV perturbation in the extratropics was driven by the dehydration in the Antarctic polar vortex during June–October 2023 through polar stratospheric clouds (PSCs) (Zhou et al., 2024; Millán et al., 2024), as well as by sub-seasonal dynamics of the Arctic polar vortex during boreal winter 2023/2024. By March 2024, water vapour in the tropics reached background levels; however, the global anomaly was only 7.7% lower than the maximum post-Hunga anomaly in late February 2022 (Figure 3.1d). Unlike the polar or tropical regions, the lifetime of excessive moisture in the midlatitude stratosphere is less constrained by vertical removal mechanisms.

As noted above and in Chapter 2, the differences in the meridional dispersion patterns of aerosols and water vapour are driven by their vertical separation. The vertical evolutions of the Hunga water vapour anomaly and sulfate aerosols for different latitudinal regions are shown in Figure 3.2. One month after the eruption, the bulk of the water vapour anomaly, ranging between 1–4 ppmv in the tropics (Figure 3.2b), was confined to altitudes between 20–30 km, which roughly corresponded to the vertical extent of the volcanic aerosol. During the first few months after the eruption, the upward propagation of the moist anomaly in the tropical upwelling was partly inhibited by radiative cooling caused by the excessive moisture (Sellitto et al., 2022; Schoeberl et al., 2022). The ascent of the tropical water vapour anomaly began in October 2022 and reached the stratopause by early 2023. The acceleration of tropical upwelling in late 2022 can be associated with a change in the QBO phase. By early 2024, the extent of the water vapour anomaly exceeding 1 ppmv was entirely above the stratosphere and occupied a broad altitude layer in the mesosphere.

In contrast to the gaseous water, the aerosol particles were subject to gravitational settling, and the bulk of aerosols remained in the lower stratosphere, between 17–25 km altitude. The ultimate vertical separation of the aerosol and water vapour perturbations at all latitude bands occurred approximately one year after the eruption. While the aerosols gradually settled to the tropopause level, the water vapour anomaly persisted in the middle stratosphere throughout 2022. The steep rise in altitude of the hydrated layer in April 2023 is associated with transport from outside the tropical pipe, as noted above. In the northern extratropics, the water vapour anomaly did not appear

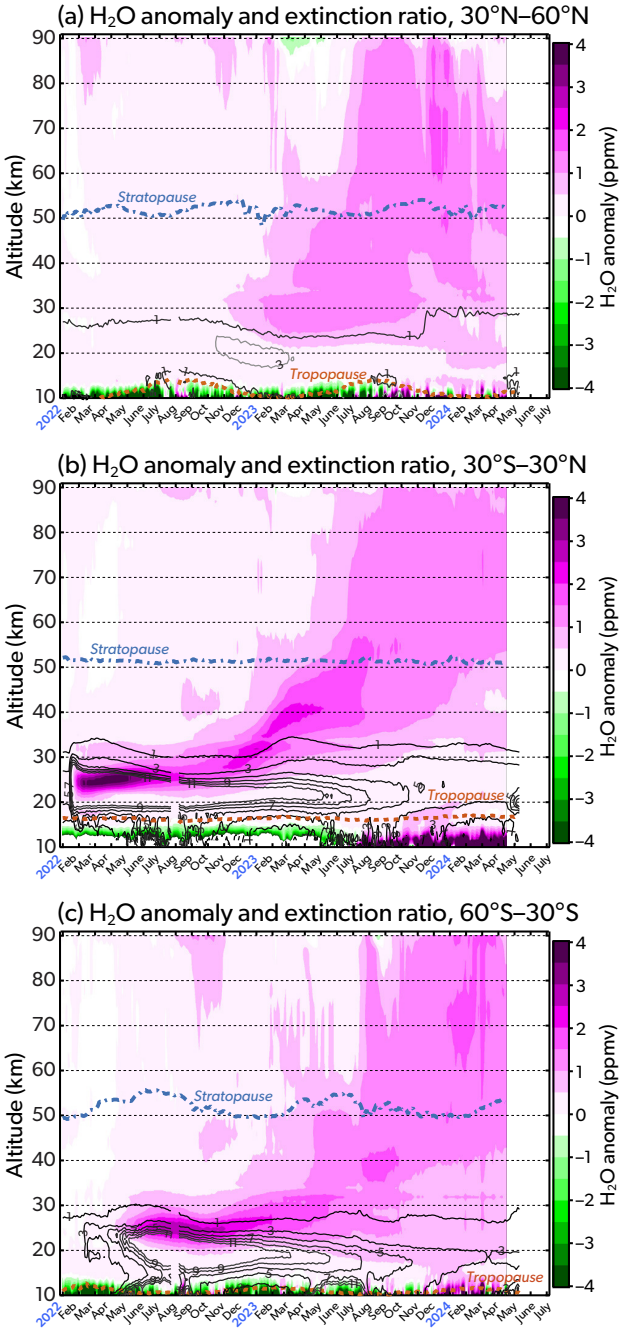

Figure 3.2: *Vertical evolution of the water vapour absolute anomaly and aerosol perturbation from MLS and OMPS-LP. Water vapour anomaly (shades) and aerosol extinction ratio (contours) as a function of time and altitude at different latitude bands: (a) 30°N–60°N, (b) 30°S–30°N, and (c) 60°S–30°S.*

before November 2022 and then largely replicated the vertical evolution pattern seen in the south. Variations of the anomaly in the mesosphere are likely linked to solar activity through molecular dissociation by Lyman-α radiation and formation of noctilucent clouds (Sonnemann and Grygalashvyly, 2005). By early 2024, two years after the eruption, the water

vapour anomaly larger than 1 ppmv extended from the tropopause to the mesopause in the extratropics, whereas the aerosols had largely settled out of the stratosphere.

3.2 Evolution of sulfate aerosols

3.2.1 Aerosol growth and changes in the size distribution

As noted in Chapter 2, the emitted SO_2 gas converted rapidly, within days, to sulfate aerosol droplets. Meanwhile, the UV-absorbing particles—likely ash—were observed only during the first week after the eruption and in relatively small amounts. Within a month, the Hunga aerosol already consisted of sulfate aerosol particles with a size distribution that was unexpectedly stable and characteristic of this eruption. Indeed, after the rapid growth phase (see Chapter 2), the particles stopped growing, unlike what has been measured in former major eruptions, e.g. the Pinatubo sulfates' modal radius up to 0.8 µm, as reported by Russell et al. (1996). Namely, the aerosol grew within a week from a typical stratospheric background radius centred around 0.15 µm to a narrower pseudo-lognormal size distribution with a modal radius of approximately 0.35 µm (e.g. Duchamp et al., 2023; Li et al., 2024).

Several complementary lines of observations corroborate this result. Balloon-borne *in-situ* profiles using the Portable Optical Particle Spectrometer (POPS) were able to assess the aerosol size in the early plume above La Réunion (see Chapter 2; Asher et al., 2023) and continued to monitor the microphysics of the plume with time and latitude from several stations (`https://csl.noaa.gov/projects/b2sap/`). These observations complement the SAGE III/ISS satellite measurements of the spectrum of aerosol extinction that allow for the retrieval of a single-mode lognormal size distribution using the methods presented in Wrana et al. (2021) and Knepp et al. (2024).

A convenient way of condensing the information on the aerosol size distribution is to compute the effective radius of the aerosol. Namely, the effective radius is the ratio of the third (volume) to the second (surface) moments of the size distribution. It represents a suitable proxy for the size distribution when calculating radiative properties of the aerosol and is a commonly retrieved quantity from optical satellite measurements. For a single-mode lognormal distribution with a known width, the effective radius relates to the modal radius with an analytic expression (Duchamp et al., 2023).

Figure 3.3 shows the evolution of the effective radius of the Hunga aerosol. The zonal mean of the SAGE III/ISS effective radius is displayed for four latitude bands, from northern to southern mid-latitudes, together with balloon-borne POPS profiles from La Réunion, France (21° S; Figure 3.3a), Hilo, Hawaii (19° N; Figure 3.3b), Lauder, New Zealand (45° S; Figure 3.3c), and Boulder, Colorado (40° N; Figure 3.3d). Although these two types of measurements use completely different techniques, the results agree well in terms of both magnitude and altitude of the effective-radius perturbation. The peak effective radius reached just above 0.4 µm in the early stage in the southern tropics. The larger particles are observed later in the southern mid-latitude reaching similar values of effective radius. In the northern hemisphere, the aerosol size does not show a large increase, with effective radius reaching up to approximately 0.2 µm. This is consistent with the observed transport of the bulk of the aerosol toward the southern hemisphere, and the mixing with the background aerosol in the northern mid-latitudes.

In addition to the satellite remote sensing and *in-situ* measurements, the size distribution of Hunga aerosols can be constrained by photometric ground observations from multiple stations of the worldwide AERONET network. A rapid growth is observed in the days following the eruption (see Chapter 2 for details), faster than that observed after the 1991 Pinatubo eruption (Boichu et al., 2023). Figure 3.4 shows that a distinct increase in aerosol peak radius of the calculated fine-mode volume size distribution (r_{peak}) to values in the range 0.3–0.5 µm was reported across the 23 AERONET stations of the Southern Hemisphere. This persisted until at least March 2024, in full agreement with SAGE III/ISS and POPS observations. Hence, despite a rapid growth in the post-eruption week—likely due to the exceptional abundance of water in the Hunga plume resulting from the phreatomagmatic nature of the eruption (interaction of water and magma)—the Hunga aerosols remained smaller than those reported after the Mt. Pinatubo eruption in 1991 (Boichu et al., 2023).

The Lauder station (New Zealand, 45° S) within the Balloon Baseline Stratospheric Aerosol Profiles project (B2SAP; `https://csl.noaa.gov/projects/b2sap/`) has been an ideal location for monitoring the fate of the Hunga aerosol plume microphysics with time. Observations from this station are representative of the volcanic aerosol that persisted in the southern mid-latitudes until 2024 (see Section 3.1). In Fig-

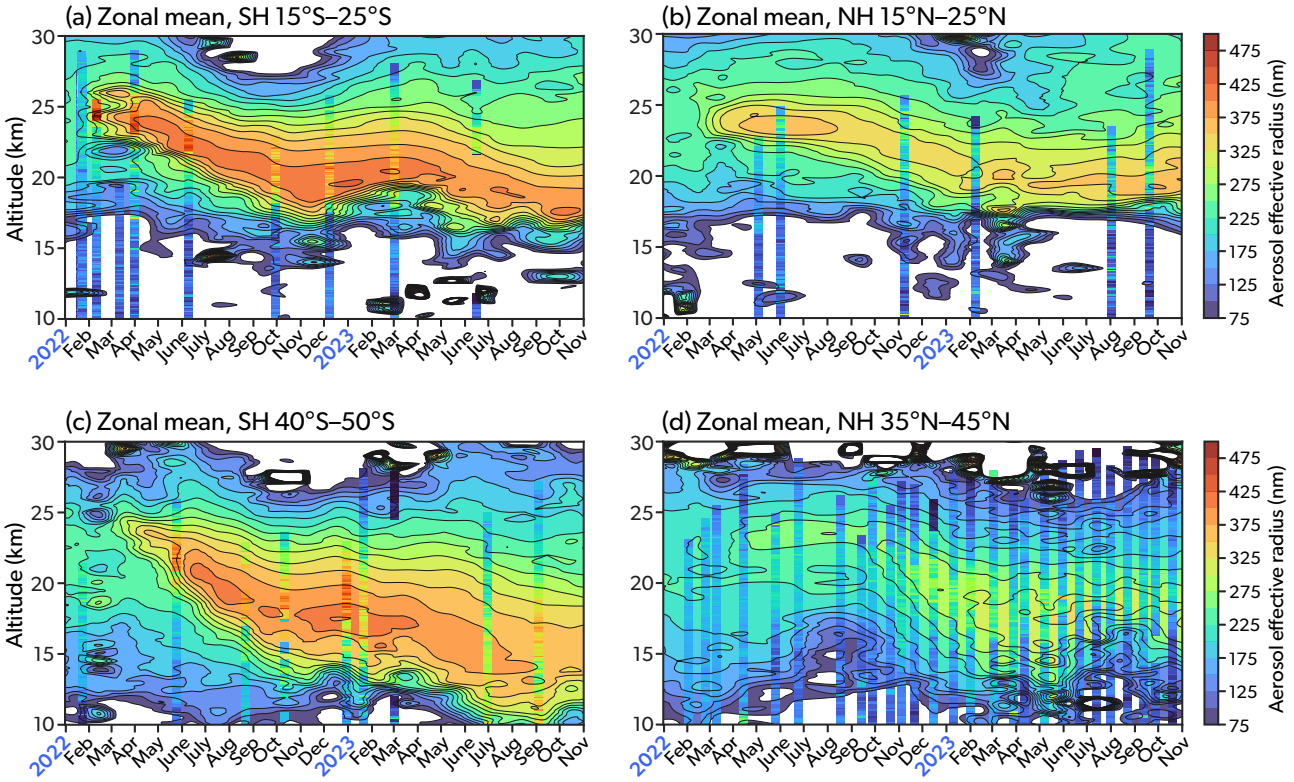

Figure 3.3: *Aerosol effective radius as a function of time and latitude in four latitude bands retrieved from SAGE III/ISS solar occultation spectra, with overlaid markers representing effective radius measured in situ by balloon sondes.*

ure 3.5, POPS-derived normalised aerosol surface size distributions are plotted in 6-month increments from January 2022 for two stratospheric regions (broadly defined as mid and lower stratosphere). The aerosol surface is both relevant for heterogeneous chemistry in the stratosphere and long-term radiative properties.

For the mid-stratosphere region, with potential temperature from 550 K to 750 K (approximately 22–28 km altitude at this latitude), the surface size distribution shifted toward larger sizes soon after the eruption. From background conditions with a modal radius below 0.1 µm, the perturbed distribution shifted to peak around 0.35 µm (Figure 3.5a, red–purple curve) during the first six months after the eruption. With time, this decreased to approximately 0.25 µm in early 2023 and remained relatively stable into 2024. At the end of 2024, this Hunga mode was fading away.

In the lower-stratosphere region, with potential temperature from 380 K to 550 K (approximately 14–22 km altitude at this latitude), a somewhat different particle evolution was observed. Six months after the eruption, the modal radius of the aerosol surface size distribution was centred at approximately 0.25 µm but increased with time to peak around 0.35 µm in 2023. By the end of 2024, a return toward background conditions (modal radius of approximately 0.11 µm) was observed (Figure 3.5b), with the perturbed mode decreasing in favour of a smaller mode (< 0.1 µm). These results from POPS profiles from Lauder demonstrate the sedimentation of larger particles, initially formed in the mid-stratosphere, to the lower stratosphere. This is further discussed in the following section.

3.2.2 Sedimentation of aerosol particles

The SAGE III/ISS extinction and derived effective-radius profiles (Knepp et al., 2024) provide a clear picture of the particle sedimentation that occurred following the Hunga eruption. Figure 3.6 shows the time evolution of average profiles in the tropics between 10° S and 10° N. For the four months preceding the eruption (Panels A–B), the particle effective radius (shown in red) was approximately 0.25 μm for most of the lower stratosphere. In the months immediately following the eruption (Panels C-D), effective radius is approximately 0.4 μm with a peak near 25 km, which is consistent with the balloon-borne and ground-based results presented in the previous section. At this point in time, the extinction at 755 nm, shown in black, has a peak that is collocated with the peak in effective radius. From May to August 2022

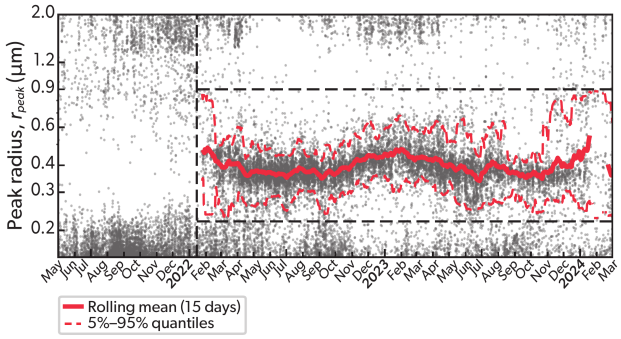

Figure 3.4: *Composite time series of aerosol peak radius (r_{peak}) ranging within the volcanic size range [0.22–0.90] µm at 23 AERONET stations of the Southern Hemisphere. r_{peak} is the radius at the peak of the aerosol volume size distribution (fine mode). The thick red line shows the rolling median computed after the Hunga eruption (vertical dashed line) with a 15-day window, restricted to data points within the volcanic size range (black dashed lines). Dashed red lines indicate the 5% and 95% quantiles. Among the 23 AERONET stations, 11 are in the southern tropics (lat < 23.5° S) and 12 are in the southern mid-latitudes (up to 45.8° S). The stations include Niassa (Mozambique), American Samoa, Mount Chacaltaya (Bolivia), La Paz (Bolivia), Huancayo IGP (Peru), Lucinda (Australia), Windpoort (Namibia), Maïdo OPAR (Réunion Island), Learmonth (Australia), HESS (Namibia), SP-EACH (Brazil), Gobabeb (Namibia), PSDA Chile (Chile), Yerba Loca (Chile), Metsi (South Africa), Upington (Zambia), Fowlers Gap (Australia), Lake Lefroy (Australia), AU NSW Lidcombe (Australia), Univ. of Auckland (New Zealand), CEILAP–Neuquén (Argentina), Trelew (Argentina), and CEILAP–Comodoro (Argentina).*

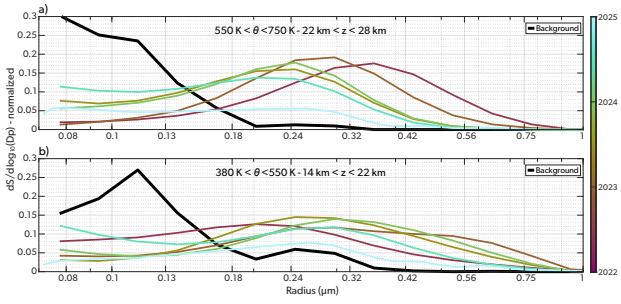

Figure 3.5: *Time evolution (6-month increments) of the resolved aerosol surface size distribution (normalised) measured in situ by balloon sondes from Lauder, New Zealand (45° S): (a) upper stratosphere (potential temperature 550–750 K, equivalent to 22–28 km), and (b) lower stratosphere (potential temperature 380–550 K, equivalent to 14–22 km).*

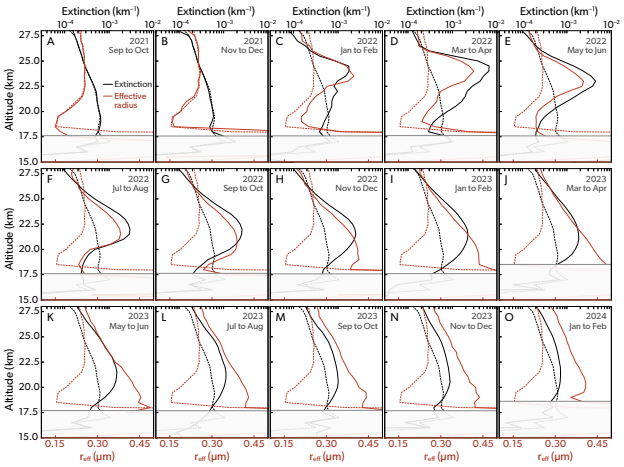

Figure 3.6: *Two-month average profiles of aerosol extinction (black, top axis) and effective radius (red, bottom axis) from SAGE III/ISS in the tropics (10° S–10° N), showing the descent of larger particles and the eventual altitude separation of the peak extinction and peak effective radius. In each panel, pre-eruption extinction (September–December) and radius profiles from late 2021 are shown as dashed curves for reference.*

(Panels E-F) this relationship between effective radius and extinction continues with both quantities having peaks that both drop and spread out in altitude. Past August 2022 (Panels G-O) there is a marked altitude separation between the extinction and effective radius peaks, with the extinction peak remaining near 22 km while the effective radius peak continues to drop. During this descent, the effective radius continues a slow increase, with values approaching 0.45 µm by September 2023. While the extinction peak remains near 22 km, it continues to broaden; coupled with the changes in effective radius this indicates a gradation of particle sizes as the larger particles sediment more rapidly.

3.2.3 Hunga aerosol in the long-term record

The longest continuous records of SAOD are provided by ground-based lidars operating within the Network for the Detection of Atmospheric Composition Change (NDACC) and merged satellite products. In order to compare the magnitude of Hunga-induced SAOD perturbation with that of past moderate and major eruptions, Figure 3.7 shows monthly-mean SAOD time series from two midlatitude and two tropical lidars sites located symmetrically with respect to the equator: Lauder (45° S), La Réunion (21° S), Mauna Loa (21° N) and Observatoire de Haute-Provence (OHP; 44° N), each compared with the Global Space-based Stratospheric Aerosol Climato-

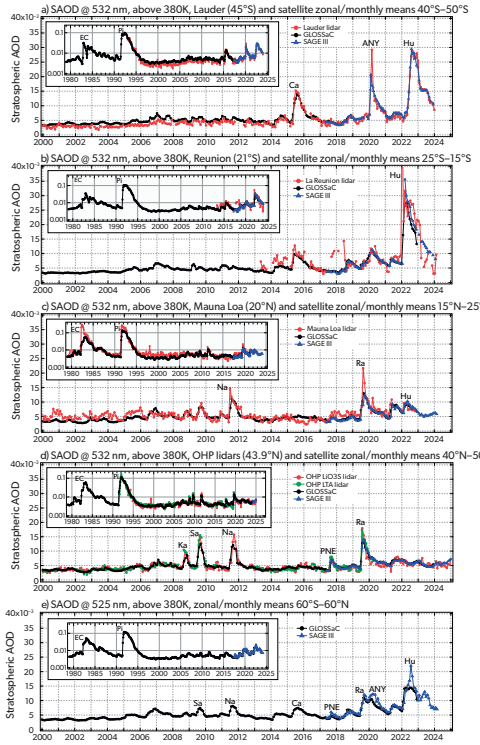

Figure 3.7: *Time series of aerosol optical depth above the 380 K potential temperature level from ground-based lidars at different sites, compared with GloSSAC V2.21 merged satellite data and SAGE III/ISS observations zonally averaged within corresponding 10° latitude bands: (a) Lauder (45° S); (b) La Réunion (21° S); (c) Mauna Loa (21° N); (d) Haute-Provence (44° N); (e) Satellite quasi-global series within 60° S–60° N.*

logy (GloSSAC; Kovilakam et al., 2020) and zonally averaged SAGE III/ISS data for the respective latitude band.

The largest SAOD perturbation magnitude was recorded at La Réunion (21° S) in January 2022, which is expected given the site's location directly downwind of Hunga at nearly the same latitude (Figure 3.7b). As the bulk of Hunga aerosols was transported to the southern mid-latitudes in June 2022 (see Section 3.1), the peak of the SAOD perturbation at Lauder (45° S) was observed during June–July 2022 (Figure 3.7a). In both Southern Hemisphere lidar records, the magnitude of the Hunga perturbation is the largest observed since Mt. Pinatubo in 1991.

In contrast, the SAOD perturbation at Mauna Loa (21° N; Figure 3.7c), at the northern edge of the tropics, was relatively weak, with SAOD returning to pre-eruption levels before the end of 2023. At the northern mid-latitudes (Figure 3.7d), the OHP record shows a small increase in SAOD in late 2022, reflecting the gradual transport of Hunga aerosols to the northern extratropics (Section 3.1). The SAOD time series averaged for the full 60° S–60° N latitude range (Figure 3.7e), from GloSSAC and SAGE III/ISS, confirms that even on a near-global scale the Hunga SAOD perturbation is the largest observed in the post-Pinatubo era. However, even at these levels, the peak magnitude of the Hunga SAOD perturbation was approximately a factor of six smaller than that of Pinatubo.

3.3 Transport of volcanic material into the polar regions

This section focuses specifically on the transport of the volcanic aerosol and water vapour into the polar regions. This process is particularly important due to its potential for impact on the size and strength of the polar vortex, and perturbation of the vortex chemistry, including ozone loss.

3.3.1 Water vapour

Manney et al. (2023) detailed the march of the Hunga water vapour plume towards the developing polar vortex in austral fall 2022. Figure 3.8 shows the global transport of the Hunga eruption water-vapour plume through 2023 as measured by MLS, using equivalent latitude as a coordinate to distinguish vortex from extra-vortex air. The bulk of the plume transported into the Southern-Hemisphere extratropics during 2022 remained between approximately 500 K and 800 K (about 50–10 hPa; 20–30 km altitude) and reached the vortex edge in early- to mid-June 2022 at those altitudes (Figures 3.8a–3.8b, 3.8f). By this time, the Antarctic stratospheric polar vortex—developing since April at these levels—had reached near-full strength and acted as an effectively impenetrable transport barrier, excluding Hunga water vapour from the 2022 vortex. Consequently, there was no discernible effect of Hunga water vapour on vortex processing in the 2022 Antarctic winter (Manney et al., 2023 and Chapter 5). Hunga-enhanced water vapour was able to reach the polar regions only after the springtime vortex breakup, in November 2022 at higher altitudes (Figure 3.8a) to December 2022 in the lower stratosphere (Figure 3.8b). By Southern-Hemisphere fall 2023, high Hunga-derived water vapour pervaded Southern-Hemisphere high latitudes (Figures 3.8a, 3.8b, 3.8i) and was entrained into the developing Antarctic vortex, with resultant impacts on polar processes as detailed in Chapter 5 (see also Santee et al., 2024; Wohltmann et al., 2024).

In the Northern Hemisphere, Hunga water vapour reached the edge of the 2022/2023 Arctic vortex in the mid-stratosphere by January 2023, after it had de-

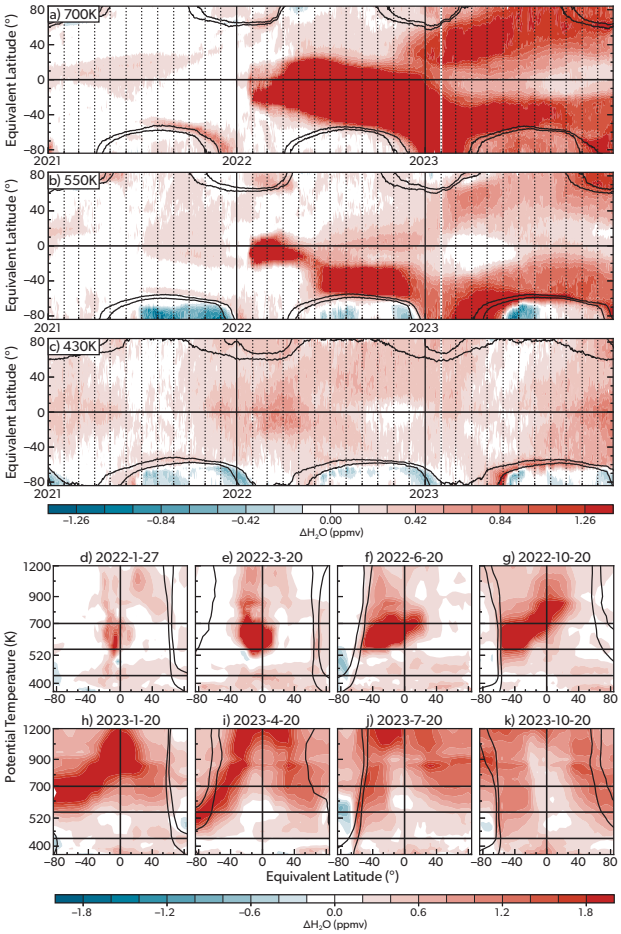

Figure 3.8: *Time series and equivalent-latitude cross-sections of water vapour anomalies from MLS. (a–c) Time series of water vapour anomalies as a function of equivalent latitude for 2021–2023 at (a) 700 K (near 27 km, 18 hPa), (b) 550 K (near 23 km, 38 hPa), and (c) 430 K (near 18 km, 82 hPa). (d–k) Equivalent-latitude / potential-temperature snapshots of water vapour anomalies on eight representative days spanning 2022–2023. Black overlays on all panels are scaled potential-vorticity contours representing the vortex-edge region. Updated from Manney et al. (2023).*

veloped and presented a substantial transport barrier (Figures 3.8a, 3.8h); in the lower stratosphere near 20 km (Figure 3.8b) enhanced extra-vortex water vapour is seen outside the vortex starting in February, having descended from higher levels (Figures 3.8h, 3.8i). This enhanced water vapour was blocked from entering the vortex region until a mid-February sudden stratospheric warming resulted in extensive mixing between vortex and extra-vortex air, mixing high water vapour that had descended in the vortex from the upper stratosphere with high water vapour transported into the region from the Hunga plume (Lee et al., 2024). As in the SH, by the second fall after the eruption, Hunga-enhanced water vapour pervaded mid-latitudes and was entrained into the vortex as it developed. The 2023/2024 Arctic winter was characterised by two major sudden stratospheric warming events; the resultant lower stratospheric temperatures increases and associated transport resulted in much less than typical chemical ozone loss in Arctic spring 2024 (Newman et al., 2024).

3.3.2 Aerosol

While the satellite measurements of aerosol extinction are not made in the polar night regions, the aerosol backscatter and depolarisation by CALIPSO CALIOP satellite lidar as well as by a ground-based cloud/aerosol lidar at Dumont d'Urville (DDU) station at 67° S can be used to study the transport of Hunga sulfate aerosols into the Antarctic region. In order to distinguish between solid polar stratospheric cloud (PSC) particles (NAT and ice) from liquid spherical particles (including PSC supercooled ternary solution, STS), we use CALIOP depolarisation ratio, providing information on the particle sphericity. In addition, we use 195 K as an approximate PSC-permitting temperature threshold (Peter, 1997) to identify the measurements unaffected by PSCs of any type.

Figure 3.9a displays the time-altitude series of scattering ratio restricted to liquid spherical aerosols (volume depolarisation below 5%; Pitts et al., 2018), which include volcanic sulfates and STS particles, from DDU lidar and CALIOP observations. While the first detection of a weak aerosol layer from Hunga over DDU was in mid-February 2022 (Khaykin et al., 2022), more substantial sulfate aerosol layers between 12-22 km altitude were observed throughout April 2022 (labelled T1 in Figure 3.9a) and afterwards between 18-23 km in mid-May (T2), just before the onset of the Antarctic polar vortex in June 2022 (grey shading in Figure 3.9a). The presence of Hunga sulfates in the southern high-latitude stratosphere by the time of vortex onset implies that the aerosols were most likely entrained by the vortex, however a reliable distinction between sulfate aerosols and subtle STS clouds that have similar optical properties is difficult using lidar observations. That said, the Hunga sulfates were present in the lowermost high-latitude stratosphere during the 2022 vortex season as suggested by the enhanced scattering ratio between 11-14 km outside the PSC-permitting temperature conditions represented by 195 K temperature isoline derived from DDU radiosoundings (white contour in Figure 3.9a).

A series of stronger enhancements in scattering ratio

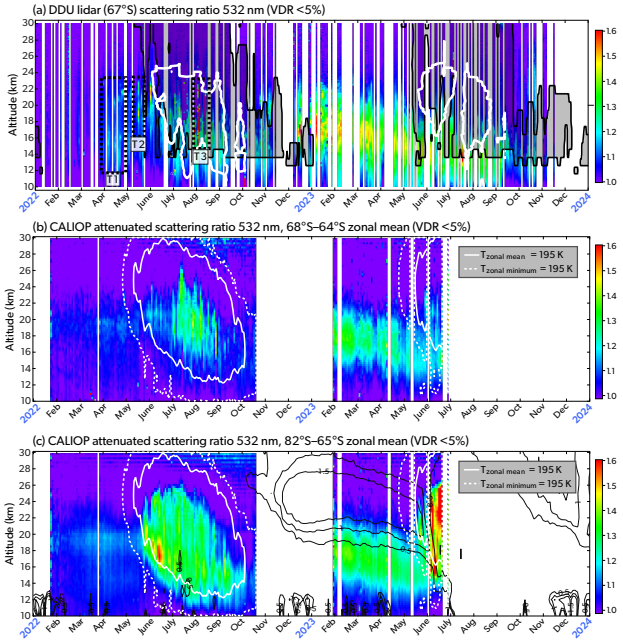

Figure 3.9: *Transport of Hunga sulfate aerosols into the Antarctic region from lidar observations. (a) Height-resolved time series of scattering ratio at 532 nm from ground-based lidar at Dumont d'Urville station (66.7° S, 140.0° E). Analysis is restricted to data with volume depolarisation ratio (VDR) < 5%, corresponding to spherical aerosols (sulfates and liquid PSC particles). Grey shading represents the polar-vortex mask defined using MERRA-2 reanalysis and the method of Lawrence et al. (2018). The white contour shows the 195 K temperature isoline (approximate PSC-formation threshold) from daily radiosoundings at DDU (minimum over a 7-day window). Black dashed rectangles labelled T1–T3 indicate the time/altitude windows referred to in the text. (b) Same as (a), but from CALIOP night-time zonally averaged measurements within the 68° S–64° S latitude band, without the vortex mask. Solid and dashed white contours indicate the 195 K temperature isoline (zonal mean and zonal minimum) from MERRA-2 data. (c) Same as (b), but for 82° S–65° S; black contours show MLS water-vapour anomalies in ppmv.*

between 14–22 km altitude during August 2022 (T3) can be attributed to STS clouds forming within the colder upper layer of the stratosphere. The locally observed time–altitude evolution of the scattering ratio from liquid aerosols is consistent with the zonal-mean CALIOP data at DDU latitudes (Figure 3.9b). After the final breakdown of the 2022 vortex, the excess aerosols from Southern-Hemisphere mid-latitudes expanded rapidly into high latitudes while slowly sedimenting. During the 2023 vortex season, the enhanced scattering ratios were observed mostly within the 10–15 km altitude layer outside the STS-permitting temperature environment (Figure 3.9a), and can thus be attributed to Hunga sulfates.

A broader perspective on the evolution of Hunga sulfates and liquid PSCs over the southern polar cap is provided by CALIOP zonal-mean observations between 82° S and 65° S (Figure 3.9c). During the 2022 Antarctic vortex, the time–altitude pattern of scattering ratio represented a typical signal of liquid PSCs (Tritscher et al., 2021), consistent with the 195 K temperature isoline. By the onset of the 2023 vortex, the Hunga sulfate aerosols were ubiquitous within the 14–18 km layer above the southern polar cap. At the same time, the MLS water vapour anomaly exceeding 0.5 ppmv was located at higher altitudes (black contours in Figure 3.9c), mostly above the aerosol layer. While both water vapour and aerosol anomalies were gradually descending at high southern latitudes, they entered the 2023 vortex at different levels, one above another. The aerosols entered the lower part of the vortex whereas the moist anomaly above 2.5 ppmv was entrained by the vortex in a wide altitude range between 19-26 km. This was immediately followed by a vortex-wide outbreak of liquid STS-type PSCs, which can be attributed to the excess of moisture. Indeed, a change in water vapour by 1 ppmv increases the threshold temperature for STS formation by about 1 K (Wohltmann et al., 2024). Another in-vortex layer of enhanced scattering ratio can be observed in early June at lower levels (15-17 km), vertically matching the aerosol layer entrainment by the vortex. It is conceivable that the pre-existing volcanic sulfate particles may also have enhanced the formation of STS clouds in the lower part of the 2023 vortex.

In addition to the lidar observations, several balloon-borne POPS soundings have been carried out from polar locations since the onset of the Hunga eruption. The unique microphysical signature of the Hunga aerosol particle size can trace the Hunga influence at polar latitudes. As shown in Figure 3.10a, at the northern high latitude station Utqiaġvik (Alaska, 71° N) in March 2023, the effective radius profiles in the stratosphere above 10 km do not present large layers with a strong Hunga signature. Note that the two profiles on 14 and 15 March 2023, sampled the polar vortex and measured lower effective radii between 15-20 km in altitude. The profile of March 14 presents some effective radius enhancement above 0.2 µm that may be attributed to Hunga particle influence. This is consistent with a mixing between smaller size background aerosol and Hunga particles, as identified in lower latitudes in the northern hemisphere (Section 3.1).

Below 10 km, the variability is likely due to aerosol transport in the free-troposphere, often impacted by wildfires even early in the season.

In the southern high latitudes (Figures 3.10b–3.10c), data from Scott Base (78° S) and the South Pole Observatory (Amundsen–Scott Station, 90° S) there is no strong evidence of concentrated Hunga plume reaching Antarctica by November 2022 (Figure 3.10b). However, the effective radius peaks just above 0.2 μm between 10-15 km and may be due to mixing with Hunga particles. In Austral spring 2023, the Hunga aerosols are unambiguously present above Antarctica with effective radius reaching up to 0.36 μm above 10 km. At South Pole (Figure 3.10c), available profiles during the Austral winter and spring 2024 highlights a return to the state observed at Scott Base during the Austral spring 2023. These profiles exhibit the low effective radius signature of the polar vortex above 15 km. During Austral summer 2025 in South Pole, Hunga signature is not perceived.

3.4 Uncertainty of observations

3.4.1 Aerosol optical depth and extinction

Uncertainty in the aerosol extinction coefficients and optical depth obtained from satellite measurements is evaluated by comparing solar occultation observations from the SAGE III/ISS instrument with limb-scatter measurements from the OMPS-LP instrument. For the latter, results from three different retrieval algorithms—NASA, the University of Bremen (IUP), and the University of Saskatchewan (USask)—are analysed (Taha et al., 2021; Bourassa et al., 2023; Rozanov et al., 2024). As those three retrievals use the same measured radiances, the resulting differences in retrieved extinction illustrate the influence of different assumptions about, e.g., aerosol particle size distribution and different retrieval techniques. In addition, results obtained from measurements of the limb-scatter OSIRIS instrument are shown. OSIRIS is in a different orbit than OMPS-LP, thus the differences between the results from those retrievals are also due to the viewing geometry, i.e. different single scattering angles, and illustrate the influence of the assumption about the aerosol particle size distribution. Dependence of the retrieval results on the assumption about the particle size distribution and viewing geometry is discussed e.g. by Rieger et al. (2019).

Figure 3.11 shows the time series of aerosol optical depth from SAGE III/ISS, OSIRIS, and all three available OMPS-LP retrievals in three latitude bands in the Southern Hemisphere. The dots show individual measurements while the solid curves are a 60-day rolling average to account for sampling gaps. In the time period with relatively weak volcanic activity before 2022, results from all satellite instruments and different retrievals agree very well in terms of the magnitude and temporal variation. The only exception is the first half of 2020 in the 50°–40° S latitude band, where the aerosol load of the stratosphere was strongly influenced by the Australian bush fires. For this period SAGE III/ISS results are on the upper range and USask OMPS-LP data are on the lower range of the spread. The differences between the minimum and maximum values reach about 50% in the beginning of 2020.

In contrast to the limb-scatter observations made by OMPS-LP and OSIRIS, SAGE III/ISS occultation measurements do not require any assumptions about aerosol type or particle size distribution to derive extinction. For this reason, SAGE III/ISS results are considered most reliable when considering single retrievals. Some issues might however arise for monthly mean data because of a sparsity of spatio-temporal sampling of the solar occultation measurements. After the Hunga eruption in January 2022, the spread between different data sets drastically increased. The NASA results are generally at the upper edge of the spread while OSIRIS values are always significantly lower in comparison to all others. OMPS-LP retrievals from IUP and USask are typically close to each other and systematically lower than SAGE III/ISS results. OMPS-LP results of NASA are typically higher than those from SAGE III/ISS. Despite the differences in the absolute values of the aerosol extinction, the shape of the extinction peak in the first half of 2022 is similar for SAGE III/ISS and all OMPS-LP retrievals. Larger differences in the temporal variation of the aerosol depth are seen in 2023. In the 50°–40° S latitude band, the second peak in the optical depth is observed in OMPS-LP NASA earlier than in the SAGE III/ISS results while OMPS-LP retrievals from IUP and USask do not show any secondary peak at all. In the 30°–20° S latitude band, the secondary peak is quite strong in OMPS-LP NASA results, much weaker in OMPS-LP USask time series and is not seen in SAGE III/ISS and OMPS-LP IUP data. In the 10° S–10° N latitude band, SAGE III/ISS and OMPS-LP IUP agree reasonably well, while OMPS-LP retrievals from NASA and USask show secondary peaks later in 2023. In 2024, the stratospheric aerosol load decreases toward the pre-eruption level and the agreement between different data sets significantly improves.

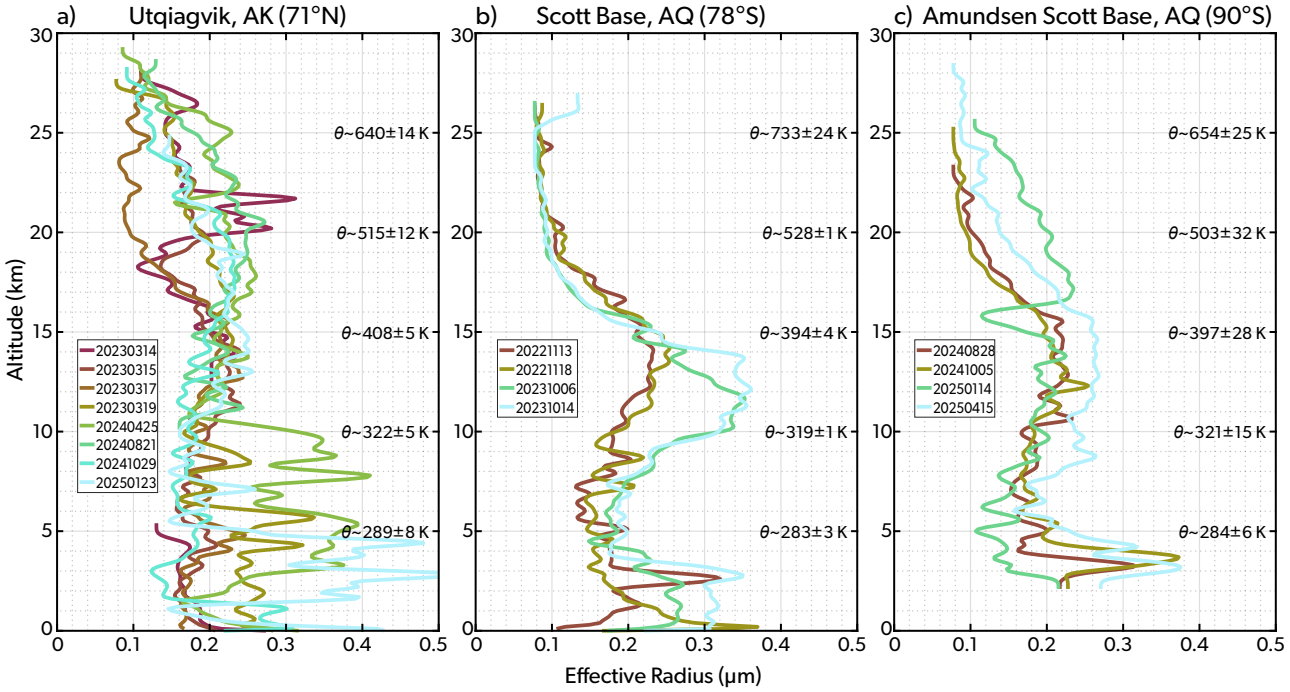

Figure 3.10: *Aerosol effective radius derived from balloon sounding measurements (radius range 0.07–1.25 μm) at polar stations: (a) Utqiaġvik (71° N), (b) Scott Base (78° S), and (c) South Pole (90° S). Potential-temperature equivalent levels averaged over the plotted profiles are displayed on the right axis of each panel.*

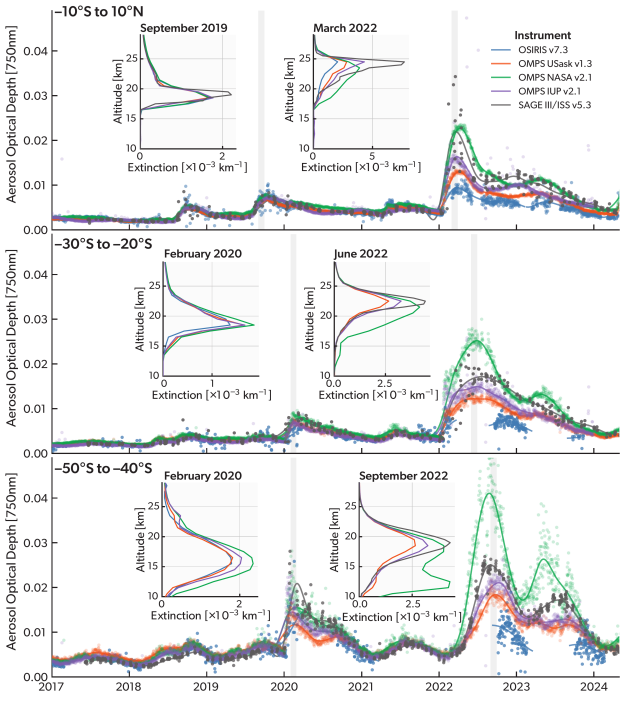

Figure 3.11: *Time series of aerosol optical depth from SAGE III/ISS, OSIRIS, and all three OMPS-LP retrievals (NASA, IUP, and USask) in three latitude bands of the Southern Hemisphere. Inset panels show the monthly mean extinction profiles from each instrument for the months marked by vertical grey shaded regions.*

A strong factor for the differences observed after the Hunga-Tonga eruption is likely the assumption of the aerosol particle size distribution needed for the limb-scatter retrieval algorithms for the radiative transfer forward model. The results indicate that a particle size distribution typical for the background aerosol conditions, which is assumed in the limb-scatter retrievals, is not adequate for the atmospheric conditions after the Hunga-Tonga eruption and adds substantial uncertainty to these data sets.

The inset panels in Figure 3.11 show the monthly average extinction profiles from each instrument for months marked by the vertical grey shaded regions. From these plots we see that for weak perturbations in the stratospheric aerosol as seen e.g. in February 2020 in the 30°–20° S latitude band and in September 2019 in the 10° S–10° N latitude band, results from all instruments agree reasonably well. For a stronger perturbation as seen in March 2020 in the 50°–40° S latitude band, larger differences are observed. NASA results show the best agreement with SAGE III/ISS while the OSIRIS data are the lowest and show higher peak altitude as compared to all other data sets. Within the Hunga aerosol, OMPS-LP retrievals from IUP and USask agree very well with SAGE III/ISS data in terms of the profile shape and peak altitude but show significantly lower values in the peak range. The OMPS

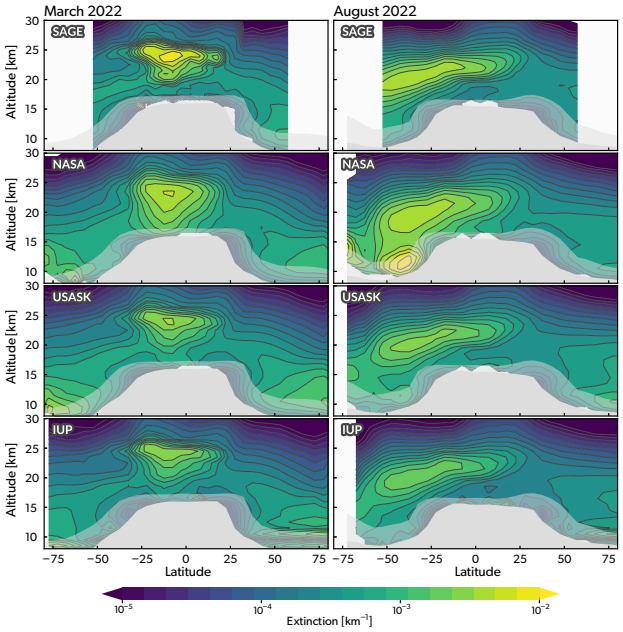

Figure 3.12: *Comparison of aerosol extinction at 750 nm from all three OMPS-LP retrievals and SAGE III/ISS. Panels show zonal averages from each instrument for March (left) and August (right) 2022. The light-grey region indicates altitudes that are sometimes in the stratosphere; the opaque grey region indicates altitudes always in the troposphere.*

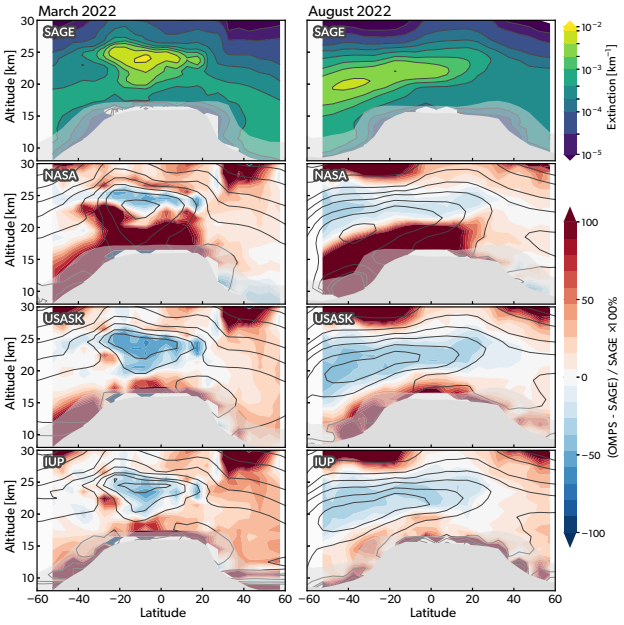

Figure 3.13: *Comparison of aerosol extinction at 750 nm from all three OMPS-LP retrievals and SAGE III/ISS. Panels show zonal averages from each instrument and the corresponding percent difference of OMPS-LP from SAGE III/ISS. Black contours show the extinction from each instrument, delineating the region of the Hunga aerosol. Light-grey regions indicate altitudes that are sometimes in the stratosphere; opaque-grey regions indicate altitudes always in the troposphere.*

NASA retrieval shows similar peak values as SAGE III/ISS (except for March 2022 in the 10° S–10° N latitude band) but somewhat lower peak altitude and very different profile shape. The aerosol extinction coefficient values below the profile peak reported by the NASA retrieval are much higher compared to all other data sets.

The high bias of the NASA retrieval below the profile peak seen in example plots in Figure 3.11 is also clearly illustrated in Figure 3.12, which shows the aerosol extinction profiles from SAGE III/ISS and three OMPS-LP retrievals for two example months (March 2022 in the left panel and August 2022 in the right panel) as a function of the altitude and longitude. This plot is done using the zonal monthly mean data for all instruments and retrievals. Figure 3.12 shows that the OMPS-LP IUP and USask retrievals reproduce the shape of the aerosol plume seen by SAGE III/ISS very well but show consistently lower values. In the OMPS-LP NASA results the shape of the aerosol plume is distorted below the peak and the resulting aerosol extinction coefficients are often higher than those from SAGE III/ISS.

The relative differences with respect to the SAGE III/ISS data for all three OMPS-LP retrievals in March and August 2022 are shown in Figure 3.13. The position of the Hunga-Tonga aerosol plume is shown by the overlaid black contours. The shape of the differences is very similar for IUP and USask retrievals with a low bias in the aerosol plume peak area and high bias outside. The differences are larger in March 2022 (within 2 months after the eruption) reaching about 60% for USask and 40% for IUP retrievals. The differences for the OMPS-LP NASA retrieval show a pronounced vertical structure around the peak altitude with a low bias of up to about 50% above the peak altitude and a positive bias exceeding 100% below. In the Northern mid-latitudes, where only occasional penetrations of the Hunga-Tonga aerosols were observed, the pattern of the differences with respect to SAGE III/ISS results is similar for all three OMPS-LP retrievals but the absolute values of the differences are somewhat higher for OMPS-IUP retrieval. Comparisons poleward of 60°N/S are not always possible due to the more limited latitudinal coverage of SAGE III/ISS compared to OMPS-LP. The feasibility of extending GloSSAC with the OMPS measurements to help fill these gaps is currently under investigation (Kovilakam et al., 2025).

The results discussed in this section show that the

results from SAGE III/ISS and different OMPS-LP retrievals agree well for background aerosol conditions. After the Hunga eruption, the spatio-temporal evolution of the volcanic plume is essentially captured by all satellite data sets considered here, but large differences occur in the magnitude of the aerosol extinction. The size of the differences depends on the retrieval and on the time after the eruption. This confirms previous findings, that a realistic assumption about the aerosol particle size distribution is important for limb-scatter retrievals (Rieger et al., 2014), and that strong volcanically perturbed particle size drives large uncertainty in these observations.

3.4.2 Water vapour

The uncertainty in the water vapour observations can also be investigated through comparison of satellite observations. Like the aerosol, the water vapour levels are substantially different from those ever encountered before in the era of space-borne observations posing potential issues for the available measurement and retrieval approaches. There are three main satellite instruments that are able to measure water vapour profiles in the stratosphere with reasonable vertical resolution and coverage across a wide range of latitudes: MLS, ACE-FTS, and SAGE III/ISS. While these are all limb sounding instruments, the measurement approaches of these three instruments are quite different in terms of spectral range and sampling. MLS measures emitted radiation from the atmosphere in the microwave spectral region, while ACE-FTS and SAGE III/ISS measure attenuated solar radiation through occultation with ACE-FTS observing in the mid-infrared, and SAGE III/ISS in the visible and near infrared.

MLS has by far the best global coverage of the three, with daily global coverage extending up to latitudes greater than 80° latitude. Figure 3.14a shows the daily zonal average time series of water vapour mass anomaly as measured by MLS for latitudes 80°S to 80°N and altitudes between 19-60 km. Note that this is essentially the same as the global percent anomaly shown in Figure 3.1d; however, here mass units are calculated following the methodology in Khaykin et al. (2022). Also, the MLS data are first corrected for the artefact reported by Millán et al. (2024), which is caused by a discontinuity in the retrieval *a priori* following the methodology suggested in that paper.

Figure 3.14a also shows the same water vapour mass anomaly but for a reduced latitude range of 50°S-50°N to facilitate the comparison with the SAGE III/ISS and

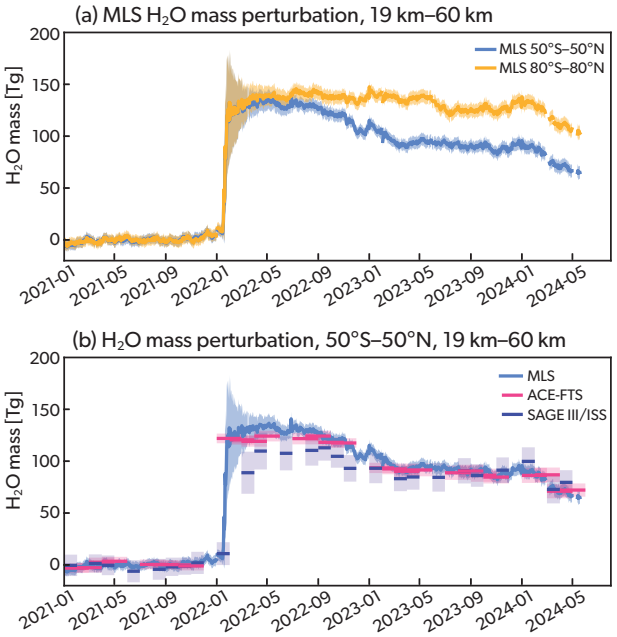

Figure 3.14: *Stratospheric water-vapour mass anomaly from MLS, ACE, and SAGE III/ISS. Daily averages are shown for MLS, whereas the coarser sampling from occultation instruments (ACE and SAGE) requires 2–3-month averages to capture the latitudinal distribution.*

AGE-FTS solar occultation observations, shown in Figure 3.14b. The reduced sampling of the solar occultation technique means it requires 1-2 months to sample the latitudinal extent enabled by the orbit, and that the highest latitudes are sampled more infrequently. One month time averages for SAGE III/ISS and 2 month time averages for ACE-FTS limited to latitudes 50°S-5°N provide a good balance between number of samples and latitudinal coverage. Even at this resolution, some bins do not cover the full range of latitudes, and bins that are not fully sampled at least every 10 degrees are removed from the analysis and left as a gap in the time series. Water vapour mass anomaly is then calculated using the same approach as for MLS with minor adjustments to handle the altitude rather than pressure level coordinates of the occultation data sets.

It is clear from Figure 3.14b that the agreement between all three measurement sets is highly robust. Aside from the first 6 months after the eruption where the atmospheric variability is quite high (as seen in the standard deviation of the measurements shown with shaded colours) the three instruments agree within about 10 Tg, which is less than 10% of the total mass anomaly. Even the decay observed in the water vapour mass starting in early 2024 is very well captured by all three data sets. SAGE III/ISS has an

unexplained but small low bias compared to ACE-FTS and MLS during approximately the first year after the eruption that is gradually rectified in early 2023. ACE-FTS and MLS agree extremely well with each other throughout the time series, even during the first few highly variable months after the eruption.

3.5 Modelling of the Hunga plume evolution

The objective of this section is to evaluate the fidelity of the simulated medium-term (1 month – 2 years) evolution of sulfate aerosol and water vapour in seven global climate models: CAM5/CARMA, WACCM6/CARMA, MIROC-CHASER, GEOSCCM, GEOS/CARMA, LMDZ6.2-LR, and WACCM6/MAM. Model skill in simulating volcanic aerosols and their impacts is typically assessed for sulfur-rich eruptions such as Mt. Pinatubo. The uniqueness of the Hunga–Tonga eruption, however, provides an unprecedented opportunity to test models under conditions markedly different from those for which they were originally developed, thereby enhancing confidence in their ability to simulate future eruptions.

In each of the subsections below, the key features of the observations are briefly summarised, followed by an evaluation of those features in the models. While the mechanisms responsible for the differences between the various models are of scientific interest, an investigation of the causes of the model differences is beyond the scope of this report. Studies examining the differences in the simulated plume evolution, the longer-term evolution of the Hunga perturbations in free-running ensemble simulations (Zhuo et al., 2025), and the radiative forcing estimates in the various models (Quaglia et al., 2025) are submitted or in preparation at the time of writing this report. These efforts augment the Tonga Model Intercomparison Project (Tonga-MIP) focused on the first three months after the eruption (Clyne et al., 2024).

The simulated global transport and evolution of Hunga materials are evaluated through analysis of *Experiment 2a* of the HTHH-MOC project (Zhu et al., 2025) (see also Supplementary S1 and S3, Part 1).

In these simulations, temperatures and/or winds are nudged to a reanalysis product to evaluate the model representation of the volcanic eruption without interannual variability. For each model, the magnitude and altitude of the injection of water vapour are chosen with the goal to retain 150 Tg of water at the MLS-observed altitude one week after the eruption. All models inject 0.5 Tg of SO_2, but the injection location is not required to be co-located with the water vapour injection. Experiment 2a models all include a prognostic aerosol module but vary in the complexity of their representation of aerosol microphysics (i.e., bulk, modal, or sectional). Detailed model descriptions and specifications for the simulations are found in Zhu et al. (2025).

3.5.1 Meridional dispersion of the volcanic aerosol and water vapour

The evolution of the sulfate aerosol and water vapour anomalies as observed by satellites (Section 3.1) suggests distinct transport pathways and episodic events. Observations of SAOD indicate the meridional dispersion of sulfate aerosols in the southern tropics within two months of the eruption, followed by a more efficient winter transport from the tropics towards the southern extratropics by June 2022 (Figures 3.1a and 3.15a). Northward cross-equatorial transport was relatively weak and sporadic, but enhanced SAOD was clearly observed as far north as 20°N within three months after eruption. After several episodic in-mixing events, the aerosols reached the northern extratropics by early 2023.

The observed aerosol transport is well simulated by all models (Figure 3.15). Most models simulate the transport from the tropics to the southern midlatitudes by June-July 2022 and to the southern high-latitudes by the end of 2022. Overall, models underestimate the magnitude of the SAOD compared to observations, as visible in the comparisons with OMPS in Figure 3.15 and with GloSSAC in Figure 3.19 (see NASA/LARC/SD/ASDC, 2023), indicating that the prescribed 0.5 Tg of SO_2 might be insufficient to reproduce the magnitude of the stratospheric aerosol perturbation (see Chapter 7 for a discussion of this issue).

Most of the Hunga aerosols remain outside of the Antarctic vortex during the first year in all models, in agreement with observations. Note that SAOD is enhanced within the Antarctic vortex in many models (except MIROC-CHASER and LMDZ6.2-LR), but the aerosol burden is due to background aerosols in the respective models (Figure S3.1 shows the simulated background SAOD from a control run without the Hunga eruption, and Figure S3.2 shows the SAOD simulated anomaly with respect to the control run). All models except for MIROC-CHASER and LMDZ6.2-LT simulate the entrainment of aerosols into the Antarctic vortex of 2023.

While some cross-equatorial transport is evident in all models within the first few months after eruption,

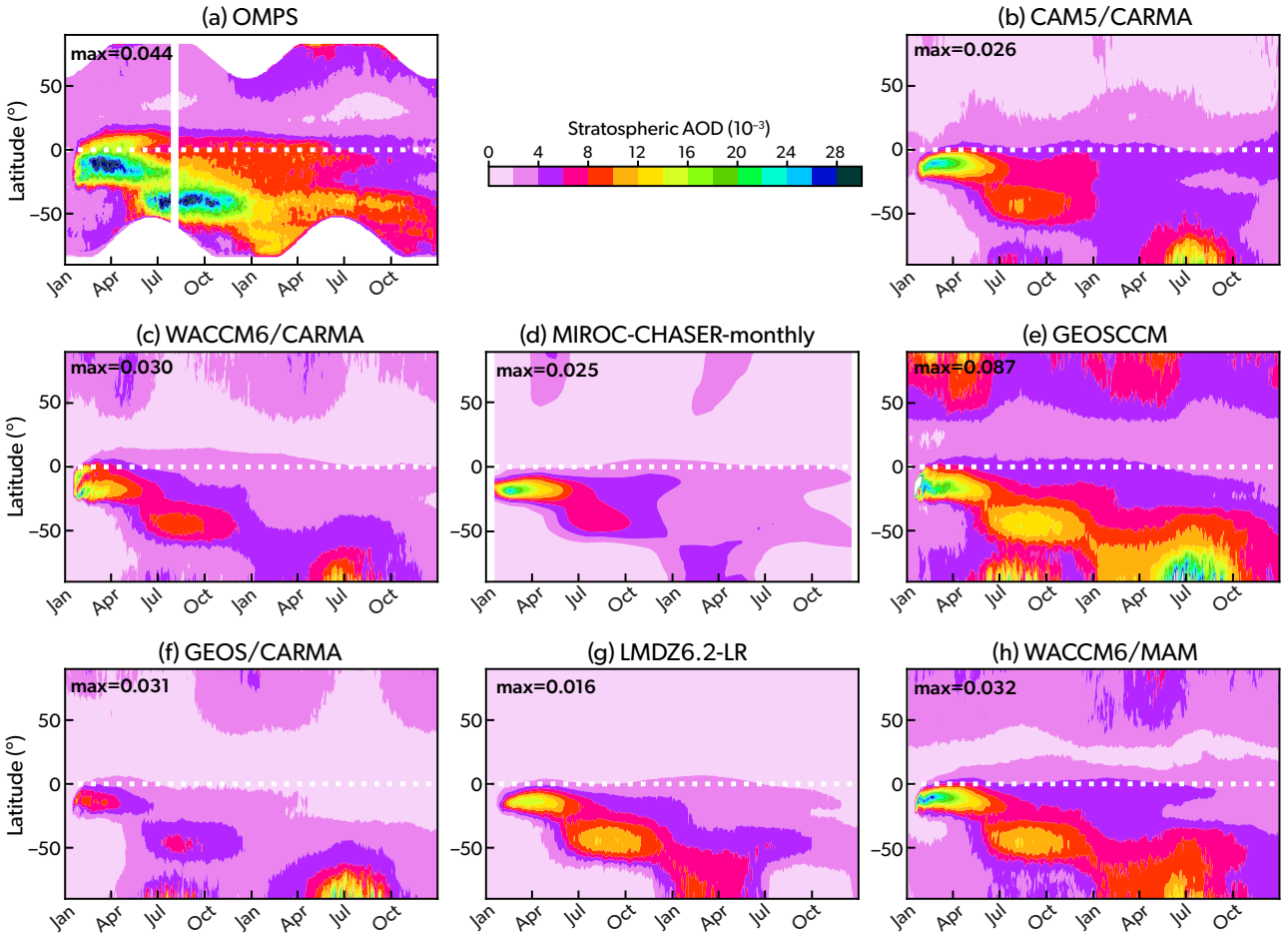

Figure 3.15: *Meridional dispersion and evolution of Hunga aerosol in global models and observations from January 2022 to December 2023. Stratospheric aerosol optical depth (SAOD) is plotted as a function of time and latitude. All panels show near-infrared SAOD. SAOD values were calculated from daily data, except for MIROC-CHASER (d), which used monthly means.*

the fraction of SAOD in the NH is generally lower than in observations (Figure S3.3). The entrainment into the developing Arctic vortex is only simulated in GEOS/CARMA (Figure S3.2f).

The water vapour transport over the first year as observed by MLS was characterised by a large perturbation in the tropics (0–20° S) within two months of the eruption followed by transport into the southern midlatitudes in mid-June 2022 and into the northern extratropics in January 2023. After reaching the stratopause in early 2023, most of the Hunga water vapour was transported to the mid and high latitudes. Hunga's water vapour was not entrained into the Antarctic and Arctic vortices until the following year. To compare the water vapour transport pattern in each of the models with observations, the simulated SCWV were computed as density-weighted water vapour mass mixing ratios vertically integrated above 100 hPa. SCWV perturbations (g m^{-2}) were calculated with respect to the simulations without water vapour and sulfur dioxide injections from the eruption (Figure 3.16 shows perturbations; Figures S3.4 and S3.5 show absolute values of the stratospheric water vapour column).

The overall pattern of the water vapour transport during the first two years is reproduced well by the models (Figure 3.16). For example, all models simulate the meridional dispersion of water vapour from the tropics to the southern midlatitudes around June 2022 and the entrainment into the Antarctic vortex in late 2022. Despite the differences in the background SCWV between the models, the timing and magnitude of the simulated SCWV perturbations are roughly in agreement with MLS observations.

The major episode of northward water vapour transport in January 2023 is reproduced well in most models (northward transport is virtually absent in MIROC-CHASER and LMDZ6.2-LR). The smaller cross-equatorial transport event in March-April 2022 is also present in all models except for MIROC-

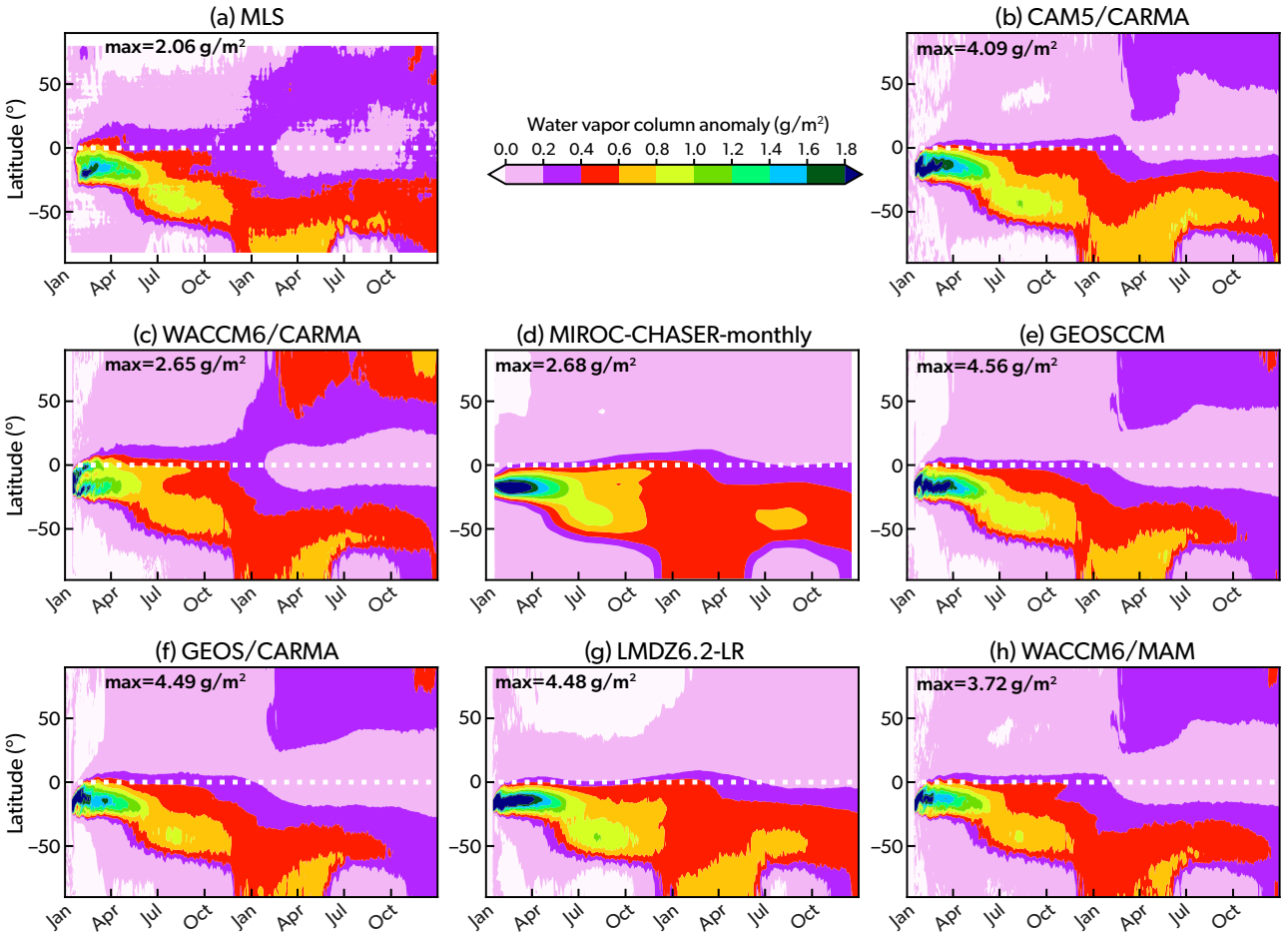

Figure 3.16: *Meridional dispersion and evolution of Hunga water-vapour perturbations in global models from January 2022 to December 2023. Perturbations are calculated relative to simulations without water-vapour and sulfur-dioxide injections, based on daily values except for MIROC-CHASER (d), which uses monthly means. Numbers in the upper left of each panel indicate the maximum anomalies reached. MLS water-vapour anomalies are calculated with respect to January 2022 using deseasonalised values for 2022–2024.*

CHASER but its latitudinal extent is underestimated. By spring 2023, most of the Hunga water vapour resides outside of the tropical belt, as in observations, except in MIROC-CHASER and LMDZ6.2-LR where moisture remains elevated in the southern tropics. The good overall agreement of the water vapour perturbations in CAM5/CARMA, WACCM6/CARMA, GEOSCCM and GEOS/CARMA with MLS observations suggests that the large-scale transport via the Brewer-Dobson circulation as well as the dynamics of the Arctic and Antarctic polar vortices are well represented in those models.

3.5.2 Vertical separation of the volcanic aerosol and water vapour and evolution of the aerosol radius

As noted in Section 3.1 and illustrated in Figure 3.2, the different meridional dispersion patterns of aerosols and water vapour starting in late 2022 are largely driven by the vertical separation of the aerosol and water vapour clouds. The water vapour began to rise through the mid stratosphere in October 2022 and subsequently experienced a steep rise in April 2023 associated with the rapid transport from the tropical pipe to northern high latitudes. After crossing the stratopause in early 2023, the bulk of the water vapour resided in the mesosphere by early 2024. Meanwhile, aerosols gradually descended towards the tropopause (Figure 3.3a and Figure S3.6).

All models show a vertical separation between the ascending water vapour and the descending aerosols in the tropics starting around late 2022 (Figure 3.17), in agreement with observations Figure 3.2a). The vertical separation in the models is primarily due to the gravitational settling of aerosol particles, which causes the aerosols to descend while water vapour ascends via the tropical upwelling branch of the Brewer-Dobson circulation (after the initial radiative cooling

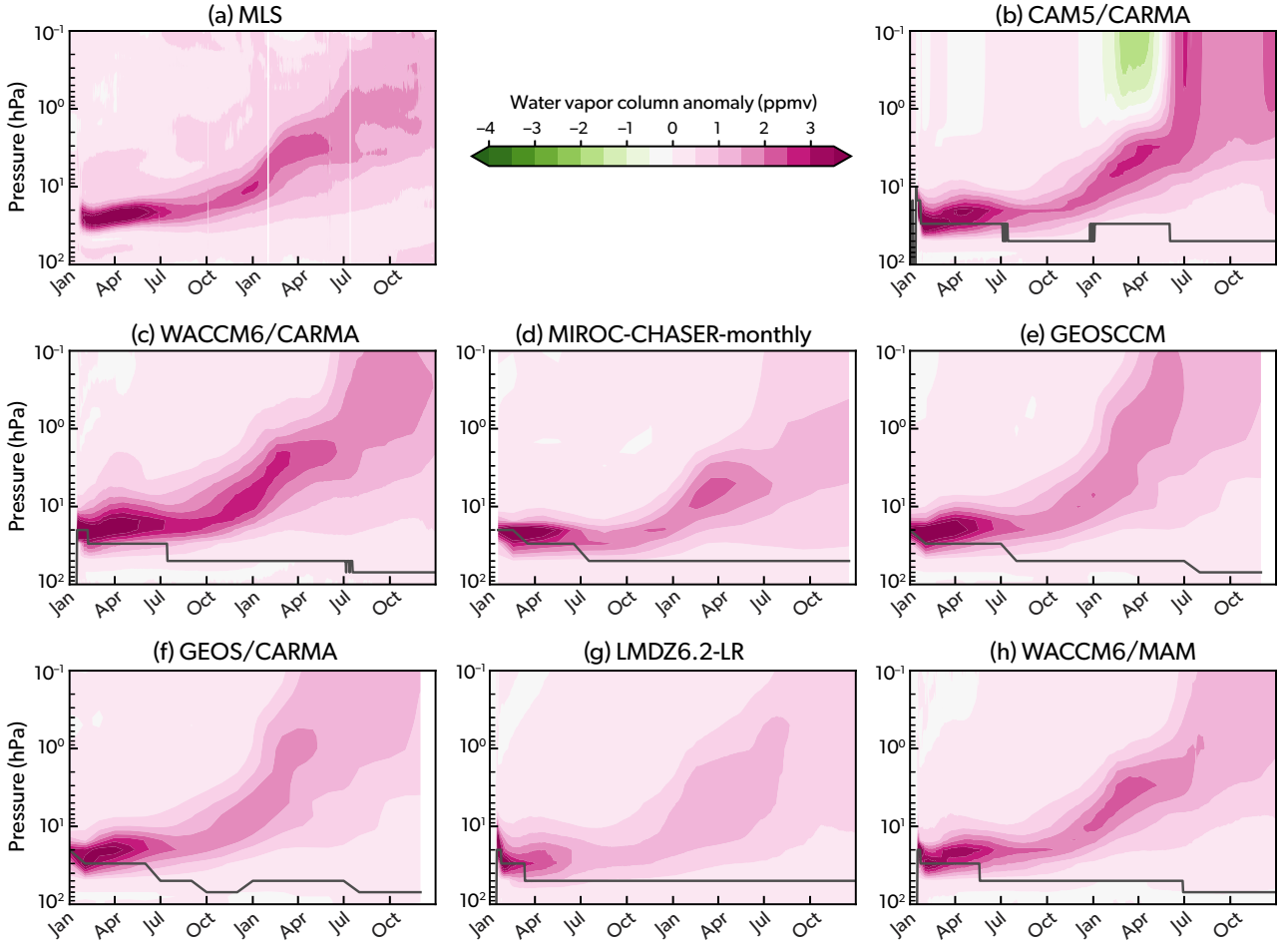

Figure 3.17: *Zonal-mean water-vapour perturbation (colour, in ppmv) as a function of time and altitude, averaged over 30° S–30° N in global models from January 2022 to December 2023. The black line shows the altitude of the maximum aerosol extinction coefficient (or mass-mixing ratio for CAM5/CARMA) above 100 hPa. Corresponding observations are shown in Figure 3.2a. Perturbations are based on daily values except for MIROC-CHASER, GEOSCCM, and GEOS/CARMA, which use monthly means.*

until October 2022). The simulated rate of tropical upwelling agrees well with observations in most models, with the Hunga moisture reaching the 1 hPa level by early 2023. Most models also simulate the steep rise of the Hunga water vapour into the mesosphere in April 2023. When compared to observations, the tropical ascent is too fast in GEOSCCM and too slow in MIROC-CHASER. Water vapour perturbations in CAM5/CARMA ascend slowly until just below the stratopause and are capped by negative water vapour perturbations in the mesosphere in early 2023. The very rapid ascent into the mesosphere in mid 2023 is much too fast compared to MLS observations. Overall, the timing and altitude of the appearances of the water vapour perturbations are simulated reasonably well in all models. The altitude of the sulfate aerosols (shown by the black line in Figure 3.17, and shown more clearly in Figures S3.6 and S3.7) is similar in all models and centered between 50 and 30 hPa (~25 km).

All of the models considered here, except for GEOSCCM, contain a parameterisation of aerosol microphysics and simulate the evolution of the particle radii (Figure 3.18 in the tropics and Figure S3.8 in the extratropics). CAM5/CARMA, WACCM6/CARMA, GEOS/CARMA, and LMDZ6/2-LR use a sectional aerosol microphysical model, while MIROC-CHASER, and WACCM6/MAM use two different versions of the MAM modal model. In all models, the effective radius grows quickly after the eruption and equilibrates between 0.2 and 0.3 μm after the larger particles settle out of the stratosphere. The increase in effective radius due to the eruption varies across models and is generally up to 2.5 times larger than the background (Figure S3.9). LMDZ6.2-LR simulates a slower growth in particle size and peaks at a much smaller radius than the other models, probably because the aerosol burden in this model is much smaller than in the others. Two years after the eruption, all models still

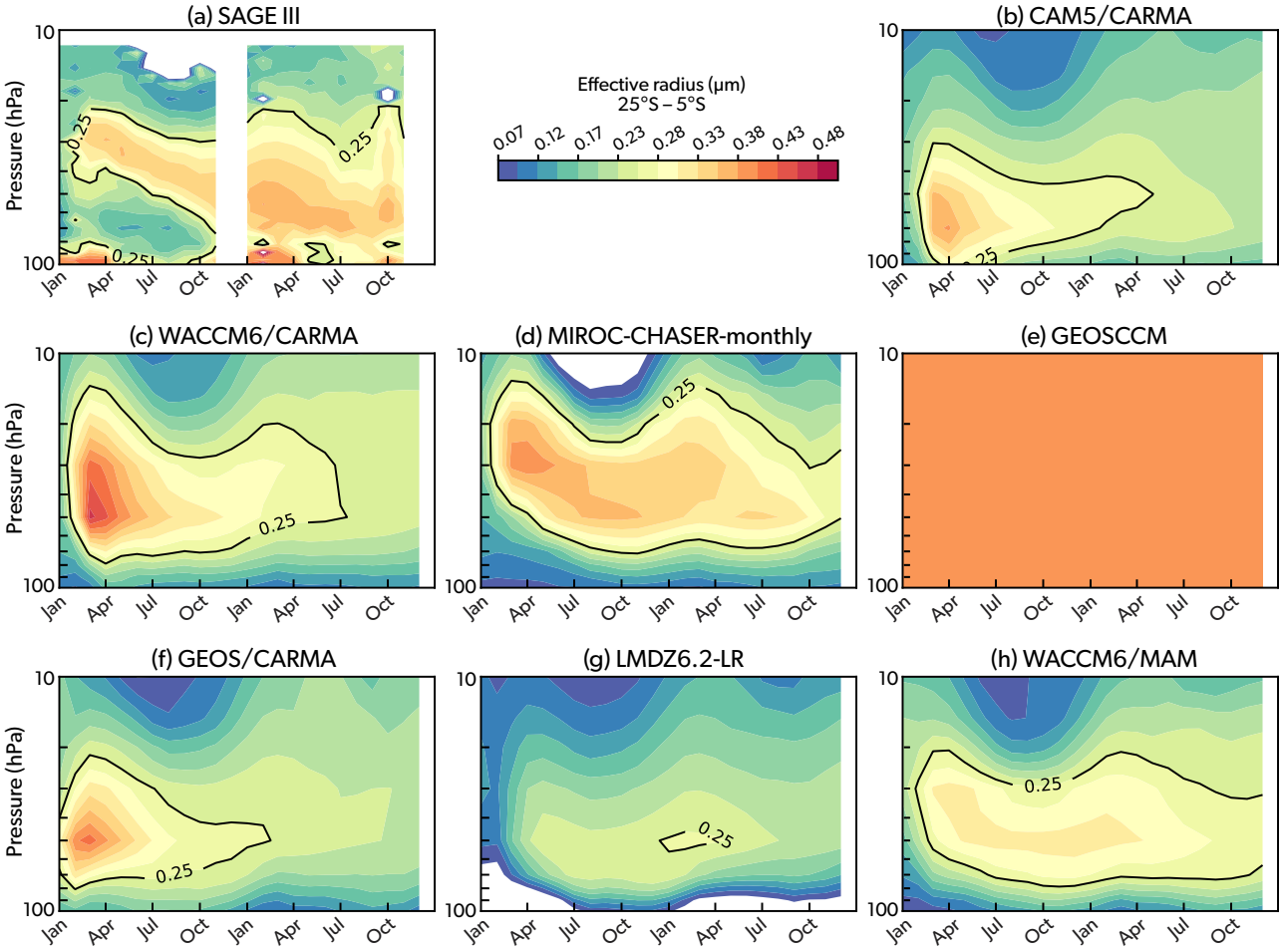

Figure 3.18: *Monthly mean aerosol effective radius averaged over the southern-hemisphere tropics (5°S–25°S) as a function of time and altitude in SAGE III/ISS and in different models from January 2022 to December 2023. GEOSCCM is a bulk model and assumes a constant effective radius of 0.4 μm.*

simulate particles size larger than the background.

3.5.3 Longevity and decay of the water-vapour and aerosol perturbations

The GloSSAC V2.21 merged satellite data set shows that the near global (60° S–60° N) SAOD anomaly grows rapidly after the eruptions reaching a maximum of approximately 0.006 in July-August 2022, followed by a decay phase (Figure 3.19). By the end of 2024, GloSSAC still records elevated SAOD with respect to the 2013 values, which we consider background conditions.

The simulated global mean SAOD perturbations reach a maximum soon after eruption and enter the decay phase in each of the models (Figure 3.19). Except for LMDZ6.2-LR and GEOS/CARMA, the initial enhancement in near-global SAOD occurs earlier than observed. This suggests that either the aerosol formation is too fast in most models, or that the observations underestimate the early peak in SAOD because

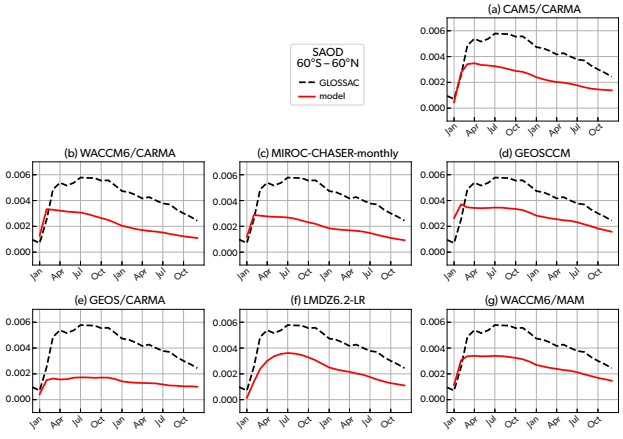

Figure 3.19: *Time series of monthly mean near-infrared (near-IR) stratospheric aerosol optical depth (SAOD) anomalies averaged over 60°S–60°N in the GloSSAC dataset (Thomason et al., 2018) (black dashed line) and in models (red solid lines) from January 2022 to December 2023. The GloSSAC anomalies are calculated relative to 2013, while the model perturbations are relative to simulations without the Hunga eruption.*

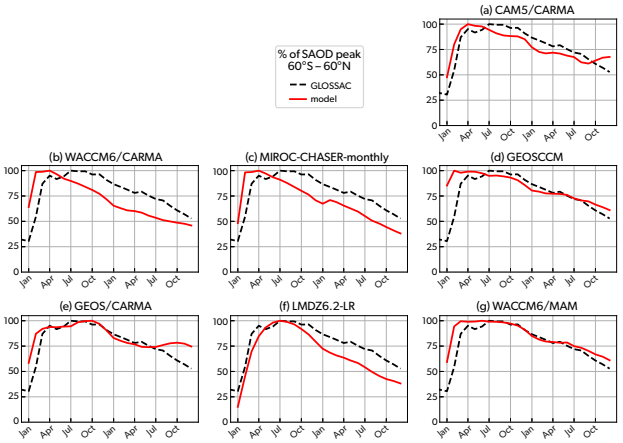

Figure 3.20: *Fraction (in %) of monthly mean near-IR SAOD with respect to its maximum, averaged over 60°S–60°N, in the GloSSAC dataset (black dashed line) and in models (red lines).*

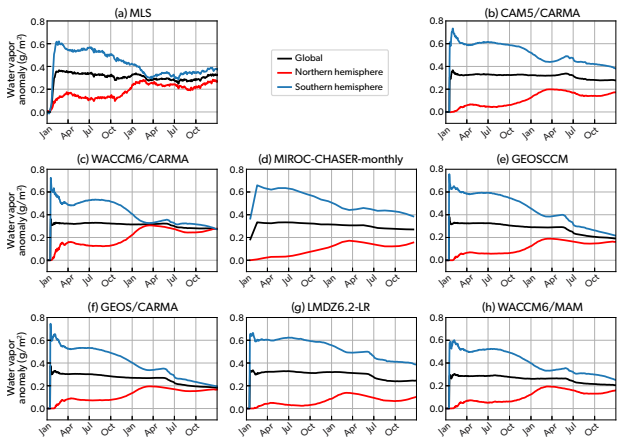

Figure 3.21: *Time series of Hunga water-vapour perturbations in global models from January 2022 to December 2023: global mean (black), Northern Hemisphere (red), and Southern Hemisphere (blue). Perturbations are calculated based on daily values, except for MIROC-CHASER, which uses monthly means. MLS-observed water vapour anomalies are calculated relative to January 2022 from deseasonalised values for 2022–2024.*

of sampling. While all models underestimate the magnitude of SAOD compared to observations, the decay rate of the global SAOD is remarkably well simulated compared to the GloSSAC dataset (Figure 3.20).

Several factors may have contributed to the lower SAOD values in the models compared to observations, primarily pointing to a too low injection of sulfur dioxide. Another likely explanation is that the simulated conversion to sulfate aerosol may have been too fast, leading to too large particles (Figure 3.18) that sediment quicker than in observations and with a lower extinction efficiency.

The Hunga eruption increased the global SCWV by more than 15% for a period of about two years (Figures 3.1c,d). The increase was most dramatic in the SH reaching 24% of climatological mean value shortly after eruption. The cross-equatorial transport to the NH in Mar-Apr 2022 decreased the SH burden to about 22% and increased the NH burden to about 11%. By March 2023, hemispheric SCWV perturbations converged with the global perturbation of about 15% and stayed at roughly the same level throughout the following year.

The time series of the global simulated SCWV perturbations show a rapid increase after the Hunga eruption of a magnitude similar to observations in all models (Figure 3.21). CAM5/CARMA, MIROC-CHASER, GEOSCCM, and LMDZ6.2-LR models simulate the correct magnitude and timing of the global and southern hemispheric perturbations, while they underestimate the perturbation in the northern hemisphere. This suggests that the meridional dispersion of the water vapour plume is underestimated in these models, which is confirmed in Figure 3.16 and Figure S3.10. In fact, the cross-equatorial transport around April and May 2022 (Figures 3.1c,d) is nearly absent in MIROC-CHASER, while evident in the other models as a small peak in the NH perturbation time series (see also Figure 3.16). The global stratospheric mixing timescales in WACCM6/CARMA, estimated from the convergence of global and hemispheric water vapour time series agree reasonably well with the 14 month timescale based on MLS observations (Figure 3.1d). In GEOSCCM, GEOS/CARMA, the time series converges near the end of the two-year simulation, suggesting a timescale of about 24 months. The mixing timescales in CAM5/CARMA, MIROC-CHASER, and LMDZ6.2-LR appear to be much longer, as seen from the separation between the northern and hemispheric averaged perturbations even at the end of 2023.

3.5.4 Summary of model performances

Overall, models reproduce the observed transport of water vapour and volcanic aerosols from the Hunga eruption quite well. Generally, the timing of the aerosol and water vapour transport outside of the tropics toward the southern hemisphere is represented remarkably well. Most models overestimate the early peak water vapour perturbation in the tropics with respect to MLS, but simulate well the water vapour perturbation after the first month from the eruption. Models also underestimate the peak SAOD with respect to OMPS (which, however, reports higher SAOD

values than other satellite instruments), indicating that the prescribed injection parameters need to be tuned. On the other hand, models simulate the decay rate of SAOD remarkably well, showing that the removal of aerosols through settling and circulation is generally well represented. In the second year after the eruption, the water vapour perturbation matches MLS observations very well, while the SAOD is still underestimated. All models underestimate the cross-equatorial transport compared to OMPS and confine most of the aerosols to the Southern Hemisphere.
All models simulate the vertical separation of water vapour and aerosols, with the water vapour ascending via the tropical upwelling branch of the Brewer-Dobson circulation and the aerosol remaining in the middle and lower stratosphere due to gravitational settling. The simulated period (2 years) was not long enough to derive the e-folding time of aerosols, which is tightly related to the aerosol effective radius. All models simulate an increase in aerosol particle size after the eruption. The aerosol size then decreases with time due to the faster settling of larger particles, and stabilises in all models around 0.2 - 0.3 μm, in agreement with observations.

References

Asher, E., M. Todt, K. Rosenlof, T. Thornberry, R.-S. Gao, G. Taha, P. Walter, S. Alvarez, J. Flynn, S. M. Davis et al. (2023). 'Unexpectedly rapid aerosol formation in the Hunga Tonga plume'. *Proc. Natl. Acad. Sci.*, 120, e2219547120. DOI: 10.1073/pnas.2219547120.

Boichu, M., R. Grandin, L. Blarel, B. Torres, Y. Derimian, P. Goloub, C. Brogniez, I. Chiapello, O. Dubovik, T. Mathurin et al. (2023). 'Growth and Global Persistence of Stratospheric Sulfate Aerosols From the 2022 Hunga Tonga–Hunga Ha'apai Volcanic Eruption'. *J. Geophys. Res.*, 128, e2023JD039010. DOI: 10.1029/2023JD039010.

Bourassa, A. E., D. J. Zawada, L. A. Rieger, T. W. Warnock, M. Toohey and D. A. Degenstein (2023). 'Tomographic retrievals of Hunga Tonga-Hunga Ha'apai volcanic aerosol'. *Geophys. Res. Lett.*, 50, e2022GL101978. DOI: 10.1029/2022GL101978.

Clyne, M., O. B. Toon, T. Sukhodolov, G. W. Mann, S. Dhomse, S. Tilmes, Y. Zhu, P. R. Colarco, K. Tsigaridis, T. Nagashima et al. (2024). 'Tonga-MIP: The Hunga Tonga-Hunga Ha'apai Volcano Model Intercomparison Project'. In M. Clyne (Ed.), *Modeling the role of volcanoes in the climate system* (Publication No. 31487034), https://www.proquest.com/dissertations-theses/modeling-role-volcanoes-climate-system/docview/3100397790/se-2. PhD thesis. University of Colorado at Boulder.

Duchamp, C., F. Wrana, B. Legras, P. Sellitto, R. Belhadji and C. von Savigny (2023). 'Observation of the aerosol plume from the 2022 Hunga Tonga–Hunga Ha'apai eruption with SAGE III/ISS'. *Geophys. Res. Lett.*, 50, e2023GL105076. DOI: 10.1029/2023GL105076.

Global Volcanism Program (2024). *Volcanoes of the World (v. 5.2.8; 6 May 2025)*. Distributed by Smithsonian Institution, compiled by Venzke, E. DOI: 10.5479/si.GVP.VOTW5-2024.5.2.

Khaykin, S., G. Taha, T. Leblanc, T. Sakai, I. Morino, B. Liley and S. Godin-Beekmann (2024). 'Stratospheric aerosols [in "State of the Climate in 2022"]'. *Bull. Am. Meteorol. Soc.*, 105, S96–S98. DOI: 10.1175/BAMS-D-24-0116.1.

Khaykin, S., B. Legras, S. Bucci, P. Sellitto, L. Isaksen, F. Tencé, S. Bekki, A. Bourassa, L. Rieger, D. Zawada et al. (2020). 'The 2019/20 Australian wildfires generated a persistent smoke-charged vortex rising up to 35 km altitude'. *Commun. Earth Environ.*, 1, 22. DOI: 10.1038/s43247-020-00022-5.

Khaykin, S., A. Podglajen, F. Ploeger, J.-U. Grooß, F. Tence, S. Bekki, K. Khlopenkov, K. Bedka, L. Rieger, A. Baron et al. (2022). 'Global perturbation of stratospheric water and aerosol burden by Hunga eruption'. *Commun. Earth Environ.*, 3, 316. DOI: 10.1038/s43247-022-00652-x.

Knepp, T. N., M. Kovilakam, L. Thomason and S. J. Miller (2024). 'Characterization of stratospheric particle size distribution uncertainties using SAGE II and SAGE III/ISS extinction spectra'. *Atmos. Meas. Tech.*, 17, pp. 2025–2054. DOI: 10.5194/amt-17-2025-2024.

Kovilakam, M., L. W. Thomason, N. Ernest, L. Rieger, A. Bourassa and L. Millán (2020). 'The Global Space-based Stratospheric Aerosol Climatology (version 2.0): 1979–2018'. *Earth Syst. Sci. Data*, 12, pp. 2607–2634. DOI: 10.5194/essd-12-2607-2020.

Kovilakam, M., L. W. Thomason, M. Verkerk, T. Aubry and T. N. Knepp (2025). 'OMPS-LP aerosol extinction coefficients and their applicability in GloSSAC'. *Atmos. Chem. Phys.*, 25, pp. 535–553. DOI: 10.5194/acp-25-535-2025.

Lawrence, Z. D., G. L. Manney and K. Wargan (2018). 'Reanalysis intercomparisons of stratospheric polar processing diagnostics'. *Atmos. Chem. Phys.*, 18, pp. 13547–13579. DOI: 10.5194/acp-18-13547-2018.

Lee, S., G. L. Manney and A. H. Butler (2024). 'The 2023 Major Sudden Stratospheric Warming [in "State of the Climate in 2023"]'. *Bull. Am. Meteorol. Soc.*, 105, S288–S289. DOI: 10.1175/BAMS-D-24-0101.1.

Li, C., Y. Peng, E. Asher, A. A. Baron, M. Todt, T. D. Thornberry, S. Evan, J. Brioude, P. Smale, R. Querel et al. (2024). 'Microphysical Simulation of the 2022 Hunga Volcano Eruption Using a Sectional Aerosol Model'. *Geophys. Res. Lett.*, 51, e2024GL108522. DOI: 10.1029/2024GL108522.

Manney, G. L., M. L. Santee, A. Lambert, L. F. Millán, K. Minschwaner, F. Werner, Z. D. Lawrence, W. G. Read, N. J. Livesey and T. Wang (2023). 'Siege in the Southern Stratosphere: Hunga Tonga-Hunga Ha'apai Water Vapor Excluded From the 2022 Antarctic Polar Vortex'. *Geophys. Res. Lett.*, 50. DOI: 10.1029/2023gl103855.

Millán, L., W. G. Read, M. L. Santee, A. Lambert, G. L. Manney, J. L. Neu, M. C. Pitts, F. Werner, N. J. Livesey and M. J. Schwartz (2024). 'The Evolution of the Hunga Hydration in a Moistening Stratosphere'. *Geophys. Res. Lett.*, 51, e2024GL110841. DOI: 10.1029/2024gl110841.

NASA/LARC/SD/ASDC (2023). *Global Space-based Stratospheric Aerosol Climatology Version 2.21*. Data set. NASA Langley Atmospheric Science Data Center DAAC. DOI: 10.5067/GLOSSAC-L3-V2.21.

Newman, P. A., L. R. Lait, N. A. Kramarova, L. Coy, S. M. Frith, L. D. Oman and S. S. Dhomse (2024). 'Record High March 2024 Arctic Total Column Ozone'. *Geophys. Res. Lett.*, 51, e2024GL110924. DOI: 10.1029/2024gl110924.

Peter, T. (1997). 'Microphysics and heterogeneous chemistry of polar startospheric clouds'. *Annu. Rev. Phys. Chem.*, 48, pp. 785–822. DOI: 10.1146/annurev.physchem.48.1.785.

Pitts, M. C., L. R. Poole and R. Gonzalez (2018). 'Polar stratospheric cloud climatology based on CALIPSO spaceborne lidar measurements from 2006 to 2017'. *Atmos. Chem. Phys.*, 18, pp. 10881–10913. DOI: 10.5194/acp-18-10881-2018.

Polvani, L. M., D. W. Waugh and R. A. Plumb (1995). 'On the Subtropical Edge of the Stratospheric Surf Zone'. *J. Atmos. Sci.*, 52, pp. 1288–1309. DOI: 10.1175/1520-0469(1995)052<1288:otseot>2.0.co;2.

Quaglia, I., D. Visioni, E. M. Bednarz, Y. Zhu, G. Stenchikov, V. Aquila, C.-C. Liu, G. W. Mann, Y. Peng, T. Sekiya et al. (2025). 'Multi-model analysis of the radiative impacts of the 2022 Hunga eruption indicates a significant cooling contribution from the volcanic plume'. *EGUsphere [preprint]*, 2025, pp. 1–35. DOI: 10.5194/egusphere-2025-3769.

Rieger, L. A., A. E. Bourassa and D. A. Degenstein (2014). 'Stratospheric aerosol particle size information in Odin-OSIRIS limb scatter spectra'. *Atmos. Meas. Tech.*, 7, pp. 507–522. DOI: 10.5194/amt-7-507-2014.

Rieger, L. A., D. J. Zawada, A. E. Bourassa and D. A. Degenstein (2019). 'A Multiwavelength Retrieval Approach for Improved OSIRIS Aerosol Extinction Retrievals'. *J. Geophys. Res.*, 124, pp. 7286–7307. DOI: 10.1029/2018jd029897.

Rozanov, A., C. Pohl, C. Arosio, A. Bourassa, K. Bramstedt, E. Malinina, L. Rieger and J. P. Burrows (2024). 'Retrieval of stratospheric aerosol extinction coefficients from sun-normalized Ozone Mapper and Profiler Suite Limb Profiler (OMPS-LP) measurements'. *Atmos. Meas. Tech.*, 17, pp. 6677–6695. DOI: 10.5194/amt-17-6677-2024.

Russell, P. B., J. M. Livingston, R. F. Pueschel, J. J. Bauman, J. B. Pollack, S. L. Brooks, P. Hamill, L. W. Thomason, L. L. Stowe, T. Deshler et al. (1996). 'Global to microscale evolution of the Pinatubo volcanic aerosol derived from diverse measurements and analyses'. *J. Geophys. Res.*, 101, pp. 18745–18763. DOI: 10.1029/96jd01162.

Santee, M. L., G. L. Manney, A. Lambert, L. F. Millán, N. J. Livesey, M. C. Pitts, L. Froidevaux, W. G. Read and R. A. Fuller (2024). 'The Influence of Stratospheric Hydration From the Hunga Eruption on Chemical Processing in the 2023 Antarctic Vortex'. *J. Geophys. Res.*, 129, e2023JD040687. DOI: 10.1029/2023jd040687.

Schoeberl, M. R., Y. Wang, R. Ueyama, G. Taha, E. Jensen and W. Yu (2022). 'Analysis and Impact of the Hunga Tonga-Hunga Ha'apai Stratospheric Water Vapor Plume'. *Geophys. Res. Lett.*, 49, e2022GL100248. DOI: 10.1029/2022gl100248.

Sellitto, P., A. Podglajen, R. Belhadji, M. Boichu, E. Carboni, J. Cuesta, C. Duchamp, C. Kloss, R. Siddans, N. Bègue et al. (2022). 'The unexpected radiative impact of the Hunga Tonga eruption of 15th January 2022'. *Commun. Earth Environ.*, 3, 288. DOI: 10.1038/s43247-022-00618-z.

Sonnemann, G. R. and M. Grygalashvyly (2005). 'Solar influence on mesospheric water vapor with impact on NLCs'. *J. Atmos. Solar-Terr. Phys.*, 67, pp. 177–190. DOI: 10.1016/j.jastp.2004.07.026.

Taha, G., R. Loughman, T. Zhu, L. Thomason, J. Kar, L. Rieger and A. Bourassa (2021). 'OMPS LP Version 2.0 multi-wavelength aerosol extinction coefficient retrieval algorithm'. *Atmos. Meas. Tech.*, 14, pp. 1015–1036. DOI: 10.5194/amt-14-1015-2021.

Thomason, L. W., N. Ernest, L. Millán, L. Rieger, A. Bourassa, J.-P. Vernier, G. Manney, B. Luo, F. Arfeuille and T. Peter (2018). 'A global space-based stratospheric aerosol climatology: 1979–2016'. *Earth Syst. Sci. Data*, 10, pp. 469–492. DOI: 10.5194/essd-10-469-2018.

Tritscher, I., M. C. Pitts, L. R. Poole, S. P. Alexander, F. Cairo, M. P. Chipperfield, J.-U. Grooß, M. Höpfner, A. Lambert, B. Luo et al. (2021). 'Polar Stratospheric Clouds: Satellite Observations, Processes, and Role in Ozone Depletion'. *Rev. Geophys.*, 59, e2020RG000702. DOI: 10.1029/2020rg000702.

Wohltmann, I., M. L. Santee, G. L. Manney and L. F. Millán (2024). 'The Chemical Effect of Increased Water Vapor From the Hunga Tonga-Hunga Ha'apai Eruption on the Antarctic Ozone Hole'. *Geophys. Res. Lett.*, 51, e2023GL106980. DOI: 10.1029/2023gl106980.

Wrana, F., C. von Savigny, J. Zalach and L. W. Thomason (2021). 'Retrieval of stratospheric aerosol size distribution parameters using satellite solar oc-

cultation measurements at three wavelengths'. *Atmos. Meas. Tech.*, 14, pp. 2345–2357. DOI: 10.5194/amt-14-2345-2021.

Xu, J., D. Li, Z. Bai, M. Tao and J. Bian (2022). 'Large Amounts of Water Vapor Were Injected into the Stratosphere by the Hunga Tonga–Hunga Ha'apai Volcano Eruption'. *Atmosphere*, 13, 912. DOI: 10.3390/atmos13060912.

Zhou, X., S. S. Dhomse, W. Feng, G. Mann, S. Heddell, H. Pumphrey, B. J. Kerridge, B. Latter, R. Siddans, L. Ventress et al. (2024). 'Antarctic Vortex Dehydration in 2023 as a Substantial Removal Pathway for Hunga Tonga-Hunga Ha'apai Water Vapor'. *Geophys. Res. Lett.*, 51, e2023GL107630. DOI: 10.1029/2023gl107630.

Zhu, Y., H. Akiyoshi, V. Aquila, E. Asher, E. M. Bednarz, S. Bekki, C. Brühl, A. H. Butler, P. Case, S. Chabrillat et al. (2025). 'Hunga Tonga–Hunga Ha'apai Volcano Impact Model Observation Comparison (HTHH-MOC) project: experiment protocol and model descriptions'. *Geosci. Model Dev.*, 18, pp. 5487–5512. DOI: 10.5194/gmd-18-5487-2025.

Zhuo, Z., X. Wang, Y. Zhu, W. Yu, E. M. Bednarz, E. Fleming, P. R. Colarco, S. Watanabe, D. Plummer, G. Stenchikov et al. (2025). 'Comparing multimodel ensemble simulations with observations and decadal projections of upper atmospheric variations following the Hunga eruption'. *Atmos. Chem. Phys.*, 25, pp. 13161–13176. DOI: 10.5194/acp-25-13161-2025.

4 Hunga effects on stratospheric temperatures and circulation

Lead authors Xinyue Wang
Lawrence Coy

Co-Authors Masatomo Fujiwara
Pu Lin
Alison Ming
Feng Li
Ewa M. Bednarz
Zhihong Zhuo
Kirstin Krüger

Contributing authors William Randel
Jon Starr
Wandi Yu
Simone Tilmes
Chengyun Yang
Yunqian Zhu
Jun Zhang
Simchan Yook
Eric Fleming
Peter Colarco
Shingo Watanabe
Mijeong Park
Martin Jucker

Cite this as:

Wang, X., L. Coy et al. (2025): Hunga effects on stratospheric temperatures and circulation. In APARC, 2025: The Hunga Eruption Atmospheric Impacts Report [Yunqian Zhu, Graham Mann, Paul A. Newman, William Randel (Eds.)]. APARC Report No. 11, WCRP Report No. 10/2025, DOI: 10.34734/FZJ-2025-05241, available at `https://aparc-climate.org/publications/aparc-report-no-11/`.

Key points

- The Hunga H_2O cloud, injected into the stratosphere in 2022, was spread globally by the residual mean circulation and lateral mixing along surfaces of constant potential temperature. The water vapour anomaly reached the polar region of each hemisphere after the breakdown of the Southern and Northern polar vortices in December 2022 and April 2023, respectively, and continues to persist over much of the stratosphere to the present (2025).

- The Hunga eruption led to a 0.5-1 K cooling of the global stratosphere in early 2022, which has extended through 2024. Larger temperature anomalies are observed in specific regions, but local Hunga impacts are entangled with dynamically forced variability.

- Cooling in the stratosphere is mainly due to radiative impact of the Hunga H_2O. The Hunga forced cooling contrasts to the stratospheric warming associated with aerosols in other major volcanic eruptions.

- The Southern Hemisphere winter stratospheric circulation was significantly disrupted following the Hunga eruption in 2022, with an unusually strengthened and equatorward shifted of the winter stratospheric jet, weakened residual mean circulation, and reduced planetary wave forcing. Models reproduce this observed behaviour but also exhibit significant internal variability of the same amplitude. Model simulations for spring 2023 show a wide range of Northern Hemisphere stratospheric responses, making it challenging to attribute changes to the Hunga eruption given the influence of internal variability.

- Observed temperature and circulation changes following Hunga eruption in the SH mid latitude stratosphere during the first austral winter are captured by global data assimilation systems. The MERRA-2 reanalysis, which assimilates MLS temperature observations above the 5-hPa level, follows best the MLS observations in and above the upper stratosphere. Without knowledge of the water vapour anomaly, these systems tracked Hunga induced changes in assimilated temperature observations, thus providing gridded global analysis of meteorological fields during 2022 and following years.

- Current pieces of evidence are insufficient to draw conclusions on whether the Hunga eruption affected the QBO, given the inconsistency between observations and the model simulations and the possible large internal variability in the system and the unrealistic QBO representation in the models.

Contents

4.1 The large-scale evolution of the Hunga H_2O cloud 92
4.2 Stratospheric transport, temperatures and zonal winds 92
4.2.1 Observations of temperature anomalies following the eruption of Hunga 92
4.2.2 Assimilated temperature and wind anomalies following the Hunga eruption 94
4.2.3 Hunga induced temperature and circulation anomalies in models 96
4.3 Residual mean meridional circulation and Eliassen-Palm flux 98
4.3.1 Residual mean meridional circulation and EP flux in the global data assimilation systems 98
4.3.2 Residual mean circulation and EP flux changes in models 99
4.4 Interaction of Hunga with the Quasi-Biennial Oscillation (QBO) 101
4.5 Summary 102

Preamble

The Hunga submarine volcano erupted on 15th January 2022 injected a massive plume of water vapour into the stratosphere. It increased the global stratospheric water burden by ~15% (Chapter 3), setting a record high for direct water vapour injection into the stratosphere in the modern satellite era and differentiating itself from previous major volcanic eruptions (Vömel et al., 2022; Khaykin et al., 2022). Most of the Hunga H_2O cloud then dispersed globally, remaining in the upper atmosphere through 2024 (Millán et al., 2022; Khaykin et al., 2022; Zhou et al., 2024). In addition to the water vapour, a moderate amount of sulfur-containing gas, equivalent to 0.5–1 Tg sulfur dioxide (SO_2), was lofted into the stratosphere by the Hunga eruption according to Carn et al. (2022), and converted to sulfate aerosol particles within one to two weeks (Zhu et al., 2022). After three months, the Hunga aerosol separated from the H_2O due to aerosol growth and sedimentation (Legras et al., 2022) and was mainly transported into the Southern Hemisphere (SH) lower stratosphere (Duchamp et al., 2023). Additional details on plume dispersion are discussed in Chapter 3. The large H_2O and aerosol perturbations affected stratospheric temperatures, circulation, and transport, as analysed in this chapter.

4.1 The large-scale evolution of the Hunga H_2O cloud

Satellite observations show that the Hunga H_2O plume has persisted in the stratosphere and evolved from 2022 through the end of 2024 (Millán et al., 2024). The global, latitude and altitude evolution of the Hunga H_2O anomaly followed the well-known residual mean (or Brewer-Dobson) circulation in the stratosphere (Figure 4.1). During January 2022, the initial volcanic cloud, near 20°S, 175°W, spread longitudinally around the globe with most of the water vapour anomaly remaining near the 20°S, 20 hPa (Figure 4.1a). The H_2O then spread laterally within the tropical pipe (Plumb, 1996), reaching 10 hPa by Feb 2022. It spread deep into the SH in December 2022, when the austral polar vortex broke down removing the mixing barrier. It then spread deeper into the Northern Hemisphere (NH) a few months later, in March, when its vortex broke down, removing mixing barriers in the north. Furthermore, by the start of 2023 the initial water vapour perturbation had been advected upward in the tropics and was now replaced by the typical dryer air through the tropopause (Figure 4.1b). Note that the upward motion at the equator was initially slow until June 2022.

4.2 Stratospheric transport, temperatures and zonal winds

4.2.1 Observations of temperature anomalies following the eruption of Hunga

Substantial stratospheric warming linked to enhanced aerosols has been observed following major volcanic eruptions such as El Chichón and Pinatubo (Labitzke and McCormick, 1992). However, the unprecedented H_2O perturbation after the Hunga eruption presents a distinct case in the observational record. Unlike sulfate aerosol, stratospheric water vapour acts as a greenhouse gas and is a strong emitter of longwave radiation, leading to localised cooling effect in the stratosphere (Sellitto et al., 2022). The dynamical variability and cooling trends in the stratosphere, along with the potential non-local dynamical effects from H_2O and aerosol clouds, make it challenging to isolate the stratospheric temperature impacts of the Hunga eruption. To address these complications, we have detrended the entire historical datasets from the Stratospheric Sounding Unit (SSU) channels and Microwave Limb Sounder (MLS) using regression fits based on the pre-Hunga period and additionally removed the influence of the 11-year solar cycle (Steiner et al., 2020; Randel et al., 2024). The Hunga-related temperature anomalies are compared to variability in the longer-term stratospheric climate record across several stratospheric layers over the modern satellite era in Figure 4.2. The time series in the stratosphere captures two distinct warming spikes in 1982 and 1991, corresponding to the El Chichón and Pinatubo volcanic eruptions. The warming in 2020 caused by the smoke injected from the Australian New Year's fires can also be seen (Rieger et al., 2021). Cooling effects from the Hunga eruption are noticeable in the middle to upper stratosphere during 2022–2023, with temperature residuals revealing anomalies of approximately -0.5 to -1 K throughout the stratosphere. The Hunga-related cooling is comparable in magnitude, though opposite in sign, to the warming anomalies associated with the El Chichón and Pinatubo eruptions. The sign difference is attributed to the intensified longwave cooling rate caused by the large amount of H_2O injected by Hunga (Wang et al., 2023; Wang and Huang, 2024; Gupta et al., 2025), as opposed to the sulfate aerosol-driven warming observed after El Chichón and Pinatubo. Additionally, the Hunga cooling anomalies increase substantially in magnitude from the lower to upper stratosphere into the meso-

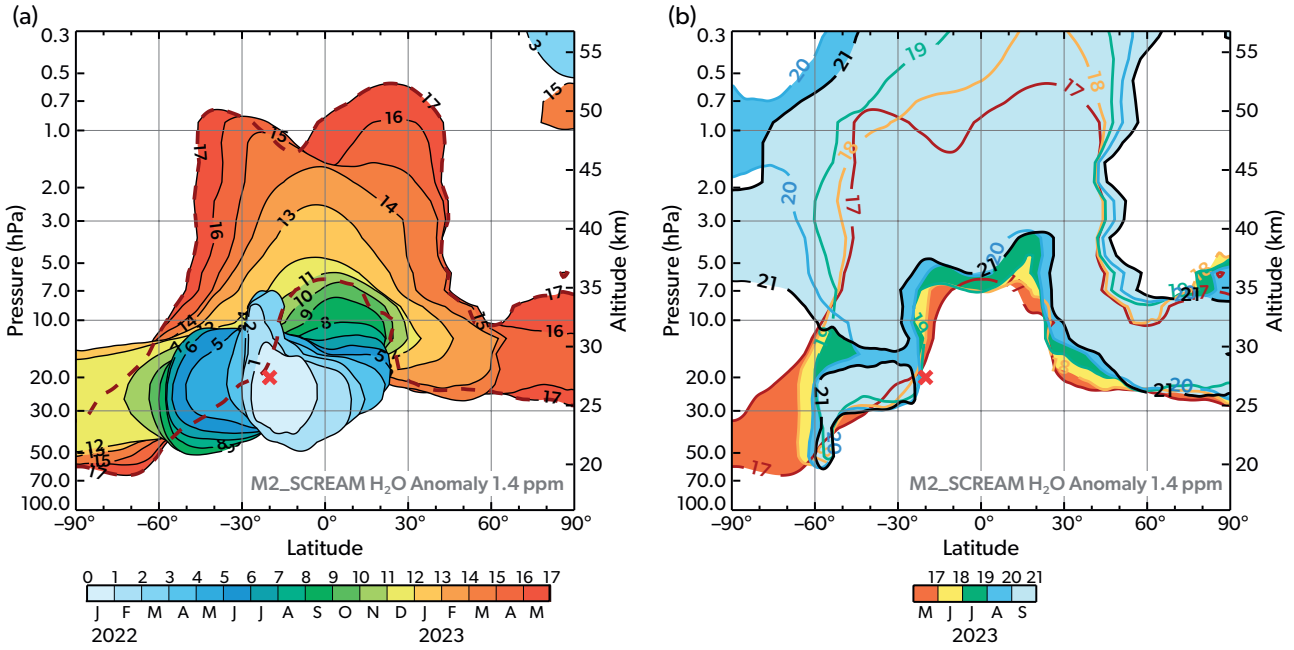

Figure 4.1: *Water vapour anomaly (1.4 ppm contour) plotted for each month starting at January 2022 (labelled 1) for a) January 2022 through May 2023, and b) May 2023 through September 2023. In a) the filled contours for earlier months are plotted on top of the later months, with the dashed curve being month seventeen.; in b) the filled contours for later months are plotted on top of the earlier months. The monthly averaged fields are taken from the MERRA-2 Stratospheric Composition Reanalysis of Aura Microwave Limb Sounder (M2-SCREAM), a global constituent data assimilation system. The red cross denotes the location 20°S, 20 hPa.*

sphere in response to ozone depletion (see discussion in Chapter 6), whereas the warming anomalies from El Chichón, Pinatubo, and the Australian wildfire peak in the lower stratosphere and decrease with altitude.

The systematic cooling influence of the Hunga eruption on global stratospheric temperatures is also evident in MLS observations. The global average MLS temperature anomalies as a function of altitude and time over 2022 to 2024 are presented in Figure 4.3. These anomalies are calculated as differences from the 2005–2021 MLS average after removing the decadal trends and natural variabilities via regression as discussed above. The black contour denotes the corresponding Hunga H_2O at 1 ppmv level. The H_2O cloud originated near 25–30 km in January 2022, with subsequent upward transport to the upper stratosphere and mesosphere by mid-2023. Cold anomalies of 0.5 K originated near 25–30 km two months after the eruption, coinciding with the altitude of the rising plume. During 2022 and 2023, cold temperature anomalies of ~0.5–1.0 K in the stratosphere closely aligned with the ascending Hunga H_2O, with slightly larger anomalies (~1.5–2.0 K) above ~45 km in the lower mesosphere after mid-2023. The vertical and temporal overlap of these temperature and H_2O anomalies provides strong evidence for the Hunga forcing on the observed temperature cooling. Gupta et al. (2025) quantified the radiative effects of stratospheric H_2O using satellite observations and radiative transfer simulations under clear sky conditions. Their results show that the Hunga H_2O caused a net radiative cooling rate of −0.15 K day^{-1} in the stratosphere in 2022, and a continued cooling of −0.1 K day^{-1} in 2023, consistent with our findings.

Notably, the mid-stratosphere experienced even more pronounced cooling in austral winter 2022. The global temperatures in the mid-stratosphere fell well below those recorded in previous years (Figure 4.4). These cold anomalies stood out one-to-two months after the eruption. This delay is consistent with a radiative response to the increased H_2O near this altitude, with a radiative damping time scale of ~10–20 days (Hitchcock et al., 2010). By July and August 2022, 20 hPa global temperatures were ~1 K below the multi-year average over 2005 to 2021. The cold anomalies persisted into 2023, becoming slightly weaker than in 2022 but remaining beyond the range of variability.

In the months following the eruption, both the water vapour and sulfur dioxide anomalies spread in latitude creating local temperature anomalies. Observed cold temperature anomalies and the H_2O plume over-

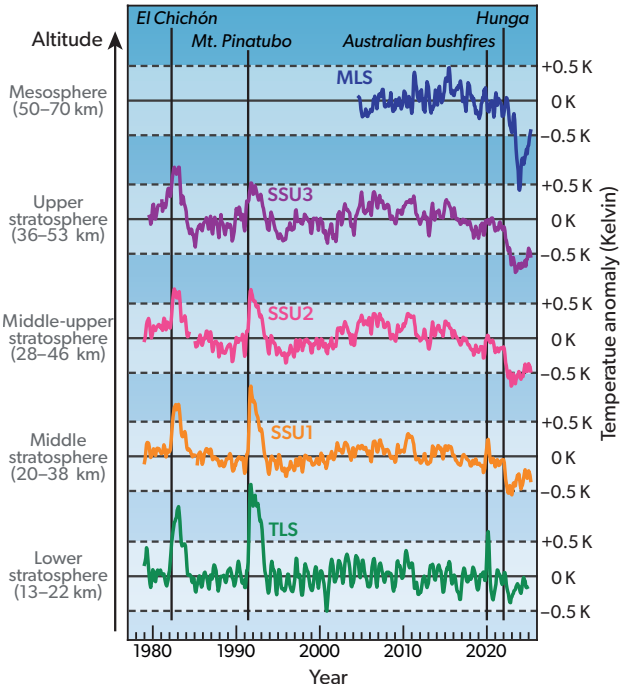

Figure 4.2: *Time series of monthly global average temperature anomalies for thick-layer averages spanning the lower to upper stratosphere (bottom to top). Linear trend and solar cycle fits have been subtracted. Lower stratosphere temperatures (TLS) are ~13-22 km layer averages from satellite microwave measurements. Middle and upper stratosphere data are from the SSU channels updated with microwave measurements, representing thick-layer averages centred near 30, 38 and 45 km (SSU1, SSU2 and SSU3, respectively). Mesospheric temperatures represent 50–70 km averages based on MLS data from 2005 to February 2025 (Randel et al., 2024). The four vertical dashed lines mark the timing of major events that caused stratospheric temperature anomalies: the eruptions of El Chichón (1982), Mount Pinatubo (1991), the 2019–2020 Australian wildfires, and the 2022 Hunga eruption. Adapted and updated from Randel et al. (2024).*

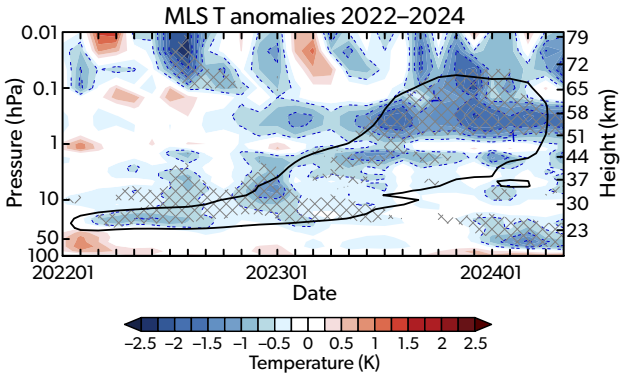

Figure 4.3: *Height and time sections of anomalous global average temperature anomalies (colour shadings) from MLS observations. Dashed blue contours indicate temperature anomalies at 0.5 K intervals. Solid black contour shows the location of Hunga H_2O plume at 1 ppmv level. The MLS observations have been detrended based on the entire MLS data (2005-2024) using fits derived from the pre-Hunga period (2004-2021) and the 11-year solar cycle, ENSO, and QBO variabilities have been removed using multilinear regression fits (adapted from Randel et al., 2024). The hatched regions are those evaluated as significant based on twice of the standard deviation of the anomalies for the period 2005-2021.*

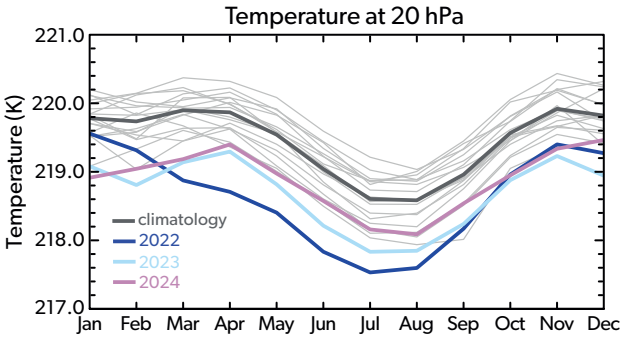

Figure 4.4: *Globally and monthly averaged temperatures at 20 hPa from the MLS observations showing persistent anomalous cooling since 2022. Gray lines show time series of MLS temperatures for 2005–2021 while the black line is the climatology. Navy/light-blue/purple lines show 20 hPa temperature for 2022/2023/2024, respectively.*

lapped until April (Figure 4.5a) and decoupled in early SH winter. In particular, 2022 austral winter months exhibited a striking cold anomaly in the mid latitudes of the SH, not directly overlapping the H_2O plume, as illustrated in Figure 4.5b. This significant cooling, in excess of 15 K in the mid-latitude upper stratosphere, is surprising in that much of it was located well above the water vapour anomaly, suggesting a non-local dynamical response to the volcanic perturbations. Part of the tropical and extratropical temperature maxima could be related to the phase of the QBO in 2022 (Coy et al., 2022). The temperature contrast between high and low latitudes is suggestive of a meridional shift of the zonal winds and associated changes in the mean meridional circulation (Yulaeva et al., 1994; Wang et al., 2023).

4.2.2 Assimilated temperature and wind anomalies following the Hunga eruption

Global atmospheric reanalyses are one of the fundamental data sets to understand atmospheric variability, and there are multiple reanalyses available, which sometimes show different results for the same diagnostic (SPARC, 2022). Here, we evaluate the influences of the Hunga eruption on stratospheric temper-

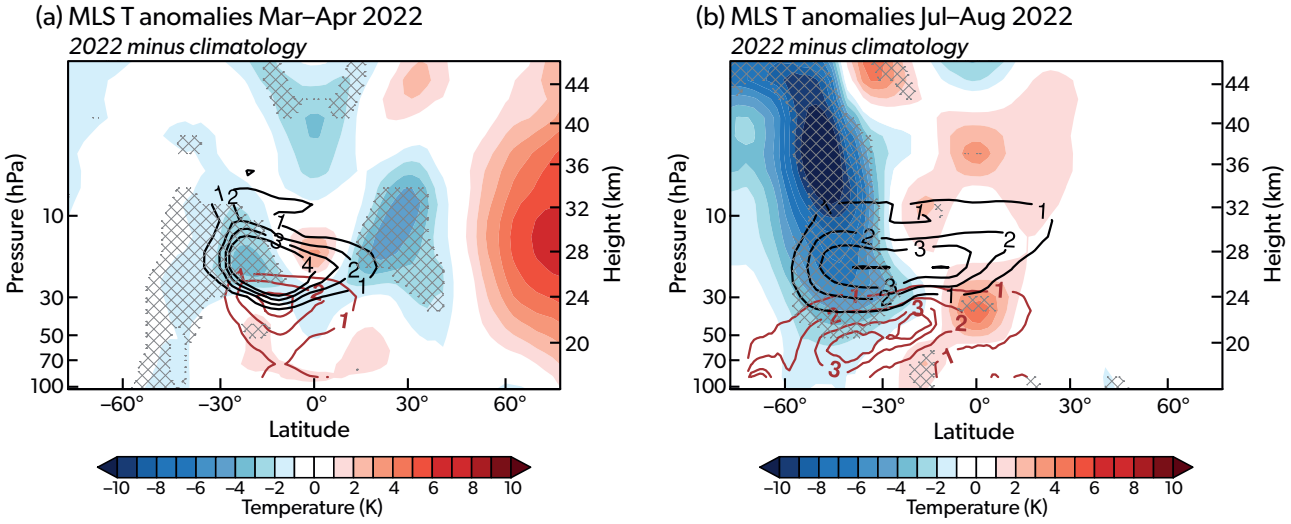

Figure 4.5: *MLS observed temperature anomalies averaged in (a) March and April and (b) July and August 2022 (colour shading, K), calculated as differences between the 2022 and the 2005–2021 average. Red line contours denote the sulfate aerosol extinction in 10^{-3} km^{-1}, and black line contours denote the anomalous H_2O concentration in ppmv. Hatched regions indicate where the 2022 anomalies are outside the range of all variability during 2005–2021 (Wang et al., 2023).*

ature and circulation across the global data assimilation (DA) systems, including MERRA-2 (Gelaro et al., 2017), JRA-3Q (Kosaka et al., 2024), ERA5 (with the period 2000–2006 replaced with ERA5.1) (Hersbach et al., 2020; Simmons et al., 2020), and JRA-55 (Kobayashi et al., 2015). Note that none of these reanalyses include the enhanced water vapour due to the Hunga eruption in the radiative transfer calculations in their forecast model. Thus, the temperature signals mainly come from various assimilated temperature observations. Coy et al. (2022) analysed MERRA-2 data and found that adjustments made during data assimilation compensated for the missing radiative cooling caused by the Hunga water vapour. This suggests that while the direct radiative impact of the eruption was not explicitly modelled, the resulting meridional circulation signals are likely realistic.

The temperature anomaly time series at 20 hPa at 45° S shows the strongest cooling in August 2022 following the Hunga eruption based on four reanalyses (Figure 4.6). These anomalies are calculated with respect to the 2005–2021 climatology. All four reanalyses track the temperature changes from month to month nearly identically, and all show negative anomalies after the Hunga eruption at 20 hPa, 45° S mid-stratosphere, with temperatures down to ~-8 K in the middle of 2022, comparing well with the MLS observation (Figure 4.5b).

For examination of changes at all latitudes and pressures, we focus on the months of July and August 2022, when the SH stratospheric polar vortex is strongest.

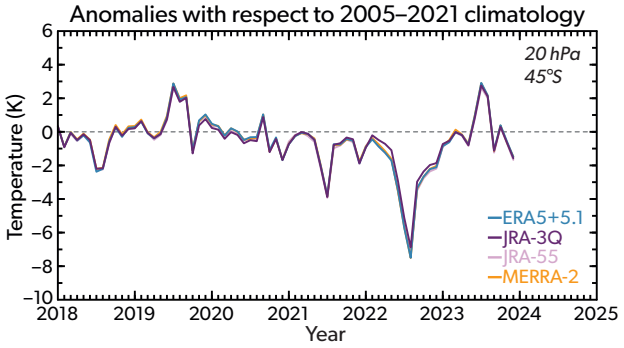

Figure 4.6: *Temperature anomaly times series at 20 hPa, 45°S for the four reanalyses. These anomalies are with respect to the 2005-2021 climatology.*

During this period, record low stratospheric temperature in the satellite era were just equatorward of the polar vortex edge (Figure 4.5b). These months are also when stratospheric planetary activity becomes important to the circulation variability. Hunga may impact stratospheric circulation not only through radiative forcing but also by modifying wave–mean flow interactions.

Temperature anomalies with horizontal gradients imply the existence of vertical wind shear anomalies through thermal wind balance. In austral winter 2022, the maximum stratospheric cooling was consistent with positive and negative vertical wind shears equatorward and poleward, respectively, leading to positive wind anomalies of over 40 m s^{-1} at 40°S in the upper stratosphere shown in MERRA-2 (Figure 4.7). The location of the large wind anomaly amplitudes coin-

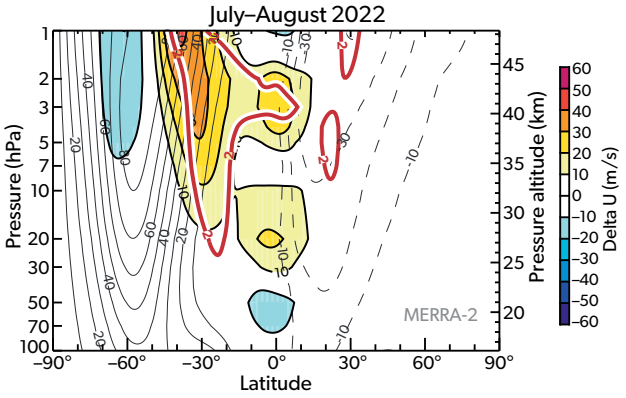

Figure 4.7: *Zonal mean zonal wind anomaly for July and August 2022. The grey contours show the background zonal winds with an interval of 10 m s^{-1}. MERRA-2 wind anomalies are calculated relative to the 2005-2021 mean and 2005-2023 trend. Red contours highlight anomalies exceeding 2 standard deviations.*

cided with the location of the polar vortex at these altitudes. The enhanced zonal winds in this region exceeded the range of internal variability observed in previous years (Wang et al., 2023). The other three reanalyses produce a similar pattern and magnitude (not shown).

In addition, we investigated the evolution of the global averaged temperature anomalies using the Reanalysis Intercomparison Dataset (Martineau et al., 2018) for the four reanalyses. Global temperature anomalies for the years 2022 to 2024 are shown in Figure 4.8. The anomalies were obtained by regressing out the components of the seasonal cycle, linear trend, the QBO, solar cycle, and ENSO (Niño 3.4) for the period 1980–2023, excluding the 24 months after the three major tropical eruptions (from January 2022 to December 2023 for the Hunga eruption). In MERRA-2, negative temperature anomalies first appeared around 20 hPa in April 2022, ascending to around 5 hPa by one year later. Separately, there is a continuous negative temperature anomaly around 1 hPa throughout the year 2022. These features are similar to the MLS measurements shown in Figure 4.3, in part because MLS temperature retrievals have been assimilated in this reanalysis.

Other reanalyses JRA-3Q, ERA5, and JRA-55 show generally similar negative anomalies of -0.5 K in the mid-stratosphere around 20–10 hPa, but do not show ascending anomalies up to 5 hPa. This is probably because these latter three reanalyses do not assimilate MLS temperatures, and other temperature-sensitive microwave and infrared satellite sounders may not be able to strongly constrain upper stratospheric temperatures in these reanalysis systems. Also, the negative anomalies are much weaker in JRA-3Q than in the other three reanalyses; this is in part because in JRA-3Q, mid-stratospheric subtropical positive anomalies are much greater, partially cancelling the SH mid latitude negative anomalies in the global means.

Overall, global DA systems tracked the observed cooling anomalies up to the mid-stratosphere despite the modelling component being unaware of the composition perturbation following the Hunga eruption. Above about the 10 hPa level, MERRA-2 is the only reanalysis that provides similar temperature signals to those in the MLS observations because MERRA-2 is the only reanalysis that assimilates MLS temperature retrievals above the 5 hPa level. In addition, these reanalyses provide global information on winds and circulation patterns, with multi-year reanalysis products enabling potential identification of post-Hunga eruption anomalies.

4.2.3 Hunga induced temperature and circulation anomalies in models

Global atmospheric models can isolate the effects of the Hunga eruption on temperatures and winds through the use of control and ensemble simulations, aiding in our understanding of these impacts. Using multiple ensemble members with slightly perturbed initial conditions can capture natural variability while the volcanic perturbations to atmospheric composition can be excluded in control runs or included in volcano runs. The forced signal induced by Hunga can be extracted by the statistically significant differences between the volcano and the control ensembles.

Here, we analyse four models that participated in the Hunga Tonga-Hunga Ha'apai Volcano Impact Model Observation Comparison (HTHH-MOC) Project (Zhuo et al., 2025): Community Earth System Model, version 2 / Whole Atmosphere Community Climate Model version 6 (CESM2/WACCM6, hereafter referred to as WACCM) with modal aerosol module (MAM), Goddard Earth Observing System earth system model (GEOSCCM), Goddard Space Flight Center two-dimensional model (GSFC2D), and the Model for Interdisciplinary Research on Climate – Chemical Atmospheric general circulation model for Study of atmospheric Environment and Radiative forcing (MIROC-CHASER). After adding realistic amounts of H_2O and SO_2 perturbations from the Hunga eruption in January 2022, all models can capture the evolution of the water vapour and temperature perturbations on a global scale (see detailed com-

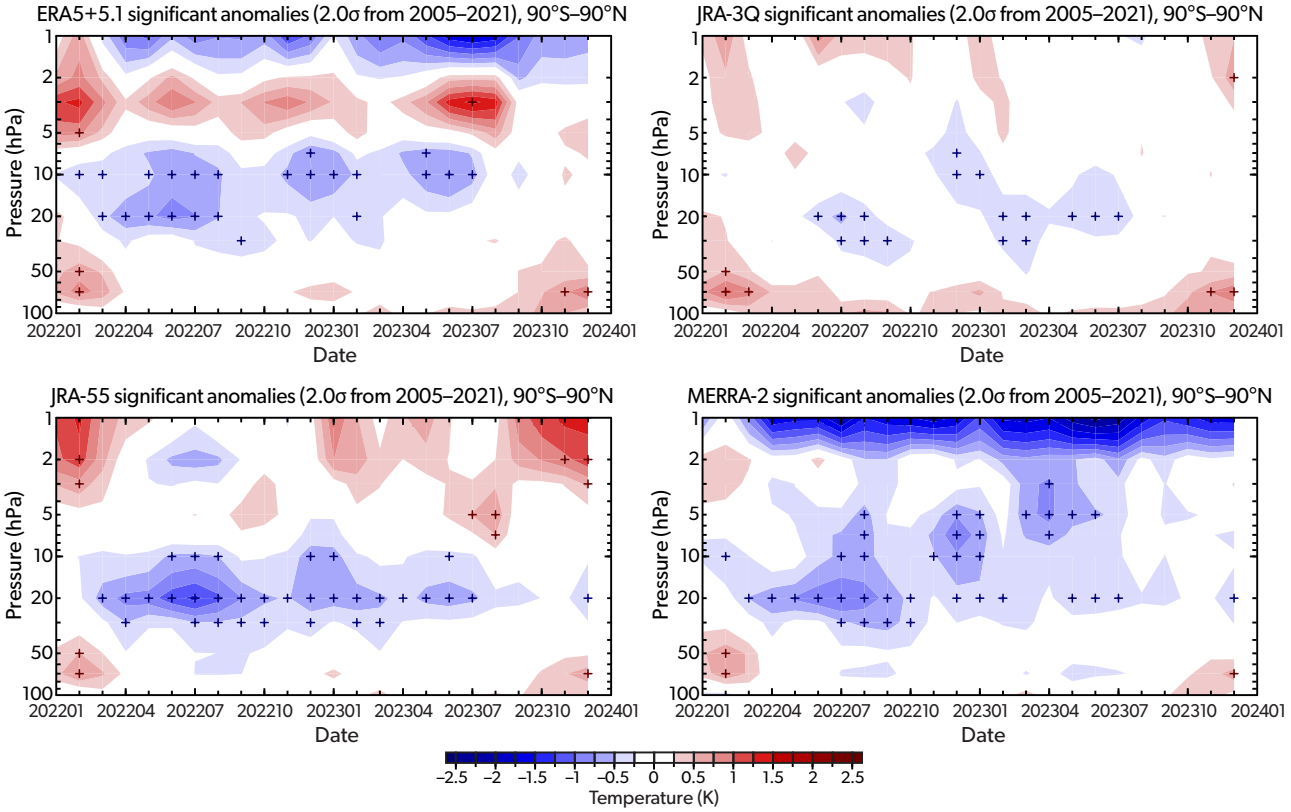

Figure 4.8: *Global-mean temperature anomalies in the stratosphere from the ERA5, JRA-3Q, JRA-55, and MERRA-2 reanalyses. These anomalies were obtained by regressing out the components of seasonal cycle, linear trend, the QBO, solar cycle, and ENSO for the period 1980-2023, excluding the 24 months after the three major tropical eruptions, for each reanalysis. The hatched regions are those evaluated as significant based on twice of the standard deviation of the anomalies for the period 2005-2021. Note that MERRA-2 assimilated temperature retrievals from Aura MLS at pressures 5 hPa and less, but the other three did not.*

parison and Figure 4 in Zhuo et al., 2025). The global time-height temperature response from WACCM is shown in Figure 4.9 as a reference. Notable similarities to the observations (Figure 4.3) include the ascent of the cooling of ~0.5 K overlapping the H_2O cloud, followed by a systematically larger temperature response in the mesosphere. Note that global average data show very small warming effects from Hunga aerosol in the lower stratosphere in both observations and model simulations, so the main Hunga impacts on temperature appear to be due to the radiative cooling effects of H_2O.

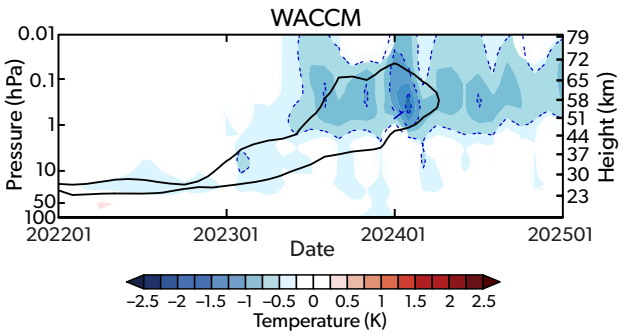

Figure 4.9: *Modelled global mean temperature perturbation (color shading at 0.5 K intervals) as a function of pressure and time from CESM2-WACCM6. Solid black contour shows the location of forecasted H_2O plume at 1 ppmv level. Regions where differences are not significant at the 95% level using t-test are shaded white.*

During austral winter months in 2022, the WACCM ensemble mean averaged over 60 ensemble members reproduced the strong monthly mean negative temperature anomaly in the SH (Figure 4.10a), matching the altitudes and latitudes in the observations (Figure 4.5b), but with a weaker magnitude. The simulated zonal wind changes also show a strengthening and equatorward displacement of the winter westerlies in response to the Hunga forcing (Figure 4.10b), with patterns similar to the observed anomalies (Figure 4.7). Both the ensemble mean temperature and mean wind anomalies in the model ensemble are only about half as pronounced as those observed in 2022. Despite the smaller magnitude, the similarity in timing and

spatial structure of observed and modelled temperature and wind patterns is strongly suggestive of an Hunga attribution for the observed anomalies. GEOSCCM with 10 ensemble members did show a cooling signal in this region during the same months, but it was not statistically significant at 95% level (Figure 4.10c). The GSFC2D model (Figure 4.10d) uses specified lower tropospheric forcing for the planetary and gravity wave parameterisations that is identical for both the control and Hunga runs, thus lacking possible wave–mean flow feedbacks due to the Hunga eruption. The internal variability is very small in the 2D model, and it captures only small dynamical changes due to the direct radiative impacts of the Hunga H_2O and aerosol. It simulates significant cooling of about 2 to 3 K in the tropical stratosphere near 20 hPa, with weaker warming below the cooling layer. The 2D model does not reproduce the mid latitude cooling in the ensemble mean, which is consistent with the hypothesis that the observed mid latitude cooling anomalies in austral winter 2022 are a combination of the dynamical (wave) response to Hunga's radiative forcing and internal (unforced) variability. The MIROC-CHASER model simulates cooling in regions overlapping the Hunga H_2O, but it does not reproduce the mid latitude cooling and underestimates sulfate concentrations and the associated infrared heating (Figure 4.10e).

These discrepancies among the models and observations suggest that while the radiative effect of H_2O is a robust feature of the Hunga eruption's impact, not all global climate models reproduce the strong mid latitude cooling pattern with statistical significance, indicating that the observed response may contain significant internal variability (Yu et al., 2023).

Reasons behind the specific patterns of temperature and wind observed in 2022, and how those patterns are related to the Hunga water and aerosol anomalies, continue to be an active research topic (Yook et al., 2025). Ongoing research should provide additional insights into the dynamical processes, that is, the relationships between the temperature, wind, and wave anomalies, in these observed fields.

As the water vapour anomaly spread into the NH it was blocked by the formation of the NH stratospheric jet (Figure 4.1b), and did not reach the coldest regions of NH 2022/2023 winter stratospheric polar vortex (Chapter 3). However, the possibility of anomalous cooling outside of the vortex and at upper levels, modifying the evolution of the NH polar region, remains to be fully explored (Kuchar et al., 2025). Reanalysis shows that zonal mean zonal winds during the 2022/2023 winter were within the range of internal variability (supplementary Figure S4.1), and the MLS temperatures show no clear or persistent departures from the mean state (supplementary Figure S4.2). Current modelling research suggests Hunga effects at a level much smaller than annual variability (Figure S3.28), and therefore it is difficult to identify or quantify any Hunga signal (Bednarz et al., 2026). These results highlight the need for additional studies using larger model ensemble sizes to constrain the role of the Hunga eruption in modulating the NH stratospheric circulation (Figure S3.33).

4.3 Residual mean meridional circulation and Eliassen-Palm flux

Comparisons between global DA systems and models can provide complete diagnostics on the effects of the Hunga eruption on the atmospheric circulation. Here, the focus is on the effects of the Hunga eruption on the mean meridional transport circulation (residual mean circulation RMC) and its wave forcing as diagnosed by the Eliassen-Palm flux (EP flux).

4.3.1 Residual mean meridional circulation and EP flux in the global data assimilation systems

In the austral winter months following the Hunga eruption, the RMC developed a clockwise anomaly, which indicates anomalous SH mid-latitude upwelling and low-latitude downwelling that opposes and weakens the normal background circulation (Figure 4.11a). By austral winter of 2022, this RMC anomaly encompassed the vertical extent of the SH stratosphere and extended into the NH in the lower stratosphere in MERRA-2 (Figure 4.11a). It is important to note that the full RMC remained downward in the SH high latitudes. However, it was weakened by the anomaly. These circulation anomalies remained as strong clockwise circulation anomalies during June to August 2022, based on the 43-year (1980–2022) MERRA-2 dataset (Coy et al., 2022). Note that the "upward" residual circulation anomaly in the SH extratropics is consistent with the cold anomaly (Figure 4.6), as the RMC anomaly reduced the adiabatic heating from the climatological downward RMC. The downward anomaly in the tropics, however, would be associated with anomalous warming, which would oppose the radiative signal.

The wave forcing of the stratosphere also displayed significant changes after the Hunga eruption. EP

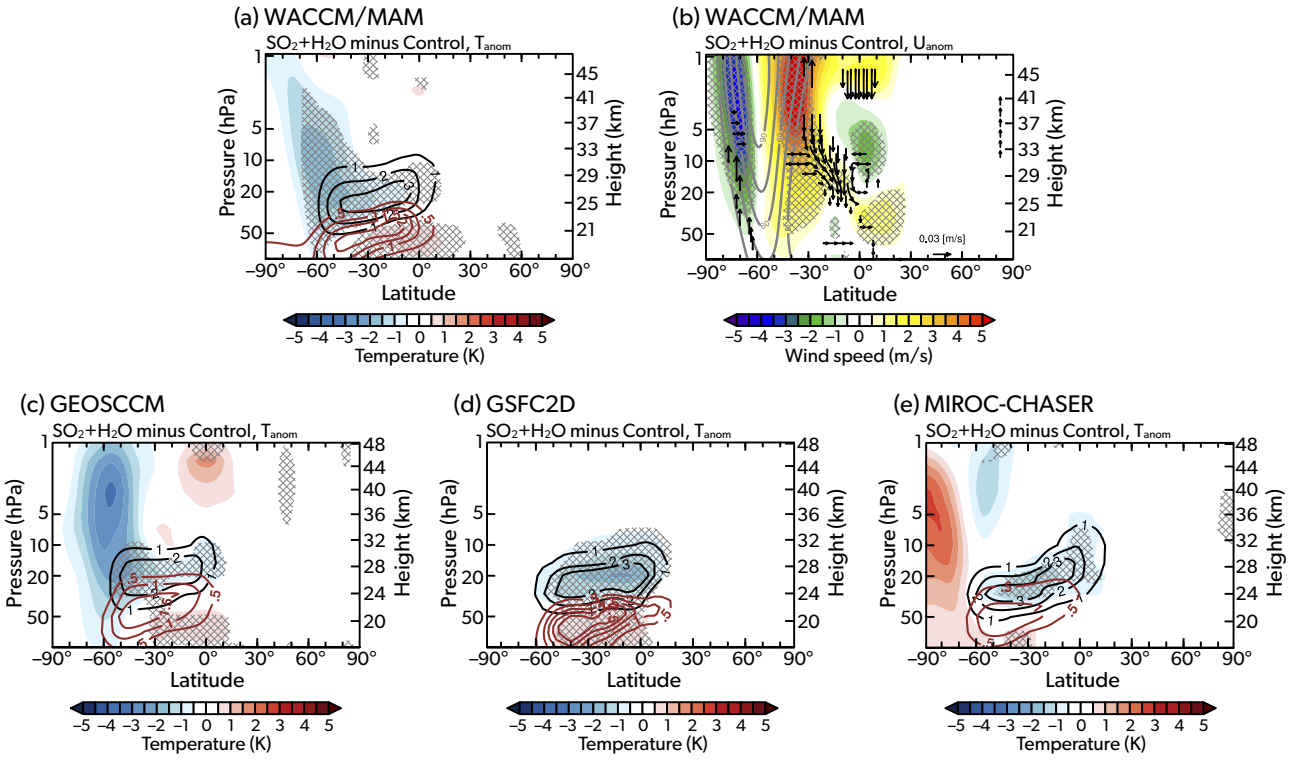

Figure 4.10: *Modelled temperature differences in July and August 2022 (colour shading, K) from (a) WACCM with modal aerosol module (MAM), (c) GEOSCCM, (d) GSFC2D, and (e) MIROC-CHASER. Red contours denote the sulfate aerosol extinction at 745 nm in 10^{-3} km^{-1}, and black contours denote the anomalous H_2O concentration in ppmv. (b) Zonal mean zonal wind differences averaged in July and August 2022. Colours show zonal mean zonal wind anomalies in WACCM simulations compared to the control runs. Gray contours show the background zonal winds with an interval of 15 m s^{-1}. The vectors depict the significant anomalies in the residual mean circulation. Hatched regions indicate where anomalies are statistically significant at the 95% level according to Student's* t*–test.*

fluxes are a measure of the propagation of wave activity. In the SH winter climatology, EP fluxes are upward and equatorward, as these waves are typically forced from the troposphere. Along with the zonal wind, temperature, and RMC anomalies, the July–August 2022 upward and equatorward EP fluxes were reduced in high latitudes at 60°S throughout the stratosphere (Figure 4.11b). Since the climatological EP fluxes are upward, the downward EP flux anomalies in Figure 4.11b indicate weaker upward EP flux from the mid-stratosphere upward over 40°S–60°S and hence, reduced planetary wave activity in austral winter 2022. Note that there was some increase in the upward and equatorward EP flux vectors in the lower to mid stratosphere near 45°S. Since the planetary waves preferably propagate in the regions of strong potential vorticity gradients, this equatorward shift in EP flux was consistent with a more equatorward expanded polar vortex in 2022 (Wang et al., 2023).

With reduced upward EP fluxes, the wave forcing of the zonal mean zonal flow from the flux divergence results in reduced drag, leading to strengthening of the polar vortex. Climatologically, wave activity acts to decelerate the zonal mean zonal wind in the region of the polar vortex, i.e., EP flux divergence is negative. The July–August 2022 EP flux divergence anomaly is accelerating the zonal mean zonal wind in the SH upper stratosphere (Figure 4.10b), and thus acting to reduce the climatological drag on the zonal wind.

4.3.2 Residual mean circulation and EP flux changes in models

Detailed comparisons of simulated anomalies from global models against DA results confirm the models' ability to simulate the RMC and EP fluxes. The WACCM simulation, used as an example, has been able to represent the RMC anomalies in austral winter months during 2022. The upward residual circulation anomaly at 60°S and downward anomaly extending across the equator (Figure 4.10b) compares well with the DA-derived RMC in Figure 4.11a. The changes in the RMC are associated with adiabatic cooling in the stratosphere in the SH extratropics, consistent with a weakened planetary-scale wave forcing in the middle

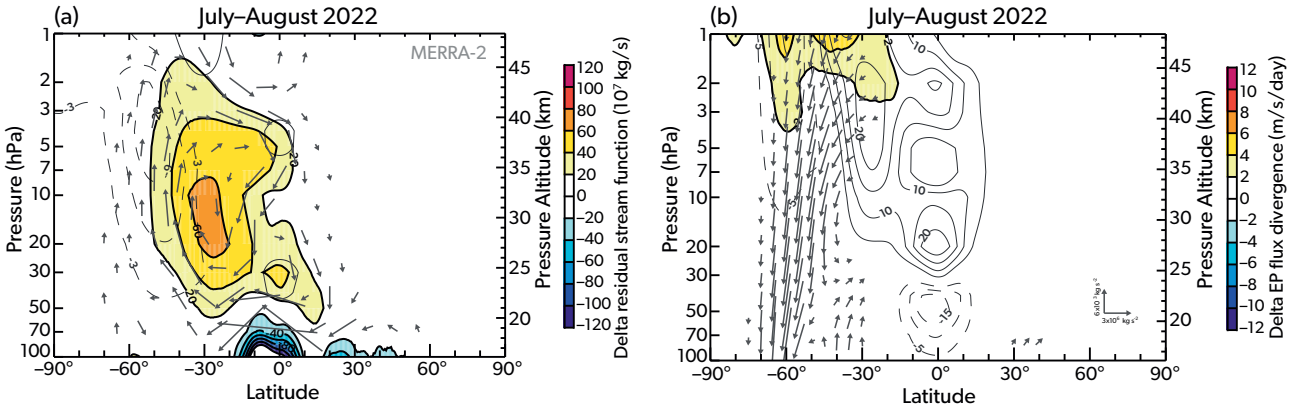

Figure 4.11: *(a) Monthly mean residual circulation anomaly for July-August 2022. The arrows show the circulation calculated from the stream function anomaly. The dashed contours show the corresponding temperature anomaly (K) for the same month. (b) EP flux divergence anomalies for July-August 2022 (filled contours) and EP flux anomaly vectors (arrows). The scale arrows are 3x10^6 kg s^{-2} for the meridional component and 6x10^3 kg s^{-2} for the vertical component. The grey contours show the corresponding zonal mean zonal wind anomaly (m s^{-1}). Fields are shown relative to the 2005-2021 mean, with the 2005-2023 linear trend subtracted.*

and upper stratosphere.

The coupling of planetary wave amplitudes and stratospheric temperature is a well-known feature of the winter stratosphere (Andrews et al., 2016; Randel and Newman, 1998). The correlation is evident in Figure 4.12, which shows results from all available WACCM ensemble members in the HTHH-MOC Project (Zhuo et al., 2025), consisting of 60 Hunga-forced and 60 control simulations. Over July and August from 2022 to 2031, a significant positive correlation (r = 0.76, p-value < 0.0001) is found between polar temperature versus the vertical component of the EP flux in the lower stratosphere (grey dots). Among the 60 Hunga-forced ensemble members, 44 runs exhibit a cold temperature anomaly in 2022 (red dots in Figure 4.12), and several simulations produce temperature and wave responses comparable to the observations (black dot in Figure 4.12). There is a systematic shift in temperatures and wave activity in the integrations with the eruption in 2022 (red dots in Figure 4.12) with respect to the 10-year control ensemble background (grey dots in Figure 4.12). Specifically, 39 out of 60 ensemble members (65%) exhibit both colder temperatures and weaker upward EP fluxes in response to the Hunga eruption, compared to 42% in the control ensemble. We view this shift as a fingerprint of the response to the Hunga forcing in WACCM simulations. However, there is considerable stochastic variability among the volcano realisations. We conclude that internal variability in the ensemble model simulations contributes to the weaker amplitudes of the ensemble average temperature and wind anomalies compared to the observed pattern in 2022. Similar strong correlations between temperature and wave activities are found in the other two 3D models (supplementary Figure S4.3). However, the Hunga-forced simulations in these models exhibit considerable spread, and with only 10 ensemble members, it is difficult to determine whether there is a clear shift toward colder temperatures.

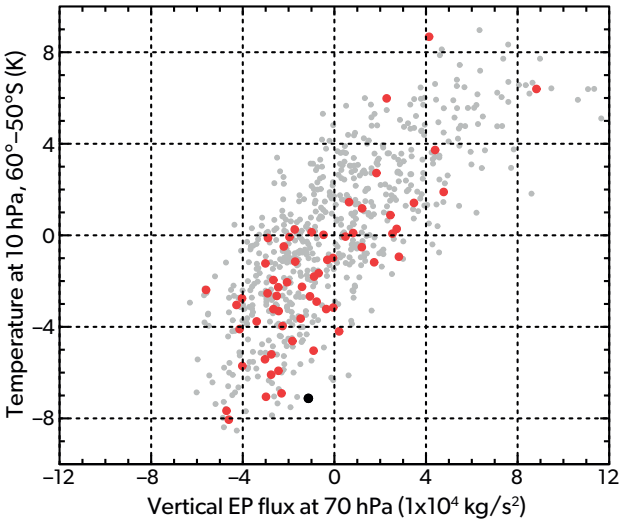

Figure 4.12: *Relationship between July–August average temperatures at 10 hPa and upward EP flux at 70 hPa over 55°S–65°S. Red dots represent the Hunga-forced minus control WACCM simulation for July–August 2022, based on 60 ensemble members. Gray dots represent deviations from the control ensemble mean for July–August averages across 2022–2031 (60 ensemble members over 10 years). The black dot indicates the July–August 2022 average from ERA5.*

4.4 Interaction of Hunga with the Quasi-Biennial Oscillation (QBO)

The Quasi-Biennial Oscillation (QBO) occurs in the lower stratosphere near the equator, manifesting as alternating easterlies and westerlies that descend from the stratopause to the tropopause with a period of ~28 months (Baldwin et al., 2001). Such equatorial zonal wind anomalies are balanced by a meridional circulation that extends temperature anomalies throughout the tropical stratosphere (Plumb and Bell, 1982). Depending on the QBO phase, the QBO meridional circulation may reinforce or weaken the background RMC.

In early 2022, QBO had easterly winds in the lower stratosphere with westerly winds above (Figure 4.13), a configuration associated with a lower stratosphere secondary circulation descending at the equator and ascending at the subtropics. Such a circulation may have enhanced the cross-equatorial transport of water vapour following the Hunga eruption (Schoeberl et al., 2023). Jucker et al. (2024) further suggested from their chemistry-climate model simulations that excessive stratospheric water vapour like that injected by the Hunga eruption tends to stay longer in the middle atmosphere if the QBO is in the easterly phase than the westerly phase at 50 hPa, as observed in 2022, and effects of the initial easterly QBO phase could persist over a few years (Diallo et al., 2018; Jucker et al., 2024).

Given the potential impact of the QBO on RMC, austral winter 2022 offers an opportunity for comparing the QBO-induced circulation anomaly to the changes caused by the Hunga eruption. The QBO signal in RMC is derived from the 1980-2021 MERRA-2 record by averaging daily July–August residual mean circulations on days with a similar QBO phase to July–August 2022. The estimated QBO effect on the RMC (Figure 4.14a) generally opposed the August 2022 residual circulation in the SH (Figure 4.11b), resulting in a slight reduction in the strength of the austral winter 2022 residual circulation anomaly (Figure 4.14b), especially equatorward of 30°S latitude. The QBO-induced residual circulation anomaly in the upper stratosphere (above the main QBO region) shows a downward circulation just equatorward of the main cold anomaly, which may have had a minor influence in limiting the equatorward extent of the cold anomaly. However, since the QBO signal in residual circulation is much weaker than the full residual circulation, and does not extend into the main cooling anomaly region (40°–60°S) during July–August 2022,

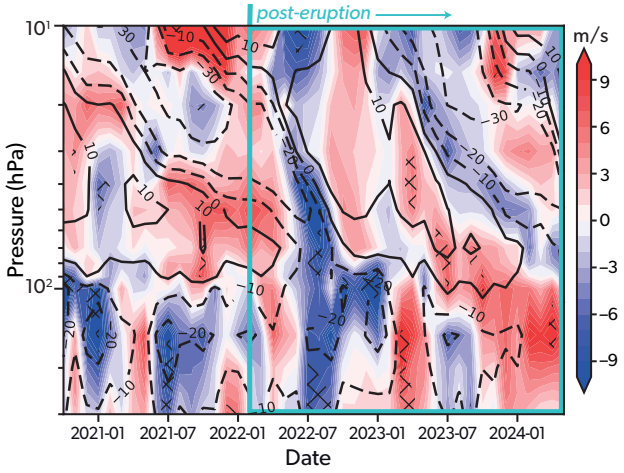

Figure 4.13: *Monthly mean zonal wind measured by radiosondes from the Meteorological Service Singapore Upper Air Observatory (station code 48698) (black contours) and its differences with respect to the months between 1979-2014 that has similar QBO phase (colour shading, unit: m/s). QBO phase is determined by the two leading EOFs in the Singapore wind between 100-10 hPa following Wallace et al. (1993). We compare the wind profile in each month to those months that have QBO phase within ±0.1π of this month, representing a small fraction of the QBO cycle. Hatches indicate the differences that are statistically significant at 90% confidence level based on the Student's t-test. The turquoise box marks the period after the eruption. The turquoise box marks the common region plotted in Figure 4.15.*

it does not appear to have played a major role in the creation and maintenance of the cold anomaly. Therefore, this suggests that the anomalous temperature and RMC responses in the mid-latitude were primarily caused by the large internal variability and the Hunga forcing.

The QBO progression before and after the Hunga eruption in radiosonde observations shows that the equatorial zonal wind was easterly between 20 hPa and 60 hPa in early 2022 when the Hunga volcano erupted (Figure 4.13). These easterlies descended over the next few months, and westerlies dominated the equatorial stratosphere in late 2022. By early 2024, the wind profile returned to a similar structure as in early 2022, corresponding to a period of ~2 years. This particular QBO cycle is faster than the average period (~28 months) but is still within the range of variations seen in observations over the past few decades.

The amplitude of the QBO following the eruption showed some significant regions of stronger than usual westerlies and easterlies (Figure 4.13). However, the easterly anomalies are significant only for one month below 60 hPa in 2022, and the westerlies

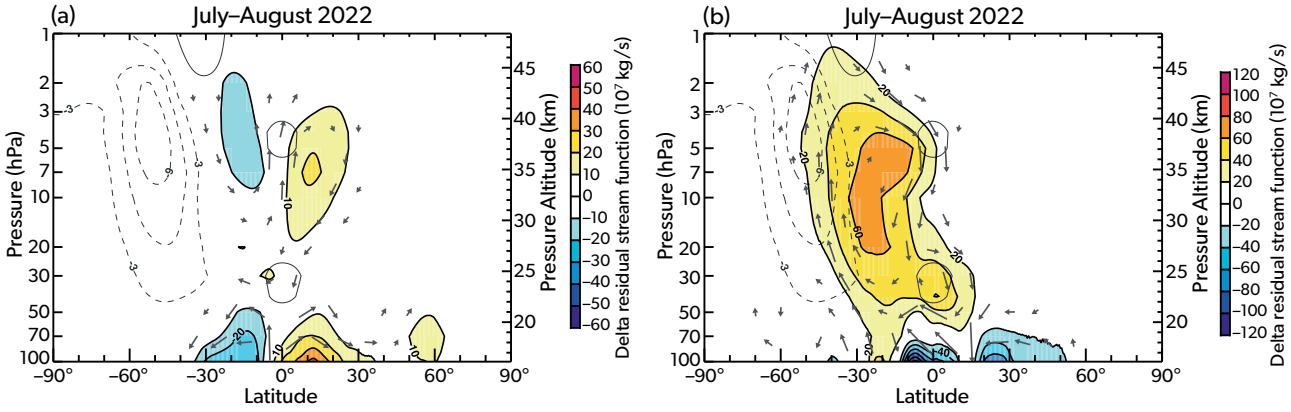

Figure 4.14: *(a) Estimated QBO signal in the residual mean circulation, calculated as the average circulation during July-August of years with similar QBO phase as in 2022; (b) Residual mean circulation after QBO-induced circulation shown in (a) from the full circulation shown in Figure 4.11a. Gray contours denote the July-August 2022 temperature anomaly. The arrow lengths, based on the stream function, are scaled by pressure. Note that the contour interval is halved in (a) relative to (b) and that the scale of the arrows in (a) are double the arrow scale in (b). All fields are from MERRA-2.*

appear for just three months in the lower stratosphere. It is difficult to attribute these changes to the Hunga eruption given the complicated interaction between the waves generated from convection in the troposphere and the stratospheric circulation responsible for creating the highly variable QBO.

We also examined the QBO simulated across all models participating in HTHH-MOC, enabling the examination of equatorial zonal wind anomalies due to the additional sulfate aerosols and water vapour from the eruption (Figure 4.15). The models did not simulate a statistically significant response to the Hunga eruption in the equatorial winds over most of the stratosphere and mesosphere. Instead, they revealed a generally insignificant weakening of QBO amplitude from 2023 onward, a result that disagrees with the stronger anomalies observed. Models are known to have problems simulating the QBO, including producing a wind oscillation that is too weak in the lower stratosphere, not capturing the ozone feedback, and not having the correct gravity wave spectrum (Anstey et al., 2022). The possible inability of models to simulate a realistic QBO limits our ability to say whether the QBO changes in observations are part of natural variability or a result of the forced response to the eruption.

4.5 Summary

Satellite and reanalysis systems demonstrated persistent perturbations in stratospheric temperature and circulation following the Hunga eruption. The Hunga H_2O injected by the eruption in 2022 remains until the present in 2025. It was spread globally by the Brewer-Dobson circulation, which includes vertical and meridional transport by the residual mean circulation and mixing along isentropic surfaces.

During the austral winter months in 2022, observations showed large-scale SH stratospheric cooling, consistent with the equatorward shift of the SH winter stratospheric jet and the slowing of the residual mean circulation with reduced wave activity seen in the DA system. In the first two years following the Hunga volcanic eruption, the global average stratospheric temperatures decreased by 0.5 to 1.0 K. This impact was mainly due to radiative cooling from H_2O injected into the stratosphere by the Hunga eruption. The observed cooling patterns rose in altitude over time following the evolution of the H_2O plume. Unlike earlier sulfur-rich volcanoes, satellite observations provide little evidence of global warming impacts from Hunga aerosols in the lower stratosphere.

Global atmospheric models were used to isolate the effects of the Hunga eruption on stratospheric temperatures and winds by distinguishing volcanic forcing from natural variability. Simulations from the HTHH-MOC Project, including WACCM, GEOSCCM, GSFC2D, and MIROC-CHASER, tracked the evolution of water vapour and temperature perturbations, showing ~0.5 K global stratospheric cooling overlapping the H_2O cloud and a stronger response in the mesosphere. While all models captured the radiative cooling due to Hunga H_2O, not all global chemistry-climate models reproduced the large-scale Southern Hemisphere cooling and equatorward-shifted polar vortex. This suggests that the observed mid latitude temperature anomalies might contain substantial

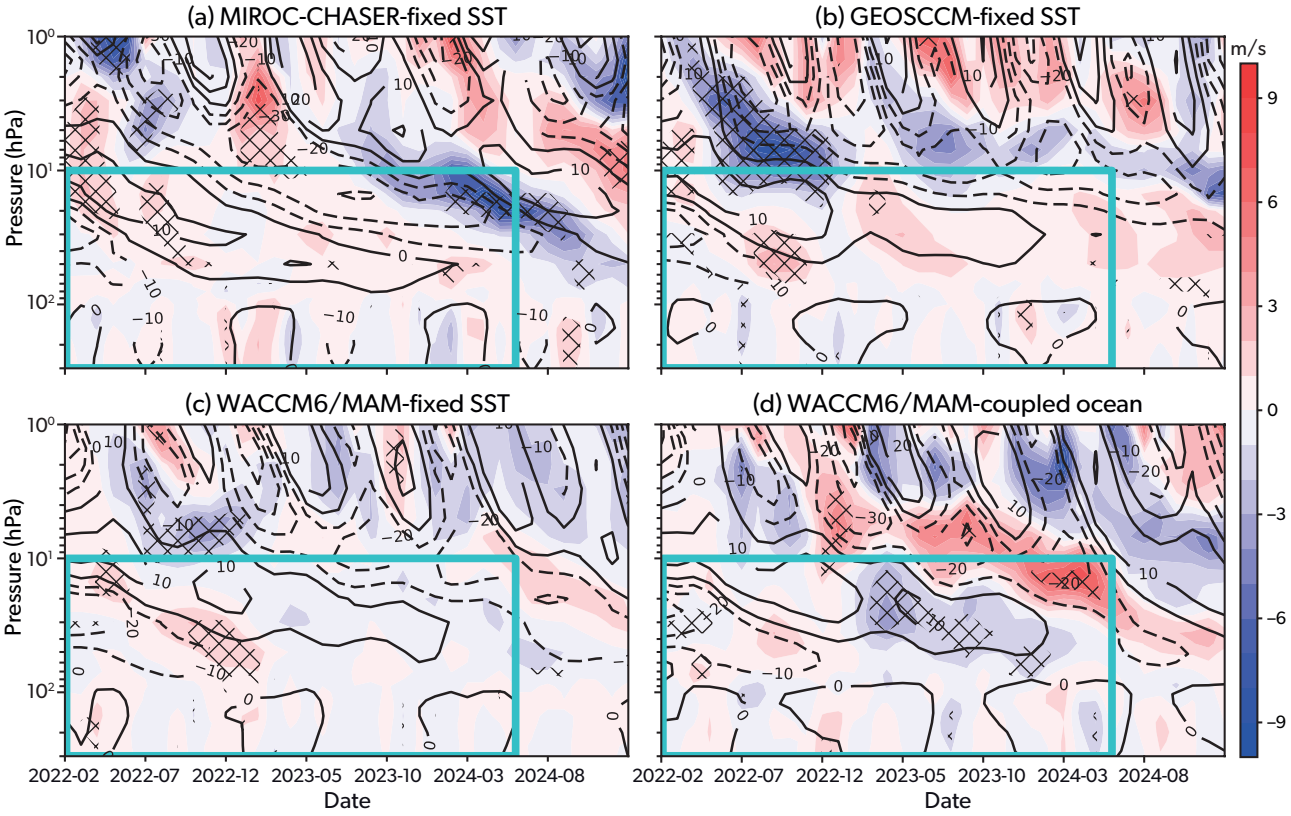

Figure 4.15: *Ensemble mean equatorial zonal mean zonal wind averaged over 5°N-5°S simulated in (a) MIROC-CHASER fixed SST runs (b) GEOSCCM fixed SST runs (c) WACCM fixed SST runs and (d) WACCM coupled ocean runs. Black contours represent the equatorial winds in no-volcano runs, while colour shading shows anomalies due to volcanic aerosols and water vapour in units of m s^{-1}. Diagonal hatches indicate differences between the two simulations are statistically significant at 90% confidence level. Statistical significance is estimated based on the two-sided Student's t–test. The turquoise box marks the common region plotted in Figure 4.13.*

internal variability, with local Hunga impacts intertwined with dynamically forced anomalies.

While a slightly faster and stronger QBO was observed following the Hunga eruption, this change was within the range of variability and was not simulated across the participating models in the HTHH-MOC activity, indicating that the eruption likely had no significant impact on the QBO.

References

Andrews, D. G., C. B. Leovy and J. R. Holton (2016). *Middle Atmosphere Dynamics*. Vol. 40. Academic Press.

Anstey, J. A., S. M. Osprey, J. Alexander, M. P. Baldwin, N. Butchart, L. Gray, Y. Kawatani, P. A. Newman and J. H. Richter (2022). 'Impacts, processes and projections of the quasi-biennial oscillation'. *Nature Rev. Earth Environ.*, 3, pp. 588–603. DOI: 10.1038/s43017-022-00323-7.

Baldwin, M. P., L. J. Gray, T. J. Dunkerton, K. Hamilton, P. H. Haynes, W. J. Randel, J. Holton, M. J. Alexander, I. Hirota and T. Horinouchi (2001). 'The quasi-biennial oscillation'. *Rev. Geophys.*, 39, pp. 179–229. DOI: 10.1029/1999rg000073.

Bednarz, E. M., A. H. Butler, X. Wang, Z. Zhuo, W. Yu, G. Stenchikov, M. Toohey and Y. Zhu (2026). 'Indirect climate impacts of the Hunga eruption'. *Atmos. Chem. Phys.*, 26, pp. 197–215. DOI: 10.5194/acp-26-197-2026.

Carn, S. A., N. A. Krotkov, B. L. Fisher and C. Li (2022). 'Out of the blue: volcanic SO_2 emissions during the 2021-2022 Hunga Tonga-Hunga Ha'apai eruptions'. *Front. Earth Sci.*, 13. DOI: 10.3389/feart.2022.976962.

Coy, L., P. Newman, K. Wargan, G. Partyka, S. Strahan and S. Pawson (2022). 'Stratospheric Circulation Changes Associated with the Hunga Tonga-Hunga Ha'apai Eruption'. *Geophys. Res. Lett.*, 49, e2022GL100982. DOI: 10.1029/2022GL100982.

Diallo, M., M. Riese, T. Birner, P. Konopka, R. Müller, M. I. Hegglin, M. L. Santee, M. Baldwin, B. Legras and F. Ploeger (2018). 'Response of stratospheric water vapor and ozone to the unusual timing of El Niño and the QBO disruption in 2015–2016'. *Atmos. Chem. Phys.*, 18, pp. 13055–13073. DOI: 10.5194/acp-18-13055-2018.

Duchamp, C., F. Wrana, B. Legras, P. Sellitto, R. Belhadji and C. von Savigny (2023). 'Observation of the aerosol plume from the 2022 Hunga Tonga–Hunga Ha'apai eruption with SAGE III/ISS'. *Geophys. Res. Lett.*, 50, e2023GL105076. DOI: 10.1029/2023GL105076.

Gelaro, R., W. McCarty, M. J. Suárez, R. Todling, A. Molod, L. Takacs, C. A. Randles, A. Darmenov, M. G. Bosilovich and R. Reichle (2017). 'The Modern-Era Retrospective Analysis for Research and Applications, Version 2 (MERRA-2)'. *J. Climate*, 30, pp. 5419–5454. DOI: 10.1175/jcli-d-16-0758.1.

Gupta, A. K., T. Mittal, K. E. Fauria, R. Bennartz and J. F. Kok (2025). 'The January 2022 Hunga eruption cooled the Southern Hemisphere in 2022 and 2023'. *Commun. Earth Environ.*, 6, 240. DOI: 10.1038/s43247-025-02181-9.

Hersbach, H., B. Bell, P. Berrisford, S. Hirahara, A. Horányi, J. Muñoz-Sabater, J. Nicolas, C. Peubey, R. Radu, D. Schepers et al. (2020). 'The ERA5 global reanalysis'. *Q. J. R. Meteorol. Soc.*, 146, pp. 1999–2049. DOI: 10.1002/qj.3803.

Hitchcock, P., T. G. Shepherd and S. Yoden (2010). 'On the approximation of local and linear radiative damping in the middle atmosphere'. *J. Atmos. Sci.*, 67, pp. 2070–2085. DOI: 10.1175/2009jas3286.1.

Jucker, M., C. Lucas and D. Dutta (2024). 'Long-term climate impacts of large stratospheric water vapor perturbations'. *J. Climate*, 37, pp. 4507–4521. DOI: 10.1175/JCLI-D-23-0437.1.

Khaykin, S., A. Podglajen, F. Ploeger, J.-U. Grooß, F. Tence, S. Bekki, K. Khlopenkov, K. Bedka, L. Rieger, A. Baron et al. (2022). 'Global perturbation of stratospheric water and aerosol burden by Hunga eruption'. *Commun. Earth Environ.*, 3, 316. DOI: 10.1038/s43247-022-00652-x.

Kobayashi, S., Y. Ota, Y. Harada, A. Ebita, M. Moriya, H. Onoda, K. Onogi, H. Kamahori, C. Kobayashi and H. Endo (2015). 'The JRA-55 reanalysis: General specifications and basic characteristics'. *J. Meteorol. Soc. Japan. Ser. II*, 93, pp. 5–48. DOI: 10.2151/jmsj.2015-001.

Kosaka, Y., S. Kobayashi, Y. Harada, C. Kobayashi, H. Naoe, K. Yoshimoto, M. Harada, N. Goto, J. Chiba and K. Miyaoka (2024). 'The JRA-3Q reanalysis'. *J. Meteorol. Soc. Japan. Ser. II*, 102, pp. 49–109. DOI: 10.2151/jmsj.2024-004.

Kuchar, A., T. Sukhodolov, G. Chiodo, A. Jörimann, J. Kult-Herdin, E. Rozanov and H. H. Rieder (2025). 'Modulation of the northern polar vortex by the Hunga Tonga–Hunga Ha'apai eruption and the associated surface response'. *Atmos. Chem. Phys.*, 25, pp. 3623–3634. DOI: 10.5194/acp-25-3623-2025.

Labitzke, K. and M. P. McCormick (1992). 'Stratospheric temperature increases due to Pinatubo aerosols'. *Geophys. Res. Lett.*, 19, pp. 207–210. DOI: 10.1029/91gl02940.

Legras, B., C. Duchamp, P. Sellitto, A. Podglajen, E. Carboni, R. Siddans, J.-U. Grooß, S. Khaykin and F. Ploeger (2022). 'The evolution and dynamics of the Hunga Tonga–Hunga Ha'apai sulfate aerosol plume in the stratosphere'. *Atmos. Chem. Phys.*, 22, pp. 14957–14970. DOI: 10.5194/acp-22-14957-2022.

Martineau, P., J. S. Wright, N. Zhu and M. Fujiwara (2018). 'Zonal-mean data set of global atmospheric reanalyses on pressure levels'. *Earth Syst. Sci. Data*, 10, pp. 1925–1941. DOI: 10.5194/essd-10-1925-2018.

Millán, L., W. G. Read, M. L. Santee, A. Lambert, G. L. Manney, J. L. Neu, M. C. Pitts, F. Werner, N. J. Livesey and M. J. Schwartz (2024). 'The Evolution of the Hunga Hydration in a Moistening Stratosphere'. *Geophys. Res. Lett.*, 51, e2024GL110841. DOI: 10.1029/2024gl110841.

Millán, L., M. L. Santee, A. Lambert, N. J. Livesey, F. Werner, M. J. Schwartz, H. C. Pumphrey, G. L. Manney, Y. Wang, H. Su et al. (2022). 'The Hunga Tonga-Hunga Ha'apai Hydration of the Stratosphere'. *Geophys. Res. Lett.*, 49, e2022GL099381. DOI: 10.1029/2022gl099381.

Plumb, R. A. and R. C. Bell (1982). 'A model of the quasi-biennial oscillation on an equatorial beta-plane'. *Q. J. R. Meteorol. Soc.*, 108, pp. 335–352. DOI: 10.1002/qj.49710845604.

Plumb, R. A. (1996). 'A "tropical pipe" model of stratospheric transport'. *J. Geophys. Res.*, 101, pp. 3957–3972. DOI: 10.1029/95JD03002.

Randel, W. J. and P. A. Newman (1998). 'The stratosphere in the Southern Hemisphere'. *Meteorol. South. Hemisphere*. Springer, pp. 243–282. DOI: 10.1007/978-1-935704-10-2_9.

Randel, W. J., X. Wang, J. Starr, R. R. Garcia and D. Kinnison (2024). 'Long-Term Temperature Impacts of the Hunga Volcanic Eruption in the Stratosphere and Above'. *Geophys. Res. Lett.*, 51. DOI: 10.1029/2024gl111500.

Rieger, L. A., W. J. Randel, A. E. Bourassa and S. Solomon (2021). 'Stratospheric temperature and ozone anomalies associated with the 2020 Australian New Year fires'. *Geophys. Res. Lett.*, 48, e2021GL095898. DOI: 10.1029/2021gl095898.

Schoeberl, M. R., Y. Wang, R. Ueyama, G. Taha and W. Yu (2023). 'The Cross Equatorial Transport of the Hunga Tonga-Hunga Ha'apai Eruption Plume'. *Geophys. Res. Lett.*, 50, e2022GL102443. DOI: 10.1029/2022gl102443.

Sellitto, P., A. Podglajen, R. Belhadji, M. Boichu, E. Carboni, J. Cuesta, C. Duchamp, C. Kloss, R. Siddans, N. Bègue et al. (2022). 'The unexpected radiative impact of the Hunga Tonga eruption of 15th January 2022'. *Commun. Earth Environ.*, 3, 288. DOI: 10.1038/s43247-022-00618-z.

Simmons, A., C. Soci, J. Nicolas, B. Bell, P. Berrisford, R. Dragani, J. Flemming, L. Haimberger, S. Healy, H. Hersbach et al. (2020). 'Global stratospheric temperature bias and other stratospheric aspects of ERA5 and ERA5.1'. *ECMWF Technical Memoranda*, DOI: 10.21957/rcxqfmg0.

SPARC (2022). *Reanalysis Intercomparison Project (S-RIP) Final Report*. Tech. rep. SPARC Report No. 10, WCRP-6/2021. https://www.aparc-climate.org/sparc-reports/sparc-report-no-10/. SPARC/WCRP.

Steiner, A. K., F. Ladstädter, W. J. Randel, A. C. Maycock, Q. Fu, C. Claud, H. Gleisner, L. Haimberger, S.-P. Ho and P. Keckhut (2020). 'Observed temperature changes in the troposphere and stratosphere from 1979 to 2018'. *J. Climate*, 33, pp. 8165–8194. DOI: 10.1175/jcli-d-19-0998.1.

Vömel, H., S. Evan and M. Tully (2022). 'Water vapor injection into the Stratosphere by Hunga Tonga-Hunga Ha'apai'. *Science*, 377, pp. 1444–1447. DOI: 10.1126/science.abq2299.

Wallace, J. M., R. L. Panetta and J. Estberg (1993). 'Representation of the Equatorial Stratospheric Quasi-Biennial Oscillation in EOF Phase Space'. *J. Atmos. Sci.*, 50, pp. 1751–1762. DOI: 10.1175/1520-0469(1993)050<1751:ROTESQ>2.0.CO;2.

Wang, X., W. Randel, Y. Zhu, S. Tilmes, J. Starr, W. Yu, R. Garcia, O. B. Toon, M. Park, D. Kinnison et al. (2023). 'Stratospheric Climate Anomalies and Ozone Loss Caused by the Hunga Tonga-Hunga Ha'apai Volcanic Eruption'. *J. Geophys. Res.*, 128, e2023JD039480. DOI: 10.1029/2023jd039480.

Wang, Y. and Y. Huang (2024). 'Compensating atmospheric adjustments reduce the volcanic forcing from Hunga stratospheric water vapor enhancement'. *Sci. Adv.*, 10, eadl2842. DOI: 10.1126/sciadv.adl2842.

Yook, S., S. Solomon and X. Wang (2025). 'The impact of 2022 Hunga Tonga-Hunga Ha'apai (Hunga) eruption on stratospheric circulation and climate'. *J. Geophys. Res.*, 130, e2024JD042943. DOI: 10.1029/2024JD042943.

Yu, W., R. Garcia, J. Yue, A. Smith, X. Wang, W. Randel, Z. Qiao, Y. Zhu, V. L. Harvey, S. Tilmes et al. (2023). 'Mesospheric temperature and circulation response to the Hunga Tonga-Hunga-Ha'apai volcanic eruption'. *J. Geophys. Res.*, 128, e2023JD039636. DOI: 10.1029/2023JD039636.

Yulaeva, E., J. R. Holton and J. M. Wallace (1994). 'On the cause of the annual cycle in tropical lower-stratospheric temperatures'. *J. Atmos. Sci.*, 51, pp. 169–174. DOI: 10.1175/1520-0469(1994)051<0169:otcota>2.0.co;2.

Zhou, X., S. S. Dhomse, W. Feng, G. Mann, S. Heddell, H. Pumphrey, B. J. Kerridge, B. Latter, R. Siddans, L. Ventress et al. (2024). 'Antarctic Vortex Dehydration in 2023 as a Substantial Removal Pathway for Hunga Tonga-Hunga Ha'apai Water Vapor'. *Geophys. Res. Lett.*, 51, e2023GL107630. DOI: 10.1029/2023gl107630.

Zhu, Y., C. G. Bardeen, S. Tilmes, M. J. Mills, X. Wang, V. L. Harvey, G. Taha, D. Kinnison, R. W. Portmann, P. Yu et al. (2022). 'Perturbations in stratospheric aerosol evolution due to the water-rich plume of the 2022 Hunga-Tonga eruption'. *Commun. Earth Environ.*, 3, 248. DOI: 10.1038/s43247-022-00580-w.

Zhuo, Z., X. Wang, Y. Zhu, W. Yu, E. M. Bednarz, E. Fleming, P. R. Colarco, S. Watanabe, D. Plummer, G. Stenchikov et al. (2025). 'Comparing multimodel ensemble simulations with observations and decadal projections of upper atmospheric variations following the Hunga eruption'. *Atmos. Chem. Phys.*, 25, pp. 13161–13176. DOI: 10.5194/acp-25-13161-2025.

5 Effects of the Hunga eruption on stratospheric ozone and related trace gases

Lead authors Freja F. Østerstrøm
Michelle L. Santee

Co-authors Martyn P. Chipperfield
Stéphanie Evan
Dan Smale
Krzysztof Wargan
David M. Wilmouth
Ingo Wohltmann

Contributing authors Ewa M. Bednarz
Sandip Dhomse
Eric L. Fleming
Stacey M. Frith
Gloria L. Manney
Luis F. Millán
Jun Zhang
Xin Zhou

Cite this as:

Østerstrøm, F. F., M. L. Santee et al. (2025): Effects of the Hunga eruption on stratospheric ozone and related trace gases. In APARC, 2025: The Hunga Eruption Atmospheric Impacts Report [Yunqian Zhu, Graham Mann, Paul A. Newman, William Randel (Eds.)]. APARC Report No. 11, WCRP Report No. 10/2025, DOI: 10.34734/FZJ-2025-05242, available at `https://aparc-climate.org/publications/aparc-report-no-11/`.

Key points

This chapter presents the current state of knowledge of the immediate and longer-term effects of Hunga on global stratospheric composition. The extraordinary water vapour enhancement from the eruption triggered both heterogeneous and gas-phase chlorine activation, leading to rapid ozone loss in the fresh plume within one week. Over subsequent months, further heterogeneous chemical processing led to widespread perturbations in stratospheric chlorine and nitrogen partitioning of unprecedented magnitude and duration in the southern tropics and midlatitudes. Record-low abundances of stratospheric ozone were also seen at some altitudes in some regions; however, the degree of ozone destruction due to altered chemistry was minor, with ozone at low and middle latitudes being largely controlled by transport. Overall, Hunga did not strongly perturb total column ozone. The Hunga hydration was effectively excluded from the winter polar vortices in the first post-eruption winters in both hemispheres. While comparatively high humidity inside the 2023 Antarctic vortex prompted unusually early and vertically extensive chlorine activation and intensified dehydration, by mid-winter those processes had essentially run to completion, as is typical in the Antarctic, preventing an exceptionally severe springtime ozone hole. The Arctic vortex in the 2023/2024 winter/spring was also unusually moist, but dynamically disturbed conditions were unfavourable for chlorine-catalysed ozone loss. The effects on stratospheric composition from Hunga will diminish over the next decade as the excess water vapour is removed from the stratosphere through Antarctic dehydration and stratosphere-to-troposphere exchange. The observed anomalous chemical processing following the eruption, on both short and longer-term timescales, resulted from well-known chemical reactions occurring on volcanic sulfate aerosol under conditions of highly enhanced stratospheric humidity unique in the observational record. No evidence of novel or previously unknown chemical mechanisms has been found.

Initial chemical processing and ozone loss in the fresh plume

- **The Hunga eruption triggered significant rapid ozone loss in the stratosphere over the tropical southwestern Pacific and Indian Ocean region, with ozone decreasing by 5% in less than two weeks.** The ozone loss was driven by the Hunga excess water vapour intensifying HO_x and ClO_x catalytic cycles, as well as heterogeneous chemistry on humidified volcanic aerosols; these mechanisms differ from those responsible for polar ozone loss. Although the eruption produced an unprecedented number of lightning flashes, lightning-generated NO_x was not a significant contributor to the initial in-plume ozone depletion. The extent to which similarly rapid ozone depletion may have occurred after previous major eruptions, such as El Chichón and Mount Pinatubo, is difficult to assess because comparable satellite and rapid-response observations were not available for those events. This highlights not only the exceptional nature of the Hunga eruption, but also the need for early-response campaigns and satellite instruments capable of monitoring stratospheric composition after major volcanic eruptions.

Longer-term impacts on stratospheric composition

Midlatitudes

- **Widespread changes in stratospheric composition of magnitude and duration unprecedented in the satellite record were observed at Southern Hemisphere (SH) midlatitudes in the months following the eruption.** In particular, perturbations in H_2O, HNO_3, HCl, ClO, and O_3 were seen.
- **The observed perturbations in trace gas distributions in the SH midlatitudes were brought about by altered chemistry and, more importantly in most cases, by altered transport.** The main heterogeneous reaction driving chemical changes was N_2O_5 hydrolysis, in contrast to the heterogeneous chlorine activation reactions that lead to lower stratospheric polar ozone destruction. Ozone-loss cycles involving HO_x and ClO_x were enhanced, while NO_x-driven ozone loss slowed. However, although heterogeneous chemistry also played a role, as evidenced by correlations with the transport tracer N_2O as well as atmospheric modelling, changes in stratospheric circulation (possibly linked to Hunga) were primarily responsible for the observed anomalies in HCl, HNO_3, and O_3.

Tropics

- **Satellite observations reveal substantial post-eruption perturbations in the composition of the tropical stratosphere. Model simulations show that these perturbations arise from heterogeneous chemical processing on volcanic sulfate aerosol.** Impacts are seen in the tropics several months before they become evident at midlatitudes, consistent with the evolution of the Hunga water vapour and aerosol. N_2O_5 hydrolysis is identified as the main mechanism driving chlorine and nitrogen repartitioning.
- **Although the ClO enhancements observed in the tropics in 2022 were exceptional for that latitude band, they were still more than an order of magnitude weaker than those seen during a typical polar winter/spring in either hemisphere.** The evolution of ozone abundances in the tropical stratosphere in 2022, while affected by anomalous chemistry to some degree, was dominated by transport. The extent to which transport anomalies in the tropics were causally connected to the eruption is not clear.

Antarctic winters/springs of 2022, 2023, and 2024

- **The Hunga water vapour was effectively excluded from the 2022 Antarctic polar vortex by the strong transport barrier at the vortex edge, and consequently the heterogeneous chemical processing and ozone loss that took place within it were near average.** After the vortex broke down in November–December 2022, enhanced stratospheric water vapour and aerosols pervaded the southern high latitudes.
- **Although Hunga enhanced polar stratospheric cloud (PSC) formation and chlorine activation early in the 2023 season, by July/August lower stratospheric abundances of HCl, ClO, HNO_3, and H_2O had returned to their respective climatological mean values. Thus chlorine activation, denitrification, and dehydration processes had saturated by mid-winter, as is typical in the Antarctic, preventing an exceptionally severe ozone hole in 2023.** The extraordinary moisture from Hunga prompted unusually early and vertically extensive PSCs, and dehydration subsequently removed ~50% more water vapour than typical. Heterogeneous chlorine activation also occurred weeks earlier and at higher altitudes than previously observed, but the early-winter upper-level activation was too weak to cause substantial ozone loss. For the most part, observational and modelling studies found only a minor effect on the 2023 Antarctic ozone hole, with the additional Hunga-induced ozone loss (which largely occurred in the region along the vortex edge where chlorine is typically not fully activated) being within the observed year-to-year variability.
- **As a result of unusually strong planetary wave activity, the Antarctic vortex was relatively warm through much of the 2024 season; although conditions inside the vortex were again moister than usual, lower stratospheric chemical processing mostly followed typical patterns, and ozone abundances were near or slightly above average.**

Arctic winters/springs of 2021/2022, 2022/2023, and 2023/2024

- **Hunga hydration has so far had minimal impact on chemical processing and ozone loss in the Arctic winter polar vortex.** The Hunga water vapour had not yet reached the northern polar latitudes by boreal spring 2022, while in spring 2023 it was not able to penetrate the Arctic vortex. Although extraordinarily high water vapour abundances were present inside the 2023/2024 Arctic vortex, comparatively warm and dynamically disturbed conditions during that winter/spring were unfavourable for substantial chemical ozone loss.

Predictions of the future impacts on the stratospheric ozone layer

- **Observations and model simulations indicate that the Hunga hydration will persist through the end of this decade.** MLS measurements and model simulations identify dehydration through sedimentation of ice PSCs in Antarctic winter as the primary removal pathway for the excess Hunga water vapour at work initially. Stratosphere-to-troposphere transport (STT) at middle and high latitudes as part of the meridional Brewer–Dobson circulation began to play a major role after the Hunga-hydrated

air parcels had descended to sufficiently low altitudes in late 2023. Once removal processes commenced, the e-folding decay time estimated from both measurements and models is 2.5–4 years, leading to a lifetime (i.e., mean stratospheric residence time) of 4–5.5 years.

- **Minor effects on ozone, in most cases indistinguishable against the backdrop of interannual variability, can be expected to continue until the excess Hunga water vapour has been removed from the stratosphere.** Model studies indicate that the largest Hunga impacts on column ozone occur in the polar regions, in particular the Antarctic.

Contents

5.1 Overview of Hunga effects on total column ozone . . . 112
5.2 Initial chemical processing and ozone loss in the fresh plume . . . 112
5.3 Longer-term impacts on stratospheric composition . . . 116
5.3.1 Midlatitudes . . . 116
5.3.2 Tropics . . . 121
5.3.3 Antarctic winters/springs of 2022, 2023, and 2024 . . . 124
5.3.4 Arctic winters/springs of 2021/2022, 2022/2023, and 2023/2024 . . . 131
5.4 Predictions of the future impacts on the stratospheric ozone layer . . . 132
5.4.1 Future evolution of stratospheric water vapour . . . 132
5.4.2 Future Hunga-related changes in stratospheric composition . . . 133

Preamble

Chapter 5 presents and assesses the current understanding of the immediate and longer-term impacts on stratospheric composition of the eruption of the Hunga volcano (see Chapter 1 for details of the eruption). Observational and modelling studies that have examined the effects of Hunga on composition at low, middle, and high latitudes throughout the stratosphere are concisely summarised. The chapter also describes projections of the Hunga water vapour evolution and how its effects on stratospheric composition are expected to diminish over the next decade.

Observations of stratospheric chemical composition, aerosol, and clouds reported here come mainly from satellite-borne sensors: the Aura Microwave Limb Sounder (MLS), the SCISAT Atmospheric Chemistry Experiment-Fourier Transform Spectrometer (ACE-FTS), the Suomi-NPP Ozone Mapping and Profiler Suite Limb Profiler (OMPS-LP) and Nadir Profiler (OMPS-NP), the Solar Backscatter Ultraviolet (SBUV, SBUV/2) series of instruments, and the Cloud-Aerosol Lidar and Infrared Pathfinder Satellite Observations (CALIPSO) Cloud-Aerosol Lidar with Orthogonal Polarization (CALIOP). High-resolution profiles of ozone and water vapour from balloon-borne sondes are also used. An overview of observational platforms that sampled the compositional changes following the Hunga eruption, including descriptions of observational techniques, data coverage, and measurement quality, can be found in Supplementary S2 of this report.

Intermodel and model-to-measurement comparisons of the impact of the Hunga eruption are being undertaken as part of the Hunga Tonga–Hunga Ha'apai Model Observations Comparison (HTHH-MOC) and Hunga Tonga–Hunga Ha'apai Volcano Model Intercomparison Project (Tonga-MIP). The specifics of the model experiment protocol and descriptions of the different chemical transport models (CTMs) and chemistry–climate models (CCMs) participating in these efforts are given in Supplementary S1 for HTHH-MOC and Supplementary S5 for Tonga-MIP. In addition to those included here, other HTHH-MOC results relevant to the chapter are shown in Supplementary S3. Chapter 5 also discusses simulations from models that are not part of those intercomparisons; descriptions of these models are provided in Supplementary S4.

5.1 Overview of Hunga effects on total column ozone

To set the stage for subsequent discussion, Figure 5.1 shows the long-term (1979–2025) record of anomalies (i.e., deviations from climatological values) in total column ozone. While a substantial reduction in total column ozone is seen in much of the Southern Hemisphere (SH) in 2022, negative (and positive) anomalies of comparable or greater magnitude have occurred throughout the observational record, and the post-Hunga changes do not stand out in the context of the considerable interannual variability in total column ozone. Hunga-induced anomalies in ozone and related trace gases are more striking at some altitudes in some regions, as discussed in detail in the following sections.

5.2 Initial chemical processing and ozone loss in the fresh plume

The eruption of the Hunga volcano on 15 January 2022 offered a unique opportunity to investigate the early impacts of a tropical eruption on stratospheric composition. A balloon campaign was set up within a week at the Maïdo Observatory, Réunion Island (21°S, 55°E). From 20 to 24 January 2022, meteorological balloons carrying aerosol, water vapour (H_2O), sulfur dioxide (SO_2), and ozone (O_3) instruments measured the plume's composition. These and other observations revealed the unprecedented stratospheric injection of water vapour (see Chapter 2). This rapid-response campaign provided a rare dataset for studying early chemical processes in a fresh volcanic plume.

Significant stratospheric composition changes following the Hunga eruption were reported based on a combination of satellite data from Aura MLS and balloon-borne as well as ground-based measurements (Evan et al., 2023). The night of 22 January 2022, when the Cryogenic Frostpoint Hygrometer instrument at Maïdo Observatory recorded the highest post-eruption stratospheric water vapour mixing ratio (350 ppmv at 26.5 km), also corresponded to the largest ozone decreases observed in the balloon profiles (10–45%, relative to the 1998–2021 climatology; Figure 5.2a). This specific case helped define the H_2O threshold of 100 ppmv used to extract MLS anomalies of O_3, HCl, and ClO shown in Figure 5.2b, ensuring that these anomalies represent Hunga plume conditions. Balloon-borne and MLS observations near 20°S indicated an average ozone anomaly of −0.5 ppmv and −0.4 ppmv, respectively, within the altitude range 25–29 km (corresponding to approximately 14–25 hPa

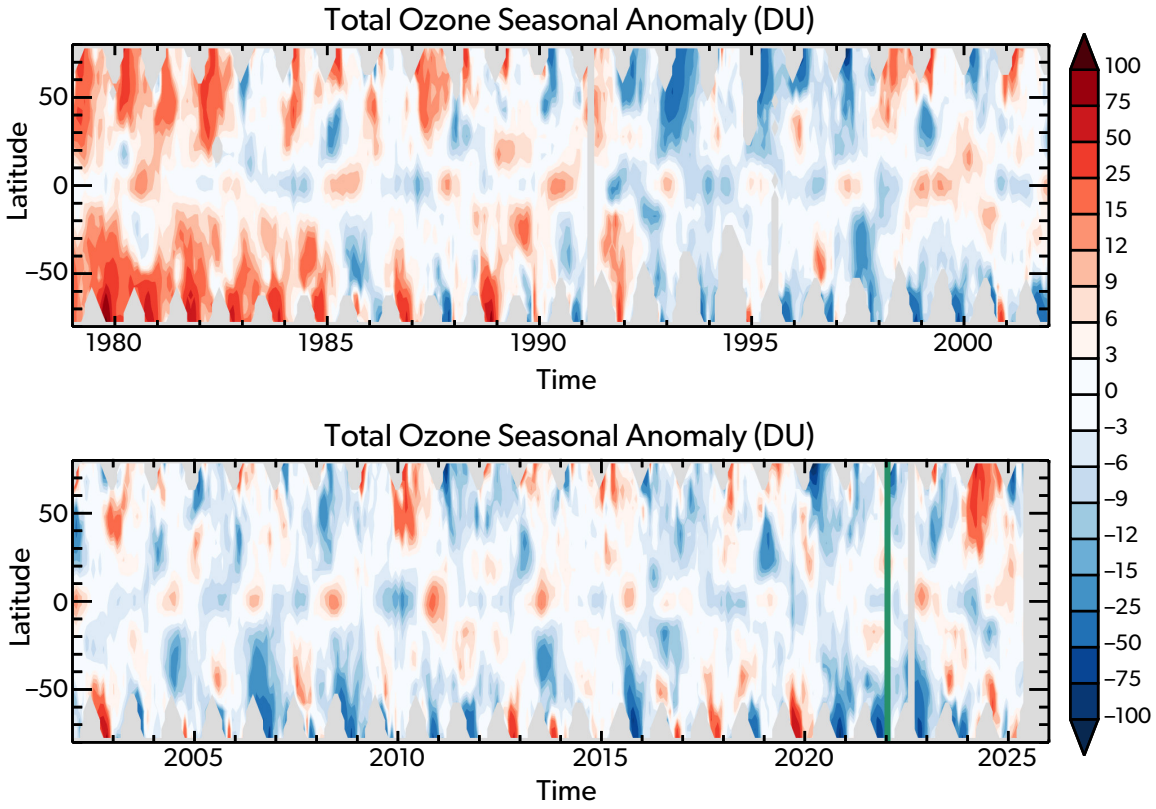

Figure 5.1: *Total column ozone seasonal anomalies (in Dobson Units, DU), plotted as a function of time (1979 to mid-2025) and latitude (80°S to 80°N). Total ozone anomalies were computed from the version 8.7 SBUV Merged Ozone Data (SBUV MOD) record (Frith et al., 2014; Frith et al., 2017; Godin-Beekmann et al., 2022). SBUV MOD is a combined record of total and profile ozone measurements from the SBUV, SBUV/2, and OMPS-NP instrument series. Seasonal anomalies were computed by subtracting the 1979–2025 seasonal climatology. Grey shading marks regions of missing data, and the vertical green line marks the date of the Hunga eruption.*

or 620–770 K) over the period 16–24 January (Figure 5.2b). The 0.4 ppmv decrease in ozone observed over 25–29 km exceeds ±1 standard deviation of the MLS ozone climatology, indicating that it lies outside the typical range of variability (not shown). This decline corresponds to an approximate 5% reduction in ozone at these altitudes. Additionally, MLS observations indicated a 0.25 ppbv decrease in hydrochloric acid (HCl, the main reservoir for chlorine in the stratosphere), corresponding to an approximate 20% reduction over the same altitude range (Figure 5.2b). In parallel, chlorine monoxide (ClO, the primary form of ozone-destroying reactive chlorine) increased by 0.37 ppbv (Figure 5.2b).

Heterogeneous chlorine activation on humidified volcanic aerosols was found to play a major role in facilitating the observed rapid ozone depletion (Evan et al., 2023). These processes were further explored using 3-D CCM simulations from the Whole Atmosphere Community Climate Model version 6 (WACCM6) to distinguish the chemical and dynamical drivers of the initial in-plume ozone reduction (Zhu et al., 2023). The model simulations tested various injection scenarios involving H_2O, SO_2, HCl, and ClO to assess their respective impacts on ozone depletion. There is no observational evidence for a direct injection of ClO into the stratosphere by the Hunga eruption, and although MLS did measure elevated HCl abundances in a handful of profiles immediately following the eruption (Millán et al., 2022; Santee et al., 2023), the relatively modest HCl injection from Hunga is unlikely to have had a major impact on available chlorine in the plume. Nevertheless, both of these scenarios were tested in the model to investigate the effects of the presence of additional reactive chlorine, and the ClO injection case yielded results equivalent to those obtained when injecting HCl.

The simulations highlighted the key role of the H_2O injection in amplifying chlorine activation and ozone depletion through enhanced heterogeneous and gas-phase chemical processes. Figure 5.2c shows that the average simulated ozone anomaly is −0.22 ppmv at

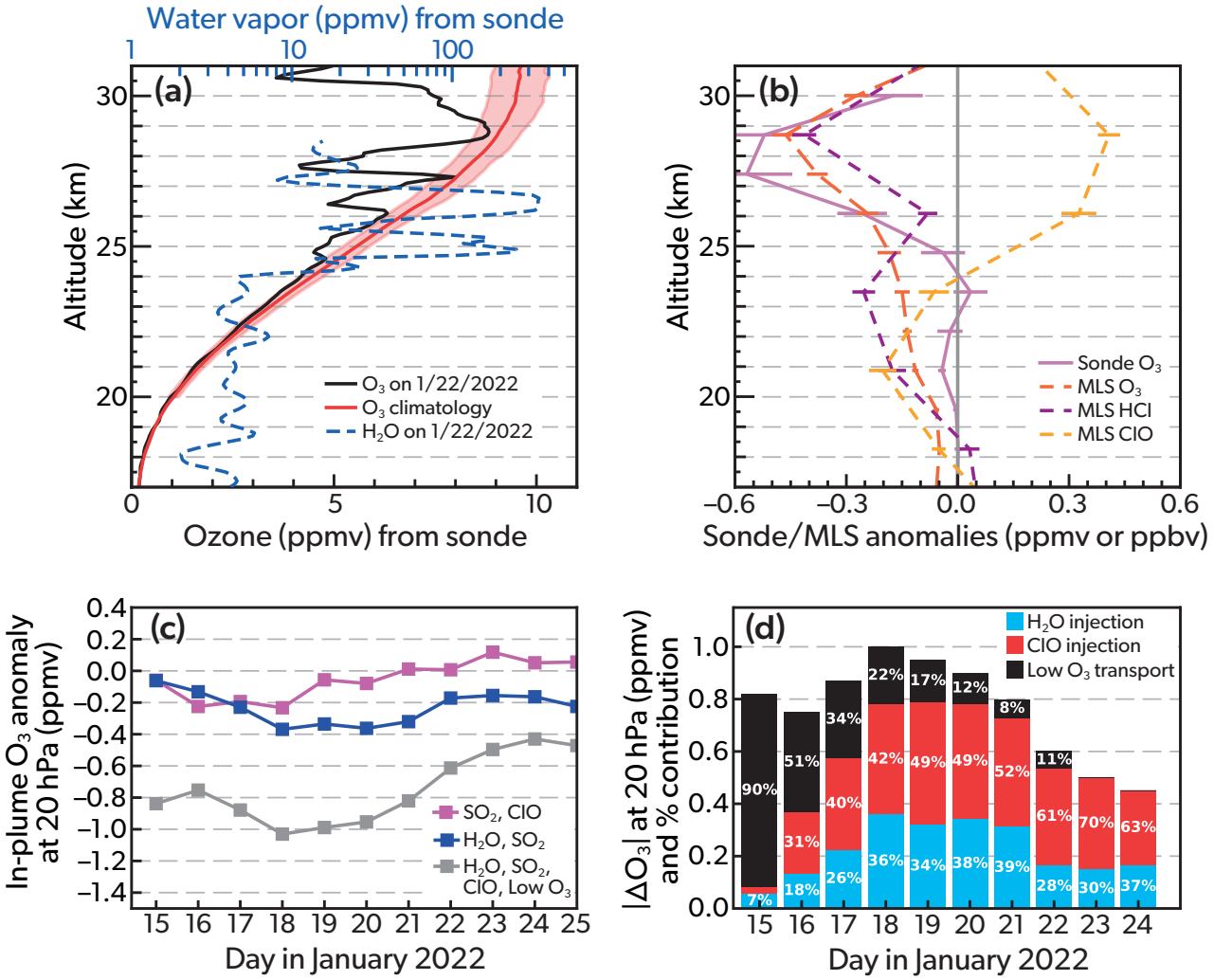

Figure 5.2: *(a) Ozone and water vapour soundings at Maïdo Observatory on 22 January 2022, the night of the highest water vapour mixing ratio recorded by the Cryogenic Frostpoint Hygrometer (dashed blue line). The solid black line shows the ozone mixing ratio measured at Maïdo on 22 January, exhibiting multiple ozone loss layers compared to the Réunion climatology (1998–2021, solid red line). Red shading indicates ±1 standard deviation of the Réunion climatology. (b) Ozonesonde-derived mean anomalies for O_3 (solid magenta line), as well as MLS-derived mean anomalies for O_3 (dashed red line), HCl (dashed purple line), and ClO (dashed orange line), averaged over 16–24 January. MLS anomaly profiles were computed using an H_2O threshold of 100 ppmv to ensure that they represent Hunga plume conditions. Error bars on each anomaly profile represent the standard error of the mean anomaly. (c) Daily average simulated in-plume ozone anomaly at 20 hPa from WACCM6 model runs. Different model scenarios are represented: H_2O and SO_2 co-injection (blue); SO_2 and ClO co-injection (magenta); and H_2O, SO_2, and ClO co-injection with transport of ozone-poor air from the troposphere (grey). (d) Percentage contributions to the absolute values of daily mean ozone anomaly ($|\Delta O_3|$) at 20 hPa in WACCM6 simulations from H_2O injection (blue), ClO injection (red), and low-O_3 air transported from the troposphere (black). Contributions were estimated by incrementally adding each process: the H_2O contribution reflects the ozone loss from comparing the H_2O/SO_2 injection scenario to the no-volcano baseline; the ClO contribution compares the H_2O/SO_2/ClO scenario to the H_2O/SO_2 case; and the low-O_3 contribution compares the H_2O/SO_2/ClO/LowO_3 scenario to the H_2O/SO_2/ClO scenario (Zhu et al., 2023). While no observational evidence exists for direct ClO injection by the Hunga eruption, this scenario was tested in the model and produced results equivalent to those obtained assuming HCl injection. Thus, results for the "ClO injection" scenario are shown in (c) and (d). Data from Evan et al. (2023).*

20 hPa (~27 km) over 15–25 January for the "H_2O, SO_2" scenario, reflecting ozone depletion driven by Hunga H_2O-enhanced activation of background chlorine (either via gas-phase chemical processes or via heterogeneous chemistry subsequent to the formation of sulfate aerosols). This is smaller than the observed anomalies of −0.5 ppmv and −0.4 ppmv measured by ozonesondes and MLS, respectively, within the 25–29 km altitude range (Figure 5.2b). Notably, in the "SO_2, ClO" scenario, in which no H_2O is injected, the average simulated ozone anomaly is only −0.05 ppmv, indicating that ClO alone, without the presence of enhanced water vapour, results in minimal ozone depletion.

In the "H_2O, SO_2, ClO, low-O_3" scenario, the simulated ozone anomalies deepen to −0.75 ppmv over the same period, with two additional processes contributing to this enhanced depletion. During the first few days (15–16 January), the injection of ozone-poor air from the troposphere dominates, accounting for more than 50% of the ozone loss at 20 hPa (Figure 5.2d). However, this contribution declines rapidly and becomes minor (<10%) by 21 January. After this date, the enhanced ozone loss is primarily driven by elevated ClO levels, introduced in the model as a sensitivity test to isolate the effect of additional reactive chlorine, analogous to what might result if HCl were injected and subsequently activated, as discussed by Zhu et al. (2023).

The somewhat larger simulated ozone anomalies in the WACCM6 "H_2O, SO_2, ClO, low-O_3" scenario, particularly during the early simulation period (15–21 January; Figure 5.2c), likely stem from challenges in representing the initial dispersion of the highly humidified plume with WACCM6's relatively coarse vertical and horizontal resolution, as well as uncertainties in modelling rapid chlorine activation processes and the transport and mixing of ozone-poor air from the troposphere. However, when considering the mean simulated ozone decrease for the later period (22–25 January), when the transport and mixing of low-O_3 air from the troposphere had stabilised, the simulated average ozone decrease for the "H_2O, SO_2, ClO, low-O_3" scenario is −0.5 ppmv (Figure 5.2c). This value agrees well with the mean O_3 anomaly derived from measurements in Figure 5.2b.

The massive injection of water vapour led to a substantial rise in hydroxyl radical (OH) production rates (Zhu et al., 2022; Zhu et al., 2023; Fleming et al., 2024). Elevated OH abundances played a critical role in accelerating ozone depletion by participating in catalytic cycles that convert ozone into molecular oxygen (O_2). The increased H_2O levels enhanced the hydrogen oxide (HO_x = OH + HO_2) catalytic cycles, which consist of OH and hydroperoxyl (HO_2) radicals in various reactions with ozone and oxygen atoms. Specifically, the rates of key reactions increased by a factor of four. This heightened activity of OH and HO_2 radicals not only contributed to the rapid ozone loss observed, but also facilitated interactions with chlorine compounds, further driving the depletion of ozone through HO_x–chlorine oxide (ClO_x = Cl + ClO + 2 × ClOOCl) cycles. These chemical processes were largely confined within the layer around ~20 hPa, where the highest H_2O mixing ratios were observed. At this altitude, the extreme water vapour injection significantly enhanced chlorine activation, amplifying catalytic ozone loss (Zhu et al., 2023). Overall, the model results (Figures 5.2c–5.2d) indicated that the primary drivers of the observed reduction in ozone were threefold: increased H_2O injection enhanced the HO_x catalytic cycle and its interaction with the ClO_x catalytic cycle; enhanced ClO abundances, which arose through both heterogeneous and gas-phase reactions, induced ozone loss; and the rising volcanic plume introduced ozone-poor tropospheric air into the stratosphere.

Additionally, a large enhancement in HOCl and its photolysis rate within the plume were found to play a critical role in gas-phase chlorine repartitioning (Zhu et al., 2023). Moreover, the rate of the heterogeneous reaction (see Reaction R5.1 in Box 5.1) between HOCl and HCl, forming molecular chlorine (Cl_2) and H_2O, increased by 10 orders of magnitude, making it a major driver of chlorine activation. This distinguishes the chlorine activation mechanism in the fresh Hunga plume from that in the winter polar lower stratospheric vortices, where Reaction R5.2 between HCl and chlorine nitrate ($ClONO_2$) plays a dominant role.

The Hunga eruption also generated significant lightning activity (e.g., Van Eaton et al., 2023), leading to potential production of nitrogen oxides (NO_x = NO + NO_2). Thus, the impact of lightning-generated NO_x within the Hunga volcanic plume was also explored (Zhu et al., 2023). The simulations, which included an injection of 0.003 Tg of nitrogen monoxide (NO), inferred from the number of lightning flashes detected after the eruption, indicated that the additional NO_x had little effect on ozone loss in the first 10 days after the eruption. This is likely because the high water vapour content in the plume rapidly converted NO to nitric acid (HNO_3), limiting its influence

on ozone depletion. Satellite observations from MLS did not indicate a significant enhancement of HNO_3 in the initial volcanic plume in January 2022 (Millán et al., 2022; Santee et al., 2023). The measured HNO_3 remained within the range of typical variability, suggesting that the total NO production was insufficient to cause a noticeable increase in HNO_3. Therefore, lightning-generated NO_x was not considered a significant contributor to the initial in-plume ozone depletion observed immediately following the Hunga eruption.

In summary, the rapid (within one week) ozone loss observed in the Hunga plume resulted from well-known chemical reactions occurring under the highly unusual atmospheric conditions triggered by the eruption. While sulfate aerosols typically promote heterogeneous chemistry after major eruptions, in this case, the exceptional water vapour injection (which far exceeded typical variability) played a critical role in enhancing chlorine activation and ozone loss.

The ~5% ozone loss in the Hunga plume immediately following the eruption appears to stand out in the observational record of stratospheric ozone changes after major volcanic eruptions, such as El Chichón in 1982 and Mount Pinatubo in 1991. However, no comparable rapid-response campaigns were conducted after those eruptions, nor were they initially observed with satellite instruments capable of providing detailed stratospheric composition measurements like MLS. As a result, it is difficult to determine whether similarly rapid tropical ozone depletion occurred immediately following previous major eruptions but went unobserved due to limited measurements. This highlights both the exceptional nature of the Hunga eruption and the importance of rapid-response observations for fully capturing the immediate atmospheric impacts of major volcanic eruptions.

Box 5.1. Heterogeneous reactions important to stratospheric ozone

Heterogeneous reactions involve interactions between gas-phase molecules and aerosols in the stratosphere and play an important role in stratospheric ozone chemistry. Aerosols can have many different compositions, but the most common form is an aqueous suspension of sulfuric acid (Junge et al., 1961). At the extremely low temperatures typical of the stratospheric polar regions in wintertime, polar stratospheric clouds (PSCs) can form. PSCs vary in composition but most commonly consist of hydrated droplets of nitric acid and sulfuric acid (Tritscher et al., 2021). PSCs provide surfaces for heterogeneous reactions to take place that drive large seasonal ozone losses in the polar regions in both hemispheres in winter and spring. Important heterogeneous reactions on aerosol surfaces relevant to ozone in the stratosphere include (e.g., Solomon, 1999 and references therein):

$$HCl + HOCl \rightarrow Cl_2 + H_2O \quad \text{(R5.1)}$$
$$HCl + ClONO_2 \rightarrow Cl_2 + HNO_3 \quad \text{(R5.2)}$$
$$ClONO_2 + H_2O \rightarrow HOCl + HNO_3 \quad \text{(R5.3)}$$
$$N_2O_5 + H_2O \rightarrow 2 \times HNO_3 \quad \text{(R5.4)}$$
$$BrONO_2 + H_2O \rightarrow HOBr + HNO_3 \quad \text{(R5.5)}$$
$$HOBr + HCl \rightarrow BrCl + H_2O \quad \text{(R5.6)}$$

These reactions serve to both (1) shift chlorine and bromine from reservoir forms to more active forms that can be readily photolyzed to release Cl and Br and thus destroy ozone, and (2) shift nitrogen into the longer-lived reservoir form of HNO_3. The heterogeneous reaction rates involving chlorine (all but R5.4 and R5.5) are extremely temperature dependent. All of the reactions listed become enhanced (although not necessarily to the point of stratospheric significance) when sulfate surface area density is elevated, such as following a volcanic eruption.

5.3 Longer-term impacts on stratospheric composition

5.3.1 Midlatitudes

Following the initial early impacts of the Hunga eruption (Section 5.2), significant and prolonged changes in stratospheric composition were observed at SH midlatitudes (Santee et al., 2023; Wilmouth et al., 2023). MLS measurements taken in 2022 show anomalies of unprecedented magnitude and duration in H_2O, ClO, HNO_3, HCl, and O_3 relative to previous years in the data record, which began in 2004. Other instruments similarly observed substantial perturbations to stratospheric composition at SH midlatitudes. These changes were caused by both altered transport and altered chemistry following the stratospheric injection of H_2O and SO_2 (Santee et al., 2023; Wilmouth et al., 2023; Zhang et al., 2024a; Bednarz et al., 2025).

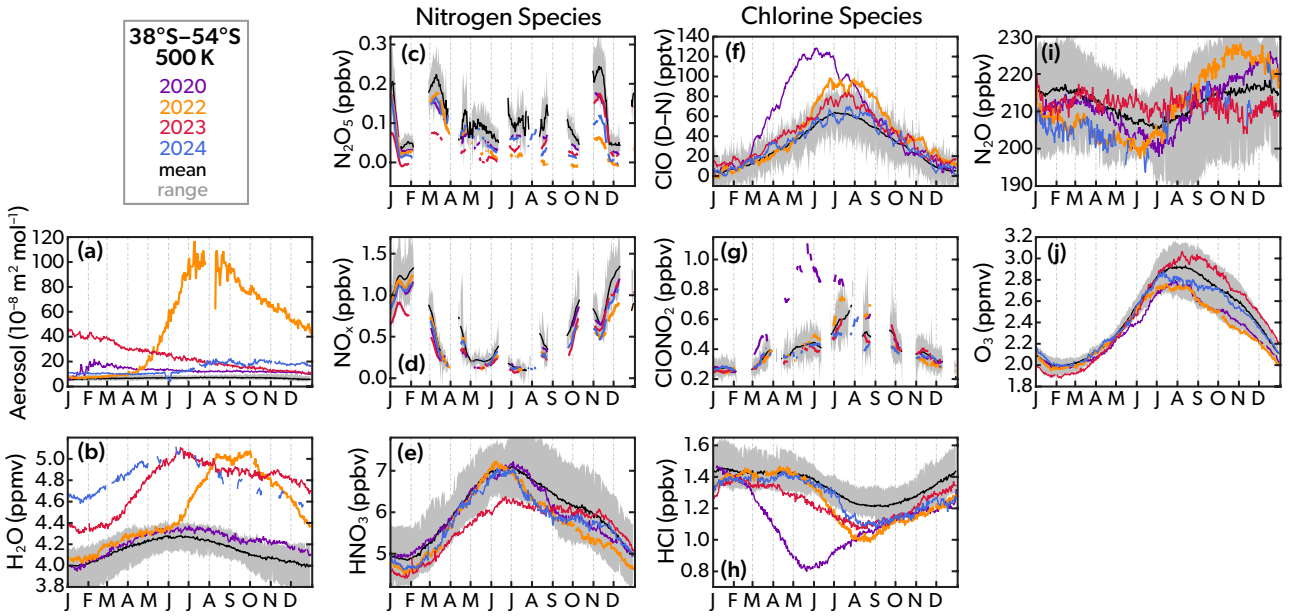

Figure 5.3: *Satellite observations averaged over 38°S–54°S EqL (SH midlatitudes) at 500 K (~47–57 hPa, ~20 km) of (a) OMPS-LP aerosol cross section at 869 nm, (b) MLS H_2O, (c) ACE-FTS N_2O_5, (d) ACE-FTS NO_x ($NO+NO_2$), (e) MLS HNO_3, (f) MLS ClO (day minus night), (g) ACE-FTS $ClONO_2$, (h) MLS HCl, (i) MLS N_2O, and (j) MLS O_3. Individual years are highlighted as indicated in the legend: 2020 in purple, 2022 in orange, 2023 in red, and 2024 in blue. Grey shading depicts the range of values observed by MLS (2005–2024), ACE-FTS (2005–2024), and OMPS-LP (2012–2024), excluding the highlighted years; black lines represent the mean of the grey-shaded data. To facilitate interpolation to isentropic surfaces, the aerosol data are converted from extinction coefficient (in units of km^{-1}) to extinction cross section per mole of air (in units of m^2 mol^{-1}), a quantity conserved under changes of atmospheric pressure in the absence of aerosol formation or loss (Santee et al., 2023). There are gaps in the 2024 MLS H_2O and N_2O data because it became necessary to duty cycle the MLS subsystem used to measure these species; thus, starting in May 2024, H_2O and N_2O measurements are available only for approximately week-long intervals in the middle of each month. ClO is shown as the day-minus-night difference to mitigate measurement bias at the lowest retrieval levels; the highlighted years and mean for ClO (but not the envelope) have been smoothed using a boxcar of width 10 days. ACE-FTS fields were also smoothed with a 10-day boxcar average. Adapted from Santee et al. (2023).*

Satellite observations for aerosol and a number of chemical constituents following the eruption, along with previous years of data for climatological context, are shown in Figure 5.3. Data have been averaged over a range of SH midlatitudes, 38°S–54°S equivalent latitude (EqL, a Lagrangian coordinate calculated from potential vorticity), and are shown at 500 K potential temperature (~47–57 hPa, ~20 km). Although in this EqL band the peak in the Hunga water vapour occurred around 600 K (where the maximum anomaly reached ~3.5 ppmv, as opposed to ~1 ppmv at 500 K), results are presented at 500 K because ClO enhancements were largest there (Santee et al., 2023). Showing this surface also facilitates comparison with the stratospheric impact of the Australian New Year's (ANY) fires in late 2019/early 2020. Focusing on 2022, aerosol from the Hunga eruption began arriving in the 38°S–54°S EqL region in mid-April (Figure 5.3a), with water vapour slightly delayed, arriving in mid-June (Figure 5.3b); both then quickly and dramatically exceeded the envelope of data in all previous years. A faster aerosol sedimentation rate relative to the rate of water vapour descent in the stratospheric circulation likely explains the time difference in the onset of the enhancements (Santee et al., 2023).

Like the aerosol and water vapour, mixing ratios of the nitrogen species were fairly typical for the first few months of 2022 in this EqL range, with dinitrogen pentoxide (N_2O_5, a nighttime reservoir species for NO_x), NO_x, and HNO_3 plotted in Figures 5.3c, 5.3d, and 5.3e, respectively. However, by early June, values of N_2O_5 fell well below any previous measurements in this region by ACE-FTS. NO_x was also below average, setting new lower limits in October, November, and December. HNO_3 had a small positive anomaly in early June, with somewhat larger enhancements at higher altitudes, but the values rapidly decreased from July onward, redefining the bottom of the MLS mission envelope at some levels (Santee et al., 2023, their Figure 3). The inorganic chlorine species also

showed significant perturbations due to the Hunga eruption. ClO increased rapidly beginning in early May (Figure 5.3f) at 500 K, coincident with increasing aerosol but before water vapour increased, and maintained elevated values well above the climatological range for a period of months, with peak positive anomalies in early August approaching 40 pptv. $ClONO_2$ exhibited elevated values during the intervals of ACE-FTS sampling from June to August (Figure 5.3g), coincident with the observations of enhanced ClO. Values of HCl were typical from mid-February to mid-May but dropped sharply thereafter (Figure 5.3h), falling outside the envelope of previous years for a period of months and reaching a minimum in August. N_2O did not depart from the range of previously observed variability (Figure 5.3i) but was lower than normal in the first half of the year and higher than typical in the second half. Mixing ratios of O_3 at 500 K (Figure 5.3j) were below average in 2022, similar to the behaviour in 2020 following the ANY fires, and were among the lowest values recorded by MLS in the final few months of 2022.

Based on Figure 5.3, it is clear that 2022 was an exceptional year for midlatitude stratospheric composition due to the Hunga eruption; in the 38°S–54°S EqL band, only the perturbations to chlorine species following the ANY fires in 2020 (when ClO attained peak positive anomalies of ~80 pptv) significantly separate from the climatological range prior to the eruption. Also shown in Figure 5.3 are measurements for the subsequent years 2023 and 2024. In most cases, observed compositional anomalies remain outside the background range of previous years for at least part of 2023, with 2024 values generally falling within the background envelope. The most notable exception is water vapour, which remains far higher than normal three years after the eruption.

In many cases, the peak compositional anomalies caused by the Hunga eruption occurred higher in the stratosphere and were larger in magnitude than those at 500 K (e.g., Santee et al., 2023). Figure 5.4 highlights the most significant anomalies in O_3, ClO (shown as day and night average), HCl, and HNO_3 induced by Hunga between 60°S and 60°N latitudes in 2022. To determine these values, zonal-mean, monthly average vertical profiles for each variable were calculated over 15° latitude bins using MLS data, with anomalies over the pressure range 5–60 hPa in 2022 determined relative to the previous 17 years of MLS measurements (2005–2021). Significant, widespread, and prolonged anomalies were evident in the MLS record in 2022 throughout the SH midlatitudes and tropics, and to a lesser extent, in the Northern Hemisphere (NH) tropics (Figure 5.4). Hunga had little to no significant impact on the NH midlatitudes. The dominant features in the SH are losses in O_3 and HCl, increases in ClO, and both increases and decreases in HNO_3. Focusing on the SH midlatitudes, the initial appearance of anomalies in all four species was delayed relative to that in the tropics, with the first points appearing in April or May for 30°S–45°S and July for 45°S–60°S. While the largest positive anomalies in ClO and HNO_3 were observed at tropical latitudes throughout 2022, the largest negative anomalies in O_3 and HCl were observed at SH midlatitudes in the second half of the year. Peak anomalies in O_3 and HCl were −14% and −22%, respectively, relative to the previous 17-year MLS mean for the respective month and 15° latitude bin (Wilmouth et al., 2023). For HNO_3, the shift from positive to negative anomalies going from the SH tropics to the midlatitudes occurred because a higher-altitude (pressures <20 hPa) increase was replaced as the dominant feature in the vertical profile by a lower-altitude HNO_3 loss. Indeed, there was a large vertical region of HNO_3 loss, typically peaking at 31.6 hPa, from 15°S to 60°S for July to December, but it did not always satisfy the selection criteria (see the Figure 5.4 caption). Finally, considering stratospheric column ozone, record-low negative anomalies were observed at SH midlatitudes in austral spring (Wilmouth et al., 2023; Weber et al., 2024). With values calculated as monthly averages in 15° latitude bins for the 1.2–100 hPa region, the largest observed monthly anomalies in stratospheric column ozone were approximately −7% for 45°S–60°S in October and −5% for 30°S–45°S in September (Wilmouth et al., 2023).

Examination of the peak perturbations (most of which were between 20 and 40 hPa) as shown in Figure 5.4 provides a compelling picture of the substantial and persistent anomalies the Hunga eruption induced. Taken together, Figures 5.3 and 5.4 provide unmistakable evidence that changes in stratospheric composition of unprecedented magnitude and duration occurred in the SH midlatitudes following the Hunga eruption. To further elucidate the vertical structure of these changes, Figure 5.5 shows compositional anomalies in 2022 as a function of pressure for selected points in Figure 5.4. The exact MLS pressure levels of the peak perturbations in Figure 5.5 vary with latitude, month, and the species being considered, but it is apparent that there were unprecedented enhancements

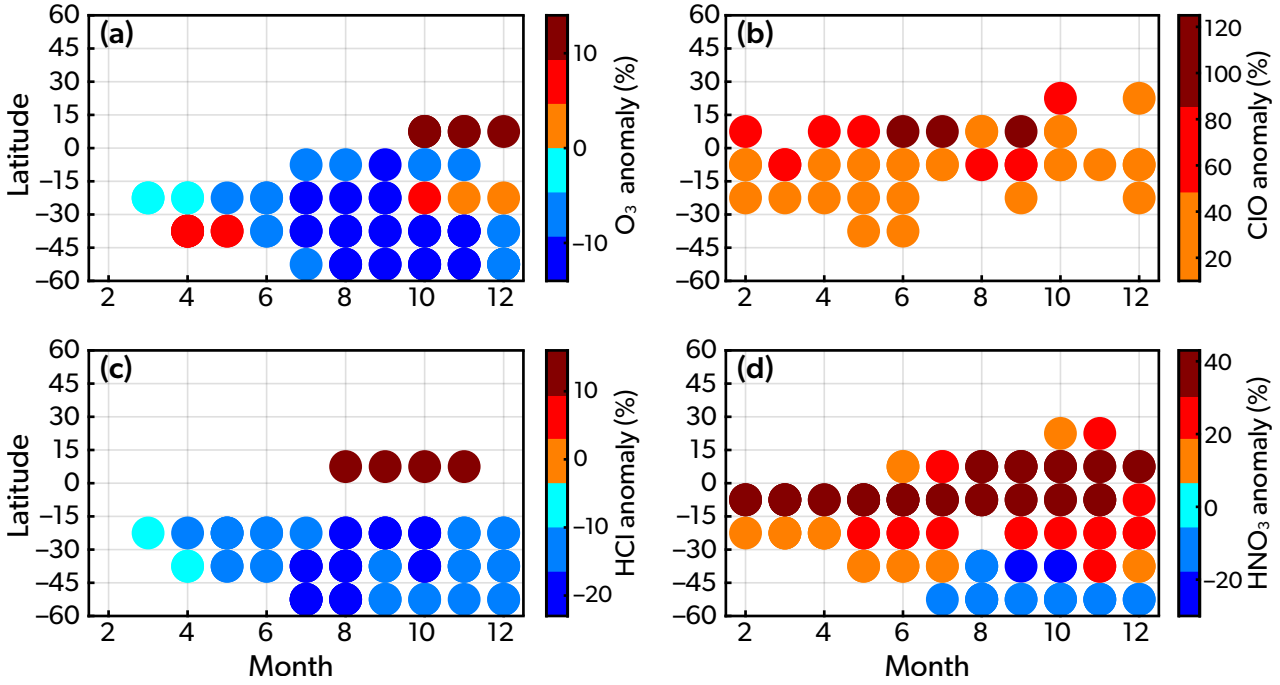

Figure 5.4: *Peak anomalies in monthly mean vertical profiles of MLS (a) O_3, (b) ClO, (c) HCl, and (d) HNO_3 for February to December 2022, labelled with the month number of the year. Note that the colour bar ranges differ for each panel, but in this figure shades of blue always indicate decreases in mixing ratio, while shades of red always indicate increases. The points are zonal-mean monthly averages over 15° latitude bins between 60°S and 60°N, with coloured circles representing the maximum outlier in mixing ratio (expressed as a percentage) over the pressure range 5–60 hPa, the region of maximum water vapour enhancement from Hunga. Only data points that satisfy the following criteria are shown: (1) mixing ratio in 2022 was greater than two standard deviations (2σ) from the 2005–2021 MLS monthly mean for the respective variable and latitude range; (2) anomaly was coincident in month, latitude bin, and pressure level with water vapour being more than 2σ above its 2005–2021 MLS mean; (3) anomaly did not already exist prior to the water vapour being elevated; and (4) anomaly persisted for more than one month. It is important to note that it is statistically possible that a few points meeting these selection criteria are not attributable to Hunga. From Wilmouth et al. (2023).*

in (a) ClO and (b) HNO_3 in July in the SH tropics, unprecedented reductions in (c) O_3 and (d) HCl in August at SH midlatitudes, and anomalously high (e) O_3 and (f) HCl in October in the NH tropics (Wilmouth et al., 2023). In most cases, multiple MLS pressure levels were substantially perturbed. The compositional anomalies for the months and latitudes shown in Figure 5.5 were more significant for the Hunga eruption in 2022 than for the ANY fires in 2020. The tropical anomalies are addressed further in Section 5.3.2.

The observed changes in SH midlatitude composition in the months following the eruption (as shown in Figures 5.3, 5.4, 5.5c,d) were caused by both chemistry and transport. First considering chemistry, important heterogeneous reactions in the stratosphere are summarised in Box 5.1. Reactions R5.1–R5.3 are known to be the primary cause of chlorine activation in polar winter that can lead to large Antarctic and Arctic ozone depletion, and these reactions are enhanced in the presence of elevated volcanic sulfate aerosol and water vapour. However, CCM simulations with SOCOL-AERv2-Volc (SOCOL = modeling tools for studies of SOlar Climate Ozone Links, AER = 2-D aerosol model, Volc = heat flux, mixed-layer ocean, and SSP implementation; Wilmouth et al., 2023) and rate constant analyses (Santee et al., 2023) show that even though these reactions are faster following the Hunga eruption, all three are too slow at temperatures in the middle stratosphere to have played any significant role in driving the observed compositional changes in 2022.

Reactions R5.4 and R5.5 are enhanced following the Hunga eruption and, unlike R5.1–R5.3, they are relatively insensitive to temperature. Indeed, the N_2O_5 hydrolysis reaction (R5.4) on elevated sulfate aerosol was the dominant heterogeneous reaction driving chemical changes following the Hunga eruption (Santee et al., 2023; Wilmouth et al., 2023; Zhang et al., 2024a; Bednarz et al., 2025), as it was following the Mount Pinatubo eruption (e.g., Fahey et al., 1993;

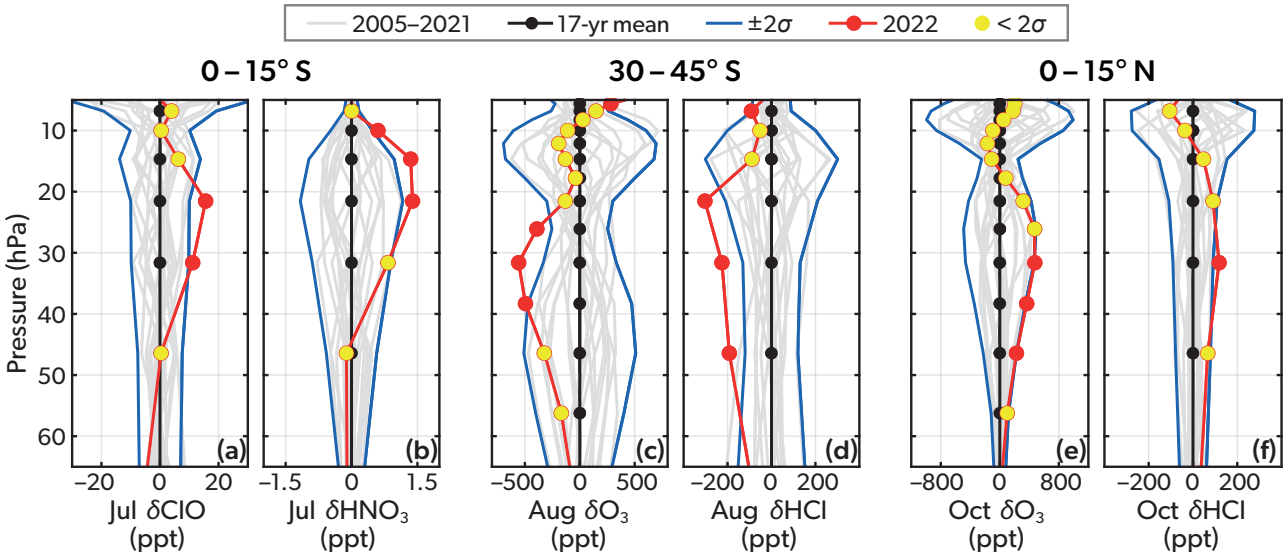

Figure 5.5: *Anomalies in the monthly mean vertical profiles of selected MLS measurements for each year from 2005 to 2022 relative to the 2005–2021 mean value. Mixing ratio anomalies are shown for (a) ClO and (b) HNO_3 for July at 0°–15°S, (c) O_3 and (d) HCl for August at 30°S–45°S, and (e) O_3 and (f) HCl for October at 0°–15°N. All longitudes are included in the averages. Data for each of the 17 years from 2005–2021 are shown in grey, the 17-year mean is shown in black, lines representing ±2σ from the 17-year mean are shown in blue, data points from 2022 that fall inside the 2σ lines are plotted in yellow, and data from 2022 outside the 2σ lines are shown in red. Adapted from Wilmouth et al. (2023).*

Kinnison et al., 1994). It is noteworthy that the chemical changes induced by the N_2O_5 hydrolysis reaction would have been even more substantial had this reaction not reached saturation (Santee et al., 2023). Saturation occurs because N_2O_5 formation (mainly from NO_2+NO_3 at night) is slower than Reaction R5.4 when stratospheric aerosol loading is sufficiently elevated, i.e., N_2O_5 is hydrolysed as fast as it can be formed. The bromine nitrate ($BrONO_2$) hydrolysis reaction (R5.5), when coupled with a subsequent heterogeneous reaction of hypobromous acid (HOBr) with HCl (R5.6), has also been suggested to play a significant role in the chemical loss of HCl following the Hunga eruption (Zhang et al., 2024b; Bednarz et al., 2025).

In addition to heterogeneous reactions, gas-phase reactions were significantly impacted (e.g., Santee et al., 2023; Wilmouth et al., 2023; Zhang et al., 2024b). Because the chemical cycles controlling stratospheric composition are highly interconnected, perturbations in even just one or two reactions can have far-reaching impacts. The manner in which enhanced HNO_3, decreased NO_x, and elevated OH impact other chemical cycles has been discussed in detail (Santee et al., 2023; Wilmouth et al., 2023). Here, it is sufficient to summarise that ozone-loss cycles involving HO_x and ClO_x are enhanced, while NO_x-driven ozone loss slows (e.g., Zhang et al., 2024a, their Figure 3c; Fleming et al., 2024, their Figure 9b; Bednarz et al., 2025). For some of the measurements shown in Figures 5.3–5.5, the impact of altered chemistry following Hunga is clear, particularly in the record-low N_2O_5 and NO_x and record-high ClO. In other cases, such as HNO_3, HCl, and O_3, chemistry is only part of the story, and transport must be considered.

The cooling effect of the greatly elevated stratospheric water vapour following the Hunga eruption caused changes in stratospheric circulation (see Chapter 4) that led to some of the observed changes in composition. The importance of altered transport for trace-gas distributions has been demonstrated with both tracer–tracer correlations (Santee et al., 2023; Wilmouth et al., 2023) and atmospheric modelling (Wang et al., 2023; Zhang et al., 2024a; Bednarz et al., 2025). The method used in independent tracer analyses was to evaluate correlations in the anomalies of HNO_3, HCl, and O_3 with anomalies in nitrous oxide (N_2O), as N_2O represents a long-lived tracer for large-scale transport in the atmosphere. These tracer–tracer analyses (Santee et al., 2023; Wilmouth et al., 2023) showed that changes in transport were the primary factor in causing the observed anomalies in HNO_3, HCl, and O_3 mixing ratios, particularly at SH midlatitudes in the second half of 2022. For example, the dominant role of transport explains why HNO_3 decreases in the second half of 2022 in Figure 5.3e despite Reaction R5.4, while the importance of chemistry

is revealed by a plot of HNO_3/NO_y (odd nitrogen, $NO_y \approx 2{\times}N_2O_5 + NO_x + HNO_3 + ClONO_2$) showing record-high values over that same time period (Santee et al., 2023, their Figure 2), suggesting heterogeneous HNO_3 production. Similarly, the strong SH midlatitude reductions in O_3 and HCl shown in Figures 5.3j and 5.3h (seen also in Figures 5.5c,d) correlate with high values of N_2O (Figure 5.3i). In short, several analyses (Santee et al., 2023; Wilmouth et al., 2023; Zhang et al., 2024b) indicated that changes in transport played the more important role in perturbing HCl, HNO_3, and O_3 mixing ratios in the SH midlatitudes, but chemical perturbations were also significant, especially for HCl. Of these three, anomalies in ozone showed the smallest chemical signature (Santee et al., 2023; Wilmouth et al., 2023). A WACCM6 modelling study quantified the ozone loss due to chemistry to be ~4% at SH midlatitudes near ~70 hPa in August 2022, compared to a maximum modelled ozone loss of ~15% at 30–50 hPa due to combined dynamical and chemical influences. The chemical loss may be underestimated, as the simulations did not include the dynamical feedback on chemistry (Zhang et al., 2024a). On the other hand, a recent analysis of ensembles of multi-model CCM simulations performed as part of HTHH-MOC found that the chemical perturbations induced by Hunga were comparable in importance to the changes in transport in determining the overall ozone response to the eruption in the SH extratropics (Bednarz et al., 2025).

The observed anomalies in stratospheric composition following the Hunga eruption in 2022 were of distinctly different origin than the anomalies in 2020 (Santee et al., 2022; Strahan et al., 2022), when the high solubility of HCl in aged stratospheric smoke particles from the ANY fires apparently prompted heterogeneous chlorine activation via Reaction R5.2, leading to larger perturbations in chlorine partitioning (Solomon et al., 2023). While the details of the Mount Pinatubo (e.g., Kinnison et al., 1994; Aquila et al., 2013) and Hunga eruptions differ substantially, they were similar in that the significant and prolonged changes in stratospheric composition that followed were caused by a combination of altered chemistry and transport.

5.3.2 Tropics

Evidence from satellite observations reveals substantial impacts of the Hunga eruption on chlorine and nitrogen chemistry in the tropical stratosphere (Santee et al., 2023; Wilmouth et al., 2023). While perturbations in the abundances of those species were remarkable for the tropics, they were too small to affect ozone in the lower stratosphere to a significant degree. Evolution of ozone in that layer was instead dominated by transport. However, in the second half of 2022, anomalous nitrogen partitioning triggered by the eruption suppressed the NO_x catalytic loss cycle, resulting in a notable increase in middle-stratospheric ozone.

The impacts on composition were seen in the tropics several months before they were evident at midlatitudes (Figure 5.4), consistent with the evolution of the water vapour and aerosol (see Chapter 3). Similar to the situation in the SH midlatitudes, the perturbations of the ClO_x, NO_x, and HO_x species were significant (Santee et al., 2023; Wang et al., 2023; Fleming et al., 2024). Peak ClO anomalies (Figure 5.4b) were positive in the tropics throughout the year, with ClO abundances reaching up to twice their climatological values in June, July, and September 2022. There is a consistent pattern of high maximum HNO_3 abundances throughout 2022 (Figure 5.4d), as well as more moderate peak HCl values north of the equator and negative values between 15°S and 30°S (Figure 5.4c). Peak O_3 anomalies in the tropics in 2022 were mostly negative, except in the latter part of the year starting in October (Figure 5.4a).

The vertical structure of some of these anomalies is shown in Figure 5.5. The maximum ClO enhancements of over two standard deviations (2σ) from the climatological mean in the latitude band 0°–15°S in July occurred near 20 hPa (~26.5 km; Figure 5.5a). When adjusted for trends and dynamical variability, large increases in ClO due to chemistry were also observed in the upper stratosphere up to about 36.5 km (4.6 hPa) in 2023 (Nedoluha et al., 2025, not shown here). The ClO enhancements in the upper stratosphere were attributed to increased OH from the additional water vapour. HNO_3 mixing ratios exceeded the 2σ threshold in a broad layer between 30 hPa and 10 hPa (~24–31 km; Figure 5.5b). In October, positive maximum ozone and HCl anomalies immediately north of the equator occurred at altitudes below (i.e., pressures greater than) 30 hPa (~24 km; Figures 5.5e,f). The presence of strongly negative N_2O anomalies at the same time and altitudes (Wilmouth et al., 2023, their Figure S14) suggests that transport was the direct driver of the high HCl and ozone in that latitude band. It is not known whether radiative effects of the Hunga eruption were responsible for this circulation anomaly in the tropics (see Chapter 4).

Chlorine and nitrogen chemistry in 2022 was dominated by the hydrolysis of N_2O_5 (Reaction R5.4) on volcanic sulfate aerosol and subsequent gas-phase reactions (Santee et al., 2023). This is different from the typical pathway of heterogeneous chlorine activation in the winter polar lower stratosphere, which involves reactions between chlorine reservoir species (R5.1–R5.3). At 620 K (~26 hPa, ~25 km), the level where the initial enhancements in water vapour from the eruption were maximum in the tropics, there was a rapid initial increase in HNO_3 and ClO, concomitant with a drop in N_2O_5 and NO_x (Figures 5.6c–f). The 2022 values redefine the envelopes of previously observed abundances for these four species based on data collected between 2005 and 2021. The timing of those initial changes closely followed the increases in water vapour and aerosols in the tropics in late January 2022 (Figures 5.6a,b). A more moderate increase in $ClONO_2$ and a decrease in HCl (Figures 5.6g,h) are also seen. Evidence for N_2O_5 hydrolysis being the primary mechanism of this repartitioning of chlorine and nitrogen species is provided by the subsequent evolution of HNO_3 and ClO. Specifically, after the rapid initial increase, HNO_3 mixing ratios reached a plateau between March and May 2022 and then followed their typical seasonal trajectory while remaining about 10% above the mean. This March–May plateau is also seen in HNO_3 anomalies at other altitudes (Santee et al., 2023, their Figure 8). After reaching its maximum anomaly in mid-March, ClO was also roughly constant through May, after which values declined slowly while remaining significantly higher than average throughout most of 2022. The fact that the rise in the abundances of these gases stalled in late February or March despite the continuing increases in aerosol and water vapour loading, combined with an increase in $ClONO_2$ (rather than a decrease, as would be expected if direct heterogeneous chlorine activation Reactions R5.2 or R5.3 were at work), suggests that it was N_2O_5 hydrolysis, which is subject to saturation, that dominated their production.

The evolution of ozone in the tropical lower stratosphere in 2022 was mainly driven by transport. Ozone mixing ratios were mostly above average at 620 K (~26 hPa, ~25 km), with significant up- and downswings throughout the year (Figure 5.6j), suggesting that the chlorine activation had only a limited impact on ozone at that level, and any chemical loss that might have occurred was masked by much stronger dynamical variability. This assertion is strengthened by a quantitative analysis of the perturbations in chlorine chemistry. As exceptional as they were, the ClO enhancements in the tropics in 2022 were still more than an order of magnitude weaker than those during a typical polar winter. For example, the maximum ClO enhancements observed between 22°S and 6°S EqL following the Hunga eruption were about 0.04 ppbv (Figure 5.6f), compared to at least 1 ppbv observed in the lower stratosphere over the Antarctic in September (World Meteorological Organization (WMO) (2022); see also Section 5.3.3).

Mixing ratios of the transport tracer, N_2O, were low between February and June 2022 (Figure 5.6i), suggesting anomalously slow tropical upwelling consistent with the observed circulation anomalies in 2022. However, it is difficult to determine how much of this transport anomaly resulted from the eruption, given strong interannual and quasi-biennial oscillation (QBO) variability in tropical upwelling (see Chapter 4). Examination of joint distributions of chemically active gases and N_2O provides further insights into the relative importance of chemistry and transport for the observed composition anomalies in 2022 (Figure 5.7). Based on MLS data between 2005 and 2021, both the N_2O/HNO_3 and N_2O/HCl anomaly distributions exhibit compact relationships (Figures 5.7a–c and 5.7d–f, respectively). This reflects the relatively long chemical lifetimes of these species in the lower stratosphere. Consequently, deviations from the climatological distributions indicate anomalous chemical production or loss. The HNO_3 values in the broad layer between 580 K and 660 K are slightly outside of the 2005–2021 envelope between February and July 2022, consistent with chemical processing, as discussed above. HCl mixing ratios at and above 620 K between July and October 2022 are lower than can be explained by transport, providing further evidence for heterogeneous chemical processing, consistent with highly elevated HNO_3 and ClO. Correlations between N_2O and ozone (Figures 5.7g–i) are weaker than those for HNO_3 and HCl, but the joint distributions of these gases still provide insights into mechanisms responsible for tropical ozone anomalies in 2022. At 620 K and 580 K (~32 hPa, ~24 km; Figures 5.7h,i), ozone anomalies are within previously observed ranges. The lack of significant departure from the climatological N_2O/O_3 relationship supports the conclusion stated earlier that no substantial chemical ozone loss occurred at that level. A clearer chemical signal is present at 660 K (~22 hPa, ~26 km; Figure 5.7g) and above (not shown), where ozone anomalies reached record-high values in the second half of the year (see

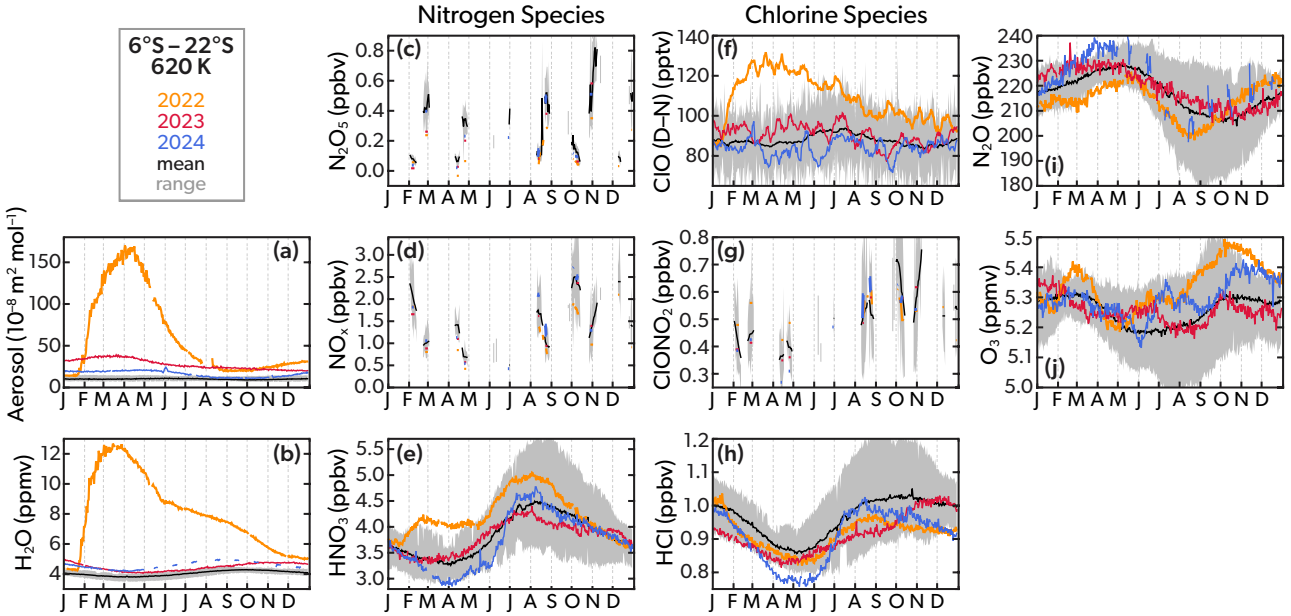

Figure 5.6: *Satellite observations averaged over 6°S–22°S EqL (SH tropics) at 620 K (~26 hPa, ~25 km) of (a) OMPS-LP aerosol cross sections at 869 nm, (b) MLS H_2O, (c) ACE-FTS N_2O_5, (d) ACE-FTS NO_x, (e) MLS HNO_3, (f) MLS ClO (day minus night), (g) ACE-FTS $ClONO_2$, (h) MLS HCl, (i) MLS N_2O, and (j) MLS O_3. Individual years are highlighted as indicated in the legend: 2022 in orange, 2023 in red, and 2024 in blue. Grey shading depicts the range of values observed by MLS (2005–2024), ACE-FTS (2005–2024), and OMPS-LP (2012–2024), excluding the highlighted years; black lines represent the mean of the grey-shaded data. To facilitate interpolation to isentropic surfaces, the aerosol data are converted from extinction coefficient (in units of km^{-1}) to extinction cross section per mole of air (in units of m^2 mol^{-1}), a quantity conserved under changes of atmospheric pressure in the absence of aerosol formation or loss (Santee et al., 2023). There are gaps in the 2024 MLS H_2O and N_2O data because it became necessary to duty cycle the MLS subsystem used to measure these species; thus, starting in May 2024, H_2O and N_2O measurements are available only for approximately week-long intervals in the middle of each month. ClO is shown as the day-minus-night difference to mitigate measurement bias at the lowest retrieval levels; the highlighted years and mean for ClO (but not the envelope) have been smoothed using a boxcar of width 10 days. ACE-FTS fields were also smoothed with a 10-day boxcar average. Adapted from Santee et al. (2023).*

also Figure 5.6j). The absence of corresponding large anomalies in N_2O suggests that this ozone enhancement is not readily explained by transport. Rather, the elevated ozone abundances are consistent with anomalously low NO_x abundances (Figure 5.6d) and the resulting suppressed chemical loss from the catalytic NO_x cycle.

Ensemble simulations using the 3-D global CCM SOCOL-AERv2-Volc with injected water vapour and SO_2 leading to water vapour and sulfate aerosol enhancements reflecting those from the eruption produce responses in stratospheric composition in the tropics (0°–30°S) that are in qualitative agreement with observations in April 2022 (Wilmouth et al., 2023). The model simulation finds enhanced HO_x, HOCl, HNO_3, and ClO and reduced HCl, NO_x, and N_2O_5 compared to a control experiment. Modelled O_3 and ClO closely agree with MLS observations. Qualitative agreement between modelled and measured HCl and HNO_3 is also seen, although the model overestimates the observed HNO_3 enhancement and the reduction in HCl (Wilmouth et al., 2023). In addition, these simulations show significant changes in chemically active compounds unobserved from space; in particular, they produce peak increases of 50% for HO_x and 100% for HOCl.

Finally, we briefly discuss the composition of the tropical stratosphere in the years following 2022. While water vapour and aerosols remained elevated throughout 2023 and 2024, HNO_3, ClO, HCl, and ozone largely returned to their climatological abundances in 2023 (Figures 5.6e,f,h,j). N_2O_5 remained low through April 2023 but was well within its climatological envelope in the latter part of the year (Figures 5.6c,d). Between March and July 2024, HCl, $ClONO_2$, and HNO_3 reached record or near-record low values. The origin of these anomalies is not known, but a corresponding strong positive anomaly in N_2O (Figure 5.6i) suggests that they may have been transport related. Ozone, on the other hand,

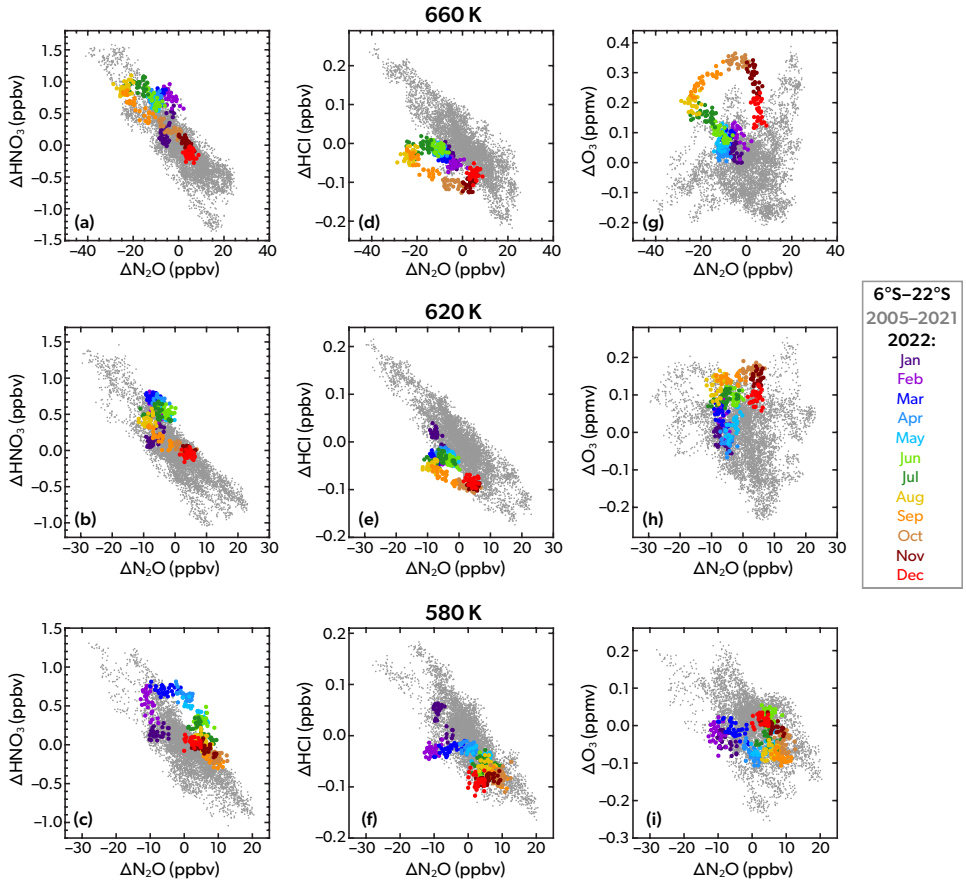

Figure 5.7: *Scatter plots of daily N_2O anomalies versus anomalies of HNO_3 (a–c), HCl (d–f), and O_3 (g–i) from MLS observations averaged between 6°S and 22°S EqL at selected potential temperature levels: 660 K (~22 hPa, ~26 km; a, d, g), 620 K (~26 hPa, ~25 km; b, e, h), and 580 K (~32 hPa, ~24 km; c, f, i). Data from 2005–2021 are shown in grey; 2022 data are coloured by month as indicated by the legend. Adapted from Santee et al. (2023).*

is generally only weakly correlated with N_2O at the altitude considered here (Figure 5.7h). It was close to its long-term average during the first half of 2024 and above average for the rest of the year, with the exception of September (Figure 5.6j).

5.3.3 Antarctic winters/springs of 2022, 2023, and 2024

Antarctic winter/spring of 2022 The Hunga eruption had minimal impact on Antarctic stratospheric polar chemistry in 2022. The 2022 austral winter polar vortex was large, cold, and stable, and its dynamical characteristics were well within the range of pre-Hunga values (Figure 5.8; Manney et al., 2023; Wargan et al., 2025). A small increase in aerosol loading was observed at high southern latitudes in the lowermost stratosphere (430 K and below) before the vortex had fully formed at those levels (Khaykin et al., 2022; Taha et al., 2022; Manney et al., 2023). In contrast, the Hunga water vapour was effectively excluded from the 2022 Antarctic vortex by the strong transport barrier at the vortex edge (Schoeberl et al., 2022; Manney et al., 2023), and water vapour was not fully entrained into the deep branch of the Brewer–Dobson circulation (BDC) until 2023 (Zhou et al., 2024); see Chapter 3. While some observational studies showed evidence that the heterogeneous chemical processing (chlorine activation, denitrification, dehydration) and ozone loss that took place within the vortex were near average (Figure 5.8; Manney et al., 2023), others reported Antarctic polar-cap-averaged observed (and simulated) ozone abundances with values in October that were ~30% less than typical, though still within the climatological range (Wang et al., 2023; Fleming et al., 2024; Zhang et al., 2024a; Zhou et al., 2024). This apparent inconsistency may be explained by the studies' examination of averages calculated over different regions of interest—geographic latitude bands vs. the vortex. The dynamical characteristics (e.g., size, shape, and position) of the Antarctic vortex are highly variable; since polar-cap (i.e., 60°S–90°S) averages do not account for undulations of the vortex

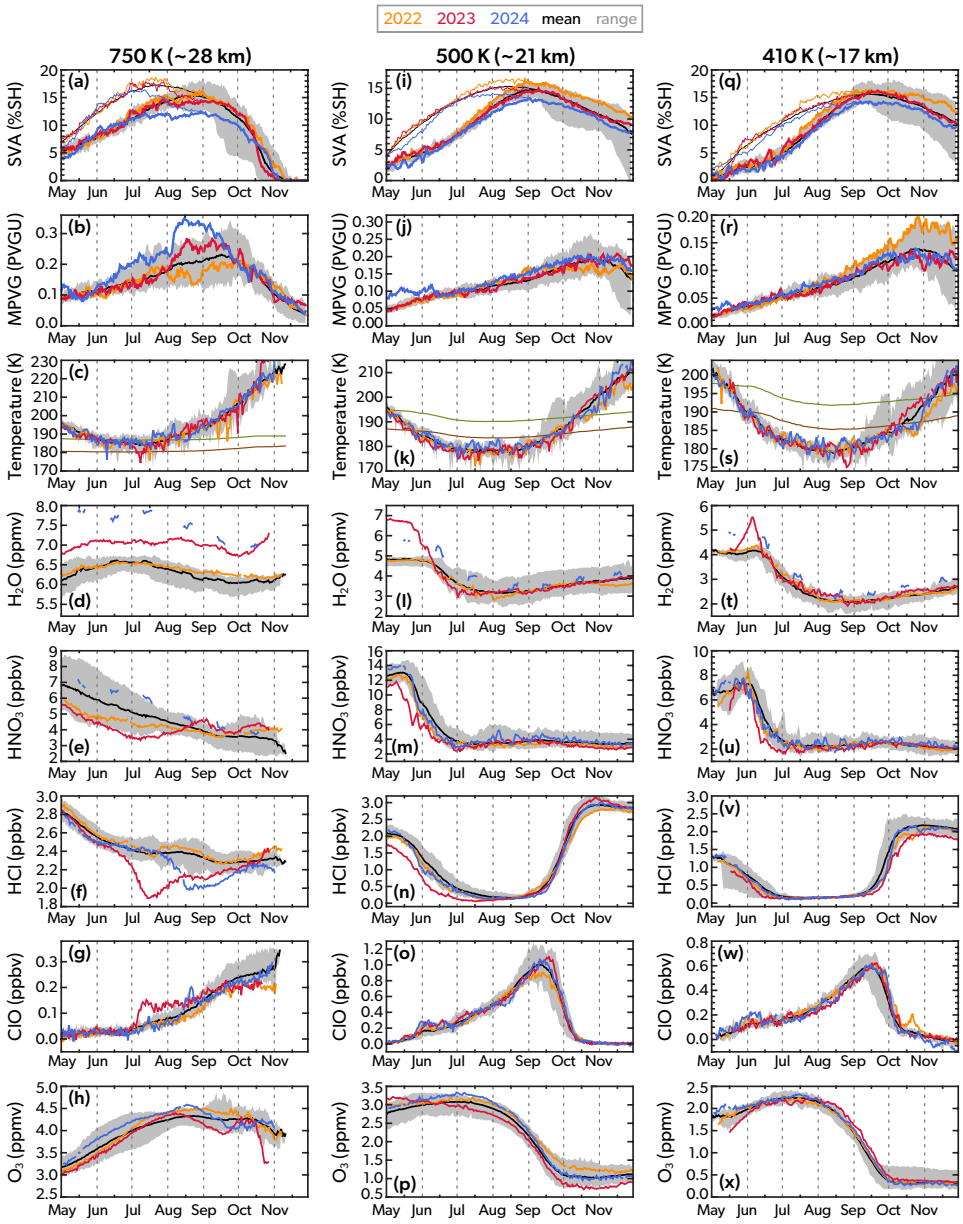

Figure 5.8: *Time series from May through November of daily quantities in the SH polar region on three selected isentropic surfaces: 750 K (left), 500 K (middle), and 410 K (right). For all panels, grey shading depicts the range of observed values and black lines the mean over 2005–2021. The coloured lines represent different years as indicated in the legend: 2022 (orange), 2023 (red), and 2024 (blue). (a, i, q) MERRA-2 Antarctic total vortex area (thinner lines) and sunlit vortex area (SVA, thicker lines), both expressed as a percentage of the hemisphere (%SH). SVA is smaller than the total vortex area for the first few months, as a portion of the vortex remains in darkness, but later in the season the two curves converge. Vortex area calculations require definition of the approximate "edge" of the polar vortex, identified here using specified contours of scaled potential vorticity (PV) that vary with altitude, as described by Lawrence et al. (2018). The total vortex area envelope is omitted for clarity. (b, j, r) MERRA-2 maximum scaled-PV gradient (MPVG, a measure of vortex strength), in units of 10^{-4} s^{-1} deg^{-1} (PVGU). (c, k, s) MLS minimum temperatures inside the vortex. Thinner lines mark the formation thresholds for HNO_3-containing (green) and water-ice (brown) PSCs, respectively. (d, l, t) Vortex averages of MLS H_2O. There are gaps in the 2024 data because it became necessary to duty cycle the MLS subsystem used to measure H_2O; thus, starting in May 2024, H_2O measurements are available only for approximately week-long intervals in the middle of each month. Vortex averages of (e, m, u) HNO_3, (f, n, v) HCl, (g, o, w) daytime-only ClO, and (h, p, x) O_3. Adapted from Santee et al. (2024).*

edge, they inevitably mix inside- and outside-vortex air, especially after September, when stronger dynamical variability in austral spring increasingly confounds signatures of chemical ozone loss. Modelled chemical impact on Antarctic ozone from the excess Hunga water vapour was found to be negligible using the TOMCAT CTM (Zhou et al., 2024), and the low polar-cap-averaged ozone was largely attributed to internal variability in the climate system and dynamical changes that may have been forced by the eruption based on WACCM6 results (Wang et al., 2023; Zhang et al., 2024a). After the vortex broke down in November–December 2022, enhanced stratospheric water vapour and aerosols pervaded the southern middle and high latitudes (Manney et al., 2023) and persisted into 2023. Thus it was extraordinarily humid over the Antarctic when the 2023 vortex formed, and concentrations of large aerosol particles (with diameters greater than 0.5 μm) were also greatly increased (by as much as an order of magnitude; Deshler et al., 2024).

Antarctic winter/spring of 2023 As in 2022, the 2023 Antarctic polar vortex was large, stable, and cold. Dynamical characteristics (such as the maximum gradient in scaled potential vorticity, a measure of vortex strength) were generally unremarkable and, along with vortex temperature, within climatological norms (Figure 5.8; Santee et al., 2024; Zhou et al., 2024; Wargan et al., 2025). However, relatively weak planetary-scale wave activity from mid-October onwards slowed the seasonal transition to summer, with the breakdown of the vortex delayed until mid-December, nearly two weeks later than usual (Kramarova et al., 2024). The prolonged duration of the 2023 Antarctic lower stratospheric vortex was similar to that of the prior three years (2020–2022), which also saw weaker-than-average wave activity in late austral spring (Kramarova et al., 2024).

Water vapour was exceptionally high at the start of austral winter in May, 10–40% higher than normal over much of the stratosphere (Figures 5.8d,l,t; Santee et al., 2024; Wohltmann et al., 2024), and the vortex remained unusually moist throughout 2023 at altitudes at and above 600 K (e.g., Figure 5.8d). Enhanced water vapour abundances both reduced vortex minimum temperatures by ~1–2 K (within the climatological range) in early winter (June; Fleming et al., 2024) and raised the threshold temperatures for the formation of water ice and HNO_3-containing polar stratospheric clouds (PSCs) by ~1–2 K above typical values (Santee et al., 2024; Wohltmann et al., 2024). The cold, humid conditions caused earlier (May) and more extensive PSC formation than usual. Ice PSC volume in late June was the largest ever observed by CALIOP, estimated at ~55 million km^3 (compared to the mission average of ~20 million km^3; Figure 5.9a). Such an increase in ice PSC abundance was predicted in model simulations considering the Hunga hydration (Fleming et al., 2024; Zhou et al., 2024). HNO_3-containing PSC volume in late June was also elevated but within climatological variability (Figure 5.9b). Consistent with these results, the season-integrated volume of PSC occurrence inferred from (daytime-only) OMPS-LP aerosol measurements was the largest in the 13-year OMPS-LP record (DeLand and Schoeberl, 2025).

The availability of excess water vapour above the saturation limit might be expected to produce larger particles with correspondingly greater sedimentation velocity (Wohltmann et al., 2024). ACE-FTS aerosol observations in September and October 2023 support this hypothesis, as inferred aerosol sulfate radius was the largest ever reported (Lecours et al., 2024). Extensive PSC sedimentation caused early-season (May–June) large-scale dehydration and denitrification of the lower stratospheric vortex. It was estimated that ice PSC sedimentation removed ~35 Tg of water vapour from the stratosphere in 2023, compared to ~23 Tg in a typical Antarctic winter (Millán et al., 2024). By mid-July, water vapour in the lower stratosphere was "reset" back to the typical range (3–4 ppmv) observed in earlier years and essentially followed the climatological mean thereafter (Figures 5.8l,t). In other words, the dehydration process had run to completion by mid-winter (July–August). Substantial hydration (of ~1 ppmv) from evaporation of ice particles falling from above also occurred over 380–460 K (~102–46 hPa, ~15–19 km) in the lower stratosphere in late May/early June (e.g., Figure 5.8t); such PSC-related hydration had not been previously reported as early in the season or at as high altitudes as observed in 2023 (Santee et al., 2024). Rapid denitrification of the vortex occurred in May and June 2023 (see the sharp declines in HNO_3 in Figures 5.8e,m,u). However, as with water vapour, HNO_3 evolution mostly followed the climatological mean after mid-July, indicating that the denitrification process had run its course. Ground-based remote-sensing measurements of HNO_3, NO, and NO_2 made at Arrival Heights, Antarctica, confirm that Hunga did not cause excess denitrification during the 2023 season (Smale et al., 2025).

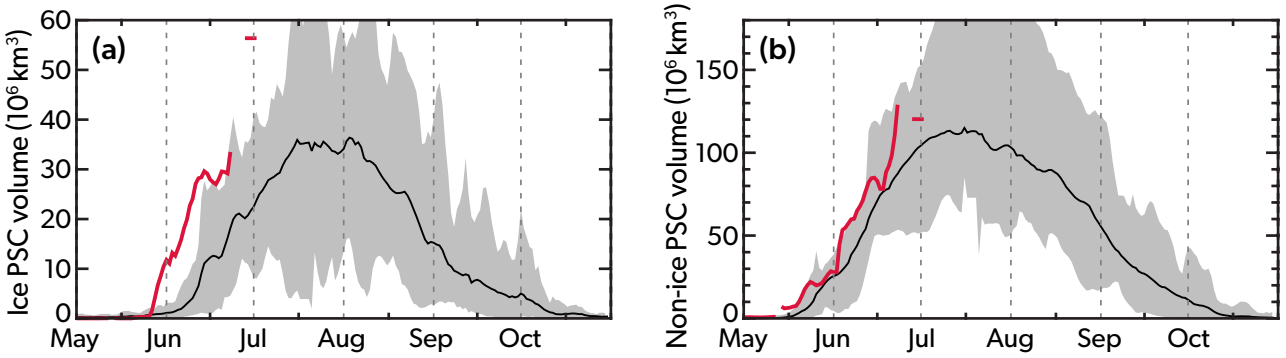

Figure 5.9: *Daily values of Antarctic (a) ice and (b) HNO_3-containing (liquid and solid, labelled as "non-ice") PSC spatial volumes, calculated by integrating PSC areal coverage values over the altitude range 12–30 km, derived from the CALIOP cloud mask product. These time series terminate at the end of October, as PSC activity typically ceases by that time. Grey shading depicts the range of values from the climatology of PSC volume, and black lines show the mean over 2006–2022 (excluding 2023, shown in red). Regular daily CALIOP measurements ceased in late June 2023; therefore, PSCs were observed directly only during the early part of the 2023 Antarctic winter. Adapted from Santee et al. (2024).*

Unprecedented early-winter chlorine activation was seen at higher altitudes of 600–800 K (~18–8 hPa, ~25–30 km), where record-low HCl (Figure 5.8f) and an associated increase in ClO (Figure 5.8g) were observed in June–August 2023. Early and moderately strong chlorine activation was observed in the layer around 500 K as well (Figures 5.8n,o). Such anomalous chlorine activation in early winter is a consequence of increased PSC surface area, lower temperatures, and enhanced water vapour causing a faster rate of Reaction R5.2 (Fleming et al., 2024). However, by the end of July, HCl and ClO mixing ratios throughout the lower stratosphere were within their usual ranges. Thus, while chlorine activation was observed earlier in the winter than usual, HCl depletion and ClO enhancement eventually plateaued due to saturation of heterogeneous chemical processing (irrespective of elevated water vapour and PSC abundances) within the vortex core. Consistent with lingering below-average temperatures (Figures 5.8k,s), chlorine deactivation was slightly delayed throughout the lower stratosphere, with enhanced ClO persisting longer than usual into mid-September and then dropping to near-average values from October onwards (Figures 5.8o,w). Chlorine species measured at the Arrival Heights ground station also indicate persistent chlorine activation in September 2023 (Smale et al., 2025).

Although the early-winter chlorine activation at 600–800 K temporarily redefined the envelope of behaviour, the ClO enhancement in that layer was still nearly an order of magnitude smaller than that seen in the sunlit vortex later in the season at lower altitudes (~500 K) and thus was too weak to induce substantial ozone depletion. The August–September decrease in ozone at 750 K was tentatively ascribed to destruction induced by solar energetic particles, rather than chemical processing on PSCs, while the sharp decline in late October was attributed primarily to descent of ozone-poor air from higher potential temperatures (Figure 5.8h; Santee et al., 2024). At 500 K, the persistence of very high ClO abundances (and thus strong chemical loss) likely brought about the low ozone mixing ratios at the end of the winter at that level (Figure 5.8p; Santee et al., 2024). At 410 K, ozone remained at or above the climatological mean through most of the season (Figure 5.8x).

Chemical ozone destruction is quantified in several ways. One approach is "MLS-Match," whereby trajectory calculations are used to identify air parcels sampled multiple times by MLS to account for transport effects. The MLS-Match analysis in a study by Santee et al. (2024) covered the period from 1 May through 15 October, chosen to encompass the bulk of the chemical ozone destruction while excluding the much greater dynamical variability at the end of the season; similar results were obtained employing the MLS-Match method over 1 June–30 September by Wargan et al. (2025). At the upper levels (600–800 K), the MLS-Match–derived cumulative amount of ozone destroyed over the course of the winter (~1 ppmv or less) was only slightly above average and well within the typical range (Figure 5.10a; Santee et al., 2024). At 410–550 K (~74–24 hPa, ~17–23 km) in the lower stratosphere, cumulative chemical ozone losses were relatively large (~2.3–3.6 ppmv, depending on level) but not unprecedented (Figure 5.10a). Integrating the MLS-Match height-resolved cumulative chemical ozone changes over the vertical do-

main from 375 to 900 K yielded an estimate of vortex-averaged stratospheric partial column ozone loss for 2023 that was ~2 DU less than the 2005–2022 MLS mission mean estimated partial column loss, well within the observed year-to-year variability (Santee et al., 2024). In another study, subtracting from the MLS ozone values a modelled passive ozone tracer initialised on 1 June using the ATLAS CTM yielded somewhat smaller estimates of observed vortex-averaged ozone loss on 1 October of ~1.5–2.6 ppmv in the lower stratosphere (Wohltmann et al., 2024). The modelled vortex-averaged stratospheric partial column (133.4–23.7 hPa) ozone loss, calculated by subtracting from modelled ozone fields the modelled passive ozone tracer, underestimated the MLS-derived loss by about 30% (Figure 5.10b). While ATLAS ozone abundances in the lower stratosphere were significantly higher than those observed by MLS in 2023 (Wohltmann et al., 2024, their Figure 2), better agreement between ATLAS and MLS ozone is seen in other Antarctic winters. A possible explanation for the larger model/measurement discrepancy in 2023 is that water vapour is not assimilated in the ECMWF ERA5 reanalysis used to drive the model. Since post-eruption ERA5 water vapour abundances deviated substantially from observed values, the representation of vertical transport in the vortex in ERA5 (and thus the modelled passive ozone tracer) may be unrealistic in 2023.

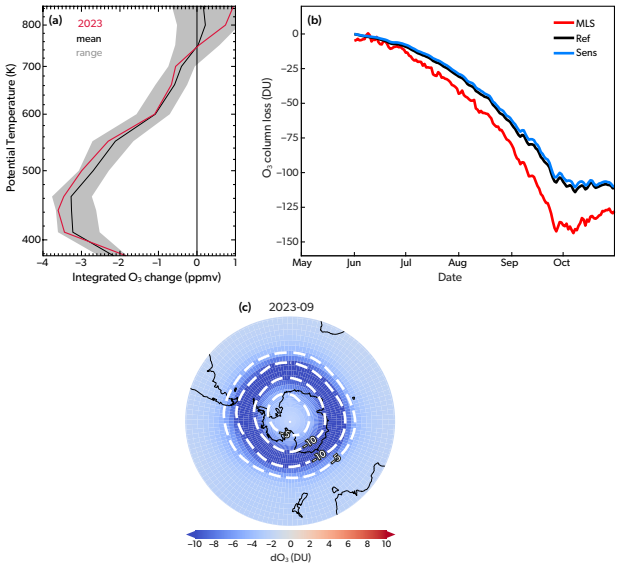

Figure 5.10: *(a) Vertical profiles of vortex-averaged chemical ozone change from the MLS-Match analysis integrated over the Antarctic winter from 1 May to 15 October. Grey shading depicts the range of values and the black line the climatological mean over 2005–2022; the red line denotes 2023 values. Adapted from Santee et al. (2024). (b) Temporal evolution of vortex-averaged chemical loss of ozone for the partial column from 133.4–23.7 hPa (~360–550 K, ~13–23 km) in 2023. Chemical ozone loss was determined by subtracting a passive ozone tracer initialised on 1 June from modelled and measured ozone values. The black line shows modelled results from the reference run ("Ref") initialised with MLS measurements from 2023, while the blue line shows modelled results from a sensitivity run ("Sens") initialised with MLS water vapour data from 2022 (i.e., without the effect of Hunga on water vapour), utilising the 3-D CTM ATLAS. The difference between the Ref and Sens runs quantifies the ozone loss attributable to the Hunga-induced increase in water vapour. The red line quantifies the observed chemical ozone loss through subtraction of the passive ozone tracer from the ozone values observed by MLS in 2023 and shows that the CTM (ATLAS) consistently underestimates ozone loss compared to MLS. Adapted from Wohltmann et al. (2024). (c) Modelled monthly mean difference in column ozone between a control simulation and one including the Hunga hydration for September 2023 using the 3-D CTM TOMCAT. White dashed lines mark the −5 and −10 DU contours. Adapted from Zhou et al. (2024).*

Modelling studies have generally found weak impacts from the Hunga hydration on the 2023 Antarctic ozone hole. The chemical ozone loss attributable to the eruption was quantified by comparing simulations with and without the Hunga water vapour perturbation. Subtracting a passive ozone tracer from simulated ozone fields from the ATLAS CTM, the direct effect of the excess water vapour on modelled vortex-averaged stratospheric partial column ozone loss was found to be less than 4 DU, compared to ~145 DU of loss in the vortex-averaged stratospheric partial column estimated from MLS measurements (Figure 5.10b; Wohltmann et al., 2024). TOMCAT simulations indicated Hunga-induced column ozone loss of ~10 DU (~4% of the background) over June–September 2023, with most of the additional loss occurring in the collar region along the vortex edge (Figure 5.10c; Zhou et al., 2024; Smale et al., 2025), where chlorine is typically not fully activated. Projections by the NASA GSFC2D model indicated that Hunga exacerbated polar-cap-average column ozone loss in 2023 by 13–23 DU, depending on the planetary wave driving scenario used (e.g., Figure 5.11a); in simulations with relatively weak wave forcing (resulting in a colder vortex than in the standard case), the excess moisture from Hunga makes less difference since ozone depletion is already severe under those conditions (Fleming et al., 2024). It should be noted that those numerical modelling studies only perturbed

water vapour, not stratospheric SO_2 or aerosols. In contrast, simulations with three CCMs conducted as part of HTHH-MOC included the effects of both the water vapour and aerosol perturbations from Hunga, each in isolation as well as the two in combination to assess their relative contributions. In these three models, the Hunga-induced impact on the 2023 Antarctic ozone hole ranged from statistically non-significant reductions of less than 10 DU to significant reductions of as much as 50 DU, with about half the decrease due to chemical destruction (Figure 5.12, Figure S3.41; see also Figures S3.42 and S3.43 for the simulated post-Hunga halogen repartitioning in the SH lower stratosphere; Bednarz et al., 2025). The Hunga SO_2 injection and subsequent aerosol formation, rather than the H_2O injection, was determined to be the primary driver of the additional chemical ozone loss (Figure 5.12; Figures S3.41- S3.43). Given the relatively weak forced response to the eruption, multi-member ensembles should be performed by each model to ensure robust diagnosis (Bednarz et al., 2025), and further multi-model evaluation should aim to reduce the spread in results. Across most modelling studies, the additional total column ozone loss in the polar vortex attributed to Hunga was within typical climatological variability and thus may not be readily detectable in the current observational record.

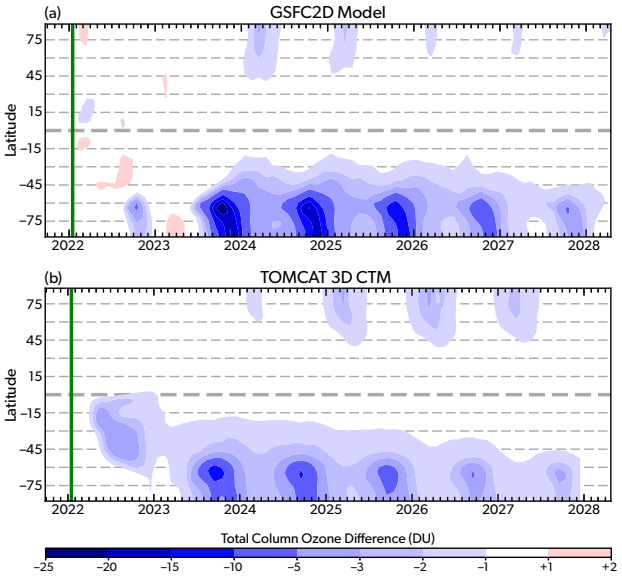

Figure 5.11: *Calculated impact over 2022–2028 of the Hunga eruption on total column ozone, quantified by taking differences between simulations with and without inclusion of the Hunga injection of H_2O. Total ozone differences (in DU) are shown from (a) a 2-D model (GSFC2D), adapted from Fleming et al. (2024), and (b) a 3-D CTM (TOMCAT), adapted from Zhou et al. (2024). The vertical green line marks the date of the Hunga eruption.*

Antarctic winter/spring of 2024 The Antarctic vortex was unusually dynamically disturbed in 2024, with two consecutive sudden stratospheric warming (SSW) events occurring in July and August (Zi et al., 2025). Unusually large values of the maximum gradient in scaled potential vorticity are consistent with increased wave activity (Figures 5.8b,j,r; Santee et al., 2024). Consequently, temperatures were near or above average through most of the season (Figures 5.8c,k,s). Water vapour remained exceptionally high, especially at 750 K (Figure 5.8d), where mixing ratios were initially about 1–2 ppmv higher than those observed in 2023, consistent with continued slow transport in the BDC bringing the Hunga hydration to the southern polar middle stratosphere (Millán et al., 2024). In the lower stratosphere (Figures 5.8l,t), the anomalously moist conditions at the start of May again led to greater-than-average dehydration during the winter, albeit to a lesser degree than in 2023. Such year-to-year reduction in the magnitude of Hunga-enhanced Antarctic dehydration is in line with expectations (Millán et al., 2024; Zhou et al., 2024) and is also consistent with the generally slightly higher temperatures in 2024. The evolution of HNO_3 (Figures 5.8e,m,u) was mostly within its climatological range, suggesting that the denitrification process was not substantially perturbed. The chlorine species also more or less followed typical seasonal patterns in the lower stratosphere. At 750 K, however, anomalous chlorine activation, with unprecedented low HCl and a spike in ClO (Figures 5.8f,g), was observed in mid-August during a period of strong wave activity (Figure 5.8b; Zi et al., 2025). Although the highly perturbed vortex shrank considerably at this time (Figure 5.8a), it was elongated and shifted off the pole (not shown), enabling greater exposure to sunlight and thus atypically large vortex-averaged ClO values. The SSW event also transported ozone poleward, causing vortex-averaged ozone to be marginally above the previously observed range at this level in mid-August (Figure 5.8h). Consistent with the unremarkable progression of chlorine activation in the lower stratosphere, ozone abundances there were near or slightly above average through most of the season (Figures 5.8p,x). Common metrics of Antarctic springtime ozone (e.g., September ozone hole area, ozone mass deficit, and polar-cap-averaged column ozone) similarly show values well within the climatological range (Wargan et al., 2025).

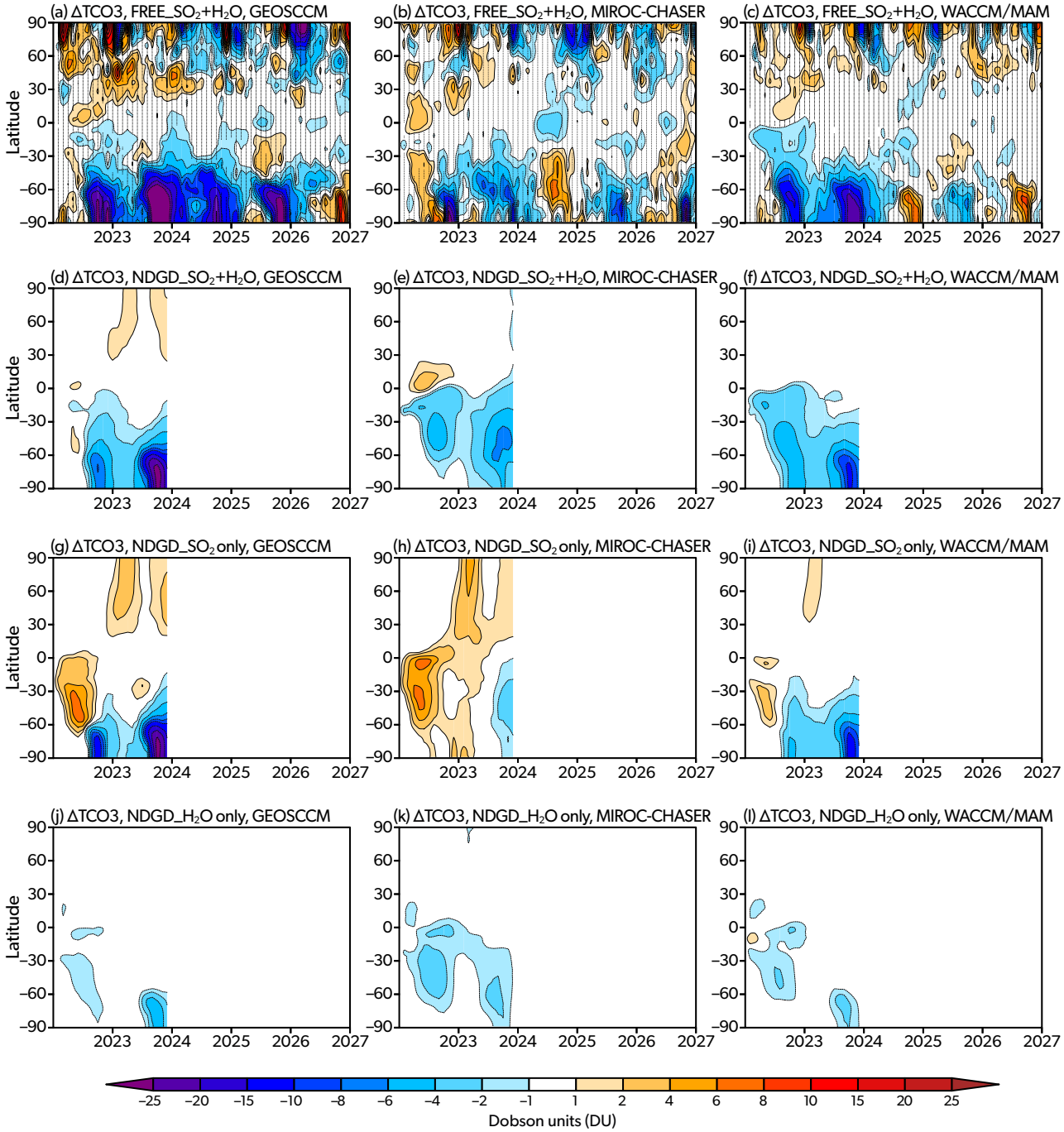

Figure 5.12: *Hunga-induced changes in total column ozone, calculated as the differences (perturbed minus control) between simulations with and without Hunga forcing. Results are from the NASA GEOSCCM (a,d,g,j), the MIROC-CHASER version 6 (b,e,h,k), and WACCM6 coupled to the MAM module version 4 (c,f,i,l). In all cases the ensemble-mean response is shown. (a–c) Results from free-running experiments including injection of both 0.5 Tg of SO_2 and ~150 Tg of H_2O from Hunga (FREE_SO_2+H_2O). Stippling marks regions where the response in total ozone is not statistically significant. (d–f) Results from specified-dynamics experiments driven by atmospheric winds and temperatures from MERRA-2 and including injection of both SO_2 and H_2O (NDGD_SO_2+H_2O). Since the meteorology is identical for the perturbed and control runs, these experiments quantify the direct chemical effects of the eruption on ozone and do not reflect those arising from changes in temperature or circulation. (g–i) Results from specified-dynamics experiments in which only SO_2 is injected (NDGD_SO_2only). (j–l) Results from specified-dynamics experiments in which only H_2O is injected (NDGD_H_2Oonly). The bottom two rows allow the effects of the aerosol and water-vapour perturbations from Hunga to be isolated. From Bednarz et al. (2025).*

5.3.4 Arctic winters/springs of 2021/2022, 2022/2023, and 2023/2024

The 2021/2022 polar vortex was colder than usual, especially between late January and March 2022, when minimum temperatures in the lower stratosphere were about one standard deviation below the climatological mean (Figure 5.13a; Bernhard et al., 2023). While the 2022/2023 Arctic winter started with temperatures below the long-term average in January 2023 (Figure 5.13a), a major SSW on 16 February 2023 caused the vortex to break up by the end of February, before chlorine-catalysed ozone loss could have a major effect (Druckenmiller et al., 2024). The 2023/2024 Arctic vortex was weaker, warmer, and more dynamically active than typical (Newman et al., 2024). Although the vortex recovered from an early major SSW on 16 January 2024, a second major SSW on 4 March caused the early breakup of the vortex (Figure 5.13a; Lee et al., 2024). Conditions during the 2022/2023 and 2023/2024 seasons were unfavourable for ozone loss catalysed by heterogeneous reactions, precluding a significant effect from the Hunga eruption on ozone depletion in these years. Whether the generally warm and disturbed conditions in these years were, at least partly, a consequence of dynamical changes induced by the eruption remains an open question. In a first study, results from the SOCOLv4 CCM suggest that the increased water vapour from Hunga reduced the temperature gradient between the tropics and the polar regions, weakening the Arctic stratospheric polar vortex in 2022/2023 and possibly causing conditions conducive to an SSW event (Kuchar et al., 2025). Ongoing analysis of HTHH-MOC simulations may shed further light on this issue.

We now turn to the evolution of water vapour, ozone, and related constituents in the years following the eruption. In spring 2022, the increased water vapour from Hunga had not yet reached the northern polar latitudes (Chapter 3, Figure 3.8), while in the winter/spring season of 2022/2023, it was not able to penetrate the polar vortex (Druckenmiller et al., 2024). Thus, through most of the late winter/spring in both 2021/2022 and 2022/2023, water vapour mixing ratios were close to the long-term mean (Figure 5.13b). Consistent with the meteorological conditions, the minimum daily total column ozone observed in March 2022 in the polar vortex was slightly lower than the climatological mean (Bernhard et al., 2023), whereas in spring 2023 it was slightly higher (Druckenmiller et al., 2024).

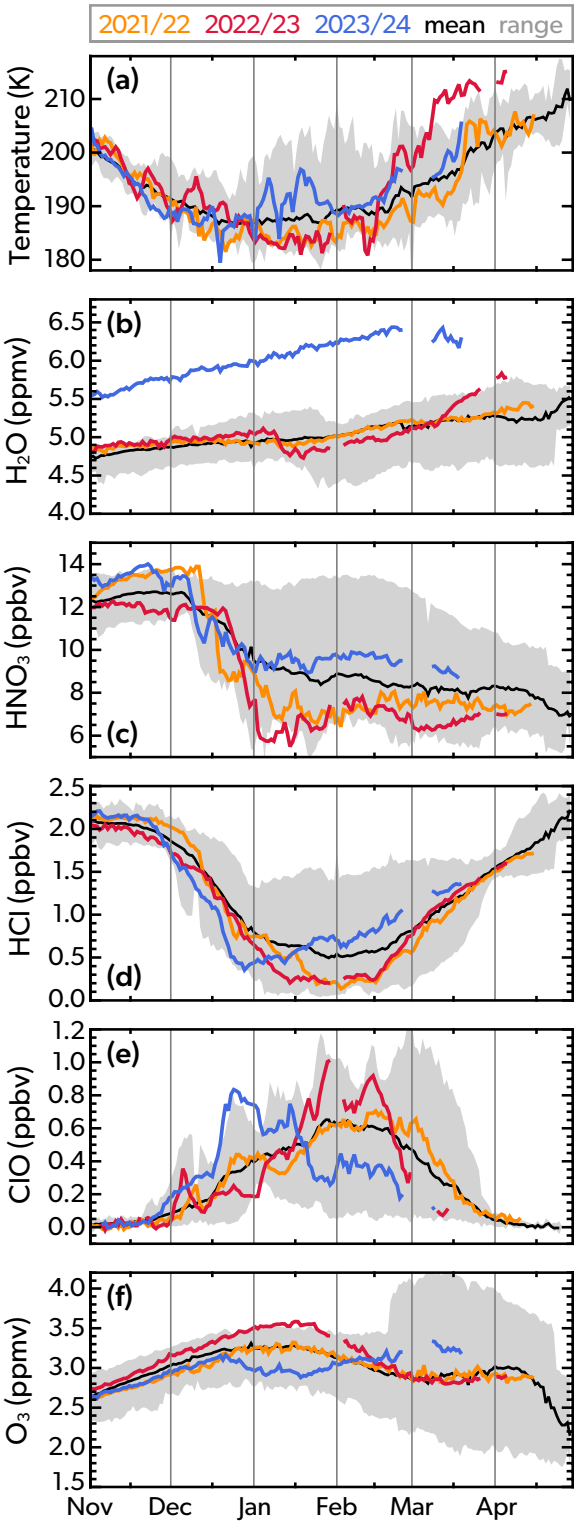

Figure 5.13: *Evolution from November through April of daily MLS (a) minimum temperature inside the Arctic polar vortex, and (b) H_2O, (c) HNO_3, (d) HCl, (e) daytime-only ClO, and (f) O_3, averaged within the vortex at 500 K (~42 hPa, ~21 km) for selected winters/springs: 2021/2022 (orange), 2022/2023 (red), and 2023/2024 (blue). Grey shading marks the range of values and the black line the climatological mean over 2005–2021.*

In contrast to the prior two years, increased water vapour values were observed by MLS inside the 2023/2024 Arctic vortex (Figure 5.13b). The 2023/2024 season also showed relatively high ClO abundances (Figure 5.13e) and corresponding low HCl abundances (Figure 5.13d) at 500 K (~42 hPa, ~21 km) compared to the long-term mean in December and January, consistent with an increased probability of PSCs induced by the increased water vapour. In addition, vortex minimum temperatures at that level were below average from late November to late December 2023, and the vortex shifted off the pole into sunlit regions, enabling strong ClO enhancement; ClO abundances then declined after mid-January 2024 as the temperatures rose and the vortex moved back over the pole (Figure 5.13a,e; Lee et al., 2024). Ozone values at 500 K were observed to be below average in late December 2023/January 2024, but they returned to near or above average in February (Figure 5.13f), consistent with the variations in chlorine activation. Chemical changes in vortex-averaged ozone can arise from variations in PSC occurrence induced by both temperature fluctuations and changes in water vapour. Furthermore, it is important to emphasise that ozone is controlled by both chemical and dynamical effects. Indeed, over the 2023/2024 winter/spring, a series of planetary-scale wave events propagating upward from the troposphere forced poleward and downward advection of ozone into the lower stratosphere, resulting in record-high Arctic polar-cap total column ozone amounts in March 2024 (Figure 5.1; Newman et al., 2024). Note, however, that the caution stated earlier (in the description of the 2022 Antarctic winter in Section 5.3.3)—that polar-cap averages and vortex averages encompass very different regions and thus are not directly comparable—is even more applicable in the Arctic, where the vortex is typically elongated, shifted off the pole, and tilted with altitude. Quantification of chemical ozone loss in the Arctic requires a detailed accounting of transport effects; such studies have not yet been conducted for any of the post-Hunga Arctic winters.

The increase of Arctic ozone loss through the combined effects of the Hunga water vapour and temperature perturbations projected by the GSFC2D model is small (4–5 DU) and does not start until spring 2024 (Figure 5.11a; Fleming et al., 2024). The model is not constrained by observed meteorological conditions, but rather uses constant tropospheric planetary-wave driving for the lower boundary conditions, based on a 30-year (1991–2020) average of MERRA-2 data. Sensitivity calculations with the strength of the wave driving varied to mimic the interannual range of observed stratospheric temperatures show that the Hunga water vapour and temperature perturbations have only a small effect on the expected interannual range of ozone loss (Fleming et al., 2024). Similarly, HTHH-MOC simulations including the effects of both the water vapour and the aerosol perturbations show no statistically significant changes in Arctic total column ozone in any post-Hunga winter (Figure 5.12; Bednarz et al., 2025).

5.4 Predictions of the future impacts on the stratospheric ozone layer

Predictions based on current observations and model simulations indicate that the Hunga hydration will persist for some time, with removal occurring on a timescale of several years to a decade. Accordingly, the effects on ozone and other trace gases discussed in Section 5.3 for 2022–2024 can be expected to continue over the coming years, albeit to a decreasing extent as the excess water vapour is slowly removed. This section discusses observational and global modelling studies that have examined these effects. At the time of publication, work on HTHH-MOC experiments is ongoing. We expect that these and other model studies will further elucidate the possible impacts from the Hunga eruption on stratospheric chemistry and composition in the future.

5.4.1 Future evolution of stratospheric water vapour

It took ~1–1.5 years for the water vapour injected into the stratosphere by the eruption to be distributed globally (see Chapters 3 and 4; Millán et al., 2024; Zhou et al., 2024). The stratosphere is dehydrated primarily by stratosphere-to-troposphere transport (STT) at middle and high latitudes as part of the meridional Brewer–Dobson circulation and by sedimentation of ice PSCs in the Antarctic vortex (dehydration); photodissociation in the mesosphere also plays a small role (see discussion in Millán et al., 2024). Measurements and model simulations identify dehydration in Antarctic winter as the primary removal pathway at work initially (Millán et al., 2024; Zhou et al., 2024). Because the Hunga water vapour was effectively excluded from the 2022 Antarctic vortex (see Section 5.3.3), removal did not begin until dehydration in the 2023 austral winter. Removal through STT did not come into play until the Hunga-hydrated air parcels had descended to sufficiently low altitudes (below ~16 km,

~100 hPa, ~380 K), but loss via STT started to exceed that from Antarctic dehydration in late 2023 (Zhou et al., 2025). Both removal processes (STT and dehydration through ice PSC sedimentation) will continue over the coming years. Estimates based on observations and model simulations of the e-folding timescale for the decay of the excess Hunga water vapour once removal commenced range between 2.5 and 4 years (Fleming et al., 2024; Khaykin et al., 2022; Kuchar et al., 2025; Schoeberl et al., 2025; Zhou et al., 2024; Zhou et al., 2025; Zhuo et al., 2025). Accounting for the ~1.5-year lag time before removal processes began, the lifetime (i.e., mean stratospheric residence time) of the Hunga water vapour is estimated to be about 4–5.5 years (Schoeberl et al., 2025).

5.4.2 Future Hunga-related changes in stratospheric composition

The long-term impact of Hunga water vapour on ozone and related gases is clearly controlled by the timescale of the removal of the additional water vapour (Section 5.4.1). The decreasing chemical impacts will also extend over this same timescale of the next decade or so.

Global model studies indicate that the largest impact of Hunga on column ozone will occur in the polar regions, particularly the Antarctic. Transport of the Hunga cloud to the Arctic took longer (see Chapters 3 and 4), by which time the magnitude of the additional water vapour had decreased through global mixing. Moreover, the occurrence of cold conditions leading to substantial ozone depletion exhibits strong interannual variability. Figure 5.11 shows the predicted effect of the Hunga water vapour alone on column ozone from simulations using the GSFC2D 2-D model (Fleming et al., 2024) and the TOMCAT 3-D CTM (Zhou et al., 2024). It should be noted that neither of these studies considered the effects of enhanced stratospheric aerosol following the eruption. Both models show the largest column impact of the excess water vapour in the Antarctic from 2023 onwards, although the modelled impact is substantially larger in GSFC2D (Figure 5.11a) than in TOMCAT (Figure 5.11b). Note that the GSFC2D simulation shown in the figure uses standard wave driving, which gives an additional depletion of 20 DU, at the high end of the 13–23 DU range for different forcings discussed in the description of the 2023 Antarctic winter in Section 5.3.3. However, aside from the difference in absolute impact, the qualitative behaviour of a decreasing effect in the SH is similar in both models, particularly from 2024 onwards. In the NH, the GSFC2D model produces the largest impact in 2024, whereas in TOMCAT, which has slower transport to the Arctic, the effect is largest in 2026. HTHH-MOC CCM simulations, in which both the water vapour and the aerosol perturbations from Hunga are considered, similarly show that the largest impacts on column ozone occur in the Antarctic and generally diminish after 2024, with the timing of the strongest effects in the Arctic varying between the different models (Figure 5.12; Bednarz et al., 2025). The modelled effects of Hunga on ozone persist until approximately 2030, although they become relatively small as the excess water vapour is removed from the stratosphere (Figure 5.11). Observations obtained by late 2024 suggest that additional chemical depletion attributable to Hunga in the Antarctic in 2023 and 2024 was small (see Section 5.3.3), so the impact may be overestimated in the models.

The impact of the Hunga H_2O anomaly on total ozone is generally less than ~10% (Figures 5.11 and 5.12), smaller than the year-to-year variability characteristic of the stratospheric polar regions during winter and spring. The standard deviation of the observed SH October–November polar-cap total ozone (~35 DU during 1991–2022; Fleming et al., 2024) exceeds most of the maximum model-estimated changes. Therefore, the fingerprint of the response to the Hunga eruption may not be easily detectable above the background variability in the current record of total ozone observations. However, the transient suppression of ozone abundances by the additional water vapour and aerosol may affect the estimation of long-term trends during the Hunga period and complicate detection of the signal of ozone recovery.

References

Aquila, V., L. D. Oman, R. Stolarski, A. R. Douglass and P. A. Newman (2013). 'The Response of Ozone and Nitrogen Dioxide to the Eruption of Mt. Pinatubo at Southern and Northern Midlatitudes'. *J. Atmos. Sci.*, 70, pp. 894–900. DOI: 10.1175/jas-d-12-0143.1.

Bednarz, E. M., V. Aquila, A. H. Butler, P. Colarco, E. Fleming, F. F. Østerstrøm, D. Plummer, I. Quaglia, W. Randel, M. L. Santee et al. (2025). 'Multi-model assessment of impacts of the 2022 Hunga eruption on stratospheric ozone and its chemical and dynamical drivers'. *EGUsphere [preprint]*, 2025, pp. 1–24. DOI: 10.5194/egusphere-2025-4609.

Bernhard, G. H., V. E. Fioletov, J.-U. Grooß, I. Ialongo, B. Johnson, K. Lakkala, G. L. Manney, R. Müller and T. Svendby (2023). 'Ozone and UV radiation [in "State of the Climate in 2022"]'. *Bull. Amer. Meteor. Soc.*, 104, S308–S310. DOI: 10.1175/BAMS-D-23-0079.1.

DeLand, M. T. and M. R. Schoeberl (2025). 'Polar Stratospheric Cloud Observations From the OMPS Limb Profiler'. *J. Geophys. Res.*, 130, e2024JD042632. DOI: 10.1029/2024jd042632.

Deshler, T., L. E. Kalnajs, M. Norgren, Y. Zhu and J. Zhang (2024). 'In Situ Aerosol Size Spectra Measurements in the Austral Polar Vortex Before and After the Hunga Tonga-Hunga Ha'apai Volcanic Eruption'. *Geophys. Res. Lett.*, 51, e2024GL111388. DOI: 10.1029/2024gl111388.

Druckenmiller, M. L., R. L. Thoman, T. A. Moon, L. M. Andreassen, T. J. Ballinger, L. T. Berner, G. H. Bernhard, U. S. Bhatt, S. Bigalke, J. W. Bjerke et al. (2024). 'The Arctic'. *Bull. Am. Meteorol. Soc.*, 105, S277–S330. DOI: 10.1175/bams-d-24-0101.1.

Evan, S., J. Brioude, K. H. Rosenlof, R.-S. Gao, R. W. Portmann, Y. Zhu, R. Volkamer, C. F. Lee, J.-M. Metzger, K. Lamy et al. (2023). 'Rapid ozone depletion after humidification of the stratosphere by the Hunga Tonga eruption'. *Science*, 382, eadg2551. DOI: 10.1126/science.adg2551.

Fahey, D. W., S. R. Kawa, E. L. Woodbridge, P. Tin, J. C. Wilson, H. H. Jonsson, J. E. Dye, D. Baumgardner, S. Borrmann, D. W. Toohey et al. (1993). 'In situ measurements constraining the role of sulphate aerosols in mid-latitude ozone depletion'. *Nature*, 363, pp. 509–514. DOI: 10.1038/363509a0.

Fleming, E. L., P. A. Newman, Q. Liang and L. D. Oman (2024). 'Stratospheric Temperature and Ozone Impacts of the Hunga Tonga-Hunga Ha'apai Water Vapor Injection'. *J. Geophys. Res.*, 129, e2023JD039298. DOI: 10.1029/2023jd039298.

Frith, S. M., N. A. Kramarova, R. S. Stolarski, R. D. McPeters, P. K. Bhartia and G. J. Labow (2014). 'Recent changes in total column ozone based on the SBUV Version 8.6 Merged Ozone Data Set'. *J. Geophys. Res.*, 119, pp. 9735–9751. DOI: 10.1002/2014jd021889.

Frith, S. M., R. S. Stolarski, N. A. Kramarova and R. D. McPeters (2017). 'Estimating uncertainties in the SBUV Version 8.6 merged profile ozone data set'. *Atmos. Chem. Phys.*, 17, pp. 14695–14707. DOI: 10.5194/acp-17-14695-2017.

Godin-Beekmann, S., N. Azouz, V. F. Sofieva, D. Hubert, I. Petropavlovskikh, P. Effertz, G. Ancellet, D. A. Degenstein, D. Zawada, L. Froidevaux et al. (2022). 'Updated trends of the stratospheric ozone vertical distribution in the 60°S–60°N latitude range based on the LOTUS regression model'. *Atmos. Chem. Phys.*, 22, pp. 11657–11673. DOI: 10.5194/acp-22-11657-2022.

Junge, C. E., C. W. Chagnon and J. E. Manson (1961). 'Stratospheric aerosols'. *J. Atmos. Sci.*, 18, pp. 81–108. DOI: 10.1175/1520-0469(1961)018<0081:sa>2.0.co;2.

Khaykin, S., A. Podglajen, F. Ploeger, J.-U. Grooß, F. Tence, S. Bekki, K. Khlopenkov, K. Bedka, L. Rieger, A. Baron et al. (2022). 'Global perturbation of stratospheric water and aerosol burden by Hunga eruption'. *Commun. Earth Environ.*, 3, 316. DOI: 10.1038/s43247-022-00652-x.

Kinnison, D. E., K. E. Grant, P. S. Connell, D. A. Rotman and D. J. Wuebbles (1994). 'The chemical and radiative effects of the Mount Pinatubo eruption'. *J. Geophys. Res.*, 99, pp. 25705–25731. DOI: 10.1029/94jd02318.

Kramarova, N. A., P. A. Newman, L. R. Lait, B. Johnson, M. Pitts, M. L. Santee, I. Petropavlovskikh, L. Coy and J. De Laat (2024). '2023 Antarctic ozone hole [in "State of the Climate in 2023"]'. *Bull. Amer. Meteor. Soc.*, 105, S358–S361. DOI: 10.1175/BAMS-D-24-0099.1.

Kuchar, A., T. Sukhodolov, G. Chiodo, A. Jörimann, J. Kult-Herdin, E. Rozanov and H. H. Rieder (2025). 'Modulation of the northern polar vortex by the Hunga Tonga–Hunga Ha'apai eruption and the associated surface response'. *Atmos. Chem. Phys.*, 25, pp. 3623–3634. DOI: 10.5194/acp-25-3623-2025.

Lawrence, Z. D., G. L. Manney and K. Wargan (2018). 'Reanalysis intercomparisons of stratospheric polar processing diagnostics'. *Atmos. Chem. Phys.*, 18,

pp. 13547–13579. DOI: 10.5194/acp-18-13547-2018.

Lecours, M., C. D. Boone and P. F. Bernath (2024). 'Antarctic Polar Stratospheric Cloud Analysis of ACE-FTS Data From 2005 to 2023'. *J. Geophys. Res.*, 129, e2024JD040990. DOI: 10.1029/2024jd040990.

Lee, S. H., A. H. Butler and G. L. Manney (2024). 'Two major sudden stratospheric warmings during winter 2023/2024'. *Weather*, 80, pp. 45–53. DOI: 10.1002/wea.7656.

Manney, G. L., M. L. Santee, A. Lambert, L. F. Millán, K. Minschwaner, F. Werner, Z. D. Lawrence, W. G. Read, N. J. Livesey and T. Wang (2023). 'Siege in the Southern Stratosphere: Hunga Tonga-Hunga Ha'apai Water Vapor Excluded From the 2022 Antarctic Polar Vortex'. *Geophys. Res. Lett.*, 50. DOI: 10.1029/2023gl103855.

Millán, L., W. G. Read, M. L. Santee, A. Lambert, G. L. Manney, J. L. Neu, M. C. Pitts, F. Werner, N. J. Livesey and M. J. Schwartz (2024). 'The Evolution of the Hunga Hydration in a Moistening Stratosphere'. *Geophys. Res. Lett.*, 51, e2024GL110841. DOI: 10.1029/2024gl110841.

Millán, L., M. L. Santee, A. Lambert, N. J. Livesey, F. Werner, M. J. Schwartz, H. C. Pumphrey, G. L. Manney, Y. Wang, H. Su et al. (2022). 'The Hunga Tonga-Hunga Ha'apai Hydration of the Stratosphere'. *Geophys. Res. Lett.*, 49, e2022GL099381. DOI: 10.1029/2022gl099381.

Nedoluha, G. E., R. M. Gomez, I. Boyd, H. Neal, D. R. Allen, A. Parrish, B. J. Connor and D. E. Siskind (2025). 'Measurements of Stratospheric ClO From Mauna Kea: 1992–2023'. *J. Geophys. Res.*, 130, e2024JD041848. DOI: 10.1029/2024jd041848.

Newman, P. A., L. R. Lait, N. A. Kramarova, L. Coy, S. M. Frith, L. D. Oman and S. S. Dhomse (2024). 'Record High March 2024 Arctic Total Column Ozone'. *Geophys. Res. Lett.*, 51, e2024GL110924. DOI: 10.1029/2024gl110924.

Santee, M. L., A. Lambert, L. Froidevaux, G. L. Manney, M. J. Schwartz, L. F. Millán, N. J. Livesey, W. G. Read, F. Werner and R. A. Fuller (2023). 'Strong Evidence of Heterogeneous Processing on Stratospheric Sulfate Aerosol in the Extrapolar Southern Hemisphere Following the 2022 Hunga Tonga-Hunga Ha'apai Eruption'. *J. Geophys. Res.*, 128, e2023JD039169. DOI: 10.1029/2023jd039169.

Santee, M. L., A. Lambert, G. L. Manney, N. J. Livesey, L. Froidevaux, J. L. Neu, M. J. Schwartz, L. F. Millán, F. Werner, W. G. Read et al. (2022). 'Prolonged and Pervasive Perturbations in the Composition of the Southern Hemisphere Midlatitude Lower Stratosphere From the Australian New Year's Fires'. *Geophys. Res. Lett.*, 49, e2021GL096270. DOI: 10.1029/2021gl096270.

Santee, M. L., G. L. Manney, A. Lambert, L. F. Millán, N. J. Livesey, M. C. Pitts, L. Froidevaux, W. G. Read and R. A. Fuller (2024). 'The Influence of Stratospheric Hydration From the Hunga Eruption on Chemical Processing in the 2023 Antarctic Vortex'. *J. Geophys. Res.*, 129, e2023JD040687. DOI: 10.1029/2023jd040687.

Schoeberl, M. R., M. Toohey, Y. Wang and R. Ueyama (2025). 'Stratospheric Injection Lifetimes'. *J. Geophys. Res.*, 130, e2025JD043928. DOI: 10.1029/2025jd043928.

Schoeberl, M. R., Y. Wang, R. Ueyama, G. Taha, E. Jensen and W. Yu (2022). 'Analysis and Impact of the Hunga Tonga-Hunga Ha'apai Stratospheric Water Vapor Plume'. *Geophys. Res. Lett.*, 49, e2022GL100248. DOI: 10.1029/2022gl100248.

Smale, D., M. P. Chipperfield, R. Querel, G. E. Nedoluha, U. Frieß, J. Robinson, S. Nichol, S. Heddell, W. Feng, R. M. Gomez et al. (2025). 'The impact of the Hunga Tonga-Hunga Ha'apai volcanic eruption on the 2023 Antarctic Ozone hole, as observed from Arrival Heights, Antarctica'. *J. Atmos. Chem.*, 82. DOI: 10.1007/s10874-025-09478-1.

Solomon, S. (1999). 'Stratospheric ozone depletion: A review of concepts and history'. *Rev. Geophys.*, 37, pp. 275–316. DOI: 10.1029/1999rg900008.

Solomon, S., K. Stone, P. Yu, D. M. Murphy, D. Kinnison, A. R. Ravishankara and P. Wang (2023). 'Chlorine activation and enhanced ozone depletion induced by wildfire aerosol'. *Nature*, 615, pp. 259–264. DOI: 10.1038/s41586-022-05683-0.

Strahan, S. E., D. Smale, S. Solomon, G. Taha, M. R. Damon, S. D. Steenrod, N. Jones, B. Liley, R. Querel and J. Robinson (2022). 'Unexpected repartitioning of stratospheric inorganic chlorine after the 2020 Australian wildfires'. *Geophys. Res. Lett.*, 49, e2022GL098290. DOI: 10.1029/2022GL098290.

Taha, G., R. Loughman, P. R. Colarco, T. Zhu, L. W. Thomason and G. Jaross (2022). 'Tracking the 2022 Hunga Tonga-Hunga Ha'apai Aerosol Cloud in the Upper and Middle Stratosphere Using Space-Based Observations'. *Geophys. Res. Lett.*, 49, e2022GL100091. DOI: 10.1029/2022gl100091.

Tritscher, I., M. C. Pitts, L. R. Poole, S. P. Alexander, F. Cairo, M. P. Chipperfield, J.-U. Grooß, M. Höpfner, A. Lambert, B. Luo et al. (2021). 'Polar Stratospheric Clouds: Satellite Observations, Processes,

and Role in Ozone Depletion'. *Rev. Geophys.*, 59, e2020RG000702. DOI: 10.1029/2020rg000702.

Van Eaton, A. R., J. Lapierre, S. A. Behnke, C. Vagasky, C. J. Schultz, M. Pavolonis, K. Bedka and K. Khlopenkov (2023). 'Lightning Rings and Gravity Waves: Insights Into the Giant Eruption Plume From Tonga's Hunga Volcano on 15 January 2022'. *Geophys. Res. Lett.*, 50, e2022GL102341. DOI: 10.1029/2022gl102341.

Wang, X., W. Randel, Y. Zhu, S. Tilmes, J. Starr, W. Yu, R. Garcia, O. B. Toon, M. Park, D. Kinnison et al. (2023). 'Stratospheric Climate Anomalies and Ozone Loss Caused by the Hunga Tonga-Hunga Ha'apai Volcanic Eruption'. *J. Geophys. Res.*, 128, e2023JD039480. DOI: 10.1029/2023jd039480.

Wargan, K., G. L. Manney and N. J. Livesey (2025). 'Factors Contributing to the Unusually Low Antarctic Springtime Ozone in 2020–2023'. *J. Geophys. Res.*, 130, e2025JD043621. DOI: 10.1029/2025jd043621.

Weber, M., W. Steinbrecht, C. Arosio, R. van der A, S. Frith, J. Anderson, L. Ciasto, M. Coldewey-Egbers, S. Davis, D. Degenstein et al. (2024). 'Stratospheric ozone [in "State of the Climate in 2023"]'. *Bull. Amer. Meteor. Soc.*, 105, S99–S100. DOI: 10.1175/BAMS-D-24-0116.1.

Wilmouth, D. M., F. F. Østerstrøm, J. B. Smith, J. G. Anderson and R. J. Salawitch (2023). 'Impact of the Hunga Tonga volcanic eruption on stratospheric composition'. *Proc. Natl. Acad. Sci.*, 120, e2301994120. DOI: 10.1073/pnas.2301994120.

Wohltmann, I., M. L. Santee, G. L. Manney and L. F. Millán (2024). 'The Chemical Effect of Increased Water Vapor From the Hunga Tonga-Hunga Ha'apai Eruption on the Antarctic Ozone Hole'. *Geophys. Res. Lett.*, 51, e2023GL106980. DOI: 10.1029/2023gl106980.

World Meteorological Organization (WMO) (2022). *Scientific Assessment of Ozone Depletion: 2022*. Tech. rep. GAW Report No. 278. Geneva, Switzerland.

Zhang, J., D. Kinnison, Y. Zhu, X. Wang, S. Tilmes, K. Dube and W. Randel (2024a). 'Chemistry Contribution to Stratospheric Ozone Depletion After the Unprecedented Water-Rich Hunga Tonga Eruption'. *Geophys. Res. Lett.*, 51, e2023GL105762. DOI: 10.1029/2023gl105762.

Zhang, J., P. Wang, D. Kinnison, S. Solomon, J. Guan, K. Stone and Y. Zhu (2024b). 'Stratospheric Chlorine Processing After the Unprecedented Hunga Tonga Eruption'. *Geophys. Res. Lett.*, 51, e2024GL108649. DOI: 10.1029/2024gl108649.

Zhou, X., Q. Chen, W. Feng, S. Heddell, S. S. Dhomse, G. Mann, H. C. Pumphrey, L. Millán, M. L. Santee and M. P. Chipperfield (2025). 'When will the stratospheric water vapour return to pre-Hunga level?' *Commun. Earth Environ.*, submitted, manuscript COMMSENV-25-4119-T.

Zhou, X., S. S. Dhomse, W. Feng, G. Mann, S. Heddell, H. Pumphrey, B. J. Kerridge, B. Latter, R. Siddans, L. Ventress et al. (2024). 'Antarctic Vortex Dehydration in 2023 as a Substantial Removal Pathway for Hunga Tonga-Hunga Ha'apai Water Vapor'. *Geophys. Res. Lett.*, 51, e2023GL107630. DOI: 10.1029/2023gl107630.

Zhu, Y., C. G. Bardeen, S. Tilmes, M. J. Mills, X. Wang, V. L. Harvey, G. Taha, D. Kinnison, R. W. Portmann, P. Yu et al. (2022). 'Perturbations in stratospheric aerosol evolution due to the water-rich plume of the 2022 Hunga-Tonga eruption'. *Commun. Earth Environ.*, 3, 248. DOI: 10.1038/s43247-022-00580-w.

Zhu, Y., R. W. Portmann, D. Kinnison, O. B. Toon, L. Millán, J. Zhang, H. Vömel, S. Tilmes, C. G. Bardeen, X. Wang et al. (2023). 'Stratospheric ozone depletion inside the volcanic plume shortly after the 2022 Hunga Tonga eruption'. *Atmos. Chem. Phys.*, 23, pp. 13355–13367. DOI: 10.5194/acp-23-13355-2023.

Zhuo, Z., X. Wang, Y. Zhu, W. Yu, E. M. Bednarz, E. Fleming, P. R. Colarco, S. Watanabe, D. Plummer, G. Stenchikov et al. (2025). 'Comparing multimodel ensemble simulations with observations and decadal projections of upper atmospheric variations following the Hunga eruption'. *Atmos. Chem. Phys.*, 25, pp. 13161–13176. DOI: 10.5194/acp-25-13161-2025.

Zi, Y., Z. Long, J. Sheng, G. Lu, W. Perrie and Z. Xiao (2025). 'The Sudden Stratospheric Warming Events in the Antarctic in 2024'. *Geophys. Res. Lett.*, 52, e2025GL115257. DOI: 10.1029/2025gl115257.

6 Upper stratosphere to thermosphere effects and H_2O transport in the deep Brewer-Dobson branch

Lead authors	Corwin Wright Jia Yue
Co-authors	Neil Hindley Jinhou Lei Luis F. Millán David Themens Sandra Wallis Wandi Yu
Contributing authors	Ewa M. Bednarz Eric Fleming Ruoxi Li David Plummer Simone Tilmes Xinyue Wang Jun Zhang Yunqian Zhu Zhihong Zhuo

Cite this as:

Wright, C., J. Yue et al. (2025): Upper stratosphere to thermosphere effects and H_2O transport in the deep Brewer-Dobson branch. In APARC, 2025: The Hunga Eruption Atmospheric Impacts Report [Yunqian Zhu, Graham Mann, Paul A. Newman, William Randel (Eds.)]. APARC Report No. 11, WCRP Report No. 10/2025, DOI: 10.34734/FZJ-2025-05243, available at `https://aparc-climate.org/publications/aparc-report-no-11/`.

Key points

- The Hunga eruption produced short-term gravity wave and Lamb wave responses unprecedented in the observational record which traversed the world for several days, reaching the top of the terrestrial atmosphere and with major impacts as high as the ionosphere-thermosphere system.
- Major ionospheric impacts were recorded which significantly advanced our understanding of TIDs, including some of the largest amplitude lower atmospherically-driven TIDs ever observed. Neutral atmospheric impacts were similarly dramatic and have significantly advanced our knowledge of wave propagation and dynamics in the stratosphere and above.
- Water vapour was initially injected into the stratosphere and by May 2023 was subsequently transported up to the mesosphere where a large fraction remains at time of writing. The vapour has been distributed globally since August 2023, and has had significant impacts on the dynamical and chemical state of the mesosphere.
- Models reproduce the observed water and ozone effects well. Mesospheric water vapour increased by ~3-4 Tg in 2023 via vertical transport from the stratosphere, while HOx chemistry led to depletion of mesospheric ozone. The resulting reduction in ozone shortwave heating and water vapour cooling led to a >1K temperature decrease in global mean mesospheric temperatures. Models however had much more difficulty reproducing the observed dynamical and temperature effects induced by stratospheric wind changes and gravity wave drag during 2022.
- Model simulations indicate that perturbations to mesospheric temperature, water vapour, and ozone concentrations are expected to persist beyond 2026. MLS observations substantiate model evidence that the maximum anomaly occurred in 2023, followed by a gradual decline. By 2027, the residual effects are likely to fall below statistical significance relative to climatological variability.

Contents

6.1 Introduction . . . 140
6.2 Short-term dynamical impacts on the middle atmosphere . . . 140
6.2.1 Stratosphere and mesosphere . . . 140
6.2.2 Impacts on the thermosphere . . . 142
6.3 Impacts on the ionosphere . . . 143
6.4 Water vapour transport in the middle and upper atmosphere . . . 144
6.5 Modelling of long-term middle-atmospheric impacts . . . 145
6.5.1 Overview . . . 145
6.5.2 Water vapour plume in the mesosphere . . . 145
6.5.3 Mesospheric cooling in 2023 . . . 147
6.5.4 Mesospheric circulation and temperature response in 2022 . . . 148
6.6 Summary . . . 149

Preamble

This chapter describes the impact of the Hunga eruption on Earth's upper-middle and upper atmosphere, from the upper stratosphere to the thermosphere-ionosphere system. The explosion and plume triggered both direct and indirect chemical, radiative and dynamical impacts on all these layers, providing a dramatic natural experiment elucidating many key aspects of their structure and dynamics. In the initial hours after the eruption, Lamb waves and acoustic-gravity waves penetrated deep into the upper atmosphere and were observed propagating at global scales through the ionosphere and thermosphere. The eruption simultaneously injected large volumes of water vapour into the stratosphere, and the upward transport and radiative effects of this water proved to be the longest-term impact in these atmospheric layers: leading to mesospheric cooling and ozone depletion. Dynamically, it also led to record-breaking warming over the extratropical southern hemisphere and cooling throughout the rest of the mesosphere during boreal summer 2022. Climate models have been able to reproduce these chemical and dynamic effects of water vapour, but with varying degrees of success. Based on these models, we believe that the residual effects of this injected water vapour are likely to fall below statistical significance relative to climatological variability by 2027.

6.1 Introduction

Above the stratosphere lies the Earth's upper atmosphere, consisting of the mesosphere and thermosphere. Due to incoming solar UV radiation, part of the thermosphere is ionised, a region known as the ionosphere.

Air densities in the upper atmosphere are extremely low, and consequently are often treated as part of space - indeed, objects in LEO, including the international space station, actually fly within the thermosphere. Simultaneously, radio wave communications and GNSS navigation rely on the propagation of electromagnetic signals through the ionosphere. As such, it is important to characterise and quantify the variability of the upper atmosphere as driven by Earth system sources such as the Hunga eruption.

A highly unusual feature of the Hunga eruption was that it penetrated deep into the middle and upper layers of the atmosphere, with the initial plume reaching 58 km in height, an altitude above the stratopause at this time of year and location (Proud et al., 2022). At this altitude the explosion and plume triggered both direct and indirect chemical, radiative and dynamical impacts on the middle and upper neutral atmosphere and on the charged ionosphere, which we discuss in this chapter.

Within the initial hours after the eruption, Lamb waves (Lamb, 1881) and acoustic-gravity waves penetrated deep into the upper atmosphere and were observed across the global ionosphere. These immediate effects, and their implications are discussed in Sections 6.2 and 6.3. The underlying mechanisms driving these thermospheric responses remain elusive and are an object of active research. We next consider the much longer timescale processes by which water vapour injected into the stratosphere reached the lower mesosphere, taking over a year to reach lower mesospheric altitudes via the slow progress of the global general circulation. This had concomitant impacts on the temperature structure and chemical composition of the upper atmosphere, which are discussed in Sections 6.4 and 6.5.

6.2 Short-term dynamical impacts on the middle atmosphere

As mentioned in Chapter 2, the initial eruption of Hunga triggered Lamb, acoustic and gravity waves which propagated in a period of hours from the surface to the upper thermosphere, coupling directly into the ionosphere (Wright et al., 2022; Matoza et al., 2022; Themens et al., 2022). Observations of these waves provide a dramatic demonstration of deep vertical coupling between atmospheric layers unique in the long-term satellite observational record, as well as a key scientific test for large parts of linear wave theory. In particular, this event represents the first time a Lamb wave has been observed in the middle and upper atmospheres by satellite.

6.2.1 Stratosphere and mesosphere

In the stratosphere and mesosphere, an extremely broad spectrum of waves was seen after the eruption, produced by generation mechanisms both immediate and also spread out over most of the day following the initial eruption.

The initial eruption immediately produced intense atmospheric waves which became visible in the stratospheric portion of the plume within 20 minutes of the eruption (Smart, 2022; Proud et al., 2022; Carr et al., 2022; Wright et al., 2022). The observed spectrum at these timescales was dominated by a single high-amplitude Lamb wave which propagated radially outwards from the eruptive centre with a phase

speed of ~318 m s^{-1}. This wave was present throughout the entire depth of the middle atmosphere. The Lamb wave rapidly propagated out of the plume but remained clearly visible in stratospheric radiance (i.e. emitted atmospheric radiant flux) measurements from a range of satellite platforms including AIRS, ATMS CIPS, CRIS, and IASI, and was tracked over a period of days as it propagated around the Earth multiple times (Ern et al., 2022; Wright et al., 2022; Lee et al., 2023; Zhou et al., 2023, Figure 6.1). During these multiple laps around the Earth, the wave showed no significant evidence of any dispersion. This 'primary' Lamb wave's propagation across the globe was almost entirely radial, but with deviations from a purely radial path consistent with the column-mean atmospheric state, large-scale winds and surface topography rather than the state at any specific height level (Inchin et al., 2023; Sepúlveda et al., 2023; Wright et al., 2022). At least two lower-amplitude Lamb waves were subsequently produced by later phases of the eruption, and were also observed propagating through the stratosphere at global scales (Wright et al., 2022). Along with the Lamb waves, a slower horizontal phase speed internal Pekeris wave, a resonance oscillation inherent to the Earth's atmosphere, was excited as a normal mode of the global atmosphere (Watanabe et al., 2022; Ohya et al., 2024).

The same initial eruptive burst that produced the first high-amplitude Lamb wave also produced internal gravity waves across a broad spectrum of horizontal wavelengths, all with extremely long vertical wavelengths of comparable depth to the homosphere (i.e. the layer of the atmosphere between the surface and 100 km where longer-lived atmospheric gases are well mixed; Liu et al., 2022; Ern et al., 2022; Wright et al., 2022). These waves propagated rapidly outwards at their upper-bound phase speed in a radial direction. On planetary scales, the waves separated out by horizontal wavelength as a result of fundamental physical limits on their horizontal phase speeds, which covered an extremely broad range from near-zero up to a "speed limit" of ~270 m s^{-1} (Wright et al., 2022). Within hours, a clear spatial gap was visible between the initial-burst Lamb waves and gravity waves, consistent with a theoretically-forbidden phase speed range between Lamb waves and gravity waves which had not previously been observed but which is consistent with linear wave theory (Figure 6.1). Gravity waves were subsequently generated by the plume over a period of hours, which propagated visibly across the entire Pacific basin but at slower speeds than the theoretical limit of the initial gravity wave burst emitted along with the initial Lamb wave. Despite their large amplitudes, these waves transferred very little momentum to the background, and no short-term impact was seen on stratospheric dynamics due to their passage (Wright et al., 2022). No significant evidence of these waves being refracted by the large-scale background winds was seen, likely due to their very high phase speed.

Globe-spanning gravity and Lamb waves are completely unprecedented in the satellite record from any source. For comparison, gravity waves generated by large-scale hurricanes typically dissipate within a few thousand kilometres at most (Wright, 2019), while waves refracted into the polar night jet streams travel shorter distances than this. The lack of observations of this type of wave could partly be due to the limited length of the data record, since satellite instruments of the types used to study the Hunga-produced atmospheric waves by e.g. Ern et al. (2022), Matoza et al. (2022), Wright et al. (2022) and Lee et al. (2023) have only been available since the 2000s, i.e. well after the 1991 Pinatubo eruption.

Ground-based data records of atmospheric waves observed by airglow imagers, radar and lidar extend back some decades with no evidence of similar wave activity. The lack of an atmospheric dataset record of such events is also consistent with long-term surface pressure measurements, which would be able to measure the surface aspect of a Lamb wave of the magnitude seen after the Hunga eruption. Such features have previously been seen in ionospheric data, e.g. by Liu et al. (1982) for the 1980 Mt. St. Helens eruption.

Smaller convective waves of the type seen at stratospheric and mesospheric levels in the plume have however been seen after previous volcanic eruptions, consistent with our broader knowledge of convective gravity wave physics. In particular, previous studies have discussed internal gravity waves seen in airglow after the smaller-magnitude La Soufriere (2021, VEI 4) and Calbuco (2015, VEI 4) eruptions (Miller et al., 2015; Yue et al., 2022). Retrospective analysis of AVHRR radiances measured during the 1991 eruption of Pinatubo carried out after the Hunga eruption also shows evidence of gravity wave phase fronts in the plume (Wright et al., 2022). It is thus likely that smaller gravity waves are generated in the plumes of many large volcanic eruptions, albeit with a much smaller magnitude and propagation range relative to those observed after the 2022 Hunga eruption (e.g. Wright

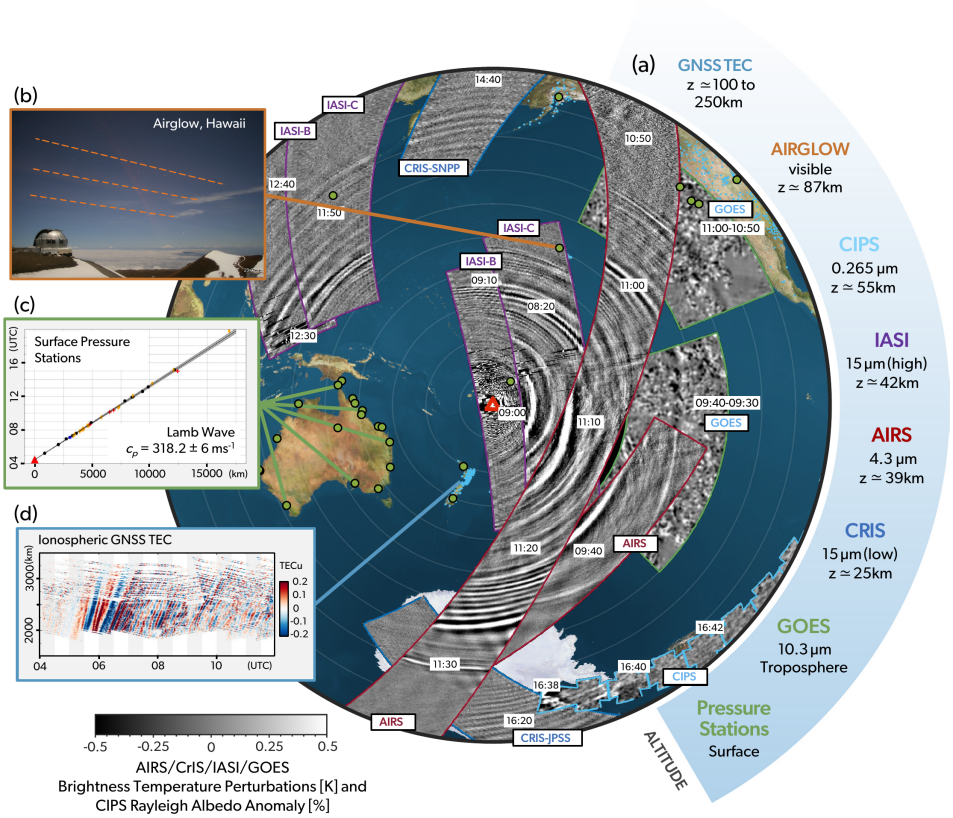

Figure 6.1: *Atmospheric waves from the initial eruption observed across the Pacific Ocean by a range of instruments. Coloured outlines of swaths identify each instrument using the key at right, with observation times overlaid in white boxes. Reproduced with minor modifications from Wright et al. (2022).*

et al., 2022). However, in contrast to Hunga, such wave activity seen in the stratosphere after previous 20th and 21st century eruptions has been significantly more spatially-localised, lower-amplitude and of shorter duration, and the waves have not propagated long distances from the initial eruptive source (e.g. Yue et al., 2022).

6.2.2 Impacts on the thermosphere

The Hunga-triggered atmospheric disturbances also reached above the middle atmosphere, extending as high as the upper thermosphere (Li et al., 2023a; Wright et al., 2022). These disturbances in turn coupled into the overlapping charged ionosphere, and we discuss these ionospheric impacts separately in Section 6.3 below.

In the neutral (i.e. uncharged) thermosphere, global-scale variations in wind and temperature associated with the Hunga eruption were captured by ICON-MIGHTI and GOLD (Aryal et al., 2023; Harding et al., 2022) and by methods including the MANGO network (Inchin et al., 2023) and hydroxyl airglow (Wright et al., 2022). Additionally, eruption-induced mesospheric local wind changes were also detected by ground-based meteor radars (Poblet et al., 2023; Stober et al., 2023). Furthermore, Li et al. (2023b) derived thermospheric mass densities from GRACE-FO (Landerer et al., 2020) satellite accelerometer data, and demonstrated the existence of globally-propagating post-eruption thermospheric waves and subsequent mass density redistributions. The underlying mechanisms driving these thermospheric responses remain elusive and are an object of active research.

Various physical models have been employed to elucidate the upper atmospheric reaction to the eruption (Huba et al., 2023; Liu et al., 2023; Wu et al., 2023; Vadas et al., 2023a; Vadas et al., 2023b). Liu et al. (2023) used WACCM-X to replicate the global propagation of the L0 and L1 modes (i.e. two leading-order modes) of the Lamb waves emitted in the initial eruption, and demonstrated consistency with ICON-MIGHTI wind observations in terms of wind perturbations, wavefront tilting, and propagation speeds. Moreover, a large observed wind perturbation along the northwest coast of South America coincided with the simulated L1 mode (Poblet et al., 2023; Chau et al., 2024).

Studies such as those of Vadas et al. (2023a) and Stober et al. (2023) and Stober et al. (2024) have instead argued for a significant role for 'secondary' gravity waves (i.e. gravity waves triggered within the atmospheric column due to the breakdown of other 'primary' waves from near-surface sources) instead of Lamb waves in generating the observed large-scale fluctuations in wind. Vadas et al. (2023a) employed the MESORAC to compute primary gravity waves, subsequently utilising the associated local body forces as input into the HIAMCM to simulate secondary gravity waves, with results aligning with far-field wind observations. However, the scarcity of thermospheric measurements makes it challenging to elucidate the primary energy transformation process from the eruption epicentre to a global scale, and the exact transfer mechanism thus remains an open question.

6.3 Impacts on the ionosphere

Waves generated in the thermosphere by the Hunga eruption generated a wide range of different waves in the ionosphere and produced a global-scale ionospheric response (Themens et al., 2022; Wright et al., 2022; Zhang et al., 2022). Ionospheric responses to the eruption included gravity wave-induced MSTIDs with wavelengths of tens to hundreds of kilometres and LSTIDs with wavelengths greater than a thousand kilometres, strong electrical currents, magnetically conjugate disturbances, and a deep ionospheric depletion near the location of the eruption.

MSTIDs were among the first documented features of the event, where waves in the ionosphere of similar scale and propagation characteristics to the gravity waves generated in the stratosphere and mesosphere were observed in ionospheric observations of the column integrated plasma density of the ionosphere, i.e. TEC (Themens et al., 2022; Wright et al., 2022; Zhang et al., 2022). MSTIDs were observed globally (Themens et al., 2022) across all continents (e.g., Asia: Li et al., 2023b; Europe: Verhulst et al., 2022; North America: Zhang et al., 2022; South America: Takahashi et al., 2023; Pacheco et al., 2024; Africa: Themens et al., 2022), and for several days following the eruption (Zhang et al., 2022).

The exact nature of the coupling mechanisms through which the gravity waves in the lower atmosphere generated waves in the thermosphere, and correspondingly in the ionosphere, is still a subject of extensive research. Themens et al. (2022) and Zhang et al. (2022) observed these TIDs propagating globally. However, studies such as Vadas et al. (2023a) and Vadas et al. (2023b) and Stober et al. (2023) and Stober et al. (2024) argue through both modelling and ionospheric and mesospheric observations, that these TIDs, as with the Lamb waves discussed above, are the result of secondary gravity waves generated by wave breaking in the mesosphere. Meanwhile, other modelling studies by (Wu et al., 2023; Liu et al., 2023; Miyoshi and Shinagawa, 2023) suggest Lamb waves as their origin, Ohya et al. (2024) discuss their relationship to Pekeris waves, and Inchin et al. (2023) highlight the diversity of potential mechanisms and the importance of the Hunga event as a natural laboratory for expanding our understanding of wave source processes, atmospheric gravity wave (AGW) propagation, and coupling across scales. To this end, the TIDs generated by the Hunga eruption are some of the most broadly modelled ionospheric responses to lower atmospheric external forcing, with studies carried out using WACCM-X (Liu et al., 2023), GAIA (Miyoshi and Shinagawa, 2023), grid-refined TIE-GCM (Wu et al., 2023), and SAMI3 coupled to HIAMCM and MESORAC (Huba et al., 2023; Vadas et al., 2023a; Vadas et al., 2023b).

In addition to MSTIDs, LSTIDs were also generated by the eruption and were observed both locally within a few thousand kilometres of the eruption (Themens et al., 2022; Wright et al., 2022; Zhang et al., 2022) and globally over North and South America (Figueiredo et al., 2023; Vadas et al., 2023b). Near the eruption, these LSTIDs had amplitudes of 3-8 TEC Units (TECU) depending on detrending scale and processing method (Zhang et al., 2022), making them some of the largest-amplitude lower atmospherically-driven TIDs ever observed. Ionosonde observations of the bottomside ionosphere also show LSTID variations in peak electron density of greater than 50% and variations in the height of the ionospheric peak by 100 to 150 km (Vadas et al., 2023b). Modelling by Vadas et al. (2023b) demonstrated good agreement with observations and suggests that these LSTIDs were directly caused by secondary gravity waves induced by the eruptive primary wave.

Waves generated locally by the eruption were also found to generate TIDs in the magnetically conjugate hemisphere, i.e. on the other end of the magnetic field lines where primary TIDs were observed, both broadly over Asia (Shinbori et al., 2022; Lin et al., 2022) and directly under the eruption's magnetic conjugate footprint near Hawaii (Themens et al., 2022). This resulted in TIDs appearing at these conjugate points nearly coincidently with their hemispheric counter-

parts and, in some cases, interfering with later arriving TIDs that propagate directly from the eruption (Themens et al., 2022).

In addition to the TIDs generated by this event, the eruption generated unprecedented electric field disturbances in the vicinity of the eruption (Gasque et al., 2022; Harding et al., 2022; Le et al., 2022; Yamazaki et al., 2022), observed through in situ satellite measurements by the Swarm satellites and by ground-based magnetometer observations. The large-scale ionospheric response also included the generation of a large ionospheric "hole" of up to 13 TECU near the eruption location that did not recover before sunset (Astafyeva et al., 2022; He et al., 2023; Choi et al., 2023). This plasma density depletion was coincident with a corresponding large thermospheric density depletion, but the relationship between these is still not fully understood (Li et al., 2023a). The work of Zettergren et al. (2017) would suggest that the ionospheric depletion may be the result of nonlinear, dissipating acoustic waves following the initial shock. While this work strongly correlates with the impact observed for this event, more modelling of this type for this event is necessary in order to conclusively attribute this mechanism as the cause of the depletion. This is particularly important given that Zettergren et al. (2017) only modelled waves generated through surface displacements, while this event also included substantial water vapour deposition in the stratosphere and lower mesosphere which could significantly change the nature and source of the waves at play in this case. There remain considerable opportunities for the modelling of the observed response to this event.

The TIDs and electric field disturbances generated by this event are observed (Aa et al., 2022a; Aa et al., 2022b; Carter et al., 2023; Rajesh et al., 2022; Pacheco et al., 2024; Shinbori et al., 2023) and modelled (Huba et al., 2023) to have seeded equatorial plasma bubbles of unprecedented scale (exceeding altitudes of ~1900 km), depth (exceeding 43 TECU), and resulting in GNSS positioning challenges over Australia (Carter et al., 2023).

The event also stimulated considerable interest in the use of the resulting ionospheric waves for monitoring and, potentially, warning against ensuing tsunamis (Han et al., 2023; Pradipta et al., 2023; Maletckii and Astafyeva, 2022). However, there remains considerable research required in order to translate these observations into actionable warnings or measurement techniques, as the relationship between ionospheric wave characteristics and the properties of tsunami waves remains uncertain (Ravanelli et al., 2023).

This event has served as a natural laboratory in which to test and push the boundaries of our understanding of TIDs, their generation, and atmosphere-ionosphere coupling as a whole. The collective observations and simulations of the ionospheric response to this eruption are unprecedented compared to any past seismological or meteorological events occurring in the lower atmosphere and the magnitude of the signature, observed the world over, made this event unique. This allowed this event to stimulate extensive discussions in the community on the nature of atmosphere-ionosphere coupling, with still-unknown outcomes and untested hypotheses, particularly related to the role of nonlinear and higher order wave dynamics in the observed ionospheric response, as well as related to the internal processes within TIDs (Klenzing et al., 2025). In the coming years, we may yet see studies of this event substantially advance our capacity to develop early warning systems for tsunamis, build better models of the ionosphere, and solve many of our outstanding questions related to how waves in the lower atmosphere drive ionospheric dynamics.

6.4 Water vapour transport in the middle and upper atmosphere

We now consider the effects of the eruption on middle- and upper-atmospheric water vapour, arguably the largest impact of Hunga on this large region of the neutral atmosphere. Evolution of the water vapor plume in the stratosphere is thoroughly discussed in Chapters 2 and 3, and we refer the reader there for further contextual details.

The initial eruption injected water vapour across the whole depth of the stratosphere, reaching directly into the lower mesosphere (Millán et al., 2022; Proud et al., 2022). The plume rapidly descended from this absolute peak, likely due to longwave radiative cooling of its upper part (Sellitto et al., 2022; Niemeier et al., 2023), and the majority settled between 20-40 hPa (approximately 20-30 km), i.e. in the lower stratosphere, where it remained for several months (Millán et al., 2022; Legras et al., 2022; Niemeier et al., 2023). Thus, the initial injection did not affect the mesosphere.

Hunga-hydrated air re-entered the mesosphere 16 months after the eruption in May 2023 (Figure 6.2a,j), where it split into northward and southward branches, consistent with transport via the climatological Brewer Dobson Circulation. By June 2023 (Figure 6.2b), it reached into the northern tropical lower mesosphere, and by August 2023 (Figure 6.2c)

blanketed the entire lower mesosphere in the southern hemisphere and most of the northern hemisphere. By the beginning of 2024, i.e. two years after the eruption (Figure 6.2f), the vapour was almost entirely absent from the tropical stratosphere, displaced by dryer air entering through the tropical tropopause. At higher altitudes however, the vapour had expanded through much of the lower mesosphere, reaching maximal altitudes of 0.07 hPa at southern high latitudes (Nedoluha et al., 2024; Millán et al., 2024). In the following months, i.e. the beginning and middle of 2024 (Figures 6.2g–6.2i), the additional vapour oscillated between the Northern and Southern Hemispheres in response to the mesospheric general circulation.

Figure 6.3a,b contextualises the additional water vapour introduced into the middle and upper atmosphere by showing the observed annual cycle of near-global (82°S-82°N) mesospheric water vapour mass over the 20+ years of the Microwave Limb Sounder (MLS) record, with post-2022 data highlighted. Independently of the Hunga eruption, we see elevated water vapour mass in late 2022 and early 2023 which arises partly due to dynamical conditions that enhanced methane oxidation and increased water vapour (Nedoluha et al., 2023). Despite this, the impact of the Hunga eruption is clearly visible from May 2023, when the mesospheric water vapour burden jumped from 23 to 26 Tg in just 3 months, up to 4 Tg above climatological values. These anomalously moist mesospheric conditions led in turn to an unprecedentedly low global mesospheric ozone burden beginning around August 2023 and lasting until June 2024 (Figure 6.3c,d), which may have been driven, at least in part, by the impact of the additional humidity on the HOx catalytic cycles (e.g., Brasseur and Solomon, 2005; Randel et al., 2024). The evolution of global mid-mesospheric (0.1 hPa) temperatures has remained within the climatological range, except in October 2023 and a few days in August 2023 and February 2024 (Figure 6.3e,f), when the values in the MLS record were marginally cooler by about 1 K than in previous years. Randel et al. (2024) argue that this cooling was mostly caused by the low ozone burden associated with HOx chemistry from the elevated water vapor values and the water vapour related cooling.

PMCs or noctilucent clouds form in the polar mesopause summer when ambient temperatures drop below 150 K and water vapour is saturated. The first sighting of noctilucent clouds was reported 2 years after the 1883 Krakatau volcanic eruption (VEI 6) (Leslie, 1885). After the 2022 Hunga eruption, no clear response in PMCs occurrence frequency was detected from OMPS-LP measurements during the 2023/2024 and 2024 season. Although a 1 ppmv water vapour anomaly reached the polar summer mesopause in the Northern Hemisphere during 2024, ice particle formation may have been hindered by anomalous warming (Wallis et al., 2025).

6.5 Modelling of long-term middle-atmospheric impacts

6.5.1 Overview

Climate models are a vital tool to help understand and describe the dynamical and chemical response to the Hunga volcanic eruption. As such, the Hunga volcanic eruption is an excellent natural testbed for general model performance, and careful interpretation of the results could provide vital guidance on how to improve such models.

In this section, we describe the upper-atmospheric results of the Hunga Tonga-Hunga Ha'Pai Model Observations Comparison (HTHH-MOC, Zhu et al., 2025), experiment 1. We include only models which have a fully-resolved mesosphere, i.e. WACCM6/MAM (Mills et al., 2016; Zhu et al., 2022), GSFC2D (Fleming et al., 2020; Fleming et al., 2024), and CMAM (Jonsson et al., 2004; Scinocca et al., 2008). WACCM has both required fixed-SST and additional optional coupled ocean settings, with 30 ensemble members and both H_2O and SO_2 injection in the two settings. CMAM has 10 ensemble members with fixed SST fields and with H_2O injection only. GSFC2D has 10 ensemble members with fixed SST fields and with H_2O injection only for 5 years, and additional 20 ensemble members with both H_2O and SO_2 injection but runs 2 years. We use the GSFC2D H2O only ensemble to check the long-term evaluation of the field in Section 6.5.2 and 6.5.3, and use the H_2O and SO_2 ensemble to check the dynamics response in Section 6.5.4. More details of HTHH-MOC data analysis related to Chapter 6 can be found in Supplementary S3 PartS3.5.

6.5.2 Water vapour plume in the mesosphere

The multi-model mean of the runs clearly shows evidence of the Hunga-injected water vapour plume starting to enter the mesosphere following the eruption. The water vapour burden anomaly reached 2 Tg by May 2023, with a maximum of 3.30 Tg reached in November 2023. For context, Feofilov et al. (2009) estimate the normal mesospheric water vapour burden as between 1 hPa and 0.01 hPa as lying in the

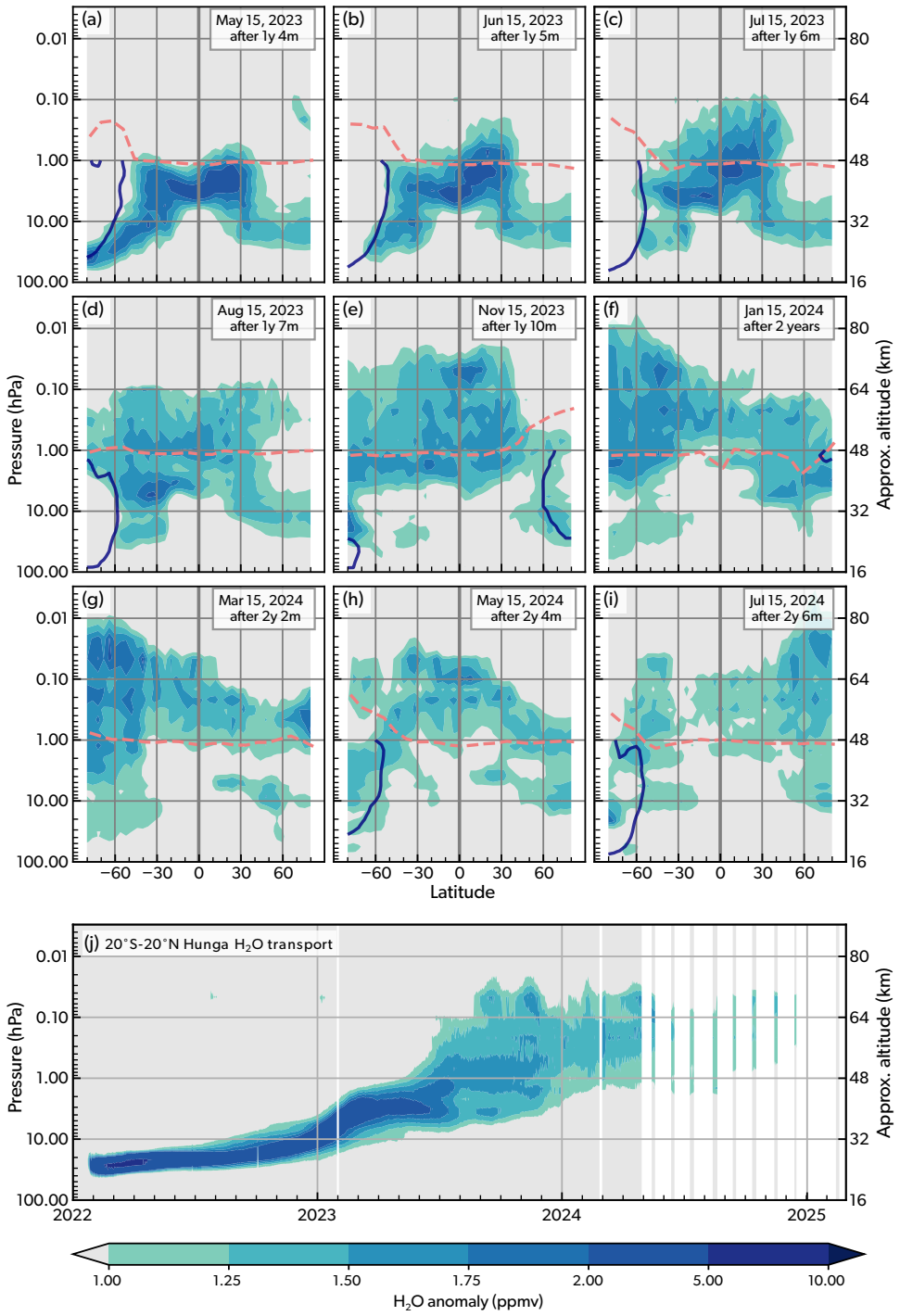

Figure 6.2: *(a–i) Daily zonal-mean water vapour anomalies measured by MLS relative to the 2005–2021 climatology for each day. The stratopause, as determined from MLS temperature measurements, is represented by dashed pink lines. Dark blue lines show contours of scaled potential vorticity (see, e.g., Dunkerton and Delisi, 1986; Manney et al., 1994) approximating the stratospheric polar vortex edge region. Adapted from Millán et al. (2024). (j) Zonal-mean tropical (20°S–20°N) anomalies displaying the Hunga transport through the Brewer–Dobson circulation, demonstrating that water vapour injected by the plume reached the mesosphere (i.e., ~1 hPa) around May 2023.*

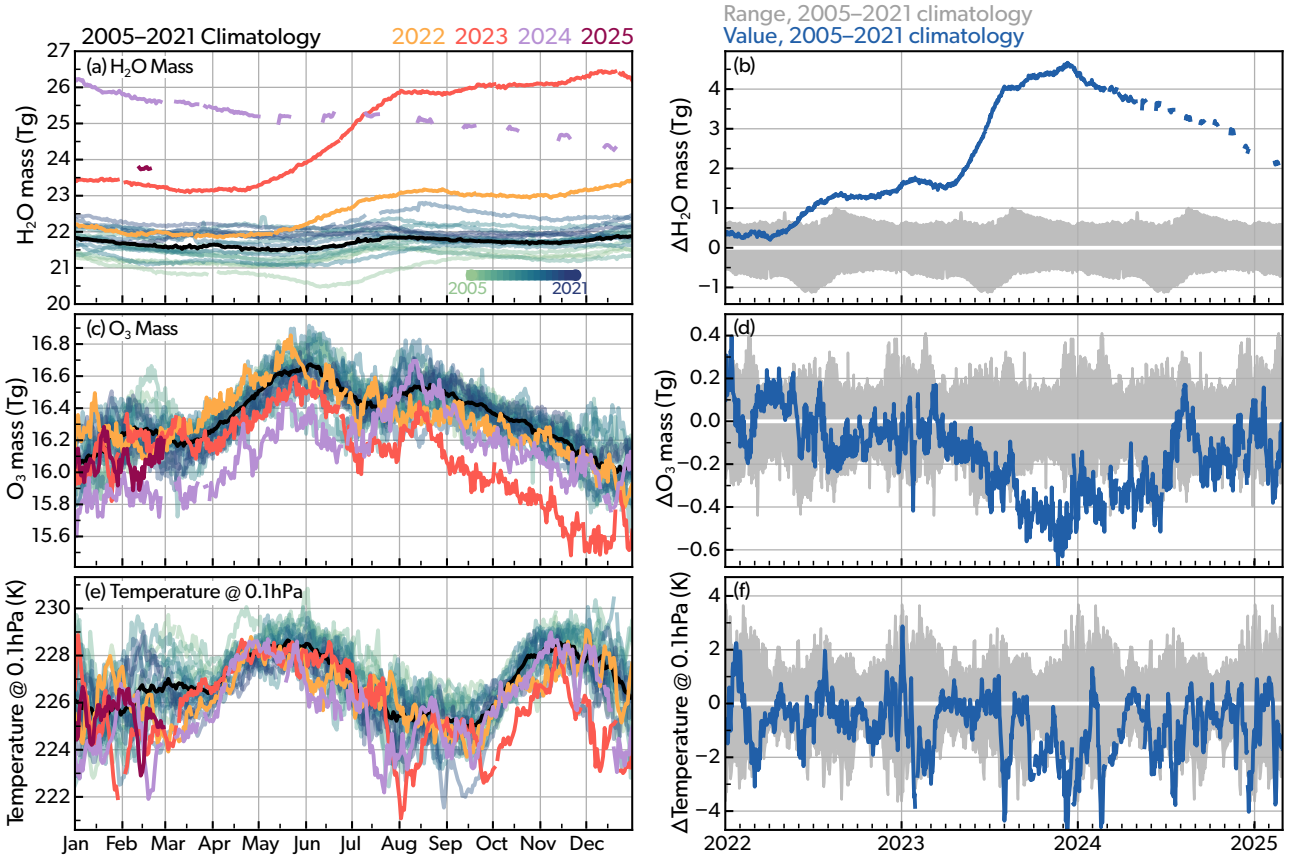

Figure 6.3: *MLS-derived estimates (left side) of the evolution of the (a) global [82°S-82°N] mesospheric [1–0.01 hPa] water vapour burden, (c) global mesospheric ozone burden, (e) mid-mesospheric [0.1 hPa] temperature. The right side shows the same variables, but with the annual cycle removed.*

range 17–21 Tg, and thus this represents an 16% increase in the total mesospheric water vapour burden (Figure 6.4a). This multi-model mean is reasonably comparable to but lower than the anomaly calculated from MLS (Figure 6.4a; cf. Section 6.4). From November 2023 the injected water vapour began to descend, and by the end of 2026, 0.63 Tg of injected water vapour remained in the mesosphere, accounting for 3% of the total mesospheric water vapour burden (Figure 6.4a).

In general, the model results exhibit only relatively small variations in the water vapour plume and match observations well (Figure 6.4a). GSFC2D shows the highest water vapour burden anomaly at 4.07 Tg, with the other models' maximum water vapour burden lying in the range 3.1-3.3 Tg. When interpreting these results, it is important to remember that the water vapour burden anomaly as calculated from the models is defined as the difference between the volcanic and control runs, while for the observations it is defined as the difference from climatology and thus includes natural variability. In temporal terms, the maximum water vapour burden in the GSFC2D ocean run agrees well with the observations and with the multi model mean, 1-2 months early in WACCM and multi-model mean, and 3-4. All models predict a water vapour burden anomaly lower than 1 Tg by the end of 2026.

6.5.3 Mesospheric cooling in 2023

The water vapour plume had a net radiative cooling effect (cross cf. Chapter 4). Additionally, in 2023 after the Hunga-associated water vapour entered the mesosphere, additional HOx reactions led to the depletion of mesospheric ozone, which combined with the water vapour related cooling to produce a >1 K decrease in the global mean mesospheric temperature (Randel et al., 2024).

Our model results are consistent with the changes of ozone and temperature described by Randel et al. (2024). The multi-model-mean global-mean ozone burden started to significantly decrease in 2023 after the water vapour plume entered the mesosphere, and almost simultaneously the mesospheric temperature began to decrease in response to the ozone depletion (Figure 6.5). In general, all models capture the cooling and the ozone depletion, and the model-to-model

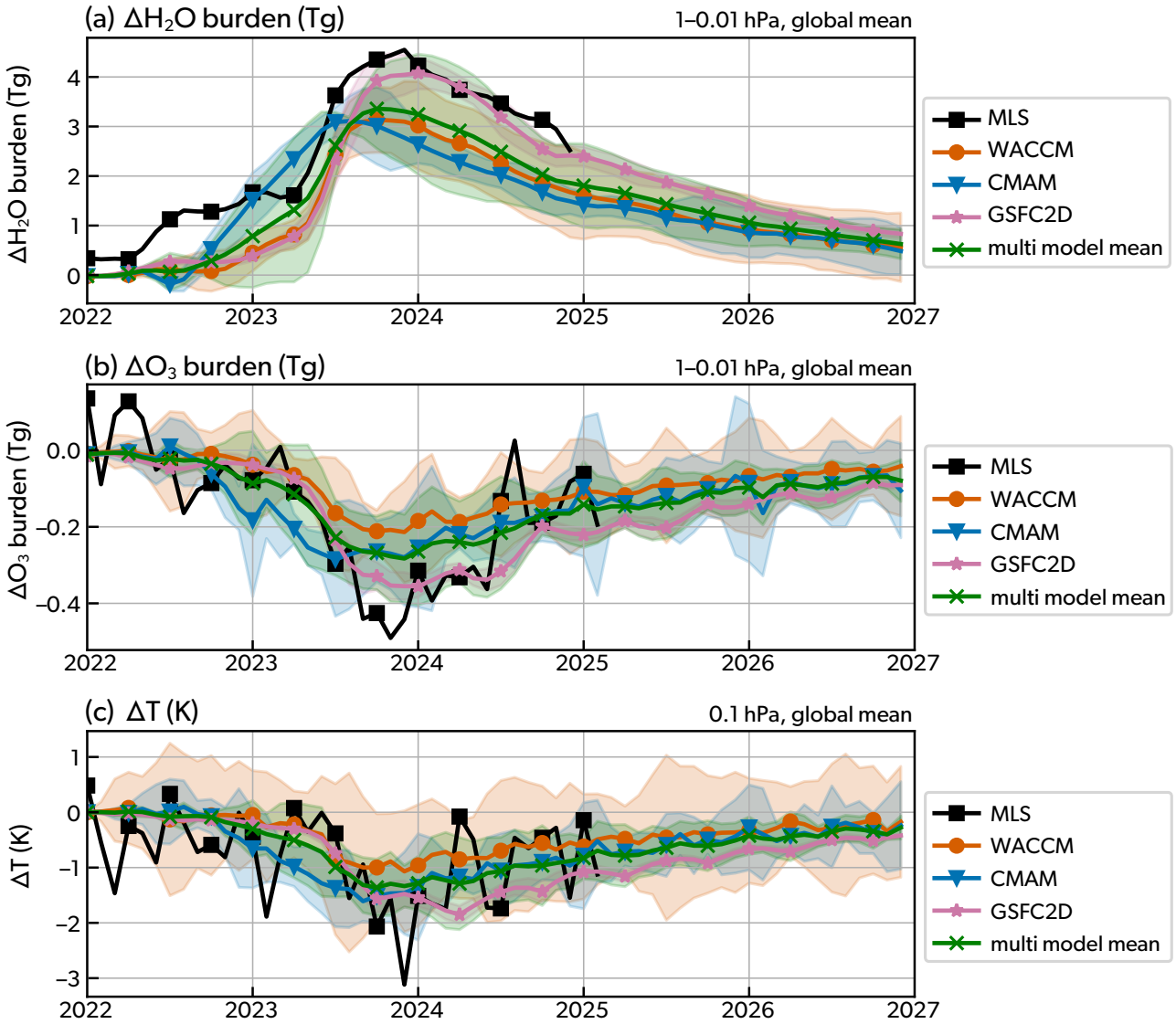

Figure 6.4: *Anomalies of (a) mesospheric water vapor burden, (b) mesospheric ozone burden, and (c) 0.1 hPa global mean temperature, observed by (black with square markers) MLS, and as differences between the volcanic case(H_2O & SO_2 in WACCM, or H_2O only in CMAM and GSFC2D) and the control case in the (red with round markers) WACCM, (blue with triangle markers) CMAM, and (pink with star markers) GSFC2D models, and as (green with cross markers) a multi model mean. Shading denotes the range within 1 standard deviation of the mean.*

variation of ozone follows the variation of the water vapour burden in the models (Figure 6.4b).

6.5.4 Mesospheric circulation and temperature response in 2022

One of the most important mesospheric responses to the Hunga volcanic eruption was a large change in temperature. This was observed by the Sounding of the Atmosphere using Broadband Emission Radiometry (SABER) instrument during boreal summer 2022, which saw record-breaking warming over the southern hemisphere extra tropics and cooling throughout of the rest parts of the mesosphere (Yu et al., 2023, Figure 6.6a). Results from WACCM suggest that this was a response to the record-breaking stronger stratospheric westerlies after the eruption (cross cf. Chapter 4). These stronger stratospheric westerlies enhanced westward gravity wave drag in the mesosphere, resulting in a 20% stronger mesospheric meridional circulation, and corresponding record-breaking temperature variations (Yu et al., 2023). This temperature response in 2022 was an indirect impact of Hunga's dynamically-driven water injection, as it occurred prior to the appearance of water anomalies in the mesosphere in 2023.

However, it has turned out to be technically challenging to reproduce this dynamical process in models. The response in this model is statistically significant

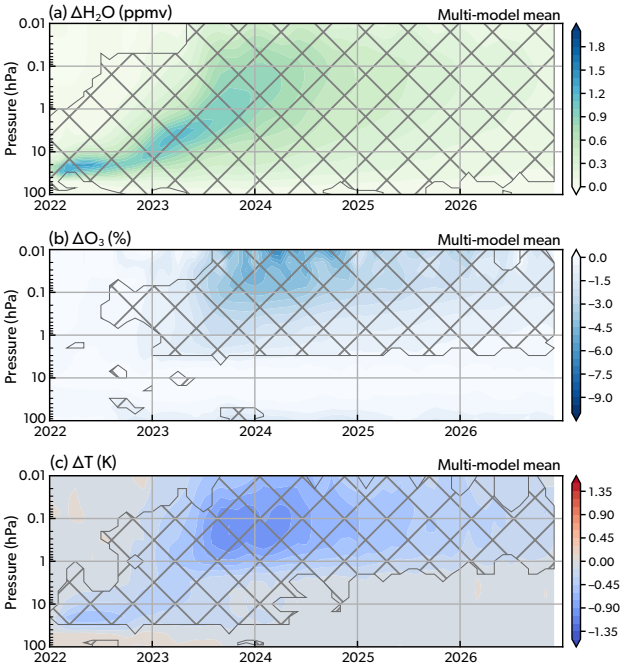

Figure 6.5: *Multi-model mean global differences in (a) water vapour (ppmv), (b) ozone (in percentage), and (c) temperature (K) between the volcanic case (H_2O and SO_2 in WACCM, or H_2O only in CMAM and GSFC2D) and the control case. Areas with hatching indicate statistically significant differences.*

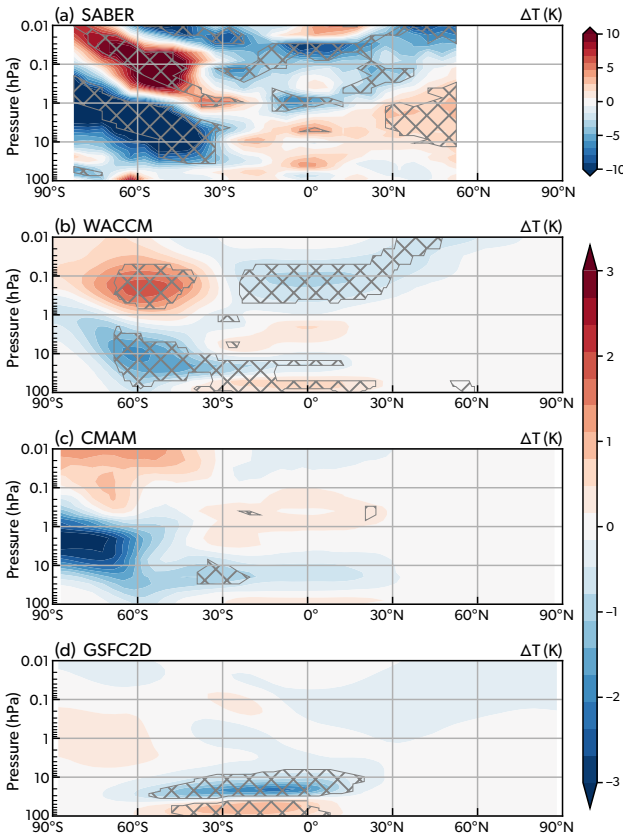

Figure 6.6: *Zonal mean temperature differences between the volcanic case (H_2O and SO_2 in WACCM and GSFC2D, or H_2O only in CMAM) and the control case in July-August 2022, (a) as observed by SABER and adapted from Yu et al. (2023), and as simulated in the (b) WACCM, (c) CMAM, and (d) GSFC2D models. Areas with hatching indicate statistically significant differences.*

in the WACCM, which has 60 ensemble members that can better disentangle the Hunga dynamics forcing and the internal variability. However, the magnitude of the response of WACCM is much smaller than the observed anomaly. It is of correct sign but not significant in CMAM, with almost no response seen in GSFC2D. The very small response in GSFC2D is likely due to concomitantly small internal variability, as dynamical responses in the model are driven by a combination of radiative forcing and tropospheric planetary and gravity wave forcing which are the same for the control and Hunga perturbation simulations. The resulting circulation and dynamically induced temperature responses are weak compared to 3D models which have much larger internal variability. These unpromising model simulation results are consistent with the idea that the response was to some degree stochastic in nature (Yu et al., 2023).

6.6 Summary

The Hunga eruption of 2022 had profound short-term dynamical impacts on the middle and upper atmosphere. The initial explosion triggered a complex array of Lamb, acoustic, and gravity waves that propagated rapidly from the surface to the thermosphere and ionosphere and transversed the globe several times, demonstrating strong and direct dynamical coupling across the depth of the atmosphere. The eruption's short- and long-term influences extended into both the neutral thermosphere and charged ionosphere, generating disturbances including MSTIDs and LSTIDs and causing significant ionospheric depletion and electric field disturbances. MSTIDs were also observed in the magnetic conjugate location to the eruptive wave release (Lin et al., 2022). These effects highlight the complex coupling mechanisms between atmospheric layers and the geomagnetic environment and may have important research implications for applied topics such as tsunami warning systems as well as into fundamental aspects of atmospheric science theory.

Chemically, the eruption injected substantial water vapour into the stratosphere, which was then transported into the mesosphere during 2023 via the

Brewer-Dobson circulation, leading to mesospheric cooling and ozone depletion via HOx chemistry and radiative processes. Dynamically, the Hunga eruption caused strong stratospheric westerlies in 2022 and enhanced westward gravity wave drag in the mesosphere, leading to record-breaking warming over the Southern hemisphere extra tropics and cooling throughout the rest of the mesosphere during boreal summer 2022. Climate models have subsequently been employed to simulate these effects, with varying degrees of success. Models are able to reproduce the mesospheric water vapour, ozone and cooling responses well. The response reached a maximum in late 2023, then gradually diminished and is expected to return to its pre-eruption state in 2027. Only the ocean-coupled climate model showed the significant dynamical and temperature response observed in summer 2022.

It is important to note that the impact of this water vapour operates at long timescales, and is still ongoing at time of writing, and thus we are not able to fully describe all upper-atmospheric impacts in this report. However, results at time of writing suggest that the models generally captured the water vapour transport and its direct impact on mesospheric temperature and ozone, but have had challenges in reproducing dynamical processes. This highlights the complexity of the eruption's influence on the middle and upper atmospheric system and the nonlinear chemical and dynamical interactions driven by the eruption.

References

Aa, E., S.-R. Zhang, P. J. Erickson, J. Vierinen, A. J. Coster, L. P. Goncharenko, A. Spicher and W. Rideout (2022a). 'Significant Ionospheric Hole and Equatorial Plasma Bubbles After the 2022 Tonga Volcano Eruption'. *Space Weather*, 20, e2022SW003101. DOI: 10.1029/2022SW003101.

Aa, E., S.-R. Zhang, W. Wang, P. J. Erickson, L. Qian, R. Eastes, B. J. Harding, T. J. Immel, D. K. Karan, R. E. Daniell et al. (2022b). 'Pronounced Suppression and X-Pattern Merging of Equatorial Ionization Anomalies After the 2022 Tonga Volcano Eruption'. *J. Geophys. Res.*, 127, e2022JA030527. DOI: 10.1029/2022ja030527.

Aryal, S., Q. Gan, J. S. Evans, F. I. Laskar, D. K. Karan, X. Cai, K. R. Greer, W. Wang, W. E. McClintock and R. W. Eastes (2023). 'Tongan Volcanic Eruption Induced Global-Scale Thermospheric Changes Observed by the GOLD Mission'. *Geophys. Res. Lett.*, 50, e2023GL103158. DOI: 10.1029/2023gl103158.

Astafyeva, E., B. Maletckii, T. D. Mikesell, E. Munaibari, M. Ravanelli, P. Coisson, F. Manta and L. Rolland (2022). 'The 15 January 2022 Hunga Tonga Eruption History as Inferred From Ionospheric Observations'. *Geophys. Res. Lett.*, 49, e2022GL098827. DOI: 10.1029/2022GL098827.

Brasseur, G. P. and S. Solomon (2005). *Aeronomy of the middle atmosphere*. Dordrecht, The Netherlands: Springer.

Carr, J. L., Á. Horváth, D. L. Wu and M. D. Friberg (2022). 'Stereo Plume Height and Motion Retrievals for the Record-Setting Hunga Tonga-Hunga Ha'apai Eruption of 15 January 2022'. *Geophys. Res. Lett.*, 49, e2022GL098131. DOI: 10.1029/2022gl098131.

Carter, B. A., R. Pradipta, T. Dao, J. L. Currie, S. Choy, P. Wilkinson et al. (2023). 'The ionospheric effects of the 2022 Hunga Tonga volcano eruption and the associated impacts on GPS precise point positioning across the Australian region'. *Space Weather*, 21, e2023SW003476. DOI: 10.1029/2023SW003476.

Chau, J. L., F. L. Poblet, H.-L. Liu, A. Liu, N. Gulbrandsen, C. Jacobi, R. R. Rodriguez, D. Scipion and M. Tsutsumi (2024). 'Mesosphere and lower thermosphere wind perturbations due to the 2022 Hunga Tonga–Hunga Ha'apai eruption as observed by multistatic specular meteor radars'. *Radio Sci.*, 59. DOI: 10.1029/2024RS008013.

Choi, J. M., C. C. H. Lin, P. K. Rajesh et al. (2023). 'Giant ionospheric density hole near the 2022 Hunga–Tonga volcanic eruption: Multi-point satellite observations'. *Earth Planets Space*, 75, 184. DOI: 10.1186/s40623-023-01933-1.

Dunkerton, T. J. and D. P. Delisi (1986). 'Evolution of potential vorticity in the winter stratosphere of January–February 1979'. *J. Geophys. Res.*, 91, pp. 1199–1208. DOI: 10.1029/JD091iD01p01199.

Ern, M., L. Hoffmann, S. Rhode and P. Preusse (2022). 'The mesoscale gravity wave response to the 2022 Tonga volcanic eruption: AIRS and MLS satellite observations and source backtracing'. *Geophys. Res. Lett.*, 49, e2022GL098626. DOI: 10.1029/2022GL098626.

Feofilov, A. G., A. A. Kutepov, W. D. Pesnell, R. A. Goldberg, B. T. Marshall, L. L. Gordley and J. M. I. Russell (2009). 'Daytime SABER/TIMED observations of water vapor in the mesosphere: Retrieval approach and first results'. *Atmos. Chem. Phys.*, 9, pp. 8139–8158. DOI: 10.5194/acp-9-8139-2009.

Figueiredo, C. A. O. B., S. L. Vadas, E. Becker, C. M. Wrasse, H. Takahashi, P. K. Nyassor and D. Barros (2023). 'Secondary gravity waves from the Tonga volcano eruption: Observation and modeling over New Zealand and Australia'. *J. Geophys. Res.*, 128, e2023JA031476. DOI: 10.1029/2023JA031476.

Fleming, E. L., P. A. Newman, Q. Liang and J. S. Daniel (2020). 'The Impact of Continuing CFC-11 Emissions on Stratospheric Ozone'. *J. Geophys. Res.*, 125, e2019JD031849. DOI: 10.1029/2019jd031849.

Fleming, E. L., P. A. Newman, Q. Liang and L. D. Oman (2024). 'Stratospheric Temperature and Ozone Impacts of the Hunga Tonga-Hunga Ha'apai Water Vapor Injection'. *J. Geophys. Res.*, 129, e2023JD039298. DOI: 10.1029/2023jd039298.

Gasque, L. C., Y.-J. Wu, B. J. Harding, T. J. Immel and C. C. Triplett (2022). 'Rapid volcanic modification of the E-region dynamo: ICON's first glimpse of the Tonga eruption'. *Geophys. Res. Lett.*, 49, e2022GL100825. DOI: 10.1029/2022GL100825.

Han, S.-C., S. McClusky, T. D. Mikesell, L. Rolland, E. Okal and C. Benson (2023). 'CubeSat GPS observation of traveling ionospheric disturbances after the 2022 Hunga–Tonga Hunga–Ha'apai volcanic eruption and its potential use for tsunami warning'. *Earth Space Sci.*, 10, e2022EA002586. DOI: 10.1029/2022EA002586.

Harding, B. J., Y.-J. J. Wu, P. Alken, Y. Yamazaki, C. C. Triplett, T. J. Immel, L. C. Gasque, S. B. Mende and C. Xiong (2022). 'Impacts of the January 2022 Tonga volcanic eruption on the ionospheric dynamo: ICON–MIGHTI and Swarm observations of extreme neutral winds and currents'. *Geophys. Res.*

Lett., 49, e2022GL098577. DOI: 10.1029/2022GL098577.

He, J., E. Astafyeva, X. Yue, F. Ding and B. Maletckii (2023). 'The giant ionospheric depletion on 15 January 2022 around the Hunga Tonga–Hunga Ha'apai volcanic eruption'. *J. Geophys. Res.*, 128, e2022JA030984. DOI: 10.1029/2022JA030984.

Huba, J. D., E. Becker and S. L. Vadas (2023). 'Simulation study of the 15 January 2022 Tonga event: Development of super equatorial plasma bubbles'. *Geophys. Res. Lett.*, 50, e2022GL101185. DOI: 10.1029/2022GL101185.

Inchin, P. A., A. Bhatt, S. A. Cummer, S. D. Eckermann, B. J. Harding, D. D. Kuhl, J. Ma, J. J. Makela, R. Sabatini and J. B. Snively (2023). 'Multilayer evolution of acoustic-gravity waves and ionospheric disturbances over the United States after the 2022 Hunga Tonga volcano eruption'. *AGU Adv.*, 4, e2023AV000870. DOI: 10.1029/2023AV000870.

Jonsson, A. I., J. de Grandpré, V. I. Fomichev, J. C. McConnell and S. R. Beagley (2004). 'Doubled CO2-induced cooling in the middle atmosphere: Photochemical analysis of the ozone radiative feedback'. *J. Geophys. Res.*, 109, D24103. DOI: 10.1029/2004JD005093.

Klenzing, J., K. Zawdie, E. Astafyeva, A. Belehaki, M. Burleigh, A. G. Burrell, C. A. O. B. Figueiredo, N. A. Frissell, W. Fu, D. Hickey et al. (2025). 'Resolving the generation mechanisms and electrodynamical effects of medium-scale traveling ionospheric disturbances (MSTIDs)'. *Front. Astron. Space Sci.*, 12, 1539821. DOI: 10.3389/fspas.2025.1539821.

Lamb, H. (1881). 'On the vibrations of an elastic sphere'. *Proc. Lond. Math. Soc.*, s1-13, pp. 189–212. DOI: 10.1112/plms/s1-13.1.189.

Landerer, F. W., F. M. Flechtner, H. Save, F. H. Webb, T. Bandikova, W. I. Bertiger, S. V. Bettadpur, S. H. Byun, C. Dahle, H. Dobslaw et al. (2020). 'Extending the global mass change data record: GRACE Follow-On instrument and science data performance'. *Geophys. Res. Lett.*, 47, e2020GL088306. DOI: 10.1029/2020GL088306.

Le, G., G. Liu, E. Yizengaw and C. R. Englert (2022). 'Intense equatorial electrojet and counter electrojet caused by the 15 January 2022 Tonga volcanic eruption: Space- and ground-based observations'. *Geophys. Res. Lett.*, 49, e2022GL099002. DOI: 10.1029/2022GL099002.

Lee, Y.-K., N. Hindley, C. Grassotti and Q. Liu (2023). 'The Hunga Tonga–Hunga Ha'apai volcanic eruption as seen in satellite microwave observations and MiRS temperature retrievals'. *Geophys. Res. Lett.*, 50, e2023GL106439. DOI: 10.1029/2023GL106439.

Legras, B., C. Duchamp, P. Sellitto, A. Podglajen, E. Carboni, R. Siddans, J.-U. Grooß, S. Khaykin and F. Ploeger (2022). 'The evolution and dynamics of the Hunga Tonga–Hunga Ha'apai sulfate aerosol plume in the stratosphere'. *Atmos. Chem. Phys.*, 22, pp. 14957–14970. DOI: 10.5194/acp-22-14957-2022.

Leslie, R. C. (1885). 'Sky glows'. *Nature*, 32, 245. DOI: 10.1038/032245a0.

Li, R., J. Lei, J. Kusche, T. Dang, F. Huang, X. Luan, S.-R. Zhang, M. Yan, Z. Yang, F. Liu et al. (2023a). 'Large-scale disturbances in the upper thermosphere induced by the 2022 Tonga volcanic eruption'. *Geophys. Res. Lett.*, 50, e2022GL102265. DOI: 10.1029/2022GL102265.

Li, X., F. Ding, X. Yue, T. Mao, B. Xiong and Q. Song (2023b). 'Multiwave structure of traveling ionospheric disturbances excited by the Tonga volcanic eruptions observed by a dense GNSS network in China'. *Space Weather*, 21, e2022SW003210. DOI: 10.1029/2022SW003210.

Lin, J.-T., P. K. Rajesh, C. C. H. Lin, M.-Y. Chou, J.-Y. Liu, J. Yue, T.-Y. Hsiao, H.-F. Tsai, H.-M. Chao and M.-M. Kung (2022). 'Rapid conjugate appearance of the giant ionospheric Lamb wave signatures in the northern hemisphere after Hunga Tonga volcano eruptions'. *Geophys. Res. Lett.*, 49, e2022GL098222. DOI: 10.1029/2022GL098222.

Liu, C. H., J. Klostermeyer, K. C. Yeh, T. B. Jones, T. Robinson, O. Holt, R. Leitinger, T. Ogawa, K. Sinno, S. Kato et al. (1982). 'Global dynamic responses of the atmosphere to the eruption of Mount St. Helens on May 18, 1980'. *J. Geophys. Res.*, 87, pp. 6281–6290. DOI: 10.1029/JA087iA08p06281.

Liu, H.-L., W. Wang, J. D. Huba, P. H. Lauritzen and F. Vitt (2023). 'Atmospheric and ionospheric responses to the Hunga–Tonga volcano eruption simulated by WACCM-X'. *Geophys. Res. Lett.*, 50, e2023GL103682. DOI: 10.1029/2023GL103682.

Liu, X., J. Xu, J. Yue and M. Kogure (2022). 'Strong gravity waves associated with the Tonga volcano eruption revealed by SABER observations'. *Geophys. Res. Lett.*, 49, e2022GL098339. DOI: 10.1029/2022GL098339.

Maletckii, B. and E. Astafyeva (2022). 'Near-real-time analysis of the ionospheric response to the 15 January 2022 Hunga Tonga–Hunga Ha'apai volcanic eruption'. *J. Geophys. Res.*, 127, e2022JA030735. DOI: 10.1029/2022JA030735.

Manney, G. L., R. W. Zurek, M. E. Gelman, A. J. Miller and R. Nagatani (1994). 'The anomalous Arctic lower stratospheric polar vortex of 1992–1993'. *Geophys. Res. Lett.*, 21, pp. 2405–2408. DOI: 10.1029/94gl02368.

Matoza, R. S., D. Fee, J. D. Assink, A. M. Iezzi, D. N. Green, K. Kim, L. Toney, T. Lecocq, S. Krishnamoorthy, J.-M. Lalande et al. (2022). 'Atmospheric waves and global seismoacoustic observations of the January 2022 Hunga eruption, Tonga'. *Science*, 377, pp. 95–100. DOI: 10.1126/science.abo7063.

Millán, L., W. G. Read, M. L. Santee, A. Lambert, G. L. Manney, J. L. Neu, M. C. Pitts, F. Werner, N. J. Livesey and M. J. Schwartz (2024). 'The Evolution of the Hunga Hydration in a Moistening Stratosphere'. *Geophys. Res. Lett.*, 51, e2024GL110841. DOI: 10.1029/2024gl110841.

Millán, L., M. L. Santee, A. Lambert, N. J. Livesey, F. Werner, M. J. Schwartz, H. C. Pumphrey, G. L. Manney, Y. Wang, H. Su et al. (2022). 'The Hunga Tonga-Hunga Ha'apai Hydration of the Stratosphere'. *Geophys. Res. Lett.*, 49, e2022GL099381. DOI: 10.1029/2022gl099381.

Miller, S. D., W. C. Straka, J. Yue, S. M. Smith, M. J. Alexander, L. Hoffmann, M. Setvák and P. T. Partain (2015). 'Upper atmospheric gravity wave details revealed in nightglow satellite imagery'. *Proc. Natl. Acad. Sci. U.S.A.*, 112, E6728–E6735. DOI: 10.1073/pnas.1508084112.

Mills, M. J., A. Schmidt, R. Easter, S. Solomon, D. E. Kinnison, S. J. Ghan et al. (2016). 'Global volcanic aerosol properties derived from emissions, 1990–2014, using CESM1 (WACCM)'. *J. Geophys. Res.*, 121, pp. 2332–2348. DOI: 10.1002/2015jd024290.

Miyoshi, Y. and H. Shinagawa (2023). 'Upward propagation of gravity waves and ionospheric perturbations triggered by the 2022 Hunga–Tonga volcanic eruption'. *Earth Planets Space*, 75, 68. DOI: 10.1186/s40623-023-01827-2.

Nedoluha, G. E., R. M. Gomez, I. Boyd, H. Neal, D. R. Allen and A. Lambert (2024). 'The Spread of the Hunga Tonga H2O Plume in the Middle Atmosphere Over the First Two Years Since Eruption'. *J. Geophys. Res.*, 129, e2024JD040907. DOI: 10.1029/2024jd040907.

Nedoluha, G. E., R. M. Gomez, I. Boyd, H. Neal, D. R. Allen, A. Lambert and N. J. Livesey (2023). 'Mesospheric Water Vapor in 2022'. *J. Geophys. Res.*, 128, e2023JD039196. DOI: 10.1029/2023jd039196.

Niemeier, U., S. Wallis, C. Timmreck, T. van Pham and C. von Savigny (2023). 'How the Hunga Tonga—Hunga Ha'apai Water Vapor Cloud Impacts Its Transport Through the Stratosphere: Dynamical and Radiative Effects'. *Geophys. Res. Lett.*, 50, e2023GL106482. DOI: 10.1029/2023gl106482.

Ohya, H., F. Tsuchiya, T. Takamura, H. Shinagawa, Y. Takahashi and A. B. Chen (2024). 'Lower ionospheric resonance caused by Pekeris wave induced by the 2022 Tonga volcanic eruption'. *Sci. Rep.*, 14, 15659. DOI: 10.1038/s41598-024-65929-x.

Pacheco, E. E., J. P. Velasquez, R. Flores, L. Condori, G. Fajardo, K. Kuyeng, D. E. Scipion, M. Milla, J. F. Conte, F. L. Poblet et al. (2024). 'The impact of the Hunga Tonga–Hunga Ha'apai volcanic eruption on the Peruvian atmosphere: From the sea surface to the ionosphere'. *Earth Planets Space*, 76, 79. DOI: 10.1186/s40623-024-02022-7.

Poblet, F. L., J. L. Chau, J. F. Conte, J. Vierinen, J. Suclupe, A. Liu and R. R. Rodriguez (2023). 'Extreme horizontal wind perturbations in the mesosphere and lower thermosphere over South America associated with the 2022 Hunga eruption'. *Geophys. Res. Lett.*, 50, e2023GL103809. DOI: 10.1029/2023GL103809.

Pradipta, R., B. A. Carter, J. L. Currie, S. Choy, P. Wilkinson, P. Maher and R. Marshall (2023). 'On the propagation of traveling ionospheric disturbances from the Hunga Tonga–Hunga Ha'apai volcano eruption and their possible connection with tsunami waves'. *Geophys. Res. Lett.*, 50, e2022GL101925. DOI: 10.1029/2022GL101925.

Proud, S. R., A. T. Prata and S. Schmauß (2022). 'The January 2022 eruption of Hunga Tonga-Hunga Ha'apai volcano reached the mesosphere'. *Science*, 378, pp. 554–557. DOI: 10.1126/science.abo4076.

Rajesh, P. K., C. C. H. Lin, J. T. Lin, C. Y. Lin, J. Y. Liu, T. Matsuo, C. Y. Huang, M. Y. Chou, J. Yue, M. Nishioka et al. (2022). 'Extreme poleward expanding super plasma bubbles over the Asia–Pacific region triggered by the Tonga volcano eruption during the recovery phase of a geomagnetic storm'. *Geophys. Res. Lett.*, 49, e2022GL099798. DOI: 10.1029/2022GL099798.

Randel, W. J., X. Wang, J. Starr, R. R. Garcia and D. Kinnison (2024). 'Long-Term Temperature Impacts of the Hunga Volcanic Eruption in the Stratosphere and Above'. *Geophys. Res. Lett.*, 51. DOI: 10.1029/2024gl111500.

Ravanelli, M., E. Astafyeva, E. Munaibari, L. Rolland and T. D. Mikesell (2023). 'Ocean–ionosphere disturbances due to the 15 January 2022 Hunga Tonga–Hunga Ha'apai eruption'. *Geophys. Res. Lett.*, 50, e2022GL101465. DOI: 10.1029/2022GL101465.

Scinocca, J. F., N. A. McFarlane, M. Lazare, J. Li and D. Plummer (2008). 'Technical Note: The CCCma third generation AGCM and its extension into the middle atmosphere'. *Atmos. Chem. Phys.*, 8, pp. 7055–7074. DOI: 10.5194/acp-8-7055-2008.

Sellitto, P., A. Podglajen, R. Belhadji, M. Boichu, E. Carboni, J. Cuesta, C. Duchamp, C. Kloss, R. Siddans, N. Bègue et al. (2022). 'The unexpected radiative impact of the Hunga Tonga eruption of 15th January 2022'. *Commun. Earth Environ.*, 3, 288. DOI: 10.1038/s43247-022-00618-z.

Sepúlveda, I., M. Carvajal and D. C. Agnew (2023). 'Global Winds Shape Planetary-Scale Lamb Waves'. *Geophys. Res. Lett.*, 50, e2023GL106097. DOI: 10.1029/2023GL106097.

Shinbori, A., Y. Otsuka, T. Sori, M. Nishioka, S. Perwitasari, T. Tsuda et al. (2022). 'Electromagnetic conjugacy of ionospheric disturbances after the 2022 Hunga Tonga–Hunga Ha'apai volcanic eruption as seen in GNSS–TEC and SuperDARN Hokkaido pair of radars observations'. *Earth Planets Space*, 74, 106. DOI: 10.1186/s40623-022-01665-8.

Shinbori, A., T. Sori, Y. Otsuka, M. Nishioka, S. Perwitasari, T. Tsuda et al. (2023). 'Generation of equatorial plasma bubble after the 2022 Tonga volcanic eruption'. *Sci. Rep.*, 13, 6450. DOI: 10.1038/s41598-023-33603-3.

Smart, D. (2022). 'The first hour of the paroxysmal phase of the 2022 Hunga Tonga–Hunga Ha'apai volcanic eruption as seen by a geostationary meteorological satellite'. *Weather*, 77, pp. 81–82. DOI: 10.1002/wea.4173.

Stober, G., A. Liu, A. Kozlovsky, Z. Qiao, W. Krochin, G. Shi, J. Kero, M. Tsutsumi, N. Gulbrandsen, S. Nozawa et al. (2023). 'Identifying gravity waves launched by the Hunga Tonga–Hunga Ha'apai volcanic eruption in mesosphere/lower-thermosphere winds derived from CONDOR and the Nordic Meteor Radar Cluster'. *Ann. Geophys.*, 41, pp. 197–208. DOI: 10.5194/angeo-41-197-2023.

Stober, G., S. L. Vadas, E. Becker, A. Liu, A. Kozlovsky, D. Janches, Z. Qiao, W. Krochin, G. Shi, W. Yi et al. (2024). 'Gravity waves generated by the Hunga Tonga–Hunga Ha'apai volcanic eruption and their global propagation in the mesosphere/lower thermosphere observed by meteor radars and modeled with the High-Altitude general Mechanistic Circulation Model'. *Atmos. Chem. Phys.*, 24, pp. 4851–4873. DOI: 10.5194/acp-24-4851-2024.

Takahashi, H., C. A. O. B. Figueiredo, D. Barros, C. M. Wrasse, G. A. Giongo, R. H. Honda, L. F. R. Vital, L. C. A. Resende, P. K. Nyassor, T. T. Ayorinde et al. (2023). 'Ionospheric disturbances over South America related to the Tonga volcanic eruption'. *Earth Planets Space*, 75, 92. DOI: 10.1186/s40623-023-01844-1.

Themens, D. R., C. Watson, N. Žagar, S. Vasylkevych, S. Elvidge, A. McCaffrey, P. Prikryl, B. Reid, A. Wood and P. T. Jayachandran (2022). 'Global propagation of ionospheric disturbances associated with the 2022 Tonga volcanic eruption'. *Geophys. Res. Lett.*, 49, e2022GL098158. DOI: 10.1029/2022GL098158.

Vadas, S. L., E. Becker, C. Figueiredo, K. Bossert, B. J. Harding and L. C. Gasque (2023a). 'Primary and secondary gravity waves and large-scale wind changes generated by the Tonga volcanic eruption on 15 January 2022: Modeling and comparison with ICON-MIGHTI winds'. *J. Geophys. Res.*, 128, e2022JA031138. DOI: 10.1029/2022JA031138.

Vadas, S. L., C. Figueiredo, E. Becker, J. D. Huba, D. R. Themens, N. P. Hindley, S. Mrak, I. Galkin and K. Bossert (2023b). 'Traveling ionospheric disturbances induced by the secondary gravity waves from the Tonga eruption on 15 January 2022: Modeling with MESORAC–HIAMCM–SAMI3 and comparison with GPS/TEC and ionosonde data'. *J. Geophys. Res.*, 128, e2023JA031408. DOI: 10.1029/2023JA031408.

Verhulst, T. G. W., D. Altadill, V. Barta, A. Belehaki, D. Burešová, C. Cesaroni et al. (2022). 'Multi-instrument detection in Europe of ionospheric disturbances caused by the 15 January 2022 eruption of the Hunga volcano'. *J. Space Weather Space Clim.*, 12, 35. DOI: 10.1051/swsc/2022032.

Wallis, S., M. DeLand and C. von Savigny (2025). 'Did the 2022 Hunga eruption impact the noctilucent cloud season in 2023/24 and 2024?' *Atmos. Chem. Phys.*, 25, pp. 3635–3645. DOI: 10.5194/acp-25-3635-2025.

Watanabe, S., K. Hamilton, T. Sakazaki and M. Nakano (2022). 'First Detection of the Pekeris Internal Global Atmospheric Resonance: Evidence from the 2022 Tonga Eruption and from Global Reanalysis Data'. *J. Atmos. Sci.*, 79, pp. 3027–3043. DOI: 10.1175/JAS-D-22-0078.1.

Wright, C. J. (2019). 'Quantifying the global impact of tropical cyclone-associated gravity waves using HIRDLS, MLS, SABER, and IBTrACS data'. *Q. J. R. Meteorol. Soc.*, 145, pp. 3023–3039. DOI: 10.1002/qj.3602.

Wright, C. J., N. P. Hindley, M. J. Alexander, M. Barlow, L. Hoffmann, C. N. Mitchell, F. Prata, M. Bouillon, J. Carstens, C. Clerbaux et al. (2022). 'Surface-to-space atmospheric waves from Hunga Tonga-Hunga Ha'apai eruption'. *Nature*, 609, pp. 741–746. DOI: 10.1038/s41586-022-05012-5.

Wu, H., X. Lu, W. Wang and H.-L. Liu (2023). 'Simulation of the propagation and effects of gravity waves generated by the Tonga volcano eruption in the thermosphere and ionosphere using nested-grid TIEGCM'. *J. Geophys. Res.*, 128, e2023JA031354. DOI: 10.1029/2023JA031354.

Yamazaki, Y., G. Soares and J. Matzka (2022). 'Geomagnetic detection of the atmospheric acoustic resonance at 3.8 mHz during the Hunga Tonga eruption event on 15 January 2022'. *J. Geophys. Res.*, 127, e2022JA030540. DOI: 10.1029/2022JA030540.

Yu, W., R. Garcia, J. Yue, A. Smith, X. Wang, W. Randel, Z. Qiao, Y. Zhu, V. L. Harvey, S. Tilmes et al. (2023). 'Mesospheric temperature and circulation response to the Hunga Tonga-Hunga-Ha'apai volcanic eruption'. *J. Geophys. Res.*, 128, e2023JD039636. DOI: 10.1029/2023JD039636.

Yue, J., S. D. Miller, W. C. I. Straka, Y.-J. Noh, M.-Y. Chou, R. Kahn and V. Flower (2022). 'La Soufriere volcanic eruptions launched gravity waves into space'. *Geophys. Res. Lett.*, 49, e2022GL097952. DOI: 10.1029/2022GL097952.

Zettergren, M. D., J. B. Snively, A. Komjathy and O. P. Verkhoglyadova (2017). 'Nonlinear ionospheric responses to large-amplitude infrasonic–acoustic waves generated by undersea earthquakes'. *J. Geophys. Res.*, 122, pp. 2272–2291. DOI: 10.1002/2016JA023159.

Zhang, H., F. Wang, J. Li, Y. Duan, C. Zhu and J. He (2022). 'Potential Impact of Tonga Volcano Eruption on Global Mean Surface Air Temperature'. *J. Meteorol. Res.*, 36, pp. 1–5. DOI: 10.1007/s13351-022-2013-6.

Zhou, L., B. Yan, N. Sun, J. Huang, Q. Liu, C. Grassotti, Y.-K. Lee, W. Straka, J. Niu, A. Huff et al. (2023). 'Observed Atmospheric Features for the 2022 Hunga Tonga Volcanic Eruption from Joint Polar Satellite System Science Data Products'. *Atmosphere*, 14, 263, p. 263. DOI: 10.3390/atmos14020263.

Zhu, Y., H. Akiyoshi, V. Aquila, E. Asher, E. M. Bednarz, S. Bekki, C. Brühl, A. H. Butler, P. Case, S. Chabrillat et al. (2025). 'Hunga Tonga–Hunga Ha'apai Volcano Impact Model Observation Comparison (HTHH-MOC) project: experiment protocol and model descriptions'. *Geosci. Model Dev.*, 18, pp. 5487–5512. DOI: 10.5194/gmd-18-5487-2025.

Zhu, Y., C. G. Bardeen, S. Tilmes, M. J. Mills, X. Wang, V. L. Harvey, G. Taha, D. Kinnison, R. W. Portmann, P. Yu et al. (2022). 'Perturbations in stratospheric aerosol evolution due to the water-rich plume of the 2022 Hunga-Tonga eruption'. *Commun. Earth Environ.*, 3, 248. DOI: 10.1038/s43247-022-00580-w.

7 Radiative forcing and climate impacts caused by the 2022 Hunga volcano eruption

Lead authors Georgiy Stenchikov
Mark R. Schoeberl

Co-authors Ewa M. Bednarz
Eric Fleming
Yi Huang
Ilaria Quaglia
Pasquale Sellitto
Claudia Timmreck
Matthew Toohey
Jun Wang
Zhihong Zhuo

Contributing authors Peter Colarco
David Plummer
Takashi Sekiya
Simone Tilmes
Xinyue Wang
Shingo Watanabe
Wandi Yu
Jun Zhang

Cite this as:

Stenchikov, G., M. R. Schoeberl et al. (2025): Radiative forcing and climate impacts caused by the 2022 Hunga volcano eruption. In APARC, 2025: The Hunga Eruption Atmospheric Impacts Report [Yunqian Zhu, Graham Mann, Paul A. Newman, William Randel (Eds.)]. APARC Report No. 11, WCRP Report No. 10/2025, DOI: 10.34734/FZJ-2025-05244, available at `https://aparc-climate.org/publications/aparc-report-no-11/`.

Key points

Radiative Forcing

- **Hunga's stratospheric sulfate aerosol (SA) loading following the eruption was small compared to significant climate-impacting eruptions like the 1991 Mt. Pinatubo eruption**. The initial reported observed amount of SO_2 released in the major emission pulse on 15 January 2022 was 0.5 Tg. Global climate models require 0.65-1.0 Tg of SO_2 to produce stratospheric aerosol optical depths (SAOD) comparable with observations. This higher SO_2 value is consistent with later eruption estimates. Hunga's sulfate aerosol layer stayed in the stratosphere for less than two years.
- **Hunga injected significant amounts of water vapour (WV) into the mid-stratosphere, which will remain in the stratosphere for 4-7 years and could very slightly contribute to warming of the Earth's climate.** A portion of Hunga's water vapour layer was lifted by the Brewer-Dobson Circulation (BDC) into the upper stratosphere and, therefore, persisted in the stratosphere longer than volcanic aerosols. The Hunga water vapour layer decreases the outgoing longwave (LW) radiation at the top of the atmosphere (TOA) and increases the LW downward flux at the tropopause.
- **The net Hunga radiative forcing (RF) was dominated by SA in the first two years. The net global average volcanic RF was about −0.4±0.1 W/m^2, averaged for the two years following the eruption.** At all atmospheric levels, the negative RF caused by SA is an order of magnitude larger than Hunga's WV positive RF during the first two years after the eruption.
- **The WV-induced middle and upper stratospheric cooling (−0.2 K Day^{-1}) is stronger and more persistent than the stratospheric heating by Hunga's SA**. The WV cooling in the 10-30 hPa layer weakened in the two years after the eruption as the Hunga's water vapour ascends, disperses, and is partially removed from the stratosphere.
- **Stratospheric temperature and ozone changes in the Southern Hemisphere only slightly modified the RF**. The reduction in ozone increases the downward short wave (SW) flux at the tropopause, warming the troposphere. Stratospheric temperature adjustment (cooling) reduces the outgoing LW radiation at TOA, warming the climate system. However, during the first two years following the Hunga eruption, the contributions of ozone and stratospheric temperature adjustments to the TOA radiative forcing are significantly smaller than that of SA.
- **Beyond 2024, the Hunga aerosol loading has largely disappeared, and the stratospheric water vapour TOA RF is negligible (<0.005 W m^{-2}).**

Climate Perturbations

- **It is estimated that the Hunga eruption cooled the global average surface air temperature (SAT) by 0.05 K, but this reduction is so subtle as to be indistinguishable from the natural variability of the current climate.**
- **Beyond 2024, once the SA loading has dissipated, the residual warming from Hunga-injected water vapour will be minimal and unable to counteract the accumulated cooling from SAs.** The overall perturbation to global average climate is indistinguishable from natural climate variability.
- **Hunga-induced ozone perturbations and stratospheric cooling from WV may drive regional changes in tropospheric circulation**. Stratospheric meridional temperature gradient changes can impact the troposphere through stratosphere-troposphere dynamic coupling. Ozone depletion-driven cooling of the polar stratosphere in both hemispheres has the potential to strengthen winter polar vortices and delay stratospheric final warming. While these effects are evident in model simulations, their amplitudes remain below the threshold necessary for clear attribution in observations.

Contents

7.1 Mechanisms of volcanic climate impacts . . . 160
7.1.1 Impacts of volcanic sulfate aerosols . . . 160
7.1.2 Impact of volcanic water vapour . . . 161
7.1.3 Stratospheric chemistry and dynamics feedbacks . . . 161
7.1.4 The 2022 Hunga eruption . . . 161
7.2 Hunga's radiative forcing agents . . . 162
7.2.1 Hunga's sulfate aerosol perturbation . . . 162
7.2.2 Hunga's water vapour perturbation . . . 163
7.2.3 Hunga's ozone perturbation . . . 164
7.3 Hunga's radiative forcing . . . 164
7.3.1 IRF, ERF, and SARF . . . 164
7.3.2 Clear sky and all sky RF . . . 165
7.3.3 Hunga's sulfate aerosol and water vapour IRF . . . 166
7.3.4 Empirically calculated ERF . . . 167
7.3.5 Model calculated ERF . . . 167
7.3.6 Uncertainty in radiative forcing . . . 170
7.4 Hunga's climate impact . . . 171
7.4.1 SA-dominated climate response (2022-2023) . . . 171
7.4.2 WV-dominated climate response (2024-2030) . . . 173
7.4.3 Indirect atmospheric effects . . . 174
7.4.4 Uncertainties in climate response . . . 176
7.5 Discussion and conclusions . . . 176

Preamble

Chapter 7 assesses the tropospheric and climate impacts of the Hunga eruption. The chapter focuses on the radiative forcing associated with the Hunga volcanic eruption and its effect on tropospheric temperatures, as well as indirect effects related to ozone and temperature changes in the stratosphere. Because many of the observed stratospheric changes following the Hunga eruption are detailed in previous chapters, this chapter is closely linked to Chapters 3–5. Chapter 7 also uses the results of HTHH-MOC (see Supplementary S1 and S3) analysis to quantify Hunga's radiative forcing and climate impact, as well as the results of published empirical and modelling studies.

7.1 Mechanisms of volcanic climate impacts

Explosive volcanic eruptions release sulfur-bearing gases, volcanic ash, water vapour (WV), halogens, and other trace substances into the atmosphere, disrupting stratospheric chemistry. The injection altitude can vary from the lower stratosphere (LS, below 25 km) to the upper stratosphere (US, above 25 km), though most stratosphere-reaching eruptions inject material primarily into the LS. Sulfur gases such as SO_2 and H_2S undergo oxidation to form sulfate aerosols (SAs), which can persist in the stratosphere for several years, significantly impacting Earth's radiative balance.

Volcanoes emit large amounts of solid particles, i.e. volcanic ash. Ash comprises recondensed silicate particles with diameters typically larger than 2 μm. While ash usually settles out of the stratosphere within one to two weeks after an eruption, it can generate a short-lived but measurable radiative forcing (RF) (Niemeier et al., 2009; Stenchikov et al., 2021). However, no significant ash particles were observed in the Hunga eruption plume (see Chapters 1 and 2; Legras et al., 2022; Sellitto et al., 2022; Kloss et al., 2022; Baron et al., 2023).

If the eruption is sufficiently large in terms of SO_2 emission (>5 Tg), it can have noticeable effects on atmospheric temperatures, ocean heat content, and both atmospheric and oceanic circulation (Hansen, 2002; Robock, 2000; Timmreck, 2012; Stenchikov, 2016; Swingedouw et al., 2017; Marshall et al., 2022). The estimated Hunga SO_2 emission was between 0.5–0.7 Tg (Carn et al., 2022) based on satellite observations of SO_2 and the amount of sulfate aerosol that formed after the eruption.

7.1.1 Impacts of volcanic sulfate aerosols

Sulfate aerosol particles are typically not emitted directly by volcanic eruptions but instead form in the stratosphere through oxidation of SO_2 followed by the binary nucleation of sulfuric acid and water vapour. This process is followed by particle coagulation, condensational growth, and gravitational settling (Turco et al., 1982; Pueschel, 1996; Hamill et al., 1997). The typical timescale for the conversion of SO_2 to sulfate (SO_4) is about one month (Bluth et al., 1992; Read et al., 1993; Höpfner et al., 2015; Wang et al., 2013). However, the conversion rate can vary depending on the stage of the process and is influenced by factors such as water vapour availability and injection altitude (Höpfner et al., 2015; LeGrande et al., 2016; Carn et al., 2016; Zhu et al., 2022; Abdelkader et al., 2023).

SAs can significantly disrupt the planet's radiative energy balance, impacting stratospheric and tropospheric temperatures and the circulation (Lambert et al., 1993; Baran and Foot, 1994; Bluth et al., 1997; Barnes and Hofmann, 1997; Lacis et al., 1992; Perlwitz and Graf, 2001; Kremser et al., 2016). SAs scatter shortwave (SW) radiation in the entire solar spectrum, increasing the planetary albedo. SAs absorb solar near-IR (NIR) and longwave (LW, λ>4 μm) radiation.

SAs are dispersed throughout the stratosphere by eddies and the Brewer-Dobson Circulation (BDC) (Holton et al., 1995). In the tropical stratosphere, their movement is also influenced by the Quasi-Biennial Oscillation (QBO) (Trepte and Hitchman, 1992). The tropical upward branches of BDC and buoyancy generated by aerosol radiative heating can loft aerosols against gravitational settling, increasing their residence time. The residence time of tiny (< 0.1 μm) background aerosol particles in the stratosphere is about two to three years (Hamill et al., 1997). The residence time of stratospheric volcanic SAs is shorter than background aerosols due to their larger particle size (Deshler, 2008), which increases gravitational sedimentation rates. For example, an analysis of SA observations suggests a mean stratospheric aerosol lifetime from the 1991 Pinatubo eruption of around 22 months and tropical eruptions have longer lifetimes than extra-tropical eruptions (Toohey et al., 2025). Models simulate the formation of SAs using a variety of parametrisation schemes. This leads to discrepancies between models on the SA size distributions and the subsequent SA's radiative properties and residence time (Quaglia et al., 2023; Kremser et al., 2016; Timmreck et al., 2018).

Direct instrumental observations of the radiative forcing of SAs are rare (Dutton and DeLuisi, 1983; Dutton and Christy, 1992; Dutton et al., 1994; Minnis et al., 1993; Russell et al., 1993; Andersson et al., 2015; Solomon et al., 2011). Overall, stratospheric SAs have a net cooling effect on Earth's surface and the troposphere by reducing solar radiation while warming the stratosphere by absorbing NIR and infrared (IR) radiation. Solar spectral irradiance is relatively weak at wavelengths longer than 2.5 μm, where SAs are absorptive, resulting in relatively modest NIR heating by SAs. Consequently, IR radiative heating rates within the aerosol layer are roughly twice as large as those from SW heating. However, the volcanic SW RF at the top of the atmosphere (TOA) dominates over the LW RF (Stenchikov et al., 1998). The stratospheric heating caused by volcanic aerosols' LW and NIR absorption cannot be neglected because it influences stratospheric temperature and circulation patterns (Graf et al., 1994; Kodera, 1994; Thompson and Wallace, 1998; Stenchikov et al., 2002).

7.1.2 Impact of volcanic water vapour

Water vapour is the most abundant gas emitted through volcanic eruptions. The amount of water vapour in the volcanic plume can be significantly enhanced by entraining environmental water (Guo et al., 2004a; Guo et al., 2004b; Joshi and Jones, 2009). The amount of WV that remains in the stratosphere is influenced by the ambient temperature at the injection plume height. Lower stratospheric temperatures range from 180 to 230 K, but temperature increases with altitude, reaching around 270 K near the stratopause (~50 km). At lower temperatures, ice particles form and sediment downwards if the water vapour concentration exceeds the temperature-dependent nucleation threshold. Because stratospheric temperatures rise rapidly with altitude, higher injection levels within the stratosphere lead to greater retention of water vapour, resulting in higher stratospheric water vapour concentrations. For example, the 1991 Pinatubo eruption injected over 80 Tg of water vapour just above the tropopause; however, this vapour quickly condensed and was almost entirely removed through the sedimentation of ice crystals (Stenchikov et al., 2021; Abdelkader et al., 2023; Guo et al., 2004a; Guo et al., 2004b).

Enhanced concentrations of WV in a volcanic plume can also accelerate the conversion of SO_2 to sulfate (LeGrande et al., 2016; Abdelkader et al., 2023). Strong volcanic eruptions could potentially heat the troposphere via SA NIR and IR absorption, increasing tropospheric water vapour entering the stratosphere. While simulations have demonstrated this effect (Joshi and Shine, 2003; Robock et al., 2009; Kroll et al., 2021; Kroll and Schmidt, 2024), it has not yet been observed in real-world situations, including the 1991 Mt. Pinatubo eruption (Fueglistaler et al., 2013; Randel et al., 2004; Chiou et al., 2006).

7.1.3 Stratospheric chemistry and dynamics feedbacks

Ozone is a radiatively active tracer, absorbing solar ultraviolet (UV) and visible radiation and emitting and absorbing IR radiation primarily in a band centred at 9.6 μm. Chemically driven changes in ozone thus can lead to changes in stratospheric heating rates and temperatures. Changes in the meridional temperature gradient in the stratosphere, driven by the radiative effects of SA, WV, or ozone, can alter stratospheric circulation and trigger dynamical interactions between the stratosphere and troposphere (Graf et al., 1994; Kodera, 1994; Thompson and Wallace, 1998; Stenchikov et al., 2002; Maycock et al., 2013). The induced dynamical changes can alter the distribution of other chemical species. Volcanic radiative processes may also change the phase, strength, and duration of El Niño-Southern Oscillation (ENSO) (Predybaylo et al., 2017; Pausata et al., 2015), as well as the strength of the Atlantic Meridional Overturning Circulation (AMOC) (Stenchikov et al., 2009).

7.1.4 The 2022 Hunga eruption

The shallow-underwater eruption of Hunga was unusual in that it increased the WV content in the stratosphere by 10–15% (see Chapters 2 and 3). The Hunga eruption was rated as a Volcanic Explosivity Index (VEI) 6 eruption (see Chapter 1; Newhall and Self 1982; Carn et al. 2022). Hunga's SO_2 emission in the primary eruption on 15 January 2022 was relatively small compared to climatologically significant eruptions such as the VEI 6 1991 Pinatubo eruption. Initial estimates place Hunga's SO_2 release in the major pulse at around 0.5 Tg (Carn et al., 2022; Duchamp et al., 2023). If we account for smaller SO_2 injections before the primary eruption, the total SO_2 reaches 0.7 Tg (Carn et al., 2022), but the smaller emissions dispersed to a lower altitude than the main eruption. From the perspective of SO_2 emissions alone, Hunga's climate impact would likely resemble eruptions with moderate SO_2 output, e.g., St. Helens (1980, 0.875 Tg SO_2), Calbuco (2015, 0.4 Tg SO_2), Raikoke (2019, 1.4

Tg SO_2), Sarychev (2009, 1.2 Tg SO_2), all of which have had a negligible climate impact.

7.2 Hunga's radiative forcing agents

7.2.1 Hunga's sulfate aerosol perturbation

As already noted, the Hunga eruption injected a modest amount of SO_2 in the upper stratosphere and lower mesosphere (Carn et al., 2022; Taha et al., 2022; Witze, 2022; Sellitto et al., 2024), increasing by a factor of ~5–10 the background stratospheric sulfur burden. By comparison, the 1991 Pinatubo event increased the stratospheric sulfur burden by a factor of 100 (Bluth et al., 1992).

Satellite observations from the Ozone Mapping and Profiler Suite (OMPS) Limb Profiler (LP) instrument, the Stratospheric Aerosol and Gas Experiment III (SAGE III) onboard the International Space Station (ISS), and Infrared Atmospheric Sounder Interferometer (IASI) observations can be used to derive aerosol properties, including extinction, effective radius, surface area density (SAD), and stratospheric optical depth (SAOD) (Duchamp et al., 2023; Taha et al., 2021; Taha et al., 2022; Bourassa et al., 2023; Schoeberl et al., 2024; Sellitto et al., 2024; Johnson et al., 2025). We also use the Global Space-based Stratospheric Aerosol Climatology (GloSSAC) combined observational dataset (Thomason et al., 2018; Kovilakam et al., 2020), which mostly consists of SAGE observations. Figure 7.1a (see also Chapter 3) shows the evolution of the 1020 nm global average (60°S–60°N) SAOD following the eruption from four sources: NASA OMPS-LP (Taha et al., 2021; Johnson et al., 2025); USask OMPS-LP (Bourassa et al., 2023); SAGE III/ISS (Thomason et al., 2018); and GloSSAC (Kovilakam et al., 2020).

For the NASA OMPS-LP data shown in Figure 7.1a, we use the latest Version 2.5 product (Johnson et al., 2025), replacing the Version 2.1 product used by Taha et al. (2022). In the new NASA OMPS-LP V2.5 algorithm, convergence was improved over V2.1 by significantly increasing the number of iterations to improve the retrieval performance. The short-wavelength aerosol profiles at 510, 600, 675, and 745 nm were filtered for unrealistic values (mostly at lower altitudes and large scattering angles) using the colour ratio relative to 869 nm. To eliminate unrealistic and anomalous retrievals, the aerosol profiles were also filtered for values greater than 0.1 km^{-1} and where the retrieval residual is greater than 50%. See Supplementary S2 (Figure S.II.3) for a detailed comparison of NASA OMPS-LP V2.5 and V2.1 SAODs.

We use the SAGE Ångström Exponent to convert the NASA and USask OMPS 745 nm SAODs to 1020 nm in order to compare them with the HTHH-MOC model output, which is available at this wavelength. Additionally, we present the original SAGE 1020 nm SAOD, GloSSAC, and the NASA OMPS 997 nm SAOD. Due to limited sampling, SAGE data smooth the initial rise in Hunga's SAOD, but they provide the most reliable observations 3–4 months after the eruption and serve as the foundation for the GloSSAC combined observational dataset.

Since our focus is on Hunga's impact on SAOD, we removed the background SAOD from all observed SAOD records by defining Hunga's SAOD as the increase over a 10-day average SAOD prior to the eruption. While this approach is not entirely precise, using a climatological background SAOD seasonal cycle would also be problematic because of interannual variability. Therefore, we opted for this method as the simplest and most easily reproducible.

Figure 7.1a compares SAOD estimates described above. The NASA OMPS-V2.5 1020 nm SAOD converted from 745 nm observations is unrealistically high. The NASA OMPS-V2.5 SAOD at 997 nm is in better agreement with the other sources. It reaches ~0.006 in one month after the eruption, while the USask OMPS SAOD is a factor of 1.5 smaller. The SAGE III/ISS SAOD and GloSSAC lie between the two OMPS estimates. The differences in the SAOD estimates between the various satellite retrieval algorithms can be viewed as uncertainty in the measurement.

All the measurements show a shift in SAOD from the tropics to the extratropical Southern Hemisphere (SH) during May–June 2022 (Schoeberl et al., 2023). Models capture the transport of the SA plume throughout the stratosphere reasonably well (see Chapter 3). The stratospheric SAs are removed from the stratosphere by gravitational sedimentation, mixing into the troposphere through tropopause folds, and transport to the troposphere in the polar regions (e.g., Kremser et al., 2016). The decay time for stratospheric sulfate aerosols depends on the latitude of the eruption (Toohey et al., 2025; Oman et al., 2006). According to observations, most of the Hunga aerosol loading had disappeared by the end of 2023 (Figure 7.1a; Schoeberl et al., 2024).

To depict Hunga's SAOD from the HTHH-MOC models, Figure 7.1b presents the difference between simulations with volcanic emissions and their corresponding control runs, thereby effectively removing the background SAOD. The models exhibit a range of results, with WACCM6MAM and GEOSCCM pro-

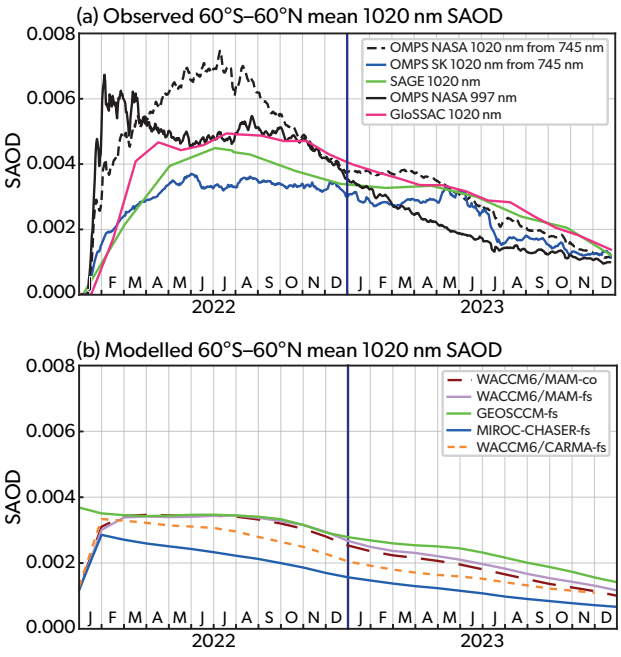

Figure 7.1: *Near-global average (60°S–60°N) Hunga SAOD for the first two years after the eruption, with background SAOD removed. (a)* Observational estimates: *NASA OMPS-LP-V2.5 at 1020 nm SAOD is derived by converting 745 nm SAOD using the SAGE III/ISS 745-to-1020 nm Ångström exponent. USask OMPS-LP 1020 nm SAOD is obtained in the same way. NASA OMPS-LP-V2.5 997 nm and SAGE III/ISS 1020 nm SAODs are shown directly, without conversion, along with GloSSAC 1020 nm. (b)* Model results: *Ensemble-mean Hunga – control SAODs from WACCM6MAM-co, WACCM6-MAM-fs, WACCM6CARMA-fs, MIROC-CHASER-fs, and GEOSCCM-fs ensembles.*

ducing the highest SAOD and MIROC-CHASER the lowest. Removing the background helps bring the model SAODs closer to the observations. Nevertheless, considering the spread in both observational and model data, the modelled SAODs are a factor of 1.3 to 2.0 lower than the observed SAOD. Assuming that the model reduced SAOD is due to smaller initial SO_2 injection, the corresponding adjusted SO_2 emission estimate would be 0.65–1.0 Tg. This higher SO_2 amount is consistent with more recent estimates reported by Stenchikov et al. (2025), Schoeberl et al. (2024), and Sellitto et al. (2024). The observational estimate of 0.7 Tg by Carn et al. (2022) lies at the lower bound of this range.

Hunga's SAOD is the largest in the observation record since the 1991 Pinatubo eruption (Khaykin et al., 2022). It was suggested that the Hunga eruption was approximately twice as effective at producing SAOD per unit mass of emitted SO_2 compared to similar or more significant eruptions like Raikoke, Calbuco, or Nabro (Sellitto et al., 2022; Taha et al., 2022); see Chapters 2 and 3 for further information. We attribute Hunga's relatively high SAOD to the fact that the volcanic materials were initially injected in the upper stratosphere and did not interact with the tropopause layer during their descent to the lower stratosphere (see Chapter 2). As a result, volcanic clouds did not lose SO_2 and SO_4 through the tropopause (Stenchikov et al., 2021; Stenchikov et al., 2025), which led to larger SAOD generation per unit mass of emitted SO_2. Stenchikov et al. (2025) demonstrated that Hunga's aerosol size enhanced SAOD per unit SO_2 mass by only 10–15% relative to Raikoke and Nabro. Thus, reconciling the simulated and observed SAOD requires assuming an SO_2 emission greater than 0.5 Tg.

7.2.2 Hunga's water vapour perturbation

The Hunga eruption injected WV directly into the upper stratosphere even reaching the lower mesosphere (Khaykin et al., 2022; Millán et al., 2022; Vömel et al., 2022). Satellite observations from the Aura Microwave Limb Sounder (MLS) revealed unprecedented stratospheric H_2O concentrations following the eruption (see Chapter 3). The amount of volcanic WV retained in the stratosphere after the eruption was unusually high, exceeding 120–130 Tg, which represents about a ~10–15% increase in the global stratospheric WV burden (Vömel et al., 2022; Millán et al., 2022; Millán et al., 2024; Santee et al., 2023). As a result, the 2022 Hunga eruption sparked considerable debate about its climate effect.

Hunga's WV cloud initially formed over the volcano at (175° W; 20°S) and spread throughout the tropics south of the equator. Millán et al. (2024) detailed the evolution of the WV anomaly using MLS observations. Models reproduce the transport of the WV cloud throughout the stratosphere reasonably well (see Chapter 3). The large injection of water vapour has the potential to alter stratospheric chemistry and circulation (Coy et al., 2022; Chen et al., 2023; Fleming et al., 2024; Niemeier et al., 2023; Maycock and Shine, 2012) and might indirectly impact other radiatively active gases, like ozone and methane, and the tropospheric climate.

The WV plume initially descended from 30–40 km to 25–27 km, then slowly ascended over the following year, reaching mesospheric altitudes (>50 km) during 2023–2024 (see Chapters 2 and 3; Sellitto et al., 2022; Nedoluha et al., 2024; Millán et al., 2024; Wallis et al., 2025; Randel et al., 2023; Niemeier et al., 2023). This initial plume descent was not seen in SAGE III/ISS

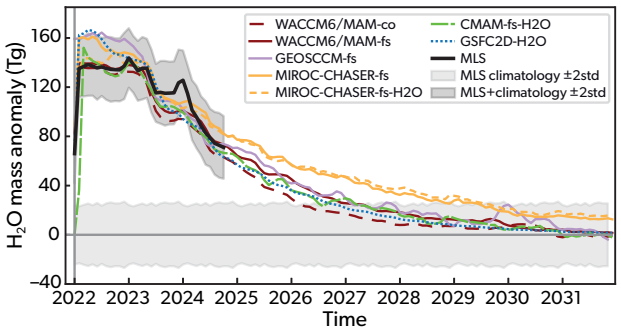

Figure 7.2: *Perturbation of the global stratospheric water vapour burden (Tg) observed by MLS (black) and simulated using several chemistry-climate models, as indicated in the legend. The light-gray shading indicates the 2σ variability range of the MLS observations calculated using data from 2005-2021, while the dark-gray shading represents 2σ variability over the MLS observational record for the 2022-2025 period. (Adapted from Zhuo et al., 2025.)*

observations, because SAGE III/ISS missed the initial stage of the plume evolution. In the model simulations (Chapter 3, e.g., WACCM6MAM) the descent phase is short-lived, as WV and SO_2 were released near 30 km, just above the level where the plume descent halted. The excess Hunga WV will ultimately return to the troposphere at mid-high latitudes via the BDC (Holton et al., 1995; Appenzeller et al., 1996) and by sedimentation of polar stratospheric cloud (PSC) ice crystals in the Antarctic polar vortex (see, e.g., Kelly et al., 1989; Fahey et al., 1990; Vömel et al., 1995; Nedoluha et al., 2002; Zhou et al., 2024).

Given the multiyear stratospheric lifetime for trace gas anomalies, the Hunga WV will have a multi-year impact. The HTHH-MOC simulations suggest that stratospheric WV will take 4–7 years to return to pre-eruption levels (Figure 7.2, see also Chapter 3). Based on model simulations, Fleming et al. (2024) and Zhou et al. (2024) suggested a ~2.5–4-year decay timescale for the Hunga water vapour anomaly, and Schoeberl et al. (2025) found that Hunga's WV lifetime is ~3.7 years, which is consistent with the HTHH-MOC's model results (Figure 7.2). MLS observations suggest a significantly longer e-folding decay timescale of 12.2 years (Millán et al., 2024). This discrepancy might be partly caused by the shorter water vapour record used by Millán et al. (2024), and how the MLS residence time was calculated (Schoeberl et al., 2025; Toohey et al., 2025).

7.2.3 Hunga's ozone perturbation

Wang et al. (2023) and Wilmouth et al. (2023) used models and observations to show that for a few months after the Hunga eruption in the SH tropics ozone mixing ratio increased in the upper and middle stratosphere but decreased in the lower stratosphere. The amplitude of ozone changes was within natural variability. The aerosol and water vapour anomalies can affect stratospheric dynamics and chemistry, resulting in detectable effects on atmospheric radiation and potentially the surface climate (Muthers et al., 2015; Wang et al., 2013; Fleming et al., 2024). The added stratospheric radiative cooling from the water vapour injection set up a secondary circulation (Coy et al., 2022) that lifted the ozone layer at southern mid-latitudes near 25 km. This decreased the mid-latitude ozone concentration in the 20–25 km layer by transporting lower concentration ozone upward. MLS also detected enhanced ClO (Santee et al., 2023) due to heterogeneous chemistry on aerosols. Relative to the climatology, the ozone perturbations in the stratosphere are within 2–3% and in the mesosphere 5–6%. However, the absolute changes in ozone content in the mesosphere are minor because of low background concentration (Santee et al., 2023; Schoeberl et al., 2024). After 2023, ozone losses in the tropics remain modest (<10 DU).

7.3 Hunga's radiative forcing

RF refers to the perturbation of the radiative energy flux at TOA, tropopause (TROP), and surface (SURF) caused by radiatively active agents of interest. RF at TOA measures the energy imbalance at the boundary of the Earth's climate system and is predictive of the global mean temperature impact of a particular radiative agent (Ramaswamy et al., 2019). The forcing at the tropopause integrates the change in the energy balance of the troposphere-surface system. RF at SURF is indicative of the radiative heating or cooling of the land and ocean. Ocean heating/cooling induced by volcanic RF initiates long-term climate changes that can persist for several decades after the volcanic event (Stenchikov et al., 2009; Delworth et al., 2006). Table 7.1 defines some standard terms used in this chapter.

7.3.1 IRF, ERF, and SARF

Depending on the methods, RF can be categorised as Instantaneous Radiative Forcing (IRF), stratosphere-adjusted radiative forcing (SARF), or effective radiative forcing (ERF) (Hansen et al., 2005; Ramaswamy

et al., 2019; Andrews et al., 2021). IRF is defined as the radiation perturbation caused by the change in the radiative agent of interest when no other changes to the atmosphere-surface system are allowed. IRF can be calculated using radiative transfer models (Sellitto et al., 2022; Jenkins et al., 2023; Stenchikov et al., 2025; Yu and Huang, 2024) following the partial radiative perturbation concept (Wetherald and Manabe, 1988) without accounting for atmospheric adjustments. IRF is also often evaluated using empirical formulas or scaling relations (Hansen et al., 2005; Larson and Portmann, 2016; Yu et al., 2023b; Schoeberl et al., 2023; Schoeberl et al., 2024; Marshall et al., 2020). Column stand-alone radiative-transfer models driven by observed meteorology and atmospheric composition are well suited for evaluating IRF. IRF calculations are also implemented in regional and global climate models by a "double call" of radiative routines (Stenchikov et al., 1998). The double-call approach computes radiative fluxes twice, once with and once without the optically active constituents of interest, using the same meteorological profiles, and defines the IRF as the difference between the two.

Unfortunately, a double-call capability is not implemented in most of the HTHH-MOC models. Instead, they calculated IRF in the runs with nudged meteorology as a difference of radiative fluxes in perturbed and control experiments. SA+WV IRF was calculated using the nudged meteorology ensemble with SA and WV emissions. WV IRF was calculated in the nudged meteorology runs with only WV emission. SA IRF was calculated in the experiments with nudged meteorology and only SO_2 emissions. Because nudging suppresses variability in meteorological fields, it typically excludes the stratospheric temperature adjustment. However, the clear-sky SA+WV, SA, and WV IRFs still inherently reflect the influence of non-nudged variables that affect radiative fluxes – such as ozone perturbations and changes in PSCs. This must be kept in mind when interpreting the IRFs obtained with HTHH-MOC models.

Subsequent to the introduction of IRF, stratospheric temperature adjustment was recognised as an essential process influencing the RF magnitude, leading to the definition of SARF, which is often quantified by the Fixed Dynamical Heating method (Fels et al., 1980). SARF does not include any tropospheric adjustments or other stratospheric adjustments than temperature. For stratospheric water vapour perturbations in the middle and upper stratosphere, IRF at the tropopause usually closely matches the SARF at the tropopause (Jenkins et al., 2023; Solomon et al., 2010).

Recently, it has been recognised that fast tropospheric adjustments can also play an important role for radiative forcing (Sherwood et al., 2015). This finding led to the introduction of ERF, which accounts for both stratospheric and tropospheric adjustments. In many forcing cases (e.g., carbon dioxide), ERF is a better predictor of eventual global mean surface air temperature change than IRF (Hansen et al., 2005; Smith et al., 2020; Andrews et al., 2021). For example, some studies have suggested that cloud adjustment in the troposphere can add an essential modification to the radiative effect of stratospheric water vapour (Huang et al., 2020; Li and Newman, 2020; Wang and Huang, 2024; He and Huang, 2025). In the HTHH-MOC experiments, ERF is calculated as the difference in radiative fluxes between perturbed (with radiatively active agents) and control (without radiatively active agents) runs with prescribed sea surface temperatures (SST). We note that this diagnosis of ERF includes chemical adjustments, e.g., via stratospheric ozone, as well as physical adjustments.

Short-wave IRF, SARF, and ERF are largely independent of changes in environmental temperature, and as a result, their values are similar. In contrast, long-wave SARF and ERF differ from the LW IRF because they are influenced by changes in atmospheric temperature, whereas the LW IRF is not (Forster et al., 2016).

7.3.2 Clear sky and all sky RF

RF can be calculated for all-sky or clear-sky conditions. The all-sky RF provides a better estimate of the global average surface temperature response. For example, Wang and Huang (2024) showed that cloud feedback in their model tends to reduce the SW radiative impact of the Hunga volcanic cloud. However, clear-sky forcing is a more meaningful metric than all-sky forcing for characterising the evolution of a volcanic cloud and comparing model performance, as cloud parametrisations vary significantly across models. We must emphasise that an all-sky forcing is acting within the models, i.e., an all-sky forcing drives the simulated climate responses in the HTHH-MOC ensembles.

Using observed distributions of WV and SA, we can calculate the 2022-2024 radiative forcing and compare it with available ground-based observations and satellite retrievals (Schoeberl et al., 2022; Schoeberl et al., 2023; Schoeberl et al., 2024; Sellitto et al., 2022;

Table 7.1: *Radiative Forcing Terminology.*

Acronym	Term	Definition
IRF	Instantaneous Radiative Forcing	Radiation perturbation at TOA, TROP, or SURF caused by the change in the radiative constituents alone.
ERF	Effective Radiative Forcing	A difference in corresponding radiative fluxes between perturbed and unperturbed experiments with prescribed SST which allow for radiative adjustments in the atmosphere and by the land surface.
SARF	Stratosphere-adjusted Radiative Forcing	Radiative forcing that accounts only for stratospheric temperature adjustment.
TOA	Top of Atmosphere	The model's top level.
TROP	Tropopause	The tropopause level, e.g., 100 hPa.
SURF	Surface	Surface level.

Sicard et al., 2025; Gupta et al., 2025). Beyond 2024, we must rely on models to estimate the RF. To increase the model's credibility, we use the observations to validate models for the 2022-2024 period. To calculate Hunga's radiative impact, we must account for the effects of stratospheric SA, WV, and changes to other radiatively active constituents, e.g., stratospheric ozone.

7.3.3 Hunga's sulfate aerosol and water vapour IRF

The radiative impact of volcanic aerosols is well-known (e.g., Ramaswamy et al., 2019; Kremser et al., 2016; Stenchikov et al., 1998). They cool the surface–troposphere system by reducing downwelling solar radiation, while simultaneously causing warming within the stratospheric aerosol layer due to absorption of solar NIR and terrestrial LW radiation. As noted in Section 7.2.1, Hunga's SO_2 injection is small compared to climatologically significant eruptions like the 1991 Pinatubo event. The SO_2-to-SO_4 conversion rate in the Hunga plume appears to be 1-2 weeks due to the enhanced WV mixing ratio (see Chapter 3). This is 2-3 times faster than in all previously observed eruptions (Carn et al., 2016). After the major Hunga eruption pulse on 15 January 2022, the SAOD increased during a few weeks after the eruption due to the rising of the SO_4 mass and particle coagulation and condensation growth (Zhu et al., 2022), which led to local IRF values reaching nearly -2.0 W m^{-2} in some locations (Sellitto et al., 2022; Sicard et al., 2025), and a global averaged IRF of -0.5 W m^{-2} through the first year (Schoeberl et al., 2023; Stenchikov et al., 2025). The LW SA IRF is positive at the TOA, SURF, and the TROP, but SW SA IRF is negative at all atmospheric levels. The absolute value of SA SW IRF is approximately five times larger than that of SA LW IRF, i.e., the net IRF due to Hunga SA is negative at all levels.

Figure 7.3 presents the all-sky and clear-sky net IRFs averaged over 0-60°S at the TOA, TROP, and SURF, calculated using the WACCM6MAM-nd ensemble with nudged meteorological fields (see Supplementary S1 for more information about HTHH-MOC). The all-sky SA+WV and SA IRFs are approximately 20–30% smaller than their clear-sky counterparts. The all-sky IRF exhibits stronger temporal changes than the clear-sky IRF due to cloud variability (Figure 7.3). The near-hemispheric (0-60°S) average clear-sky SA+WV net IRFs at TOA, TROP, and SURF generally follow the SA net IRF, averaging around -0.5 W m^{-2} over 2022-2023. The increase in SA IRF magnitude during the austral summer of 2022-2023 is attributed to the poleward spread of SA into southern mid- and high latitudes and the seasonal rise in solar insolation. As previously noted, the IRFs in Figure 7.3 are based on the simulations with a 0.5 Tg SO_2 emission. To match the observed SAOD the models would likely have to increase SO_2 emissions by a factor of 1.3-2.0. With this adjustment and considering that Figure 7.3 shows the 0–60°S average rather than global IRF, the HTHH-MOC results are consistent with findings from Schoeberl et al. (2024), Stenchikov et al. (2025) and Gupta et al. (2025).

The clear-sky WV net IRF at TOA in the WACCM6-MAM-nd run with nudged meteorology is negative in 2022, but counter-intuitively becomes slightly positive in 2023 (Figure 7.3a). This may be due to changes in ozone or PSCs, as the method used by the HTHH-MOC models to calculate IRF does not isolate or remove the effects of ozone and PSCs. The HTHH-MOC WV IRF is broadly consistent with other estimates of WV IRF (Stenchikov et al., 2025; Wang and Huang, 2024). The SW WV IRF is caused by WV NIR absorption and is at least one order of magnitude smaller than the LW WV IRF. Although it is included in

all calculations, its contribution appears negligible. Stenchikov et al. (2025) and Wang and Huang (2024) calculated the WV IRF using climate models and reported consistent WV IRFs at TOA of the order −0.05 W m^{-2}.

After the first 5-6 months following the injection, Hunga's WV layer tends to ascend in the stratosphere and thus has a longer stratospheric residence time (4-7 years) than SA (see Figures 7.1 and 7.2). SA and WV radiative impacts counteract each other for about 2 years when Hunga's SAs are present in the stratosphere. In contrast to SA, which warms the stratosphere and cools the troposphere, stratospheric WV cools the stratosphere and warms the troposphere (Forster and Shine, 1999; Solomon et al., 2010; Dessler et al., 2013). The SA RF<0 prevails during the first 2 years (Schoeberl et al., 2024; Stenchikov et al., 2025; Gupta et al., 2025). After 2 years, only Hunga WV RF>0 matters, which could potentially warm the climate (Jenkins et al., 2023; Jucker et al., 2024; Wang and Huang, 2024), even though, as assessed in this Chapter, that impact is likely to be undetectable.

The stratospheric WV layer absorbs upward LW flux, attenuating the outgoing LW irradiance above the WV layer. However, it also increases upward LW flux from local emission, compensating for this attenuation. As a result, WV LW RF at TOA remains minimal, while heating rates within the WV layer reach −0.2 K/day, causing cooling in the stratosphere (Chapter 4; Stenchikov et al., 2025). Riese et al. (2012) show that a stratospheric WV layer below 20 hPa causes a positive IRF, while a WV layer above 20 hPa causes a negative IRF. However, whether there is overall heating or cooling of the Earth's surface strongly depends on the water vapour's vertical (and perhaps horizontal) distribution and stratospheric temperature adjustment. These factors deserve further consideration.

7.3.4 Empirically calculated ERF

Schoeberl et al. (2024) computed the clear-sky SA ERF (Figure 7.4) using observed aerosol extinction and a parametrisation similar to Yu et al. (2023a), Yu and Huang (2023) and Yu et al. (2023b). In Figure 7.4, the total forcing along with the various forcing components are shown. Figures 7.4a, b show the net forcing computed using the NASA and USask OMPS aerosol SAOD estimates. The SA forcing is confined mainly to the Southern Hemisphere low- and mid-latitudes (see Figure 7.4a, b, Stenchikov et al., 2025; Schoeberl et al., 2023; Schoeberl et al., 2024). The clear-sky net ERF calculated using NASA OMPS-LP-V2.1 SAOD exceeds −1 W/m^2 in the tropics, while the ERF calculated using the USask SAOD retrievals is about half that amount. The components of ERF from various optically active agents are shown at the equator, 20°S, and 40°S, illustrating their evolution over time. The black line is the net total ERF. The SW SA forcing component is in red. As the aerosol disperses and sediments out of the stratosphere, its radiative forcing becomes negligible by the end of 2023. The SA loading, initially highest in the tropics at the beginning of 2022, shifts to the southern extra-tropics by the end of 2022. NIR absorption by WV (yellow-green) is much weaker than its LW emission (green). The WV LW flux increases the TROP ERF, whereas the NIR absorption by WV reduces it. Finally, the changes in LW flux due to stratospheric temperature changes (dark blue) also modify the net flux. The temperature anomalies are the observed 2022-2023 differences from the 10-year climatology. These anomalies reflect some natural variability and therefore do not provide a clean estimate of the temperature adjustment contribution to the ERF. The impact of natural temperature variability, which is highest in the extra-tropics, can be seen toward the end of 2023, where all the other radiative anomalies have diminished.

The secondary circulation set up by the water vapour radiative cooling in the stratosphere causes a decrease in column ozone in mid-to-late 2022 (Wang et al., 2023; Wilmouth et al., 2023). The ozone decrease could be partially caused by changes in planetary wave propagation and the BDC driven by the Hunga volcanic (WV+SA) forcing (Yu et al., 2023b). Ozone depletion causes increases in the SW downward flux at TROP and SURF, partly compensating for aerosol dimming. Schoeberl et al. (2024) computed ozone IRF directly from observed changes in stratospheric ozone (see Figure 7.4), which is surprisingly large. The stratospheric ozone reduction increases the solar flux, even though the ozone reduction is modest (orange line). Ozone LW flux (blue-green) changes are small and are included here only for completeness. It should be noted that the ozone ERF estimate presented here represents an upper bound, as it does not account for the attenuation of tropical UV flux by the Hunga aerosol layer. The ozone ERF is significantly smaller than the SA IRF.

7.3.5 Model calculated ERF

On average, the stratospheric net IRF driven by WV (and ozone) is small compared to the aerosol net IRF.

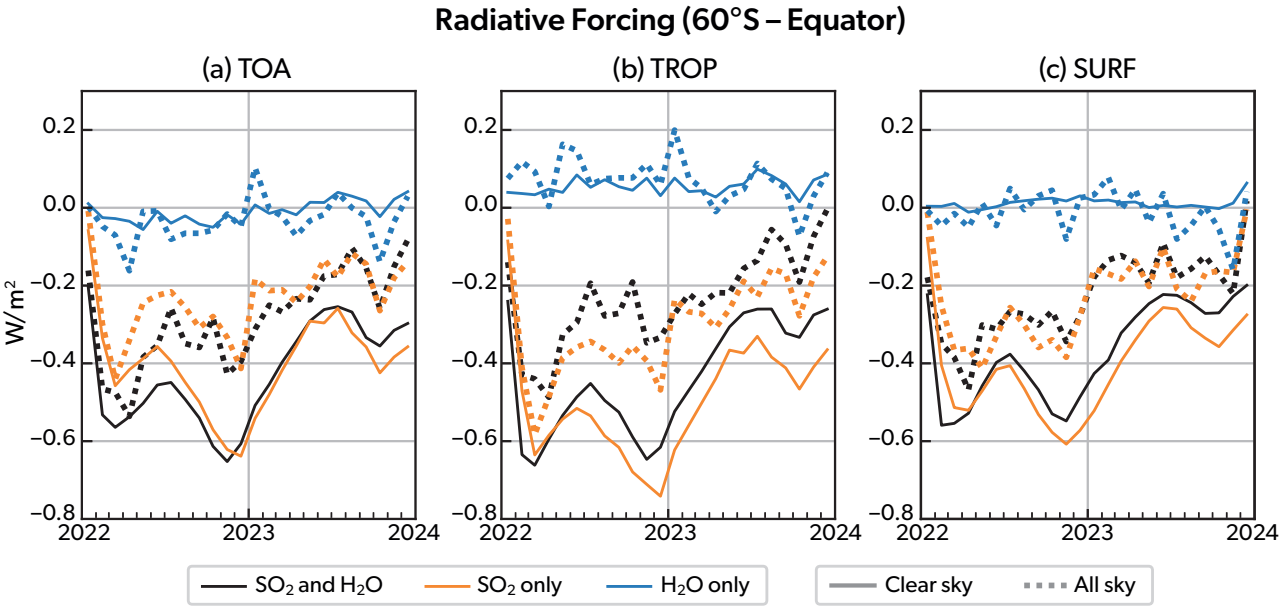

Figure 7.3: *All-sky (dotted curves) and clear-sky (solid curves) (0-60°S) average net SA+WV, WV, and SA IRFs (W m^{-2}) from the WACCM6MAM-nd run with nudged meteorology: (a) at TOA; (b) at TROP; (c) at SURF. (Adapted from Quaglia et al., 2025.)*

During the first two years, the WV and ozone IRFs were overwhelmed by a negative SA IRF, so the net global IRF at all levels was about −0.4±0.1 W m^{-2} (Schoeberl et al., 2024; Stenchikov et al., 2025). This is also found for ERF. Unlike IRF, the ERF cannot be calculated simultaneously for the SA and WV in a climate model in one run (Stenchikov et al., 2025). However, the SW components of IRF and ERF are similar at all levels. The LW ERF might differ from the LW IRF due to, e.g., stratospheric temperature adjustment. For example, the LW WV ERF at TOA has a different sign (positive) than the LW WV IRF (negative).

Stenchikov et al. (2025) calculated LW and SW WV and SA ERF, combining results from the different experiments (SA+WV and WV only) with a regional climate model, WRF-Chem, that interactively calculated the spatial-temporal distribution of volcanic plume, SAOD, and temperature responses. Wang and Huang (2024) calculated WV ERF assuming a prescribed WV perturbation in the 50-10 hPa layer using the FDH method (Fels et al., 1980). Despite different approaches, globally averaged WV ERF from Stenchikov et al. (2025) and WV ERF from Wang and Huang (2024) are consistent with each other, amounting to 0.05 W m^{-2}.

In the HTHH-MOC, SA+WV ERF is obtained from the prescribed ocean WACCM6MAM-fs ensemble, with SO_2 and WV emissions. Long-term integrated effects can be determined by computing an integrated average $\overline{\text{ERF}}$ defined as

$$\overline{ERF}(t) = \frac{1}{t} \times \int_0^t ERF(t')dt' \qquad (7.1)$$

To evaluate the long-term radiative impact of the Hunga plume, we plot in Figure 7.5 the (0-60°S) average clear-sky net time integrated ensemble mean SA+WV net $\overline{ERF}$. We also show $\overline{IRF}$

$$\overline{IRF}(t) = \frac{1}{t} \times \int_0^t IRF(t')dt' \qquad (7.2)$$

calculated within the run with nudged meteorology, WACCM6MAM-nd, and $\overline{RF}$ calculated as (Hunga-control) within the WACCM6MAM-co ensemble with coupled ocean using a similar operator:

$$\overline{RF}(t) = \frac{1}{t} \times \int_0^t RF(t')dt' \qquad (7.3)$$

In Figures 7.5a, b, c we present net $\overline{\text{ERF}}$, $\overline{\text{IRF}}$, and $\overline{\text{RF}}$ at the TOA, TROP, and SURF, respectively. At each time, $\overline{\text{ERF}}$ (as well as $\overline{\text{IRF}}$ and $\overline{\text{RF}}$) is equal to the average forcing for all previous periods starting from the time of the Hunga eruption. $\overline{\text{ERF}}$ is much smoother than the instantaneous (0-60°S) averaged ERF and is a more precise metric of the perturbation of the energy balance of the climate system. Increased stratospheric WV tends to warm the climate system on average, but SA cooling prevails for the entire simulation period.

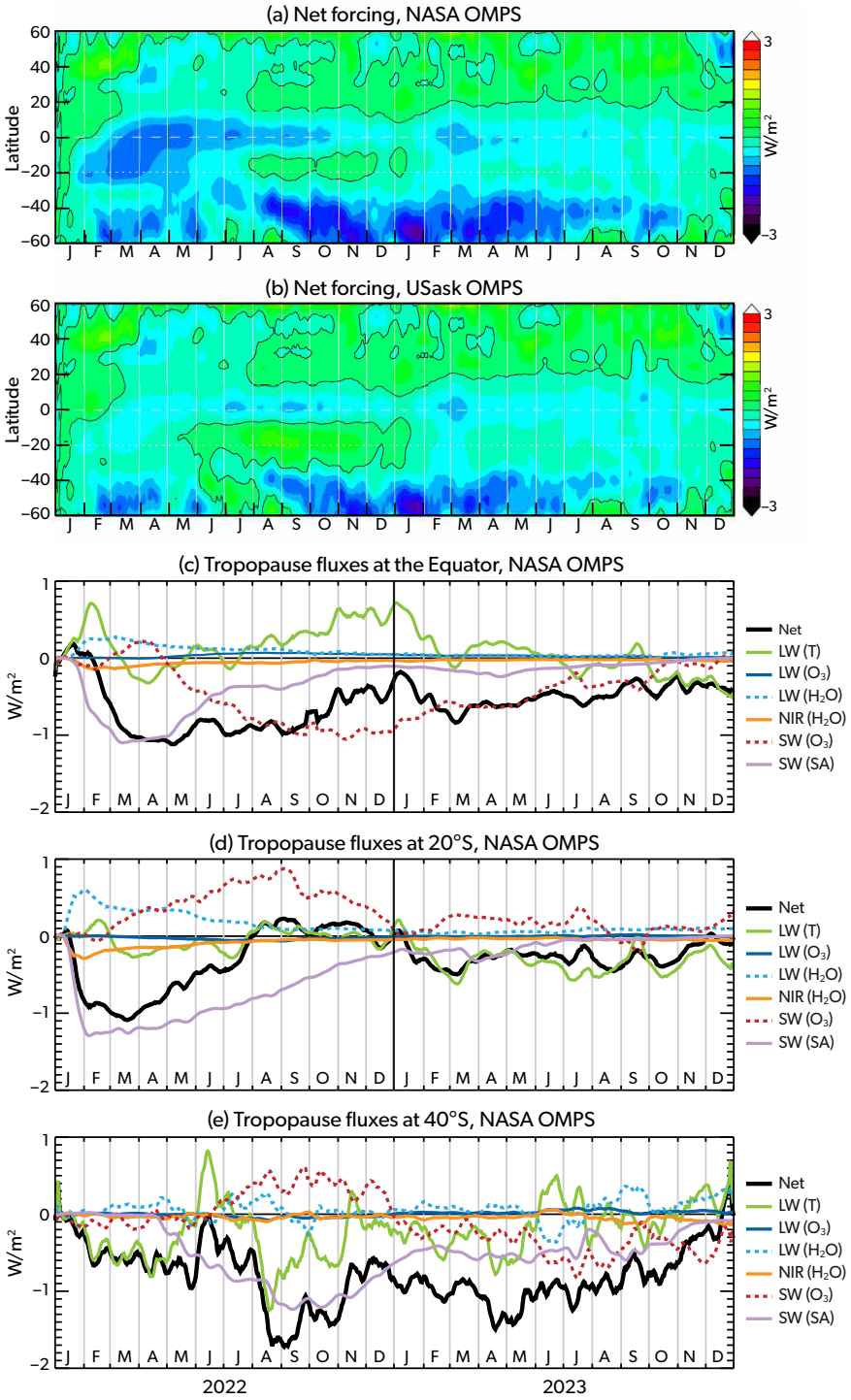

Figure 7.4: *Hunga's clear-sky empirically calculated ERF at the TROP: (a) Using SAOD obtained by the NASA OMPS-LP-V2.1 algorithm (Taha et al., 2021; Taha et al., 2022) and (b) Using SAOD obtained by the USask algorithm (Bourassa et al., 2023), which has a smaller estimated SAOD. Panels (c, d, e) show the various radiative forcing components of TOA's ERF as labelled in the legend at the Equator, 20°S, and 40°S. (Adapted from Schoeberl et al., 2024, reproduced with permission.)*

In 2023, the $\overline{\text{IRF}}$ (calculated within the run with nudged meteorology, WACCM6MAM-nd) reaches −0.5 W m^{-2} at the TOA, −0.55 W m^{-2} at the tropopause, and −0.45 W m^{-2} at the surface, with values around −0.4 W m^{-2} at all levels in 2024. The $\overline{\text{ERF}}$ (calculated within the ensemble with prescribed ocean, WACCM6MAM-fs) is slightly weaker, reaching −0.3 W m^{-2}, −0.45 W m^{-2}, and −0.4 W m^{-2} at TOA, TROP, and SURF, respectively. The $\overline{\text{RF}}$ (calculated within the ensemble with coupled ocean, WACCM6MAM-co) closely tracks $\overline{\text{ERF}}$ during the first two years following the eruption.

In 2030, $\overline{\text{ERF}}$ is still of the order of −0.1 W m^{-2}, indicating the decadal-average cooling effect of the Hunga eruption. Two years after the eruption, $\overline{\text{ERF}}$ at TOA equals −0.3 W m^{-2}, while $\overline{\text{IRF}}$ equals −0.4 W m^{-2}. This is consistent (assuming an increase of SO_2 emission by a factor of 1.3-2.0, as discussed above) with other estimates made using observations and different models (Schoeberl et al., 2024; Stenchikov et al., 2025; Gupta et al., 2025).

7.3.6 Uncertainty in radiative forcing

Discrepancies among the various estimates of the radiative forcing of Hunga primarily stem from uncertainties in the amount of injected SO_2 (Carn et al., 2022; Sellitto et al., 2024) and in the measurements of SAOD (Figure 7.1a, Taha et al., 2022; Bourassa et al., 2023; Schoeberl et al., 2024). Models may also introduce inconsistencies due to differences in their representations of SA and WV transformation processes and transport. The abundance of WV affects stratospheric temperature, chemistry, and dynamics, as described in 4 and 5, with the potential to indirectly influence the planet's radiative balance. These processes are technically included in the HTHH-MOC, but the ability of the model to quantitatively simulate these indirect effects remains a challenge.

The RFs calculated with the same model but in different experiments also could differ. The net SA+WV IRF calculated from the WACCM6MAM-nd run with nudged meteorology, ERF calculated using the WACCM6MAM-fs ensemble with prescribed SST, and RF calculated using the WACCM6MAM-co ensemble with coupled ocean are shown in Figure 7.6 at TOA, TROP, and SURF. The difference between the RFs appears to be about 10–20%.

However, the uncertainties in clear-sky IRFs calculated in four different models (Figure 7.7) reach 50% at TOA and TROP and are slightly smaller at SURF. These models all use nudged meteorology so that

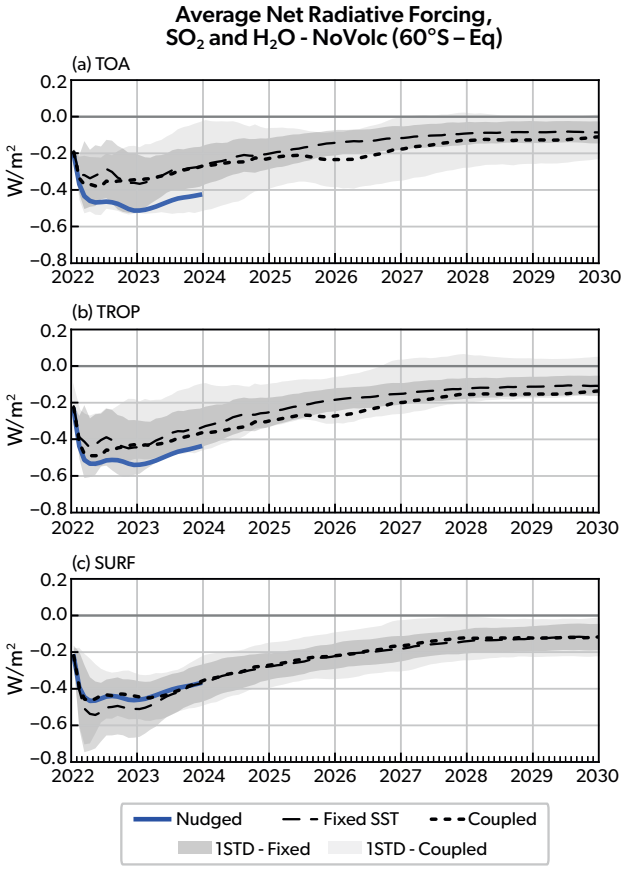

Figure 7.5: *Near-hemispheric (0–60°S) average clear-sky net ensemble-mean Hunga $\overline{ERF}$ from the WACCM6MAM-fs prescribed-ocean ensembles, $\overline{IRF}$ from the WACCM6MAM-nd run with nudged meteorology, and $\overline{RF}$ from the WACCM6MAM-co coupled-ocean ensemble: (a) at TOA; (b) at TROP; (c) at SURF. (Adapted from Quaglia et al., 2025.)*

temperature differences are minimised. Thus, the discrepancies in IRF are only due to model differences in radiatively active constituents and radiative transfer parametrisations (ozone, H_2O, aerosols, PSCs), with aerosol differences being the dominant contribution. The uncertainty between the models is likely driven by the differences in the aerosol microphysics parametrisations, as the most significant IRF differences are seen between the models with different aerosol microphysics. The net IRF is highest in WACCM6MAM, which uses mode microphysics (Mills et al., 2016). In contrast, WACCM6CARMA, which employs bin microphysics (Tilmes et al., 2023), produces a net IRF that is roughly half as strong as that of WACCM6MAM. Finally, calculating RF for WV using broadband radiative transfer models (used in all climate models) could also be associated with a 30% computational error (Maycock and Shine, 2012; Forster et al., 2011; Stenchikov et al., 2025). However,

this computational uncertainty is likely not critical, as the WV IRF is relatively small compared to the SA IRF during 2022–2024.

7.4 Hunga's climate impact

The impact of the Hunga eruption on tropospheric climate has been assessed using energy balance models (EBM) (e.g., Jenkins et al., 2023; Zhang et al., 2022), statistical relationships from past volcanic events (e.g., Schoeberl et al., 2024), or by scaling based on historical eruptions like Pinatubo in 1991 (Stenchikov et al., 2025). Clear-sky and all-sky RF are effective scaling predictors, producing comparable estimates for the Hunga eruption. From this perspective, Hunga's clear-sky SA + WV net RF is almost one order of magnitude smaller (in absolute value) than the clear-sky net SA RF generated by the 1991 Pinatubo eruption (-3.5 W/m^2; Stenchikov et al., 1998). Consistently, the maximum global mean surface temperature change in response to the Hunga eruption is expected to be about 10 times smaller than that caused by the Pinatubo eruption (Santer et al., 2001; Stenchikov et al., 2009), i.e., of the order of 0.05 K.

Climate models are more advanced tools (compared to EBMs and scaling) for assessing climate impacts. However, the internal variability in climate models can complicate the interpretation of climate responses to external forcing, especially when the forcing is small. Several studies have utilised climate models to evaluate the impact of the Hunga eruption (Zhu et al., 2022; Jucker et al., 2024; Stenchikov et al., 2025; Kuchar et al., 2025; Yook et al., 2025; Zhuo et al., 2025; Bednarz et al., 2026). Challenges arise due to the small response magnitude and RF uncertainties, complicating interpretation of the results. Here we show output from the HTHH-MOC ensemble runs (see Supplementary S3), which provide standardised simulations of the climate consequences of the Hunga eruption.

Section 7.3 describes Hunga's RFs, revealing that in the first two years following the eruption (2022–2023), SA RF dominates over the WV RF. After 2024, however, the SA RF decreases, so that the impacts of perturbations in WV and ozone become dominant. Accordingly, we divide our analysis of tropospheric climate changes into two phases: (1) the period when direct SA RF primarily drives climate perturbations (2022–2023) and (2) the period when only direct WV RF remains (2024–2031). It has been suggested (Kuchar et al., 2025; Stenchikov et al., 2025; Bednarz et al., 2026) that the direct WV radiative effect may be complicated by secondary effects resulting from the substantial chemical and dynamic feedbacks to perturbations of temperature, chemical composition, and circulation in the stratosphere caused by the Hunga eruption. If these stratospheric changes influence the troposphere, they could lead to longer-term tropospheric impacts. Therefore, we dedicate a separate section to examining tropospheric perturbations, focusing on stratosphere-troposphere dynamic interactions in high latitudes of both hemispheres and the role of stratospheric ozone changes.

7.4.1 SA-dominated climate response (2022-2023)

A detailed comparison of the models in the HTHH-MOC collection is provided in Supplementary S3 and in Zhuo et al. (2025). Here, we show the output from the WACCM6MAM ensemble, which exhibits the largest (in absolute value) IRF (see Figure 7.7), to explore the physical aspects of the response while utilising results from multiple models to assess the spread of outcomes, which we interpret as an uncertainty range.

First, we tested the global average surface air temperature (SAT) response to Hunga's RF (see Figure 7.8). We analyse the ensemble mean SAT perturbations ΔSAT calculated as the difference between perturbed WACCM6MAM-co (with coupled ocean model) and WACCM6MAM-fs (with prescribed SSTs) runs with SO_2 and WV emissions, and the corresponding control ensemble WACCM6MAM (without volcanic emissions).

We consider ΔSAT averages over land (ΔSAT_L), over the ocean (ΔSAT_O), and globally (ΔSAT_G). In the WACCM6MAM-co ensemble, ΔSAT_L is three times as large compared to ΔSAT_O, but hardly exceeds two SAT standard deviations in the control ensemble without volcanic injections during the 2022–2023 period. In other words, Hunga's climate impact remains barely distinguishable from natural internal variability, even when averaged over the 30-member ensemble. In the WACCM6MAM-fs ensemble with prescribed SSTs, the ΔSAT variability lacks the low-frequency oscillation induced by the perturbation of the ocean's ENSO cycle.

To reduce the SAT variability, we introduce an integrated time-dependent average $\overline{\Delta SAT}$

$$\overline{\Delta SAT}(t) = \frac{1}{t} \times \int_0^t \Delta SAT(t')dt' \qquad (7.4)$$

$\overline{\Delta SAT}$ represents the average of ΔSAT over a given

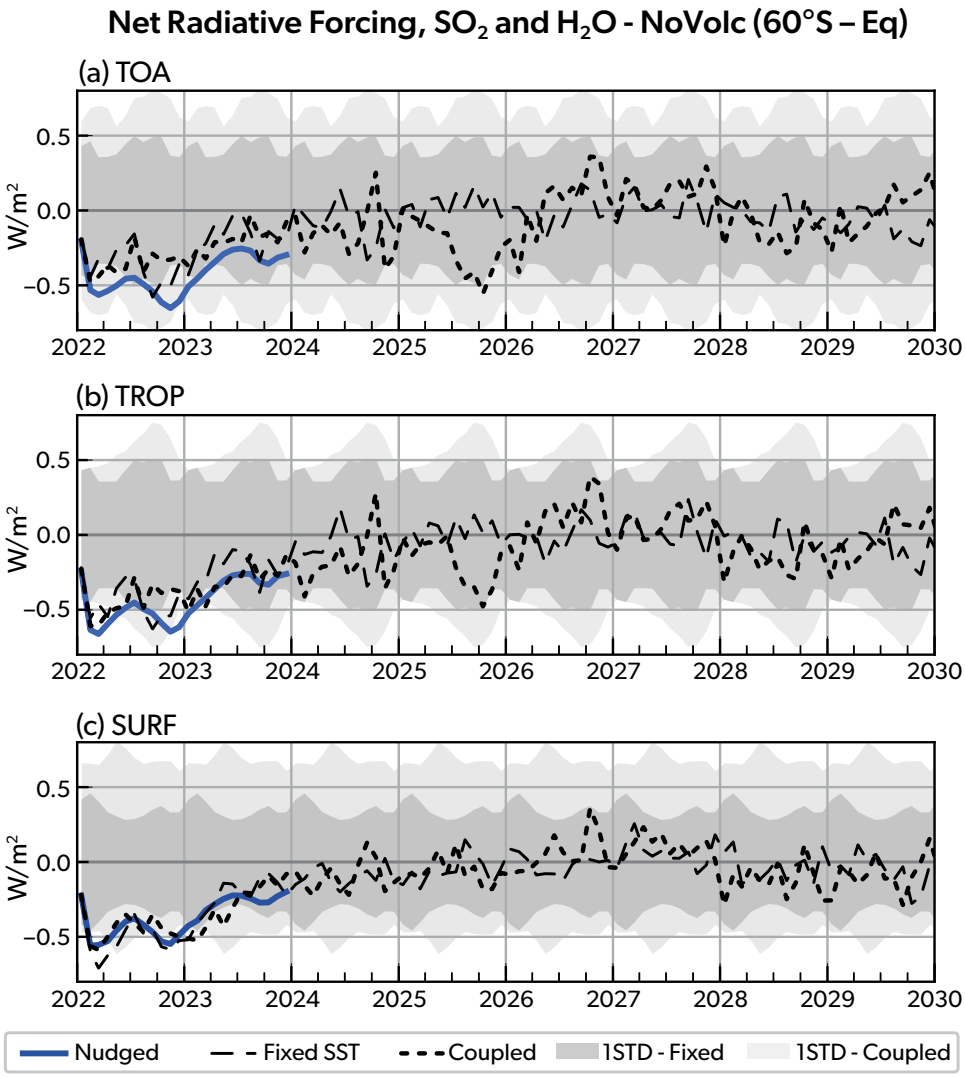

Figure 7.6: *Near-hemispheric (0-60°S) SA+WV clear-sky RFs (W m^{-2}) from the WACCM6MAM-nd run with nudged meteorology, the WACCM6MAM-co ensembles with coupled ocean, and the WACCM6MAM-fs ensembles with prescribed SSTs, shown at (a) TOA, (b) TROP, and (c) SURF. Dark shading indicates the one-standard-deviation range for WACCM6MAM-fs, while light shading indicates the one-standard-deviation range for WACCM6MAM-co. (Adapted from Quaglia et al., 2025.)*

time period starting from the Hunga eruption. $\overline{\Delta SAT}$ over land ($\overline{\Delta SAT}_L$), ocean ($\overline{\Delta SAT}_O$), and global ($\overline{\Delta SAT}_G$) areas are shown in Table 7.2. As expected, $\overline{\Delta SAT}_L$ in the coupled-ocean runs is almost three times larger than $\overline{\Delta SAT}_O$. An interactive ocean adds to the low-frequency variability (with ~3-year periodicity) in ΔSAT. The global accumulated cooling is largest at two years past the eruption, reaching −0.0303 K. This agrees with the −0.05 K cooling estimate obtained by scaling the Pinatubo *SAT* perturbation (Stenchikov et al., 2025). This magnitude of cooling is also consistent with other estimates (Zhang et al., 2022; Schoeberl et al., 2023). Such a slight temperature change would not be detectable above internal variability (see Figure 7.8).

The $\overline{\Delta SAT}$ in the WACCM6MAM-fs ensemble with prescribed SST is presented in Table 7.3. It also shows a generally small cooling response. However, the variability of the response indicates that the effect of natural variability is significant. For example, $\overline{\Delta SAT}$ over the ocean is positive (while RF < 0) during the first year, indicating that internal variability exceeds the forced signal. However, the 10-year average global mean $\overline{\Delta SAT}_G$ is negative and consistent between the coupled-ocean and fixed-SST ensembles. As expected, $\overline{\Delta SAT}_L$ in the coupled-ocean runs is almost three times larger than $\overline{\Delta SAT}_O$.

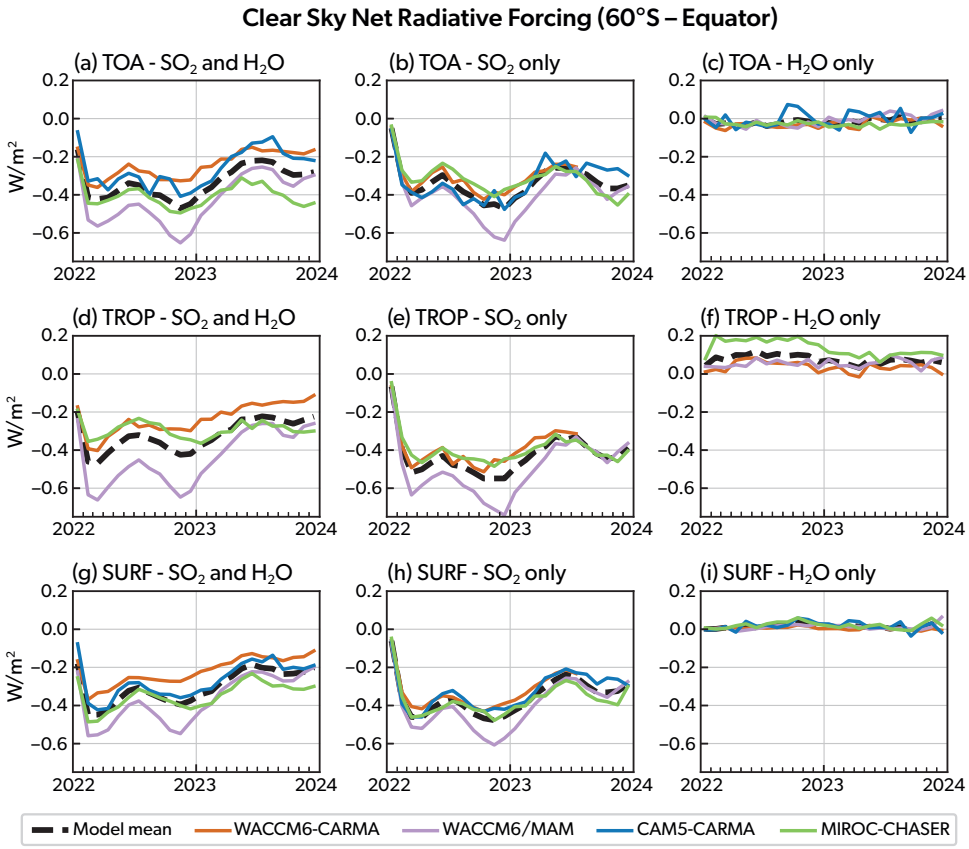

Figure 7.7: *Near-hemispheric (0–60°S) average WV+SA (a, d, g), SA (b, e, h), and WV (c, f, i) clear-sky net IRFs (W m^{-2}) calculated in runs with nudged meteorology for different models, as indicated in the legend, at: (a–c) TOA, (d–f) TROP, and (g–i) SURF. (Adapted from Quaglia et al., 2025.)*

Table 7.2: *Ensemble mean $\overline{\Delta SAT}$ (K) from the WACCM6MAM-co ensemble.*

AREA	6 MONTHS	1 YEAR	2 YEARS	5 YEARS	10 YEARS
LAND	−0.0850	−0.0240	−0.0836	−0.0274	−0.0173
OCEAN	0.0021	−0.0005	−0.0009	0.0038	0.0038
GLOBAL	−0.0295	−0.0086	−0.0303	−0.0074	−0.0004

7.4.2 WV-dominated climate response (2024-2030)

It is expected that the Hunga WV has a residence time of 4–7 years, longer than SAs (Fleming et al., 2024; Schoeberl et al., 2025). However, despite its prolonged presence in the stratosphere, WV's ability to impact surface temperature and climate depends on its altitude and latitudinal distribution (Solomon et al., 2010). Like the transient climate effects of SA, Hunga's WV impact on middle and lower stratosphere temperature and ozone concentration is limited to 2–3 years. As WV ascends into the upper stratosphere and mesosphere, its direct influence on the dynamics and chemistry of the middle and lower stratosphere diminishes. Figure 7.9 presents the ensemble mean zonally averaged temperature responses (Hunga − control) at the surface and in the stratosphere at the 20 hPa and 50 hPa pressure levels, derived from the 30-member WACCM6MAM-fs and WACCM6MAM-co ensembles. In experiments with prescribed SST, ΔSAT is negligible within the 60°S–60°N latitude band; however, in coupled ocean-atmosphere simulations, equatorial temperatures exhibit periodic fluctuations with an amplitude of approximately 0.3 K due to ENSO variability. These ensemble-mean equatorial ΔSAT perturbations remain detectable even four years post-eruption (Bednarz et al., 2026).

The La Niña could be affected by negative SA RF, and by the northward shift of the intertropical convergence zone (ITCZ) forced by the SA's cooling of the SH (Pausata et al., 2015; Predybaylo et al., 2017). The strengthening of El Niño in 2025–2026 may be

Table 7.3: *Ensemble mean $\overline{\Delta SAT}$ (K) from the WACCN6MAM-fs ensemble.*

AREA	6 MONTHS	1 YEAR	2 YEARS	5 YEARS	10 YEARS
LAND	−0.0052	0.0055	−0.0086	−0.0265	−0.0235
OCEAN	0.0148	0.0026	−0.0008	−0.0007	−0.0020
GLOBAL	0.0072	0.0034	−0.0038	−0.0102	−0.0099

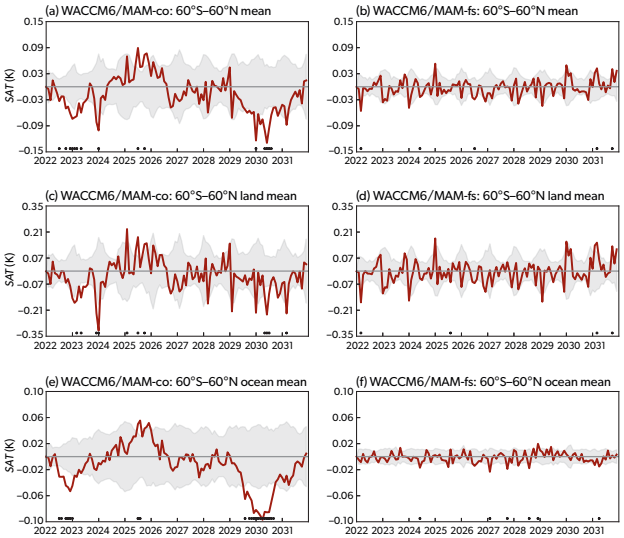

Figure 7.8: *Near-global (60°S-60°N) averaged ensemble mean surface air temperature SAT (K) change (Hunga - control) from the WACCM6MAM-co (left column) and prescribed SST WACCM6MAM-fs (right column) ensembles. Red solid lines show the 30-member ensemble mean. Gray shading belts are ± 2 SAT standard deviations from the control run. (a, b) ΔSAT_G (global), (c, d) ΔSAT_L (land), and (e, f) ΔSAT_O (ocean). Dots at the bottom of the panels indicate the time periods when the SAT perturbation exceeds 2 standard deviations.*

in response to a stronger La Niña in 2022–2023. The enhancement of the ENSO cycle amplitude might potentially affect tropospheric temperature and circulation, as well as cause perturbations in the stratosphere (Simpson et al., 2011; Walsh et al., 2022). However, the perturbations from Hunga are too weak to produce a significant global climate response, and further analysis is required to determine whether the simulated ENSO changes can be attributed to the eruption's impact.

In contrast to the troposphere, the stratosphere exhibits lasting forced temperature signals corresponding to Hunga's water vapour in the upper and lower stratosphere, as well as ozone perturbations in polar regions in both hemispheres (see Figure 7.9 and Chapters 4 and 5). Notably, the stratospheric temperature responses in the coupled-ocean and prescribed SST ensembles were nearly identical in the low and SH midlatitudes but differed in the polar stratosphere. Polar stratospheric cooling may be linked to dynamics (strengthening of the polar vortex) and/or Hunga-induced ozone depletion (see Chapter 5), which could delay (at least in the model) the spring break-up of the polar vortices.

7.4.3 Indirect atmospheric effects

Although Hunga's direct radiative impact on the tropospheric climate is limited, climate feedbacks driven by stratospheric WV perturbations may influence tropospheric conditions. Among the most significant feedback mechanisms are the chemical and dynamical effects of elevated stratospheric WV on ozone concentrations (Fleming et al., 2024; Schoeberl et al., 2024; Evan et al., 2023; Lu et al., 2023; Zhang et al., 2024; Wang et al., 2023; Wilmouth et al., 2023), as well as the stratospheric cooling resulting from WV's radiative effects (Coy et al., 2022; Schoeberl et al., 2022; Kuchar et al., 2025; Bednarz et al., 2026; Niemeier et al., 2023).

Changes in equatorial stratospheric temperatures and polar ozone concentrations modify the meridional temperature gradient between the equator and the poles, thereby influencing stratospheric circulation by strengthening or weakening the polar vortices. These changes involve wave–mean flow interactions and can propagate downward, affecting the troposphere through stratosphere–troposphere dynamical coupling. This coupling can alter the strength and position of the subtropical jet (Thompson and Wallace, 1998; Thompson and Wallace, 2000; Baldwin et al., 2001; Stenchikov et al., 2002; Kuchar et al., 2025; Bednarz et al., 2026). Such interactions may lead to modifications of the Northern Hemisphere (NH) and Southern Hemisphere (SH) annular modes (NAM and SAM), potentially enhancing or weakening them, which in turn influences winter climate in extratropical regions (Ramaswamy, 2006; Shindell et al., 2003; Shindell et al., 2004; Stenchikov et al., 2002; Stenchikov et al., 2004; Stenchikov et al., 2006; Perlwitz and Graf, 2001; Kodera, 1994; Graf et al., 1994).

Hunga's water vapour radiative forcing drives strato-

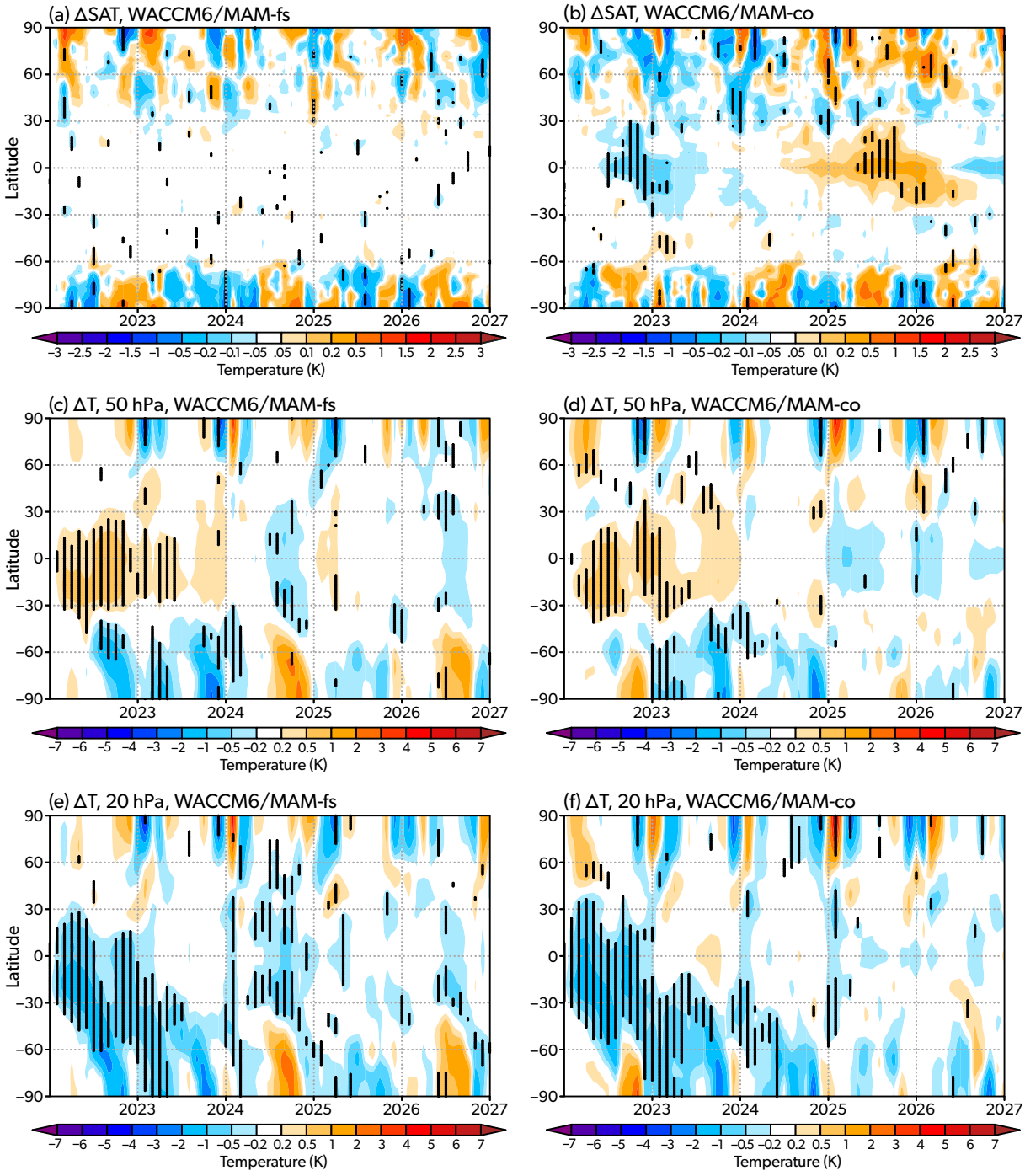

Figure 7.9: *Zonally averaged ensemble mean perturbations (Hunga - control): (a, b) surface air temperature ΔSAT (K) from WACCM6MAM ensembles with prescribed SSTs (WACCM6MAM-fs) and coupled ocean (WACCM6MAM-co); (c, d) stratospheric temperature (K) at 50 hPa from WACCM6MAM-fs and WACCM6MAM-co; (e, f) stratospheric temperature (K) at 20 hPa from WACCM6MAM-fs and WACCM6MAM-co. Stippling indicates regions where the ensemble mean perturbation exceeds two standard deviations of the corresponding control ensemble mean. (Adapted from Bednarz et al., 2026.)*

spheric temperature perturbations in the middle and upper stratosphere for at least two years, as shown in Figures 7.9c–f and discussed in Chapter 4. In simulations that include both SO_2 and WV emissions, high-latitude ozone perturbations persist for 3–4 years (see Figure 7.10 and Chapters 3 and 4 for further details). As illustrated in Figures 7.9c–f, equatorial temperature anomalies exhibit opposite signs in the lower stratosphere (around 50 hPa) and upper stratosphere (around 20 hPa). This pattern indicates that Hunga's stratospheric temperature perturbations generate positive wind shear in the LS, reinforcing the Southern Hemisphere polar vortex, while inducing negative wind shear in the US, contributing to its weakening. As a result, the Hunga-induced temperature anomalies exert opposing influences on stratospheric circulation in the LS and US, complicating the interpretation of their net effect.

Polar ozone depletion can influence polar temperatures and strengthen the polar vortices, thereby favouring the positive phases of the SAM and NAM (Stenchikov et al., 2002; Waugh and Polvani, 2010; Dennison et al., 2015; Ivy et al., 2017). In the Southern Hemisphere, ozone depletion during the austral springs of 2024 and 2025 is linked to a stronger polar vortex and a delayed final warming. For instance, in the WACCM6MAM-fs and WACCM6MAM-co ensembles, the ozone loss observed during the 2023/2024 austral spring (Figures 7.10a, b) enhances the SH polar vortex, as reflected by stronger zonal winds at 50 hPa near 60°S (Figures 7.10c, d), delays the final warming, and produces a sea-level pressure anomaly consistent with a positive SAM phase (Figures 7.10e, f). Ozone depletion is more pronounced in the WACCM6MAM-fs ensemble compared to WACCM6MAM-co, resulting in larger anomalies in both the 50 hPa zonal wind and sea-level pressure response.

After 2025, Hunga-driven polar ozone perturbations are no longer robust. It is important to emphasise that both polar stratospheric responses and stratosphere–troposphere dynamical coupling are sensitive to model configurations and experimental setups. For example, in the WACCM6MAM-fs and WACCM6MAM-co ensembles (Figures 7.9c, d and 7.10c, d), the ensemble-mean perturbations of the SH and NH polar vortices differ between the ensembles. This inconsistency arises because the forced responses to the Hunga eruption are masked by substantial internal variability in the high-latitude climate.

In contrast to ozone variations in the middle stratosphere, which are more prominent at high southern and northern latitudes (Figures 7.10a, c), ozone perturbations in the upper stratosphere and lower mesosphere are observed primarily in the low and midlatitudes starting in 2024 (see Chapter 5). However, these perturbations lead to only minor changes in the total ozone column, as ozone concentrations at these altitudes are inherently low.

7.4.4 Uncertainties in climate response

To assess the intrinsic uncertainties in model simulations of the long-term *SAT* response to the 2022 Hunga eruption, we compare the responses from different models participating in HTHH-MOC. The global monthly ensemble mean ΔSAT exhibits significant temporal variability. Among the models, the WACCM6MAM-co ensembles and MIROC-CHASER-fs with prescribed SST demonstrate the most significant variability. It is expected that the coupled model exhibits larger year-to-year variability than the model with prescribed SST. For example, the variance of WACCM6MAM-co's ΔSAT is largest among the presented HTHH-MOC ensembles. However, the MIROC-CHASER-fs (not shown) has larger variance than WACCM6MAM-fs, almost matching the WACCM6MAM-co variability. This indicates that MIROC-CHASER-fs might have larger land temperature variability than WACCM6MAM-fs and WACCM6-MAM-co, even though its SAOD perturbation (see Figure 7.1) is smaller than in the WACCM6MAM-co and WACCM6MAM-fs ensembles.

An integrated average $\overline{\Delta SAT}$ introduced in Eq. 7.4 is more stable than the instantaneous ΔSAT, allowing a more reliable conclusion (see Table 7.4). All models show a negative $\overline{\Delta SAT}$ two years following the eruption, reflecting the integrated effect of negative SA forcing (cooling). The decade-average $\overline{\Delta SAT}$ is also negative across all models. However, their absolute values vary by an order of magnitude.

7.5 Discussion and conclusions

Chapter 7 explores the direct and indirect radiative effects of stratospheric WV and SA from the Hunga eruption and their potential climate impacts. The shallow-underwater eruption of the Hunga volcano was distinctive due to the significant amount of injected WV that is expected to persist in the stratosphere for 4–7 years. Unlike the plumes from the 1991 Pinatubo and 2019 Raikoke eruptions, the Hunga plume was initially injected at altitudes of 30–40 km, with overshoots reaching up to 58 km. It then gradually descended to around 27 km over the follow-

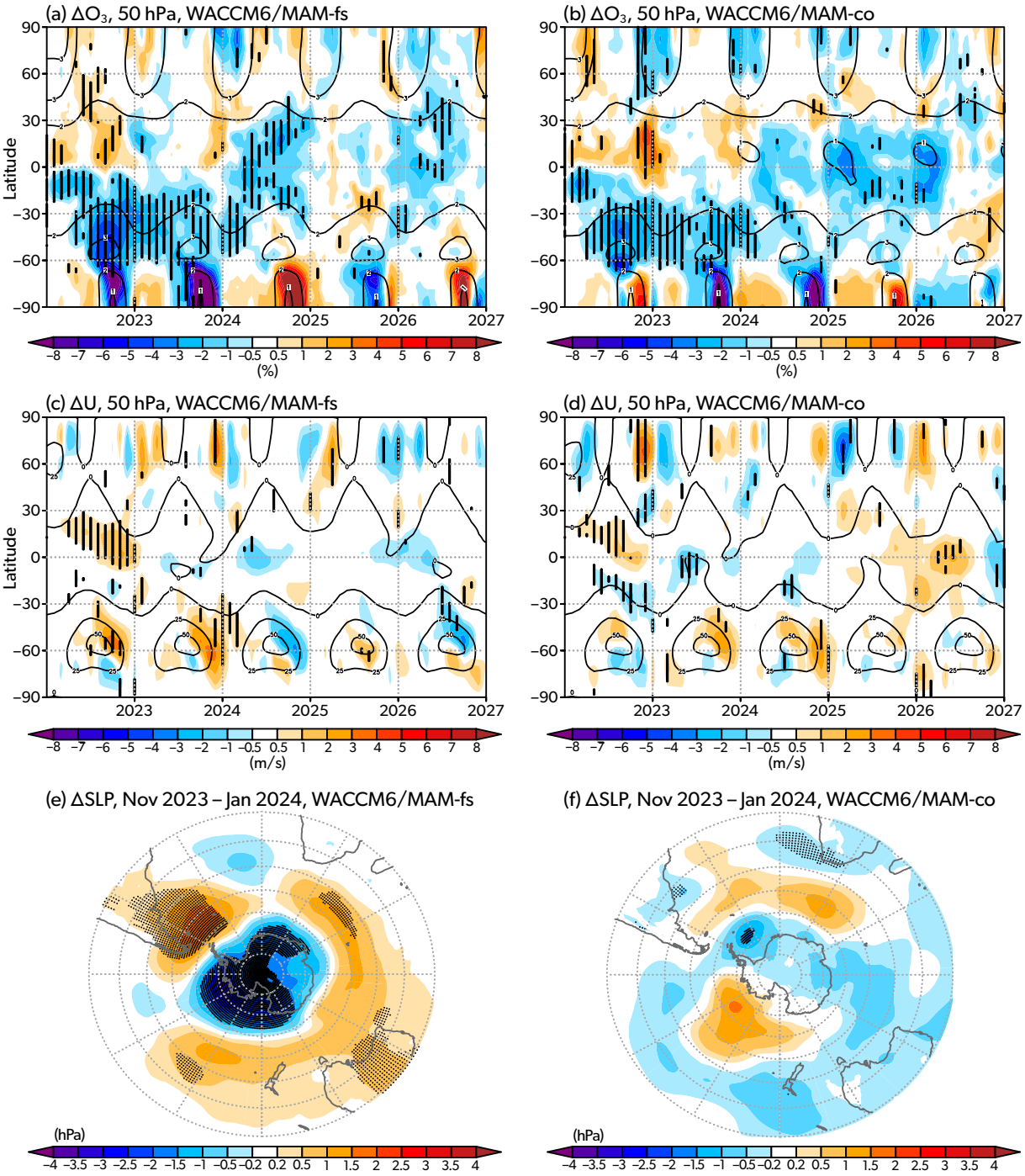

Figure 7.10: *Simulated ensemble-mean zonal-mean ozone changes (%) (Hunga – control) from (a) WACCM6MAM-fs and (b) WACCM6MAM-co. Ensemble-mean zonal-mean zonal wind changes (m s^{-1}) at 50 hPa from (c) WACCM6MAM-fs and (d) WACCM6MAM-co. Mean sea-level pressure changes (hPa) for November 2023–January 2024 (Hunga – control) from (e) WACCM6MAM-fs and (f) WACCM6MAM-co. Hatching indicates regions where the signal exceeds two standard deviations of the ensemble mean. (Adapted from Bednarz et al., 2026.)*

Table 7.4: *Ensemble means $\overline{\Delta SAT}$ (K) from different ensemble simulations.*

Model	6 MONTHS	1 YEAR	2 YEARS	5 YEARS	10 YEARS
WACCM6-MAM-co	−0.0295	−0.0086	−0.0303	−0.0074	−0.0004
WACCM6-MAM-fs	0.0072	0.0034	−0.0038	−0.0102	−0.0099
MIROC-CHASER-fs	−0.0324	−0.0045	−0.0085	−0.0055	−0.0060
GEOSCCM-fs	0.0043	−0.0041	−0.0114	0.0016	−0.0016

ing weeks, staying well above the tropopause (see Chapter 3). The injection height allowed the volcanic plume to initially persist within the high and middle stratosphere, which increased the SAOD per unit mass of emitted SO_2 compared to previous stratospheric penetrating volcanic eruptions (Stenchikov et al., 2025).

In the first two years following the Hunga eruption, the tropospheric cooling caused by stratospheric SAs outweighed the warming due to WV, possibly causing weak, undetectable surface cooling. The radiative impact of stratospheric WV on the tropospheric climate decreases rapidly with the altitude of the WV perturbation (Solomon et al., 2010; Riese et al., 2012; Dessler et al., 2013; Banerjee et al., 2019; Nowack et al., 2023). Since the Hunga eruption injected WV into the middle and upper stratosphere, its overall climate impact is relatively weak despite the substantial increase in stratospheric WV.

The overall (SA + WV) long-term direct radiative effect of Hunga's WV appears to be insignificant; that said, the Hunga eruption presents a unique opportunity to address broader questions regarding climate variability and stratospheric WV feedbacks in global warming (Forster and Shine, 2002; Solomon et al., 2010; Dessler et al., 2013; Charlesworth et al., 2023; Banerjee et al., 2019; Nowack et al., 2023). While WV leads to noticeable radiative cooling in the stratosphere, its IRF and ERF at TOA are minimal. As a result, the direct RF from WV is insufficient to trigger slow climate feedback mechanisms linked to ocean heat content (Sellitto et al., 2022; Stenchikov et al., 2025), and its radiative influence will diminish as the WV forcing decreases.

The main findings of this Chapter are as follows:

- Hunga's water vapour initially produced strong localised radiative cooling in the stratosphere, in contrast to the radiative heating typically caused by volcanic ash in the lower stratosphere following major explosive eruptions (e.g., the 1991 Pinatubo eruption).
- Accurate simulation of the Hunga cloud's initial evolution is critical, as WV phase transitions and the early dispersion of WV, SO_2, and SA strongly depend on injection altitude – a key factor in shaping its long-term behaviour. However, both observations and the HTHH-MOC models only partially capture the descent trajectory of the fresh Hunga cloud.
- Calculating IRF in HTHH-MOC models based on radiative flux differences between perturbed and control runs with nudged meteorology presents challenges in interpreting RF contributions from SA and WV. This approach introduces contamination from ozone and PSC effects, making it difficult to isolate the individual RFs of WV and SA. Integrating a double-call capability into the standard climate model configuration would help mitigate this issue, allowing for more precise attribution of radiative forcing components.
- Estimating SA radiative forcing using SO_2-only simulations may be unreliable, as the absence of WV-induced cooling prevents plume descent and leads to a markedly different evolution compared to simulations with concurrent WV and SO_2 emissions. However, in the WACCM6MAM experiments, this approach remained effective due to the relatively low injection height (~30 km), placing the plume near its level of neutral buoyancy.
- Comparison of stratospheric aerosol simulations with observations indicates that the Hunga volcano injected between 0.65 and 1.0 Tg of SO_2, with initial observational estimates falling at the lower end of this range.
- During the first two years (2022-2023), the radiative effects of WV and SAs counteract each other: WV cools the stratosphere and warms the troposphere, while SAs warm the stratosphere and cool the troposphere. This has not been observed in previous volcanic eruptions. Sulfate aerosol RF dominates in 2022-2023, while WV RF becomes dominant (but tiny) in 2024-2031. On average in 2022-2023, a

net global SA+WV IRF and ERF are about −0.4 W/m² at all atmospheric levels.

- WV IRF at TOA is negative, but ERF is positive, proving that Hunga's WV has a net (but very minor) warming effect on the planet. The WV RF is small at TOA and tropopause, and negligible at SURF, suggesting that the Hunga WV direct radiative impacts on climate are insignificant.
- Hunga's RF causes global 0.3-0.4 K cooling in the middle and upper stratosphere, but the domain average maximum $\overline{\Delta SAT}$ is weaker than −0.05 K, remaining within the bounds of natural variability.
- Climate model simulations show that Hunga may have had a very slight influence on the timing of ENSO and produced slight shifts in the subtropical jet. These changes would be overwhelmed by natural variability. The overall long-term *SAT* perturbations caused by the Hunga eruption are hardly detectable in the model simulations.

References

Abdelkader, M., G. Stenchikov, A. Pozzer, H. Tost and J. Lelieveld (2023). 'The effect of ash, water vapor, and heterogeneous chemistry on the evolution of a Pinatubo-size volcanic cloud'. *Atmos. Chem. Phys.*, 23, pp. 471–500. DOI: 10.5194/acp-23-471-2023.

Andersson, S. M., B. G. Martinsson, J. P. Vernier, J. Friberg, C. A. Brenninkmeijer, M. Hermann and A. Zahn (2015). 'Significant radiative impact of volcanic aerosol in the lowermost Stratosphere'. *Nat. Commun.*, 6, 7692. DOI: 10.1038/ncomms8692.

Andrews, T., C. J. Smith, G. Myhre, P. M. Forster, R. Chadwick and D. Ackerley (2021). 'Effective Radiative Forcing in a GCM With Fixed Surface Temperatures'. *J. Geophys. Res.*, 126, e2020JD033880. DOI: 10.1029/2020jd033880.

Appenzeller, C., J. R. Holton and K. H. Rosenlof (1996). 'Seasonal variation of mass transport across the tropopause'. *J. Geophys. Res.*, 101, pp. 15071–15078. DOI: 10.1029/96JD00821.

Baldwin, M. P., L. J. Gray, T. J. Dunkerton, K. Hamilton, P. H. Haynes, W. J. Randel, J. Holton, M. J. Alexander, I. Hirota and T. Horinouchi (2001). 'The quasi-biennial oscillation'. *Rev. Geophys.*, 39, pp. 179–229. DOI: 10.1029/1999rg000073.

Banerjee, A., G. Chiodo, M. Previdi, M. Ponater, A. J. Conley and L. M. Polvani (2019). 'Stratospheric water vapor: an important climate feedback'. *Clim. Dynam.*, 53, pp. 1697–1710. DOI: 10.1007/s00382-019-04721-4.

Baran, A. J. and J. S. Foot (1994). 'New application of the operational sounder HIRS in determining a climatology of sulphuric acid aerosol from the Pinatubo eruption'. *J. Geophys. Res.*, 99, pp. 25673–25679. DOI: 10.1029/94JD02044.

Barnes, J. E. and D. J. Hofmann (1997). 'Lidar measurements of stratospheric aerosol over Mauna Loa Observatory'. *Geophys. Res. Lett.*, 24, pp. 1923–1926. DOI: 10.1029/97GL01943.

Baron, A., P. Chazette, S. Khaykin, G. Payen, N. Marquestaut, N. Bègue and V. Duflot (2023). 'Early Evolution of the Stratospheric Aerosol Plume Following the 2022 Hunga Tonga-Hunga Ha'apai Eruption: Lidar Observations From Reunion (21°S, 55°E)'. *Geophys. Res. Lett.*, 50, e2022GL101751. DOI: 10.1029/2022gl101751.

Bednarz, E. M., A. H. Butler, X. Wang, Z. Zhuo, W. Yu, G. Stenchikov, M. Toohey and Y. Zhu (2026). 'Indirect climate impacts of the Hunga eruption'. *Atmos. Chem. Phys.*, 26, pp. 197–215. DOI: 10.5194/acp-26-197-2026.

Bluth, G. J., W. I. Rose, I. E. Sprod and A. J. Krueger (1997). 'Stratospheric Loading of Sulfur From Explosive Volcanic Eruptions'. *J. Geol.*, 105, pp. 671–684. DOI: 10.1086/515972.

Bluth, G. J. S., S. D. Doiron, C. C. Schnetzler, A. J. Krueger and L. S. Walter (1992). 'Global tracking of the SO_2 clouds from the June, 1991 Mount Pinatubo eruptions'. *Geophys. Res. Lett.*, 19, pp. 151–154. DOI: 10.1029/91GL02792.

Bourassa, A. E., D. J. Zawada, L. A. Rieger, T. W. Warnock, M. Toohey and D. A. Degenstein (2023). 'Tomographic retrievals of Hunga Tonga-Hunga Ha'apai volcanic aerosol'. *Geophys. Res. Lett.*, 50, e2022GL101978. DOI: 10.1029/2022GL101978.

Carn, S. A., L. Clarisse and A. J. Prata (2016). 'Multi-decadal satellite measurements of global volcanic degassing'. *J. Volcanol. Geotherm. Res.*, 311, pp. 99–134. DOI: 10.1016/j.jvolgeores.2016.01.002.

Carn, S. A., N. A. Krotkov, B. L. Fisher and C. Li (2022). 'Out of the blue: volcanic SO_2 emissions during the 2021-2022 Hunga Tonga-Hunga Ha'apai eruptions'. *Front. Earth Sci.*, 13. DOI: 10.3389/feart.2022.976962.

Charlesworth, E., F. Plöger, T. Birner, R. Baikhadzhaev, M. Abalos, N. L. Abraham and M. Riese (2023). 'Stratospheric water vapor affecting atmospheric circulation'. *Nat. Commun.*, 14, 3925. DOI: s41467-023-39559-2.

Chen, P., M. Xiong, R. Wang, Y. Yao, F. Tang, H. Chen and L. Qiu (2023). 'On the ionospheric disturbances in New Zealand and Australia following the eruption of the Hunga Tonga-Hunga Ha'apai volcano on 15 January 2022'. *Geoph. Monog. Series.*, 21, e2022SW003294. DOI: 10.1029/2022SW003294.

Chiou, E. W., L. W. Thomason and W. P. Chu (2006). 'Variability of Stratospheric Water Vapor Inferred from SAGE II, HALOE, and Boulder (Colorado) Balloon Measurements'. *J. Climate*, 19, pp. 4121–4133. DOI: 10.1175/JCLI3841.1.

Coy, L., P. Newman, K. Wargan, G. Partyka, S. Strahan and S. Pawson (2022). 'Stratospheric Circulation Changes Associated with the Hunga Tonga-Hunga Ha'apai Eruption'. *Geophys. Res. Lett.*, 49, e2022GL100982. DOI: 10.1029/2022GL100982.

Delworth, T. L., A. J. Broccoli, A. Rosati, R. J. Stouffer, V. Balaji, J. A. Beesley, W. F. Cooke, K. W. Dixon, J. Dunne, K. A. Dunne et al. (2006). 'GFDL's CM2 global coupled climate models. Part I: Formulation and simulation characteristics'. *J. Climate*, 19, pp. 643–674. DOI: 10.1175/JCLI3629.1.

Dennison, F. W., A. J. McDonald and O. Morgenstern (2015). 'The effect of ozone depletion on the Southern Annular Mode and stratosphere–troposphere coupling'. *J. Geophys. Res.*, 120, pp. 6305–6312. DOI: 10.1002/2014JD023009.

Deshler, T. (2008). 'A review of global stratospheric aerosol: Measurements, importance, life cycle and local stratospheric aerosol'. *Atmos. Res.*, 90, pp. 223–232. DOI: 10.1016/j.atmosres.2008.03.016.

Dessler, A. E., M. R. Schoeberl, T. Wang, S. Davis and K. H. Rosenlof (2013). 'Stratospheric water vapor feedback'. *Proc. Natl. Acad. Sci.*, 110, pp. 18087–18091. DOI: 10.1073/pnas.1310344110.

Duchamp, C., F. Wrana, B. Legras, P. Sellitto, R. Belhadji and C. von Savigny (2023). 'Observation of the aerosol plume from the 2022 Hunga Tonga–Hunga Ha'apai eruption with SAGE III/ISS'. *Geophys. Res. Lett.*, 50, e2023GL105076. DOI: 10.1029/2023GL105076.

Dutton, E. and J. DeLuisi (1983). 'Spectral extinction of direct solar radiation by the El Chichón cloud during December 1982'. *Geophys. Res. Lett.*, 10, pp. 1013–1016. DOI: 10.1029/GL010i011p01013.

Dutton, E. G. and J. R. Christy (1992). 'Solar radiative forcing at selected locations and evidence for global lower tropospheric cooling following the eruptions of El Chichón and Pinatubo'. *Geophys. Res. Lett.*, 19, pp. 2313–2316. DOI: 10.1029/92GL02495.

Dutton, E. G., P. Reddy, S. Ryan and J. J. DeLuisi (1994). 'Features and effects of aerosol optical depth observed at Mauna Loa, Hawaii: 1982–1992'. *J. Geophys. Res.*, 99, pp. 8295–8306. DOI: 10.1029/93JD03520.

Evan, S., J. Brioude, K. H. Rosenlof, R.-S. Gao, R. W. Portmann, Y. Zhu, R. Volkamer, C. F. Lee, J.-M. Metzger, K. Lamy et al. (2023). 'Rapid ozone depletion after humidification of the stratosphere by the Hunga Tonga eruption'. *Science*, 382, eadg2551. DOI: 10.1126/science.adg2551.

Fahey, D. W., K. K. Kelly, S. R. Kawa, A. F. Tuck, M. Loewenstein, K. R. Chan and L. E. Heidt (1990). 'Observations of denitrification and dehydration in the winter polar stratospheres'. *Nature*, 344, pp. 321–324. DOI: 10.1038/344321a0.

Fels, S. B., J. D. Mahlman, M. D. Schwarzkopf and R. W. Sinclair (1980). 'Stratospheric sensitivity to perturbations in ozone and carbon dioxide: Radiative and dynamical response'. *J. Atmos. Sci.*, 37, pp. 2265–2297. DOI: 10.1175/1520-0469(1980)037%3C2265:SSTPIO%3E2.0.CO;2.

Fleming, E. L., P. A. Newman, Q. Liang and L. D. Oman (2024). 'Stratospheric Temperature and Ozone Impacts of the Hunga Tonga-Hunga Ha'apai Water Vapor Injection'. *J. Geophys. Res.*, 129, e2023JD039298. DOI: 10.1029/2023jd039298.

Forster, P. M., V. I. Fomichev, E. Rozanov, C. Cagnazzo, A. I. Jonsson, U. Langematz and K. Shibata (2011). 'Evaluation of radiation scheme performance within chemistry climate models'. *J. Geophys. Res.*, 116, D10302. DOI: 10.1029/2010JD015361.

Forster, P. M., T. Richardson, A. C. Maycock, C. J. Smith, B. H. Samset, G. Myhre and M. Schulz (2016). 'Recommendations for diagnosing effective radiative forcing from climate models for CMIP6'. *J. Geophys. Res.*, 121, pp. 12460–12475. DOI: 10.1002/2016JD025320.

Forster, P. M. D. and K. P. Shine (1999). 'Stratospheric water vapour changes as a possible contributor to observed stratospheric cooling'. *Geophys. Res. Lett.*, 26, pp. 3309–3312. DOI: 10.1029/1999GL010487.

Forster, P. M. D. F. and K. P. Shine (2002). 'Assessing the climate impact of trends in stratospheric water vapor'. *Geophys. Res. Lett.*, 29. DOI: 10.1029/2001GL013909.

Fueglistaler, S., Y. S. Liu, T. J. Flannaghan, P. H. Haynes, D. P. Dee, W. J. Read and P. F. Bernath (2013). 'The relation between atmospheric humidity and temperature trends for stratospheric water'. *J. Geophys. Res.*, 118, pp. 1052–1074. DOI: 10.1002/jgrd.50157.

Graf, H., J. Perlwitz and I. Kirchner (1994). 'Northern Hemisphere tropospheric mid-latitude circulation after violent volcanic eruptions'. *Contrib. Atmos. Phys. (also Beitr. Phys. Atmosph.)*, 67, pp. 3–13.

Guo, S., G. J. Bluth, W. I. Rose, I. M. Watson and A. J. Prata (2004a). 'Re-evaluation of SO_2 release of the 15 June 1991 Pinatubo eruption using ultraviolet and infrared satellite sensors'. *Geochem. Geophys. Geosyst.*, 5, Q04001. DOI: 10.1029/2003GC000654.

Guo, S., W. I. Rose, G. J. Bluth and I. M. Watson (2004b). 'Particles in the great Pinatubo volcanic cloud of June 1991: The role of ice'. *Geochem. Geophys. Geosyst.*, 5, Q05003. DOI: 10.1029/2003GC000655.

Gupta, A. K., T. Mittal, K. E. Fauria, R. Bennartz and J. F. Kok (2025). 'The January 2022 Hunga eruption cooled the Southern Hemisphere in 2022 and 2023'. *Commun. Earth Environ.*, 6, 240. DOI: 10.1038/s43247-025-02181-9.

Hamill, P., E. J. Jensen, P. B. Russell and J. J. Bauman (1997). 'The life cycle of stratospheric aerosol particles'. *Bull. Am. Meteorol. Soc.*, 7, pp. 1395–1410.

DOI: 10.1175/1520-0477(1997)078<1395:tlcosa>2.0.co;2.

Hansen, J. (2002). 'Climate forcing in Goddard Institute for Space Studies SI2000 simulations'. *J. Geophys. Res.*, 107, 4347. DOI: 10.1029/2001jd001143.

Hansen, J., M. Sato, R. Ruedy, L. Nazarenko, A. Lacis, G. Schmidt, G. Russell, I. Aleinov, M. Bauer and S. Bauer (2005). 'Efficacy of climate forcings'. *J. Geophys. Res.*, 110, D18104. DOI: 10.1029/2005jd005776.

He, R. and Y. Huang (2025). 'Muted radiative feedback of stratospheric water vapor found in a multimodel assessment'. *J. Geophys. Res.*, 130, e2025JD043676. DOI: 10.1029/2025jd043676.

Holton, J. R., P. H. Haynes, M. E. McIntyre, A. R. Douglass, R. B. Rood and L. Pfister (1995). 'Stratosphere-troposphere exchange'. *Rev. Geophys.*, 33, pp. 403–439. DOI: 10.1029/95rg02097.

Höpfner, M., C. D. Boone, B. Funke, N. Glatthor, U. Grabowski, A. Günther, S. Kellmann, M. Kiefer, A. Linden, S. Lossow et al. (2015). 'Sulfur dioxide (SO_2) from MIPAS in the upper troposphere and lower stratosphere 2002–2012'. *Atmos. Chem. Phys.*, 15, pp. 7017–7037. DOI: 10.5194/acp-15-7017-2015.

Huang, Y., Y. Wang and H. Huang (2020). 'Stratospheric water vapor feedback disclosed by a locking experiment'. *Geophys. Res. Lett.*, 47, e2020GL087987. DOI: 10.1029/2020gl087987.

Ivy, D. J., S. Solomon, N. Calvo and D. W. Thompson (2017). 'Observed connections of Arctic stratospheric ozone extremes to Northern Hemisphere surface climate'. *Environ. Res. Lett.*, 12, 024004. DOI: 10.1088/1748-9326/aa57a4.

Jenkins, S., C. Smith, M. Allen and R. Grainger (2023). 'Tonga eruption increases chance of temporary surface temperature anomaly above 1.5° C'. *Nat. Clim. Change*, 13, pp. 127–129. DOI: 10.1038/s41558-022-01568-2.

Johnson, J., G. Taha, R. Loughman, T. Zhu and M. DeLand (2025). *README Document for the Suomi-NPP OMPS LP L2 AER Daily Product, Collection 2.5, Version 2.5*. Tech. rep. https://disc.gsfc.nasa.gov/, Last access: 14 August 2025. Greenbelt, MD, USA: NASA GES DISC.

Joshi, M. M. and G. S. Jones (2009). 'The climatic effects of the direct injection of water vapour into the stratosphere by large volcanic eruptions'. *Atmos. Chem. Phys.*, 9, pp. 6109–6118. DOI: 10.5194/acp-9-6109-2009.

Joshi, M. M. and K. P. Shine (2003). 'A GCM Study of Volcanic Eruptions as a Cause of Increased Stratospheric Water Vapor'. *J. Climate*, 16, pp. 3525–3534. DOI: 10.1175/1520-0442(2003)016<3525:AGSOVE>2.0.CO;2.

Jucker, M., C. Lucas and D. Dutta (2024). 'Long-term climate impacts of large stratospheric water vapor perturbations'. *J. Climate*, 37, pp. 4507–4521. DOI: 10.1175/JCLI-D-23-0437.1.

Kelly, K. K., A. F. Tuck, D. M. Murphy, M. H. Proffitt, D. W. Fahey, R. L. Jones, D. S. McKenna, M. Loewenstein, J. R. Podolske, S. E. Strahan et al. (1989). 'Dehydration in the lower Antarctic stratosphere during late winter and early spring, 1987'. *J. Geophys. Res.*, 94, pp. 11317–11357. DOI: 10.1029/jd094id09p11317.

Khaykin, S., A. Podglajen, F. Ploeger, J.-U. Grooß, F. Tence, S. Bekki, K. Khlopenkov, K. Bedka, L. Rieger, A. Baron et al. (2022). 'Global perturbation of stratospheric water and aerosol burden by Hunga eruption'. *Commun. Earth Environ.*, 3, 316. DOI: 10.1038/s43247-022-00652-x.

Kloss, C., P. Sellitto, J.-B. Renard, A. Baron, N. Bègue, B. Legras, G. Berthet, E. Briaud, E. Carboni, C. Duchamp et al. (2022). 'Aerosol characterization of the stratospheric plume from the volcanic eruption at Hunga Tonga 15 January 2022'. *Geophys. Res. Lett.*, 49, e2022GL099394. DOI: 10.1029/2022GL099394.

Kodera, K. (1994). 'Influence of volcanic eruptions on the troposphere through stratospheric dynamical processes in the Northern Hemisphere winter'. *J. Geophys. Res.*, 99, pp. 1273–1282. DOI: 10.1029/93JD02731.

Kovilakam, M., L. W. Thomason, N. Ernest, L. Rieger, A. Bourassa and L. Millán (2020). 'The Global Space-based Stratospheric Aerosol Climatology (version 2.0): 1979–2018'. *Earth Syst. Sci. Data*, 12, pp. 2607–2634. DOI: 10.5194/essd-12-2607-2020.

Kremser, S., L. W. Thomason, M. Von Hobe, M. Hermann, T. Deshler, C. Timmreck, M. Toohey, A. Stenke, J. P. Schwarz, R. Weigel et al. (2016). 'Stratospheric aerosol-Observations, processes, and impact on climate: Stratospheric Aerosol'. *Rev. Geophys.*, 54, pp. 278–335. DOI: 10.1002/2015RG000511.

Kroll, C. A., S. Dacie, A. Azoulay, H. Schmidt and C. Timmreck (2021). 'The impact of volcanic eruptions of different magnitude on stratospheric water vapor in the tropics'. *Atmos. Chem. Phys.*, 21, pp. 6565–6591. DOI: 10.5194/acp-21-6565-2021.

Kroll, C. A. and A. Schmidt (2024). 'Indirect stratospheric moisture increase after a Pinatubo-magnitude eruption can be comparable to direct in-

crease after 2022 Hunga'. *Commun. Earth Environ.*, 5, 497. DOI: 10.1038/s43247-024-01651-w.

Kuchar, A., T. Sukhodolov, G. Chiodo, A. Jörimann, J. Kult-Herdin, E. Rozanov and H. H. Rieder (2025). 'Modulation of the northern polar vortex by the Hunga Tonga–Hunga Ha'apai eruption and the associated surface response'. *Atmos. Chem. Phys.*, 25, pp. 3623–3634. DOI: 10.5194/acp-25-3623-2025.

Lacis, A., J. Hansen and M. Sato (1992). 'Climate forcing by stratospheric aerosols'. *Geophys. Res. Lett.*, 19, pp. 1607–1610. DOI: 10.1029/92gl01620.

Lambert, A., R. G. Grainger, J. J. Remedios, C. D. Rodgers, M. Corney and F. W. Taylor (1993). 'Measurements of the evolution of the Mt. Pinatubo aerosol cloud by ISAMS'. *Geophys. Res. Lett.*, 20, pp. 1287–1290. DOI: 10.1029/93gl00827.

Larson, E. J. and R. W. Portmann (2016). 'A temporal kernel method to compute effective radiative forcing in CMIP5 transient simulations'. *J. Climate*, 29, pp. 1497–1509. DOI: 10.1175/jcli-d-15-0577.1.

LeGrande, A., K. Tsigaridis and S. Bauer (2016). 'Role of atmospheric chemistry in the climate impacts of stratospheric volcanic injections'. *Nat. Geosci.*, pp. 652–655. DOI: 10.1038/ngeo2771.

Legras, B., C. Duchamp, P. Sellitto, A. Podglajen, E. Carboni, R. Siddans, J.-U. Grooß, S. Khaykin and F. Ploeger (2022). 'The evolution and dynamics of the Hunga Tonga–Hunga Ha'apai sulfate aerosol plume in the stratosphere'. *Atmos. Chem. Phys.*, 22, pp. 14957–14970. DOI: 10.5194/acp-22-14957-2022.

Li, F. and P. Newman (2020). 'Stratospheric water vapor feedback and its climate impacts in the coupled atmosphere–ocean Goddard Earth Observing System Chemistry-Climate Model'. *Clim. Dynam.*, 55, pp. 1585–1595. DOI: 10.1007/s00382-020-05348-6.

Lu, J., S. Lou, X. Huang, L. Xue, K. Ding, T. Liu, Y. Ma, W. Wang and A. Ding (2023). 'Stratospheric aerosol and ozone responses to the Hunga Tonga-Hunga Ha'apai volcanic eruption'. *Geophys. Res. Lett.*, 50, e2022GL102315. DOI: 10.1029/2022GL102315.

Marshall, L. R., E. C. Maters, A. Schmidt, C. Timmreck, A. Robock and M. Toohey (2022). 'Volcanic effects on climate: recent advances and future avenues'. *B. Volcanol.*, 84, 54. DOI: 10.1007/s00445-022-01559-3.

Marshall, L. R., C. J. Smith, P. M. Forster, T. J. Aubry, T. Andrews and A. Schmidt (2020). 'Large Variations in Volcanic Aerosol Forcing Efficiency Due to Eruption Source Parameters and Rapid Adjustments'. *Geophys. Res. Lett.*, 47, e2020GL090241. DOI: 10.1029/2020GL090241.

Maycock, A. C. and K. P. Shine (2012). 'Stratospheric water vapor and climate: Sensitivity to the representation in radiation codes'. *J. Geophys. Res.*, 117, D13102. DOI: 10.1029/2012JD017484.

Maycock, A. C., M. M. Joshi, K. P. Shine and A. A. Scaife (2013). 'The Circulation Response to Idealized Changes in Stratospheric Water Vapor'. *J. Climate*, 26, pp. 545–561. DOI: 10.1175/JCLI-D-12-00155.1.

Millán, L., W. G. Read, M. L. Santee, A. Lambert, G. L. Manney, J. L. Neu, M. C. Pitts, F. Werner, N. J. Livesey and M. J. Schwartz (2024). 'The Evolution of the Hunga Hydration in a Moistening Stratosphere'. *Geophys. Res. Lett.*, 51, e2024GL110841. DOI: 10.1029/2024gl110841.

Millán, L., M. L. Santee, A. Lambert, N. J. Livesey, F. Werner, M. J. Schwartz, H. C. Pumphrey, G. L. Manney, Y. Wang, H. Su et al. (2022). 'The Hunga Tonga-Hunga Ha'apai Hydration of the Stratosphere'. *Geophys. Res. Lett.*, 49, e2022GL099381. DOI: 10.1029/2022gl099381.

Mills, M. J., A. Schmidt, R. Easter, S. Solomon, D. E. Kinnison, S. J. Ghan et al. (2016). 'Global volcanic aerosol properties derived from emissions, 1990–2014, using CESM1 (WACCM)'. *J. Geophys. Res.*, 121, pp. 2332–2348. DOI: 10.1002/2015jd024290.

Minnis, P., E. F. Harrison, L. L. Stowe, G. G. Gibson, F. M. Denn, D. R. Doelling and W. L. J. Smith (1993). 'Radiative climate forcing by the Mt. Pinatubo eruption'. *Science*, 259, pp. 1411–1415. DOI: 10.1126/science.259.5100.1411.

Muthers, S., F. Arfeuille, C. C. Raible and E. Rozanov (2015). 'The impacts of volcanic aerosol on stratospheric ozone and the Northern Hemisphere polar vortex: separating radiative-dynamical changes from direct effects due to enhanced aerosol heterogeneous chemistry'. *Atmos. Chem. Phys.*, 15, pp. 11461–11476. DOI: 10.5194/acp-15-11461-2015.

Nedoluha, G. E., R. M. Bevilacqua and K. W. Hoppel (2002). 'POAM III measurements of dehydration in the Antarctic and comparisons with the Arctic'. *J. Geophys. Res.*, 107, 8290. DOI: 10.1029/2001JD001184.

Nedoluha, G. E., R. M. Gomez, I. Boyd, H. Neal, D. R. Allen and A. Lambert (2024). 'The Spread of the Hunga Tonga H2O Plume in the Middle Atmosphere Over the First Two Years Since Eruption'. *J.*

Geophys. Res., 129, e2024JD040907. DOI: 10.1029/2024jd040907.

Newhall, C. and S. Self (1982). 'The volcanic explosivity index (VEI) an estimate of explosive magnitude for historical volcanism'. *J. Geophys. Res.*, 87, pp. 1231–1238. DOI: 10.1029/hg002p0143.

Niemeier, U., C. Timmreck, H.-F. Graf, S. Kinne, S. Rast and S. Self (2009). 'Initial fate of fine ash and sulfur from large volcanic eruptions'. *Atmos. Chem. Phys.*, 9, pp. 9043–9057. DOI: 10.5194/acp-9-9043-2009.

Niemeier, U., S. Wallis, C. Timmreck, T. van Pham and C. von Savigny (2023). 'How the Hunga Tonga—Hunga Ha'apai Water Vapor Cloud Impacts Its Transport Through the Stratosphere: Dynamical and Radiative Effects'. *Geophys. Res. Lett.*, 50, e2023GL106482. DOI: 10.1029/2023gl106482.

Nowack, P., P. Ceppi, S. M. Davis, G. Chiodo, W. Ball, M. A. Diallo, B. Hassler, Y. Jia, J. Keeble and M. Joshi (2023). 'Response of stratospheric water vapour to warming constrained by satellite observations'. *Nat. Geosci.*, 16, pp. 577–583. DOI: 10.1038/s41561-023-01183-6.

Oman, L., A. Robock, G. Stenchikov, T. Thordarson, D. Koch, D. Shindell and C. Gao (2006). 'Modeling the distribution of the volcanic aerosol cloud from the 1783–1784 Laki eruption'. *J. Geophys. Res.*, 111, D12209. DOI: 10.1029/2005jd006899.

Pausata, F. S., L. Chafik, R. Caballero and D. S. Battisti (2015). 'Impacts of high-latitude volcanic eruptions on ENSO and AMOC'. *Proc. Nat. Acad. Sci.*, 112, pp. 13784–13788. DOI: 10.1073/pnas.1509153112.

Perlwitz, J. and H.-F. Graf (2001). 'Troposphere-stratosphere dynamic coupling under strong and weak polar vortex conditions'. *Geophys. Res. Lett.*, 28, pp. 271–274. DOI: 10.1029/2000GL012405.

Predybaylo, E., G. L. Stenchikov, A. T. Wittenberg and F. Zeng (2017). 'Impacts of a Pinatubo-Size Volcanic Eruption on ENSO'. *J. Geophys. Res.*, 122, pp. 925–947. DOI: 10.1002/2016JD025796.

Pueschel, R. F. (1996). 'Stratospheric Aerosols: Formation, Properties, Effects'. *J. Aerosol Sci.*, 27, pp. 383–402. DOI: 10.1016/0021-8502(95)00557-9.

Quaglia, I., D. Visioni, E. M. Bednarz, Y. Zhu, G. Stenchikov, V. Aquila, C.-C. Liu, G. W. Mann, Y. Peng, T. Sekiya et al. (2025). 'Multi-model analysis of the radiative impacts of the 2022 Hunga eruption indicates a significant cooling contribution from the volcanic plume'. *EGUsphere [preprint]*, 2025, pp. 1–35. DOI: 10.5194/egusphere-2025-3769.

Quaglia, I., C. Timmreck, U. Niemeier, D. Visioni, G. Pitari, C. Brodowsky, C. Brühl, S. S. Dhomse, H. Franke, A. Laakso et al. (2023). 'Interactive stratospheric aerosol models' response to different amounts and altitudes of SO_2 injection during the 1991 Pinatubo eruption'. *Atmos. Chem. Phys.*, 23, pp. 921–948. DOI: 10.5194/acp-23-921-2023.

Ramaswamy, V., W. Collins, J. Haywood, J. Lean, N. Mahowald, G. Myhre and T. Storelvmo (2019). 'Radiative forcing of climate: The historical evolution of the radiative forcing concept, the forcing agents and their quantification, and applications'. *Meteor. Mon.*, 59, pp. 14.1–14.101. DOI: 10.1175/AMSMONOGRAPHS-D-19-0001.1.

Ramaswamy, V. e. a. (2006). 'Anthropogenic and natural influences in the evolution of lower stratospheric cooling'. *Science*, 311, pp. 1138–1141. DOI: 10.1126/science.1122587.

Randel, W. J., B. R. Johnston, J. J. Braun, S. Sokolovskiy, H. Vömel, A. Podglajen and B. Legras (2023). 'Stratospheric Water Vapor from the Hunga Tonga–Hunga Ha'apai Volcanic Eruption Deduced from COSMIC-2 Radio Occultation'. *Remote Sens.*, 15, 2167, p. 2167. DOI: 10.3390/rs15082167.

Randel, W. J., F. Wu, S. J. Oltmans, K. Rosenlof and G. E. Nedoluha (2004). 'Interannual Changes of Stratospheric Water Vapor and Correlations with Tropical Tropopause Temperatures'. *J. Atmos. Res.*, 61, pp. 2133–2148. DOI: 10.1175/1520-0469(2004)061<2133:icoswv>2.0.co;2.

Read, W. G., L. Froidevaux and J. W. Waters (1993). 'Microwave limb sounder measurement of stratospheric SO_2 from the Mt. Pinatubo Volcano'. *Geophys. Res. Lett.*, 20, pp. 1299–1302. DOI: 10.1029/93GL00831.

Riese, M., F. Ploeger, A. Rap, B. Vogel, P. Konopka, M. Dameris and P. Forster (2012). 'Impact of uncertainties in atmospheric mixing on simulated UTLS composition and related radiative effects'. *J. Geophys. Res.*, 117, D16305. DOI: 10.1029/2012JD017751.

Robock, A., C. M. Ammann, L. Oman, D. Shindell, S. Levis and G. Stenchikov (2009). 'Did the Toba volcanic eruption of 74 ka B.P. produce widespread glaciation?' *J. Geophys. Res.*, 114, D10107. DOI: 10.1029/2008JD011652.

Robock, A. (2000). 'Volcanic eruptions and climate'. *Rev. Geophys.*, 38, pp. 191–219. DOI: 10.1029/1998RG000054.

Russell, P. B., J. M. Livingston, E. G. Dutton, R. F. Pueschel, J. A. Reagan, T. E. DeFoor and D. J. Hofmann

(1993). 'Pinatubo and pre-Pinatubo optical-depth spectra: Mauna Loa measurements, comparisons, inferred particle size distributions, radiative effects, and relationship to lidar data'. *J. Geophys. Res.*, 98, pp. 22969–22985. DOI: 10.1029/93JD02308.

Santee, M. L., A. Lambert, L. Froidevaux, G. L. Manney, M. J. Schwartz, L. F. Millán, N. J. Livesey, W. G. Read, F. Werner and R. A. Fuller (2023). 'Strong Evidence of Heterogeneous Processing on Stratospheric Sulfate Aerosol in the Extrapolar Southern Hemisphere Following the 2022 Hunga Tonga-Hunga Ha'apai Eruption'. *J. Geophys. Res.*, 128, e2023JD039169. DOI: 10.1029/2023jd039169.

Santer, B. D., T. M. L. Wigley, C. Doutriaux, J. S. Boyle, J. E. Hansen, P. D. Jones and K. E. Taylor (2001). 'Accounting for the effects of volcanoes and ENSO in comparisons of modeled and observed temperature trends'. *J. Geophys. Res.*, 106, pp. 28033–28059. DOI: 10.1029/2000JD000189.

Schoeberl, M. R., M. Toohey, Y. Wang and R. Ueyama (2025). 'Stratospheric Injection Lifetimes'. *J. Geophys. Res.*, 130, e2025JD043928. DOI: 10.1029/2025jd043928.

Schoeberl, M. R., Y. Wang, G. Taha, D. J. Zawada, R. Ueyama and A. Dessler (2024). 'Evolution of the Climate Forcing During the Two Years After the Hunga Tonga-Hunga Ha'apai Eruption'. *J. Geophys. Res.*, 129, e2024JD041296. DOI: 10.1029/2024jd041296.

Schoeberl, M. R., Y. Wang, R. Ueyama, G. Taha, E. Jensen and W. Yu (2022). 'Analysis and Impact of the Hunga Tonga-Hunga Ha'apai Stratospheric Water Vapor Plume'. *Geophys. Res. Lett.*, 49, e2022GL100248. DOI: 10.1029/2022gl100248.

Schoeberl, M. R., Y. Wang, R. Ueyama, G. Taha and W. Yu (2023). 'The Cross Equatorial Transport of the Hunga Tonga-Hunga Ha'apai Eruption Plume'. *Geophys. Res. Lett.*, 50, e2022GL102443. DOI: 10.1029/2022gl102443.

Sellitto, P., A. Podglajen, R. Belhadji, M. Boichu, E. Carboni, J. Cuesta, C. Duchamp, C. Kloss, R. Siddans, N. Bègue et al. (2022). 'The unexpected radiative impact of the Hunga Tonga eruption of 15th January 2022'. *Commun. Earth Environ.*, 3, 288. DOI: 10.1038/s43247-022-00618-z.

Sellitto, P., R. Siddans, R. Belhadji, E. Carboni, B. Legras, A. Podglajen and et al. (2024). 'Observing the SO_2 and sulfate aerosol plumes from the 2022 Hunga eruption with the Infrared Atmospheric Sounding Interferometer (IASI)'. *Geophys. Res. Lett.*, 51, e2023GL105565. DOI: 10.1029/2023GL105565.

Sherwood, S. C., S. Bony, O. Boucher, C. Bretherton, P. M. Forster, J. M. Gregory and B. Stevens (2015). 'Adjustments in the forcing-feedback framework for understanding climate change'. *Bull. Am. Meteorol. Soc.*, 96, pp. 217–228. DOI: 10.1175/bams-d-13-00167.1.

Shindell, D. T., G. A. Schmidt, M. Mann and G. Faluvegi (2004). 'Dynamic winter climate response to large tropical volcanic eruptions since 1600'. *J. Geophys. Res.*, 109, D05104. DOI: 10.1029/2003JD004151.

Shindell, D. T., G. A. Schmidt, R. L. Miller and M. Mann (2003). 'Volcanic and solar forcing of climate change during the preindustrial era'. *J. Climate*, 16, pp. 4094–4107. DOI: 10.1175/1520-0442(2003)016<4094:vasfoc>2.0.co;2.

Sicard, M., A. Baron, M. Ranaivombola, D. Gantois, T. Millet, P. Sellitto, N. Bègue, H. Bencherif, G. Payen, N. Marquestaut et al. (2025). 'Radiative impact of the Hunga stratospheric volcanic plume: role of aerosols and water vapor over Réunion Island (21° S, 55° E)'. *Atmos. Chem. Phys.*, 25, pp. 367–381. DOI: 10.5194/acp-25-367-2025.

Simpson, I. R., T. G. Shepherd and M. Sigmond (2011). 'Dynamics of the lower stratospheric circulation response to ENSO'. *J. Atmos. Sci.*, 68, pp. 2537–2556. DOI: 10.1175/jas-d-11-05.1.

Smith, C. J., R. J. Kramer, G. Myhre, K. Alterskjær, W. Collins, A. Sima, O. Boucher, J.-L. Dufresne, P. Nabat and M. Michou (2020). 'Effective radiative forcing and adjustments in CMIP6 models'. *Atmos. Chem. Phys.*, 20, pp. 9591–9618. DOI: 10.5194/acp-20-9591-2020.

Solomon, S., J. S. Daniel, R. R. Neely, J.-P. Vernier, E. G. Dutton and L. W. Thomason (2011). 'The Persistently Variable "Background" Stratospheric Aerosol Layer and Global Climate Change'. *Science*, 333, pp. 866–870. DOI: 10.1126/science.1206027.

Solomon, S., K. H. Rosenlof, R. W. Portmann, J. S. Daniel, S. M. Davis, T. J. Sanford and G.-K. Plattner (2010). 'Contributions of Stratospheric Water Vapor to Decadal Changes in the Rate of Global Warming'. *Science*, 327, pp. 1219–1223. DOI: 10.1126/science.1182488.

Stenchikov, G. (2016). 'The role of volcanic activity in climate and global change'. *Climate Change: Observed Impact on Planet Earth, 2nd Edition*. Ed. by T. Letcher. Elsevier, pp. 419–448.

Stenchikov, G., T. L. Delworth, V. Ramaswamy, R. J. Stouffer, A. Wittenberg and F. Zeng (2009). 'Vol-

canic signals in oceans'. *J. Geophys. Res.*, 114, D16104. DOI: 10.1029/2008jd011673.

Stenchikov, G., K. Hamilton, A. Robock, V. Ramaswamy and M. D. Schwarzkopf (2004). 'Arctic Oscillation response to the 1991 Pinatubo eruption in the SKYHI GCM with a realistic quasi-biennial oscillation'. *J. Geophys. Res.*, 109, D03112. DOI: 10.1029/2003JD003699.

Stenchikov, G., K. Hamilton, R. J. Stouffer, A. Robock, V. Ramaswamy, B. Santer and H.-F. Graf (2006). 'Arctic oscillation response to volcanic eruptions in the IPCC AR4 climate models'. *J. Geophys. Res.*, 111, D07107. DOI: 10.1029/2005JD006286.

Stenchikov, G., A. Robock, V. Ramaswamy, M. D. Schwarzkopf, K. Hamilton and S. Ramachandran (2002). 'Arctic Oscillation response to the 1991 Mount Pinatubo eruption: effects of volcanic aerosols and ozone depletion'. *J. Geophys. Res.*, 107, 4803. DOI: 10.1029/2002JD002090.

Stenchikov, G., A. Ukhov and S. Osipov (2025). 'Modeling the Radiative Forcing and Atmospheric Temperature Perturbations Caused by the 2022 Hunga Volcano Explosion'. *J. Geophys. Res.*, e2024JD041940. DOI: 10.1029/2024JD041940.

Stenchikov, G., A. Ukhov, S. Osipov, R. Ahmadov, G. Grell, K. Cady-Pereira, E. Mlawer and M. Iacono (2021). 'How does a Pinatubo-size volcanic cloud reach the middle stratosphere?' *J. Geophys. Res.*, 126, e2020JD033829. DOI: 10.1029/2020jd033829.

Stenchikov, G. L., I. Kirchner, A. Robock, H.-F. Graf, J. C. Antuña, R. G. Grainger, A. Lambert and L. Thomason (1998). 'Radiative forcing from the 1991 Mount Pinatubo volcanic eruption'. *J. Geophys. Res.*, 103, pp. 13837–13857. DOI: 10.1029/98jd00693.

Swingedouw, D., J. Mignot, P. Ortega, M. Khodri, M. Menegoz, C. Cassou and V. Hanquiez (2017). 'Impact of explosive volcanic eruptions on the main climate variability modes'. *Global Planet. Change*, 150, pp. 24–45. DOI: 10.1016/j.gloplacha.2017.01.006.

Taha, G., R. Loughman, P. R. Colarco, T. Zhu, L. W. Thomason and G. Jaross (2022). 'Tracking the 2022 Hunga Tonga-Hunga Ha'apai Aerosol Cloud in the Upper and Middle Stratosphere Using Space-Based Observations'. *Geophys. Res. Lett.*, 49, e2022GL100091. DOI: 10.1029/2022gl100091.

Taha, G., R. Loughman, T. Zhu, L. Thomason, J. Kar, L. Rieger and A. Bourassa (2021). 'OMPS LP Version 2.0 multi-wavelength aerosol extinction coefficient retrieval algorithm'. *Atmos. Meas. Tech.*, 14, pp. 1015–1036. DOI: 10.5194/amt-14-1015-2021.

Thomason, L. W., N. Ernest, L. Millán, L. Rieger, A. Bourassa, J.-P. Vernier, G. Manney, B. Luo, F. Arfeuille and T. Peter (2018). 'A global space-based stratospheric aerosol climatology: 1979–2016'. *Earth Syst. Sci. Data*, 10, pp. 469–492. DOI: 10.5194/essd-10-469-2018.

Thompson, D. W. and J. M. Wallace (1998). 'The Arctic Oscillation signature in the wintertime geopotential height and temperature fields'. *Geophys. Res. Lett.*, 25, pp. 1297–1300. DOI: 10.1029/98GL00950.

Thompson, D. W. and J. M. Wallace (2000). 'Annular modes in the extratropical circulation. Part I: Month-to-month variability'. *J. Climate*, 13, pp. 1000–1016. DOI: 10.1175/1520-0442(2000)013<1000:amitec>2.0.co;2.

Tilmes, S., M. J. Mills, Y. Zhu, C. G. Bardeen, F. Vitt, P. Yu, D. Fillmore, X. Liu, B. Toon and T. Deshler (2023). 'Description and performance of a sectional aerosol microphysical model in the Community Earth System Model (CESM2)'. *Geosci. Model Dev.*, 16, pp. 6087–6125. DOI: 10.5194/gmd-16-6087-2023.

Timmreck, C. (2012). 'Modeling the climatic effects of significant explosive volcanic eruptions'. *Wiley Interdiscip. Rev. Clim. Change*, 3, pp. 545–564. DOI: 10.1002/wcc.192.

Timmreck, C., G. W. Mann, V. Aquila, R. Hommel, L. A. Lee, A. Schmidt, C. Brühl, S. Carn, M. Chin, S. S. Dhomse et al. (2018). 'The interactive stratospheric aerosol model intercomparison project (ISA-MIP): motivation and experimental design'. *Geosci. Model Dev.*, 11, pp. 2581–2608. DOI: 10.5194/gmd-11-2581-2018.

Toohey, M., Y. Jia, S. Khanal and S. Tegtmeier (2025). 'Stratospheric residence time and the lifetime of volcanic stratospheric aerosols'. *Atmos. Chem. Phys.*, 25, pp. 3821–3839. DOI: 10.5194/acp-25-3821-2025.

Trepte, C. R. and M. H. Hitchman (1992). 'Tropical stratospheric circulation deduced from satellite aerosol data'. *Nature*, 355, pp. 626–628. DOI: 10.1038/355626a0.

Turco, R. P., R. C. Witten and O. B. Toon (1982). 'Stratospheric Aerosols: Observation and Theory'. *Rev. Geophys. Space Phys.*, 20, pp. 233–279. DOI: 10.1029/RG020i002p00233.

Vömel, H., S. Evan and M. Tully (2022). 'Water vapor injection into the Stratosphere by Hunga Tonga-Hunga Ha'apai'. *Science*, 377, pp. 1444–1447. DOI: 10.1126/science.abq2299.

Vömel, H., S. J. Oltmans, D. J. Hofmann, T. Deshler and J. M. Rosen (1995). 'The evolution of the dehydration in the Antarctic stratospheric vortex'. *J. Geophys. Res.*, 100, pp. 13919–13926. DOI: 10.1029/95JD01000.

Wallis, S., M. DeLand and C. von Savigny (2025). 'Did the 2022 Hunga eruption impact the noctilucent cloud season in 2023/24 and 2024?' *Atmos. Chem. Phys.*, 25, pp. 3635–3645. DOI: 10.5194/acp-25-3635-2025.

Walsh, A., J. A. Screen, A. A. Scaife and D. M. Smith (2022). 'Non-Linear response of the extratropics to tropical climate variability'. *Geophys. Res. Lett.*, 49, e2022GL100416. DOI: 10.1029/2022GL100416.

Wang, J., S. Park, J. Zeng, C. Ge, K. Yang, S. Carn, N. Krotkov and A. H. Omar (2013). 'Modeling of 2008 Kasatochi volcanic sulfate direct radiative forcing: assimilation of OMI SO 2 plume height data and comparison with MODIS and CALIOP observations'. *Atmos. Chem. Phys.*, 13, pp. 1895–1912. DOI: 10.5194/acp-13-1895-2013.

Wang, X., W. Randel, Y. Zhu, S. Tilmes, J. Starr, W. Yu, R. Garcia, O. B. Toon, M. Park, D. Kinnison et al. (2023). 'Stratospheric Climate Anomalies and Ozone Loss Caused by the Hunga Tonga-Hunga Ha'apai Volcanic Eruption'. *J. Geophys. Res.*, 128, e2023JD039480. DOI: 10.1029/2023jd039480.

Wang, Y. and Y. Huang (2024). 'Compensating atmospheric adjustments reduce the volcanic forcing from Hunga stratospheric water vapor enhancement'. *Sci. Adv.*, 10, eadl2842. DOI: 10.1126/sciadv.adl2842.

Waugh, D. W. and L. M. Polvani (2010). 'Stratospheric polar vortices'. *The stratosphere: Dynamics, transport, and chemistry*. Ed. by L. M. Polvani, A. H. Sobel and D. W. Waugh. Vol. 190. Geophysical Monograph Series. American Geophysical Union, pp. 43–57. DOI: 10.1029/GM190.

Wetherald, R. T. and S. Manabe (1988). 'Cloud feedback processes in a general circulation model'. *J. Atmos. Sci.*, 45, pp. 1397–1416. DOI: 10.1175/1520-0469(1988)045<1397:CFPIAG>2.0.CO;2.

Wilmouth, D. M., F. F. Østerstrøm, J. B. Smith, J. G. Anderson and R. J. Salawitch (2023). 'Impact of the Hunga Tonga volcanic eruption on stratospheric composition'. *Proc. Natl. Acad. Sci.*, 120, e2301994120. DOI: 10.1073/pnas.2301994120.

Witze, A. (2022). 'Why the Tongan eruption will go down in the history of volcanology'. *Nature*, 602, pp. 376–378. DOI: 10.1038/d41586-022-00394-y.

Yook, S., S. Solomon and X. Wang (2025). 'The impact of 2022 Hunga Tonga-Hunga Ha'apai (Hunga) eruption on stratospheric circulation and climate'. *J. Geophys. Res.*, 130, e2024JD042943. DOI: 10.1029/2024JD042943.

Yu, P., R. W. Portmann, Y. Peng, C.-C. Liu, Y. Zhu, E. Asher, Z. Bai, Y. Lu, J. Bian, M. Mills et al. (2023a). 'Radiative Forcing From the 2014–2022 Volcanic and Wildfire Injections'. *Geophys. Res. Lett.*, 50, e2023GL103791. DOI: 10.1029/2023GL103791.

Yu, Q. and Y. Huang (2023). 'A Dissection of the Inter-Model Spread of the Aerosol Direct Radiative Effect in CMIP6 Models'. *Geophys. Res. Lett.*, 50, e2023GL105112. DOI: 10.1029/2023GL105112.

Yu, Q. and Y. Huang (2024). 'Quantifying the Direct Radiative Effect of Stratospheric Aerosols Using Radiative Kernels'. *ESS Open Archive*, DOI: 10.22541/essoar.172374105.56686934/v1.

Yu, W., R. Garcia, J. Yue, A. Smith, X. Wang, W. Randel, Z. Qiao, Y. Zhu, V. L. Harvey, S. Tilmes et al. (2023b). 'Mesospheric temperature and circulation response to the Hunga Tonga-Hunga-Ha'apai volcanic eruption'. *J. Geophys. Res.*, 128, e2023JD039636. DOI: 10.1029/2023JD039636.

Zhang, H., F. Wang, J. Li, Y. Duan, C. Zhu and J. He (2022). 'Potential Impact of Tonga Volcano Eruption on Global Mean Surface Air Temperature'. *J. Meteorol. Res.*, 36, pp. 1–5. DOI: 10.1007/s13351-022-2013-6.

Zhang, J., D. Kinnison, Y. Zhu, X. Wang, S. Tilmes, K. Dube and W. Randel (2024). 'Chemistry Contribution to Stratospheric Ozone Depletion After the Unprecedented Water-Rich Hunga Tonga Eruption'. *Geophys. Res. Lett.*, 51, e2023GL105762. DOI: 10.1029/2023gl105762.

Zhou, X., S. S. Dhomse, W. Feng, G. Mann, S. Heddell, H. Pumphrey, B. J. Kerridge, B. Latter, R. Siddans, L. Ventress et al. (2024). 'Antarctic Vortex Dehydration in 2023 as a Substantial Removal Pathway for Hunga Tonga-Hunga Ha'apai Water Vapor'. *Geophys. Res. Lett.*, 51, e2023GL107630. DOI: 10.1029/2023gl107630.

Zhu, Y., C. G. Bardeen, S. Tilmes, M. J. Mills, X. Wang, V. L. Harvey, G. Taha, D. Kinnison, R. W. Portmann, P. Yu et al. (2022). 'Perturbations in stratospheric aerosol evolution due to the water-rich plume of the 2022 Hunga-Tonga eruption'. *Commun. Earth Environ.*, 3, 248. DOI: 10.1038/s43247-022-00580-w.

Zhuo, Z., X. Wang, Y. Zhu, W. Yu, E. M. Bednarz, E. Fleming, P. R. Colarco, S. Watanabe, D. Plum-

mer, G. Stenchikov et al. (2025). 'Comparing multi-model ensemble simulations with observations and decadal projections of upper atmospheric variations following the Hunga eruption'. *Atmos. Chem. Phys.*, 25, pp. 13161–13176. DOI: 10.5194/acp-25-13161-2025.

Acknowledgements

We acknowledge the scientific coordination and sponsorship of the World Climate Research Programme (WCRP), within the framework of the WCRP activity Atmospheric Processes And their Role in Climate (APARC). We thank the APARC co-chairs Amanda Maycock, Karen Rosenlof, Seok-Woo Son and Olaf Morgenstern, for their guidance and advice during the proposal phase of the project, and their continuing support through the Hunga cross-activity project. We are grateful to the chapter lead authors, co- and contributing authors and review editors (over 150 scientists) for their leadership, and for generously giving their time for the volunteer roles.

We acknowledge the key role satellite observational programs funded by US, European, Canadian, Japanese, and other atmospheric and space science agencies played, enabling global monitoring of the evolving Hunga volcanic cloud. In particular, the MLS instrument on the Aura satellite, the SAGE-III instrument on the International Space Station, and many others (e.g., ACE-FTS, OMPS, OSIRIS, MISR, MODIS, GPS-RO, DSCOVR/EPIC, N20/NPP NM), provided benchmark measurement datasets for the Hunga-excess water vapour and volcanic aerosol in the stratosphere. We note Hunga is the first time lidar measurements from satellite have monitored a deep-stratosphere injecting volcanic eruption cloud. And we acknowledge the joint public investment from NASA and the French space agency (CNES) that enabled this, to measure the vertical structure of the full extent of the dispersing Hunga volcanic cloud, from the CALIOP lidar on the CALIPSO satellite.

In the initial hours and days after the Hunga eruption, the geostationary GOES and Himawari satellite instruments measured the atmospheric waves and properties of the umbrella cloud of ice, ash and sulfate aerosol, these capabilities funded by NOAA and NASA, and the Japanese meteorological agency (JMA) respectively. A key element of the early-phase post-eruption satellite monitoring of such an explosive event requires quantifying the sulfur released to the stratosphere, for potential climate and ozone impacts. In this regard, the Aura, Sentinel-5 and MetOp-B satellite hosting the OMI, TROPOMI and IASI instruments, were key to establishing a reliable consensus on the emitted sulfur.

We acknowledge also the value of in-situ measurements and ground-based remote sensing networks (e.g. TAC/BUFR radiosonde, NDACC, NOAA B2SAP, AERONET, WMO GAW, GNSS, and other ground-based balloon and lidar systems hosted by different countries) in providing ground-truth information to validate satellite assessments and to ensure reliable model predictions. We are grateful for the international collaborations that led to two field campaigns specifically to measure the progressing global dispersion of the Hunga cloud: the balloon and lidar monitoring in the TR2Ex rapid response campaign from Reunion Island, and the BraVo field campaigns from Sao Paulo. We recognise also the value of prior co-ordination via the NASA VolRes coordination activity to prepare for future major eruption (see Carn et al., 2021).

We acknowledge also the investment leading to the long-term record of air temperatures in the stratosphere from the SSU (1978-2006) and AMSU (2001-present) sounders on the NOAA series of satellites. The long-term records provide important datasets to understand the opposite-sign post-volcanic cooling of the stratosphere after Hunga, compared to the warming after El Chichón and Pinatubo (see Figure ES-3). We also acknowledge other valuable atmospheric data for monitoring the gravity wave propagation into the upper atmosphere, and the atmospheric waves and ionospheric perturbations from the initial Hunga explosions.

This report has aligned closely with two of APARC's activities, the Stratospheric Sulfur and its Role in Climate (SSiRC) and Chemistry Climate Model Initiative (CCMI). We thank the support of University of Leeds and Ecole Normale Superieure, Paris, for hosting the Hunga activity open science workshops in 2022 and 2024, and NSF NCAR Boulder for hosting the Hunga assessment meeting in 2025. Funding from NASA and APARC provided travel support for early career and scientists from the global south to attend the meetings in person.

We thank the reanalysis centres for providing their support and data products, key input datasets for the HTHH-MOC co-ordinated modelling and other analysis. We acknowledge all the participating models (detailed in Supplementary S1, S4 and S5). In particular, we are grateful to the UK Centre for Environmental Data Analysis (CEDA) for hosting the group workspace for the Hunga modelling activities, within the UK collaborative Joint Analysis System Meeting Infrastructure Needs system (JASMIN, Lawrence et al., 2012). We also thank the APARC International Project Office at Forschungszentrum Jülich (Rolf Müller, Ines Tritscher, Lars Hoffmann and Olaf Stein), for their support, and in particular for organising the typesetting and printing of the report.

Appendices

Acronym dictionary

A

AERONET	Aerosol Robotic Network
ACE-FTS	Atmospheric Chemistry Experiment-Fourier Transform Spectrometer, onboard the Canadian Space Agency SCISAT satellite
AGU	American Geophysical Union
AGW	Atmospheric gravity waves
AIRS	Advanced Infrared Sounder
AMOC	Atlantic Meridional Overturning Circulation
ANY fires	Australian New Year's fires in December 2019/January 2020
AOD	Aerosol Optical Depth
APARC	Atmospheric Processes And their Role in Climate
ATLAS	Alfred Wegener InsTitute LAgrangian Chemistry/Transport System (a 3-D global chemical transport model, not included in HTHH-MOC or TongaMIP)
ATMS	Advanced Technology Microwave Sounder
AVHRR	Advanced Very High Resolution Radiometer

B

B^2SAP	Baseline Balloon Stratospheric Aerosol Profiles
BDC	Brewer-Dobson circulation
BraVo	Bridging the Gap between the Aerosol-Cloud Interactions and the Variability of the Earth's Climate

C

CALIOP	Cloud-Aerosol Lidar with Orthogonal Polarization, onboard the NASA CALIPSO satellite
CALIPSO	Cloud-Aerosol Lidar and Infrared Pathfinder Satellite Observations
CAM5	NCAR's Community Atmosphere Model
CCM	Chemistry-climate model
CCMI	Chemistry-Climate Model Initiative
CEDA	Centre for Environmental Data Analysis
CESM1-CARMA	Community Earth System Model 1.0 – Community Aerosol and Radiation Model for Atmospheres
CESM2	Community Earth System Model, version 2
CIPS	Cloud Imaging and Particle Size Experiment
CIRES	Cooperative Institute for Research in Environmental Sciences
CMAM	Canadian Middle Atmosphere Model
CNES	Centre National d'Études Spatiales
CNMI	Commonwealth of the Northern Mariana Islands
COSMIC	Constellation Observing System for Met- eorology, Ionosphere, and Climate
CRIS	Cross-Track Infrared Sounder
CTM	Chemical transport model

D

DA	Data assimilation
DART	Deep-ocean Assessment and Reporting of Tsunamis
DDU	Dumont d'Urville (French Antarctic station)
DRE	Dense Rock Equivalent
DSCOVR/EPIC	Deep Space Climate Observatory / Earth Polychromatic Imaging Camera
DU	Dobson Unit

E

EBM	Energy balance models
ECMWF	European Centre for Medium-Range Weather Forecasts
EJ	Exajoule (1 EJ = 10^{18} Joules)
EMI-2	The Environmental Monitoring Instrument
ENTLN	Earth Networks Total Lightning Location Network
ENSO	El Niño-Southern Oscillation
EP flux	Eliassen-Palm flux
EqL	Equivalent latitude
ERA5	The fifth generation of European ReAnalysis
ERF	Effective radiative forcing

G

GAIA	Ground-to-topside Model of Atmospheric and Ionosphere for Aeronomy
GEOSCCM	Goddard Earth Observing System earth system model
GISP2	Greenland Ice Sheet Project 2
GLD360	Vaisala's Global Lightning Detection Network
GLM	Geostationary Lightning Mapper
GloSSAC	Global Space-based Stratospheric Aerosol Climatology
GNSS	Global Navigation Satellite System
GNS Science	Geological and Nuclear Sciences
GOES-17	Geostationary Operational Environment Satellite-17
GOLD	Global Observation of the Limb and Disk
GPS	Global Positioning System
GRACE-FO	Gravity Recovery and Climate Experiment Follow-On
GSFC2D	NASA Goddard Space Flight Center two-dimensional model (a 2-D chemical transport model)
GVP	Global Volcanism Program
GW	Gravity waves

H

HIAMCM	High Altitude Mechanistic general Circulation Model
HTHH	Hunga Tonga-Hunga Ha'apai
HTHH-MOC	Hunga Tonga-Hunga Ha'apai Model Observations Comparison

I

IASI	Infrared Atmospheric Sounder Interferometer
ICON	ICOsahedral Nonhydrostatic model
ICON-ART	ICOsahedral Nonhydrostatic model with Aerosols and Reactive Tracer gases
ICON-MIGHTI	Ionospheric Connection Explorer-Michelson Interferometer for Global High-resolution Thermospheric Imaging
IMS	International Monitoring System
IR	Infrared
IRF	Instantaneous radiative forcing
ISS	International Space Station
ITCZ	The intertropical convergence zone
IUP	Institute of Environmental Physics (University of Bremen)

J

JASMIN	Joint Analysis System for Multidisciplinary Investigations
JMA	Japanese Meteorological Agency
JRA-3Q	Japanese Reanalysis for Three Quarters of a Century
JRA-55	The Japanese 55-year Reanalysis

L

LEO	Low Earth orbit
LMDZ	General circulation model of the Laboratoire de Météorologie Dynamique
LOAC	Light Optical Aerosol Counter
LP	Limb Profiler
LS	Lower stratosphere
LSTIDs	Large-scale ionospheric disturbances
LW	Longwave

M

M2-SCREAM	The MERRA-2 Stratospheric Composition Reanalysis of Aura Microwave Limb Sounder
MAM	Modal Aerosol Module
MANGO	Midlatitude All-sky-imaging Network for GeoSpace Observations
MER	Mass Eruption Rate
MERRA-2	Modern-Era Retrospective Analysis for Research and Applications, Version 2
MESORAC	Model for Gravity Wave Source, Ray Tracing, and Reconstruction
MetOp-B	Meteorological Operational Satellite B
MFCI	Molten Fuel-Coolant Interaction
MIP	Model Intercomparison Project
MIROC-CHASER	Model for Interdisciplinary Research on Climate – CHemical Atmospheric general circulation model for Study of atmospheric Environment and Radiative forcing
MIRS	Microwave Integrated Retrieval System
MISR	Multi-Angle Imaging SpectroRadiometer
MLS	Microwave Limb Sounder, onboard the NASA Aura satellite
MLS-Match	"Match" technique, whereby changes in ozone between two or more observations of the same air mass provide a measure of chemical ozone loss
MODIS	Moderate Resolution Imaging Spectroradiometer (onboard NASA Terra and Aqua)
MOR	Mid-oceanic ridge
MSTIDs	Medium-scale ionospheric disturbances

N

NAT	Nitric acid trihydrate
NASA	National Aeronautics and Space Administration
NCAR	National Center for Atmospheric Research
N20	National Oceanic and Atmospheric Administration 20 (satellite)
NEIC	National Earthquake Information Center
NH	Northern Hemisphere
NAM	Northern annular mode
NIR	Near-IR
NIWA	National Institute for Water and Atmospheric Research (New Zealand)
NDACC	Network for Detection of Atmospheric Composition Change
NOAA	National Oceanic and Atmospheric Administration
NOAA CSL	NOAA Chemical Sciences Laboratory
NSF	National Science Foundation

O

OHP	Observatoire de Haute Provence
OMI	Ozone Monitoring Instrument
OMPS	Ozone Mapping and Profiler Suite
OMPS-LP	Ozone Mapping and Profiler Suite Limb Profiler, onboard the Suomi-NPP satellite
OMPS-NP	Ozone Mapping and Profiler Suite Nadir Profiler, onboard the Suomi-NPP satellite
OPAR	Observatoire de Préhistoire et d'Archéologie des Hautes Terres
OSIRIS	Optical Spectrograph and Infra-Red Imaging System

P

PDC	Pyroclastic density current
POPS	Portable Optical Particle Spectrometer
PMC	Polar mesospheric cloud
PSC	Polar stratospheric cloud
PSDA	Plataforma de Datos Ambientales - environmental data platform in Chile
Pyro-Cb	Pyro-cumulonimbus

Q

QBO	Quasi-biennial oscillation

R

r_{eff}	Effective radius
RF	Radiative forcing
RMC	Residual mean circulation
RO	GPS radio occultation
ROV	Remotely operated vehicle

S

SA	Sulfate aerosols
SABER	Sounding of the Atmosphere using Broadband Emission Radiometry
SAD	Surface area density
SAGE III	Stratospheric Aerosol and Gas Experiment III
SAGE III/ISS	Stratospheric Aerosol and Gas Experiment onboard the International Space Station
SAM	Southern annular mode
SAMI3	Sami3 is Also a Model of the Ionosphere
SAOD / sAOD	Stratospheric aerosol optical depth
SARF	Stratosphere-adjusted radiative forcing
SAT	Surface air temperature
SBUV, SBUV/2	Solar Backscatter Ultraviolet series of instruments
SCISAT	SCience and Technology SATellite
SCWV	Stratospheric columnar water vapour
SH	Southern Hemisphere
SNPP	Suomi National Polar-orbiting Partnership
SOCOL-AERv2-Volc	modeling tools for studies of SOlar Climate Ozone Links, AER = 2-D aerosol model, Volc = heat flux, mixed-layer ocean, and SSP implementation

SOCOLv4	SOlar Climate Ozone Links version 4
SPARC	Stratospheric Processes and their Role in Climate
SP-EACH	Southeast Pacific - Eastern Antarctic Climate and Hydrography
S-RIP	SPARC Reanalysis Intercomparison Project
SSA	Single scattering albedo
SSiRC	Stratospheric Sulfur and its Role in Climate
SST	Sea surface temperatures
SSU	Stratospheric Sounding Unit
SSW	Sudden stratospheric warming
STS	Supercooled ternary solution
STT	Stratosphere-to-troposphere transport
SURF	Surface
SVA	Sunlit vortex area
SW	Shortwave

T

TEC	Total electron content
TECU	Total electron content units
TESMaP	Tonga Eruption Seabed Mapping Project
TID	Travelling ionospheric disturbance
TIE-GCM	NCAR Thermosphere-Ionosphere-Electrodynamics General Circulation Model
TOA	The top of the atmosphere
TOMCAT	University of Leeds 3-D chemical transport model (not included in HTHH-MOC or TongaMIP)
Tonga-MIP	Hunga Tonga-Hunga Ha'apai Volcano Model Intercomparison Project
TR^2Ex	Tonga volcano Rapid Response Experiment
TROP	Tropopause
TROPOMI	Tropospheric Monitoring Instrument

U

UNEP	United Nations Environment Programme
US	Upper stratosphere
USask	University of Saskatoon
USGS	United States Geological Survey
USV	Uncrewed surface vessel
UTC	Coordinated universal time
UTLS	Upper troposphere and lower stratosphere
UV	Ultraviolet

V

VDR	Volume depolarisation ratio
VEI	Volcanic explosivity index
VolMIP	Volcanoes and Climate Model Intercomparison Project
VOTW	Volcanoes of the world (database)

W

WV	Water vapour
WACCM6	Whole Atmosphere Community Climate Model version 6
WACCM6/MAM	Whole Atmosphere Community Climate Model version 6 with Modal Aerosol Model
WACCM-X	Whole Atmosphere Community Climate Model with thermosphere and ionosphere extension
WCRP	World Climate Research Program
WMO-GAW	World Meteorological Organization's Global Atmosphere Watch Program
WWLLN	World Wide Lightning Location Network

Chemical acronyms

Br	Bromine atom
BrCl	Bromine chloride
BrO	Bromine monoxide
$BrONO_2$	Bromine nitrate
$CaSO_4$	Calcium sulfate
Cl	Chlorine atom
Cl_2	Molecular chlorine
ClO	Chlorine monoxide
$ClONO_2$	Chlorine nitrate
ClOOCl	Dichlorine monoxide
ClO_x	Chlorine oxides, ClO_x = Cl + ClO + 2×ClOOCl
CO_2	Carbon dioxide
HBr	Hydrobromic acid
HCl	Hydrochloric acid
H_2O	Water (vapour)
H_2S	Hydrogen sulfide
H_2SO_4	Sulfuric acid
HNO_3	Nitric acid
HO_2	Hydroperoxyl radical
HOBr	Hypobromous acid
HOCl	Hypochlorous acid
HO_x	Hydrogen oxides, HO_x = OH + HO_2
K	Potassium
Mg	Magnesium
N_2O	Nitrous oxide
N_2O_5	Dinitrogen pentoxide
NO	Nitric oxide
NO_2	Nitrogen dioxide
NO_x	Nitrogen oxides, NO_x = NO + NO_2
NO_y	Odd nitrogen, approximated here as $NO_y \approx 2\times N_2O_5 + NO_x + HNO_3 + ClONO_2$
NaCl	Sodium chloride
O_2	Molecular oxygen
O_3	Ozone
OH	Hydroxyl radical
SO_2	Sulfur dioxide
SO_4	Sulfate
SiO_2	Silicon dioxide

Supplements

S1 Hunga Tonga-Hunga Ha'apai volcano impact Model Observation Comparison (HTHH-MOC) project: experiment protocol and model descriptions

Authors

Yunqian Zhu, Hideharu Akiyoshi, Valentina Aquila, Elisabeth Asher, Ewa M. Bednarz, Slimane Bekki, Christoph Brühl, Amy H. Butler, Parker Case, Simon Chabrillat, Gabriel Chiodo, Margot Clyne, Peter R. Colarco, Sandip Dhomse, Lola Falletti, Eric Fleming, Ben Johnson, Andrin Jörimann, Mahesh Kovilakam, Gerbrand Koren, Ales Kuchar, Nicolas Lebas, Qing Liang, Cheng-Cheng Liu, Graham Mann, Michael Manyin, Marion Marchand, Olaf Morgenstern, Paul A. Newman, Luke D. Oman, Freja F. Østerstrøm, Yifeng Peng, David Plummer, Ilaria Quaglia, William Randel, Samuel Rémy, Takashi Sekiya, Stephen Steenrod, Timofei Sukhodolov, Simone Tilmes, Kostas Tsigaridis, Rei Ueyama, Daniele Visioni, Xinyue Wang, Shingo Watanabe, Yousuke Yamashita, Pengfei Yu, Wandi Yu, Jun Zhang, Zhihong Zhuo

This supplement is a preprint of (with adjustment to the assessment style): Zhu et al. (2025).

Zhu, Y., Akiyoshi, H., Aquila, V., Asher, E., Bednarz, E. M., Bekki, S., Brühl, C., Butler, A. H., Case, P., Chabrillat, S., Chiodo, G., Clyne, M., Colarco, P. R., Dhomse, S., Falletti, L., Fleming, E., Johnson, B., Jörimann, A., Kovilakam, M., Koren, G., Kuchar, A., Lebas, N., Liang, Q., Liu, C.-C., Mann, G., Manyin, M., Marchand, M., Morgenstern, O., Newman, P., Oman, L. D., Østerstrøm, F. F., Peng, Y., Plummer, D., Quaglia, I., Randel, W., Rémy, S., Sekiya, T., Steenrod, S., Sukhodolov, T., Tilmes, S., Tsigaridis, K., Ueyama, R., Visioni, D., Wang, X., Watanabe, S., Yamashita, Y., Yu, P., Yu, W., Zhang, J., and Zhuo, Z.: Hunga Tonga–Hunga Ha'apai Volcano Impact Model Observation Comparison (HTHH-MOC) project: experiment protocol and model descriptions, *Geosci. Model Dev.*, 18, 5487–5512, https://doi.org/10.5194/gmd-18-5487-2025, 2025.

Abstract

The 2022 Hunga volcanic eruption injected a significant amount of water vapour and a moderate amount of sulfur dioxide into the stratosphere, causing observable responses in the climate system. We have developed a model–observation comparison project to investigate the evolution of volcanic water and aerosols and their impacts on atmospheric dynamics, chemistry, and climate, using several state-of-the-art chemistry climate models. The project goals are (1) to evaluate the current chemistry–climate models to quantify their performance in comparison to observations and (2) to understand atmospheric responses in the Earth system after this exceptional event and investigate the potential impacts in the projected future. To achieve these goals, we designed specific experiments for direct comparisons to observations, for example from balloons and the Microwave Limb Sounder satellite instrument. Experiment 1 consists of two sets of free-running ensemble experiments from 2022 to 2031: one with fixed sea-surface temperatures and sea ice and one with coupled ocean. These experiments will help to understand the long-term evolution of water vapour and aerosols; quantify HTHH effects on stratospheric and mesospheric temperatures, dynamics, and transport; understand the impact of dynamic changes on ozone chemistry; quantify the net radiative forcings; and evaluate any surface climate impact. Experiment 2 is a nudged-run experiment from 2022 to 2023 using observed meteorology. To allow participation of more climate models with varying complexities of aerosol simulation, we include two sets of simulations in Experiment 2: Experiment 2a is designed for models with internally generated aerosol, while Experiment 2b is designed for models using prescribed aerosol surface area density. This experiment will help to analyse H_2O and aerosol evolution, quantify the net radiative forcings, understand the impacts on mid-latitude and polar O_3 chemistry, and allow close comparisons with observations.

S1.1 Introduction and motivations of this project

The Hunga Tonga–Hunga Ha'apai (HTHH) Impacts activity was established in the World Climate Research Programme (WCRP) Atmosphere Processes And their Role in Climate (APARC) as a limited-term focused cross-activity with a duration of 3 years. It aims to assess the impacts of the 15 January 2022 Hunga volcanic eruption and produce an assessment to document the Hunga impact on the climate system. The Hunga eruption injected an unprecedented amount of water (H_2O) and moderate sulfur dioxide (SO_2) into the stratosphere (Millán et al., 2022), presenting a unique opportunity to understand the impacts on the stratosphere of a large-magnitude explosive phreatomagmatic eruption. The wide range of satellite observations of the stratospheric water and sulfate plumes, global transport and dispersion of volcanic materials, and unusual chemical and temperature signals are helpful in assessing model representations of stratospheric chemistry, aerosol, and dynamics. For example, the Aura Microwave Limb Sounder (MLS) observed ~150 Tg of water injected by the Hunga eruption (Millán et al., 2022), which slowly decayed due to the polar stratospheric cloud (PSC) dehydration process and stratosphere–troposphere exchange (Fleming et al., 2024; Zhou et al., 2024). Large aerosol optical depth is observed by the Ozone Mapping and Profiler Suite (OMPS) (Taha et al., 2022), due to fast formation of sulfate (Zhu et al., 2022) and the high optical efficiency of Hunga aerosol particles (Li et al., 2024). Unlike the stratospheric warming patterns observed from previous large volcanic eruptions (El Chichón in 1982 and Pinatubo in 1991), global stratospheric temperatures decreased by 0.5 to 1.0 K in the first 2 years following the Hunga eruption, largely due to radiative cooling from injected water vapour (Randel et al., 2024). Satellite observations in June, July, and August 2022 reveal reduced lower-stratospheric ozone (O_3) over the Southern Hemisphere (SH) midlatitudes and subtropics, with high levels near the Equator, exceeding previous variability. These ozone anomalies coincide with a weakening of the Brewer–Dobson circulation during this period (Wang et al., 2023). Changes in stratospheric winds also influence the mesosphere, leading to a stronger mesospheric circulation and corresponding temperature changes (Yu et al., 2023). These observed phenomena provide a unique opportunity to test the ability of chemistry–climate models to simulate the evolution of volcanic aerosols combined with such a large amount of water vapour, as well as understand how volcanic water vapour and aerosols modify radiative balances and stratospheric ozone.

The APARC Hunga Impacts activity aims to provide a benchmark analysis of the eruption impacts so far and projections of eruption climate impacts over the next few years. Two multi-model evaluation projects are designed to facilitate the success of this activity: the Tonga Model Intercomparison Project (Tonga-MIP) (Clyne et al., 2024) and the Hunga

Tonga–Hunga Ha'apai Volcano Impact Model Observation Comparison (HTHH-MOC) project (this paper). The HTHH-MOC provides a foundation for a coordinated multi-model evaluation of global chemistry–climate models' performance in response to the Hunga volcanic eruption. It defines a set of perturbation experiments, where volcanic forcings – injected water vapour and aerosol concentrations – are consistently applied across participating model members. HTHH-MOC aims to assess how reliably global chemistry–climate models simulate the climate responses to this unprecedented volcanic forcing. This project enhances our confidence in attributing and interpreting observations following the Hunga eruption. The scientific questions related to the HTHH-MOC are as follows:

- How does the Hunga volcanic plumes' transport relate to or impact stratospheric dynamics (such as Brewer–Dobson circulation, polar vortex, and the quasi-biennial oscillation) and the upper atmosphere?
- What are the chemical impacts of the Hunga eruption in the stratosphere and mesosphere?
- What and how long is the radiative effect of the Hunga eruption?
- Does Hunga impact the tropospheric/surface climate?

Therefore, the HTHH-MOC project is focused on evaluating global chemistry–climate models regarding the following three science themes: (1) plume evolution, dispersion, and large-scale transport; (2) impacts on stratospheric chemistry and the ozone layer; and (3) radiative effect from the eruption and surface climate impacts. Besides the HTHH-MOC project, the assessment also includes analysis of observations and models that are not global climate models. In the following paragraph, we describe the HTHH-MOC experiment design and participating models.

S1.2 Experiment design

There are two experiments (Exp1 and Exp2 detailed below) designed to fulfill the scientific goals. Each experiment includes a set of simulations with different volcanic injections (i.e., with and without water and/or SO_2), to explore the separate impacts of volcanic water and aerosols during the post-eruption period: (a) control case (no eruption),(b) H_2O (~150 Tg) and SO_2 (0.5 Tg), (c) only H_2O (~150 Tg), and (d) only SO_2 (0.5 Tg). Simulations with the injection of SO_2 only (d) are optional and designed for aerosol-focused models. The SO_2 and water injections are prescribed based on Millán et al. (2022) and Carn et al. (2022). Note that~150 Tg of water is not the injection amount but the amount retained after the first couple of days. This is because some models form ice particles that fall out of the stratosphere due to large H2O supersaturation during the initial injection (Zhu et al., 2022); these models will have to inject more H_2O to counterbalance the ice formation (see Table S1.6). The only requirement is that the model should have reasonable comparison to the MLS observations for water vapour, as shown in Figure S1.1. Aside from retaining ~150 Tg of water, the water vapour enhancement should be near 10 to 50 hPa, and most of the water vapour should be located between 10°N and 30°S by March 2022.

The first experiment (Exp1) is a free-running ensemble simulation covering the period from 2022 to 2031. The experiment has been designed to answer questions on the following:

1. understanding the long-term evolution of Hunga water vapour and aerosols in free-running models;
2. quantifying Hunga effects on stratospheric temperatures, dynamics, and transport;
3. understanding the impact of dynamic changes on ozone chemistry;
4. quantifying the net radiative effects;
5. estimating surface impacts (e.g., temperature, El Niño–Southern Oscillation, monsoon precipitation).

Simulations with free-running meteorology are required to properly understand the impacts of the eruption on atmospheric dynamics and transport processes and the resulting impacts of those on chemical species (e.g., ozone) and surface climate. Since coupling of the atmosphere with ocean and land processes is required to fully simulate many aspects of the surface impacts, the use of coupled atmosphere, ocean, and land models is recommended. However, since such a fully interactive setup imposes additional computing requirements, an alternative model setup with fixed sea-surface temperatures (SSTs) and sea ice is also allowed. In that case, the prescribed climatological SSTs and sea-ice data are obtained by averaging SST during the past decade (2012–2021), with the same data imposed in both the H_2O + SO_2 (b) and control (a) simulations. It is important to note that

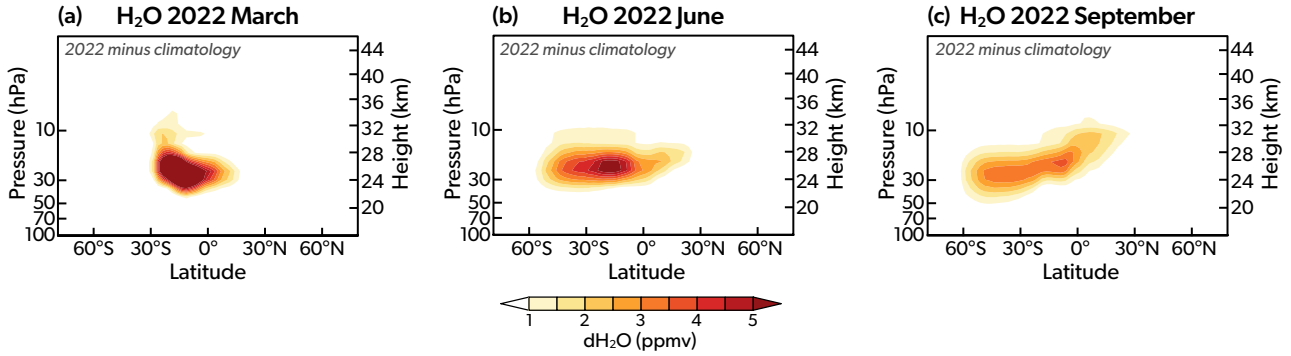

Figure S1.1: *Monthly average water vapour perturbation after the Hunga eruption from MLS. Panels (a)–(c) show the observed dispersion of the H_2O enhancement in 2022 in the months of (a) March, (b) June, and (c) September.*

both initial and boundary conditions in a model come with uncertainties, and model processes are simplified. Therefore, model simulations are influenced by the characteristics of the model itself and the background state of the atmospheric system (Jones et al., 2016; Brodowsky et al., 2021). To address some of the inherent uncertainties and reduce contribution of interannual variability to the forced response, we use a large ensemble of simulations with slightly varied initial conditions. Note that in the projection of stratospheric volcanic forcing, we only considered the Hunga eruption since 2022, and no future explosive eruptions are included. For example, the 2024 Mt. Ruang eruption contributed to elevated stratospheric aerosol optical depth, but it is not included. Particularly, the first 5 years of qualified model output of Exp1 is used to understand climate impacts on the mesosphere and ionosphere from 2022–2027, such as gravity wave drag, temperature changes, polar mesospheric clouds (PMCs), and atmospheric circulation. The qualified models need to resolve the upper atmosphere with vertical resolutions higher than or equal to what we request in Section S1.3.

Since some aspects of the response, e.g., impacts on the radiative effect, may be too noisy from free-running model simulations even with large ensembles, we have also designed the second experiment, which uses nudged temperature and meteorology to ensure that the meteorology will be as close as possible to the one observed and thus isolate chemical changes and their radiative effect. Experiment 2 (Exp2) is a 2-year simulation that runs from 2022 to 2023 with nudged winds and/or temperature to answer questions on H_2O and aerosol evolution, quantification of the net radiative effects, and impacts on mid-latitude and polar ozone chemistry. Exp2 has two distinct realisations: Experiment 2a (Exp2a) and Experiment 2b (Exp2b). The models participating in Exp2a all have a prognostic aerosol module but vary in the complexity of their representation of aerosol microphysics (i.e., bulk, modal, or sectional). Models participating in Exp2b use prescribed aerosol surface area density (SAD) and radiative properties as input to the models (Jörimann et al., 2025). The prescribed aerosol properties are calculated using Global Space-based Stratospheric Aerosol Climatology (GloSSAC; Thomason et al., 2018; Kovilakam et al., 2020; Kovilakam et al., 2023) version 2.22 aerosol data from 1979–2023. Note that for the period after the Hunga eruption, GloSSAC uses the Stratospheric Aerosol and Gas Experiment (SAGEIII/ISS) version 5.3 interpolated along the time axis and the Optical Spectrograph and InfraRed Imager System (OSIRIS) version 7.3 to fill in any missing data poleward of 60°N/S due to the unavailability of the Cloud-Aerosol Lidar and Infrared Pathfinder Satellite Observations (CALIPSO) data since January 2022. Therefore, when conducting analyses north/south of 60°N/S it should be noted that the aerosols may be underestimated due to the OSIRIS instrument retrieval biases. We ask for the models to check their initial chemical fields against the MLS to see if the models are qualified to evaluate their ozone chemistry. The nudged runs of Exp2 enable isolation of the chemical impact of the Hunga eruption from the volcanically induced changes in dynamics by comparing the runs with and without H_2O + SO_2 injection. The net radiative effect anomaly due to water and sulfate aerosol can also be calculated by comparing the control run (a) with the H_2O + SO_2 injection run (b).

Table S1.1 shows the forcings and emissions data used for the HTHH-MOC experiments. Table S1.2 shows the settings specific to each experiment. For volcanic injection for Exp1 and 2, we recommend the injections of H_2O and SO_2 at 04:00 UTC on 15 January 2022. All the models are required to retain

a similar amount of water as observed by the MLS (~150 Tg). The models are recommended to compare with the MLS evolution for validation (Figure S1.1). The goal is to retain the same amount of water and similar altitude to start with, so we can analyse the water's impact on the stratosphere and climate. If injecting 25–30 km cannot retain 150 Tg, models can inject higher than 30 km. The SO_2 injection is required to be 0.5 Tg for all models. The injection locations are not required to be co-injected with H_2O.

The data analysis of this project is designed to do inter-model comparisons, as well as inter-experiment comparisons. For example, the comparisons between Exp2a and Exp2b can help to understand how well we simulate the sulfate SAD and the importance of SAD variation for stratospheric ozone chemistry. Comparing Exp1 and Exp2 for the same period can help understand instantaneous and adjusted radiative effects. In addition, large (10–20) member ensembles are requested for free-running simulations to better quantify the role of internal variability in the climate response.

A parallel model intercomparison project, Tonga-MIP (Clyne et al., 2024), will also be part of the 2025 Hunga assessment. It is designed to explore the plume evolution between 1 day and up to 1–2 months after the eruption. Tonga-MIP was initiated before the APARC Hunga activity started. It will be described in a separate paper, but we list it here to document the comprehensiveness of the modelling effort for the Hunga assessment. Two objectives of Tonga-MIP cannot be achieved by Exp1 and Exp2:

1. The nudged experiment of Tonga-MIP aims to intercompare the microphysical processes (i.e., cloud and aerosol physics and sulfur chemistry) between different models. Therefore, all models are requested to inject 150 Tg of water, but the retained amount of water varies between models, differing from Exp1 and Exp2, which require retaining ~150 Tg of water in the stratosphere. The SO_2 injection is 0.5 Tg, the same as in the HTHH-MOC experiments. The injections are required to occur between 25–30 km altitude, within the latitude and longitude box of 22–14° S and 182–186° E, at a constant vertical volume mixing ratio for 6 h starting at 04:00 UTC on 15 January 2022.
2. The free-running experiment of Tonga-MIP aims to study the radiative effect of water and SO_2 on the Hunga plume's descending and ascending behaviour during the first month after the eruption, since the Hunga water and aerosol plumes were observed to descend several kilometres during the first month after the eruption (Sellitto et al., 2022; Randel et al., 2024). Therefore, Tonga-MIP is designed to nudge the atmosphere up until several different dates and then explore the plume-descending patterns in free-running mode after those dates. The selected dates are 21, 26, and 31 January 2022. Most of the models that participate in Tonga-MIP also participate in the HTHH-MOC.

S1.3 Model output

The model output covers variables based on the Chemistry–Climate Modeling Initiative (CCMI) output list, with some additions specific to this study. The detailed list is provided in `https://doi.org/10.5194/gmd-18-5487-2025-supplement`. All participating models are requested to generate the same variable names, units, and ordering of dimensions (longitude from 0 to 360° E, latitude from 90° S to 90° N, and pressure levels from 1000 to 0.03 hPa, or altitude from 0 to 73 000 m), as well as consistent file name structures, such as `variable_domain_modelname_experimentname.nc` or `domain_modelname_experimentname.variable.nc`. Examples of `Experiment_name` are `HTHHMOC-Exp1` and `HTHHMOC-Exp2`. Example file names include `Monthlymean_WACCM6MAM_HTHHMOC-Exp1-NoVolc-fixedSST.ensemble001.O3.nc` or `O3_Dailymean_WACCM6MAM_HTHHMOC-Exp1-H2Oonly-CoupledOcean.ensemble001.nc`.

The 3-D model output is requested both on native model levels (hybrid pressure or height) and interpolated to the CMIP6 `plev39` grid (`plev39`: 1000, 925, 850, 700, 600, 500, 400, 300, 250, 200, 170, 150, 130, 115, 100, 90, 80, 70, 50, 30, 20, 15, 10, 7, 5, 3, 2, 1.5, 1.0, 0.7, 0.5, 0.4, 0.3, 0.2, 0.15, 0.1, 0.07, 0.05, 0.03 hPa), and, for mesospheric analysis, additional levels are added: 0.02, 0.01, 0.007, 0.005, 0.003, and 0.001 hPa above the plev39 grid.

Monthly mean output is requested for all variables in Exp1, with some fields (as specified in the accompanying Excel sheet) requested as daily means. Some daily mean variables are limited to surface fields or to a reduced number of pressure levels. Daily mean output is requested for all variables in Exp2.

The total model output (approximately 33 TB) from Exp1 and Exp2 is archived at the JASMIN workspace (`https://jasmin.ac.uk/`, last access: 12 August 2025). JASMIN provides large storage capacity

Table S1.1: *Summary of forcings and emissions data used in HTHH-MOC experiments.*

Category	Description
Spin-up*	5-year nudged runs.
Degassing and eruptive volcano source**	Need both degassing and eruptive volcanic input for 5-year spin-up. Degassing continues during the experiment runs (e.g. 10 years for Exp1, 2 years for Exp2). recommended references: Volcanic degassing (Carn et al., 2016; Carn et al., 2017); Eruptive volcanoes (Neely III and Schmidt 2016 `https://archive.researchdata.leeds.ac.uk/96/` or Carn et al. 2017; Assume no more explosive volcanoes after Hunga.
Surface emission	Coupled Model Intercomparison Project phase 6 (CMIP6) emissions follow SSP2-4.5 (Gidden et al., 2019), which adopts an intermediate greenhouse gas (GHG) emission: CO_2 emissions around current levels before beginning to decline by 2050.
Chemical initialisation	Stratospheric chemistry fields (e.g., O_3, H_2O) at the beginning of 2022 should be compared with MLS observations for validation if the model participates in evaluation of the Hunga stratospheric chemistry impact.

* Five years are sufficient to reach sulfate equilibrium in the stratosphere; water may require up to 7 years (each model may adjust spin-up time based on its configuration).

** Recommended degassing volcanic emissions are injected at the cone altitude with constant flux based on Carn et al. (2017). Database is updated through 2022 here: `https://doi.org/10.5067/MEASURES/SO2/DATA406`.

Table S1.2: *Experiment design for the HTHH-MOC simulations.*

Experiment	Meteorology	Period	Aerosol Treatment	QBO	SST Configuration	Ensemble Members
Exp1.FixedSST	Free run starts 1 Feb (nudged until 31 Jan).	2022–2031 (10 years; first 5 years for mesospheric analysis).	Model-simulated aerosol or prescribed.	Internally generated (nudge if model does not generate).	Fixed climatology = mean of monthly averages 2012–2021, repeating annually. This applies to spin-up time as well.	10–20
Exp1.CoupledOcean	Free run starts 1 Feb (nudged until 31 Jan).	2022–2031 (10 years; first 5 years for mesospheric analysis).	Model-simulated aerosol or prescribed.	Internally generated (nudge if model does not generate).	Coupled ocean (optional); initialise with observed ocean state (see Section S1.4 for model descriptions).	10–20
Exp2a	Nudged wind only and/or nudged T and wind*.	2022–2023 (2 years).	Model-simulated aerosol.	Nudged.	Observed SST.	1
Exp2b	Nudged wind only and/or nudged T and wind*.	2022–2023 (2 years).	Prescribed.	Nudged.	Observed SST.	1

* "Nudged T and wind" indicates specified-dynamics (SD) configurations in which temperature and/or wind fields are relaxed toward reanalysis data. Coupled configurations are optional depending on individual model capability.

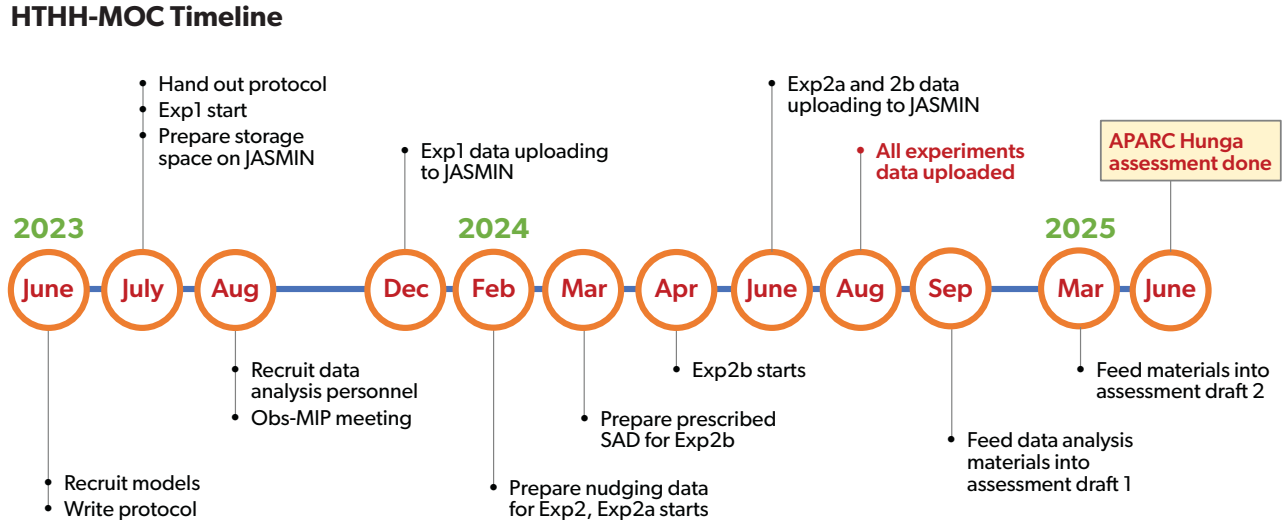

Figure S1.2: *Timeline designed for the HTHH-MOC project to coordinate with the APARC Hunga Impact assessment.*

and computing resources to facilitate data archiving and post-processing analysis for this project. This setup reduces the need for data transfers and allows reproducible computational workflows. Seddon et al. (2023) describe the facility in detail. The next project phase will publicly release the data by transferring it to the Centre for Environmental Data Analysis (CEDA) archiving system.

S1.4 Model descriptions and the Hunga volcanic injection specification

As part of the 3-year Hunga Impact activity, this project is highly time-sensitive. We designed the timeline for each experiment (Figure S1.2) to facilitate the completion of the 2025 Hunga Impact assessment. However, the JASMIN workspace will remain open for the uploading of modelling data after the deadline denoted in Figure S1.2 until 2025.

This paper only includes model descriptions for those models that submitted the output following the assessment timeline. The model setup follows the protocols listed in Section S1.2 unless specified below. Tables S1.3 to S1.6 provide key information on the participant models, which are described in detail in the following paragraphs for each model.

Table S1.3: *Participating models and contact information for HTHH-MOC and Tonga-MIP.*

Model name	Description reference paper	Developing institutions	Primary contact
CAM5/CARMA	Yu et al. (2015)	CU Boulder; Jinan Univ.	Pengfei Yu (pengfei.yu@colorado.edu); Yifeng Peng (pengyf16@lzu.edu.cn)
CCSRNIES-MIROC3.2	Akiyoshi et al. (2023) and Akiyoshi et al. (2016)	NIES	Yousuke Yamashita (yamashita.yosuke@nies.go.jp); Hideharu Akiyoshi (hakiyosi@nies.go.jp)
CMAM	Jonsson et al. (2004) and Scinocca et al. (2008)	CCCma, ECCC	David Plummer (david.plummer@ec.gc.ca)
EMAC MPIC	Schallock et al. (2023)	MPI-C, MPI-M, DLR	Christoph Brühl (christoph.bruehl@mpic.de)
GA4 UM-UKCA	Dhomse et al. (2020)	Univ. Leeds	Graham Mann (G.W.Mann@leeds.ac.uk); Sandip Dhomse (S.S.Dhomse@leeds.ac.uk)
GEOSCCM	Nielsen et al. (2017)	NASA	Peter Colarco (peter.r.colarco@nasa.gov)
GEOS/CARMA	Nielsen et al. (2017)	NASA	Parker Case (parker.a.case@nasa.gov)
GSFC2D	Fleming et al. (2024)	NASA	Eric Fleming (eric.l.fleming@nasa.gov)
IFS-COMPO Cy49R1	Huijnen et al. (2016) and Rémy et al. (2022)	ECMWF; team CAMS2_35	Simon Chabrillat (Simon.chabrillat@aeronomie.be); Samuel Rémy (sr@hygeos.com)
LMDZ6.2-LR-STRATAER / LMDZ6.2-LR-STRATAER-REPROBUS	Boucher et al. (2020) and Marchand et al. (2012)	CNRS, Sorbonne Univ., IPSL, LATMOS, LOCEAN	Marion Marchand (marion.marchand@latmos.ipsl.fr); Slimane Bekki (slimane.bekki@latmos.ipsl.fr); Nicolas Lebas (nicolas.lebas@locean.ipsl.fr); Lola Falletti (lola.falletti@latmos.ipsl.fr)
MIROC-CHASER	Sekiya et al. (2016)	JAMSTEC	Shingo Watanabe (wnabe@jamstec.go.jp); Takashi Sekiya (tsekiya@jamstec.go.jp)
MIROC-ES2H	Tatebe et al. (2019) and Kawamiya et al. (2020)	JAMSTEC; NIES	Shingo Watanabe (wnabe@jamstec.go.jp); Takashi Sekiya (tsekiya@jamstec.go.jp); Tatsuya Nagashima (nagashima.tatsuya@nies.go.jp); Kengo Sudo (kengo@nagoya-u.jp)
SOCOLv4	Sukhodolov et al. (2021)	PMOD/WRC; ETH-Zurich	Timofei Sukhodolov (timofei.sukhodolov@pmodwrc.ch)
UKESM1.1	Sellar et al. (2019), Sellar et al. (2020) and Dennison et al. (2019)	UK Met Office; UK Universities; NCAS	Graham Mann (g.w.mann@leeds.ac.uk); Sandip Dhomse (s.s.dhomse@leeds.ac.uk); Ben Johnson (ben.johnson@metoffice.gov.uk); Mohit Dalvi (mohit.dalvi@metoffice.gov.uk); Luke Abraham (nla27@cam.ac.uk); James Keeble (j.keeble2@lancaster.ac.uk)
WACCM6/CARMA	Tilmes et al. (2023)	NCAR	Simone Tilmes (tilmes@ucar.edu); Cheng-Cheng Liu (chengcheng.liu@lasp.colorado.edu); Yunqian Zhu (yunqian.zhu@noaa.gov); Margot Clyne (Tonga-MIP, margot.clyne@colorado.edu)
WACCM6/MAM	Mills et al. (2016)	NCAR	Xinyue Wang (xinyuew@colorado.edu); Simone Tilmes (tilmes@ucar.edu); Jun Zhang (jzhan166@ucar.edu); Wandi Yu (yu44@llnl.gov); Zhihong Zhuo (zhuo.zhihong@uqam.ca); Ewa Bednarz (ewa.bednarz@noaa.gov); Margot Clyne (Tonga-MIP, margot.clyne@colorado.edu)

CAM5/CARMA

The atmospheric component of the Community Atmosphere Model version 5 (CAM5; Lamarque et al. 2012) is the atmospheric component of the Community Earth System Model, version 1 (CESM1.2.2; Hurrell et al. 2013), with a top at around 45 km. CAM5 has a horizontal resolution of 1.9° latitude × 2.5° longitude, utilising the finite-volume dynamical core (Lin and Rood, 1996). The model has 56 vertical levels, with a vertical resolution of approximately 1 km in the upper troposphere and lower stratosphere.

The modeled winds and temperatures were nudged to the 3 h Goddard Earth Observing System 5 (GEOS-5) reanalysis dataset (Molod et al., 2015) every time step (30 min) by 1 % (i.e., a 50 h Newtonian relaxation timescale). The aerosol is interactively simulated using a sectional aerosol microphysics model, CARMA (Community Aerosol and Radiation Model for Atmospheres; Yu et al. 2015). The model uses the Model for Ozone and Related Chemical Tracers (MOZART) chemistry that is used for both tropospheric (Emmons et al., 2010) and stratospheric chemistry (English et al., 2011; Mills et al., 2016). The volcanic emissions from continuously degassing volcanoes use the emission inventory RCP8.5 and FINNv1.5. No volcanic eruptions except the Hunga 2022 eruption are included.

The initial volcanic injection altitude and area are determined by validating the water and aerosol transportation in months shown in S1.1 following the tests in Zhu et al. (2022), Wang et al. (2023), and Zhang et al. (2024). In these simulations, the H2O is injected at 25 to 35 km altitude, and SO2 is injected at 20 to 28 km altitude. The injection latitude ranges from 22 to 14° S, and longitude ranges from 182 to 186° E (Zhu et al., 2022). The initial injection of H2O is 150 Tg, with approximately 135 Tg left after the first week following the eruption.

CCSRNIES-MIROC3.2

The Center for Climate System Research / National Institute for Environmental Studies–Model for Interdisciplinary Research on Climate version 3.2 Chemistry–Climate Model (CCSRNIES-MIROC3.2 CCM; Akiyoshi et al. 2023) is based on version 3.2 of the MIROC atmospheric general circulation model (AGCM), incorporating a stratospheric chemistry module developed at the National Institute for Environmental Studies (NIES) and the University of Tokyo. The model has a horizontal resolution of T42 (2.8° latitude × 2.8° longitude) and 34 vertical levels, with a vertical resolution of approximately 1 km in the lower stratosphere–upper troposphere and 3 km in the upper stratosphere and mesosphere. The model top is located at 0.01 hPa (approximately 80 km).

The chemistry in the CCSRNIES-MIROC3.2 CCM is a stratospheric chemistry module including 42 photolysis reactions, 142 gas-phase chemical reactions, and 13 heterogeneous reactions for multiple aerosol types (Akiyoshi et al., 2023). Tropospheric chemistry is not included, but the stratospheric chemistry scheme is used for both the troposphere and the mesosphere. In the CCSRNIES-MIROC3.2 CCM, only Exp2b can be performed. The atmospheric temperature and horizontal winds are nudged toward Modern-Era Retrospective analysis for Research and Applications Version 2 (MERRA-2) reanalysis (Gelaro et al., 2017) with a 1-day relaxation using instant values at 6-hour intervals (Akiyoshi et al., 2016). The HadISST data are used during the simulation.

The CCSRNIES-MIROC3.2 CCM does not have any microphysics scheme for volcanic aerosols. The surface area and spectral optical parameters of extinction, single scattering albedo, and asymmetric factor for Hunga aerosols were prescribed in the model from the GloSSAC version 2.22 aerosol data (Jörimann et al., 2025). H2O was injected instantly on 15 January 2022 at the 12 grids of the model in the region 181.4–187.0° E in longitude, 14.0–22.3° S in latitude, and 12.0–27.6 hPa in pressure level. A uniform number density of 1.709×10^{15} molec. cm^{-3} H_2O was injected in each of the 12 grids, which amounts to approximately 150 Tg.

CMAM

The Canadian Middle Atmosphere Model (CMAM) is based on a vertically extended version of CanAM3.1, the third-generation Canadian Atmospheric Model (Scinocca et al., 2008). Compared to the standard configuration of CanAM3.1, for CMAM the model top was raised to 0.0006 hPa (approximately 95 km), and the parameterisation of non-orographic gravity wave drag (Scinocca, 2003) and additional radiative processes important in the middle atmosphere (Fomichev et al., 2004) have been included.

The gas-phase chemistry includes a comprehensive description of the inorganic O_x, NO_x, HO_x, ClO_x, and BrO_x families, along with CH_4, N_2O, six chlorine-containing halocarbons, CH_3Br and, to account for an additional 5 ppt of bromine from short-lived source gases, CH_2Br_2 and $CHBr_3$ (Jonsson et al., 2004). A prognostic description of, and associated heterogeneous chemical reactions on, water ice PSCs (PSC Type II) and liquid ternary solution (PSC Type Ib) particles

Table S1.4: *Participating models in HTHH-MOC and Tonga-MIP.*

Model names	Exp1.FixedSST	Exp1.CoupledOcean	Exp2a	Exp2b	Tonga-MIP (Clyne et al. 2024)
CAM5/CARMA			**X**		
CCSRNIES-MIROC3.2				**X**	
CMAM	**X** (H_2O-only)(*)				
EMAC MPIC			**X**		
GA4 UM-UKCA					**X**
GEOSCCM	**X**		**X**		**X**
GEOS/CARMA			**X**		
GSFC2D	**X**(*)			**X**	
IFS-COMPO			**X**		
LMDZ6.2-LR-STRATAER			**X**		**X**
LMDZ6.2-LR-STRATAER-REPROBUS			**X**		**X**
MIROC-CHASER	**X**		**X**		
MIROC-ES2H					**X**
SOCOLv4					**X**
UKESM1.1			**X**		**X**
WACCM6/CARMA			**X**		**X**
WACCM6/MAM	**X**(*)	**X**(*)	**X**		**X**

* Models qualified to analyse mesospheric components are marked with an asterisk.

is included, although gravitational settling (dehydration or denitrification) is not calculated, and species return to the gas phase when conditions no longer support the existence of PSC particles.

The simulations for the HTHH-MOC simulations were performed at T47 spectral resolution (approximately 3.8° resolution on the linear transform grid used for the model physics), with 80 vertical levels giving a vertical resolution of approximately 0.8 km at 100 hPa, increasing to 2.3 km above 0.1 hPa. The CMAM does not internally generate a QBO, so the zonal winds in the equatorial region were nudged towards a dataset based on observed variations up to December 2023, constructed using the method ofNaujokat (1986) and extended into the future by repeating a historical period that is congruent with the observed QBO in late 2023. Water vapour from the Hunga eruption was added as a zonally averaged perturbation to the model water over 5 days from 00:00 UTC on 20 February 2022. The spatial distribution of the anomaly was designed to reproduce the water vapour anomaly observed in mid-February by the Atmospheric Chemistry Experiment – Fourier Transform Spectrometer (ACE-FTS) (Bernath et al., 2005) satellite (Patrick Sheese, personal communication, 2022), with a maximum value of 13.3 ppm at 17°S and 25.5 km and producing an anomaly of ~150 Tg H_2O in the stratosphere.

EMAC MPIC

The chemistry–climate model EMAC (ECHAM5/MESSy Atmospheric Chemistry) consists of the European Centre Hamburg general circulation model (ECHAM5) and the Modular Earth Submodel System (MESSy) (e.g., Jöckel et al., 2010). Here we use the version of Schallock et al. (2023) in horizontal resolution T63 (1.87° × 1.87°) with 90 levels between the surface and 0.01 hPa.

Vorticity, divergence, and temperatures between surface and 100 hPa are nudged to the ERA5 reanalysis of ECMWF (Hersbach et al., 2020), as well as surface pressure. SSTs and sea ice cover are prescribed by ERA5 data. The model can generate an internal QBO, but for comparison with observations it was slightly nudged to the Singapore data compiled by the Free University of Berlin and Karlsruhe Institute

Table S1.5: *Model resolutions and schemes used for HTHH-MOC experiments.*

Model names	Horizontal resolution	nlevels	Model Top	Vertical resolution in the stratosphere	Aerosol scheme	Specified dynamic source	QBO (free run)	Chemistry package (tropospheric chemistry?)
CAM5/CARMA	~2°	56	45 km	1–4 km	CARMA sectional (20 bins)	GEOS-5	–	MOZART (yes)
CCSRNIES-MIROC3.2	T42	34	0.01 hPa	1–3 km	None	MERRA-2	–	full strat; no tropo
CMAM	T47	80	0.0006 hPa	0.8–2.5 km	None	ERA-5	nudged	strat + CH_4–NOx (tropo)
EMAC MPIC	T63	90	0.01 hPa	0.5 km in LS	GMXE (modal)	ERA-5	–	MECCA (simplified tropo)
GEOSCCM	c90 (~1°)	72	0.01 hPa	~1 km	GOCART (Bulk)	MERRA-2/GEOS-FP	Internal	GMI (yes)
GEOS/CARMA	c90 (~1°)	72	0.01 hPa	~1 km	CARMA (sectional 24 bins)	MERRA-2/GEOS-FP	–	GMI (yes)
GSFC2D	4°	76	0.002 hPa (~92 km)	1 km	Prescribed only	MERRA-2	Internal	full strat; partial trop
IFS-COMPO	T_L511 (~40 km)	137	0.01 hPa	0.5–1.5 km	Bulk	ERA-5	–	BASCOE (strat) + CB05 (tropo)
LMDZ6.2-LR-STRATAER	2.5° × 1.3°	79	80 km	1–5 km	S3A (sectional 36 bins)	ERA-5	–	No
LMDZ6.2-LR-STRATAER-REPROBUS	2.5° × 1.3°	79	80 km	1–5 km	S3A (sectional 36 bins)	ERA-5	–	REPROBUS
MIROC-CHASER	T85	81	0.004 hPa	0.7–1.2 km	MAM3	MERRA-2	Internal	tropo-strato chemistry
UKESM1.1	N96	85	80 km	0.6–0.7 km in LS	GLOMAP-mode	ERA-5	Internal	CheST (strat-trop chem.)
WACCM6/CARMA	~1°	70	140 km	1–2 km	Sectional (20 bins)	MERRA-2	–	MOZART (yes)
WACCM6/MAM	~1°	70	140 km	1–2 km	MAM4	MERRA-2	Internal	MOZART (yes)

of Technology (Giorgetta et al., 2006).

The model contains gas-phase and heterogeneous chemistry on PSCs and interactive aerosols. Surface mixing ratios of chlorine- and bromine-containing halocarbons and other long-lived gases are nudged to Advanced Global Atmospheric Gases Experiment (AGAGE) observations. The microphysical modal aerosol module contains four soluble and three insoluble modes for sulfate, nitrate, dust, organic and black carbon, and aerosol water (Pringle et al., 2010). The instantaneous radiative effect by tropospheric and stratospheric aerosols can be calculated online by multiple calls of the radiation module.

Volcanoes injecting material into the stratosphere are considered as in Schallock et al. (2023) using the perturbations of stratospheric SO_2 observed by the Michelson Interferometer for Passive Atmospheric Sounding (MIPAS) and aerosol extinction observed by OSIRIS. This method, based typically on data of a 10-day period, distributes the injected SO2 over a larger volume than typical point source approaches using the same integrated mass (see also Kohl et al., 2025). For Hunga this method has the disadvantage that H_2O and SO_2 are not co-injected since H_2O is injected over a 12-hour period as a slab consisting of four horizontal boxes and a Gaussian vertical distribution centred at 21.5 hPa. For Exp2a we continue the 30-year transient simulation presented in Schal-

Table S1.6: *Hunga volcanic injection profile for HTHH-MOC experiments.*

Model names	Date and duration	H_2O amount (after 1 week)	H_2O altitude	H_2O location / area	SO_2 amount	SO_2 altitude	SO_2 location / area
CAM5/CARMA	Jan 15, 6 h	150 Tg (~135 Tg)	25–35 km	22–14° S, 182–186° E	0.5 Tg	20–28 km	22–14° S, 182–186° E
CCSRNIES-MIROC3.2	Jan 15, instant	150 Tg (~150 Tg)	12–27.6 hPa	181.4–187.0° E, 14.0–22.3° S	–	–	–
CMAM	Feb 20, 5 days	150 Tg (~150 Tg)	~25.5 km	zonally averaged	–	–	–
EMAC MPIC	Jan 16, 12 h	136 Tg (~130 Tg)	Gaussian centered 21.5 hPa	23–19° S, 177–173° W	0.4 Tg (obs.)	23–27 km (obs.)	30° S–5° N, 90–120° W
GEOSCCM	Jan 15, 6 h	150 Tg (~150 Tg)	25–30 km	22–14° S, 182–186° E	0.5 Tg	25–30 km	22–14° S, 182–186° E
GEOS/CARMA	Jan 15, 6 h	150 Tg (~150 Tg)	25–30 km	22–14° S, 182–186° E	0.5 Tg	25–30 km	22–14° S, 182–186° E
GSFC2D	MLS H_2O profile until Mar 1	~150 Tg (~150 Tg)	–	zonally averaged	–	–	–
IFS-COMPO	Jan 15, 3 h	190 Tg (~150 Tg)	25–30 km	400×200 km area (20° S, 175° W)	0.5 Tg	25–30 km	400×200 km area (20° S, 175° W)
LMDZ6.2-LR-STRATAER	Jan 15, 1 day	150 Tg (~150 Tg)	Gaussian 27.5 km (σ = 2.5 km)	22–14° S, 182–186° E	0.5 Tg	Gaussian 27.5 km (σ = 2.5 km)	22–14° S, 182–186° E
LMDZ6.2-LR-STRATAER-REPROBUS	Jan 15, 1 day	150 Tg (~150 Tg)	Gaussian 27.5 km (σ = 2.5 km)	22–14° S, 182–186° E	0.5 Tg	Gaussian 27.5 km (σ = 2.5 km)	22–14° S, 182–186° E
MIROC-CHASER	Jan 15 (04 UTC), 6 h	186 Tg (~150 Tg)	25–30 km	22–14° S, 182–186° E	0.5 Tg	25–30 km	22–14° S, 182–186° E
UKESM1.1	Jan 15, 6 h	150 Tg	25–30 km	22–14° S, 182–186° E	0.5 Tg	25–30 km	22–14° S, 182–186° E
WACCM6/CARMA	Jan 15, 6 h	150 Tg (~150 Tg)	25–35 km	22–6° S, 182.5–202.5° E	0.5 Tg	26.5–36 km	22–6° S, 182.5–202.5° E
WACCM6/MAM	Jan 15, 6 h	150 Tg (~135 Tg)	25–35 km	22–14° S, 182–186° E	0.5 Tg	20–28 km	22–14° S, 182–186° E

lock et al. (2023) with and without Hunga Tonga. The simulated H_2O perturbation is consistent with S1.1. The SO_2 injection is derived based on the extinction from the OSIRIS observation averaged over about 10 days (Figure S1.3; Bruehl et al. 2023).

GEOSCCM

The NASA Goddard Earth Observing System Chemistry–Climate Model (GEOSCCM) is based on the GEOS Earth system model (Reinecker et al., 2008; Molod et al., 2015). For the HTHH-MOC experiments, the model was run on a cubed-sphere horizontal grid at a C90 resolution (approximately 100 km) with 72 vertical hybrid-sigma levels extending from the surface to 0.01 hPa (approximately 80 km). Dynamics are solved using the finite-volume dynamical core (Putman and Lin, 2007). Deep and shallow convection are parameterised following Grell and Freitas (2014) and Bretherton and Park (2009), respectively, while the moist physics parameterisation is from Bacmeister et al. (2006). Turbulent mixing follows the non-local scheme of Lock et al. (2000). Shortwave and longwave radiative fluxes are calculated using the Rapid Radiative Transfer Model for GCMs (RRTMG) in 30 spectral bands (Iacono et al., 2008).

Stratospheric chemistry and tropospheric chemistry are from the Global Modeling Initiative (GMI) mechanism (Duncan et al., 2007; Strahan et al., 2007; Nielsen et al., 2017), updated here to include reactions for sulfur species. The GMI mechanism in GEOSCCM has been extensively evaluated for its stratospheric ozone-related photochemistry and trans-

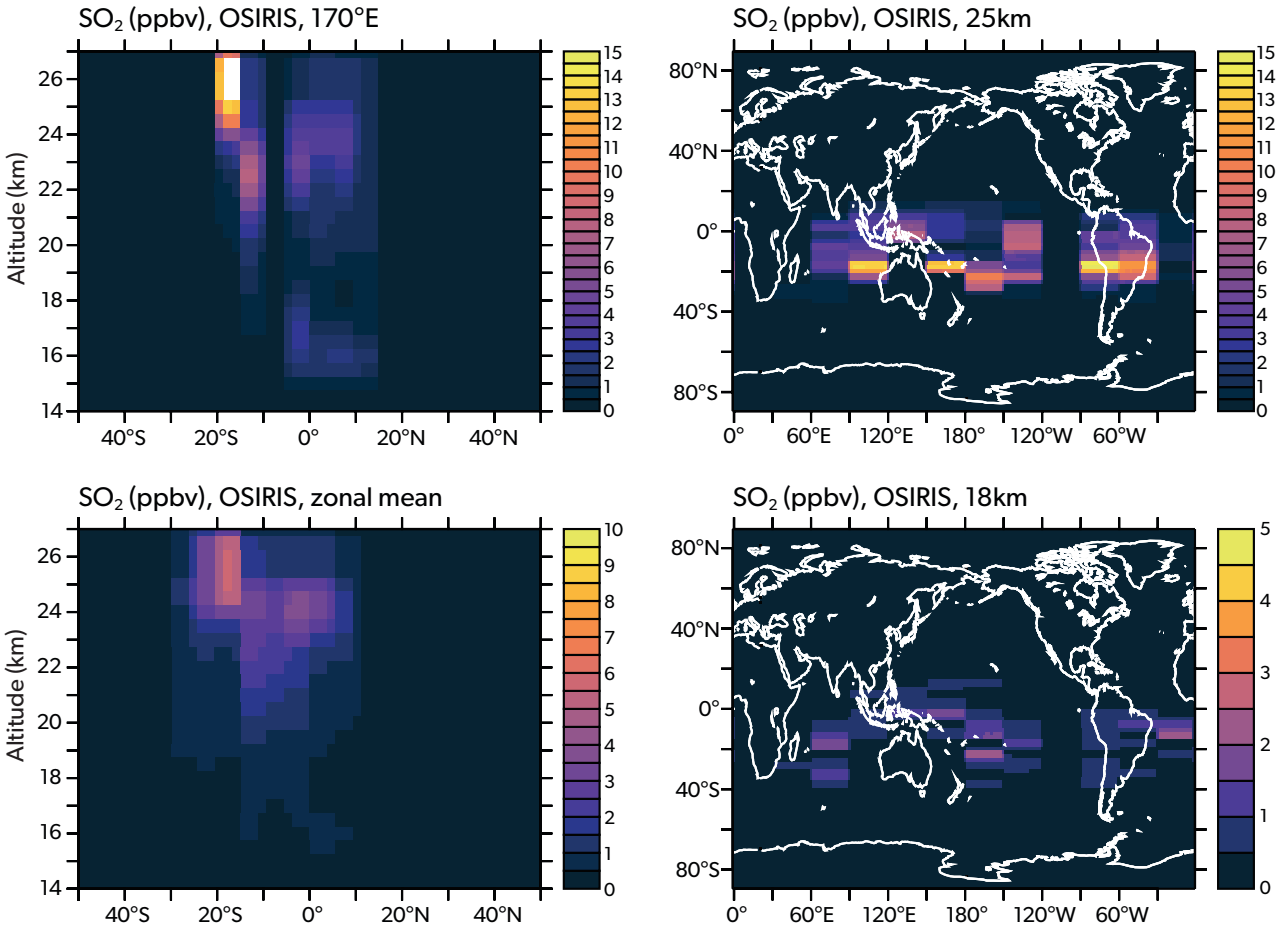

Figure S1.3: *The SO_2 injection used in the EMAC MPIC model is based on the Hunga SO_2 perturbation derived from extinction observed by OSIRIS, averaged over approximately 10 days, i.e., including several snapshots of the westward-moving plume. For conversion from extinction to volume mixing ratio, Eq. (1) of Schallock et al. (2023) is applied with $f = 3$ because of data gaps. Five-day averaged gridded OSIRIS data, averaged from 24 January at 00:00 UTC to 3 February at 00:00 UTC, were used. Note that the colour bars are not identical in each panel.*

port in various model intercomparisons, including Stratosphere-troposphere Processes and their Role in Climate (SPARC) Chemistry Climate Model Validation (CCMVal), CCMVal-2, and the CCMI (SPARC, 2010; Eyring et al., 2010; Eyring et al., 2013; Morgenstern et al., 2017).

Aerosol species are simulated by the Goddard Chemistry, Aerosol, Radiation, and Transport, second-generation (GOCART-2G) module (Collow et al., 2024), which includes a sectional approach for dust (five bins), sea salt (five bins), and nitrate (three bins) and a bulk approach for sulfate (DMS, SO_2, MSA, and SO_4^{2-}) aerosol and carbonaceous species (hydrophobic and hydrophilic modes of "white" and "brown" organics and black carbon).

For the GEOSCCM simulations performed with the GOCART-2G module we use the nominal GOCART-2G sulfate mechanism, updated here to use the online hydroxyl (OH), nitrate (NO_3), and hydrogen peroxide (H_2O_2) from the GMI mechanism instead of climatological fields provided from offline files (Collow et al., 2024). While not a full coupling to the GMI sulfur cycle it nevertheless allows the GOCART-2G sulfate mechanism to have the impact of the Hunga water vapour perturbation on the oxidants. A second "instance" of the GOCART-2G sulfate mechanism is run that is specifically for the volcanic SO_2 and resultant sulfate from the Hunga eruption. This allows us to track the eruptive volcanic aerosol separately from the nominal sulfate instance that sees mainly tropospheric sources. We assign this volcanic instance optical properties consistent with SAGE retrievals of the sulfate aerosol properties, using an effective radius of 0.4 µm.

We find that 750 Tg of H_2O is needed in the initial injection to provide a residual approximately 150 Tg of water in the stratosphere after a week. All other injection parameters follow the protocol.

The model spin-up was performed by "replaying" to the MERRA-2 meteorology (Gelaro et al., 2017), and is used throughout the Exp2a results. A MERRA-2 2012–2021 climatology of SST and sea ice fractions are used based on Reynolds et al. (2002).

GEOS/CARMA

A second configuration of the GEOSCCM, coupled to the sectional aerosol microphysics package CARMA, also simulated the eruption (GEOS/CARMA). This configuration is the same as above except for the aerosol package and its coupling to the GMI chemistry mechanism. For this version of GEOSCCM, we use the configuration of CARMA described in Case et al. (2023). This configuration uses 24 size bins, spread logarithmically in volume between 0.25 nm and 6.7 μm in radius, and simulates the nucleation, condensational growth, evaporation, coagulation, and settling of sulfate aerosols in these simulations following the mechanism of English et al. (2013).

For these simulations, CARMA is fully coupled to the GMI sulfur cycle by the production (i.e., oxidation of SO_2 and evaporation of sulfate aerosols) and loss (i.e., nucleation and condensation of sulfate aerosols) of sulfuric acid (H_2SO_4) vapour. Optical properties for the CARMA aerosols are calculated based on the interactively calculated aerosol size distribution. The same injection parameters for GEOSCCM described above are used by this configuration. This model configuration contributed to Exp2a and "replayed" to MERRA-2 meteorology as above.

GSFC2D

The NASA/Goddard Space Flight Center two-dimensional (2D) chemistry–climate model (GSFC2D) has a domain extending from the surface to approximately 92 km (0.002 hPa). The model has 76 levels, with 1 km vertical resolution from the surface to the lower mesosphere (60 km) and 2 km resolution above (60–92 km). The horizontal resolution is 4° latitude, and the model uses a 2D (latitude–altitude) finite-volume dynamical core (Lin and Rood, 1996) for advective transport. The model has detailed stratospheric chemistry and reduced tropospheric chemistry, with a diurnal cycle computed for all constituents each day (Fleming et al., 2024). The model uses prescribed zonal mean surface temperature as a function of latitude and season based on a multi-year average of MERRA-2 data (Gelaro et al., 2017). Zonal mean latent heating, tropospheric water vapour, and cloud radiative properties as a function of latitude, altitude, and season are also prescribed (Fleming et al., 2020).

For the free-running simulations, the model planetary wave parameterisation follows Bacmeister et al. (1995) and Fleming et al. (2024) and uses lower boundary conditions (750 hPa, approximately 2 km) of geopotential height amplitude and phase for zonal wave numbers 1–4. These are derived as a function of latitude and season using (1) a 30-year average (1991–2020) of MERRA-2 data for the standard yearly repeating climatological-dynamics simulations ("Clim-NoQBO") and (2) individual years of MERRA-2 data (1980–2020), randomly rearranged in time to generate interannual variations in stratospheric dynamics ("ensemble1", "ensemble2", … "ensemble10"). For the inter-annually varying dynamics simulations, the model includes an internally generated QBO (Fleming et al., 2024).

For experiments that include the Hunga volcanic aerosols, the simulations go through the end of 2023, using prescribed aerosol properties for 2022–2023 both from the GloSSAC dataset and from the OMPS-LP data (Taha et al., 2021; Taha et al., 2022). For experiments that include the Hunga H_2O injection, Aura/MLS observations are used to derive a daily zonal mean Hunga water vapour anomaly in latitude–altitude, which is added to the baseline H_2O (no volcano) through the end of February 2022. This combined water vapor field is then fully model computed starting 1 March 2022 through the end of 2031.

For Exp2b, the model zonal mean temperature and transport fields are computed from the MERRA-2 reanalysis data. These are input into the model and used as prescribed fields (no nudging is done).

IFS-COMPO

The Copernicus Atmosphere Monitoring Service (CAMS) provides daily global analysis and 5-day forecasts of atmospheric composition (aerosols, trace gases, and greenhouse gases, GHGs) (Peuch et al., 2022). CAMS is coordinated by the European Centre for Medium Range Weather Forecasts (ECMWF) and uses, for its global component, the Integrated Forecasting System (IFS), with extensions to represent aerosols, trace, and GHGs, being called "IFS-COMPO" (also previously known as "C-IFS", Flemming et al. 2015).

IFS-COMPO is composed of IFS(AER) for aerosols, as described in Rémy et al. (2022), while the atmospheric chemistry is based on the chemistry module as described in Williams et al. (2022) for the tropo-

sphere (IFS-CB05) and Huijnen et al. (2016) for the stratosphere (IFS-CBA). The stratospheric chemistry module of IFS-COMPO is derived from the Belgian Assimilation System for Chemical ObsErvations (BASCOE; Errera et al. 2019). IFS-COMPO stratospheric chemistry is used since the operational implementation of cycle 48R1 on 27 June 2023 (Eskes et al., 2024).

The aerosol component of IFS-COMPO is a bulk aerosol scheme for all species except sea salt aerosol and desert dust, for which a sectional approach is preferred, with three bins for each of these two species. Since the implementation of operational cycle 48R1 in June 2023, the prognostic species are sea salt, desert dust, organic matter (OM), black carbon (BC), sulfate, nitrate, ammonium, and secondary organic aerosols (SOAs).

For Exp2a, cycle 49R1 IFS-COMPO has been used, which will become operational for CAMS production in November 2024, at a resolution of TL511 (approximately 40 km) over 137 model levels from surface to 0.01 hPa. Cycle 49R1 IFS-COMPO integrates a number of updates of tropospheric and stratospheric aerosols and chemistry. The most relevant aspect for this work concerns the representation of stratospheric aerosols, which has been revisited with the implementation of a coupling to the stratospheric chemistry through a simplified stratospheric sulfur cycle including nucleation/condensation and evaporation processes, as shown in Figure 1.4. Direct injection of water vapour into the stratosphere is expected to enhance the nucleation and condensation of sulfate through the reaction with SO_3 and production of gas-phase H2SO4. The volcanic injection takes place between 03:00 and 06:00 UTC on 15 January 2022, with a uniform vertical distribution between 25 and 30 km of altitude, over a rectangular region of 400 km (latitude) × 200 km (longitude) centred on the coordinates of the Hunga volcano. The injected quantities are 0.5 Tg SO2 and 190 Tg H_2O.

LMDZ6.2-LR-STRATAER and LMDZ6.2-LR-STRATAER-REPROBUS

The Institut Pierre-Simon Laplace Climate Modelling Centre (IPSL CMC; `https://cmc.ipsl.fr/`, last access: 12 August 2025) has set up a new version of its climate model in the runup to CMIP6. Further description of the IPSL-CM6A-LR climate model can be found in Boucher et al. (2020) and in Lurton et al. (2020). New development of the model is now ongoing to prepare the IPSLCM7 version.

The IPSLCM7 climate model is using the general circulation model named LMDZ (Laboratoire de Météorologie Dynamique-Zoom; Hourdin et al. 2006). The LMDZ version used for this study is based on a regular horizontal grid with 144 points regularly spaced in longitude and 142 in latitude, corresponding to a resolution of 2.5° × 1.3°. The model has 79 vertical layers and extends up to 80 km, which makes it a "high-top" model. The model shows a self-generated quasi-biennial oscillation (QBO), whose period has been tuned to the observed one for the present-day climate (Boucher et al., 2020).

The aerosol is interactively simulated in the STRATAER module using a sectional scheme with 36 size bins. STRATAER is an improved version of the Sectional Stratospheric Sulfate Aerosol (S3A) module (Kleinschmitt et al., 2017). It now takes into account the photolytic conversion of H_2SO_4 into SO_2 in the upper stratosphere (Mills et al., 2005). The size-dependent composition of H_2SO_4/H_2O aerosols is now computed iteratively to ensure that the surface tension, density, and composition are consistent in the calculation of the Kelvin effect. The surface tension, density, H_2SO_4 vapour pressure, and nucleation rates are calculated based on Vehkamäki et al. (2002). The version of the LMDZ6.2-LR-STRATAER atmospheric model used in the HTHH Impact project accounts for the stratospheric H_2O source from methane oxidation. The chemistry is simulated using the REPROBUS (REactive Processes Ruling the Ozone BUdget in the Stratosphere) chemistry module that includes 55 chemical species and a comprehensive description of the stratospheric chemistry (Marchand et al., 2012; Lefèvre et al., 1994; Lefèvre et al., 1998).

For Exp2a, the H_2O and SO_2 are injected at 27.5 km altitude using a Gaussian distribution and standard deviation of 2.5 km. The injection latitude ranges from 22 to 14°S, and longitude ranges from 182 to 186°E. The injections of H_2O and SO_2 are 150 and 0.5 Tg, respectively. The SSTs are taken from the IPSL climate-coupled simulation run under the CMIP6 Tier 1 SSP2-4.5 scenario (O'Neill et al., 2016).

MIROC-CHASER

The Model for Interdisciplinary Research On Climate – CHemical Atmospheric general circulation model for Study of atmospheric Environment and Radiative forcing (MIROC-CHASER) version 6 (Sekiya et al., 2016) is a chemistry climate model, with a top at around 0.004 hPa. The present version of MIROC-CHASER is built on MIROC6 (Tatebe et al., 2019) and has a spectral horizontal resolution of T85 (1.4° lat-

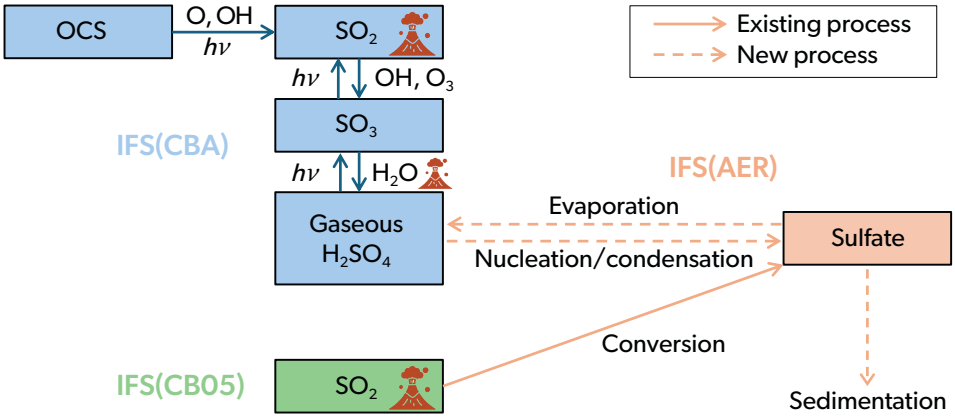

Figure S1.4: *Architecture of the stratospheric extension of IFS(AER) and its coupling with IFS(CBA) and IFS(CB05), with existing and new processes implemented in cycle 49R1 of IFS-COMPO. hν represents photolysis, and the volcano symbols represent direct injections by volcanic eruptions. Sedimentation is indicated as a new process because it has been revisited.*

itude × 1.4° longitude). The model has 81 vertical levels, with a vertical resolution 0.7 km in the lower stratosphere, ~1.2 km in the upper stratosphere, and ~3 km in the lower mesosphere. In the free-running simulations, the model generates the QBO internally. The ensemble members have different initial conditions (1 January 2022), which are generated using slightly different nudging relaxation time during the spin-up. The aerosols are interactively simulated using a three-mode modal aerosol module (Sekiya et al., 2016). The chemistry uses comprehensive troposphere–stratosphere chemistry (Watanabe et al., 2011). The volcanic emission from continuously degassing volcanoes uses the emission inventory of Fioletov et al. (2022). For the explosive volcanic eruptions during the spin-up time, explosive volcanic emissions follow Carn et al. (2022).

For Exp1 fixed-SST simulations, the model uses the observed SST from 10-year climatological mean from 2012 to 2021 using the monthly-1deg CMIP6 AMIP SST (Gates et al., 1999).

For Exp2a, the atmospheric temperature and winds are nudged to MERRA-2 reanalysis with a 12 h relaxation using 3 h meteorology. The observed SST uses the NOAA 1/4° Daily Optimum Interpolation Sea Surface Temperature (OISST) from 2022 to 2023 (Huang et al., 2020).

The initial volcanic injection altitude and area are not tuned but follow the experimental protocol. For Exp1 and Exp2a, the H2O and SO2 are injected at 25 to 30 km altitude. The injection latitude ranges from 22 to 14°S, and longitude ranges from 182 to 186°E. The initial injection of H_2O is 186 Tg, with ~150 Tg left after the first week following the eruption. The large initial H_2O injection is necessary to keep 150 Tg in the stratosphere as requested by the experimental protocol because a large amount of ice clouds generates and falls to the troposphere soon after the eruption.

UKESM1.1

The United Kingdom Earth System Model (UKESM, Sellar et al. 2019; Sellar et al. 2020) is the successor to the HadGEM2-ES model (Collins et al., 2011), jointly developed by the UK Met Office and the Natural Environment Research Council (NERC) to deliver simulations to the Coupled Model Intercomparison Project Phase 6 (CMIP6; Eyring et al. 2016). For HTHH-MOC, we run the updated UKESM1.1 system (Mulcahy et al., 2023), which consists of the physical climate model HadGEM3-GC3.1 (Kuhlbrodt et al., 2018; Williams et al., 2018) and has improved tropospheric aerosol processes and aerosol radiative forcings (Mulcahy et al., 2018; Mulcahy et al., 2020). The GC3.1 system comprises the GA7.1 global atmosphere model configuration (Walters et al., 2019), which uses the ENDGAME dynamics system (Wood et al., 2014), at a resolution of 1.875° longitude by 1.25° latitude, with 85 levels extending to 85 km. Specifically the simulations apply the UKESM1.1-AMIP academic community release job (at v12.1 of the Unified Model), as supported by the UK National Centre for Atmospheric Science.

The interactive atmospheric chemistry module UKCA (UK Chemistry and Aerosols) has a number of chemistry configurations, with UKESM1.0 for CMIP6 applying the combined stratosphere and troposphere chemistry (CheST) option (Archibald et al., 2020), essentially a combination of the stratosphere chemistry (Morgenstern et al., 2009) and tropospheric chem-

istry (O'Connor et al., 2014) UKCA schemes. The UKCA aerosol scheme is the GLOMAP-mode aerosol microphysics module (Mann et al., 2010; Mann et al., 2012; Bellouin et al., 2013), with UKESM1.0 including the initial set of adaptations to GLOMAP for simulating stratospheric aerosol Dhomse et al. (2014). For all UKESM1.0 integrations for CMIP6, the system was applied with evaporation of sulfate aerosol de-activated, stratospheric aerosol properties enacted from the CMIP6-prescribed zonal mean dataset (Luo, 2017; Jörimann, 2025), but for the integrations here we have applied the system for interactive aerosol across the troposphere and stratosphere, enacting a Hunga emission of volcanic SO2 following the 0.5 Tg at 25–30 km Tonga-MIP protocols (see Table S1.6).

For the improved UKESM1.1 version applied here, the other most relevant development, compared to UKESM1.0 used for CMIP6, is the interactive atmospheric chemistry module UKCA (UK Chemistry and Aerosols), which has the updates to heterogeneous chemistry added by Dennison et al. (2019), to represent reactions occurring on the surfaces of polar stratospheric clouds and sulfate aerosol more realistically, with modified uptake coefficients of the five existing reactions and the addition of a further eight reactions involving bromine species. For these simulations, for the first time we have added the equilibrium liquid PSC scheme of Carslaw et al. (1995) to UKESM; this scheme is an interim implementation here coupling the five existing heterogeneous reactions of chlorine activation here then occurring on solid and now also liquid ternary-aerosol PSCs.

For Exp2, UKESM1.1 is run in a specified dynamics configuration (Telford et al., 2008; Telford et al., 2009), the atmospheric temperature and winds nudged to ERA5 every 6 h, the Newton relaxation applied for levels 12 to 80 of 85 (between 1 and 60 km). Sea-surface temperatures and sea ice are prescribed from the Reynolds v2.1 datasets, during both the 2017 to 2022 spin-up period and the 2-year Exp2 period to December 2023. Monthly varying anthropogenic atmospheric chemistry and aerosol emissions were set following the CMIP6 SSP2-4.5 datasets.

WACCM6/MAM4

The Whole Atmosphere Community Climate Model version 6 (WACCM6; Gettelman et al. 2019) is the high-top version of the atmospheric component of the Community Earth System Model, version 2 (CESM2), with a top at around 140 km. WACCM6 has a horizontal resolution of 0.9° latitude × 1.25° longitude, utilising the finite-volume dynamical core (Lin and Rood, 1996). The model has 70 vertical levels, with a vertical resolution of ~1 km in the lower stratosphere, ~1.75 km in the upper stratosphere, and ~3.5 km in the upper mesosphere and lower thermosphere (Garcia et al., 2017). In the free-running simulations, the model generates QBO internally (Mills et al., 2017; Gettelman et al., 2019). The ensemble members differ in the last date of nudging (from 27 January to 5 February 2022). The aerosol is interactively simulated using a four-mode modal aerosol module (MAM4; Liu et al. 2012; Liu et al. 2016; Mills et al. 2016), in which we used the Vehkamäki nucleation scheme Vehkamäki et al. (2002). The chemistry uses comprehensive troposphere–stratosphere–mesosphere–lower thermosphere (TSMLT) chemistry (Gettelman et al., 2019). The volcanic emissions from continuously degassing volcanoes use the emission inventory of Andres and Kasgnoc (1998). For the explosive volcanic eruptions during the spin-up time, explosive volcanic emissions follow Mills et al. (2016) and Neely III and Schmidt (2016), with updates until 2022.

For Exp1_CoupledOcean simulations, the ocean and sea ice are initialised on 3 January 2022 with output from a standalone ocean model forced by atmospheric state fields and fluxes from the Japanese 55-year Reanalysis (Tsujino et al., 2018). To accurately simulate the early plume structure and evolution, the winds and temperatures in WACCM are nudged toward the Analysis for Research and Applications, MERRA-2 meteorological data (Gelaro et al., 2017) throughout January 2022. After 1 February 2022, the model is free-running to capture fully coupled variability. For the fixed-SST simulation, the model uses the 10-year climatology SST from 2012 to 2021. The SST data are OISSTv2, which is a NOAA High-resolution (0.25 × 0.25) Blended Analysis of Daily SST and Ice (Banzon et al., 2022).

For Exp2, the atmospheric temperature and winds are nudged to MERRA-2 reanalysis with a 12 h relaxation using 3 h meteorology (Davis et al., 2022). The observed SST uses the 10-year climatological mean from 2012 to 2021.

The initial volcanic injection altitude and area are the same as described in Section S1.4 for CAM5/CARMA.

WACCM6/CARMA

WACCM6/CARMA only performed Exp2 and used a configuration similar to WACCM6/MAM4 with

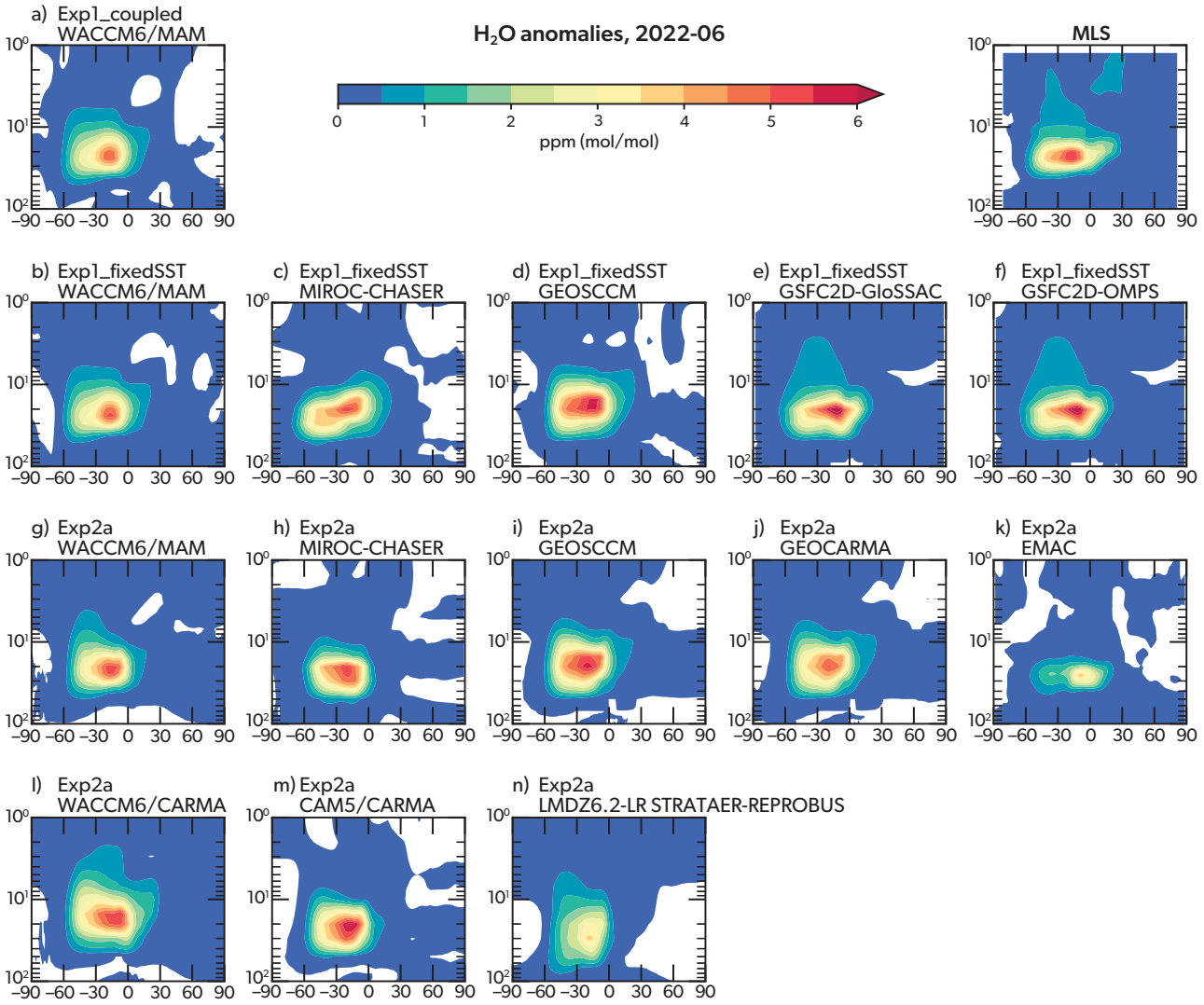

Figure S1.5: *The zonal average H_2O anomaly in June 2022 from MLS, Exp1_fixedSST, Exp1_CoupledOcean, and Exp2a. The simulated anomaly is using the H_2O + SO_2 run minus the control run. And the MLS uses the 2022 data minus the climatology.*

the same horizontal and vertical resolution, SSTs, and meteorological nudging. Differences compared to WACCM6/MAM4 are the chemistry and aerosol configuration used. WACCM6/CARMA used the middle atmosphere chemistry with limited chemistry in the troposphere and comprehensive chemistry in the stratosphere, mesosphere, and lower thermosphere (Davis et al., 2022). Furthermore, we use the Community Aerosol and Radiation Model for Atmospheres (CARMA, Tilmes et al. 2023), based on Yu et al. (2015) with some updates) as the aerosol module, in which we used the Vehkamäki nucleation scheme (Vehkamäki et al., 2002). CARMA defines 20 mass bins and tracks the dry mass of the particles and assumes particle water is in equilibrium with the environmental water vapour. The approximate radius ranges from 0.2 nm to 1.3 μm in radius for the pure sulfate group that sulfate homogeneous nucleation occurs in and ranges from 0.05 to 8.7 μm in the mixed group that tracks all major tropospheric aerosol types (i.e., black carbon, organic carbon, sea salt, dust, sulfate).

The initial volcanic injection altitude and area are determined by validating the water and aerosol transportation in the first 6 months against MLS and OMPS observations. In these simulations, the H_2O is injected to 25 to 35 km altitude following Zhu et al. (2022), while the SO_2 is injected 82% of the total mass to 26.5–28 km and 18% to 28–36 km altitude. The injection latitude ranges from 22 to 6°S, and longitude ranges from 182.5 to 202.5°E.

S1.5 Preliminary results

The models' performances will be evaluated focusing on the following aspects: the stratospheric aerosol optical depth will be compared with GloSSAC and other satellite instruments individually such as OMPS-LP, SAGEIII-ISS, and OSIRIS; the aerosol effective radius will be compared with balloon observations (Asher et al., 2023), SAGEIII-ISS-retrieved size distribution, and AeroNet-retrieved particle radius; the water vapour lifetime, ozone, and its related chemicals (such as HCl, HNO_3, and ClO) will be compared with MLS observations; and the temperature anomaly will be compared with the MLS detrended temperature field (Randel et al., 2024). All the evaluations will be conducted before looking into the climate impact of this eruption, such as radiative impact and tropospheric responses. This work will be described in a follow-up paper.

As the time of writing, we are still completing the model output inspection and validation phase. So, we can only provide preliminary results from some models. Figure S1.5 shows the preliminary results from Exp1 and Exp2 in June 2022 compared with the MLS v5 water vapour anomaly. The model results shown here generally agree with the MLS anomaly regarding the vertical (10–50 hPa) and horizontal distribution (60°S to 20°N) and the anomaly peaking at ~6 ppmv for most of the models. This consistency of water vapour anomaly 6 months after the eruption helps us have confidence in these models for the analysis of climate and chemistry impacts and will be evaluated in detail in the follow up studies.

S1.6 Summary

A multi-model observation comparison project is designed to evaluate the impact of the 2022 Hunga eruption. Two experiments are designed to cover various research interests for this eruption, including sulfate and water plume dispersion and transport, dynamical and chemical responses in the stratosphere, and climate impact. The project will not only benefit the Hunga Impact assessment but also benchmark the model performance in simulating stratospheric explosive volcanic eruption events and stratospheric water vapour injections. These events have a potentially large impact on the Earth system, especially on the stratospheric ozone layer and radiative balance.

Code/Data availability

The data used to produce the results used in this paper is archived on Zenodo:

`https://doi.org/10.5281/zenodo.14962954` (Wang, 2025).

`https://doi.org/10.5281/zenodo.14963276` (Quaglia et al., 2023; Zhuo et al., 2025).

`https://doi.org/10.5281/zenodo.14961868` (Jörimann, 2025).

`https://doi.org/10.5281/zenodo.14962925` (Brühl, 2025).

References

Akiyoshi, H., M. Kadowaki, Y. Yamashita and T. Nagatomo (2023). 'Dependence of column ozone on future ODSs and GHGs in the variability of 500-ensemble members'. *Sci. Rep.*, 13, 320. DOI: 10.1038/s41598-023-27635-y.

Akiyoshi, H., T. Nakamura, T. Miyasaka, M. Shiotani and M. Suzuki (2016). 'A nudged chemistry-climate model simulation of chemical constituent distribution at northern high-latitude stratosphere observed by SMILES and MLS during the 2009/2010 stratospheric sudden warming'. *J. Geophys. Res.*, 121, pp. 1361–1380. DOI: 10.1002/2015JD023334.

Andres, R. J. and A. D. Kasgnoc (1998). 'A time-averaged inventory of subaerial volcanic sulfur emissions'. *J. Geophys. Res.*, 103, pp. 25251–25261. DOI: 10.1029/98JD02091.

Archibald, A. T., F. M. O'Connor, N. L. Abraham, S. Archer-Nicholls, M. P. Chipperfield, M. Dalvi, G. A. Folberth, F. Dennison, S. S. Dhomse, P. T. Griffiths et al. (2020). 'Description and evaluation of the UKCA stratosphere–troposphere chemistry scheme (StratTrop vn 1.0) implemented in UKESM1'. *Geosci. Model Dev.*, 13, pp. 1223–1266. DOI: 10.5194/gmd-13-1223-2020.

Asher, E., M. Todt, K. Rosenlof, T. Thornberry, R.-S. Gao, G. Taha, P. Walter, S. Alvarez, J. Flynn, S. M. Davis et al. (2023). 'Unexpectedly rapid aerosol formation in the Hunga Tonga plume'. *Proc. Natl. Acad. Sci.*, 120, e2219547120. DOI: 10.1073/pnas.2219547120.

Bacmeister, J. T., M. R. Schoeberl, M. E. Summers, J. E. Rosenfield and X. Zhu (1995). 'Descent of long-lived trace gases in the winter polar vortex'. *J. Geophys. Res.*, 100, pp. 11669–11684. DOI: 10.1029/94JD02958.

Bacmeister, J. T., M. J. Suarez and F. R. Robertson (2006). 'Rain reevaporation, boundary layer–convection interactions, and Pacific rainfall patterns in an AGCM'. *J. Atmos. Sci.*, 63, pp. 3383–3403. DOI: 10.1175/jas3791.1.

Banzon, V., R. Reynolds and N. C. for Atmospheric Research Staff (Eds.) (2022). *The Climate Data Guide: SST data: NOAA High-resolution (0.25×0.25) Blended Analysis of Daily SST and Ice, OISSTv2.* https://climatedataguide.ucar.edu/climate-data/sst-data-noaa-high-resolution-025x025-blended-analysis-daily-sst-and-ice-oisstv2. Last access: 4 February 2025.

Bellouin, N., G. W. Mann, M. T. Woodhouse, C. Johnson, K. S. Carslaw and M. Dalvi (2013). 'Impact of the modal aerosol scheme GLOMAP-mode on aerosol forcing in the Hadley Centre Global Environmental Model'. *Atmos. Chem. Phys.*, 13, pp. 3027–3044. DOI: 10.5194/acp-13-3027-2013.

Bernath, P. F., C. T. McElroy, M. C. Abrams, C. D. Boone, M. Butler, C. Camy-Peyret, M. Carleer, C. Clerbaux, P.-F. Coheur, R. Colin et al. (2005). 'Atmospheric Chemistry Experiment (ACE): Mission overview'. *Geophys. Res. Lett.*, 32, L15S01. DOI: 10.1029/2005GL022386.

Boucher, O., J. Servonnat, A. L. Albright, O. Aumont, Y. Balkanski, V. Bastrikov, S. Bekki, R. Bonnet, S. Bony, L. Bopp et al. (2020). 'Presentation and evaluation of the IPSL-CM6A-LR climate model'. *J. Adv. Model. Earth Syst.*, 12, e2019MS002010. DOI: 10.1029/2019MS002010.

Bretherton, C. S. and S. Park (2009). 'A new moist turbulence parameterization in the Community Atmosphere Model'. *J. Climate*, 22, pp. 3422–3448. DOI: 10.1175/2008jcli2556.1.

Brodowsky, C., T. Sukhodolov, A. Feinberg, M. Höpfner, T. Peter, A. Stenke and E. Rozanov (2021). 'Modeling the sulfate aerosol evolution after recent moderate volcanic activity, 2008–2012'. *J. Geophys. Res.*, 126, e2021JD035472. DOI: 10.1029/2021JD035472.

Bruehl, C., J. Lelieveld, J. Schallock and L. A. Rieger (2023). 'Chemistry Climate Model Studies on the Effect of the Hunga Tonga Eruption on Stratospheric Ozone in Mid and High Latitudes in 2022'. *AGU Fall Meeting Abstracts*. Vol. 2023. 2235. https://ui.adsabs.harvard.edu/abs/2023AGUFM.A21B2235B, A21B–2235.

Brühl, C. (2025). *SO_2 emission for EMAC MPIC model.* Zenodo. DOI: 10.5281/zenodo.14962925.

Carn, S., V. Fioletov, C. McLinden, C. Li and N. A. Krotkov (2017). 'A decade of global volcanic SO_2 emissions measured from space'. *Sci. Rep.*, 7, 44095. DOI: 10.1038/srep44095.

Carn, S. A., L. Clarisse and A. J. Prata (2016). 'Multi-decadal satellite measurements of global volcanic degassing'. *J. Volcanol. Geotherm. Res.*, 311, pp. 99–134. DOI: 10.1016/j.jvolgeores.2016.01.002.

Carn, S. A., N. A. Krotkov, B. L. Fisher and C. Li (2022). 'Out of the blue: volcanic SO_2 emissions during the 2021-2022 Hunga Tonga-Hunga Ha'apai eruptions'. *Front. Earth Sci.*, 13. DOI: 10.3389/feart.2022.976962.

Carslaw, K. S., B. Luo and T. Peter (1995). 'An analytic expression for the composition of aqueous HNO_3–H_2SO_4 stratospheric aerosols including gas phase

removal of HNO_3'. *Geophys. Res. Lett.*, 22, pp. 1877–1880. DOI: 10.1029/95GL01668.

Case, P., P. R. Colarco, O. B. Toon, V. Aquila and C. A. Keller (2023). 'Interactive stratospheric aerosol microphysics-chemistry simulations of the 1991 Pinatubo volcanic aerosols with newly coupled sectional aerosol and stratosphere-troposphere chemistry modules in the NASA GEOS Chemistry-Climate Model (CCM)'. *J. Adv. Model. Earth Syst.*, 15, e2022MS003147. DOI: 10.1029/2022MS003147.

Clyne, M., O. B. Toon, T. Sukhodolov, G. W. Mann, S. Dhomse, S. Tilmes, Y. Zhu, P. R. Colarco, K. Tsigaridis, T. Nagashima et al. (2024). 'Tonga-MIP: The Hunga Tonga-Hunga Ha'apai Volcano Model Intercomparison Project'. In M. Clyne (Ed.), *Modeling the role of volcanoes in the climate system* (Publication No. 31487034), https://www.proquest.com/dissertations-theses/modeling-role-volcanoes-climate-system/docview/3100397790/se-2. PhD thesis. University of Colorado at Boulder.

Collins, W. J., N. Bellouin, M. Doutriaux-Boucher, N. Gedney, P. Halloran, T. Hinton, J. Hughes, C. D. Jones, M. Joshi, S. Liddicoat et al. (2011). 'Development and evaluation of an Earth-System model – HadGEM2'. *Geosci. Model Dev.*, 4, pp. 1051–1075. DOI: 10.5194/gmd-4-1051-2011.

Collow, A. B., P. R. Colarco, A. M. da Silva, V. Buchard, H. Bian, M. Chin, S. Das, R. Govindaraju, D. Kim and V. Aquila (2024). 'Benchmarking GOCART-2G in the Goddard Earth Observing System (GEOS)'. *Geosci. Model Dev.*, 17, pp. 1443–1468. DOI: 10.5194/gmd-17-1443-2024.

Davis, N. A., P. Callaghan, I. R. Simpson and S. Tilmes (2022). 'Specified dynamics scheme impacts on wave-mean flow dynamics, convection, and tracer transport in CESM2 (WACCM6)'. *Atmos. Chem. Phys.*, 22, pp. 197–214. DOI: 10.5194/acp-22-197-2022.

Dennison, F., J. Keeble, O. Morgenstern, G. Zeng, N. L. Abraham and X. Yang (2019). 'Improvements to stratospheric chemistry scheme in the UM-UKCA (v10.7) model: solar cycle and heterogeneous reactions'. *Geosci. Model Dev.*, 12, pp. 1227–1239. DOI: 10.5194/gmd-12-1227-2019.

Dhomse, S. S., K. M. Emmerson, G. W. Mann, N. Bellouin, K. S. Carslaw, M. P. Chipperfield, R. Hommel, N. L. Abraham, P. Telford, P. Braesicke et al. (2014). 'Aerosol microphysics simulations of the Mt. Pinatubo eruption with the UM-UKCA composition-climate model'. *Atmos. Chem. Phys.*, 14, pp. 11221–11246. DOI: 10.5194/acp-14-11221-2014.

Dhomse, S. S., G. W. Mann, J. C. Antuña Marrero, S. E. Shallcross, M. P. Chipperfield, K. S. Carslaw, L. Marshall, N. L. Abraham and C. E. Johnson (2020). 'Evaluating the simulated radiative forcings, aerosol properties, and stratospheric warmings from the 1963 Mt Agung, 1982 El Chichón, and 1991 Mt Pinatubo volcanic aerosol clouds'. *Atmos. Chem. Phys.*, 20, pp. 13627–13654. DOI: 10.5194/acp-20-13627-2020.

Duncan, B. N., J. A. Logan, I. Bey, I. A. Megretskaia, R. M. Yantosca, P. C. Novelli, N. B. Jones and C. P. Rinsland (2007). 'Global budget of CO, 1988–1997: Source estimates and validation with a global model'. *J. Geophys. Res.*, 112, D22301. DOI: 10.1029/2007JD008459.

Emmons, L. K., S. Walters, P. G. Hess, J.-F. Lamarque, G. G. Pfister, D. Fillmore, C. Granier, A. Guenther, D. Kinnison, T. Laepple et al. (2010). 'Description and evaluation of the Model for Ozone and Related chemical Tracers, version 4 (MOZART-4)'. *Geosci. Model Dev.*, 3, pp. 43–67. DOI: 10.5194/gmd-3-43-2010.

English, J. M., O. B. Toon, M. J. Mills and F. Yu (2011). 'Microphysical simulations of new particle formation in the upper troposphere and lower stratosphere'. *Atmos. Chem. Phys.*, 11, pp. 9303–9322. DOI: 10.5194/acp-11-9303-2011.

English, J. M., O. B. Toon and M. J. Mills (2013). 'Microphysical simulations of large volcanic eruptions: Pinatubo and Toba'. *J. Geophys. Res.*, 118, pp. 1880–1895. DOI: 10.1002/jgrd.50196.

Errera, Q., S. Chabrillat, Y. Christophe, J. Debosscher, D. Hubert, W. Lahoz, M. L. Santee, M. Shiotani, S. Skachko, T. von Clarmann et al. (2019). 'Technical note: Reanalysis of Aura MLS chemical observations'. *Atmos. Chem. Phys.*, 19, pp. 13647–13679. DOI: 10.5194/acp-19-13647-2019.

Eskes, H., A. Tsikerdekis, M. Ades, M. Alexe, A. C. Benedictow, Y. Bennouna, L. Blake, I. Bouarar, S. Chabrillat, R. Engelen et al. (2024). 'Technical note: Evaluation of the Copernicus Atmosphere Monitoring Service Cy48R1 upgrade of June 2023'. *Atmos. Chem. Phys.*, 24, pp. 9475–9514. DOI: 10.5194/acp-24-9475-2024.

Eyring, V., S. Bony, G. A. Meehl, C. A. Senior, B. Stevens, R. J. Stouffer and K. E. Taylor (2016). 'Overview of the Coupled Model Intercomparison Project Phase 6 (CMIP6) experimental design and organ-

ization'. *Geosci. Model Dev.*, 9, pp. 1937–1958. DOI: 10.5194/gmd-9-1937-2016.

Eyring, V., I. Cionni, G. E. Bodeker, A. J. Charlton-Perez, D. E. Kinnison, J. F. Scinocca, D. W. Waugh, H. Akiyoshi, S. Bekki, M. P. Chipperfield et al. (2010). 'Multi-model assessment of stratospheric ozone return dates and ozone recovery in CCMVal-2 models'. *Atmos. Chem. Phys.*, 10, pp. 9451–9472. DOI: 10.5194/acp-10-9451-2010.

Eyring, V., J.-F. Lamarque, P. Hess, F. Arfeuille, K. Bowman, M. P. Chipperfield, B. Duncan, A. Fiore, A. Gettelman, M. A. Giorgetta et al. (2013). *Overview of the IGAC/SPARC Chemistry-Climate Model Initiative (CCMI) Community Simulations in Support of Upcoming Ozone and Climate Assessments*. http://www.aparc-climate.org/wp-content/uploads/2017/12/SPARCnewsletter_No40_Jan2013_web.pdf. SPARC Newsletter No. 40, Last access: 21 August 2025.

Fioletov, V., C. A. McLinden, D. Griffin, I. Abboud, N. Krotkov, P. J. T. Leonard, C. Li, J. Joiner, N. Theys and S. Carn (2022). *Multi-Satellite Air Quality Sulfur Dioxide (SO_2) Database Long-Term L4 Global V2*. Ed. by P. Leonard. Greenbelt, MD, USA: Goddard Earth Science Data and Information Services Center (GES DISC). DOI: 10.5067/MEASURES/SO2/DATA406.

Fleming, E. L., P. A. Newman, Q. Liang and J. S. Daniel (2020). 'The Impact of Continuing CFC-11 Emissions on Stratospheric Ozone'. *J. Geophys. Res.*, 125, e2019JD031849. DOI: 10.1029/2019jd031849.

Fleming, E. L., P. A. Newman, Q. Liang and L. D. Oman (2024). 'Stratospheric Temperature and Ozone Impacts of the Hunga Tonga-Hunga Ha'apai Water Vapor Injection'. *J. Geophys. Res.*, 129, e2023JD039298. DOI: 10.1029/2023jd039298.

Flemming, J., V. Huijnen, J. Arteta, P. Bechtold, A. Beljaars, A.-M. Blechschmidt, M. Diamantakis, R. J. Engelen, A. Gaudel, A. Inness et al. (2015). 'Tropospheric chemistry in the Integrated Forecasting System of ECMWF'. *Geosci. Model Dev.*, 8, pp. 975–1003. DOI: 10.5194/gmd-8-975-2015.

Fomichev, V. I., C. Fu, J. de Grandpré, S. R. Beagley, V. P. Ogibalov and J. C. McConnell (2004). 'Model thermal response to minor radiative energy sources and sinks in the middle atmosphere'. *J. Geophys. Res.*, 109, D19107. DOI: 10.1029/2004JD004892.

Garcia, R. R., A. K. Smith, D. E. Kinnison, Á. de la Cámara and D. J. Murphy (2017). 'Modification of the Gravity Wave Parameterization in the Whole Atmosphere Community Climate Model: Motivation and Results'. *J. Atmos. Sci.*, 74, pp. 275–291. DOI: 10.1175/JAS-D-16-0104.1.

Gates, W. L., J. S. Boyle, C. Covey, C. G. Dease, C. M. Doutriaux, R. S. Drach, M. Fiorino, P. J. Gleckler, J. J. Hnilo, S. M. Marlais et al. (1999). 'An Overview of the Results of the Atmospheric Model Intercomparison Project (AMIP I)'. *Bull. Am. Meteorol. Soc.*, 80, pp. 29–55. DOI: 10.1175/1520-0477(1999)080<0029:aootro>2.0.co;2.

Gelaro, R., W. McCarty, M. J. Suárez, R. Todling, A. Molod, L. Takacs, C. A. Randles, A. Darmenov, M. G. Bosilovich and R. Reichle (2017). 'The Modern-Era Retrospective Analysis for Research and Applications, Version 2 (MERRA-2)'. *J. Climate*, 30, pp. 5419–5454. DOI: 10.1175/jcli-d-16-0758.1.

Gettelman, A., M. J. Mills, D. E. Kinnison, R. R. Garcia, A. K. Smith, D. R. Marsh, S. Tilmes, F. Vitt, C. G. Bardeen, J. McInerny et al. (2019). 'The Whole Atmosphere Community Climate Model Version 6 (WACCM6)'. *J. Geophys. Res.*, 124, pp. 12380–12403. DOI: 10.1029/2019JD030943.

Gidden, M. J., K. Riahi, S. J. Smith, S. Fujimori, G. Luderer, E. Kriegler, D. P. van Vuuren, M. van den Berg, L. Feng, D. Klein et al. (2019). 'Global emissions pathways under different socioeconomic scenarios for use in CMIP6: a dataset of harmonized emissions trajectories through the end of the century'. *Geosci. Model Dev.*, 12, pp. 1443–1475. DOI: 10.5194/gmd-12-1443-2019.

Giorgetta, M. A., E. Manzini, E. Roeckner, M. Esch and L. Bengtsson (2006). 'Climatology and Forcing of the Quasi-Biennial Oscillation in the MAECHAM5 Model'. *J. Climate*, 19, pp. 3882–3901. DOI: 10.1175/jcli3830.1.

Grell, G. A. and S. R. Freitas (2014). 'A scale and aerosol aware stochastic convective parameterization for weather and air quality modeling'. *Atmos. Chem. Phys.*, 14, pp. 5233–5250. DOI: 10.5194/acp-14-5233-2014.

Hersbach, H., B. Bell, P. Berrisford, S. Hirahara, A. Horányi, J. Muñoz-Sabater, J. Nicolas, C. Peubey, R. Radu, D. Schepers et al. (2020). 'The ERA5 global reanalysis'. *Q. J. R. Meteorol. Soc.*, 146, pp. 1999–2049. DOI: 10.1002/qj.3803.

Hourdin, F., I. Musat, S. Bony, P. Braconnot, F. Codron, J.-L. Dufresne, L. Fairhead, M.-A. Filiberti, P. Friedlingstein, J.-Y. Grandpeix et al. (2006). 'The LMDZ4 general circulation model: climate performance and sensitivity to parametrized physics with emphasis on tropical convection'. *Clim. Dynam.*, 27, pp. 787–813. DOI: 10.1007/s00382-006-0158-0.

Huang, Y., Y. Wang and H. Huang (2020). 'Stratospheric water vapor feedback disclosed by a locking experiment'. *Geophys. Res. Lett.*, 47, e2020GL087987. DOI: 10.1029/2020gl087987.

Huijnen, V., J. Flemming, S. Chabrillat, Q. Errera, Y. Christophe, A.-M. Blechschmidt, A. Richter and H. Eskes (2016). 'C-IFS-CB05-BASCOE: stratospheric chemistry in the Integrated Forecasting System of ECMWF'. *Geosci. Model Dev.*, 9, pp. 3071–3091. DOI: 10.5194/gmd-9-3071-2016.

Hurrell, J. W., M. M. Holland, P. R. Gent, S. Ghan, J. E. Kay, P. J. Kushner, J.-F. Lamarque, W. G. Large, D. Lawrence, K. Lindsay et al. (2013). 'The community Earth system model: A framework for collaborative research'. *Bull. Am. Meteorol. Soc.*, 94, pp. 1339–1360. DOI: 10.1175/BAMS-D-12-00121.1.

Iacono, M. J., J. S. Delamere, E. J. Mlawer, M. W. Shephard, S. A. Clough and W. D. Collins (2008). 'Radiative forcing by long-lived greenhouse gases: Calculations with the AER radiative transfer models'. *J. Geophys. Res.*, 113, D13103. DOI: 10.1029/2008JD009944.

Jöckel, P., A. Kerkweg, A. Pozzer, R. Sander, H. Tost, H. Riede, A. Baumgaertner, S. Gromov and B. Kern (2010). 'Development cycle 2 of the Modular Earth Submodel System (MESSy2)'. *Geosci. Model Dev.*, 3, pp. 717–752. DOI: 10.5194/gmd-3-717-2010.

Jones, A. C., J. M. Haywood, A. Jones and V. Aquila (2016). 'Sensitivity of volcanic aerosol dispersion to meteorological conditions: a Pinatubo case study'. *J. Geophys. Res.*, 121, pp. 6892–6908. DOI: 10.1002/2016JD025001.

Jonsson, A. I., J. de Grandpré, V. I. Fomichev, J. C. McConnell and S. R. Beagley (2004). 'Doubled CO2-induced cooling in the middle atmosphere: Photochemical analysis of the ozone radiative feedback'. *J. Geophys. Res.*, 109, D24103. DOI: 10.1029/2004JD005093.

Jörimann, A., T. Sukhodolov, B. Luo, G. Chiodo, G. Mann and T. Peter (2025). 'REtrieval Method for optical and physical Aerosol Properties in the stratosphere (REMAPv1)'. *Geosci. Model Dev.*, 18, pp. 6023–6041. DOI: 10.5194/gmd-18-6023-2025.

Jörimann, A. (2025). *REMAP-GloSSAC-2023*. Zenodo. DOI: 10.5281/zenodo.14961868.

Kawamiya, M., T. Hajima, K. Tachiiri, S. Watanabe and T. Yokohata (2020). 'Two decades of Earth system modeling with an emphasis on Model for Interdisciplinary Research on Climate (MIROC)'. *Prog. Earth Planet. Sci.*, 7, 64. DOI: 10.1186/s40645-020-00369-5.

Kleinschmitt, C., O. Boucher, S. Bekki, F. Lott and U. Platt (2017). 'The Sectional Stratospheric Sulfate Aerosol module (S3A-v1) within the LMDZ general circulation model: description and evaluation against stratospheric aerosol observations'. *Geosci. Model Dev.*, 10, pp. 3359–3378. DOI: 10.5194/gmd-10-3359-2017.

Kohl, M., C. Brühl, J. Schallock, H. Tost, P. Jöckel, A. Jost, S. Beirle, M. Höpfner and A. Pozzer (2025). 'New submodel for emissions from Explosive Volcanic ERuptions (EVER v1.1) within the Modular Earth Submodel System (MESSy, version 2.55.1)'. *Geosci. Model Dev.*, 18, pp. 3985–4007. DOI: 10.5194/gmd-18-3985-2025.

Kovilakam, M., L. Thomason and T. Knepp (2023). 'SAGE III/ISS aerosol/cloud categorization and its impact on GloSSAC'. *Atmos. Meas. Tech.*, 16, pp. 2709–2731. DOI: 10.5194/amt-16-2709-2023.

Kovilakam, M., L. W. Thomason, N. Ernest, L. Rieger, A. Bourassa and L. Millán (2020). 'The Global Space-based Stratospheric Aerosol Climatology (version 2.0): 1979–2018'. *Earth Syst. Sci. Data*, 12, pp. 2607–2634. DOI: 10.5194/essd-12-2607-2020.

Kuhlbrodt, T., C. G. Jones, A. Sellar, D. Storkey, E. Blockley, M. Stringer, R. Hill, T. Graham, J. Ridley, A. Blaker et al. (2018). 'The Low–Resolution Version of HadGEM3 GC3.1: Development and Evaluation for Global Climate'. *J. Adv. Model. Earth Syst.*, 10, pp. 2865–2888. DOI: 10.1029/2018MS001370.

Lamarque, J.-F., L. K. Emmons, P. G. Hess, D. E. Kinnison, S. Tilmes, F. Vitt, C. L. Heald, E. A. Holland, P. H. Lauritzen, J. Neu et al. (2012). 'CAM-chem: description and evaluation of interactive atmospheric chemistry in the Community Earth System Model'. *Geosci. Model Dev.*, 5, pp. 369–411. DOI: 10.5194/gmd-5-369-2012.

Lefèvre, F., G. P. Brasseur, I. Folkins, A. K. Smith and P. Simon (1994). 'Chemistry of the 1991–1992 stratospheric winter: Three-dimensional model simulations'. *J. Geophys. Res.*, 99, pp. 8183–8195. DOI: 10.1029/93JD03476.

Lefèvre, F., F. Figarol, K. S. Carslaw and T. Peter (1998). 'The 1997 Arctic Ozone depletion quantified from three-dimensional model simulations'. *Geophys. Res. Lett.*, 25, pp. 2425–2428. DOI: 10.1029/98GL51812.

Li, C., Y. Peng, E. Asher, A. A. Baron, M. Todt, T. D. Thornberry, S. Evan, J. Brioude, P. Smale, R. Querel et al. (2024). 'Microphysical Simulation of the 2022 Hunga Volcano Eruption Using a Sectional Aerosol

Model'. *Geophys. Res. Lett.*, 51, e2024GL108522. DOI: 10.1029/2024GL108522.

Lin, S. J. and R. B. Rood (1996). 'Multidimensional flux-form semi-Lagrangian transport schemes'. *Mon. Weather Rev.*, 124, pp. 2046–2070. DOI: 10.1175/1520-0493(1996)124<2046:MFFSLT>2.0.CO;2.

Liu, X., R. C. Easter, S. J. Ghan, R. Zaveri, P. Rasch, X. Shi, J.-F. Lamarque, A. Gettelman, H. Morrison, F. Vitt et al. (2012). 'Toward a minimal representation of aerosols in climate models: description and evaluation in the Community Atmosphere Model CAM5'. *Geosci. Model Dev.*, 5, pp. 709–739. DOI: 10.5194/gmd-5-709-2012.

Liu, X., P.-L. Ma, H. Wang, S. Tilmes, B. Singh, R. C. Easter, S. J. Ghan and P. J. Rasch (2016). 'Description and evaluation of a new four-mode version of the Modal Aerosol Module (MAM4) within version 5.3 of the Community Atmosphere Model'. *Geosci. Model Dev.*, 9, pp. 505–522. DOI: 10.5194/gmd-9-505-2016.

Lock, A. P., A. R. Brown, M. R. Bush, G. M. Martin and R. N. B. Smith (2000). 'A new boundary layer mixing scheme. Part I: Scheme description and single-column model tests'. *Mon. Weather Rev.*, 128, pp. 3187–3199. DOI: 10.1175/1520-0493(2000)128<3187:anblms>2.0.co;2.

Luo, B. (2017). *SAGE-3λ v4: Stratospheric aerosol data for use in CMIP6 models*. ETH Zurich. DOI: 10.3929/ethz-b-000715155.

Lurton, T., Y. Balkanski, V. Bastrikov, S. Bekki, L. Bopp, P. Braconnot, P. Brockmann, P. Cadule, C. Contoux, A. Cozic et al. (2020). 'Implementation of the CMIP6 forcing data in the IPSL-CM6A-LR model'. *J. Adv. Model. Earth Syst.*, 12, e2019MS001940. DOI: 10.1029/2019MS001940.

Mann, G. W., K. S. Carslaw, D. A. Ridley, D. V. Spracklen, K. J. Pringle, J. Merikanto, H. Korhonen, J. P. Schwarz, L. A. Lee, P. T. Manktelow et al. (2012). 'Intercomparison of modal and sectional aerosol microphysics representations within the same 3-D global chemical transport model'. *Atmos. Chem. Phys.*, 12, pp. 4449–4476. DOI: 10.5194/acp-12-4449-2012.

Mann, G. W., K. S. Carslaw, D. V. Spracklen, D. A. Ridley, P. T. Manktelow, M. P. Chipperfield, S. J. Pickering and C. E. Johnson (2010). 'Description and evaluation of GLOMAP-mode: a modal global aerosol microphysics model for the UKCA composition-climate model'. *Geosci. Model Dev.*, 3, pp. 519–551. DOI: 10.5194/gmd-3-519-2010.

Marchand, M., P. Keckhut, S. Lefebvre, C. Claud, D. Cugnet, A. Hauchecorne, F. Lefévre, M.-P. Lefebvre, J. Jumelet, F. Lott et al. (2012). 'Dynamical amplification of the stratospheric solar response simulated with the Chemistry-Climate Model LMDz-Reprobus'. *J. Atmos. Solar-Terr. Phys.*, 75–76, pp. 147–160. DOI: 10.1016/j.jastp.2011.11.008.

Millán, L., M. L. Santee, A. Lambert, N. J. Livesey, F. Werner, M. J. Schwartz, H. C. Pumphrey, G. L. Manney, Y. Wang, H. Su et al. (2022). 'The Hunga Tonga-Hunga Ha'apai Hydration of the Stratosphere'. *Geophys. Res. Lett.*, 49, e2022GL099381. DOI: 10.1029/2022gl099381.

Mills, M. J., J. H. Richter, S. Tilmes, B. Kravitz, D. G. Mac-Martin, A. A. Glanville, J. J. Tribbia, J.-F. Lamarque, F. Vitt, A. Schmidt et al. (2017). 'Radiative and chemical response to interactive stratospheric sulfate aerosols in fully coupled CESM1(WACCM)'. *J. Geophys. Res.*, 122, pp. 13061–13078. DOI: 10.1002/2017JD027006.

Mills, M. J., A. Schmidt, R. Easter, S. Solomon, D. E. Kinnison, S. J. Ghan et al. (2016). 'Global volcanic aerosol properties derived from emissions, 1990–2014, using CESM1 (WACCM)'. *J. Geophys. Res.*, 121, pp. 2332–2348. DOI: 10.1002/2015jd024290.

Mills, M. J., O. B. Toon, V. Vaida, P. E. Hintze, H. G. Kjaergaard, D. P. Schofield and T. W. Robinson (2005). 'Photolysis of sulfuric acid vapor by visible light as a source of the polar stratospheric CN layer'. *J. Geophys. Res.*, 110, D08201. DOI: 10.1029/2004JD005519.

Molod, A., L. Takacs, M. Suarez and J. Bacmeister (2015). 'Development of the GEOS-5 atmospheric general circulation model: evolution from MERRA to MERRA2'. *Geosci. Model Dev.*, 8, pp. 1339–1356. DOI: 10.5194/gmd-8-1339-2015.

Morgenstern, O., P. Braesicke, F. M. O'Connor, A. C. Bushell, C. E. Johnson, S. M. Osprey and J. A. Pyle (2009). 'Evaluation of the new UKCA climate-composition model – Part 1: The stratosphere'. *Geosci. Model Dev.*, 2, pp. 43–57. DOI: 10.5194/gmd-2-43-2009.

Morgenstern, O., M. I. Hegglin, E. Rozanov, F. M. O'Connor, N. L. Abraham, H. Akiyoshi, A. T. Archibald, S. Bekki, N. Butchart, M. P. Chipperfield et al. (2017). 'Review of the global models used within phase 1 of the Chemistry–Climate Model Initiative (CCMI)'. *Geosci. Model Dev.*, 10, pp. 639–671. DOI: 10.5194/gmd-10-639-2017.

Mulcahy, J. P., C. Jones, A. Sellar, B. Johnson, I. A. Boutle, A. Jones, T. Andrews, S. T. Rumbold, J. Mollard, N. Bellouin et al. (2018). 'Improved Aerosol Processes and Effective Radiative Forcing in HadGEM3 and UKESM1'. *J. Adv. Model. Earth Syst.*, 10, pp. 2786–2805. DOI: 10.1029/2018MS001464.

Mulcahy, J. P., C. Johnson, C. G. Jones, A. C. Povey, C. E. Scott, A. Sellar, S. T. Turnock, M. T. Woodhouse, N. L. Abraham, M. B. Andrews et al. (2020). 'Description and evaluation of aerosol in UKESM1 and HadGEM3-GC3.1 CMIP6 historical simulations'. *Geosci. Model Dev.*, 13, pp. 6383–6423. DOI: 10.5194/gmd-13-6383-2020.

Mulcahy, J. P., C. G. Jones, S. T. Rumbold, T. Kuhlbrodt, A. J. Dittus, E. W. Blockley, A. Yool, J. Walton, C. Hardacre, T. Andrews et al. (2023). 'UKESM1.1: development and evaluation of an updated configuration of the UK Earth System Model'. *Geosci. Model Dev.*, 16, pp. 1569–1600. DOI: 10.5194/gmd-16-1569-2023.

Naujokat, B. (1986). 'An update of the observed Quasi-Biennial Oscillation of the stratospheric winds over the tropics'. *J. Atmos. Sci.*, 43, pp. 1873–1877. DOI: 10.1175/1520-0469(1986)043<1873:AUOTOQ>2.0.CO;2.

Neely III, R. R. and A. Schmidt (2016). *VolcanEESM: Global volcanic sulphur dioxide (SO_2) emissions database from 1850 to present.* Centre for Environmental Data Analysis. DOI: 10.5285/76ebdc0b-0eed-4f70-b89e-55e606bcd568.

Nielsen, J. E., S. Pawson, A. Molod, B. Auer, A. M. da Silva, A. R. Douglass, B. Duncan, Q. Liang, M. Manyin, L. D. Oman et al. (2017). 'Chemical mechanisms and their applications in the Goddard Earth Observing System (GEOS) earth system model'. *J. Adv. Model. Earth Syst.*, 9, pp. 3019–3044. DOI: 10.1002/2017MS001011.

O'Connor, F. M., C. E. Johnson, O. Morgenstern, N. L. Abraham, P. Braesicke, M. Dalvi, G. A. Folberth, M. G. Sanderson, P. J. Telford, A. Voulgarakis et al. (2014). 'Evaluation of the new UKCA climate-composition model – Part 2: The Troposphere'. *Geosci. Model Dev.*, 7, pp. 41–91. DOI: 10.5194/gmd-7-41-2014.

O'Neill, B. C., C. Tebaldi, D. P. van Vuuren, V. Eyring, P. Friedlingstein, G. Hurtt, R. Knutti, E. Kriegler, J.-F. Lamarque, J. Lowe et al. (2016). 'The Scenario Model Intercomparison Project (ScenarioMIP) for CMIP6'. *Geosci. Model Dev.*, 9, pp. 3461–3482. DOI: 10.5194/gmd-9-3461-2016.

Peuch, V.-H., R. Engelen, M. Rixen, D. Dee, J. Flemming, M. Suttie, M. Ades, A. Agusti-Panareda, C. Ananasso, E. Andersson et al. (2022). 'The Copernicus Atmosphere Monitoring Service: From Research to Operations'. *Bull. Am. Meteorol. Soc.*, 103, E2650–E2668. DOI: 10.1175/BAMS-D-21-0314.1.

Pringle, K. J., H. Tost, S. Message, B. Steil, D. Giannadaki, A. Nenes, C. Fountoukis, P. Stier, E. Vignati and J. Lelieveld (2010). 'Description and evaluation of GMXe: a new aerosol submodel for global simulations (v1)'. *Geosci. Model Dev.*, 3, pp. 391–412. DOI: 10.5194/gmd-3-391-2010.

Putman, W. M. and S.-J. Lin (2007). 'Finite-volume transport on various cubed-sphere grids'. *J. Comput. Phys.*, 227, pp. 55–78. DOI: 10.1016/j.jcp.2007.07.022.

Quaglia, I., C. Timmreck, U. Niemeier, D. Visioni, G. Pitari, C. Brodowsky, C. Brühl, S. S. Dhomse, H. Franke, A. Laakso et al. (2023). 'Interactive stratospheric aerosol models' response to different amounts and altitudes of SO_2 injection during the 1991 Pinatubo eruption'. *Atmos. Chem. Phys.*, 23, pp. 921–948. DOI: 10.5194/acp-23-921-2023.

Randel, W. J., X. Wang, J. Starr, R. R. Garcia and D. Kinnison (2024). 'Long-Term Temperature Impacts of the Hunga Volcanic Eruption in the Stratosphere and Above'. *Geophys. Res. Lett.*, 51. DOI: 10.1029/2024gl111500.

Reinecker, M., M. Suarez, R. Todling, J. Bacmeister, L. Takacs and H. Liu (2008). *The GEOS-5 Data Assimilation System: Documentation of Versions 5.0.1, 5.1.0.* Tech. rep. NASA Technical Report TM-2007-104606.

Rémy, S., Z. Kipling, V. Huijnen, J. Flemming, P. Nabat, M. Michou, M. Ades, R. Engelen and V.-H. Peuch (2022). 'Description and evaluation of the tropospheric aerosol scheme in the Integrated Forecasting System (IFS-AER, cycle 47R1) of ECMWF'. *Geosci. Model Dev.*, 15, pp. 4881–4912. DOI: 10.5194/gmd-15-4881-2022.

Reynolds, R. W., N. A. Rayner, T. M. Smith, D. C. Stokes and W. Wang (2002). 'An Improved In Situ and Satellite SST Analysis for Climate'. *J. Climate*, 15, pp. 1609–1625. DOI: 10.1175/1520-0442(2002)015<1609:AIISAS>2.0.CO;2.

Schallock, J., C. Brühl, C. Bingen, M. Höpfner, L. Rieger and J. Lelieveld (2023). 'Reconstructing volcanic radiative forcing since 1990, using a comprehensive emission inventory and spatially resolved sulfur injections from satellite data in a chemistry-

climate model'. *Atmos. Chem. Phys.*, 23, pp. 1169–1207. DOI: 10.5194/acp-23-1169-2023.

Scinocca, J. F. (2003). 'An Accurate Spectral Non-Orographic Gravity Wave Parameterization for General Circulation Models'. *J. Atmos. Sci.*, 60, pp. 667–682. DOI: 10.1175/1520-0469(2003)060<0667:AASNGW>2.0.CO;2.

Scinocca, J. F., N. A. McFarlane, M. Lazare, J. Li and D. Plummer (2008). 'Technical Note: The CCCma third generation AGCM and its extension into the middle atmosphere'. *Atmos. Chem. Phys.*, 8, pp. 7055–7074. DOI: 10.5194/acp-8-7055-2008.

Seddon, J., A. Stephens, M. S. Mizielinski, P. L. Vidale and M. J. Roberts (2023). 'Technology to aid the analysis of large-volume multi-institute climate model output at a central analysis facility (PRIMAVERA Data Management Tool V2.10)'. *Geosci. Model Dev.*, 16, pp. 6689–6700. DOI: 10.5194/gmd-16-6689-2023.

Sekiya, T., K. Sudo and T. Nagai (2016). 'Evolution of stratospheric sulfate aerosol from the 1991 Pinatubo eruption: Roles of aerosol microphysical processes'. *J. Geophys. Res.*, 121, pp. 2911–2938. DOI: 10.1002/2015JD024313.

Sellar, A. A., C. G. Jones, J. P. Mulcahy, Y. Tang, A. Yool, A. Wiltshire, F. M. O'Connor, M. Stringer, R. Hill, J. Palmieri et al. (2019). 'UKESM1: Description and Evaluation of the U.K. Earth System Model'. *J. Adv. Model. Earth Syst.*, 11, pp. 4513–4558. DOI: 10.1029/2019MS001739.

Sellar, A. A., J. Walton, C. G. Jones, R. Wood, N. L. Abraham, M. Andrejczuk, M. B. Andrews, T. Andrews, A. T. Archibald, L. de Mora et al. (2020). 'Implementation of U.K. Earth System Models for CMIP6'. *J. Adv. Model. Earth Syst.*, 12, e2019MS001946. DOI: 10.1029/2019MS001946.

Sellitto, P., A. Podglajen, R. Belhadji, M. Boichu, E. Carboni, J. Cuesta, C. Duchamp, C. Kloss, R. Siddans, N. Bègue et al. (2022). 'The unexpected radiative impact of the Hunga Tonga eruption of 15th January 2022'. *Commun. Earth Environ.*, 3, 288. DOI: 10.1038/s43247-022-00618-z.

SPARC (2010). *SPARC CCMVal Report on the Evaluation of Chemistry-Climate Models*. Tech. rep. https://www.aparc-climate.org/publications/sparc-reports/sparc-report-no-5/. SPARC Report No. 5, WCRP-30/2010, WMO/TD-No. 40.

Strahan, S. E., B. N. Duncan and P. Hoor (2007). 'Observationally derived transport diagnostics for the lowermost stratosphere and their application to the GMI chemistry and transport model'. *Atmos. Chem. Phys.*, 7, pp. 2435–2445. DOI: 10.5194/acp-7-2435-2007.

Sukhodolov, T., T. Egorova, A. Stenke, W. T. Ball, C. Brodowsky, G. Chiodo, A. Feinberg, M. Friedel, A. Karagodin-Doyennel, T. Peter et al. (2021). 'Atmosphere ocean aerosol chemistry climate model SOCOLv4.0: description and evaluation'. *Geosci. Model Dev.*, 14, pp. 5525–5560. DOI: 10.5194/gmd-14-5525-2021.

Taha, G., R. Loughman, P. R. Colarco, T. Zhu, L. W. Thomason and G. Jaross (2022). 'Tracking the 2022 Hunga Tonga-Hunga Ha'apai Aerosol Cloud in the Upper and Middle Stratosphere Using Space-Based Observations'. *Geophys. Res. Lett.*, 49, e2022GL100091. DOI: 10.1029/2022gl100091.

Taha, G., R. Loughman, T. Zhu, L. Thomason, J. Kar, L. Rieger and A. Bourassa (2021). 'OMPS LP Version 2.0 multi-wavelength aerosol extinction coefficient retrieval algorithm'. *Atmos. Meas. Tech.*, 14, pp. 1015–1036. DOI: 10.5194/amt-14-1015-2021.

Tatebe, H., T. Ogura, T. Nitta, Y. Komuro, K. Ogochi, T. Takemura, K. Sudo, M. Sekiguchi, M. Abe, F. Saito et al. (2019). 'Description and basic evaluation of simulated mean state, internal variability, and climate sensitivity in MIROC6'. *Geosci. Model Dev.*, 12, pp. 2727–2765. DOI: 10.5194/gmd-12-2727-2019.

Telford, P., P. Braesicke, O. Morgenstern and J. Pyle (2009). 'Reassessment of causes of ozone column variability following the eruption of Mount Pinatubo using a nudged CCM'. *Atmos. Chem. Phys.*, 9, pp. 4251–4260. DOI: 10.5194/acp-9-4251-2009.

Telford, P. J., P. Braesicke, O. Morgenstern and J. A. Pyle (2008). 'Technical Note: Description and assessment of a nudged version of the new dynamics Unified Model'. *Atmos. Chem. Phys.*, 8, pp. 1701–1712. DOI: 10.5194/acp-8-1701-2008.

Thomason, L. W., N. Ernest, L. Millán, L. Rieger, A. Bourassa, J.-P. Vernier, G. Manney, B. Luo, F. Arfeuille and T. Peter (2018). 'A global space-based stratospheric aerosol climatology: 1979–2016'. *Earth Syst. Sci. Data*, 10, pp. 469–492. DOI: 10.5194/essd-10-469-2018.

Tilmes, S., M. J. Mills, Y. Zhu, C. G. Bardeen, F. Vitt, P. Yu, D. Fillmore, X. Liu, B. Toon and T. Deshler (2023). 'Description and performance of a sectional aerosol microphysical model in the Community Earth System Model (CESM2)'. *Geosci. Model Dev.*, 16, pp. 6087–6125. DOI: 10.5194/gmd-16-6087-2023.

Tsujino, H., S. Urakawa, H. Nakano, R. J. Small, W. M. Kim, S. G. Yeager, G. Danabasoglu, T. Suzuki, J. L. Bamber, M. Bentsen et al. (2018). 'JRA-55 based surface dataset for driving ocean–sea-ice models (JRA55-do)'. *Ocean Model.*, 130, pp. 79–139. DOI: 10.1016/j.ocemod.2018.07.002.

Vehkamäki, H., M. Kulmala, I. Napari, K. E. Lehtinen, C. Timmreck, M. Noppel and A. Laaksonen (2002). 'An improved parameterization for sulfuric acid-water nucleation rates for tropospheric and stratospheric conditions'. *J. Geophys. Res.*, 107, AAC3-1–AAC3-10. DOI: 10.1029/2002JD002184.

Walters, D., A. J. Baran, I. Boutle, M. Brooks, P. Earnshaw, J. Edwards, K. Furtado, P. Hill, A. Lock, J. Manners et al. (2019). 'The Met Office Unified Model Global Atmosphere 7.0/7.1 and JULES Global Land 7.0 configurations'. *Geosci. Model Dev.*, 12, pp. 1909–1963. DOI: 10.5194/gmd-12-1909-2019.

Wang, X. (2025). *MLS H2O anomaly 2022*. Zenodo. DOI: 10.5281/zenodo.14962954.

Wang, X., W. Randel, Y. Zhu, S. Tilmes, J. Starr, W. Yu, R. Garcia, O. B. Toon, M. Park, D. Kinnison et al. (2023). 'Stratospheric Climate Anomalies and Ozone Loss Caused by the Hunga Tonga-Hunga Ha'apai Volcanic Eruption'. *J. Geophys. Res.*, 128, e2023JD039480. DOI: 10.1029/2023jd039480.

Watanabe, S., T. Hajima, K. Sudo, T. Nagashima, T. Takemura, H. Okajima, T. Nozawa, H. Kawase, M. Abe, T. Yokohata et al. (2011). 'MIROC-ESM 2010: model description and basic results of CMIP5-20c3m experiments'. *Geosci. Model Dev.*, 4, pp. 845–872. DOI: 10.5194/gmd-4-845-2011.

Williams, J. E., V. Huijnen, I. Bouarar, M. Meziane, T. Schreurs, S. Pelletier, V. Marécal, B. Josse and J. Flemming (2022). 'Regional evaluation of the performance of the global CAMS chemical modeling system over the United States (IFS cycle 47r1)'. *Geosci. Model Dev.*, 15, pp. 4657–4687. DOI: 10.5194/gmd-15-4657-2022.

Williams, K. D., D. Copsey, E. W. Blockley, A. Bodas-Salcedo, D. Calvert, R. Comer, P. Davis, T. Graham, H. T. Hewitt, R. Hill et al. (2018). 'The Met Office Global Coupled Model 3.0 and 3.1 (GC3.0 and GC3.1) Configurations'. *J. Adv. Model. Earth Syst.*, 10, pp. 357–380. DOI: 10.1002/2017MS001115.

Wood, N., A. Staniforth, A. White, T. Allen, M. Diamantakis, M. Gross, T. Melvin, C. Smith, S. Vosper, M. Zerroukat et al. (2014). 'An inherently mass-conserving semi-implicit semi-Lagrangian discretization of the deep-atmosphere global non-hydrostatic equations'. *Q. J. R. Meteorol. Soc.*, 140, pp. 1505–1520. DOI: 10.1002/qj.2235.

Yu, P., O. B. Toon, C. G. Bardeen, M. J. Mills, T. Fan, J. M. English and R. R. Neely (2015). 'Evaluations of tropospheric aerosol properties simulated by the Community Earth System Model with a sectional aerosol microphysics scheme'. *J. Adv. Model. Earth Syst.*, 7, pp. 865–914. DOI: 10.1002/2014MS000421.

Yu, W., R. Garcia, J. Yue, A. Smith, X. Wang, W. Randel, Z. Qiao, Y. Zhu, V. L. Harvey, S. Tilmes et al. (2023). 'Mesospheric temperature and circulation response to the Hunga Tonga-Hunga-Ha'apai volcanic eruption'. *J. Geophys. Res.*, 128, e2023JD039636. DOI: 10.1029/2023JD039636.

Zhang, J., D. Kinnison, Y. Zhu, X. Wang, S. Tilmes, K. Dube and W. Randel (2024). 'Chemistry Contribution to Stratospheric Ozone Depletion After the Unprecedented Water-Rich Hunga Tonga Eruption'. *Geophys. Res. Lett.*, 51, e2023GL105762. DOI: 10.1029/2023gl105762.

Zhou, X., S. S. Dhomse, W. Feng, G. Mann, S. Heddell, H. Pumphrey, B. J. Kerridge, B. Latter, R. Siddans, L. Ventress et al. (2024). 'Antarctic Vortex Dehydration in 2023 as a Substantial Removal Pathway for Hunga Tonga-Hunga Ha'apai Water Vapor'. *Geophys. Res. Lett.*, 51, e2023GL107630. DOI: 10.1029/2023gl107630.

Zhu, Y., H. Akiyoshi, V. Aquila, E. Asher, E. M. Bednarz, S. Bekki, C. Brühl, A. H. Butler, P. Case, S. Chabrillat et al. (2025). 'Hunga Tonga–Hunga Ha'apai Volcano Impact Model Observation Comparison (HTHH-MOC) project: experiment protocol and model descriptions'. *Geosci. Model Dev.*, 18, pp. 5487–5512. DOI: 10.5194/gmd-18-5487-2025.

Zhu, Y., C. G. Bardeen, S. Tilmes, M. J. Mills, X. Wang, V. L. Harvey, G. Taha, D. Kinnison, R. W. Portmann, P. Yu et al. (2022). 'Perturbations in stratospheric aerosol evolution due to the water-rich plume of the 2022 Hunga-Tonga eruption'. *Commun. Earth Environ.*, 3, 248. DOI: 10.1038/s43247-022-00580-w.

Zhuo, Z., X. Wang, Y. Zhu, W. Yu, E. M. Bednarz, E. Fleming, P. R. Colarco, S. Watanabe, D. Plummer, G. Stenchikov et al. (2025). 'Comparing multimodel ensemble simulations with observations and decadal projections of upper atmospheric variations following the Hunga eruption'. *Atmos. Chem. Phys.*, 25, pp. 13161–13176. DOI: 10.5194/acp-25-13161-2025.

S2 Hunga impacts report observational data supplement

Authors Nathaniel Livesey
Graham Mann
David R. Themens
William Randel

Preface

This data supplement has been compiled to provide descriptions and references for the observational data sets used in the separate chapters of this report. We focus on brief overviews of the measurement characteristics and uncertainties, together with the space-time sampling for the various instruments. Further details can be found in the quoted references. Satellite remote sensing data are grouped together, followed by ground-based and balloon measurements.

S2.1 Satellite remote sensing data

ACE-FTS H_2O and other trace gases

The Atmospheric Chemistry Experiment Fourier Transform Spectrometer (ACE-FTS) provides vertical profiles of numerous atmospheric trace species, based on solar occultation measurements (Bernath, 2017; Boone et al., 2023). Additional information is available at `https://uwaterloo.ca/atmospheric-chemistry-experiment/`.

ACE-FTS has been making atmospheric measurements since February 2004, observing 15 sunrise and 15 sunset occultations per day covering a latitude range of approximately 70° N–S. The latitude sampling progresses slowly over time, and it takes approximately three months to cover the latitude range 70°S–70°N.

Figure S2.1 shows the ACE-FTS sampling pattern during January 2020–August 2023, overlaid on the Hunga water vapour plume as observed by MLS, for reference. The instrument measures atmospheric absorption spectra between 750 cm^{-1} to 4400 cm^{-1} at a spectral resolution of 0.02 cm^{-1}; volumetric mixing ratio profiles of more than 40 trace gases can be inferred from these spectra. The vertical resolution of the abundance measurements is approximately 3 km, and atmospheric retrievals are provided on an oversampled 1 km vertical grid. Data used here are from the Version 5 retrievals of ACE-FTS. Data quality flags for all species are used to appropriately screen data quality.

Aura Microwave Limb Sounder (MLS) trace gases and temperature

The Microwave Limb Sounder (MLS), launched on NASA's Aura mission in 2004, measures vertical profiles of a range of trace gases from the upper troposphere to the mesosphere on a daily near-global basis (Waters et al., 2006). MLS vertically scans the atmospheric limb in front of the Aura spacecraft roughly twice per minute and measures thermal emission in the 118, 190, 240, and 640 GHz spectral regions (the Aura MLS 2.5 THz observations have not been made since 2014). Measurements can be made both day and night, including in regions of significant aerosol loading and all but the thickest clouds. At the time of writing, it is anticipated that Aura MLS will continue observing until around May 2026, at which point reduced power availability will dictate the end of the Aura mission.

Starting in May 2024, the MLS "190 GHz" subsystem, which measures H_2O, N_2O, HCN, and upper stratospheric HNO_3, has only been operated for roughly one week each month in order to conserve remaining life for this subsystem, which is showing signs of aging. MLS measurements of other species (e.g., O_3, CO, ClO, HCl, etc.) continue to be made on an uninterrupted basis.

Findings in this report are derived from MLS "Level 2" data—vertical profiles of composition and temperature along the Aura orbit track, with around 3500 profiles reported per day for each product. The vertical coordinate is pressure, and profiles are spaced every 1.5° (approximately 165 km) along the orbit track. Typical vertical resolutions for retrieved profiles range over 2–5 km, depending on the product and altitude region. Published studies of the Hunga eruption and its impacts discussed in this report have used a combination of MLS Version 4 (Livesey et al., 2020) and Version 5 (Livesey et al., 2022) data.

In general, the Version 5 data are recommended over Version 4, particularly for studies involving the water vapour (H_2O) and nitrous oxide (N_2O) products, as a slow change in behaviour of the MLS 190 GHz receiver (likely related to the aging issues discussed above) resulted in observable and statistically significant drifts in these products in the Version 4 dataset (Hurst et al., 2016). The drifts are around 2–10% per decade (Livesey et al., 2021), depending on (1) pressure level, with the strongest drifts seen in the lower stratosphere, (2) species, with N_2O more strongly affected than H_2O, and (3) the basis of comparison (with comparisons to ACE-FTS showing about half as much drift as seen in comparisons to in-situ frost-point sondes).

The Version 5 algorithms and software correct for the slow instrumental changes such that no statistically significant drift is seen in comparisons between MLS and ACE-FTS H_2O, although drifts remain in N_2O and in comparisons of H_2O to the frost-point record.

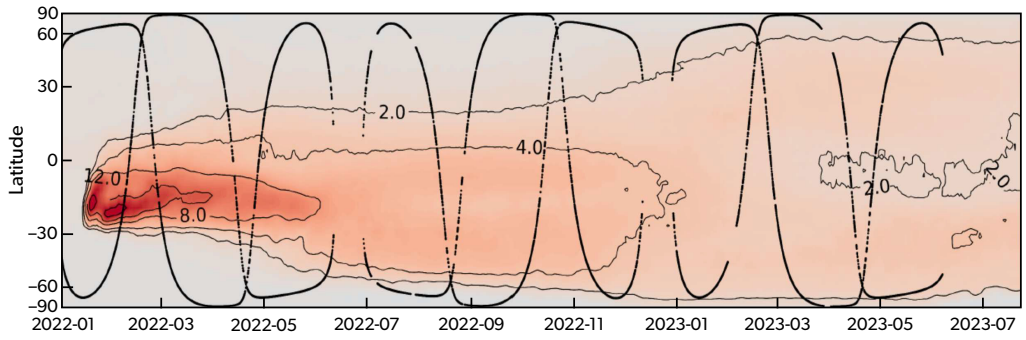

Figure S2.1: *ACE-FTS sampling locations during January 2020–August 2023 overlaying the Hunga water vapour plume as observed by MLS, as a function of time and latitude. The water vapour is expressed in terms of vertically integrated mass (Tg) over 100–1 hPa, calculated in 2.5° latitude bins using anomalies from the 2004–2021 average MLS background. Figure courtesy of Jon Starr at NSF NCAR.*

The only case where the MLS Version 4 data are recommended over Version 5 is in the immediate aftermath (within 2–3 weeks) of the Hunga eruption (Millán et al., 2022). During this period, the strong abundances of H_2O and SO_2 in the core of the stratospheric plume were larger than any seen before in the MLS record. These gave rise to microwave spectra that were very different from those for which the MLS retrievals are designed and optimised. The retrieval algorithms were not able to fit these spectra as well as is typical, resulting in many of the most Hunga-affected profiles being marked as unsuitable for scientific use. Extensive study of this period by the MLS team has concluded that (1) owing to subtle differences in the respective retrieval algorithms, the older Version 4 data are recommended over Version 5 in this specific case, and (2) in this one specific circumstance (and no other), users may waive consideration of the MLS data quality flags and use profiles marked "do not use."

CALIOP space-borne lidar

The Cloud-Aerosol Lidar with Orthogonal Polarization (CALIOP) space-borne lidar (Winker et al., 2007) was launched on the NASA Cloud-Aerosol Lidar and Infrared Pathfinder Satellite Observations (CALIPSO) satellite in April 2006; observations ceased in July 2023. Together with other satellites in the NASA A-train constellation (Stephens et al., 2002), CALIPSO flew in a 705 km altitude sun-synchronous polar orbit with equator-crossing times of about 01:30 and 13:30 local solar time, with the polar orbit ground-track repeating every 16 days.

The CALIOP lidar provided high vertical-resolution measurements of the Hunga aerosol cloud (e.g., Legras et al., 2022; Khaykin et al., 2022), and measurements of polar stratospheric clouds (PSCs) (Pitts et al., 2018), along with a wide range of other aerosol and cloud information over its mission lifetime. The CALIOP PSC type classification followed algorithms developed and validated for ground-based lidar (e.g., Adriani et al., 2004).

Aerosol scattering ratio and derived optical depth The CALIOP lidar measures backscattered light from two lasers, emitting at 532 nm and 1064 nm, with the two principal measurement quantities being total backscatter and backscatter ratio (referred to in this report as the "scattering ratio"). The latter represents the ratio of total backscatter to that from an aerosol-free atmosphere (i.e., total backscatter to Rayleigh backscatter), and thus quantifies the relative enhancement due to aerosol (or clouds).

Figures in this report mainly show backscatter ratio rather than extinction or optical depth, because derivation of the latter quantities hinges on an aerosol-type-dependent conversion from aerosol backscatter to aerosol extinction (and thence optical depth). In practice, such conversions require the assumption of an aerosol "extinction-to-backscatter ratio" – sometimes referred to as the "lidar ratio" (see, e.g., Antuña-Marrero et al., 2021 and section 1 of the supplement to Dhomse et al., 2020) – an unsafe assumption in the Hunga plume, where aerosol properties are poorly known.

The CALIOP aerosol type algorithms (Young et al., 2013) are designed to identify a specific aerosol classification that can be used to ascribe a corresponding lidar ratio, and the retrieval methods include a stratospheric aerosol type (e.g., Kar et al., 2019). For Version 4.2 of the CALIOP aerosol-type retrievals (Tackett et al., 2023), a sub-typing of the stratospheric

aerosol better resolves periods of enhanced smoke aerosol from strong PyroCb events (e.g., Khaykin et al., 2018).

During strong volcanically elevated stratospheric conditions, variations in aerosol particle size distribution modify the extinction-to-backscatter ratio, as seen, for example, by Vaughan et al. (1994) in their analysis of ground-based lidar measurements taken following the 1991 Pinatubo eruption. Research has also employed CALIOP measurements to assess individual eruptions for their varying volcanic sulfate and ash mix (e.g., Prata et al., 2017).

Even for the relatively moderate and low-ash Hunga aerosol, the substantial range in effective radius (e.g., 0.25 – 0.40 μm; Duchamp et al., 2023) affects derived aerosol optical depth from CALIOP during this period. For Pinatubo, tabulated time-varying lidar ratios (e.g., Jäger and Deshler, 2002) have been used to derive aerosol extinction from ground-based lidar backscatter ratio consistently with progressing aerosol microphysical properties (e.g., Shallcross, 2020).

Analyses of derived optical depths from CALIOP (Kim et al., 2018; Ryan et al., 2024) have indicated a general low bias compared to other observations. It is important to note that CALIOP only retrieves aerosol extinction where the particulate attenuated backscatter exceeds the layer detection thresholds (Young and Vaughan, 2009).

CALIOP depolarisation The detector for the CALIOP 532 nm channel is configured to separately measure the parallel and perpendicular polarised backscatter. The ratio of the two is referred to as "depolarisation," expressed either as a percentage or fraction. A large depolarisation value indicates non-spherical particles. This measure is a key discriminator for different types of PSCs (e.g., Adriani et al., 2004), with low depolarisation indicating spherical particles—either liquid aerosol or ternary solution "Type-1b" PSCs—with a stronger backscatter indicating the latter. More highly depolarised backscatter is indicative of either "Type-2" (solid ice) or "Type-1a" (solid nitric acid trihydrate, NAT) PSCs.

Based on the depolarisation information, the CALIOP lidar backscatter measurements can be subsampled to exclude Type-2 (ice) and Type-1a (solid NAT) PSCs, enabling the quantification of backscatter from liquid particles (sulfate aerosol and Type-1b PSCs). The liquid Type-1b PSCs are supercooled ternary solution (STS) droplets that have formed at low temperatures (approximately 3 K below the threshold for NAT PSC formation), growing much larger from the uptake of nitric acid vapour and additional water vapour into existing "binary-solution" sulfuric acid aerosol particles (e.g., Carslaw et al., 1994; Carslaw et al., 1995).

GloSSAC aerosol extinction

The Global Space-based Stratospheric Aerosol Climatology (GloSSAC) was developed in 2018 to provide a best-estimate global dataset for variations in the stratospheric aerosol layer. The main driver for GloSSAC was to provide a stratospheric aerosol dataset for climate models within the CMIP6 (Coupled Model Intercomparison Project phase 6; Eyring et al., 2016) project, and also for use within chemistry–climate models in the CCMI initiative (Chemistry–Climate Modeling Initiative; Morgenstern et al., 2017).

GloSSAC builds on earlier global gridded stratospheric aerosol datasets, notably the Pinatubo "gap-filled dataset" generated for the SPARC ASAP report (Assessment of Stratospheric Aerosol Properties; SPARC, 2006) that was geared primarily to provide Surface Area Density (SAD) information (e.g., Thomason et al., 1997; Thomason et al., 2008) for chemistry–climate models (CCMs) to represent volcanic impacts on the ozone layer (CCM-Val and CCM-Val2, see, e.g., Eyring et al., 2005).

The GloSSAC product is a global and gap-free dataset providing aerosol extinction coefficients at two reference wavelengths (525 and 1020 nm). The 2018 version dataset incorporates an improved post-Pinatubo gap-filling approach (for 1991–1993) that combines the lidar-aligned SAGE-II with data from the Cryogenic Limb Array Etalon Spectrometer (CLAES) on NASA's Upper Atmosphere Research Satellite to fill any gaps. The global dataset also used an approach to address the SAGE-II gap at wintertime high latitudes via equivalent latitude, which is a polar-vortex-oriented coordinate system. For the 2005–2017 period between the end of SAGE-II and the start of SAGE-III/ISS, the v1.0 GloSSAC dataset is primarily based on a merge of the 750 nm OSIRIS aerosol extinction with the 532 nm CALIOP aerosol extinction.

Results discussed in this report are taken from the latest v2.2 GloSSAC record (Kovilakam et al., 2025). This incorporates the latest v5.3 SAGE retrieval and OSIRIS version 7.2, rather than the version 5.07 used in GloSSAC v1.0. GloSSAC v2.2 also benefits from key advances made during the development of the earlier v2.0 dataset, including an improved monthly clima-

tology of Ångström exponent (used for converting OSIRIS extinction to 525 nm) and improved conversion of CALIOP 532 nm backscatter coefficient to 532 nm aerosol extinction (see Kovilakam et al., 2020).

IASI (Infrared Atmospheric Sounding Interferometer) SO_2 and sulfate aerosol

Information on the IASI observations is taken from Sellitto et al. (2024). The RAL (Rutherford Appleton Laboratory) Infrared/Microwave Sounder (IMS) retrieval core scheme (Siddans, 2019) uses an optimal estimation spectral fitting procedure to retrieve atmospheric and surface parameters jointly from co-located measurements by IASI, AMSU (Advanced Microwave Sounding Unit), and MHS (Microwave Humidity Sounder) on the MetOp-B spacecraft, using RTTOV-12 (Radiative Transfer for TOVS; Saunders et al., 2018) as the forward radiative transfer model.

The use of RTTOV-12 enables the quantitative retrieval of sulfate aerosols (SA) and trace gases (SO_2); the bulk of the information on SO_2 and SA in the IMS scheme comes from the IASI observations (Clerbaux et al., 2009). The IMS scheme simultaneously retrieves SO_2 and SA spectroscopic information, which is crucial for avoiding the large uncertainties on both due to their co-existence in volcanic plumes and overlapping spectral signatures (Sellitto et al., 2019). Total uncertainties in individual IMS SO_2 and SA retrievals are estimated at 0.3 DU (SO_2) and 0.002 (SA optical depth) (Siddans, 2023).

MISR aerosol extinction

The Multi-angle Imaging Spectro-Radiometer (MISR) instrument was launched aboard the NASA Terra satellite in December 1999 (e.g., Kahn et al., 2005; Limbacher et al., 2022) and measures upwelling shortwave radiance in four spectral bands centred at 446, 558, 672, and 866 nm. The instrument design has nine viewing angles and derives additional aerosol characterisation information (e.g., Kahn et al., 2010), for example regarding light absorption and particle sphericity, and has developed a sophisticated typology algorithm from the multi-wavelength information (e.g., Kahn and Gaitley, 2015).

From analysis of the MISR products during the initial Hunga aerosol plume (Kahn et al., 2024), the volcanic aerosol was predominantly spherical and non-absorbing, except for the earliest phase of the cloud monitoring. This initial monitoring (21 January 2022) showed that the main northern portion of the plume had a substantially absorbing and non-spherical signature, consistent with that seen in the 23 and 26 January LOAC observations from La Réunion (Kloss et al., 2022), this being during the 10-day period when CALIOP could not measure due to a solar flare (personal communication D. Winker, NASA LaRC).

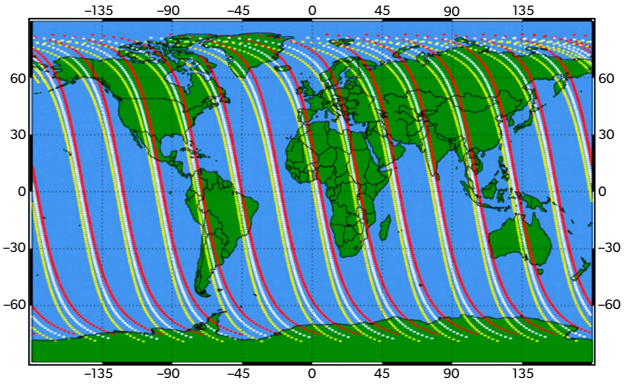

Figure S2.2: *OMPS-LP daily coverage from the S–NPP satellite, illustrating retrieval locations for the left and right slits (red and yellow circles) relative to the central slit (white circles) following the main orbital path. Figure adapted from Loughman et al. (2018).*

OMPS-LP aerosol extinction

The Ozone Mapping and Profile Suite Limb Profiler (OMPS-LP; Loughman et al., 2018; Taha et al., 2021) is a component of the Suomi National Polar-orbiting Partnership (NPP) satellite, launched in October 2011. A second OMPS-LP instrument is now operational on the NOAA-21 mission, launched in 2022, and further launches are planned. OMPS-LP uses a limb-scatter technique to retrieve vertical profiles of aerosol extinction at multiple wavelengths, alongside ozone retrievals. The vertical resolution is approximately 1–2 km. The S–NPP satellite is in a sun-synchronous orbit and provides more than 7000 profiles per day (Figure S2.2). Although OMPS-LP has three vertical slits that make measurements separated horizontally in the cross-track direction by 250 km, only the centre slit, which has the best stray-light performance, is used in the retrievals analysed here.

There are several different retrievals of aerosol extinction from OMPS-LP measurements available, offering somewhat different results. The "NASA OMPS" v2.1 retrieval from the NASA GSFC team uses a single image of the limb radiance to perform a one-dimensional (altitude) retrieval for aerosol extinction. This is performed for six spectral bands spanning 510–997 nm, and profiles are reported from cloud top to 38 km (Taha et al., 2021). The basic approach, which requires an assumption of the particle size distribu-

tion to derive the scattering phase function, follows from the original algorithm developed for limb-scatter aerosol retrievals using OSIRIS measurements (Bourassa et al., 2007). The OMPS v2.1 uses a model-derived gamma function particle size distribution (Chen et al., 2018).

Near the completion of this report, an updated version (v2.5) of NASA OMPS has become available. The v2.5 algorithm improves convergence by increasing the number of iterations, enhancing retrieval performance. Short-wavelength aerosol profiles at 510, 600, 675, and 745 nm were filtered for unrealistic values (mainly at lower altitudes and large scattering angles) using the colour ratio relative to 869 nm. Additional filtering removed profiles with extinction greater than 0.1 km^{-1} or retrieval residuals greater than 50%. Compared with v2.1, v2.5 aligns more closely with GloSSAC data (see Figure S2.3) and captures a pronounced SAOD maximum in late January–early February 2022, linked to rapid SO_2-to-SO_4 conversion in the Hunga cloud driven by elevated water vapour. This feature is absent in both GloSSAC and SAGE records.

A separate retrieval of OMPS-LP is available from the University of Saskatchewan (Bourassa et al., 2023), known as the USASK product. The USASK retrieval employs a tomographic method (Degenstein et al., 2003) to improve limb-scattering aerosol extinction retrievals, as described in Zawada et al. (2018). The tomographic two-dimensional inversion combines successive limb images from the OMPS-LP central slit. Aerosol extinction is reported at 745 nm on a retrieval grid of 1 km vertically and 125 km horizontally, which approximately matches the OMPS-LP sampling. A single-mode lognormal particle size distribution is assumed. The USASK retrieval improved characterisation of some early-phase Hunga aerosol layers (Bourassa et al., 2023) compared to the v2.1 NASA OMPS-LP aerosol extinction.

Although an additional OMPS-LP aerosol product developed by the University of Bremen (IUP) is available (Rozanov et al., 2024), those data are not used for analysis in this report but are included in the measurement uncertainty discussion in Chapter 3.

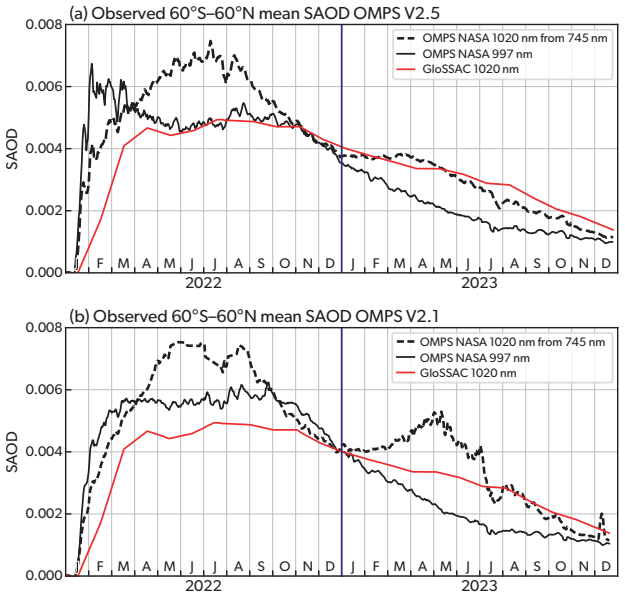

Figure S2.3: *Comparisons of near-global average (60°S–60°N) stratospheric aerosol optical depths (SAOD) from OMPS v2.1, v2.5, and GloSSAC. SAOD for the first two years after the Hunga eruption are shown with background SAOD removed. (a) NASA OMPS-LP v2.5 1020 nm values are derived by converting 745 nm SAOD using the SAGE III/ISS 745-to-1020 nm Ångström exponent; NASA OMPS-LP v2.5 997 nm SAOD shown directly, without any conversion, and GloSSAC 1020 nm SAOD. (b) NASA OMPS-LP v2.1 1020 nm values are derived by converting 745 nm SAOD using the same SAGE III/ISS Ångström exponent; NASA OMPS-LP v2.1 997 nm SAOD shown directly, without any conversion, and GloSSAC 1020 nm SAOD.*

OSIRIS aerosol extinction

The Optical Spectrograph and Infrared Imager System (OSIRIS) is a limb-scatter instrument launched aboard the Odin satellite in 2001 that continues to operate at the time of writing. The Optical Spectrograph (OS) is the primary instrument, measuring scattered sunlight between 284 and 810 nm with approximately 1.0 nm spectral resolution. The OSIRIS inversion retrieves aerosol extinction at 750 nm on a 1 km grid, with the profile information having approximately 2 km vertical resolution (Bourassa et al., 2007). The inversion requires an assumption of the particle size distribution to derive the scattering phase function. The OSIRIS sampling generally provides between 100 and 400 profiles per day over 82°S–82°N (excluding polar night), depending on the time of year, with a slight bias toward the Northern Hemisphere.

Radio occultation stratospheric H_2O

Radio Occultation (RO) measures the bending angle of radio waves propagating through the atmosphere, from which vertical profiles of atmospheric refractivity (N) can be derived with high vertical resolution (approximately 1 km). The refractivity is dependent primarily on temperature and water vapour (H_2O) in

the atmosphere according to:

$$N = 77.6\left(\frac{p}{T}\right) + 3.73 \times 10^5\left(\frac{e}{T^2}\right), \qquad \text{(S2.1)}$$

where p is pressure, T is temperature, and e is H_2O partial pressure.

Under normal conditions, the H_2O term makes virtually no contribution to N at altitudes above 10 km, and thus H_2O is not detectable by RO measurements in the stratosphere. However, in the case of extremely large stratospheric H_2O concentrations in the early Hunga plume (>1000 ppmv), the RO measurements can be combined with independent temperature observations to derive estimates of stratospheric H_2O. Details of these calculations are described in Khaykin et al. (2022) and Randel et al. (2023).

Radio occultation ionospheric electron density profiles

Radio occultation also measures the phase advance and group delay on two Global Navigation Satellite System (GNSS) frequencies, which—like ground-based GNSS measurements—can be used to measure the path-integrated electron density of the ionosphere between the transmitter and receiver satellites. During occultations, time series of this path-integrated electron density can then be inverted using an Abel transform to derive profiles of the ionospheric electron density. These profiles are often attributed to the tangent point of the occultation measurement and are frequently used for ionospheric event remote sensing (Syndergaard et al., 2006).

Some limitations of the technique are discussed in Shaikh et al. (2014), Pedatella et al. (2015), and Currie et al. (2021).

SAGE III/ISS

Water vapour and ozone The Stratospheric Aerosol and Gas Experiment (SAGE) III provides stratospheric water vapour, ozone, nitrogen dioxide, and aerosol extinction coefficient profiles using solar occultation observations from the International Space Station (ISS). SAGE III/ISS is in a mid-inclination orbit (51.6°) and provides 15 sunrise and 15 sunset measurements per day, covering the latitude range between 50°S and 50°N for most months of the year. The latitude sampling progresses slowly over time, such that it takes approximately one month to cover the latitude range 50° N–S.

Figure S2.4 shows the sampling of SAGE III/ISS during January 2020–August 2023, overlaying the Hunga H_2O plume observed by MLS for reference. Data used here are based on retrieval version v5.2. The vertical resolution of all data products is approximately 0.75 km, with profile retrievals reported on a 0.5 km grid.

The trace gas profile data are provided in units of number density on altitude and are converted to mixing ratio using the temperature and pressure profiles reported in the SAGE III/ISS data files, which originate from the Modern-Era Retrospective Analysis for Research and Applications, Version 2 (MERRA-2; Gelaro et al., 2017).

Data quality for the v5.1 retrieval of the SAGE III/ISS ozone data (the "AO3" product) is discussed in Wang et al. (2020). Water vapour retrievals for v5.1 were validated in Davis et al. (2021) and Park et al. (2021).

Aerosol extinction and derived aerosol parameters SAGE III/ISS also measures aerosol extinction at nine wavelengths (384, 449, 521, 602, 676, 756, 864, 1022, and 1544 nm). By directly measuring the extinction of the solar radiation, SAGE III/ISS provides measurements with high accuracy and precision (Thomason et al., 2021). The vertical resolution is approximately 1 km, with profiles reported in 0.5 km increments from 0.5 to 40 km altitude (Damadeo et al., 2013).

The "half-to-one-micron extinction ratio" gives a general indicator of variations in particle size distribution (e.g., Thomason et al., 2021) based on the mid-visible (525 nm) to near-infrared (1020 nm) SAGE-II aerosol extinctions. The multi-wavelength aerosol extinction coefficient measurements also provide derived aerosol parameters for variations in the stratospheric aerosol layer particle size distribution (Thomason et al., 2008; Knepp et al., 2024), within limitations discussed by Savigny and Hoffmann (2020).

The latest v5.3 SAGE III/ISS data release includes, for the first time, a suite of aerosol size distribution parameters (Knepp et al., 2024). Applying the so-called "three-lambda method" (Thomason et al., 2008), the approach relates aerosol extinction at three wavelengths to aerosol surface area density (SAD) and volume concentration, the ratio of the latter to the former then providing the effective radius.

The aerosol particle size distribution is a key factor driving the radiative and stratospheric chemistry impacts of major volcanic eruptions, and variants on the three-lambda method have been applied to generate global datasets for coordinated chemistry–climate

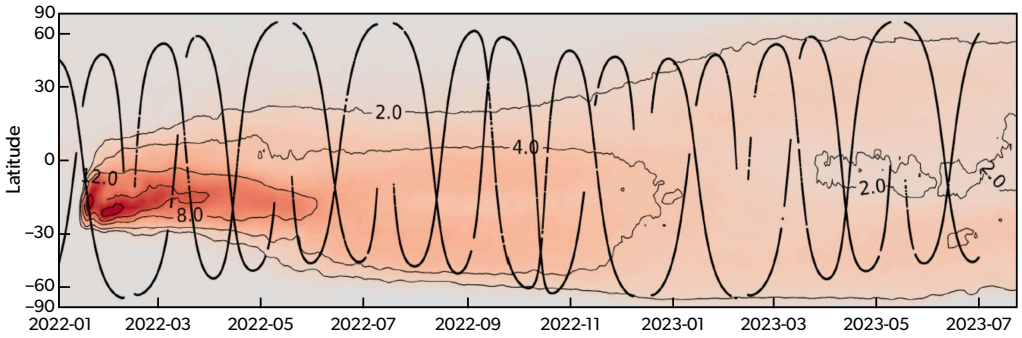

Figure S2.4: *SAGE III/ISS sampling locations overlaying the Hunga water vapour plume as observed by MLS, as a function of time and latitude. The MLS water vapour contours are the same as in Figure S2.1. Figure courtesy of Jon Starr at NSF NCAR.*

modelling assessments (Luo, 2016; Revell et al., 2017). For the Hunga HTHH-MOC experiments (Zhu et al., 2025), the CMIP6 methods from Luo (2016) were applied to generate SAD and waveband-mapped aerosol optical properties for the two years of the post-Hunga re-analysis experiment 2b (see Jörimann et al., 2025).

SSU stratospheric temperatures

Satellite data for studying long-term temperature changes in the middle and upper stratosphere include the operational Stratospheric Sounding Unit (SSU) covering 1979–2006 (Steiner et al., 2020). The SSU data represent broad-layer (approximately 15 km thick) averages centred around 30, 37, and 43 km. The SSU data originate from seven separate operational instruments, and a merged climate data record was developed by Zou et al. (2014), taking account of instrument calibration, satellite orbit drifts, and evolving CO_2 concentration.

The SSU data record beyond 2006 was extended by Zou and Qian (2016) using Advanced Microwave Sounding Unit (AMSU) measurements (the so-called SSU+AMSU data). MLS temperatures were used in Randel et al. (2016) to create an independent update to the SSU time series beyond 2006, based on constructing vertically weighted MLS averages to optimally match SSU for the overlap period 2004–2006 (the so-called SSU+MLS data).

SABER temperatures

The Sounding of the Atmosphere using Broadband Emission Radiometry (SABER) instrument on the Thermosphere, Ionosphere, Mesosphere Energetics and Dynamics (TIMED) satellite has measured temperature and chemical species in the middle atmosphere since January 2002 (Russell et al., 1999). Temperatures are retrieved from measurements of infrared CO_2 emissions from the atmospheric limb over altitudes from approximately 16 to 100 km, with a vertical resolution of 2 km (Remsberg et al., 2008).

Data used here are from retrieval version v2.08, available online at `https://saber.gats-inc.com`. SABER temperature profiles are available at two local times each day, with measurements from 53° latitude in one hemisphere to 83° latitude in the other. The local times of the measurements shift gradually from one day to the next as the TIMED orbit precesses, and this sampling pattern flips approximately every 65 days. Further data analysis details are described in Yu et al. (2023).

TROPOMI SO_2

SO_2 column abundances have been measured by the Tropospheric Monitoring Instrument (TROPOMI) operating on ESA's Sentinel-5 Precursor (S5P) satellite since 2017 (Veefkind et al., 2012). The polar-orbiting S5P satellite enables daily temporal resolution for TROPOMI SO_2 measurements at the tropical latitudes of the Hunga eruption.

TROPOMI uses observations of backscattered UV radiation to retrieve vertical column densities (VCDs) of volcanic SO_2 and is capable of detecting VCDs of less than 1 Dobson Unit (DU; 1 DU = 2.69×10^{16} molecules cm^{-2}) in a single pixel (Li et al., 2017; Theys et al., 2017). TROPOMI provides a spatial resolution of 5.5 × 3.5 km, and the total uncertainty of the TROPOMI stratospheric SO_2 measurements is approximately 35 % (Carn et al., 2022).

Reanalysis meteorological and constituent data sets

An atmospheric reanalysis system consists of a global forecast model, input observations, and a data assimilation scheme used in combination to produce

best estimates (gridded analyses) of past atmospheric states—including temperature, wind, geopotential height, and other meteorological fields.

An overview and description of atmospheric reanalysis systems, with a focus on the stratosphere, is provided by Fujiwara et al. (2017), and comprehensive evaluations of current reanalysis data in the stratosphere can be found in SPARC (2022). Stratospheric composition reanalysis is also available from the MERRA-2 Stratospheric Composition Reanalysis of Aura Microwave Limb Sounder (M2-SCREAM), which provides globally gridded analyses of the MLS constituents based on MERRA-2 winds (Wargan et al., 2023).

AIRS, IASI, CrIS temperatures, and airglow

There are several data sets used briefly in Chapter 6 regarding measurements of upper atmospheric waves observed after the initial Hunga eruption. These individual data sets are not described in detail in this Supplement, but further information can be found in Wright et al. (2022).

S2.2 Ground-based and balloon measurements

AERONET particle size distribution

The AErosol RObotic NETwork (AERONET) project (Holben et al., 1998; Zhang et al., 2006) was established to provide a harmonised network of ground-based sun photometers. AERONET observations are used to derive column-integrated aerosol parameters (Dubovik and King, 2000) and for satellite validation (e.g., Kahn et al., 2005; Remer and Kaufman, 2006), and contribute to a quantitative understanding of aerosol radiative effects (Kinne et al., 2003; Schulz et al., 2006).

The automatic Sun-tracking and sky-scanning radiometers make measurements every 15 minutes across multiple wavelengths (340, 380, 440, 500, 675, 870, 940, and 1020 nm). The detailed spectral information enables the derivation of a column particle size distribution (King et al., 1978; Eck et al., 1999). For example, Holben et al. (1996) demonstrated how measurements in the Amazon Basin during 1993 revealed a change in aerosol size distribution, transitioning from a background distribution (with modest Pinatubo enhancement) into a clear signature of biomass-burning aerosol during the dry season.

For the analysis of the Hunga aerosol size distribution in this report, the cloud-screened Level 1.5 observations are used, applying version 3 of the spectral inversion algorithm (Dubovik et al., 2006; Boichu et al., 2023).

COBALD backscatter sonde

The COBALD (Compact Optical Backscatter Aerosol Detector) instrument is a lightweight backscatter sonde designed to be flown on operational weather balloons. COBALD provides high-precision *in situ* measurements of aerosol backscatter coefficient at two wavelengths (455 and 940 nm), and detects backscattered light from air molecules, aerosol, or cloud droplets. These measurements provide detailed information on aerosol (or cloud) particle size and number density.

Ground-based GNSS Total Electron Content (TEC)

Ground-based networks of thousands of geodetic Global Navigation Satellite System (GNSS) receivers measure the phase advance and group delay on two or more frequencies, which can be used to estimate the path-integrated electron density of the ionosphere between transmitter and receiver satellites—referred to as the Total Electron Content (TEC) (Themens et al., 2013; Rideout and Coster, 2006).

This TEC is, by a wide margin, the most abundant ionospheric measurement available. While it can be subject to limitations from receiver and satellite bias calculation, for studies of the Hunga event and other mesoscale ionospheric structuring, relative TEC—where detrending has been applied—is generally accurate, albeit subject to some limitations depending on the signal ray geometry with respect to the orientation of the phase fronts of wave structures (Guerra et al., 2024).

Without projection to vertical, TEC can be determined with a precision as high as 0.005–0.02 TECU, depending on the phase stability of the receiver.

Ground-based lidar: aerosol extinction and scattering ratios

Réunion Island lidars (Maïdo observatory) A lidar facility has operated at Réunion Island (21°S, 55°E) since 1994 (Baray et al., 2013). Originally located at the coastal Université de La Réunion site in Saint-Denis (80 m a.s.l.), the system was relocated in 2012 to the Maïdo mountain observatory (2160 m a.s.l.).

The original Rayleigh–Mie 532 nm Nd:YAG lidar was upgraded in 1998 to a DIAL system to enable measurements of tropospheric ozone profiles (Baray et al., 1999). It was further adapted in 2002, incorporating Raman channels providing measurements

of water vapour profiles (Baray et al., 2013). A second aerosol-measuring DIAL lidar has been operational at Maïdo since June 2000.

As part of the NOAA Tonga Rapid Response Experiment (TR^2Ex), Baron et al. (2023) analysed the initial detections of the sheared Hunga aerosol layers, comparing results from both systems. They reported, among other findings, somewhat different lidar ratio (extinction-to-backscatter ratio) measurements between the two systems.

Lauder lidar The Lauder Atmospheric Research Station of the National Institute of Water and Atmospheric Research (NIWA), located on the South Island of New Zealand (45.0°S, 169.7°E, 370 m a.s.l.), has been operating a lidar at 532 nm since 1992 on a regular basis, with a mean measurement rate of one or two nights per week.

It provides measurements of both scattering ratio and particle depolarisation ratio. To retrieve vertical profiles of scattering ratio, a Fernald inversion method is used, assuming an aerosol extinction-to-backscatter ratio of 46 sr. The molecular backscattering coefficient is derived from the JRA-55 meteorological analysis (Nagai et al., 2010; Sakai et al., 2016).

Dumont d'Urville lidar The French Antarctic station Dumont d'Urville (66.6°S, 140°E; DDU) has hosted an aerosol and cloud lidar since April 1989, operating in the Network for the Detection of Atmospheric Composition Changes (NDACC). The main focus of the instrument is the study of polar stratospheric clouds with nighttime setup; the recent focus on aerosol plumes originating from either volcanic or biomass burning activity extended the measurement calendar to the summertime.

The Nd:YAG laser source emits at 532 nm at 10 Hz frequency with an emitted power of approximately 250 mJ. Backscattered photons are collected on a collocated 80 cm diameter Newton telescope. A polarising cube at the reception splits the beam into two components polarised parallel and perpendicular to the laser emission for the 532 nm wavelength, each component is recorded and inverted to calculate the depolarisation ratio. The Rayleigh/Mie/Raman lidar also acquires the N_2 vibrational Raman scattering at 607 nm. As the OHP lidar, the signal inversion is performed using the Klett-Fernald formalism derive scattering ratio profiles, which have a 60 m vertical resolution. ECMWF meteorological data is also used for the molecular backscattering calculation. A detailed description of the instrument, measurements processing method as well as error estimation is provided by Tencé et al. (2022).

Mauna Loa Lidar The NOAA Mauna Loa Observatory (19.5°N, 155.6°W, 3396 m a.s.l.) established a ruby laser-based lidar in the early 1970s, which operated until 1998. A Nd:YAG laser-based lidar began operation in 1994. The YAG system operates about once per week and retrieves aerosol profiles at 532 and 1064 nm at 300 m altitude resolution. Molecular profiles needed for analysis are calculated from radiosondes launched at Hilo, HI (56 km distant) and the NASA/MSIS model for altitudes above the radiosonde. The signal is usually normalised between 38 and 40 km and the Fernald-Klett inversion method is used (Barnes and Hofmann, 1997).

OHP lidar The Observatoire de Haute-Provence (OHP) located in southern France (43.9° N, 5.7° E, 670 m a.s.l.) is equipped with several lidar systems for atmospheric sounding at a wide range of altitudes. The aerosol measurements are provided by LTA lidar operating at 532 nm since 1991 on a regular basis with a mean measurement rate of 10-12 acquisition nights per month. For retrieving vertical profiles of stratospheric aerosol, a Fernald-Klett inversion method is used to provide backscatter and extinction coefficients. The scattering ratio is then computed as a ratio of total (molecular plus aerosol) to molecular backscattering, where the latter is derived from ECMWF meteorological analysis. The resulting vertical profiles of aerosol parameters are reported at 150 m vertical resolution. A more detailed description of the instruments, aerosol retrieval and error budget are provided by Khaykin et al. (2017) and references therein.

São Paulo (SPU) and Bauru (IPMET) lidars The lidar facility at São Paulo (SPU) is a multi-channel lidar system with elastic channels at 356, 532, and 1064 nm, and Raman channels at 530, 387, 408, and 530 nm (see, e.g., `https://www.spulidarstation.org/instruments`). Thanks in part to the cooperation and sharing of Hunga measurement data via the VolRes mailing list (e.g., Vernier et al., 2022; Vernier et al., 2024), a field campaign named *BraVo* took place in 2022 (Vernier et al., 2023). The campaign included lidar and balloon measurements from July to August to characterise and understand the progression of tropical Hunga aerosol and water vapour (Landulfo

et al., 2022b; Souza et al., 2025).

For the BraVo campaign, in addition to 13 balloon flights carried out (from May 24, 2022, to August 13, 2023), progression of the Hunga aerosol was monitored from the lidar facility at the Centro de Meteorologia de Bauru (IPMET-UNESP) in Bauru, Brazil (22.3°S, 49.3° W). The four-channel IPMET lidar measures at 355, 532, and 1064 nm, with the 532 nm channel measuring both parallel and perpendicular components used to derive depolarisation ratio for indicating non-spherical particles (Landulfo et al., 2022a).

Ionosonde electron density profiles

Ionosondes are ionospheric sounding instruments that use reflection in the high-frequency (HF) band (typically 1–25 MHz) to remotely sense the profile of ionospheric electron density up to the F2 peak of the ionosphere (Reinisch, 1987). These instruments have data records extending back to as early as 1932 and make up the majority of the ionospheric climate record. While these instruments are very reliable, automated processing of the radar data is challenging and often suffers critical errors during disturbed events that are not well characterised by the available quality control measures supplied with the automatically processed products (Stankov et al., 2023; Themens et al., 2022). Because of this limitation it is essential that the data from these instruments be manually processed during severe events, such as Hunga. When following the International Union of Radio Science (URSI)'s guidelines for data scaling and annotation, manually processed ionospheric peak critical frequency (f_oF2) can be taken, at the highest confidence level, as accurate to within 0.05 MHz, while h_mF2 can achieve a precision of between 5 km and 15 km, depending on ionospheric conditions and the competency of the manual scaler.

LOAC particle counter

The Light Optical Aerosol Counter (LOAC) is an optical particle counter instrument that can be operated on weather balloons for observations in the stratosphere (Renard et al., 2016). LOAC measures the number of aerosol particles at different particle sizes and additionally derives information about the absorption of the aerosol from two detectors (photodiodes) at two different angles from the light source (12 and 60 degrees). This design of the LOAC instrument allows calculation of a "particle typology" classification (Renard et al., 2016) based on the number of particles present and their light-absorbing properties.

In addition to the initial Réunion Island campaign (Kloss et al., 2022), the later Hunga aerosol was also profiled with the LOAC from South Africa in September 2022 (Cummins et al., 2023), and from Chile during 2023.

Lightweight aerosol filter samplers

A series of balloon soundings from São Paulo, Brazil deployed a lightweight filter sampling instrument to sample in-situ the composition of the Hunga aerosol. As part of the BraVo field campaign (Landulfo et al., 2022b), two phases of the campaign saw dedicated balloon soundings combining the filter sampler and POPC instrument to analyse the Hunga aerosol.

An initial series of soundings in May 2022 (Vernier et al., 2023), later soundings in August 2022 having a longer duration of sampling the Hunga aerosol (Vernier et al., 2024; Vernier et al., 2025), with the use of a radio-controlled device able to remain at a constant altitude to sample volcanic layers (personal communication Hazel Vernier, Dec 2023). The ion chromatography analysis for the samples from these two phases was carried out in two different laboratories (personal communication H. Vernier, December 2023), and the two instruments also differed in their detection limits.

For the August 2022 soundings analysed by Vernier et al. (2025), polytetrafluoroethene (PTFE) filters with a pore size of 0.45 µm were used. A key uncertainty remains regarding the collection efficiency of the finest particles, as to whether the sampler may have been unable to capture the smaller volcanic sulfate particles.

Ozonesondes and SO_2 sondes

Ozonesondes are small, lightweight, and compact balloon-borne instruments developed for measuring the vertical distribution of atmospheric ozone up to an altitude of about 30 km. Data used here are from the Electrochemical Concentration Cell (ECC) Ozonesonde, which provides ozone profile observations with an uncertainty of 10% (Tarasick et al., 2021). These measurements have a high vertical resolution of 5 m. The SO_2 sonde provides SO_2 profile measurements based on modification of an ECC ozonesonde, as described in Yoon et al. (2022). SO_2 measurements have an uncertainty of 20%.

POPS optical particle spectrometer

The Portable Optical Particle Spectrometer (POPS) is a lightweight, low-power, and relatively low-cost

research-grade optical particle counter that measures the number concentration of aerosol particles with diameters between 140 nm and 2.5 μm (Gao et al., 2016).

Since 2020, a global network of POPS launches has been established under the Balloon Baseline Stratospheric Aerosol Project (B^2SAP; e.g., Todt et al., 2023; Asher et al., 2024). Quarterly launches were conducted during 2022 from both the northern and southern tropics (Hilo, Hawaii, and Maïdo, Réunion Island, respectively) and from both northern and southern mid-latitudes (Boulder, USA, and Lauder, New Zealand).

Asher et al. (2023) use these data to study particle size variations within the Hunga volcanic cloud.

POPC Particle Counter

The BraVo balloon soundings used a POPC particle counter, a commercially available OPC instrument (Particle Plus 8306) that measures aerosol concentrations within 8 size channels, between 0.15 and 5 microns (Vernier et al., 2025).

The newer NPOPC, used on some flights, is an improved POPC instrument (Particle Plus, with similar laser, but improved signal-processing to provide 30 size channels). The POPC was also used in the DCOTSS field campaign, involving soundings from Kansas in August 2021 measuring volcanic aerosol from the La Soufrière eruption (Li et al., 2023).

STAC and L-OPC particle counters

The longest record of in-situ measurements of the stratospheric aerosol layer is from the continuing program of balloon soundings begun from Laramie, Wyoming in 1971 (Deshler et al., 2003; Deshler et al., 2019). The main basis of this record is the optical particle counter (OPC), measuring the number of scattering pulses of white light, corresponding to particles larger than approximately 300 nm diameter.

Since 2016, the Laramie record has continued with a smaller lighter-weight LASP OPC (LOPC, Kalnajs and Deshler, 2022), superseding the OPC40 that provided the Wyoming record since the late 1980s (Deshler et al., 2003). The earlier record used a similar 25 degree scattering OPC (Pinnick and Hofmann, 1973), also measuring from Minneapolis back to August 1963, originally known as a "dust-sonde" (Rosen, 1964).

In addition to the OPC, the Wyoming system also measures total particle number concentration using a condensation particle counter (CPC), counting ultrafine particles down to 10nm diameter. Now known as the Stratospheric Total Aerosol Counter (STAC; Deshler et al., 2024; Norgren et al., 2024), the instrument grows ultrafine particles to optically active sizes within a growth chamber (Rosen and Hofmann, 1977).

Soundings with the LOPC and STAC from McMurdo in 2019 and 2023 (Deshler et al., 2024) measured the long-range transport of the Hunga aerosol in April to June 2023. The LOPC has multiple size cuts, up to super-micron sizes, measuring also the size distribution of polar stratospheric clouds (Rosen et al., 1988; Deshler et al., 1994).

Radiosonde water vapour

Data from the operational upper-air network using the Vaisala RS41 radiosonde provide *in situ* observations of the large amounts of water vapour injected into the stratosphere by the Hunga eruption and allow a description of the early development of the volcanic plume as it dispersed.

Details regarding the Vaisala RS41 radiosonde observations here follows Vömel et al. (2022). The Vaisala RS41 humidity sensor relies on an integrated temperature sensor, which measures the sensor temperature in addition to air temperature, and the sensor temperature is used to eliminate any solar radiation dry bias. Furthermore, the sensor is heated to reduce icing and contamination. This allows direct exposure of the sensor to the atmosphere without any protective cap, which would otherwise reduce the ventilation around the sensor and allow for other artifacts. The Vaisala processing algorithm corrects the measured relative humidity (RH) for the difference between sensor and ambient temperature. The response time of the RS41 sensor increases strongly with decreasing temperature, reaching more than one minute at temperatures below −60 °C. The Vaisala algorithm compensates for the slow sensor response in addition to the correction due the elevated sensor temperature. The estimated detection limit of enhanced stratospheric water vapour based on these data lies around 100 ppmv at 30 km, 50 ppmv at 28 km and 15 ppmv at 25 km. Based on experience with tropospheric observations and extensive comparisons with other measurements, relative uncertainty values are in the range of 2 to 5% of the measured value. The vertical resolution of the measurements is better than 100 m.

References

Adriani, A., P. Massoli, G. Di Donfrancesco, F. Cairo, M. L. Moriconi and M. Snels (2004). 'Climatology of polar stratospheric clouds based on lidar observations from 1993 to 2001 over McMurdo Station, Antarctica'. *J. Geophys. Res.*, 109. DOI: 10.1029/2004jd004800.

Antuña-Marrero, J.-C., G. W. Mann, J. Barnes, A. Rodríguez-Vega, S. Shallcross, S. S. Dhomse, G. Fiocco and G. W. Grams (2021). 'Recovery of the first ever multi-year lidar dataset of the stratospheric aerosol layer, from Lexington, MA, and Fairbanks, AK, January 1964 to July 1965'. *Earth Syst. Sci. Data*, 13, pp. 4407–4423. DOI: 10.5194/essd-13-4407-2021.

Asher, E., A. Baron, P. Yu, M. Todt, P. Smale, B. Liley, R. Querel, T. Sakai, I. Morino, Y. Jin et al. (2024). 'Balloon Baseline Stratospheric Aerosol Profiles (B2SAP)—Perturbations in the Southern Hemisphere, 2019–2022'. *J. Geophys. Res.*, 129, e2024JD041581. DOI: 10.1029/2024jd041581.

Asher, E., M. Todt, K. Rosenlof, T. Thornberry, R.-S. Gao, G. Taha, P. Walter, S. Alvarez, J. Flynn, S. M. Davis et al. (2023). 'Unexpectedly rapid aerosol formation in the Hunga Tonga plume'. *Proc. Natl. Acad. Sci.*, 120, e2219547120. DOI: 10.1073/pnas.2219547120.

Baray, J.-L., Y. Courcoux, P. Keckhut, T. Portafaix, P. Tulet, J.-P. Cammas, A. Hauchecorne, S. Godin Beekmann, M. De Mazière, C. Hermans et al. (2013). 'Maïdo observatory: a new high-altitude station facility at Reunion Island (21° S, 55° E) for long-term atmospheric remote sensing and in situ measurements'. *Atmos. Meas. Tech.*, 6, pp. 2865–2877. DOI: 10.5194/amt-6-2865-2013.

Baray, J.-L., J. Leveau, J. Porteneuve, G. Ancellet, P. Keckhut, F. Posny and S. Baldy (1999). 'Description and evaluation of a tropospheric ozone lidar implemented on an existing lidar in the southern subtropics'. *Appl. Optics*, 38, 6808. DOI: 10.1364/ao.38.006808.

Barnes, J. E. and D. J. Hofmann (1997). 'Lidar measurements of stratospheric aerosol over Mauna Loa Observatory'. *Geophys. Res. Lett.*, 24, pp. 1923–1926. DOI: 10.1029/97GL01943.

Baron, A., P. Chazette, S. Khaykin, G. Payen, N. Marquestaut, N. Bègue and V. Duflot (2023). 'Early Evolution of the Stratospheric Aerosol Plume Following the 2022 Hunga Tonga-Hunga Ha'apai Eruption: Lidar Observations From Reunion (21°S, 55°E)'. *Geophys. Res. Lett.*, 50, e2022GL101751. DOI: 10.1029/2022gl101751.

Bernath, P. (2017). 'The Atmospheric Chemistry Experiment (ACE)'. *J. Quant. Spectrosc. Radiat. Transfer*, 186, pp. 3–16. DOI: 10.1016/j.jqsrt.2016.04.006.

Boichu, M., R. Grandin, L. Blarel, B. Torres, Y. Derimian, P. Goloub, C. Brogniez, I. Chiapello, O. Dubovik, T. Mathurin et al. (2023). 'Growth and Global Persistence of Stratospheric Sulfate Aerosols From the 2022 Hunga Tonga–Hunga Ha'apai Volcanic Eruption'. *J. Geophys. Res.*, 128, e2023JD039010. DOI: 10.1029/2023JD039010.

Boone, C. D., P. F. Bernath and M. Lecours (2023). 'Version 5 retrievals for ACE-FTS and ACE-imagers'. *J. Quant. Spectrosc. Radiat. Transfer*, 310, 108749. DOI: 10.1016/j.jqsrt.2023.108749.

Bourassa, A. E., D. A. Degenstein, R. L. Gattinger and E. J. Llewellyn (2007). 'Stratospheric aerosol retrieval with optical spectrograph and infrared imaging system limb scatter measurements'. *J. Geophys. Res.*, 112, D10217. DOI: 10.1029/2006JD008079.

Bourassa, A. E., D. J. Zawada, L. A. Rieger, T. W. Warnock, M. Toohey and D. A. Degenstein (2023). 'Tomographic retrievals of Hunga Tonga-Hunga Ha'apai volcanic aerosol'. *Geophys. Res. Lett.*, 50, e2022GL101978. DOI: 10.1029/2022GL101978.

Carn, S. A., N. A. Krotkov, B. L. Fisher and C. Li (2022). 'Out of the blue: volcanic SO_2 emissions during the 2021-2022 Hunga Tonga-Hunga Ha'apai eruptions'. *Front. Earth Sci.*, 13. DOI: 10.3389/feart.2022.976962.

Carslaw, K. S., B. Luo and T. Peter (1995). 'An analytic expression for the composition of aqueous HNO_3–H_2SO_4 stratospheric aerosols including gas phase removal of HNO_3'. *Geophys. Res. Lett.*, 22, pp. 1877–1880. DOI: 10.1029/95GL01668.

Carslaw, K. S., B. P. Luo, S. L. Clegg, T. Peter, P. Brimblecombe and P. J. Crutzen (1994). 'Stratospheric aerosol growth and HNO3 gas phase depletion from coupled HNO3 and water uptake by liquid particles'. *Geophys. Res. Lett.*, 21, pp. 2479–2482. DOI: 10.1029/94gl02799.

Chen, Z., P. K. Bhartia, R. Loughman, P. Colarco and M. DeLand (2018). 'Improvement of stratospheric aerosol extinction retrieval from OMPS/LP using a new aerosol model'. *Atmos. Meas. Tech.*, 11, pp. 6495–6509. DOI: 10.5194/amt-11-6495-2018.

Clerbaux, C., A. Boynard, L. Clarisse, M. George, J. Hadji-Lazaro, H. Herbin, D. Hurtmans, M. Pommier,

A. Razavi, S. Turquety et al. (2009). 'Monitoring of atmospheric composition using the thermal infrared IASI/MetOp sounder'. *Atmos. Chem. Phys.*, 9, pp. 6041–6054. DOI: 10.5194/acp-9-6041-2009.

Cummins, D. P., V. Guemas, C. J. Cox, M. R. Gallagher and M. D. Shupe (2023). 'Surface Turbulent Fluxes From the MOSAiC Campaign Predicted by Machine Learning'. *Geophys. Res. Lett.*, 50, e2023GL105698. DOI: 10.1029/2023GL105698.

Currie, J. L., B. A. Carter, T. Dao and M. Terkildsen (2021). 'The importance of counting: A new index to correctly quantify Equatorial Plasma Bubble occurrence in COSMIC Radio Occultation data'. *J. Geophys. Res.*, 126, e2021JA029539. DOI: 10.1029/2021JA029539.

Damadeo, R. P., J. M. Zawodny, L. W. Thomason and N. Iyer (2013). 'SAGE v7.0 algorithm: Application to SAGE II'. *Atmos. Meas. Tech.*, 6, pp. 3539–3561. DOI: 10.5194/amt-6-3539-2013.

Davis, S. M., R. Damadeo, D. Flittner, K. H. Rosenlof, M. Park, W. J. Randel et al. (2021). 'Validation of SAGE III/ISS solar water vapor data with correlative satellite and balloon-borne measurements'. *J. Geophys. Res.*, 125, e2020JD033803. DOI: 10.1029/2020JD033803.

Degenstein, D. A., E. J. Llewellyn and N. D. Lloyd (2003). 'Volume emission rate tomography from a satellite platform'. *Appl. Optics*, 42, pp. 1441–1450. DOI: 10.1364/AO.42.001441.

Deshler, T., M. E. Hervig, D. J. Hofmann, J. M. Rosen and J. B. Liley (2003). 'Thirty years of in situ stratospheric aerosol size distribution measurements from Laramie, Wyoming (41°N), using balloon-borne instruments'. *J. Geophys. Res.*, 108. DOI: 10.1029/2002JD002514.

Deshler, T., B. Luo, M. Kovilakam, T. Peter and L. E. Kalnajs (2019). 'Retrieval of aerosol size distributions from in situ particle counter measurements: Instrument counting efficiency and comparisons with satellite measurements'. *J. Geophys. Res.*, 124, pp. 5058–5087. DOI: 10.1029/2018JD029558.

Deshler, T., B. J. Johnson and W. R. Rozier (1994). 'Changes in the Character of Polar Stratospheric Clouds Over Antarctica in 1992 Due to the Pinatubo Volcanic Aerosol'. *Geophys. Res. Lett.*, 21, pp. 273–276. DOI: 10.1029/94GL00072.

Deshler, T., L. E. Kalnajs, M. Norgren, Y. Zhu and J. Zhang (2024). 'In Situ Aerosol Size Spectra Measurements in the Austral Polar Vortex Before and After the Hunga Tonga-Hunga Ha'apai Volcanic Eruption'. *Geophys. Res. Lett.*, 51, e2024GL111388. DOI: 10.1029/2024gl111388.

Dhomse, S. S., G. W. Mann, J. C. Antuña Marrero, S. E. Shallcross, M. P. Chipperfield, K. S. Carslaw, L. Marshall, N. L. Abraham and C. E. Johnson (2020). 'Evaluating the simulated radiative forcings, aerosol properties, and stratospheric warmings from the 1963 Mt Agung, 1982 El Chichón, and 1991 Mt Pinatubo volcanic aerosol clouds'. *Atmos. Chem. Phys.*, 20, pp. 13627–13654. DOI: 10.5194/acp-20-13627-2020.

Dubovik, O. and M. D. King (2000). 'A flexible inversion algorithm for retrieval of aerosol optical properties from Sun and sky radiance measurements'. *J. Geophys. Res.*, 105, pp. 20673–20696. DOI: 10.1029/2000JD900282.

Dubovik, O., A. Sinyuk, T. Lapyonok, B. N. Holben, M. Mishchenko, P. Yang, T. F. Eck, H. Volten, O. Muñoz, B. Veihelmann et al. (2006). 'Application of spheroid models to account for aerosol particle nonsphericity in remote sensing of desert dust'. *J. Geophys. Res.*, 111. DOI: 10.1029/2005JD006619.

Duchamp, C., F. Wrana, B. Legras, P. Sellitto, R. Belhadji and C. von Savigny (2023). 'Observation of the aerosol plume from the 2022 Hunga Tonga–Hunga Ha'apai eruption with SAGE III/ISS'. *Geophys. Res. Lett.*, 50, e2023GL105076. DOI: 10.1029/2023GL105076.

Eck, T. F., B. N. Holben, J. S. Reid, O. Dubovik, A. Smirnov, N. T. O'Neill, I. Slutsker and S. Kinne (1999). 'Wavelength dependence of the optical depth of biomass burning, urban, and desert dust aerosols'. *J. Geophys. Res.*, 104, pp. 31333–31349. DOI: 10.1029/1999JD900923.

Eyring, V., S. Bony, G. A. Meehl, C. A. Senior, B. Stevens, R. J. Stouffer and K. E. Taylor (2016). 'Overview of the Coupled Model Intercomparison Project Phase 6 (CMIP6) experimental design and organization'. *Geosci. Model Dev.*, 9, pp. 1937–1958. DOI: 10.5194/gmd-9-1937-2016.

Eyring, V., N. R. P. Harris, M. Rex, T. G. Shepherd, D. W. Fahey, G. T. Amanatidis, J. Austin, M. P. Chipperfield, M. Dameris, P. M. D. F. Forster et al. (2005). 'A Strategy for Process-Oriented Validation of Coupled Chemistry–Climate Models'. *Bull. Am. Meteorol. Soc.*, 86, pp. 1117–1134. DOI: 10.1175/bams-86-8-1117.

Fujiwara, M., J. S. Wright, G. L. Manney, L. J. Gray, J. Anstey, T. Birner, S. Davis, E. P. Gerber, V. L. Harvey, M. I. Hegglin et al. (2017). 'Introduction to the SPARC Reanalysis Intercomparison Project

(S-RIP) and overview of the reanalysis systems'. *Atmos. Chem. Phys.*, 17, pp. 1417–1452. DOI: 10.5194/acp-17-1417-2017.

Gao, R. S., H. Telg, R. J. McLaughlin, S. J. Ciciora, L. A. Watts, M. S. Richardson, J. P. Schwarz, A. E. Perring, T. D. Thornberry, A. W. Rollins et al. (2016). 'A lightweight, high-sensitivity particle spectrometer for PM2.5 aerosol measurements'. *Aerosol Sci. Technol.*, 50, pp. 88–99. DOI: 10.1080/02786826.2015.1131809.

Gelaro, R., W. McCarty, M. J. Suárez, R. Todling, A. Molod, L. Takacs, C. A. Randles, A. Darmenov, M. G. Bosilovich and R. Reichle (2017). 'The Modern-Era Retrospective Analysis for Research and Applications, Version 2 (MERRA-2)'. *J. Climate*, 30, pp. 5419–5454. DOI: 10.1175/jcli-d-16-0758.1.

Guerra, M., C. Cesaroni, M. Ravanelli and L. Spogli (2024). 'Travelling ionospheric disturbances detection: A statistical study of detrending techniques, induced period error and near real-time observables'. *J. Space Weather Space Clim.*, 14. DOI: 10.1051/swsc/2024017.

Holben, B. N., T. F. Eck, I. Slutsker, D. Tanré, J. P. Buis, A. Setzer, E. Vermote, J. A. Reagan, Y. J. Kaufman, T. Nakajima et al. (1998). 'AERONET—A Federated Instrument Network and Data Archive for Aerosol Characterization'. *Remote Sens. Environ.*, 66, pp. 1–16. DOI: 10.1016/S0034-4257(98)00031-5.

Holben, B. N., A. Setzer, T. F. Eck, A. Pereira and I. Slutsker (1996). 'Effect of dry-season biomass burning on Amazon basin aerosol concentrations and optical properties, 1992–1994'. *J. Geophys. Res.*, 101, pp. 19465–19481. DOI: 10.1029/96JD01114.

Hurst, D. F., W. G. Read, H. Vömel, H. B. Selkirk, K. H. Rosenlof, S. M. Davis, E. G. Hall, A. F. Jordan and S. J. Oltmans (2016). 'Recent divergences in stratospheric water vapor measurements by frost point hygrometers and the Aura Microwave Limb Sounder'. *Atmos. Meas. Tech.*, 9, pp. 4447–4457. DOI: 10.5194/amt-9-4447-2016.

Jäger, H. and T. Deshler (2002). 'Lidar backscatter to extinction, mass and area conversions for stratospheric aerosols based on midlatitude balloonborne size distribution measurements'. *Geophys. Res. Lett.*, 29. DOI: 10.1029/2002gl015609.

Jörimann, A., T. Sukhodolov, B. Luo, G. Chiodo, G. Mann and T. Peter (2025). 'REtrieval Method for optical and physical Aerosol Properties in the stratosphere (REMAPv1)'. *Geosci. Model Dev.*, 18, pp. 6023–6041. DOI: 10.5194/gmd-18-6023-2025.

Kahn, R. A. and B. J. Gaitley (2015). 'An analysis of global aerosol type as retrieved by MISR'. *J. Geophys. Res.*, 120, pp. 4248–4281. DOI: 10.1002/2015JD023322.

Kahn, R. A., B. J. Gaitley, M. J. Garay, D. J. Diner, T. F. Eck, A. Smirnov and B. N. Holben (2010). 'Multiangle Imaging Spectroradiometer global aerosol product assessment by comparison with the Aerosol Robotic Network'. *J. Geophys. Res.*, 115, D23209. DOI: 10.1029/2010JD014601.

Kahn, R. A., B. J. Gaitley, J. V. Martonchik, D. J. Diner, K. A. Crean and B. N. Holben (2005). 'Multiangle Imaging Spectroradiometer (MISR) global aerosol optical depth validation based on two years of coincident AERONET observations'. *J. Geophys. Res.*, 110, D10S04. DOI: 10.1029/2004JD004706.

Kahn, R. A., J. A. Limbacher, K. T. Junghenn Noyes, V. J. B. Flower, L. M. Zamora and K. F. McKee (2024). 'Evolving Particles in the 2022 Hunga Tonga—Hunga Ha'apai Volcano Eruption Plume'. *J. Geophys. Res.*, 129, e2023JD039963. DOI: 10.1029/2023JD039963.

Kalnajs, L. E. and T. Deshler (2022). 'A New Instrument for Balloon-Borne In Situ Aerosol Size Distribution Measurements, the Continuation of a 50 Year Record of Stratospheric Aerosols Measurements'. *J. Geophys. Res.*, 127, e2022JD037485. DOI: 10.1029/2022JD037485.

Kar, J., K.-P. Lee, M. A. Vaughan, J. L. Tackett, C. R. Trepte, D. M. Winker, P. L. Lucker and B. J. Getzewich (2019). 'CALIPSO level 3 stratospheric aerosol profile product: version 1.00 algorithm description and initial assessment'. *Atmos. Meas. Tech.*, 12, pp. 6173–6191. DOI: 10.5194/amt-12-6173-2019.

Khaykin, S. M., S. Godin-Beekmann, P. Keckhut, A. Hauchecorne, J. Jumelet, J.-P. Vernier, A. Bourassa, D. A. Degenstein, L. A. Rieger, C. Bingen et al. (2017). 'Variability and evolution of the midlatitude stratospheric aerosol budget from 22 years of ground-based lidar and satellite observations'. *Atmos. Chem. Phys.*, 17, pp. 1829–1845. DOI: 10.5194/acp-17-1829-2017.

Khaykin, S. M., S. Godin-Beekmann, A. Hauchecorne, J. Pelon, F. Ravetta and P. Keckhut (2018). 'Stratospheric smoke with unprecedentedly high backscatter observed by lidars above southern France'. *Geophys. Res. Lett.*, 45, pp. 1639–1646. DOI: 10.1002/2017GL076763.

Khaykin, S., A. Podglajen, F. Ploeger, J.-U. Grooß, F. Tence, S. Bekki, K. Khlopenkov, K. Bedka, L. Rieger, A. Baron et al. (2022). 'Global perturbation of stra-

tospheric water and aerosol burden by Hunga eruption'. *Commun. Earth Environ.*, 3, 316. DOI: 10.1038/s43247-022-00652-x.

Kim, M.-H., A. H. Omar, J. L. Tackett, M. A. Vaughan, D. M. Winker, C. R. Trepte, Y. Hu, Z. Liu, L. R. Poole, M. C. Pitts et al. (2018). 'The CALIPSO version 4 automated aerosol classification and lidar ratio selection algorithm'. *Atmos. Meas. Tech.*, 11, pp. 6107–6135. DOI: 10.5194/amt-11-6107-2018.

King, M. D., D. M. Byrne, B. M. Herman and J. A. Reagan (1978). 'Aerosol Size Distributions Obtained by Inversions of Spectral Optical Depth Measurements'. *J. Atmos. Sci.*, 35, pp. 2153–2167. DOI: 10.1175/1520-0469(1978)035<2153:ASDOBI>2.0.CO;2.

Kinne, S., U. Lohmann, J. Feichter, M. Schulz, C. Timmreck, S. Ghan, R. Easter, M. Chin, P. Ginoux, T. Takemura et al. (2003). 'Monthly averages of aerosol properties: A global comparison among models, satellite data, and AERONET ground data'. *J. Geophys. Res.*, 108, 4634. DOI: 10.1029/2001JD001253.

Kloss, C., P. Sellitto, J.-B. Renard, A. Baron, N. Bègue, B. Legras, G. Berthet, E. Briaud, E. Carboni, C. Duchamp et al. (2022). 'Aerosol characterization of the stratospheric plume from the volcanic eruption at Hunga Tonga 15 January 2022'. *Geophys. Res. Lett.*, 49, e2022GL099394. DOI: 10.1029/2022GL099394.

Knepp, T. N., M. Kovilakam, L. Thomason and S. J. Miller (2024). 'Characterization of stratospheric particle size distribution uncertainties using SAGE II and SAGE III/ISS extinction spectra'. *Atmos. Meas. Tech.*, 17, pp. 2025–2054. DOI: 10.5194/amt-17-2025-2024.

Kovilakam, M., L. W. Thomason, N. Ernest, L. Rieger, A. Bourassa and L. Millán (2020). 'The Global Space-based Stratospheric Aerosol Climatology (version 2.0): 1979–2018'. *Earth Syst. Sci. Data*, 12, pp. 2607–2634. DOI: 10.5194/essd-12-2607-2020.

Kovilakam, M., L. W. Thomason, M. Verkerk, T. Aubry and T. N. Knepp (2025). 'OMPS-LP aerosol extinction coefficients and their applicability in GloSSAC'. *Atmos. Chem. Phys.*, 25, pp. 535–553. DOI: 10.5194/acp-25-535-2025.

Landulfo, E., F. S. Lopes, J. C. Antuña, R. Arredondo and G. Taha (2022a). *Monitoring stratospheric aerosols in South America with ground-based lidar.* https://homepages.see.leeds.ac.uk/~amtgwm/SSirC_Landulfo_ForShareOffUnivLeedsSEEpage.pdf. May 2022 SSiRC workshop presentation.

Landulfo, E., F. S. Lopes, J.-P. Vernier, J. C. Antuña and the LALINET team (2022b). *VolRes and the BRAVO field campaign.* https://homepages.see.leeds.ac.uk/~amtgwm/SSirC_BRAVO_Landulfo_ForShareOffSEEpage.pdf. May 2022 SSiRC workshop presentation.

Legras, B., C. Duchamp, P. Sellitto, A. Podglajen, E. Carboni, R. Siddans, J.-U. Grooß, S. Khaykin and F. Ploeger (2022). 'The evolution and dynamics of the Hunga Tonga–Hunga Ha'apai sulfate aerosol plume in the stratosphere'. *Atmos. Chem. Phys.*, 22, pp. 14957–14970. DOI: 10.5194/acp-22-14957-2022.

Li, C., N. A. Krotkov, S. A. Carn, Y. Zhang, R. J. D. Spurr and J. Joiner (2017). 'New-generation NASA Aura Ozone Monitoring Instrument volcanic SO_2 dataset: Algorithm description, initial results, and continuation with the Suomi-NPP Ozone Mapping and Profiler Suite'. *Atmos. Meas. Tech.*, 10, pp. 445–458. DOI: 10.5194/amt-10-445-2017.

Li, Y., C. Pedersen, J. Dykema, J.-P. Vernier, S. Vattioni, A. K. Pandit, A. Stenke, E. Asher, T. Thornberry, M. A. Todt et al. (2023). 'In situ measurements of perturbations to stratospheric aerosol and modeled ozone and radiative impacts following the 2021 La Soufrière eruption'. *Atmos. Chem. Phys.*, 23, pp. 15351–15364. DOI: 10.5194/acp-23-15351-2023.

Limbacher, J. A., R. A. Kahn and J. Lee (2022). 'The new MISR research aerosol retrieval algorithm: A multi-angle, multi-spectral, bounded-variable least-squares retrieval of aerosol particle properties over both land and water'. *Atmos. Meas. Tech.*, 15, pp. 6865–6887. DOI: 10.5194/amt-15-6865-2022.

Livesey, N. J., W. G. Read, P. A. Wagner, L. Froidevaux, A. Lambert, G. L. Manney et al. (2020). *EOS MLS Version 4.2x Level 2 and 3 data quality and description document.* Technical Report JPL-D33509 Rev. E. https://mls.jpl.nasa.gov/data/v4-2_data_quality_document.pdf. Jet Propulsion Laboratory, California Institute of Technology.

Livesey, N. J., W. G. Read, P. A. Wagner, L. Froidevaux, M. L. Santee, M. J. Schwartz et al. (2022). *EOS MLS Version 5.0x Level 2 and 3 data quality and description document.* Technical Report JPL-D105336 Rev. B. https://mls.jpl.nasa.gov/data/v5-0_data_quality_document.pdf. Jet Propulsion Laboratory, California Institute of Technology.

Livesey, N. J., W. G. Read, L. Froidevaux, A. Lambert, M. L. Santee, M. J. Schwartz, L. F. Millán, R. F. Jarnot, P. A. Wagner, D. F. Hurst et al. (2021). 'Investigation and amelioration of long-term instrumental drifts in water vapor and nitrous oxide measurements

from the Aura Microwave Limb Sounder (MLS) and their implications for studies of variability and trends'. *Atmos. Chem. Phys.*, 21, pp. 15409–15430. DOI: 10.5194/acp-21-15409-2021.

Loughman, R. P., P. K. Bhartia, Z. Chen, P. Xu, E. Nyaku and G. Taha (2018). 'The Ozone Mapping and Profiler Suite (OMPS) Limb Profiler Version 1 aerosol extinction retrieval algorithm: Theoretical basis'. *Atmos. Meas. Tech.*, 11, pp. 2633–2651. DOI: 10.5194/amt-11-2633-2018.

Luo, B. (2016). *Stratospheric aerosol data for use in CMIP6 models*. ftp://iacftp.ethz.ch/pub_read/luo/CMIP6/Readme_Data_Description.pdf.

Millán, L., M. L. Santee, A. Lambert, N. J. Livesey, F. Werner, M. J. Schwartz, H. C. Pumphrey, G. L. Manney, Y. Wang, H. Su et al. (2022). 'The Hunga Tonga-Hunga Ha'apai Hydration of the Stratosphere'. *Geophys. Res. Lett.*, 49, e2022GL099381. DOI: 10.1029/2022gl099381.

Morgenstern, O., M. I. Hegglin, E. Rozanov, F. M. O'Connor, N. L. Abraham, H. Akiyoshi, A. T. Archibald, S. Bekki, N. Butchart, M. P. Chipperfield et al. (2017). 'Review of the global models used within phase 1 of the Chemistry–Climate Model Initiative (CCMI)'. *Geosci. Model Dev.*, 10, pp. 639–671. DOI: 10.5194/gmd-10-639-2017.

Nagai, T., B. Liley, T. Sakai, T. Shibata and O. Uchino (2010). 'Post-Pinatubo Evolution and Subsequent Trend of the Stratospheric Aerosol Layer Observed by Mid-Latitude Lidars in Both Hemispheres'. *Scientific Online Letters on the Atmosphere (SOLA)*, 6, pp. 69–72. DOI: 10.2151/sola.2010-018.

Norgren, M., L. E. Kalnajs and T. Deshler (2024). 'Measurements of Total Aerosol Concentration in the Stratosphere: A New Balloon-Borne Instrument and a Report on the Existing Measurement Record'. *J. Geophys. Res.*, 129, e2024JD040992. DOI: 10.1029/2024JD040992.

Park, M., W. J. Randel, R. P. Damadeo, D. E. Flittner, S. M. Davis, K. H. Rosenlof, N. Livesey, A. Lambert and W. Read (2021). 'Near-Global Variability of Stratospheric Water Vapor Observed by SAGE III/ISS'. *J. Geophys. Res.*, 126, e2020JD034274. DOI: 10.1029/2020JD034274.

Pedatella, N. M., X. Yue and W. S. Schreiner (2015). 'An improved inversion for FORMOSAT-3/COSMIC ionosphere electron density profiles'. *J. Geophys. Res.*, 120, pp. 8942–8953. DOI: 10.1002/2015JA021704.

Pinnick, R. G. and D. J. Hofmann (1973). 'Efficiency of light-scattering aerosol particle counters'. *Appl. Optics*, 12, pp. 2593–2597. DOI: 10.1364/AO.12.002593.

Pitts, M. C., L. R. Poole and R. Gonzalez (2018). 'Polar stratospheric cloud climatology based on CALIPSO spaceborne lidar measurements from 2006 to 2017'. *Atmos. Chem. Phys.*, 18, pp. 10881–10913. DOI: 10.5194/acp-18-10881-2018.

Prata, A. T., S. A. Young, S. T. Siems and M. J. Manton (2017). 'Lidar ratios of stratospheric volcanic ash and sulfate aerosols retrieved from CALIOP measurements'. *Atmos. Chem. Phys.*, 17, pp. 8599–8618. DOI: 10.5194/acp-17-8599-2017.

Randel, W. J., B. R. Johnston, J. J. Braun, S. Sokolovskiy, H. Vömel, A. Podglajen and B. Legras (2023). 'Stratospheric Water Vapor from the Hunga Tonga–Hunga Ha'apai Volcanic Eruption Deduced from COSMIC-2 Radio Occultation'. *Remote Sens.*, 15, 2167, p. 2167. DOI: 10.3390/rs15082167.

Randel, W. J., A. K. Smith, F. Wu, C.-Z. Zou and H. Qian (2016). 'Stratospheric Temperature Trends over 1979–2015 Derived from Combined SSU, MLS, and SABER Satellite Observations'. *J. Climate*, 29, pp. 4843–4859. DOI: 10.1175/jcli-d-15-0629.1.

Reinisch, B. W. (1987). 'New Techniques in Ground-Based Ionospheric Sounding and Studies'. *Radio Sci.*, 21, pp. 331–341. DOI: 10.1029/RS021i003p00331.

Remer, L. A. and Y. J. Kaufman (2006). 'Aerosol direct radiative effect at the top of the atmosphere over cloud free ocean derived from four years of MODIS data'. *Atmos. Chem. Phys.*, 6, pp. 237–253. DOI: 10.5194/acp-6-237-2006.

Remsberg, E. E., B. T. Marshall, M. Garcia-Comas, D. Krueger, G. S. Lingenfelser, J. Martin-Torres, M. G. Mlynczak, J. M. Russell III, A. K. Smith, Y. Zhao et al. (2008). 'Assessment of the quality of the Version 1.07 temperature-versus-pressure profiles of the middle atmosphere from TIMED/SABER'. *J. Geophys. Res.*, 113. DOI: 10.1029/2008JD010013.

Renard, J.-B., F. Dulac, G. Berthet, T. Lurton, D. Vignelles, F. Jégou, T. Tonnelier, M. Jeannot, B. Couté, R. Akiki et al. (2016). 'LOAC: a small aerosol optical counter/sizer for ground-based and balloon measurements of the size distribution and nature of atmospheric particles – Part 1: Principle of measurements and instrument evaluation'. *Atmos. Meas. Tech.*, 9, pp. 1721–1742. DOI: 10.5194/amt-9-1721-2016.

Revell, L. E., A. Stenke, B. Luo, S. Kremser, E. Rozanov, T. Sukhodolov and T. Peter (2017). 'Impacts of Mt Pinatubo volcanic aerosol on the tropical

stratosphere in chemistry–climate model simulations using CCMI and CMIP6 stratospheric aerosol data'. *Atmos. Chem. Phys.*, 17, pp. 13139–13150. DOI: 10.5194/acp-17-13139-2017.

Rideout, W. and A. Coster (2006). 'Automated GPS processing for global total electron content data'. *GPS Solutions*, 10, pp. 219–228. DOI: 10.1007/s10291-006-0029-5.

Rosen, J. M. (1964). 'The vertical distribution of dust to 30 km'. *J. Geophys. Res.*, 69, pp. 4673–4676. DOI: 10.1029/JZ069i021p04673.

Rosen, J. M. and D. J. Hofmann (1977). 'Balloon-borne measurements of condensation nuclei'. *J. Appl. Meteorol.*, 16, pp. 56–62. DOI: 10.1175/1520-0450(1977)016<0056:BMOCN>2.0.CO;2.

Rosen, J. M., D. J. Hofmann and J. W. Harder (1988). 'Aerosol measurements in the winter/spring Antarctic stratosphere. 2. Impact on Polar Stratospheric Cloud theories'. *J. Geophys. Res.*, 93, pp. 677–686. DOI: 10.1029/JD093iD01p00677.

Rozanov, A., C. Pohl, C. Arosio, A. Bourassa, K. Bramstedt, E. Malinina, L. Rieger and J. P. Burrows (2024). 'Retrieval of stratospheric aerosol extinction coefficients from sun-normalized Ozone Mapper and Profiler Suite Limb Profiler (OMPS-LP) measurements'. *Atmos. Meas. Tech.*, 17, pp. 6677–6695. DOI: 10.5194/amt-17-6677-2024.

Russell, J. M., M. G. Mlynczak, L. L. Gordley, J. Tansock and R. Esplin (1999). 'Overview of the SABER experiment and preliminary calibration results'. *SPIE Proc.*, 3756, pp. 277–288. DOI: 10.1117/12.366382.

Ryan, R. A., M. A. Vaughan, S. D. Rodier, J. L. Tackett, J. A. Reagan, R. A. Ferrare, J. W. Hair, J. A. Smith and B. J. Getzewich (2024). 'Total column optical depths retrieved from CALIPSO lidar ocean surface backscatter'. *Atmos. Meas. Tech.*, 17, pp. 6517–6545. DOI: 10.5194/amt-17-6517-2024.

Sakai, T., O. Uchino, T. Nagai, B. Liley, I. Morino and T. Fujimoto (2016). 'Long-term variation of stratospheric aerosols observed with lidars over Tsukuba, Japan, from 1982 and Lauder, New Zealand, from 1992 to 2015'. *J. Geophys. Res.*, 121, pp. 10, 283–10, 293. DOI: 10.1002/2016JD025132.

Saunders, R., J. Hocking, E. Turner, P. Rayer, M. Matricardi, A. Geer et al. (2018). 'An update on the RTTOV fast radiative transfer model (currently at version 12)'. *Geosci. Model Dev.*, 11, pp. 2717–2737. DOI: 10.5194/gmd-11-2717-2018.

Savigny, C. von and C. G. Hoffmann (2020). 'Issues related to the retrieval of stratospheric-aerosol particle size information based on optical measurements'. *Atmos. Meas. Tech.*, 13, pp. 1909–1920. DOI: 10.5194/amt-13-1909-2020.

Schulz, M., C. Textor, S. Kinne, Y. Balkanski, S. Bauer, T. Berntsen, T. Berglen, O. Boucher, F. Dentener, S. Guibert et al. (2006). 'Radiative forcing by aerosols as derived from the AeroCom present-day and pre-industrial simulations'. *Atmos. Chem. Phys.*, 6, pp. 5225–5246. DOI: 10.5194/acp-6-5225-2006.

Sellitto, P., H. Guermazi, E. Carboni, R. Siddans and M. Burton (2019). 'Unified quantitative observation of coexisting volcanic sulfur dioxide and sulfate aerosols using ground-based Fourier transform infrared spectroscopy'. *Atmos. Meas. Tech.*, 12, pp. 5381–5389. DOI: 10.5194/amt-12-5381-2019.

Sellitto, P., R. Siddans, R. Belhadji, E. Carboni, B. Legras, A. Podglajen and et al. (2024). 'Observing the SO_2 and sulfate aerosol plumes from the 2022 Hunga eruption with the Infrared Atmospheric Sounding Interferometer (IASI)'. *Geophys. Res. Lett.*, 51, e2023GL105565. DOI: 10.1029/2023GL105565.

Shaikh, M. M., R. Notarpietro and B. Nava (2014). 'The impact of spherical symmetry assumption on radio occultation data inversion in the ionosphere: An assessment study'. *Adv. Space Res.*, 53, pp. 599–608. DOI: 10.1016/j.asr.2013.10.025.

Shallcross, S. E. (2020). 'The role of volcanic ash in the global dispersion of the aerosol cloud from major tropical eruptions'. https://etheses.whiterose.ac.uk/id/eprint/28125/1/Sarah_Shallcross_PhD_thesis.pdf. PhD thesis. University of Leeds.

Siddans, R. (2019). *Water Vapour Climate Change Initiative (WV_cci) – Phase One, Deliverable 2.2; Version 1.0, 27 March 2019*. Technical Report. https://climate.esa.int/documents/1337/Water_Vapour_CCI_D2.2_ATBD_Part2-IMS_L2_product_v1.0.pdf. European Space Agency (ESA) / ECSAT.

Siddans, R. (2023). *Water Vapour Climate Change Initiative (WV_cci) – Phase Two, ATBD Part 2 – IMS L2 Product, Version 2.0, 21 November 2023*. Technical Report CCIWV.REP.005, D2.2. https://climate.esa.int/media/documents/Water_Vapour_CCI_D2.2_ATBD_Part2-IMS_L2_product_v2.0.pdf. European Space Agency (ESA) / ECSAT.

Souza, G., J.-P. Vernier, D. Quintão, B. Biazon, F. Lopes, J. Ricardo, A. K. Pandit, R. C. Das, H. Liu, T. N. N. Knepp et al. (2025). 'Sedimentation and growth of volcanic aerosols within the Hunga plume: Insights from unique tropical in situ and satellite measurements'. *ESS Open Archive*, DOI: 10.22541/essoar.174241613.36494891/v1.

SPARC (2006). *Assessment of Stratospheric Aerosol Properties (ASAP)*. Tech. rep. SPARC Report No. 4. https://www.aparc-climate.org/publications/sparc-reports/sparc-report-no-4/. Stratosphere–troposphere Processes and their Role in Climate (SPARC) Project, WCRP.

SPARC (2022). *Reanalysis Intercomparison Project (S-RIP) Final Report*. Tech. rep. SPARC Report No. 10, WCRP-6/2021. https://www.aparc-climate.org/sparc-reports/sparc-report-no-10/. SPARC/WCRP.

Stankov, S. M., T. G. W. Verhulst and D. Sapundjiev (2023). 'Automatic Ionospheric Weather Monitoring With DPS-4D Ionosonde and ARTIST-5 Autoscaler: System Performance at a Mid-Latitude Observatory'. *Radio Sci.*, 58, e2022RS007628. DOI: 10.1029/2022RS007628.

Steiner, A. K., F. Ladstädter, W. J. Randel, A. C. Maycock, Q. Fu, C. Claud, H. Gleisner, L. Haimberger, S.-P. Ho and P. Keckhut (2020). 'Observed temperature changes in the troposphere and stratosphere from 1979 to 2018'. *J. Climate*, 33, pp. 8165–8194. DOI: 10.1175/jcli-d-19-0998.1.

Stephens, G. L., D. G. Vane, R. J. Boain, G. G. Mace, K. Sassen, Z. Wang, A. J. Illingworth, E. J. O'connor, W. B. Rossow, S. L. Durden et al. (2002). 'The CLOUDSAT mission and the A-train: A new Dimension of Space-Based Observations of Clouds and Precipitation'. *Bull. Am. Meteorol. Soc.*, 83, pp. 1771–1790. DOI: 10.1175/bams-83-12-1771.

Syndergaard, S., W. S. Schreiner, C. Rocken, D. C. Hunt and K. F. Dymond (2006). 'Preparing for COSMIC: Inversion and Analysis of Ionospheric Data Products'. *Atmosphere and Climate: Studies by Occultation Methods*. Ed. by U. Foelsche, G. Kirchengast and A. Steiner. Berlin, Heidelberg: Springer Berlin Heidelberg, pp. 137–146. DOI: 10.1007/3-540-34121-8_12.

Tackett, J. L., J. Kar, M. A. Vaughan, B. J. Getzewich, M.-H. Kim, J.-P. Vernier, A. H. Omar, B. E. Magill, M. C. Pitts and D. M. Winker (2023). 'The CALIPSO version 4.5 stratospheric aerosol subtyping algorithm'. *Atmos. Meas. Tech.*, 16, pp. 745–768. DOI: 10.5194/amt-16-745-2023.

Taha, G., R. Loughman, T. Zhu, L. Thomason, J. Kar, L. Rieger and A. Bourassa (2021). 'OMPS LP Version 2.0 multi-wavelength aerosol extinction coefficient retrieval algorithm'. *Atmos. Meas. Tech.*, 14, pp. 1015–1036. DOI: 10.5194/amt-14-1015-2021.

Tarasick, D. W., H. G. J. Smit, A. M. Thompson, G. A. Morris, J. C. Witte, J. Davies, W. Davies, T. Nakano, R. van Malderen, R. Stübi et al. (2021). 'Improving ECC ozonesonde data quality: Assessment of current methods and outstanding issues'. *Earth Space Sci.*, 8, e2019EA000914. DOI: 10.1029/2019EA000914.

Tencé, F., J. Jumelet, S. Bekki, S. Khaykin, A. Sarkissian and P. Keckhut (2022). 'Australian Black Summer Smoke Observed by Lidar at the French Antarctic Station Dumont d'Urville'. *J. Geophys. Res.*, 127, e2021JD035349. DOI: 10.1029/2021JD035349.

Themens, D. R., B. Reid and S. Elvidge (2022). 'ARTIST ionogram autoscaling confidence scores: best practices'. *URSI Radio Sci. Lett.*, 4, pp. 1–5. DOI: 10.46620/22-0001.

Themens, D. R., P. T. Jayachandran, R. B. Langley, J. W. MacDougall and M. J. Nicolls (2013). 'Determining receiver biases in GPS-derived total electron content in the auroral oval and polar cap region using ionosonde measurements'. *GPS Solut.*, 17, pp. 357–369. DOI: 10.1007/s10291-012-0284-6.

Theys, N., I. De Smedt, H. Yu, T. Danckaert, J. van Gent, C. Hörmann, T. Wagner, P. Hedelt, H. Bauer, F. Romahn et al. (2017). 'Sulfur dioxide retrievals from TROPOMI onboard Sentinel-5 Precursor: algorithm theoretical basis'. *Atmos. Meas. Tech.*, pp. 119–153. DOI: 10.5194/amt-10-119-2017.

Thomason, L. W., S. P. Burton, B.-P. Luo and T. Peter (2008). 'SAGE II measurements of stratospheric aerosol properties at non-volcanic levels'. *Atmos. Chem. Phys.*, 8, pp. 983–995. DOI: 10.5194/acp-8-983-2008.

Thomason, L. W., L. R. Poole and T. Deshler (1997). 'A global climatology of stratospheric aerosol surface area density deduced from Stratospheric Aerosol and Gas Experiment II measurements: 1984–1994'. *J. Geophys. Res.*, 102, pp. 8967–8976. DOI: 10.1029/96JD02962.

Thomason, L. W., M. Kovilakam, A. Schmidt, C. von Savigny, T. Knepp and L. Rieger (2021). 'Evidence for the predictability of changes in the stratospheric aerosol size following volcanic eruptions of diverse magnitudes using space-based instruments'. *Atmos. Chem. Phys.*, 21, pp. 1143–1158. DOI: 10.5194/acp-21-1143-2021.

Todt, M. A., E. Asher, E. Hall, P. Cullis, A. Jordan, K. Xiong, D. F. Hurst and T. Thornberry (2023). 'Baseline Balloon Stratospheric Aerosol Profiles (B2SAP)—Systematic Measurements of Aerosol Number Density and Size'. *J. Geophys. Res.*, 128, e2022JD038041. DOI: 10.1029/2022JD038041.

Vaughan, G., D. P. Wareing, S. B. Jones, L. Thomas and N. Larsen (1994). 'Lidar measurements of Mt. Pinatubo aerosols at Aberystwyth from August 1991 through March 1992'. *Geophys. Res. Lett.*, 21, pp. 1315–1318. DOI: 10.1029/93gl02893.

Veefkind, J., I. Aben, K. McMullan, H. Förster, J. de Vries, G. Otter, J. Claas, H. Eskes, J. de Haan, Q. Kleipool et al. (2012). 'TROPOMI on the ESA Sentinel-5 Precursor: A GMES mission for global observations of the atmospheric composition for climate, air quality and ozone layer applications'. *Remote Sens. Env.*, 120, pp. 70–83. DOI: 10.1016/j.rse.2011.09.027.

Vernier, H., D. Quintão, B. Biazon, E. Landulfo, G. Souza, F. J. S. Lopes, N. Rastogi, R. Meena, H. Liu, S. Fadnavis et al. (2023). 'Understanding the impact of Hunga-Tonga undersea eruption on the stratospheric aerosol population using Balloon measurements, Satellite data, and model simulations'. *EGU General Assembly 2023*. Vienna, Austria: Copernicus Meetings, EGU23–6882. DOI: 10.5194/egusphere-egu23-6882.

Vernier, H., D. Quintão, B. Biazon, E. Landulfo, G. Souza, V. A. Santos, J. S. F. Lopes, C. P. A. Mendes, A. S. J. D. Matta, K. P. Damaris et al. (2025). 'Balloon Observations Suggesting Sea Salt Injection into the Stratosphere from Hunga Tonga-Hunga Ha'apai'. DOI: 10.5194/egusphere-2025-924.

Vernier, J.-P., C. Timmreck and S. Kremser (2022). *Atmospheric Impacts of the 2022 Hunga Tonga–Hunga Ha'apai Eruption: Summary of VolRes Discussion for the SSiRC Community*. Tech. rep. https://sparc-ssirc.org/downloads/VolRes_summary_of_the_Hunga-Vfinal.pdf. SPARC Stratospheric Sulfur and its Role in Climate (SSiRC) Initiative.

Vernier, J.-P., T. J. Aubry, C. Timmreck, A. Schmidt, L. Clarisse, F. Prata, N. Theys, A. T. Prata, G. Mann, H. Choi et al. (2024). 'The 2019 Raikoke eruption as a testbed used by the Volcano Response group for rapid assessment of volcanic atmospheric impacts'. *Atmos. Chem. Phys.*, 24, pp. 5765–5782. DOI: 10.5194/acp-24-5765-2024.

Vömel, H., S. Evan and M. Tully (2022). 'Water vapor injection into the Stratosphere by Hunga Tonga-Hunga Ha'apai'. *Science*, 377, pp. 1444–1447. DOI: 10.1126/science.abq2299.

Wang, H. J. R., R. Damadeo, D. Flittner, N. Kramarova, G. Taha, S. Davis, A. M. Thompson, S. Strahan, Y. Wang, L. Froidevaux et al. (2020). 'Validation of SAGE III/ISS Solar Occultation Ozone Products With Correlative Satellite and Ground-Based Measurements'. *J. Geophys. Res.*, 125, e2020JD032430. DOI: 10.1029/2020jd032430.

Wargan, K., B. Weir, G. L. Manney, S. E. Cohn, K. E. Knowland, P. A. Wales and N. J. Livesey (2023). 'M2-SCREAM: A Stratospheric Composition Reanalysis of Aura MLS Data With MERRA-2 Transport'. *Earth Space Sci.*, 10, e2022EA002632. DOI: 10.1029/2022ea002632.

Waters, J. W., L. Froidevaux, R. S. Harwood, R. F. Jarnot, H. M. Pickett, W. G. Read, P. H. Siegel, R. E. Cofield, M. J. Filipiak, D. A. Flower et al. (2006). 'The Earth observing system microwave limb sounder (EOS MLS) on the aura Satellite'. *IEEE Trans. Geosci. Remote Sens.*, 44, pp. 1075–1092. DOI: 10.1109/tgrs.2006.873771.

Winker, D. M., W. H. Hunt and M. J. McGill (2007). 'Initial performance assessment of CALIOP'. *Geophys. Res. Lett.*, 34. DOI: 10.1029/2007gl030135.

Wright, C. J., N. P. Hindley, M. J. Alexander, M. Barlow, L. Hoffmann, C. N. Mitchell, F. Prata, M. Bouillon, J. Carstens, C. Clerbaux et al. (2022). 'Surface-to-space atmospheric waves from Hunga Tonga-Hunga Ha'apai eruption'. *Nature*, 609, pp. 741–746. DOI: 10.1038/s41586-022-05012-5.

Yoon, S., A. Kotsakis, S. L. Alvarez, M. G. Spychala, E. Klovenski, P. Walter, G. Morris, E. Corrales, A. Alan, J. A. Diaz et al. (2022). 'Development and testing of a novel sulfur dioxide sonde'. *Atmos. Meas. Tech.*, 15, pp. 4373–4384. DOI: 10.5194/amt-15-4373-2022.

Young, S. A. and M. A. Vaughan (2009). 'The Retrieval of Profiles of Particulate Extinction from Cloud-Aerosol Lidar Infrared Pathfinder Satellite Observations (CALIPSO) Data: Algorithm Description'. *J. Atmos. Ocean. Tech.*, 26, pp. 1105–1119. DOI: 10.1175/2008JTECHA1221.1.

Young, S. A., M. A. Vaughan, R. E. Kuehn and D. M. Winker (2013). 'The Retrieval of Profiles of Particulate Extinction from Cloud–Aerosol Lidar and Infrared Pathfinder Satellite Observations (CALIPSO) Data: Uncertainty and Error Sensitivity Analyses'. *J. Atmos. Ocean. Tech.*, 30, pp. 395–428. DOI: 10.1175/jtech-d-12-00046.1.

Yu, W., R. Garcia, J. Yue, A. Smith, X. Wang, W. Randel, Z. Qiao, Y. Zhu, V. L. Harvey, S. Tilmes et al. (2023). 'Mesospheric temperature and circulation response to the Hunga Tonga-Hunga-Ha'apai volcanic eruption'. *J. Geophys. Res.*, 128, e2023JD039636. DOI: 10.1029/2023JD039636.

Zawada, D. J., L. A. Rieger, A. E. Bourassa and D. A. Degenstein (2018). 'Tomographic retrievals of ozone with the OMPS Limb Profiler: algorithm descrip-

tion and preliminary results'. *Atmos. Meas. Tech.*, 11, pp. 2375–2393. DOI: 10.5194/amt-11-2375-2018.

Zhang, C., C. Hu, S. Shang, F. E. Müller-Karger, Y. Li, M. Dai, B. Huang, X. Ning and H. Hong (2006). 'Bridging between SeaWiFS and MODIS for continuity of chlorophyll-a concentration assessments off Southeastern China'. *Remote Sens. Environ.*, 102, pp. 250–263. DOI: 10.1016/j.rse.2006.02.015.

Zhu, Y., H. Akiyoshi, V. Aquila, E. Asher, E. M. Bednarz, S. Bekki, C. Brühl, A. H. Butler, P. Case, S. Chabrillat et al. (2025). 'Hunga Tonga–Hunga Ha'apai Volcano Impact Model Observation Comparison (HTHH-MOC) project: experiment protocol and model descriptions'. *Geosci. Model Dev.*, 18, pp. 5487–5512. DOI: 10.5194/gmd-18-5487-2025.

Zou, C.-Z. and H. Qian (2016). 'Stratospheric Temperature Climate Data Record from Merged SSU and AMSU-A Observations'. *J. Atmos. Ocean. Tech.*, 33, pp. 1967–1984. DOI: 10.1175/JTECH-D-16-0018.1.

Zou, C.-Z., H. Qian, W. Wang, L. Wang and C. Long (2014). 'Recalibration and merging of SSU observations for stratospheric temperature trend studies'. *J. Geophys. Res.*, 119, pp. 13, 180–13, 205. DOI: 10.1002/2014JD021603.

S3 HTHH-MOC model validation and analysis results

S3.1 Evolution of water and aerosol plumes (Exp2)

Authors Valentina Aquila
Adam Bourassa
Sergey Khaykin
Alexandre Baron
Landon Rieger
Alexei Rozanov
Rei Ueyama

Contributors Slimane Bekki
Ewa M. Bednarz
Christoph Brühl
Parker Case
Simon Chabrillat
Margot Clyne
Peter R. Colarco
Lola Falletti
Nicolas Lebas
Cheng-Cheng Liu
Marion Marchand
Yifeng Peng
Samuel Rémy
Takashi Sekiya
Simone Tilmes
Xinyue Wang
Shingo Watanabe
Pengfei Yu
Wandi Yu
Jun Zhang
Yunqian Zhu
Zhihong Zhuo

While the figures in Chapter 3 focus on the comparison between Exp2a simulations and observations, the figures in the supplementary material help the analysis of the model simulations and the characterisation of the behaviour of models by showing, for instance, results for the simulated background conditions.

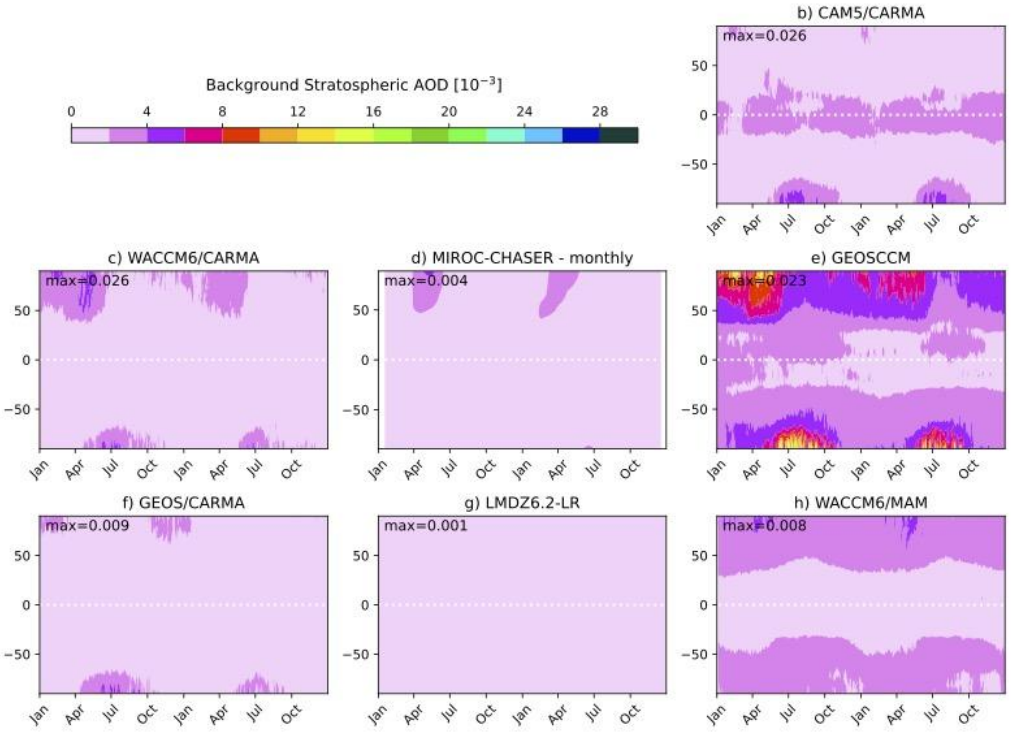

Figure S3.1: *Zonal mean background near-IR SAOD in the Exp2a models, as simulated in the experiment without Hunga injection. The SAOD of all models was calculated based on daily values, except for MIROC-CHASER which was calculated based on monthly means. The upper left value indicates the maximum SAOD value.*

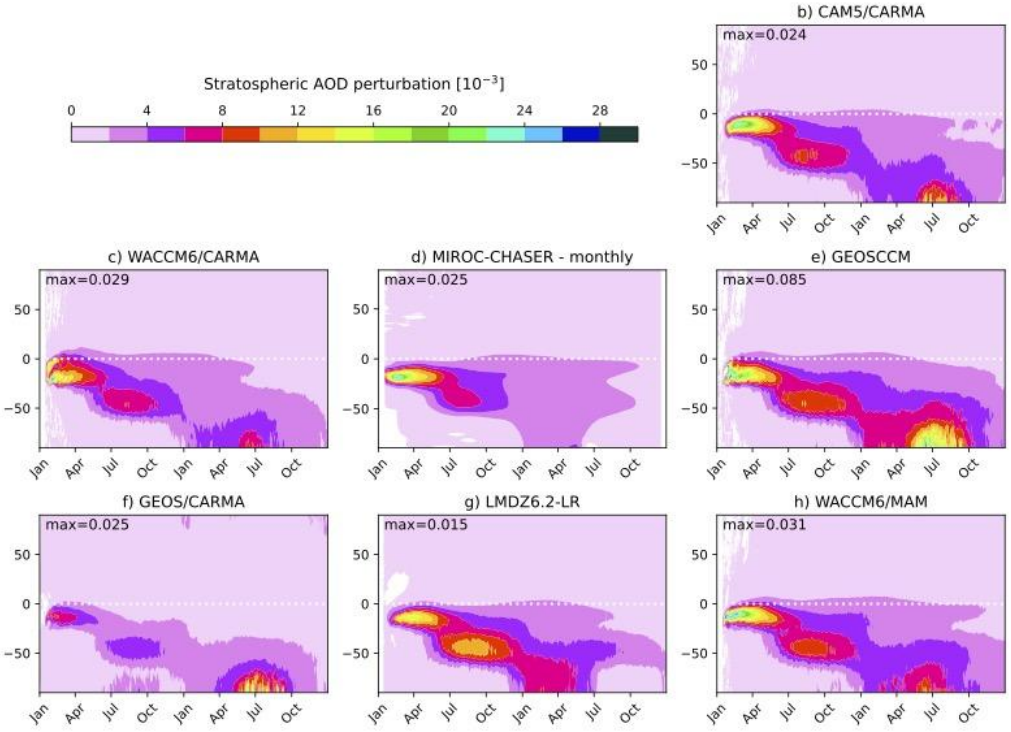

Figure S3.2: *Simulated zonal mean near-IR SAOD perturbation as a function of time and latitude in different global climate models, calculated as the difference between the simulation with and without Hunga. The SAOD of all models was calculated based on daily values, except for MIROC-CHASER and EMAC MPIC which only provided monthly means. The number in the upper left indicates the maximum value.*

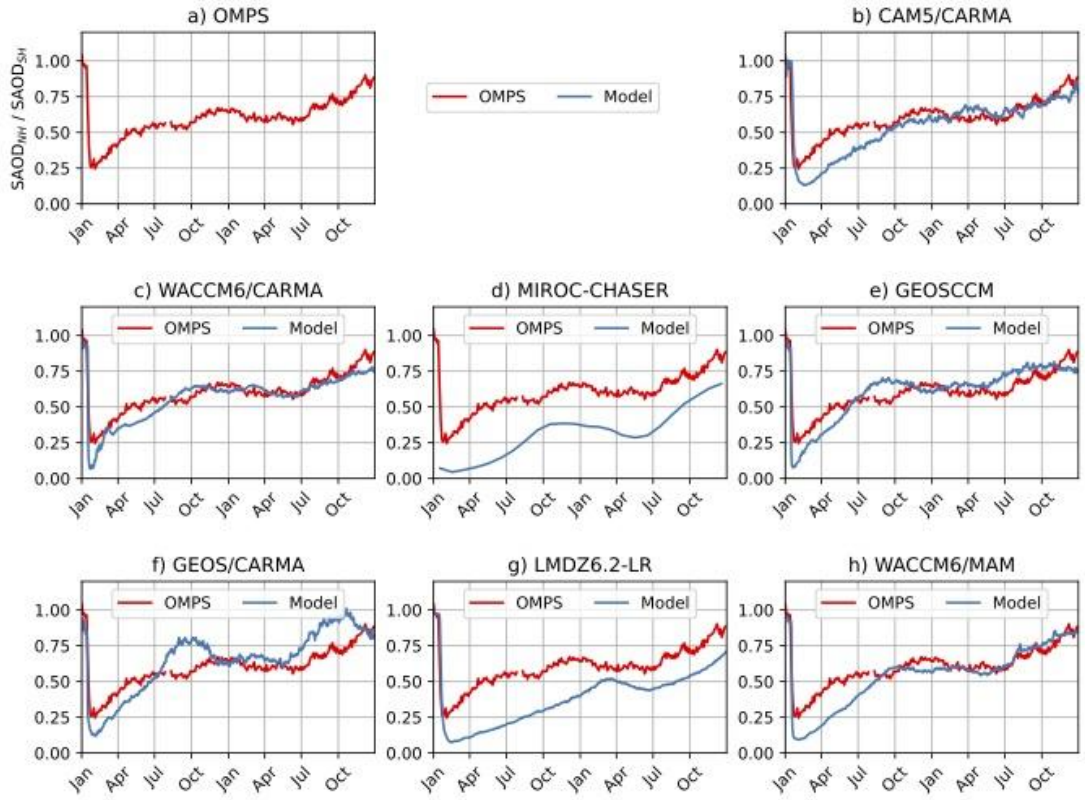

Figure S3.3: *Ratio of the average SAOD between Equator–20°N to SAOD between Equator–20°S in the Exp2a models (blue) and OMPS observations (red). The simulated ratio is lower than the observed one, indicating that models underestimate the SAOD in the northern tropics and therefore the cross-equatorial transport.*

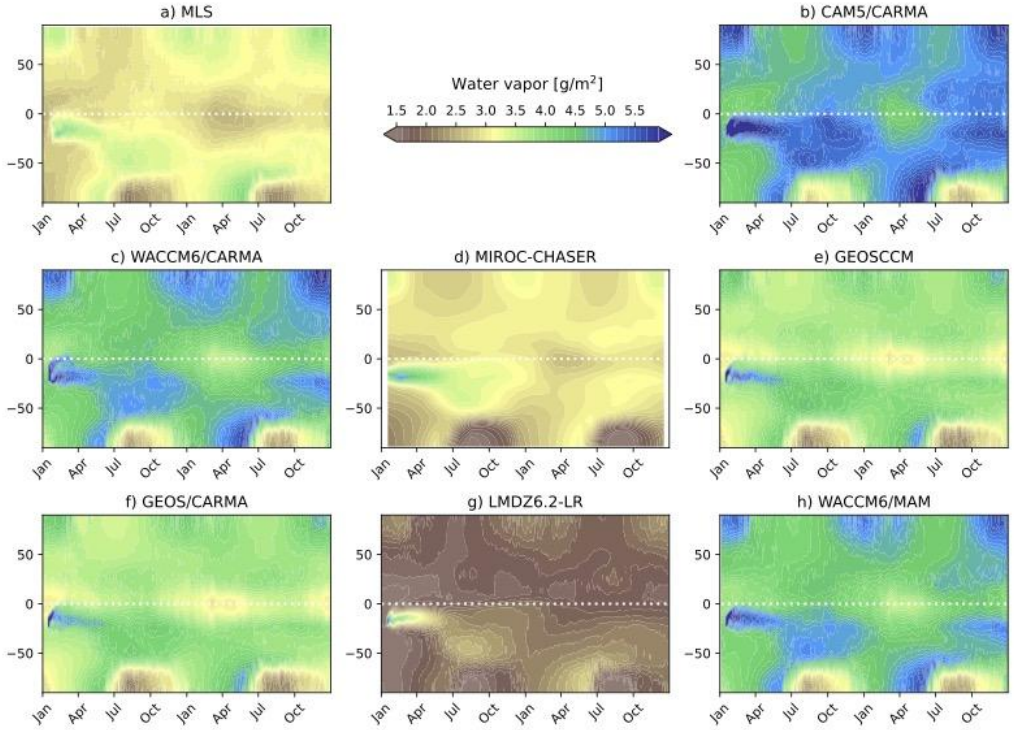

Figure S3.4: *Zonal mean stratospheric water vapour column in MLS water vapour and in the Exp2a simulation with the Hunga eruption. The simulated stratospheric water column is calculated above 100 hPa.*

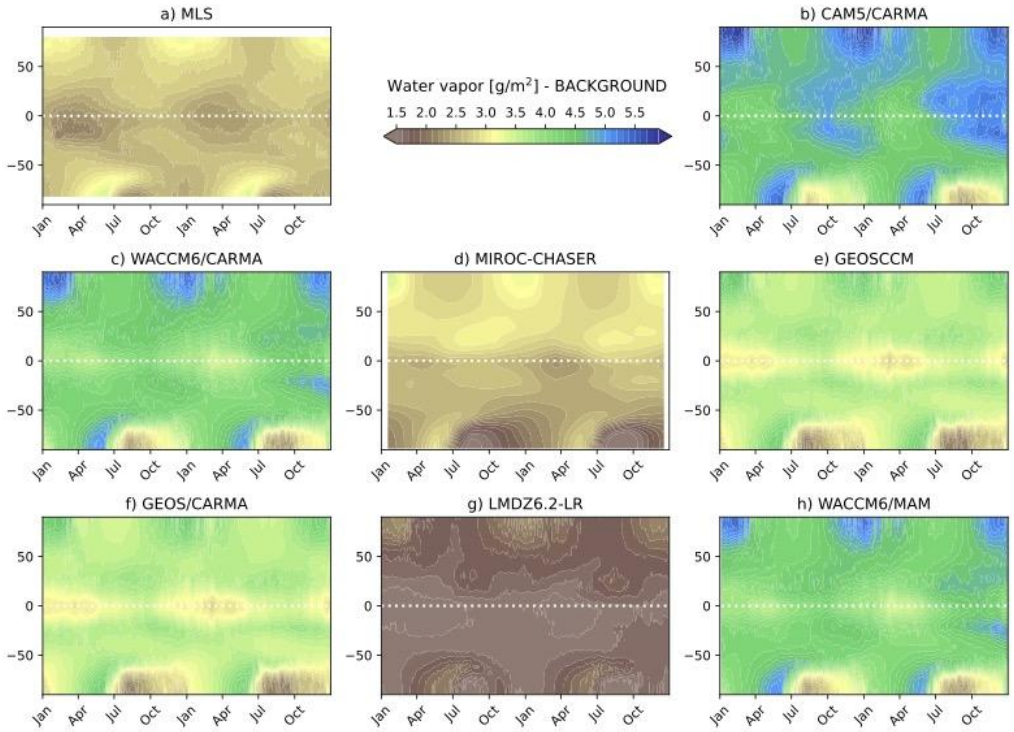

Figure S3.5: *Zonal mean stratospheric water vapour column in the MLS climatology calculated over 2005–2021 and the Exp2a simulation without the Hunga eruption. The simulated stratospheric water column is calculated above 100 hPa.*

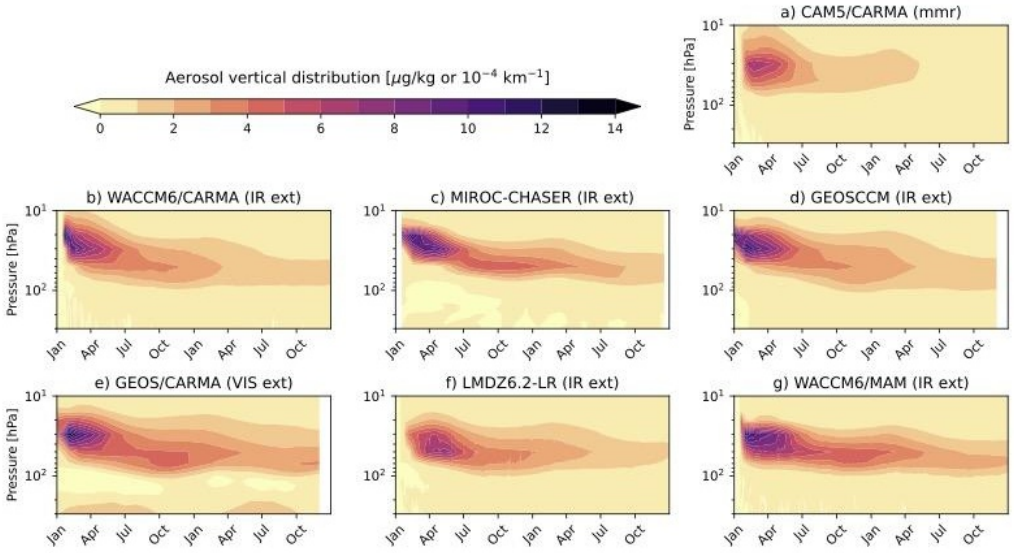

Figure S3.6: *Zonal mean aerosol perturbation as a function of time and altitude averaged over 30˚S to 30˚N in Exp2a simulations. Shown are the extinction coefficients (in 10^{-4} km^{-1}) in the near-IR range for all models except for GEOS/CARMA (e), which reports the extinction in the visible range, and CAM5/CARMA (a), which reports the sulfate mass mixing ratio (in $\mu g\ kg^{-1}$). Perturbations are based on daily values, except for MIROC-CHASER, which were calculated from monthly means.*

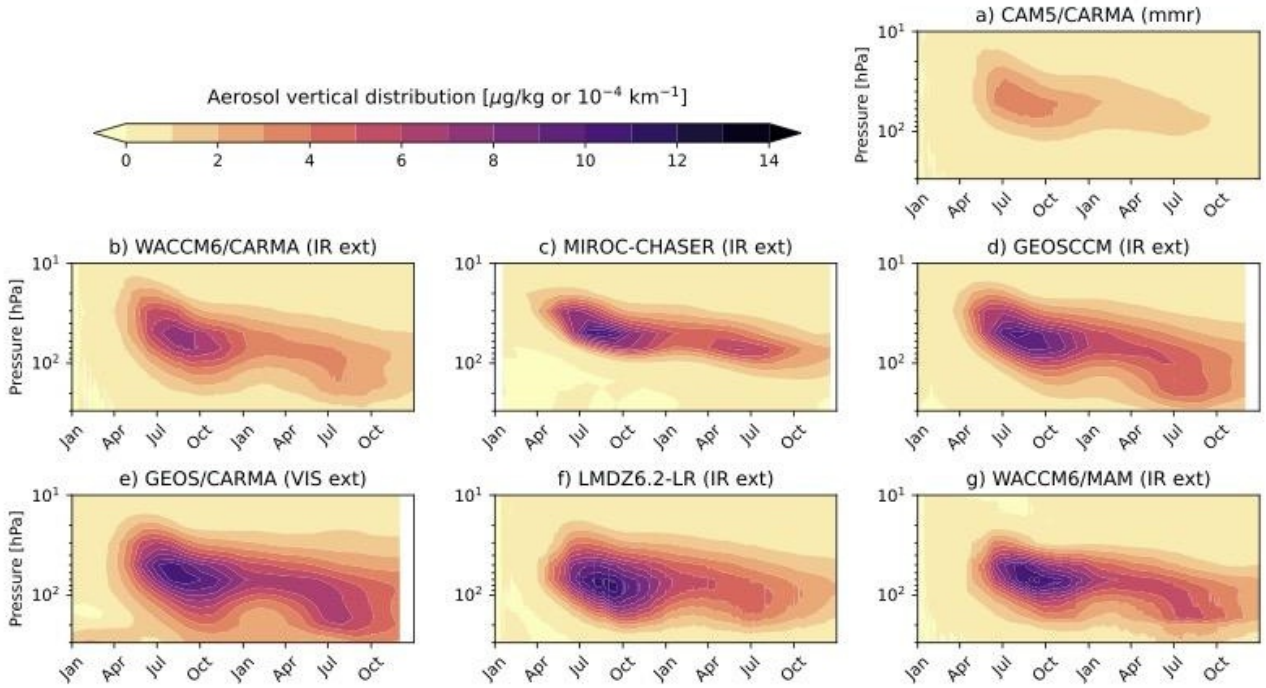

Figure S3.7: *As for Figure S3.6, but for 30˚S to 60˚S.*

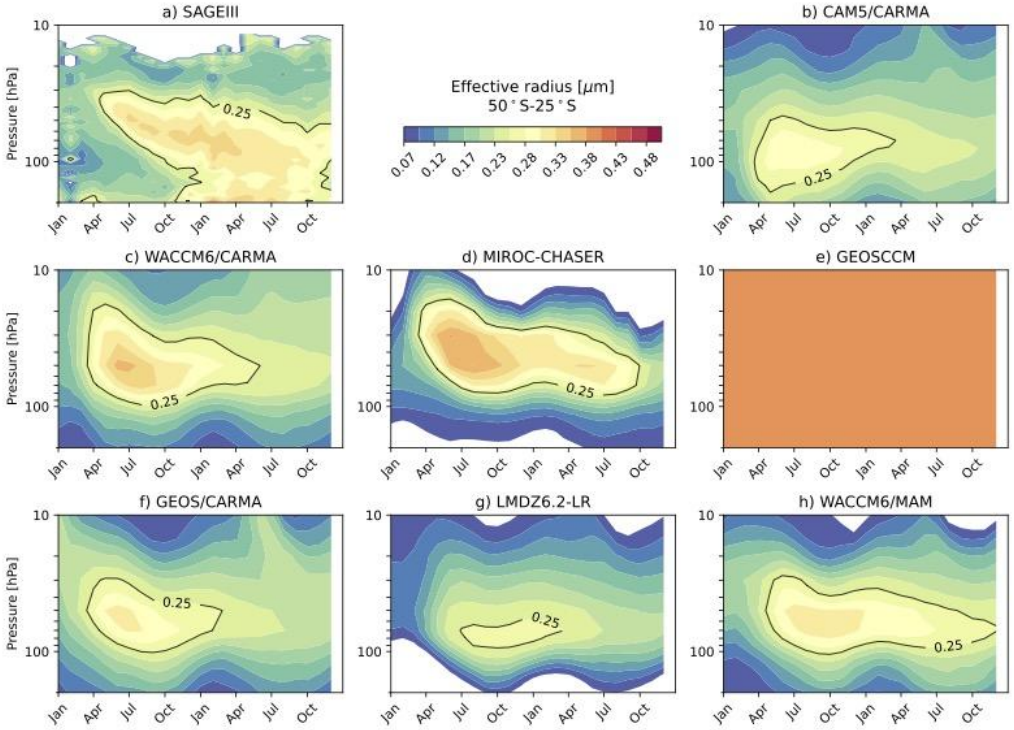

Figure S3.8: *Monthly mean aerosol effective radius averaged over the southern midlatitudes (25°S–50°S) as a function of time and altitude in SAGE III/ISS and in Exp2a models from January 2022 to December 2023. GEOSCCM is a bulk model and assumes a constant effective radius equal to 0.4 μm.*

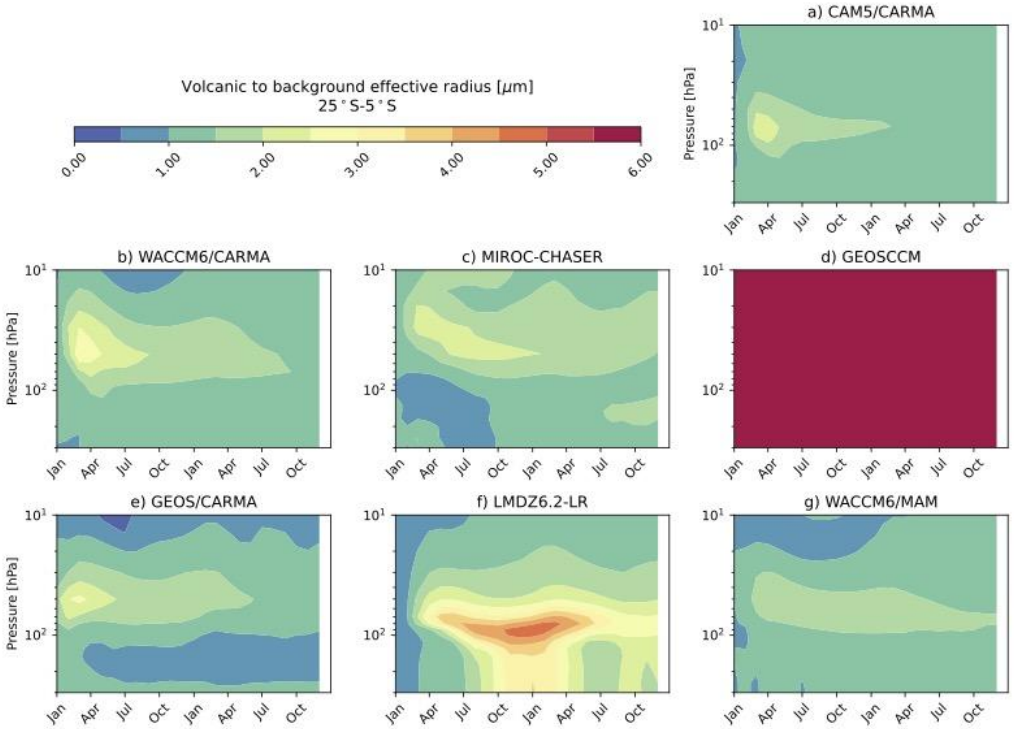

Figure S3.9: *Ratio between the monthly mean aerosol effective radius in the Exp2a simulation with and without Hunga eruption, averaged over 5°S–25°S. GEOSCCM is a bulk model and assumes a constant effective radius equal to 0.4 μm for the Hunga aerosols and 0.069511 μm for the background aerosols.*

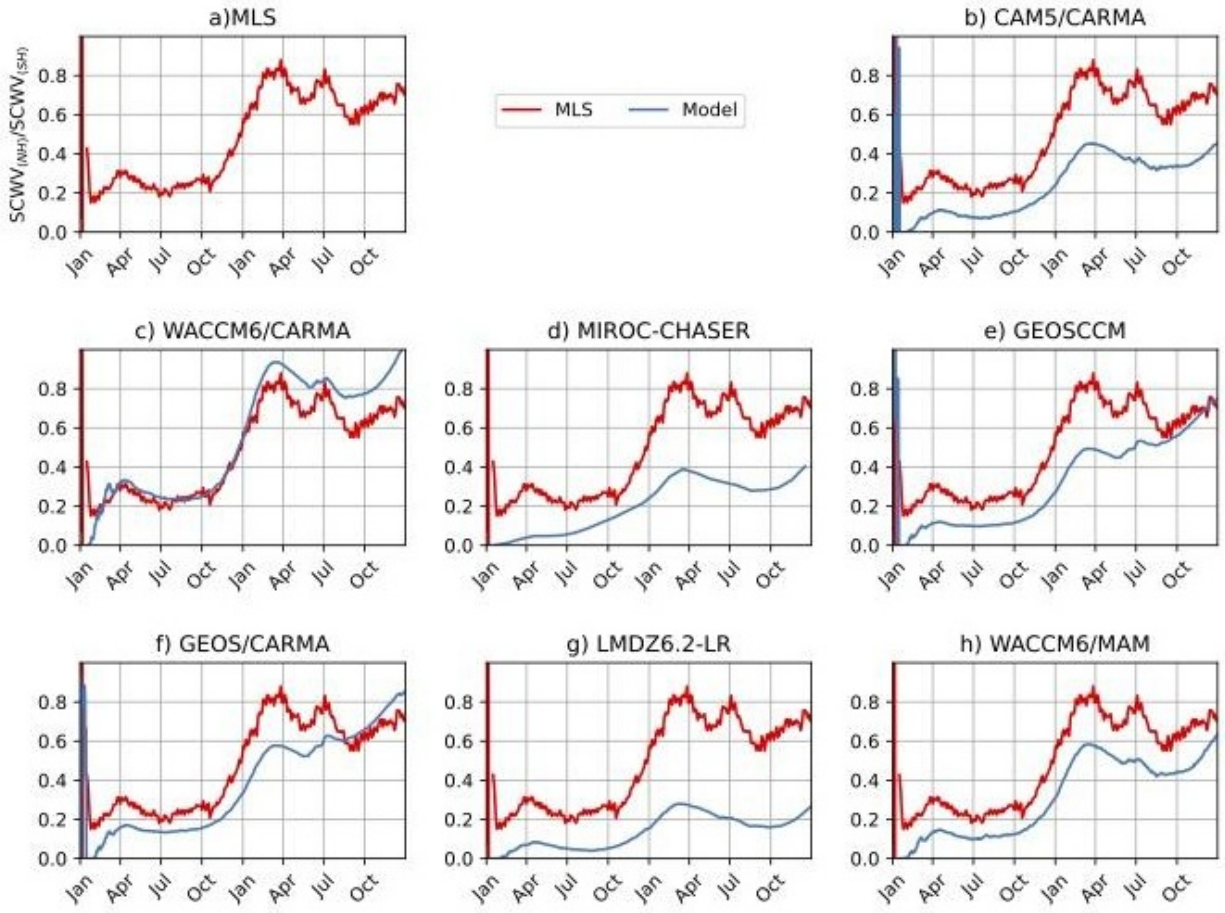

Figure S3.10: *Ratio between the mean stratospheric water vapour column in the northern hemisphere (equator–90°N) to the one in the southern hemisphere (equator–90°S) in MLS observations (red) and in Exp2a models (blue). Except for WACCM6/CARMA (c), all models underestimate the cross-equatorial transport of water vapour.*

S3.2 Hunga plumes evolution and stratospheric responses (based on EXP1 10-year output analysis)

Authors Zhihong Zhuo
Xinyue Wang
Yunqian Zhu
Wandi Yu
Ewa M. Bednarz
Eric Fleming
Peter R. Colarco
Shingo Watanabe
David Plummer
Georgiy Stenchikov
William Randel
Adam Bourassa
Valentina Aquila
Takashi Sekiya
Mark R. Schoeberl
Simone Tilmes
Jun Zhang
Paul J. Kushner
Francesco S. R. Pausata

This section is based on: Zhuo et al. (2025).

Zhuo, Z., Wang, X., Zhu, Y., Yu, W., Bednarz, E. M., Fleming, E., Colarco, P. R., Watanabe, S., Plummer, D., Stenchikov, G., Randel, W., Bourassa, A., Aquila, V., Sekiya, T., Schoeberl, M. R., Tilmes, S., Zhang, J., Kushner, P. J., and Pausata, F. S. R.: Comparing multi-model ensemble simulations with observations and decadal projections of upper atmospheric variations following the Hunga eruption, *Atmos. Chem. Phys.*, 25, 13161–13176, https://doi.org/10.5194/acp-25-13161-2025, 2025.

Multi-model ensemble and observation comparison using all available model simulations in Exp1 (coupled ocean and fixed SSTs), GloSSAC, OMPS, and MLS data.

S3.2.1 Stratospheric aerosol optical depth (SAOD) anomaly

GloSSAC data indicate that the volcanic aerosols are predominantly concentrated in the Southern Hemisphere (SH), with a smaller fraction transported to the Northern Hemisphere (NH) tropics (Figure S3.11). In the first few months of 2022, the aerosols remain largely trapped in the low latitudes of the tropical pipe (Taha et al., 2022). The SH (0–30°S) experiences a higher aerosol concentration compared to the NH tropics (0–30°N). From mid-2022, during the austral winter, more aerosols are transported to the SH mid-latitudes (30°-60°S). The strong polar vortex in the austral winter and spring prevents further poleward transport (Manney et al., 2023). However, at the end of 2022 and the beginning of 2023, the break-up of the polar vortex during austral late spring-early summer allows for a slight poleward movement of aerosols toward the southern polar regions, with a minor portion also being transported northward toward the tropics. Following this, the aerosols are predominantly confined and transported in the SH mid-latitudes. This pattern reflects the influence of seasonal changes in the polar vortex and the Brewer-Dobson circulation on stratospheric aerosol transport (Butchart, 2014). OMPS observations show a similar latitudinal transport pattern over time, although exhibit stronger SAOD values in the tropics and southern mid-latitudes compared to GloSSAC.

Model simulations demonstrate reasonable agreement with observed latitudinal SAOD distribution patterns (Figure S3.11). Both GloSSAC and OMPS show a decrease in SAOD over time as aerosols are transported toward SH high latitudes. WACCM6MAM-CO, WACCM6MAM-FS, and MIROC-CHASER-FS all exhibit similar trends, though with stronger SAOD in the tropics compared to observations. In contrast, GEOSCCM-FS displays weaker SAOD in the tropics and stronger SAOD in the polar regions (60–90°S) by mid-2023 compared to mid-latitudes (30–60°S) in mid-2022. Additionally, models show that the anomaly diminishes mostly by the end of 2024. These differences may stem from uncertainties in both modelling and satellite observation, including variations in simulated aerosol microphysics and dynamics, as well as uncertainties in aerosol estimates from GloSSAC and OMPS retrievals. Understanding these differences and uncertainties is a key objective of the Tonga Model Intercomparison Project (Tonga-MIP; Clyne et al., 2024), which, as a parallel initiative, will also contribute to the Hunga Assessment Report (Zhu et al., 2025).

Both observational data and model simulations show that the SAOD anomaly induced by the Hunga eruption lasts for approximately two years in the SH low latitudes. Additionally, both sources are consistent in identifying a secondary peak in SAOD over SH mid-latitudes during the second austral winter in 2023. Model projections further suggest minor extensions of the SAOD anomaly into the third and fourth years in SH high latitudes, with the third-year signal being particularly robust across climate models and also independent of ocean–atmosphere coupling.

S3.2.2 Water vapour variation

Global stratospheric water vapour (SWV) mass anomaly The Hunga eruption led to an unprecedented increase in stratospheric water vapour (SWV), significantly influencing global SWV loading. After removing background water vapour, the MLS-observed SWV mass anomaly from the Hunga eruption initially stabilised at approximately 135 Tg before beginning to decline in the spring of 2023 (Figure S3.12). Following a slight increase in late 2023, it began decreasing more rapidly in early 2024, reaching approximately 70 Tg by the end of 2024. The initial SWV mass analyzed based on the v5 retrieval of MLS is slightly lower than previous estimates using the v4 retrieval, which indicated a ~150 Tg water vapour injection by the Hunga eruption (Carr et al., 2022; Millán et al., 2022).

Compared to MLS observations, the modelled SWV mass anomalies exhibit varying evolutionary trends. WACCM6MAM-CO and WACCM6MAM-FS replicate the MLS observations well, with an initial mass of approximately 135–140 Tg and a continuous plateau in SWV mass before it begins decreasing in early 2023. Despite an initial injection mass of 150 Tg, the rapid reduction of 10–15 Tg is attributed to the water vapour saturation effect, which converts water vapour into ice clouds during the first week after injection, as described by Zhu et al. (2022). GEOSCCM-FS also shows a similar initial plateau but with a larger magnitude of SWV mass compared to MLS in early 2022. A more pronounced decrease begins at the end of 2022, with the SWV mass eventually decreasing to a level comparable to MLS by early 2023. MIROC-CHASER-FS exhibits a larger initial water mass but with a shorter plateau, beginning its decrease by mid-2022, and decreasing to a comparable mass to MLS in early 2023. In contrast, MIROC-CHASER-FS-H_2O shows a similar initial mass and plateau to MLS, but with a slightly faster decrease at the end of 2023 compared to both MLS and MIROC-CHASER-FS. CMAM-

FS-H_2O shows a slightly larger initial SWV mass but displays a similar variation in 2023 and a comparable decreasing trend thereafter. Simulations from GSFC2D-GLOSSAC, GSFC2D-OMPS, and GSFC2D-H_2O exhibit nearly identical SWV mass evolution, characterised by a shorter plateau and a more significant decline starting in mid-2022.

Background variability in the MLS observational record was calculated using 2-sigma interannual deviations over the 2005–2021 pre-Hunga period. When considering this variability, all modelled SWV mass anomalies fall within the two-standard-deviation range of the MLS data, indicating that the model simulations reasonably reproduce the observed evolution patterns. Additionally, the modelled SWV mass decrease slope in late 2023 is not as sharp as in early 2023, with a slight increase observed at the end of 2023 or early 2024 in models such as WACCM6MAM-CO, GEOSCCM-FS, and MIROC-CHASER-FS, although this increase is less pronounced compared to the one observed in MLS at the end of 2023.

Millán et al. (2024) estimated that the anomalous state induced by the Hunga eruption could diminish within 5–7 years based on an exponential decay using MLS observations—a timescale that closely aligns with projections from the model simulations in this study. Among the simulations, the only one with a coupled ocean (WACCM6MAM-CO) exhibits the shortest perturbation duration, with stratospheric H_2O mass returning to climatological levels within four years (by 2026). This may reflect faster transport and more efficient H_2O removal in the coupled ocean simulation compared to the fixed-SST configuration. Additional coupled-ocean simulations are needed to confirm this. The longest perturbation, lasting up to seven years (until 2029), is projected by MIROC-CHASER-FS, while the other models suggest a duration of approximately five years, until 2027. The current decreasing trend in MLS H_2O mass lies within the range of model projections, suggesting a potential perturbation lasting around five years. This prolonged anomaly has significant implications for the climate system.

The e-folding time of stratospheric H_2O mass is typically calculated from the initial injection; however, the HTHH-MOC protocol mandates a retained H_2O mass of approximately 150 Tg in January 2022. Due to variations in how models simulate the initial ice cloud formation and removal processes, the initial H_2O injection methods and magnitudes differ across models, as summarised in the second column of Table 2. The lowest initial injection occurs in WACCM6MAM-CO and WACCM6MAM-FS (150 Tg), whereas GEOSCCM-FS injects the highest amount (750 Tg). Given this disparity, calculating e-folding time from the initial injection would be inappropriate. Instead, we use the e-folding time from the peak H_2O mass as a more consistent metric for assessing H_2O lifetime.

The maximum H_2O mass across models generally falls within 130–160 Tg. Prior to initiating ensemble simulations, model adjustments were made to achieve the protocol target of 150 Tg retained by the end of January 2022. However, due to internal variability within free-running models, ensemble members exhibit different evolutionary trajectories, leading to variations in maximum H_2O burden among members (Figure S3.13). Additionally, differences in microphysical and dynamical processes across models further contribute to variations in both peak H_2O mass and timing of peak occurrence. WACCM6MAM-CO reaches its 136 Tg peak the fastest (within two months), whereas MIROC-CHASER-FS-H_2O takes the longest (ten months) to reach 148 Tg. The earliest e-folding time from peak mass occurs in November 2024 in GSFC2D-H_2O, while MIROC-CHASER-FS-H_2O exhibits the latest, in May 2026, with corresponding e-folding times of 31 and 43 months, respectively.

Interestingly, MIROC-CHASER-FS-H_2O reaches a lower peak mass and does so later than MIROC-CHASER-FS, yet both exhibit the same 43-month e-folding time. This suggests that co-injection of SO_2 with H_2O primarily influences the magnitude of H_2O mass in the early months—likely reducing ice cloud formation initially—but has limited impact on the long-term H_2O lifetime. In contrast, GSFC2D-H_2O shows no notable differences from GSFC2D-OMPS and GSFC2D-GLOSSAC. Among all models, GSFC2D predicts the shortest e-folding time of 31 months from peak H_2O mass. This is similar to a global decay time with a lifetime of 30 months starting from July 2023 and assuming a constant first-order loss previously estimated from a H_2O-only GSFC2D simulation (Fleming et al., 2024). Using an offline 3D CTM, Zhou et al. (2024) projected an overall e-folding decay timescale of 48 months from July 2023. Notably, this timescale reflects removal of water vapour from the entire atmosphere, rather than from the stratosphere as considered here. As shown above, different quantities yield varying estimates of the H_2O mass lifetime. Therefore, it is crucial to specify which quantity is used when quantifying H_2O mass lifetime to ensure consistency and comparability across studies.

Water vapour distribution The observed MLS H_2O cloud (red inset box in Figure S3.14) experiences an initial subsidence phase, characterised by downward transport to approximately 40 hPa within the first few weeks, as also noted by Niemeier et al. (2023). This is followed by a stable phase, during which H_2O remains confined to the middle stratosphere, and a subsequent rising phase, where H_2O ascends into the upper stratosphere and gradually enters the lower mesosphere by the end of 2022. The initial subsidence and stable phases are attributed to the radiative cooling effects of H_2O injection (Niemeier et al., 2023), while the final rising phase—associated with strong upward transport—is linked to the Quasi-Biennial Oscillation (QBO) phase (Schoeberl et al., 2024). Beyond this phase, stratospheric water vapour transport is increasingly dominated by upward flux into the mesosphere above 1 hPa, resulting in a peak mesospheric burden of approximately 3–4 Tg by late 2023 (Figure S3.15). However, this mesospheric contribution represents only a small fraction of the total H_2O injected by the eruption (cf. Figures S3.15 and S3.12). The majority is progressively removed through stratosphere–troposphere exchange, particularly at high latitudes. For instance, in January 2025 (Figure S3.16a), a wedge-shaped region just above the tropopause marks a sharp decline in H_2O concentration, indicating a key region where much of the Hunga H_2O is removed from the stratosphere. Above this feature, high-latitude maxima in H_2O in both hemispheres are consistent with enhanced transport driven by the Brewer–Dobson circulation. This behaviour is further supported by evidence of pronounced dehydration in the Southern Hemisphere polar stratosphere during winter, as illustrated in July 2025 (Figure S3.16b), aligning with Antarctic vortex-induced dehydration mechanisms described by Zhou et al. (2024). These pathways are expected to continue dominating the removal of Hunga-injected H_2O as it is gradually transported downward by the global stratospheric circulation (Figure 10 in Randel et al., 2024). The anomalous H_2O distribution near 10 hPa is an artefact resulting from the placement of the MLS spectral channels (Niemeier et al., 2023).

The MLS anomaly is calculated relative to the 10-year climatology, and since the model anomalies are derived from Hunga eruption experiments relative to control runs without volcanic emissions, direct comparisons of detailed values are inappropriate. Therefore, our focus is on comparing the transport pattern. As shown in Figure S3.14, all models successfully reproduce the three-phase transport pattern. Among them, WACCM6MAM-FS, WACCM6MAM-CO, MIROC-CHASER-FS, and MIROC-CHASER-FS-H_2O exhibit slightly weaker upward transport, whereas GEOSCCM-FS, GSFC2D-GLOSSAC, GSFC2D-OMPS, and GSFC2D-H_2O show slightly stronger upward transport compared to MLS. However, the differences among GSFC2D-GLOSSAC, GSFC2D-OMPS, and GSFC2D-H_2O are quite small.

The three-phase transport pattern is also captured by the ICON-Seamless model in Niemeier et al. (2023), which simulated H_2O-only injection. That study highlighted that co-injection of SO_2 primarily affects the magnitude of vertical transport but does not alter the three-phase structure. This finding is further supported by comparisons between MIROC-CHASER-FS and MIROC-CHASER-FS-H_2O, as well as between GSFC2D-GLOSSAC, GSFC2D-OMPS, and GSFC2D-H_2O.

In the long term, significant H_2O anomalies in the stratosphere and lower mesosphere are projected to persist for at least six years, until 2028, in WACCM6MAM-CO. The longest projection indicates that a substantial anomaly could persist for over a decade, lasting until the end of the simulation in 2031, as indicated by MIROC-CHASER-FS and MIROC-CHASER-FS-H_2O. This prolonged anomaly may be attributed to weaker upward transport, particularly in MIROC-CHASER-FS-H_2O, as indicated by both the anomaly pattern and the position of the 1 ppmv H_2O contour line. The extended H_2O lifetime in MIROC-CHASER-FS-H_2O, as shown in Figure S3.11, further supports this conclusion.

S3.2.3 Global-mean air temperature evolution

The upper atmospheric global-mean air temperature anomaly calculated from MLS data indicates slight warming in the lower stratosphere during 2022, particularly in the first half of the year (Figure S3.17). Above this warming layer, strong cooling is observed in the middle and upper stratosphere, which extends into the lower mesosphere above 1 hPa from late 2022 onward.

The upper-level cooling and lower-level warming dipole response pattern is reasonably reproduced by the model simulations, although with a smaller magnitude in most models compared to MLS. The significant cooling in the middle stratosphere (10–40 hPa) is more persistent than in the upper stratosphere (1–10 hPa), lasting between 3.5 and 4.5 years—until mid-2025 in WACCM6MAM-CO and mid-2026 in

GEOSCCM-FS. The strongest cooling is observed in the mesosphere above 1 hPa, where it persists for at least five years, until 2027, in GEOSCCM-FS and CMAM-FS-H_2O. This cooling persists even longer in simulations by WACCM6MAM, MIROC-CHASER, and GSFC2D, with the longest duration—up to 10 years—observed in MIROC-CHASER-FS-H_2O. The modelled significant warming in the lower stratosphere is most prominent in 2022 in GEOSCCM-FS and MIROC-CHASER-FS. However, a more prolonged warming, extending into early and mid-2023, is observed in WACCM6MAM-CO and WACCM6MAM-FS. This warming is also evident—and even stronger—in GSFC2D-GLOSSAC and GSFC2D-OMPS.

The cooling observed in the middle and upper stratosphere corresponds to the ascent of H_2O, while the warming in the lower stratosphere is associated with the descent of aerosols that absorb solar near-infrared and terrestrial infrared radiation (Wang et al., 2023). Compared to MIROC-CHASER-FS, MIROC-CHASER-FS-H_2O exhibits stronger and more prolonged cooling in the middle stratosphere but less pronounced warming in the lower stratosphere. A similar pattern is observed when comparing GSFC2D-H_2O with GSFC2D-GLOSSAC and GSFC2D-OMPS, where the former shows enhanced middle stratosphere cooling but weaker lower stratosphere warming. Although the greenhouse effect of stratospheric H_2O contributes to lower stratospheric warming, the significant warming is primarily driven by the co-injection of aerosols.

S3.2.4 Global-mean ozone variation

MLS data indicate ozone depletion in the lower stratosphere (20–100 hPa), an ozone increase in the middle stratosphere (around 10 hPa), and ozone depletion in the upper stratosphere (1–5 hPa), with the most pronounced depletion occurring in the lower mesosphere (0.1–1 hPa) during mid-2023 to 2024 (Figure S3.18). This triple-response pattern—characterised by middle-stratospheric ozone enhancement flanked by depletion above and below—is well captured by all model simulations, except for CMAM-FS-H_2O, which exhibits very limited ozone depletion in the lower stratosphere. However, the magnitude and timing of these ozone changes vary among models.

All simulations project long-lasting ozone depletion in the lower mesosphere, persisting for at least seven years. MIROC-CHASER-FS shows the most prolonged ozone depletion, extending to the end of the simulation (December 2031), and also exhibits the most pronounced ozone increase in the middle stratosphere, as well as extended significant ozone depletion in the lower stratosphere between 2022 and 2025.

Compared to MIROC-CHASER-FS, MIROC-CHASER-FS-H_2O shows a smaller ozone increase in the middle stratosphere and less ozone depletion in the lower stratosphere. The significant ozone depletion between 20 and 40 hPa observed in GSFC2D-GLOSSAC and GSFC2D-OMPS in 2022 is less pronounced in GSFC2D-H_2O. This highlights the crucial role of co-injected SO_2 in driving ozone depletion in the lower stratosphere. These findings confirm the combined effect of both H_2O and SO_2, as discussed by Wang et al. (2023).

Ozone depletion in the lower stratosphere is driven by heterogeneous chlorine activation and enhanced dinitrogen pentoxide on hydrated aerosols (Evan et al., 2023; Zhang et al., 2024; Zhu et al., 2022; Zhu et al., 2023). In contrast, ozone depletion in the lower mesosphere is linked to increased reactive hydrogen and a corresponding reduction in equilibrium ozone (Fleming et al., 2024; Randel et al., 2024), resulting from the upward transport of water vapour (Figure S3.14) that leads to significant cooling (Figure S3.17). The depleted ozone layer absorbs less ultraviolet (UV) radiation, further amplifying cooling at these altitudes. Consequently, stronger UV radiation enhances ozone production in the middle stratosphere, while ozone concentrations decrease above this layer.

Furthermore, direct chemical effects contribute to increased ozone in the mid-stratosphere. These include the heterogeneous reaction

$$N_2O_5 + H_2O \rightarrow 2 \times HNO_3$$

on enhanced sulfate aerosols, which reduces NO_x and the odd-nitrogen ozone loss cycle at altitudes where aerosols are abundant (Wilmouth et al., 2023; Santee et al., 2023; Zhang et al., 2024). The enhanced OH from the H_2O injection converts NO_2 to the reservoir HNO_3, also reducing the odd-nitrogen ozone loss cycle in the mid-stratosphere (Fleming et al., 2024). Beyond the chemical feedback effects, the increase in ozone in the middle stratosphere is also influenced by transport changes associated with a weakening of the midlatitude Brewer–Dobson circulation (Wang et al., 2023).

The ozone response mechanisms discussed here draw on previous single-model studies that conducted detailed photochemical analyses using the same modelling frameworks. While the current study does not

include new quantitative calculations of individual reaction rates or radiative effects, a dedicated multi-model analysis of the ozone response and its underlying mechanisms is currently underway.

S3.2.5 Summary and conclusions

The 2022 Hunga eruption was the most explosive volcanic event since the 1991 Pinatubo eruption. In contrast to Pinatubo, which injected a large amount of SO_2, Hunga released only approximately 0.5 Tg of SO_2 but was distinguished by an unprecedented injection of roughly 150 Tg of water vapour into the stratosphere, with some reaching the lower mesosphere. To investigate the evolution of SO_2 and H_2O perturbations and their subsequent atmospheric and climate impacts, the HTHH-MOC activity was endorsed by the WCRP APARC, fostering collaboration between the observational and modelling communities. In this study, we evaluate multi-model simulations against observations for the first two years, along with subsequent projections of their evolution, using Experiment 1—the only long-term simulation extending up to 10 post-eruption years. This assessment aims to evaluate model reliability in capturing the evolution of volcanic emissions and predicting their impacts on temperature and ozone in the stratosphere and lower mesosphere.

Our results indicate that models successfully reproduce the latitudinal distribution of aerosols, which initially exhibit southward transport in the first year and reach Southern Hemisphere (SH) polar latitudes by the austral winter of 2023, reflecting stratospheric transport dominated by the Brewer–Dobson circulation. Aerosols persist for approximately two years, with some models suggesting an additional 0.5 to 1.5 years of persistence in polar latitudes.

MLS observations show a plateau in H_2O mass between 1 and 70 hPa during the first year, followed by a continuous decline starting in late 2022. Models generally reproduce this plateau in 2022, with a subsequent sharp decline beginning in 2023. However, MIROC-CHASER-FS deviates by showing a shorter plateau, with a continuous decrease starting from mid-2022. The significant H_2O perturbation is projected to last four years (until 2026) in WACCM6MAM-CO and seven years (until 2029) in MIROC-CHASER-FS. The impact of this 4–7 year stratospheric water vapour perturbation on stratospheric and lower mesospheric chemistry and dynamics remains an open question and requires further investigation. Understanding these effects is crucial for improving climate change detection and attribution in the coming years.

To comply with the experiment protocol, different models simulated H_2O injection using various methods and initial injection amounts, ranging from 150 Tg in WACCM6MAM-CO and WACCM6MAM-FS to 750 Tg in GEOSCCM-FS. This variation in injection amounts results in differences in the maximum H_2O mass across models, which range from 139 Tg in WACCM6MAM-FS to 166 Tg in GSFC2D-H_2O. The e-folding time is calculated based on the maximum mass rather than the initial injection amount, given the substantial differences in initial injection sizes. The estimated e-folding times range from 31 months in GSFC2D-H_2O to 43 months in MIROC-CHASER-FS and MIROC-CHASER-FS-H_2O.

Both observations and model simulations indicate warming in the lower stratosphere and significant cooling above, accompanied by ozone depletion in the lower stratosphere, an ozone increase in the middle stratosphere, and severe ozone depletion in the upper stratosphere and lower mesosphere. The ozone depletion persists for at least seven years, with some model projections extending up to at least a decade. Comparisons between simulations with combined SO_2 and H_2O injection and those with H_2O-only injection reveal that the significant cooling and ozone depletion in the upper stratosphere and lower mesosphere result from the presence of excessive water vapour. Additionally, the co-injection of SO_2 with H_2O is necessary to reproduce the significant warming and ozone depletion in the lower stratosphere, albeit with a limited amount of SO_2 injection.

In conclusion, the models effectively reproduce the overall transport patterns of SO_2 and H_2O, with varying lifetimes projected across different models. They also reproduce the observed patterns of temperature and ozone variations following the eruption, albeit with differences in timescales and magnitudes. As the first study to utilise multi-model simulations of the Hunga eruption, this research provides valuable insights into the long-term evolution of Hunga-injected water vapour and aerosols, as well as their impacts on stratospheric temperatures and ozone. Furthermore, this study demonstrates the reliability of these model simulations in assessing the underlying physical and dynamical mechanisms and their potential atmospheric and climate impacts in the coming years.

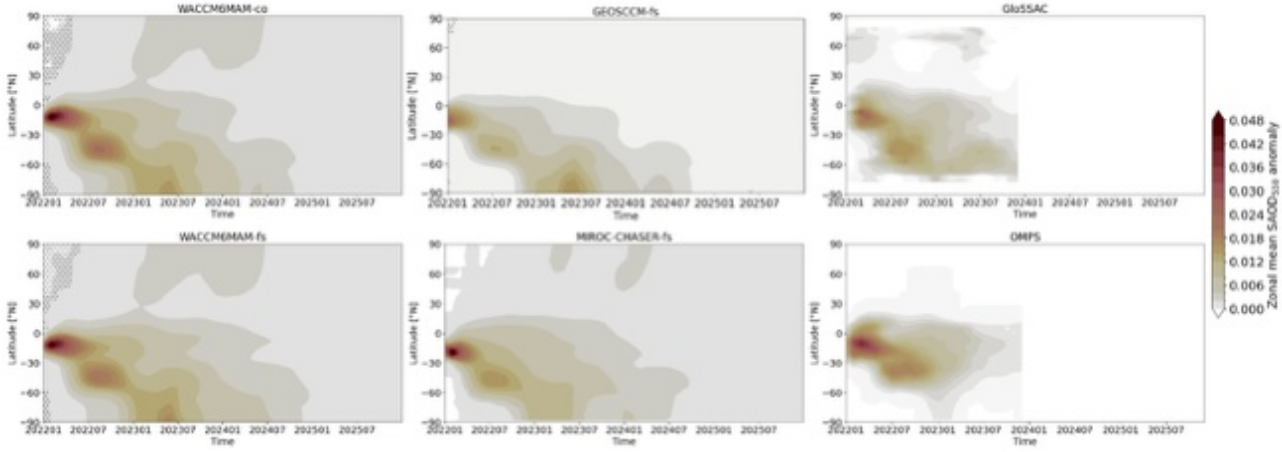

Figure S3.11: *Hovmöller diagrams of global mean stratospheric aerosol optical depth (SAOD) anomalies following the Hunga eruption. The four left panels present ensemble mean anomalies from different models relative to the control run, with dotted areas indicating statistically insignificant anomalies at the 95% confidence level based on Student's* t*-tests. The top-right panel shows the observed anomaly from the Global Space-based Stratospheric Aerosol Climatology (GloSSAC), relative to the 2012–2021 climatological period. The aerosol extinction of the GloSSAC data was used in the GSFC2D model as their prescribed aerosol field input (Zhu et al., 2025). The bottom-right panel displays the Stratospheric Aerosol Optical Depth (SAOD) calculated from aerosol extinction data obtained from the Ozone Monitoring and Profiler Suite Limb Profiler (OMPS), which was utilised in the GSFC2D model.*

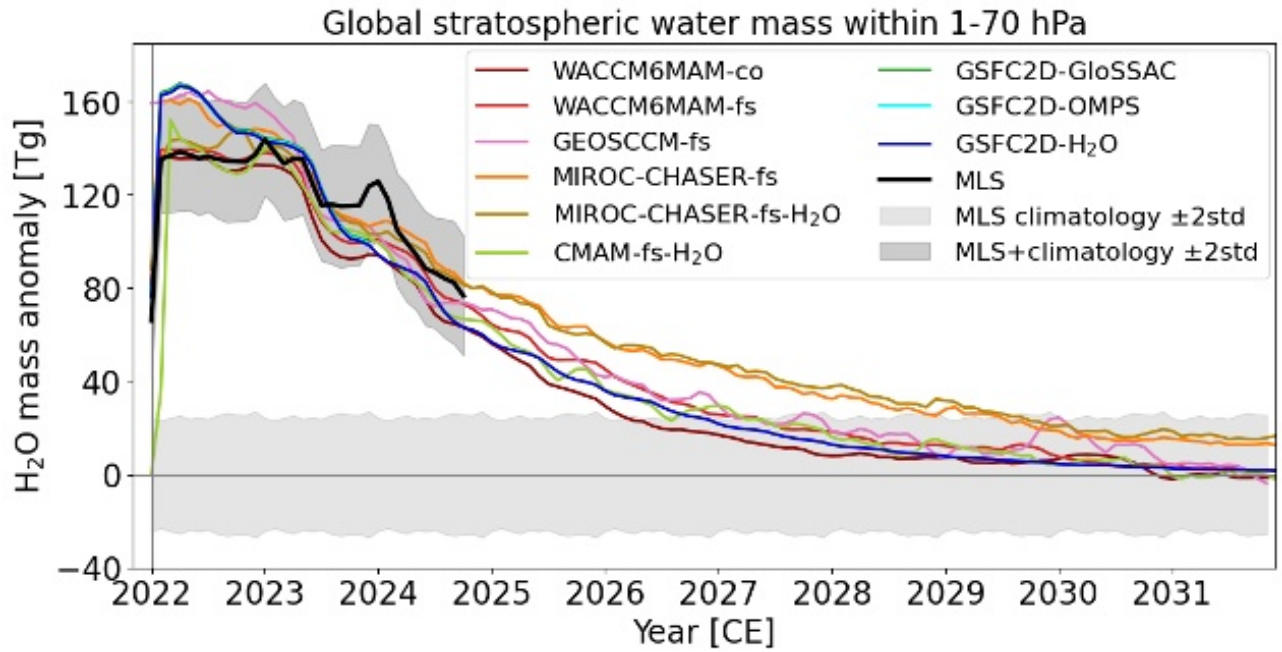

Figure S3.12: *Simulated and observed global stratospheric H_2O mass anomalies within the 1–70 hPa range following the Hunga eruption. The coloured lines represent ensemble mean anomalies relative to the control run, while the black line and grey shading depict the observed anomaly from the Microwave Limb Sounder (MLS) water vapour mass, along with its ±2 standard deviation range from the 2012–2021 climatology period. GSFC2D-GloSSAC and GSFC2D-OMPS have only two years of simulations and are superseded by GSFC2D-H_2O with ten years of simulations.*

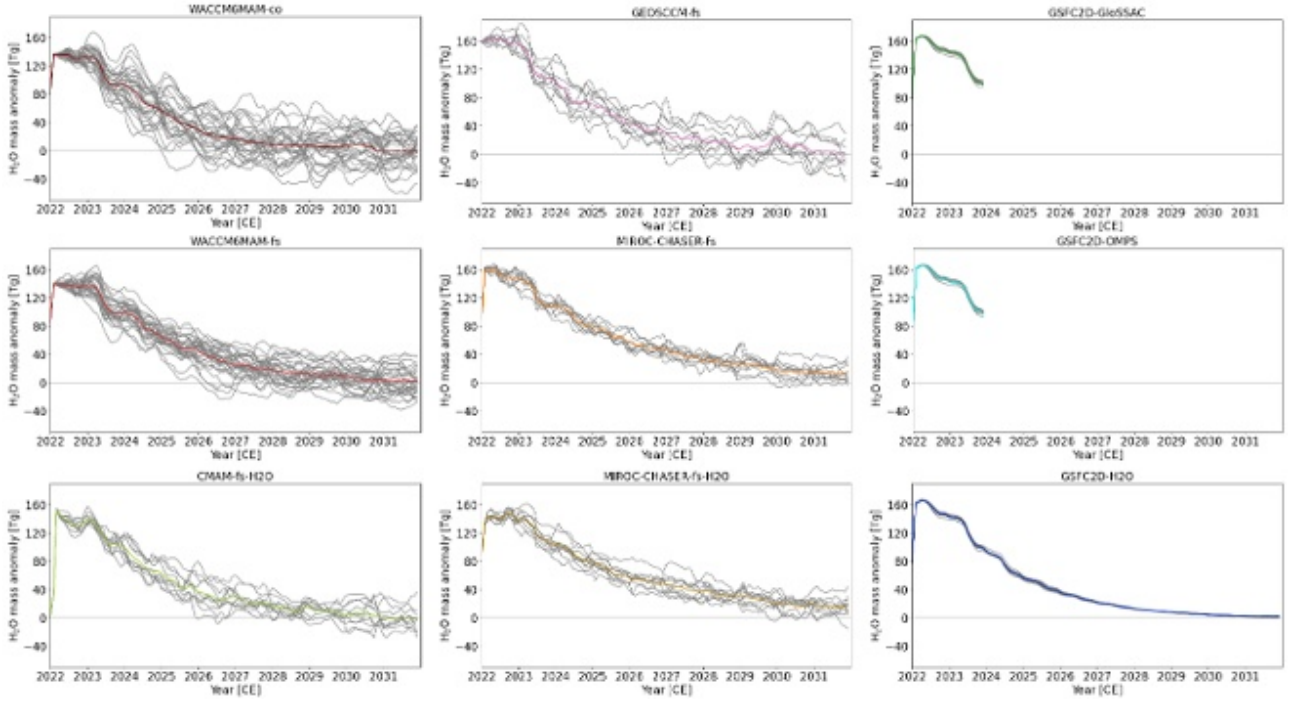

Figure S3.13: *Simulated global stratospheric H_2O mass anomalies within the 1–70 hPa range following the Hunga eruption. Coloured lines represent ensemble mean anomalies relative to the control run, while grey lines indicate individual ensemble member anomalies.*

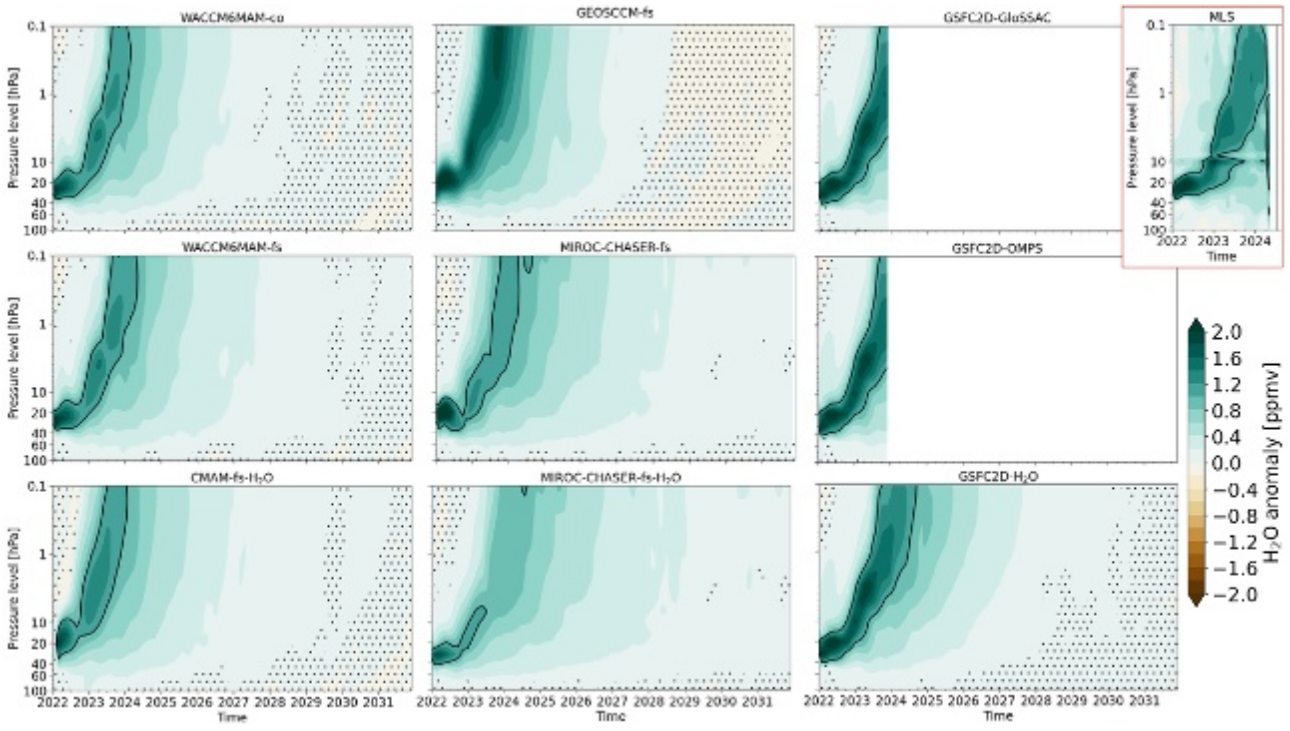

Figure S3.14: *Simulated and observed (red inset box) global mean H_2O anomalies following the Hunga eruption. The modelled anomalies are relative to the control run. Dotted grids indicate statistically insignificant anomalies at the 95% confidence level based on Student's* t*-tests. The solid black contours indicate an anomalous H_2O concentration of 1 ppmv.*

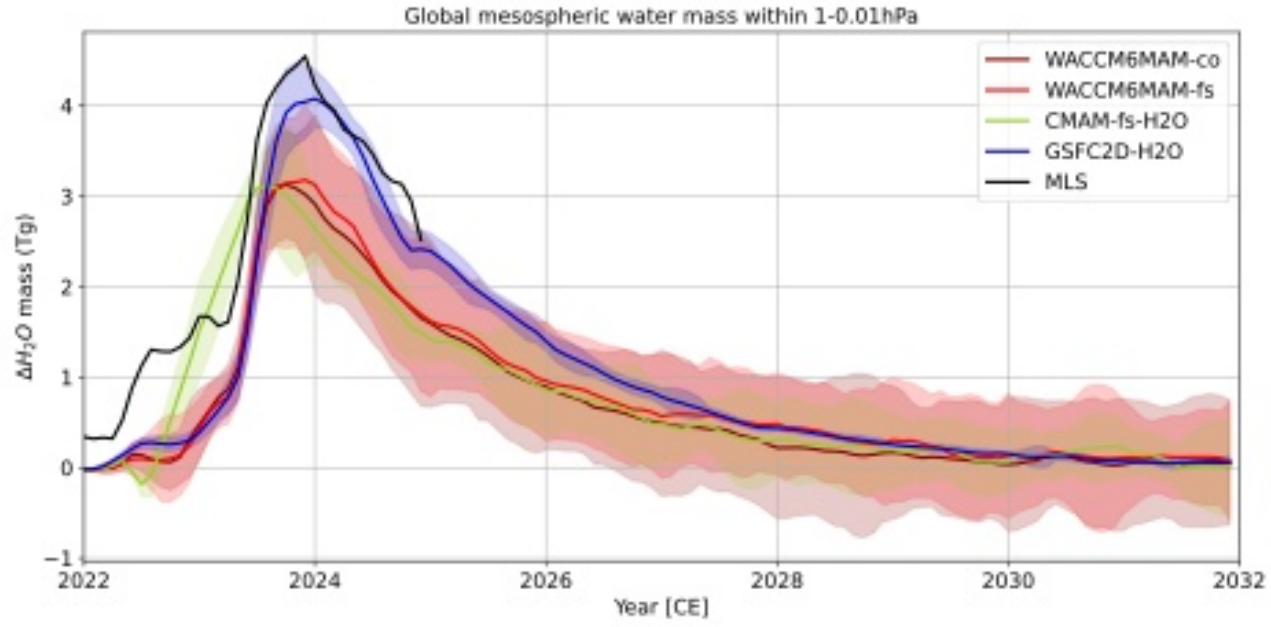

Figure S3.15: *Simulated and observed global stratospheric H_2O mass anomalies within the 1–0.01 hPa pressure range following the Hunga eruption. Coloured lines show ensemble mean anomalies relative to the control simulations for each model, with shading indicating the respective ensemble spreads. The black line represents the observed anomaly derived from Microwave Limb Sounder (MLS) water vapour measurements.*

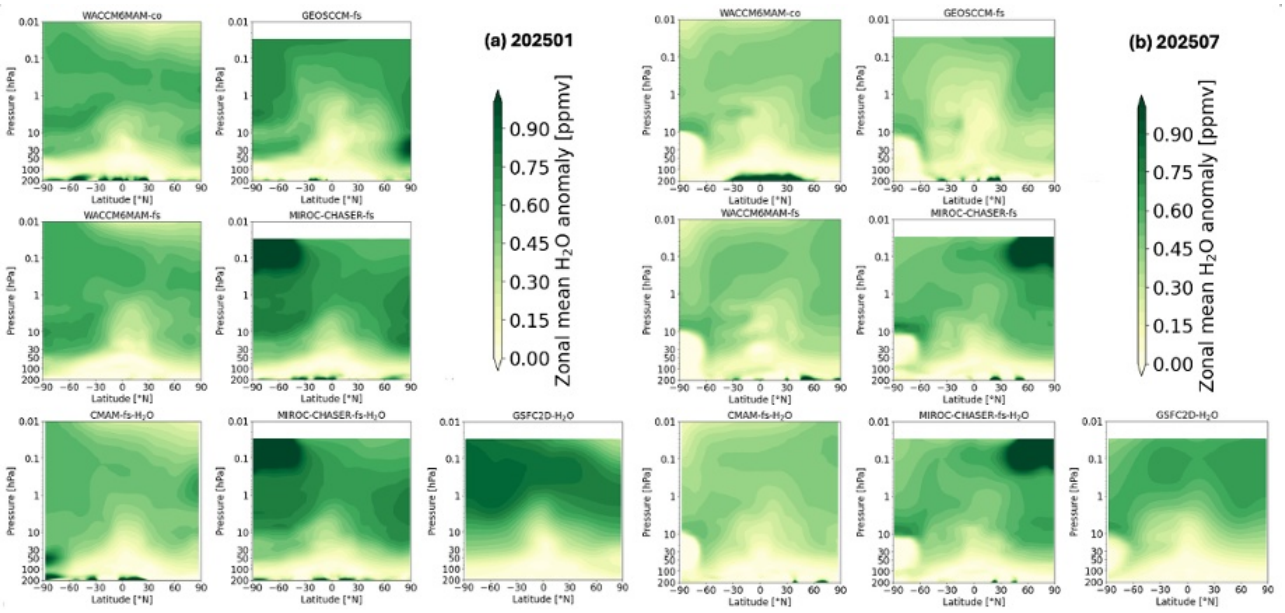

Figure S3.16: *Latitude–pressure distribution of simulated zonal mean water vapour anomalies in the upper atmosphere following the Hunga eruption, shown for (a) January 2025 and (b) July 2025. Anomalies are computed as differences between the ensemble mean of the experiment and control simulations.*

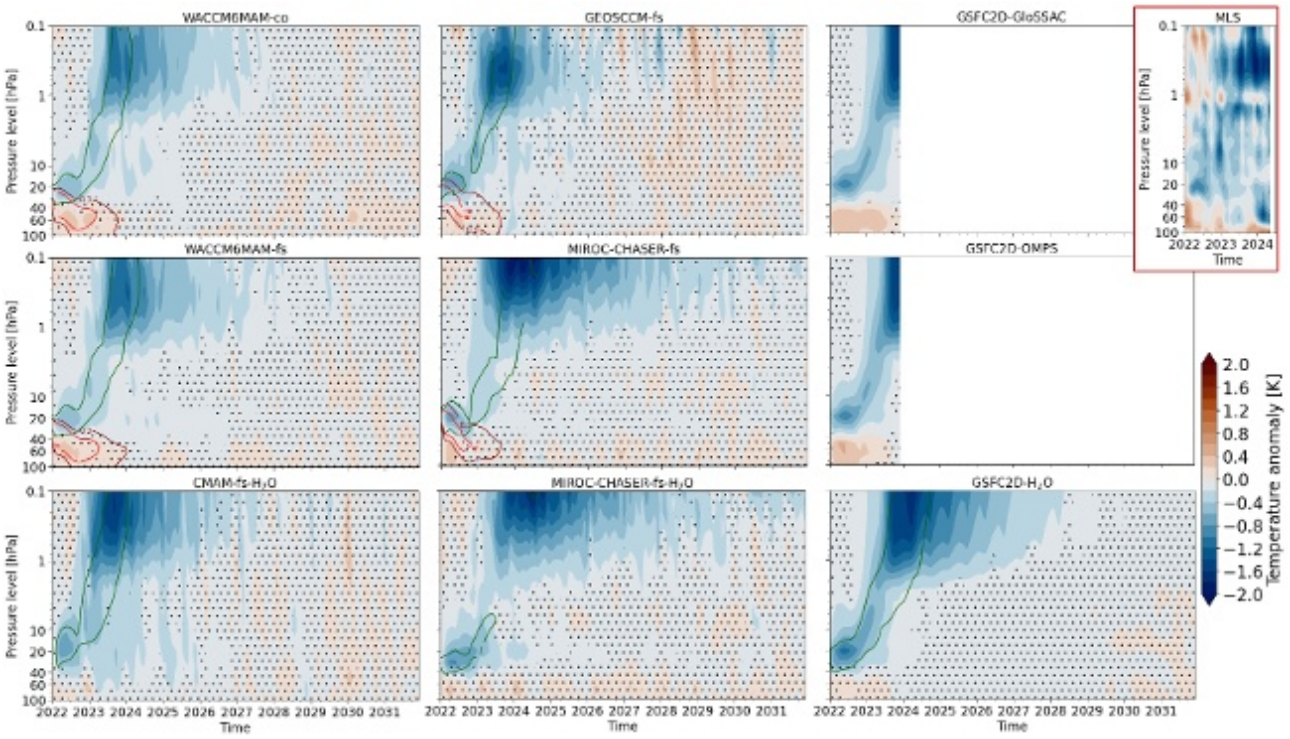

Figure S3.17: *Simulated and observed (red inset box) global mean air temperature anomalies following the Hunga eruption. The modelled anomalies are relative to the control run. Dotted grids indicate statistically insignificant anomalies at the 95% confidence level based on Student's* t*-tests. Dark red and red contour lines denote modelled aerosol extinction coefficients at 0.3 and 0.6×10^{-3} km^{-1}, respectively, while dark green contour lines indicate modelled water vapour concentrations of 1 ppmv.*

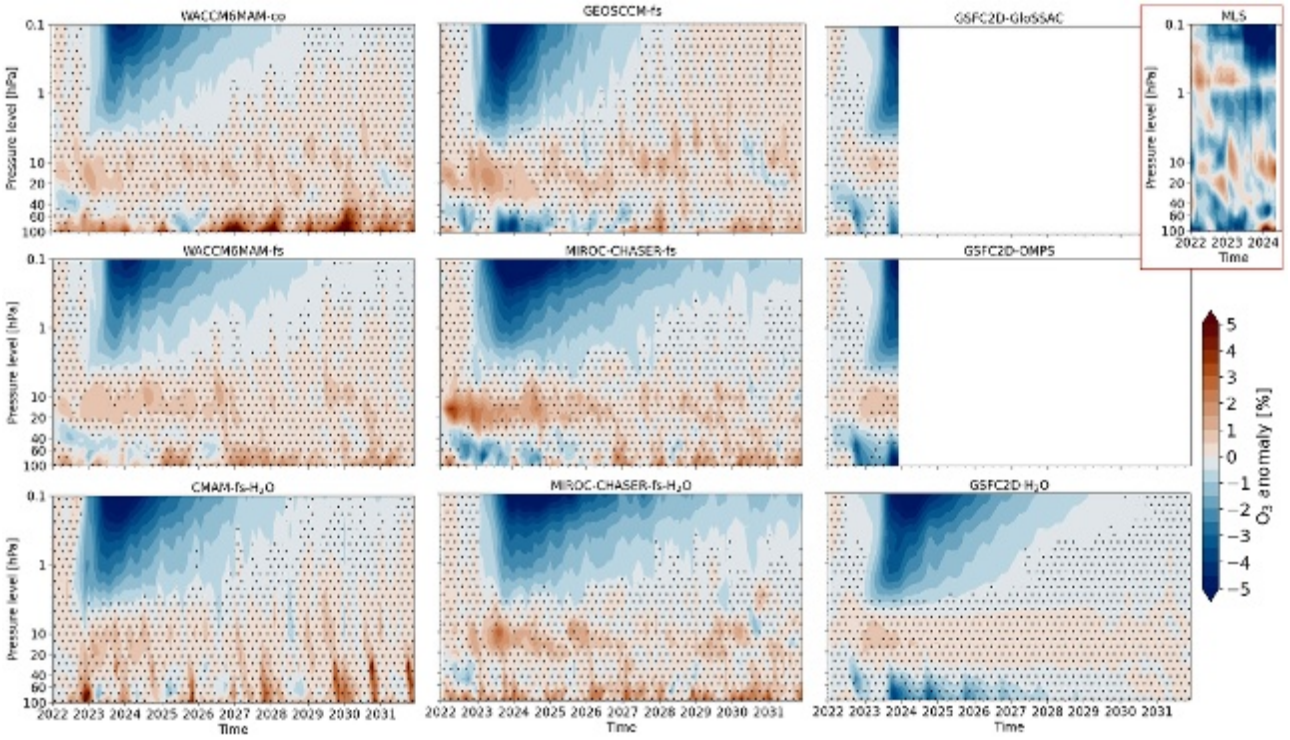

Figure S3.18: *Simulated and observed (red inset box) global mean ozone anomalies following the Hunga eruption. The modelled anomalies are relative to the control run. Dotted grids indicate statistically insignificant anomalies at the 95% confidence level based on Student's* t*-tests.*

S3.3 Hunga impact on radiative forcing

Authors Ilaria Quaglia
Daniele Visioni
Ewa M. Bednarz
Yunqian Zhu
Georgiy Stenchikov
Valentina Aquila
Cheng-Cheng Liu
Graham W. Mann
Yifeng Peng
Takashi Sekiya
Simone Tilmes
Xinyue Wang
Shingo Watanabe
Pengfei Yu
Jun Zhang
Zhihong Zhuo
Wandi Yu

This section is based on: Quaglia et al. (2025).

Quaglia, I., Visioni, D., Bednarz, E. M., Zhu, Y., Stenchikov, G., Aquila, V., Liu, C.-C., Mann, G. W., Peng, Y., Sekiya, T., Tilmes, S., Wang, X., Watanabe, S., Yu, P., Zhang, J., and Yu, W.: Multi-model analysis of the radiative impacts of the 2022 Hunga eruption indicates a significant cooling contribution from the volcanic plume, *EGUsphere [preprint]*, https://doi.org/10.5194/egusphere-2025-3769, 2025.

This section presents an inter-model comparison using both Exp1 and Exp2 results to quantify the direct radiative forcing contributions of aerosols and water vapour perturbations following the Hunga eruption.

Chapter 7: methodology – radiative forcing calculation

Instantaneous Radiative Forcing (IRF) is computed as the difference between the perturbed and unperturbed cases, using simulations with nudged meteorological fields (Exp2a, hereafter "Nudged"). The IRF of combined sulfate aerosols and water vapour, as well as of each component separately, is derived from the nudged experiments SO_2 AND H_2O, SO_2 ONLY, and H_2O ONLY, respectively.

The Effective Radiative Forcing (ERF) and Radiative Forcing (RF) are calculated analogously to the IRF, but based on free-running simulations with either fixed sea surface temperatures (SSTs) or coupled ocean configurations: Exp1_fixedSST (here "Fixed SST") and Exp1_coupled (here "Coupled"). In figure titles and captions, these cases are collectively referred to simply as *radiative forcing*.

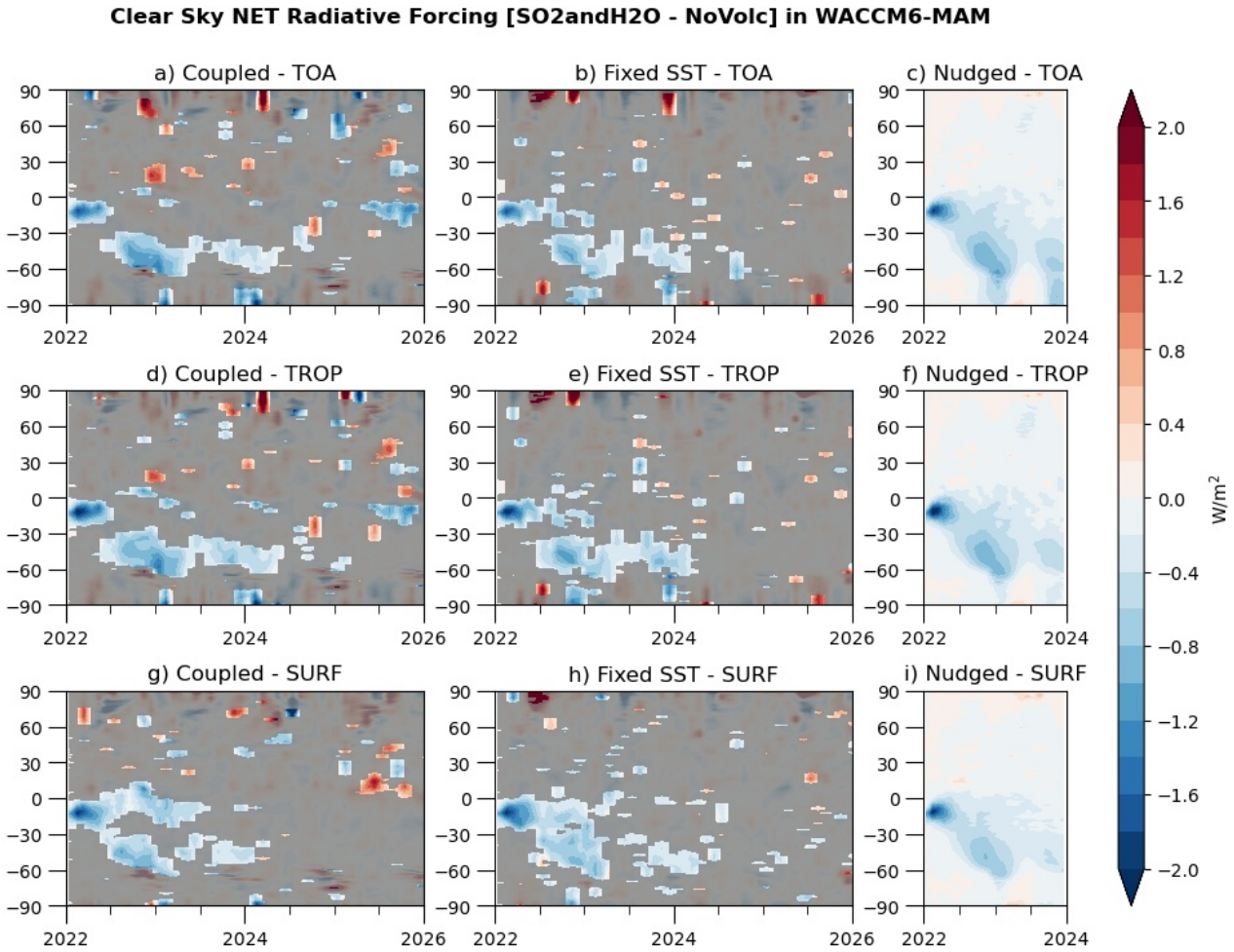

Figure S3.19: *Time series of zonal mean radiative forcing under clear-sky conditions for the SO_2 AND H_2O experiment in WACCM6-MAM, at (a–c) the top of the atmosphere (TOA), (d–f) the tropopause (TROP), and (g–i) the surface (SURF). Each column represents a different model setup: first column shows nudged simulations (Exp2a), second column fixed sea surface temperature simulations (Exp1–Fixed SST), third column coupled ocean simulations (Exp1–Coupled). Results from Exp1–Fixed SST and Exp1–Coupled are ensemble means. Gray areas indicate regions where the differences are not statistically significant at the 5% level based on Student's* t*-test.*

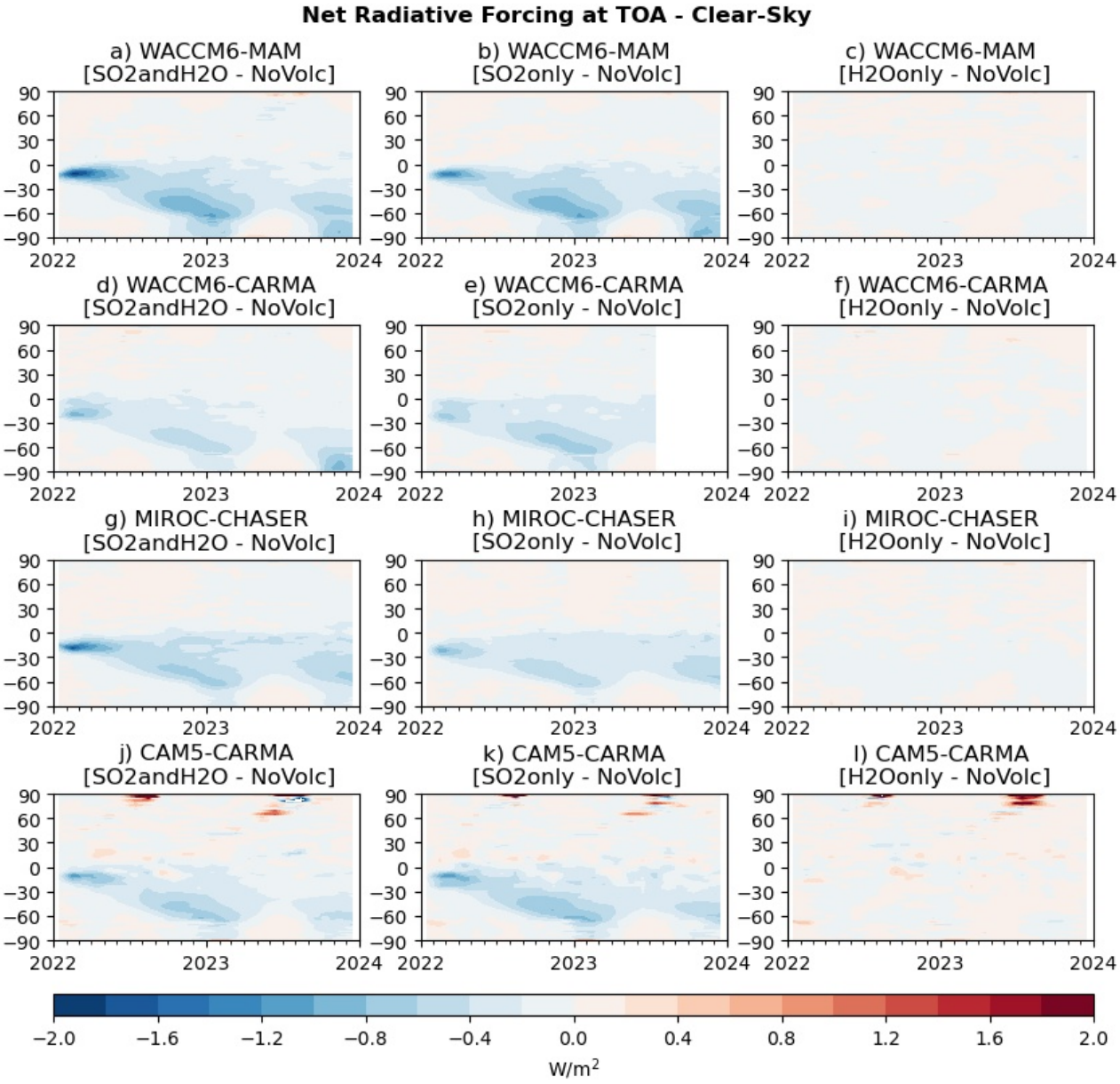

Figure S3.20: *Time series of zonal mean radiative forcing at the top of the atmosphere (TOA) under clear-sky conditions from five models: WACCM6-MAM (a–c), WACCM6/CARMA (d–f), MIROC-CHASER (g–i), and CAM5/CARMA (j–l). Each column corresponds to a different perturbation scenario from the nudged experiment (Exp2a): the first column shows SO_2ANDH_2O, the second SO_2ONLY, and the third H_2OONLY.*

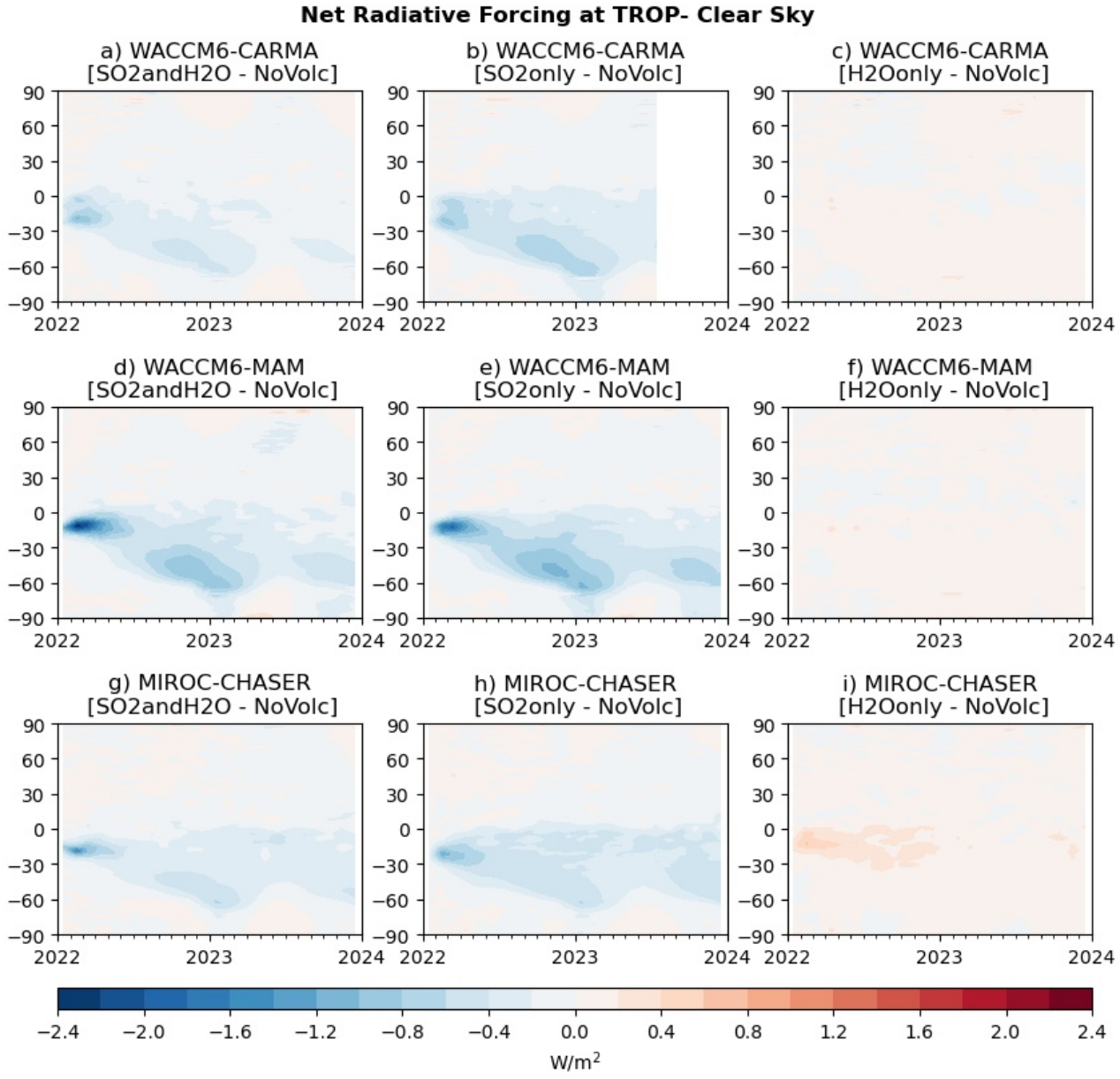

Figure S3.21: *As in Figure S3.20, but showing radiative forcing at the tropopause (TROP).*

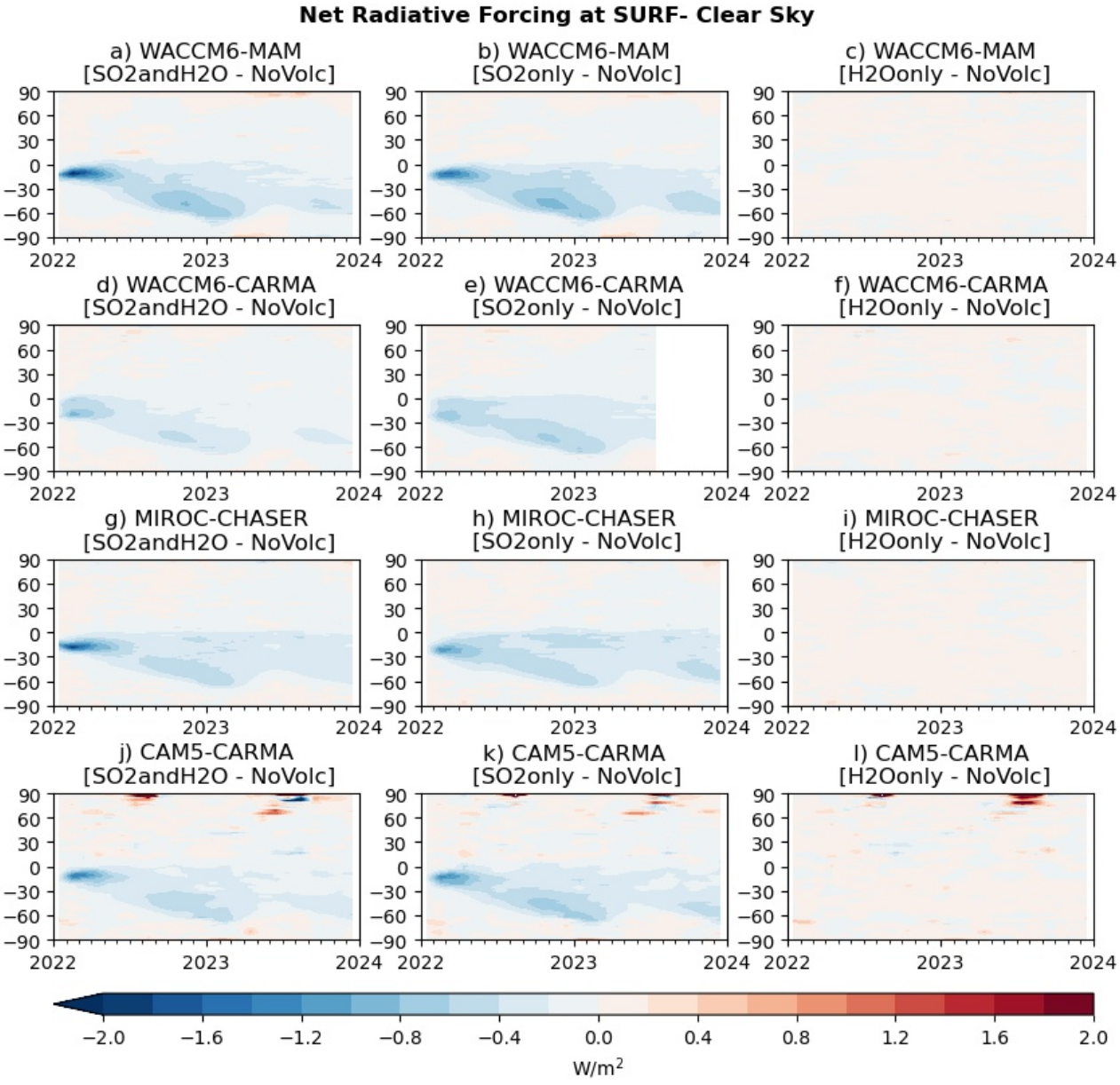

Figure S3.22: *As in figure S3.20, but showing radiative forcing at the surface (SURF).*

S3.4 Indirect climate impacts of the Hunga eruption

Authors Ewa M. Bednarz
Amy H. Butler
Xinyue Wang
Zhihong Zhuo
Wandi Yu
Georgiy Stenchikov
Matthew Toohey
Yunqian Zhu

This section is based on: Bednarz et al. (2026).

Bednarz, E. M., Butler, A. H., Wang, X., Zhuo, Z., Yu, W., Stenchikov, G., Toohey, M., and Zhu, Y.: Indirect climate impacts of the Hunga eruption, *EGUsphere [preprint]*, https://doi.org/10.5194/egusphere-2025-1970, 2025.

Using two 30-member WACCM6MAM Exp1 ensembles run with either fixed SSTs/sea-ice (HUNGA_fix) or coupled ocean configuration (HUNGA_cpl).

S3.4.1 Simulated changes in near-surface air temperatures following the eruption

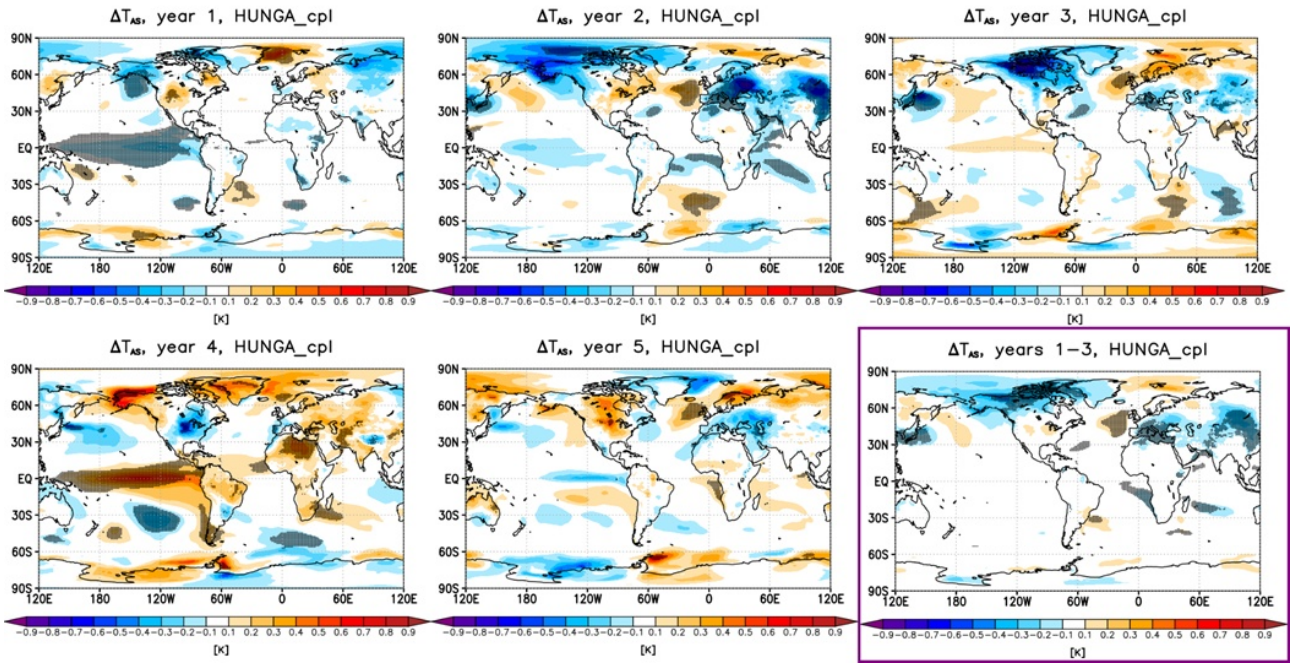

Figure S3.23: *Yearly mean changes in near-surface air temperature between the forced simulation and the control in the coupled ocean simulations for each of the five years following the eruption (2022–2027). The bottom right panel shows the response averaged over the first three years (2022–2024). Stippling indicates statistical significance, defined as differences exceeding ±2 standard errors in the difference of means.*

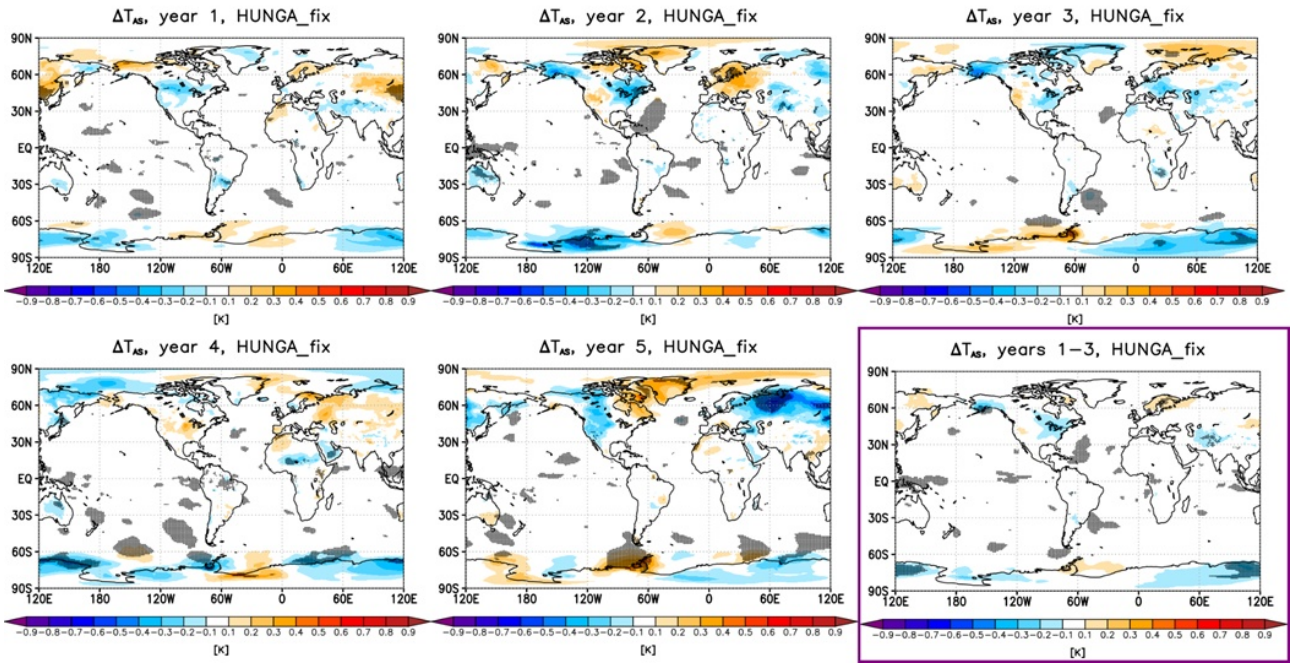

Figure S3.24: *As in Figure S3.23, but for the changes in the atmosphere-only simulations.*

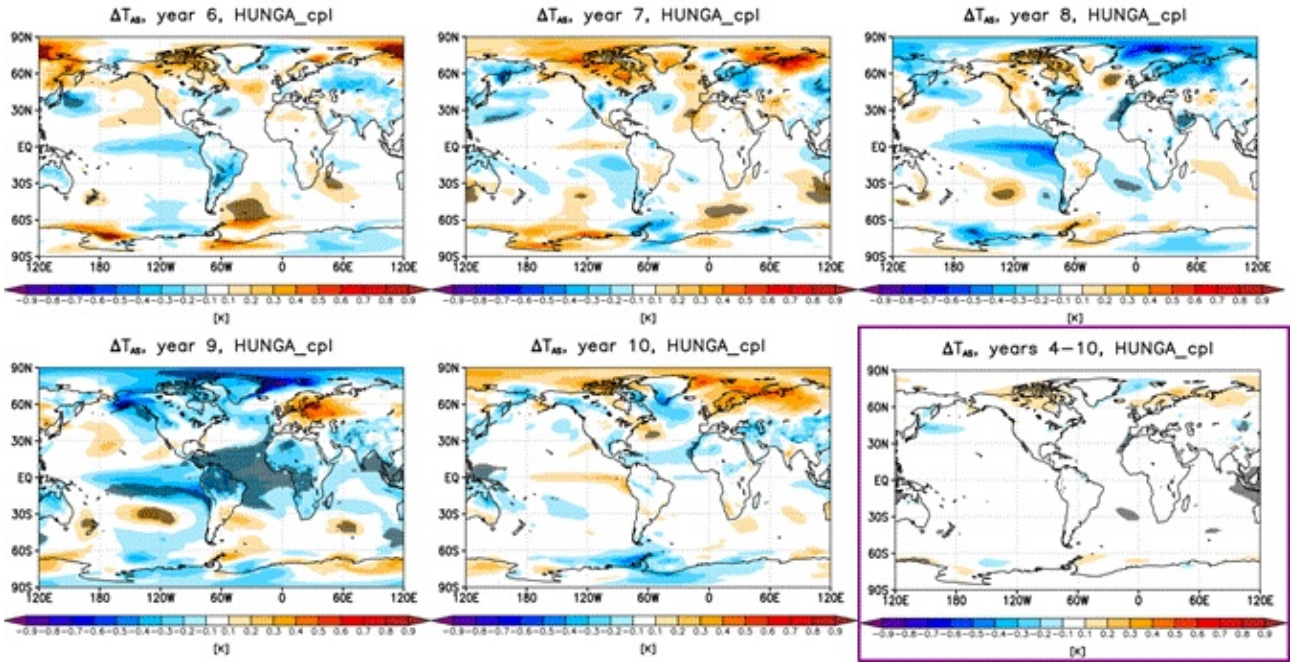

Figure S3.25: *As in figure S3.23, but for years 5–10.*

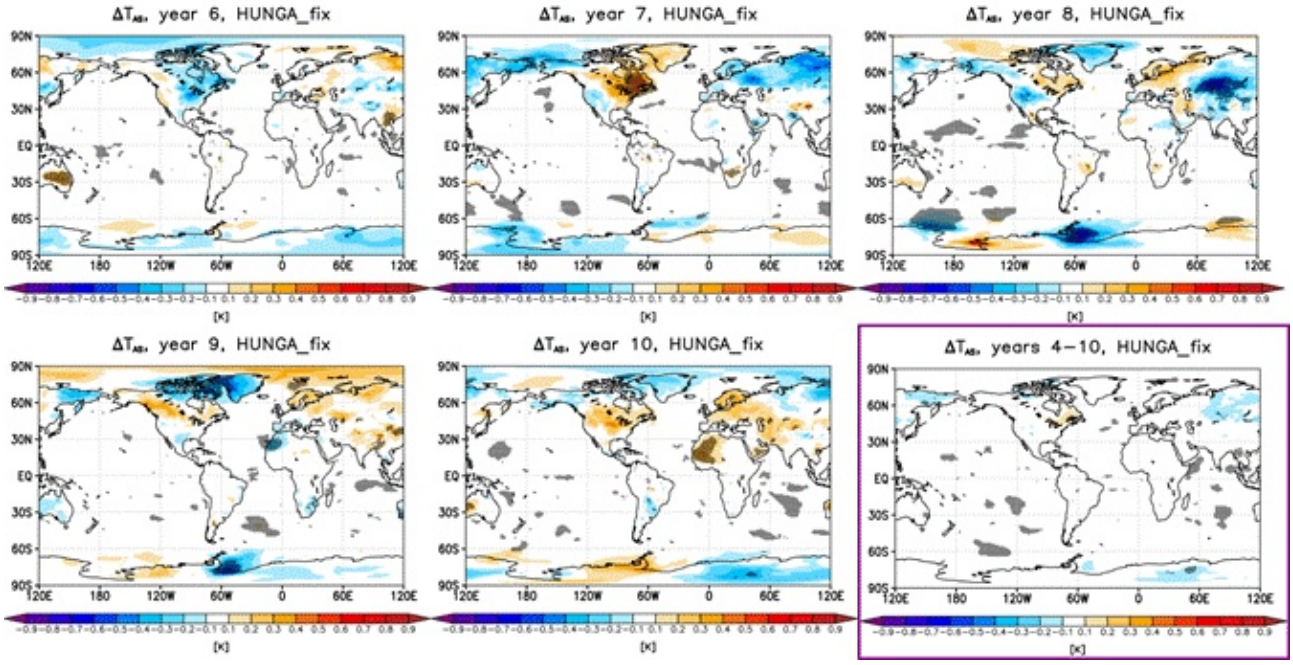

Figure S3.26: *As in Figure S3.24, but for years 5–10.*

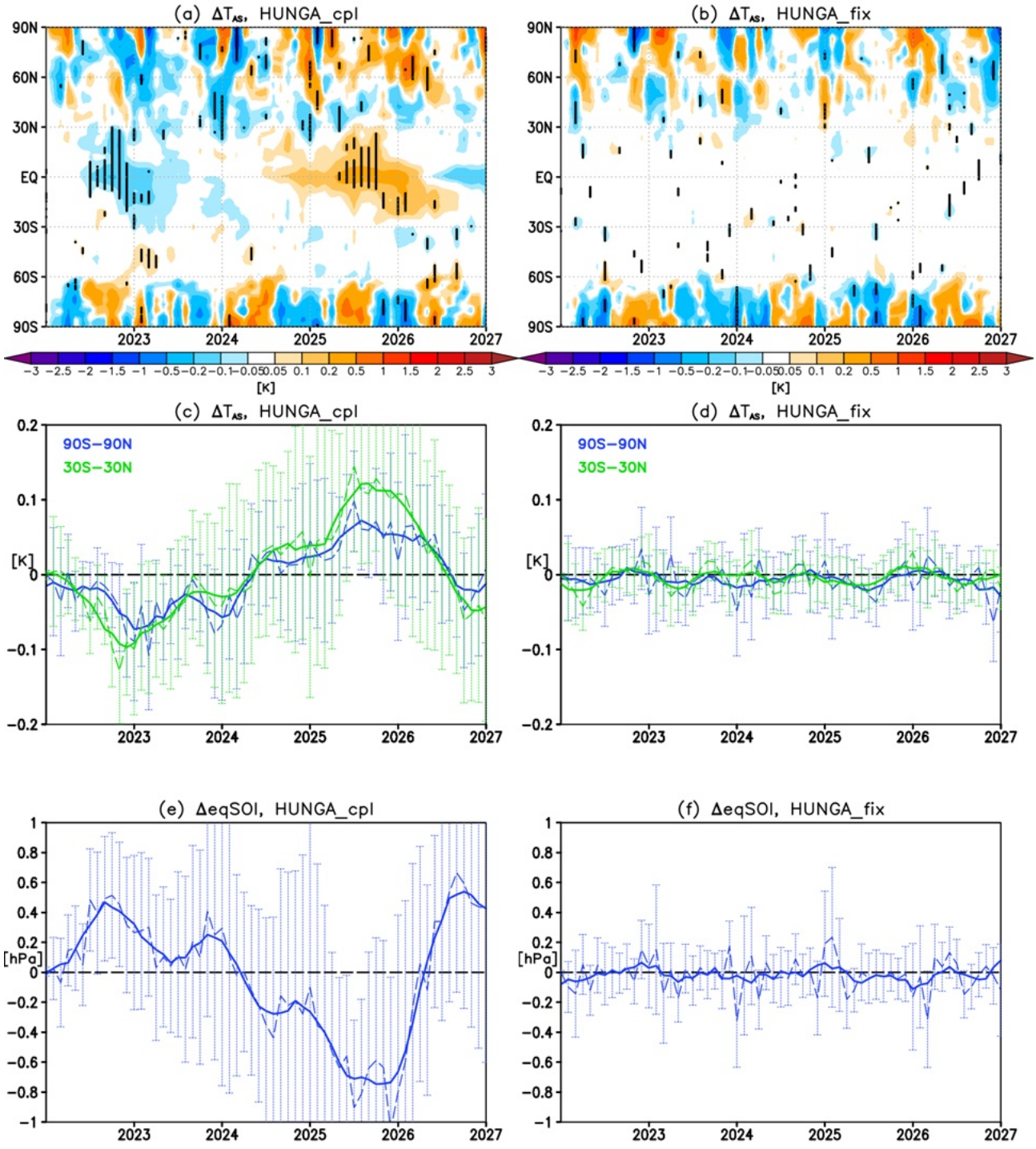

Figure S3.27: *Time series of changes in (a–b) zonal mean near-surface air temperature, (c–d) global and tropical mean near-surface air temperature, and (e–f) the eqSOI index between the forced simulation and the control in the coupled ocean (left) and atmosphere-only (right) simulations. Dashed lines in panels (c–f) indicate ensemble mean changes and solid lines their five-month running means. Error bars in panels (c–f) denote confidence intervals of the ensemble mean changes (±2 standard errors).*

S3.4.2 Seasonal changes in the NH polar vortex and impacts on the extratropical surface climate

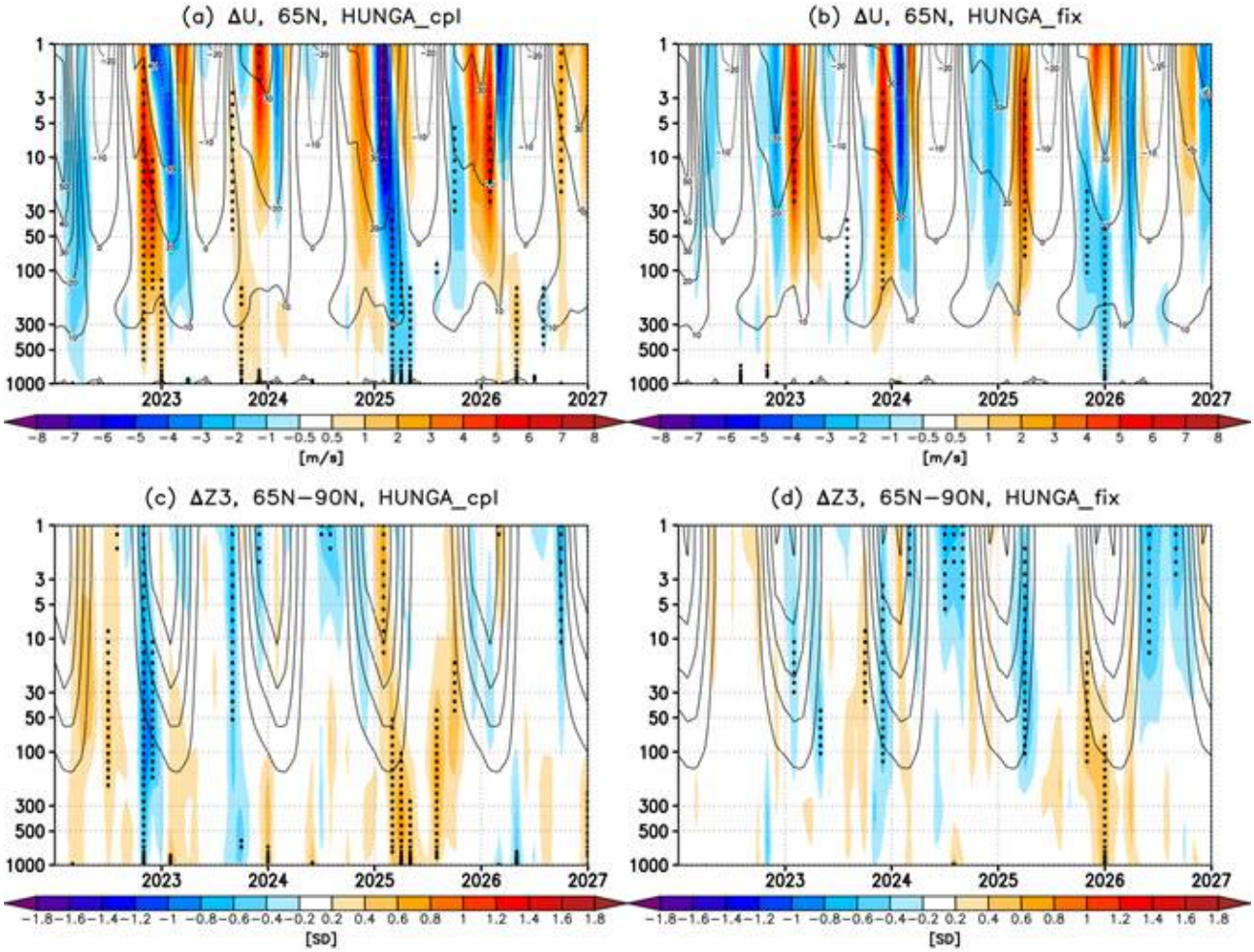

Figure S3.28: *Evolution of the Northern Hemisphere (NH) polar vortex. Shading: time series of ensemble-mean changes in (a–b) zonal wind at 65°N (in m s^{-1}) and (c–d) geopotential height (in standard deviations) averaged over the polar cap (65°–90°N) between the forced simulation and the control. Left panels correspond to the coupled ocean simulations, right panels to the atmosphere-only simulations. Stippling denotes statistical significance (defined as in Figure S3.23). Contours indicate values in the control for reference.*

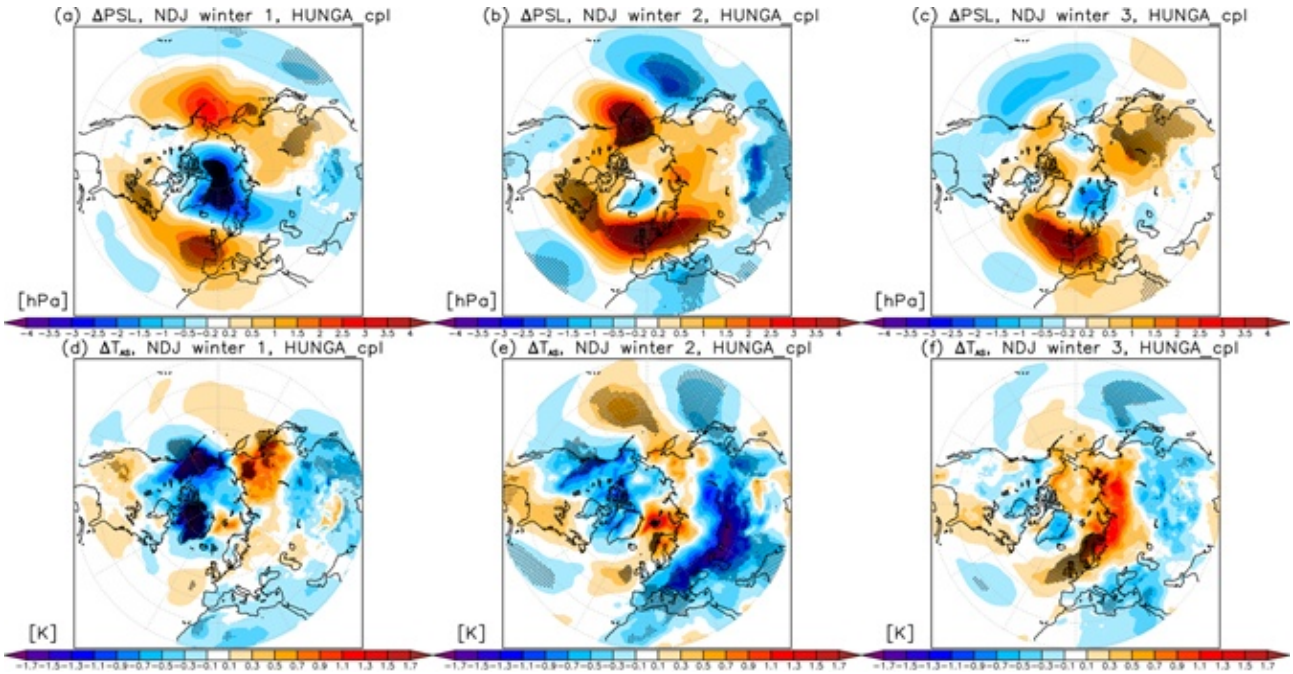

Figure S3.29: *Changes in early NH winter (November–December–January) ensemble-mean (top) sea-level pressure and (bottom) near-surface air temperature between the forced simulation and the control in the coupled ocean simulations for the first (2022/2023), second (2023/2024), and third (2024/2025) winters following the eruption (columns). Stippling denotes statistical significance (defined as in Figure S3.23).*

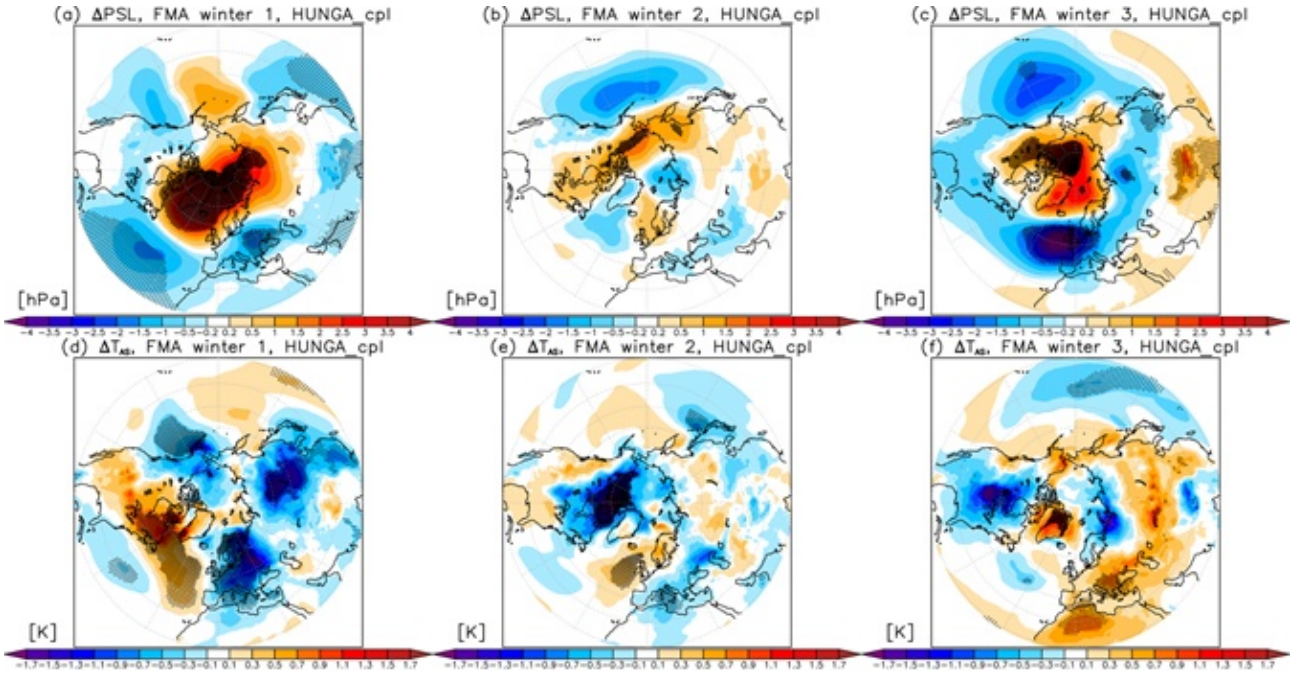

Figure S3.30: *As in Figure S3.29, but for the corresponding late NH winter (February–March–April) changes.*

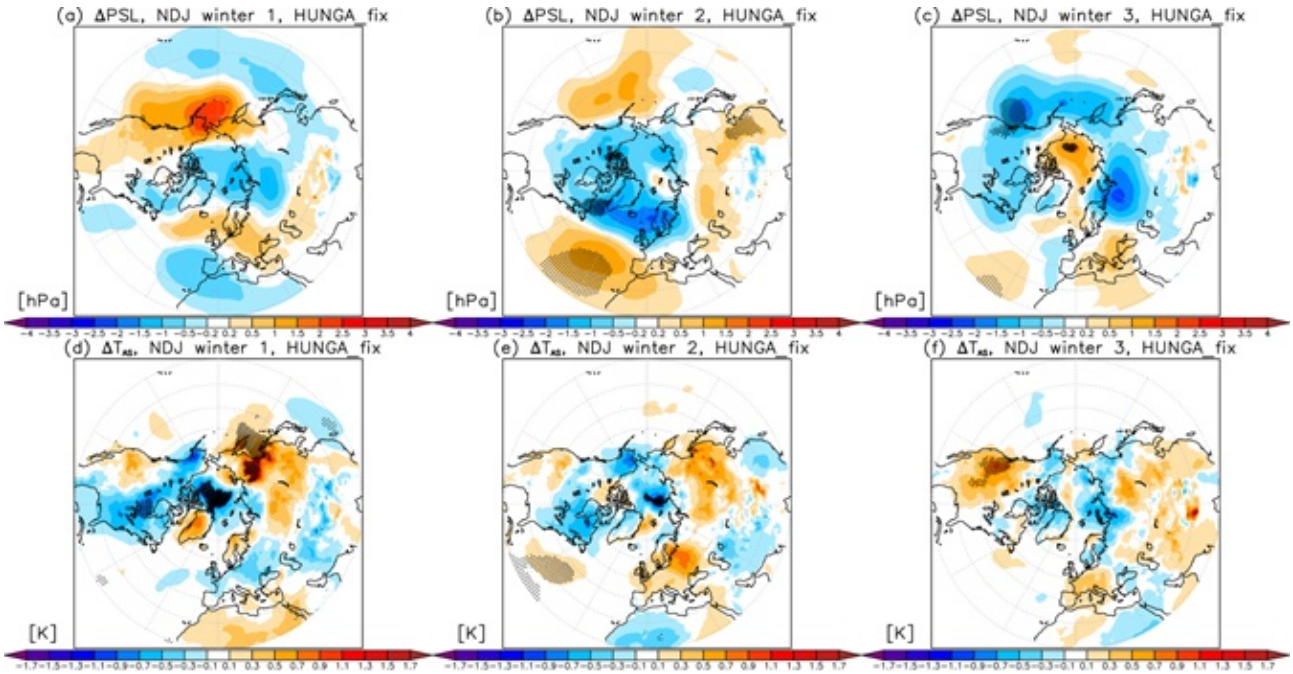

Figure S3.31: *As in Figure S3.29, but for the changes in the atmosphere-only simulations.*

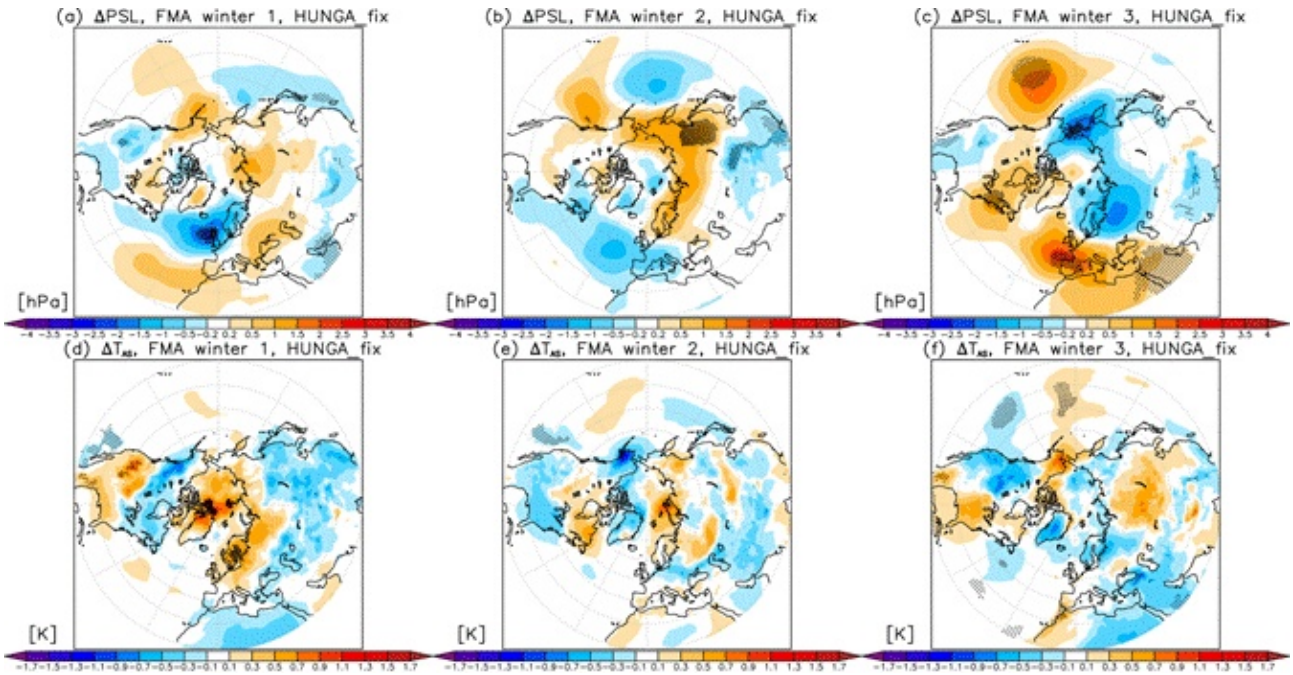

Figure S3.32: *As in Figure S3.31, but for years 5–10 in the atmosphere-only simulations.*

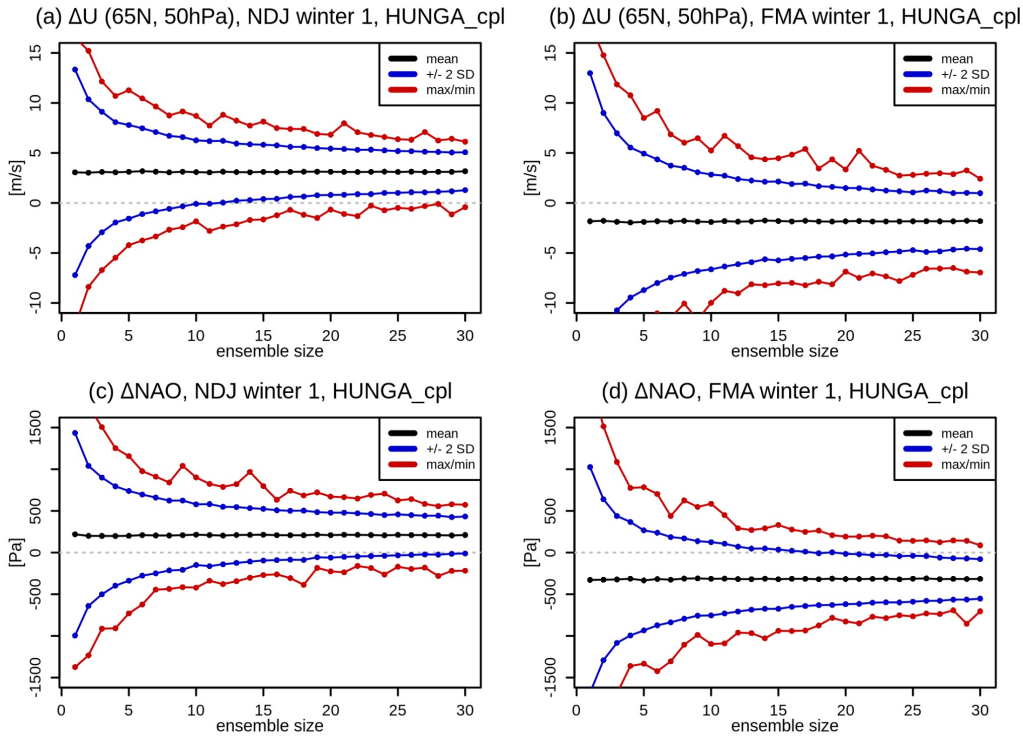

Figure S3.33: *Detectability of the early winter (a,c) and late winter (b,d) NH stratospheric vortex (a,b) and NAO (c,d) responses in the coupled ocean simulations during the first winter following the eruption (2022/2023). Black lines denote the mean response; blue and red lines indicate the ±2 standard deviation and maximum/minimum ranges, respectively, obtained by randomly subsampling the ensemble with replacement to generate 2000 artificial ensembles for each ensemble size.*

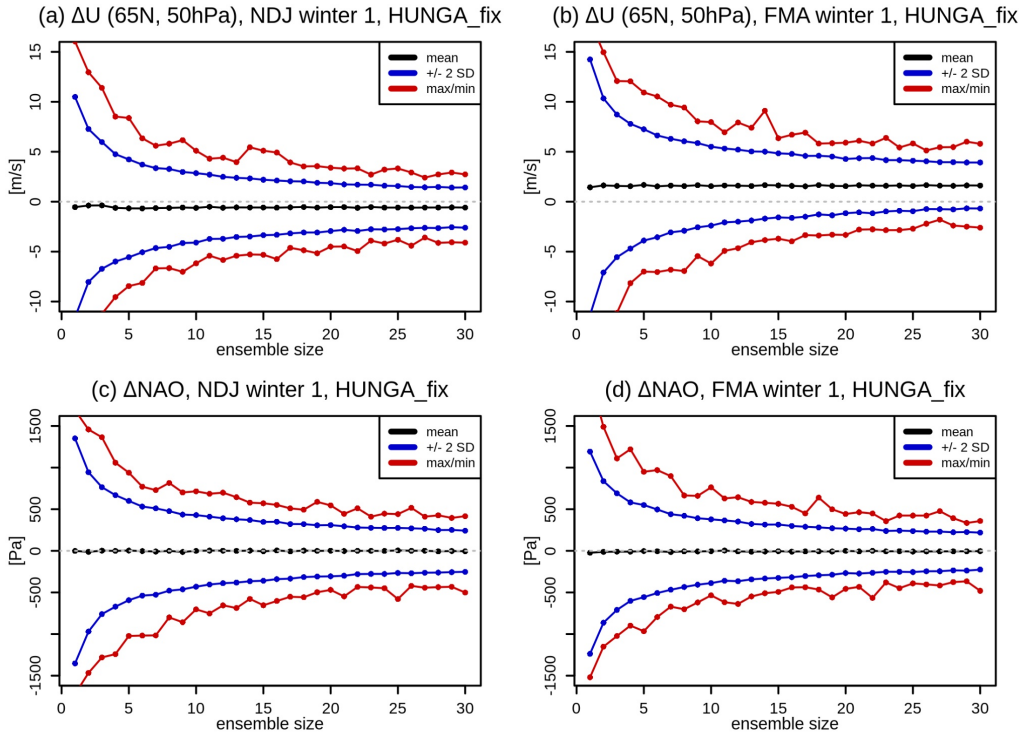

Figure S3.34: *As in Figure S3.33, but for the detectability of the changes in the atmosphere-only simulations.*

S3.4.3 Seasonal changes in the SH polar vortex and impacts on the extratropical surface climate

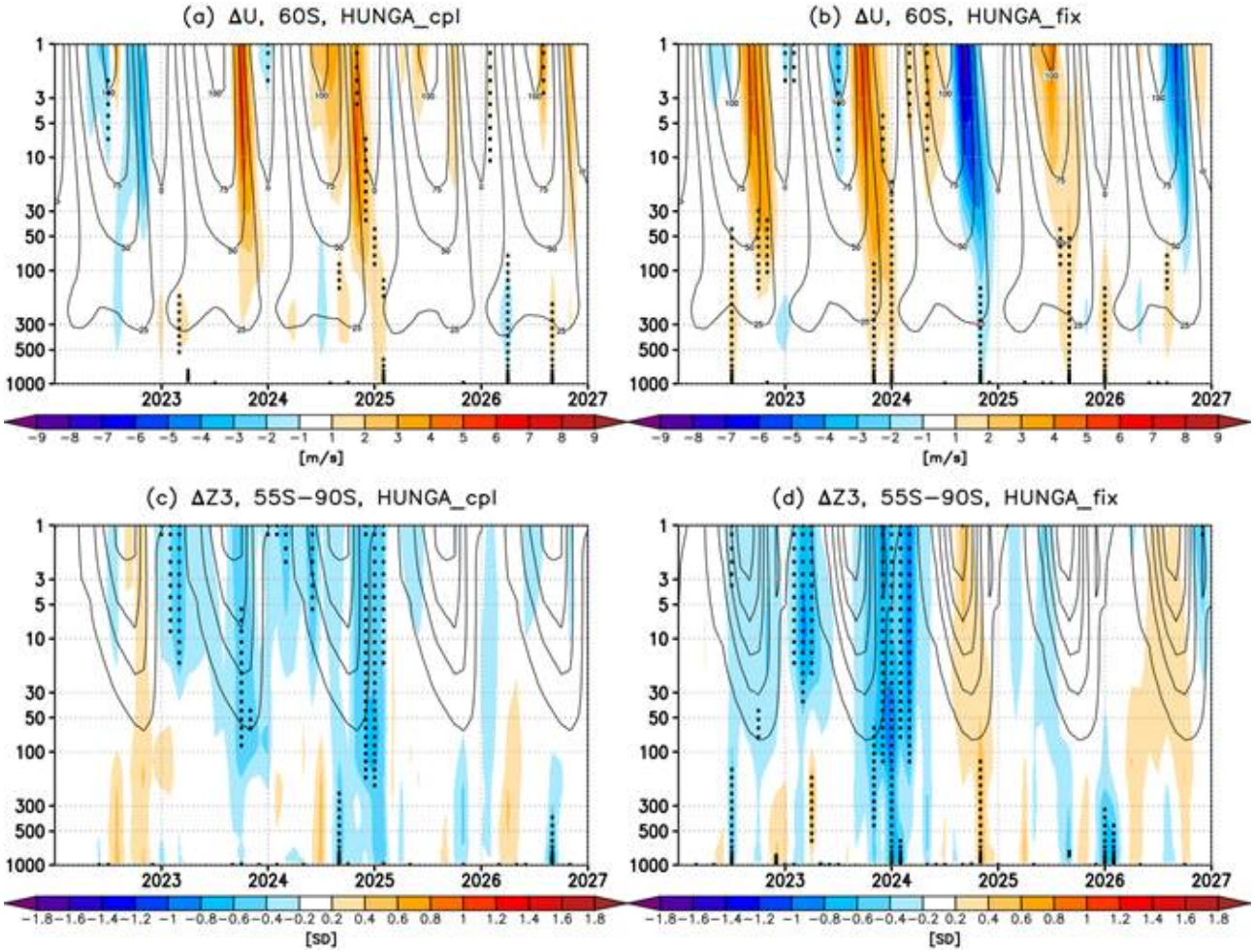

Figure S3.35: *Evolution of the Southern Hemisphere (SH) polar vortex. Shading: time series of changes in (a–b) zonal wind at 60°S (in m s^{-1}) and (c–d) geopotential height (in standard deviations) averaged over the Antarctic polar cap (55°–90°S) between the forced simulation and the control. Left panels correspond to the coupled ocean simulations, right panels to the atmosphere-only simulations. Stippling denotes regions where the response is statistically significant (defined as in Figure S3.23).*

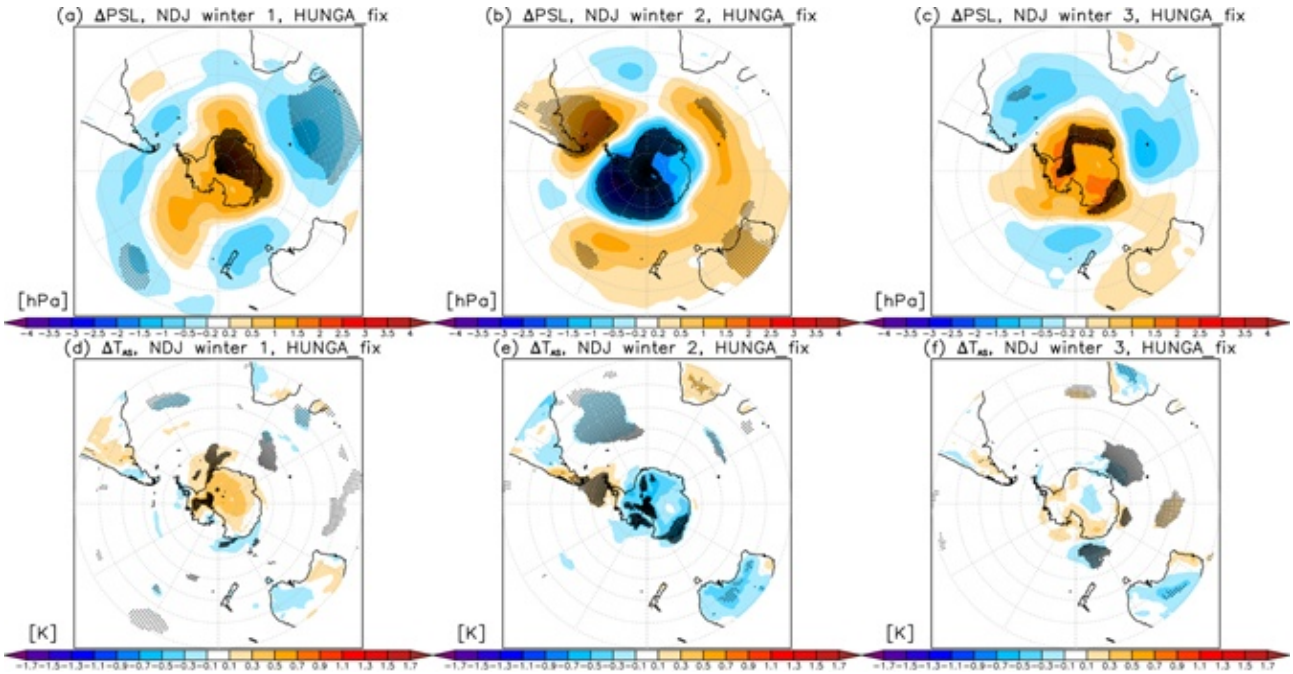

Figure S3.36: *Changes in late austral spring and early summer (November–December–January) (top) sea-level pressure and (bottom) near-surface air temperature between the forced simulation and the control in the atmosphere-only simulations for the first (2022/2023), second (2023/2024), and third (2024/2025) years following the eruption (columns). Stippling denotes statistical significance (defined as in Figure S3.23).*

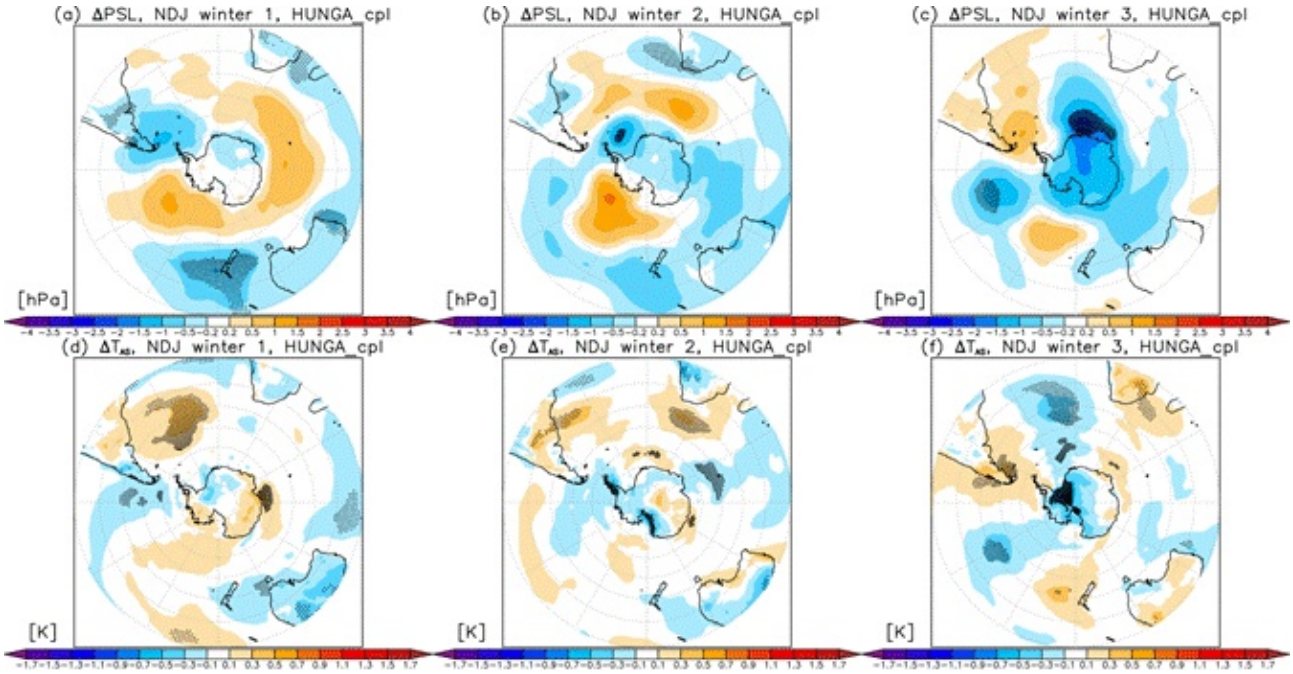

Figure S3.37: *As in Figure S3.36, but for the changes in the coupled ocean simulations.*

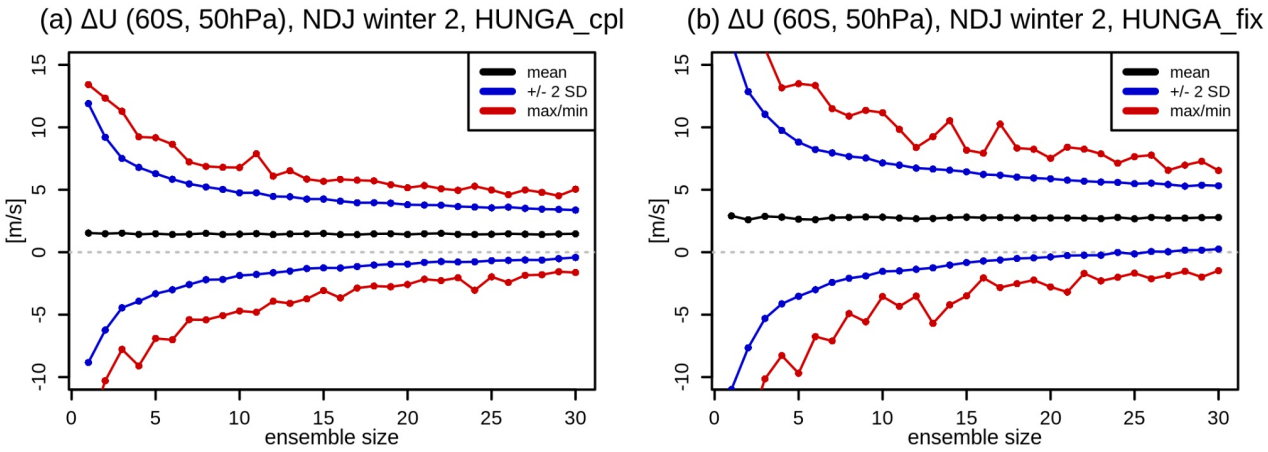

Figure S3.38: *Detectability of the changes in the 2023–2024 November–December–January SH lower stratospheric vortex in the coupled ocean (a) and atmosphere-only (b) simulations. Different lines correspond to those shown in Figure S3.33.*

S3.5 Upper stratosphere to thermosphere effects and H_2O transport in the deep Brewer–Dobson branch: modelling of long-term middle-atmospheric impacts

Authors Wandi Yu
Jia Yue
Yunqian Zhu
Xinyue Wang
Simone Tilmes
Jun Zhang
Zhihong Zhuo
Ewa M. Bednarz
Eric Fleming
David Plummer

This section analyses the upper-stratospheric to thermospheric responses to the Hunga eruption using multi-model ensemble simulations. The analysis focuses on changes in large-scale circulation, wave-driven transport, and water vapour propagation through the deep Brewer–Dobson branch, highlighting their long-term implications for the middle and upper atmosphere.

Simulations are based on 60-member WACCM6MAM Exp4 ensembles (30 with fixed SSTs/sea-ice and 30 with coupled ocean configurations) with combined H_2O and SO_2 injections, a 10-member CMAM ensemble (H_2O only), and a 20-member GSFC2D ensemble (H_2O and SO_2) conducted under fixed SSTs configuration.

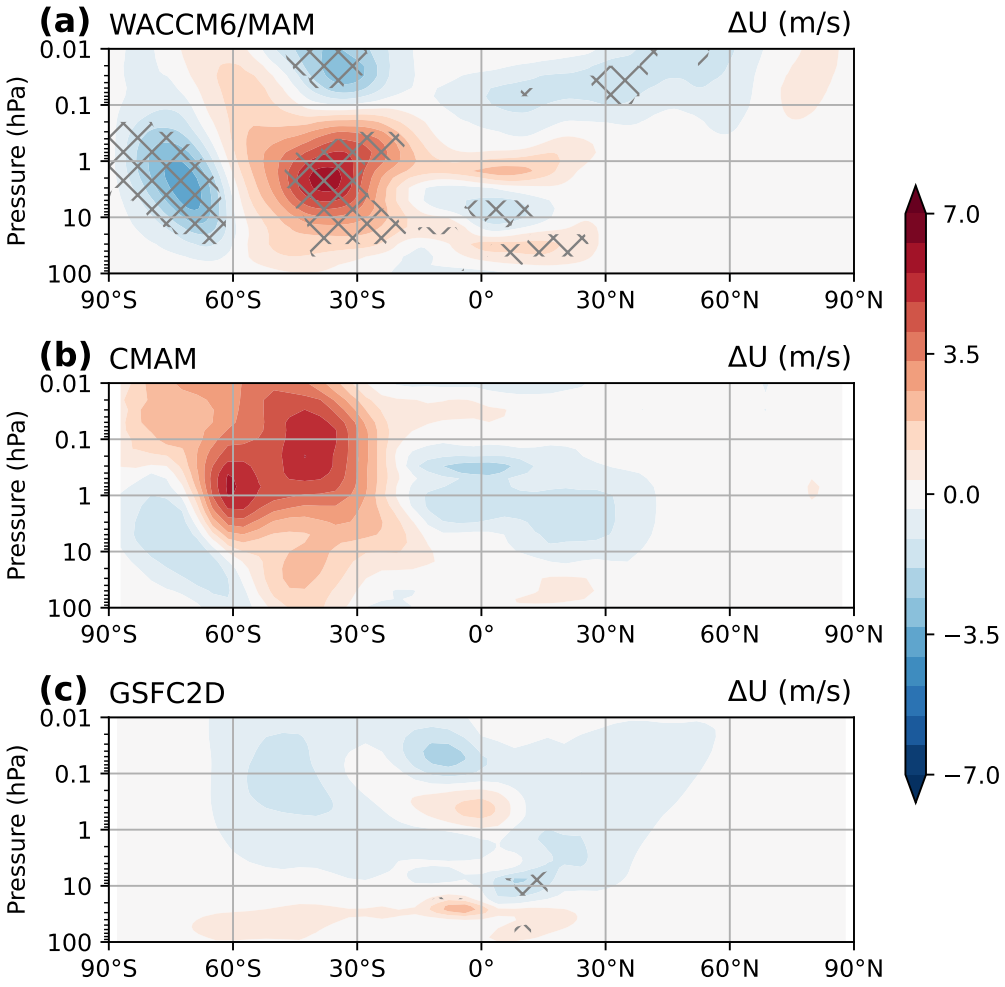

Figure S3.39: *Zonal mean zonal wind differences between the volcanic and control cases in July–August 2022, as simulated in (a) WACCM6MAM, (b) CMAM, and (c) GSFC2D. Areas with hatching indicate statistically significant differences.*

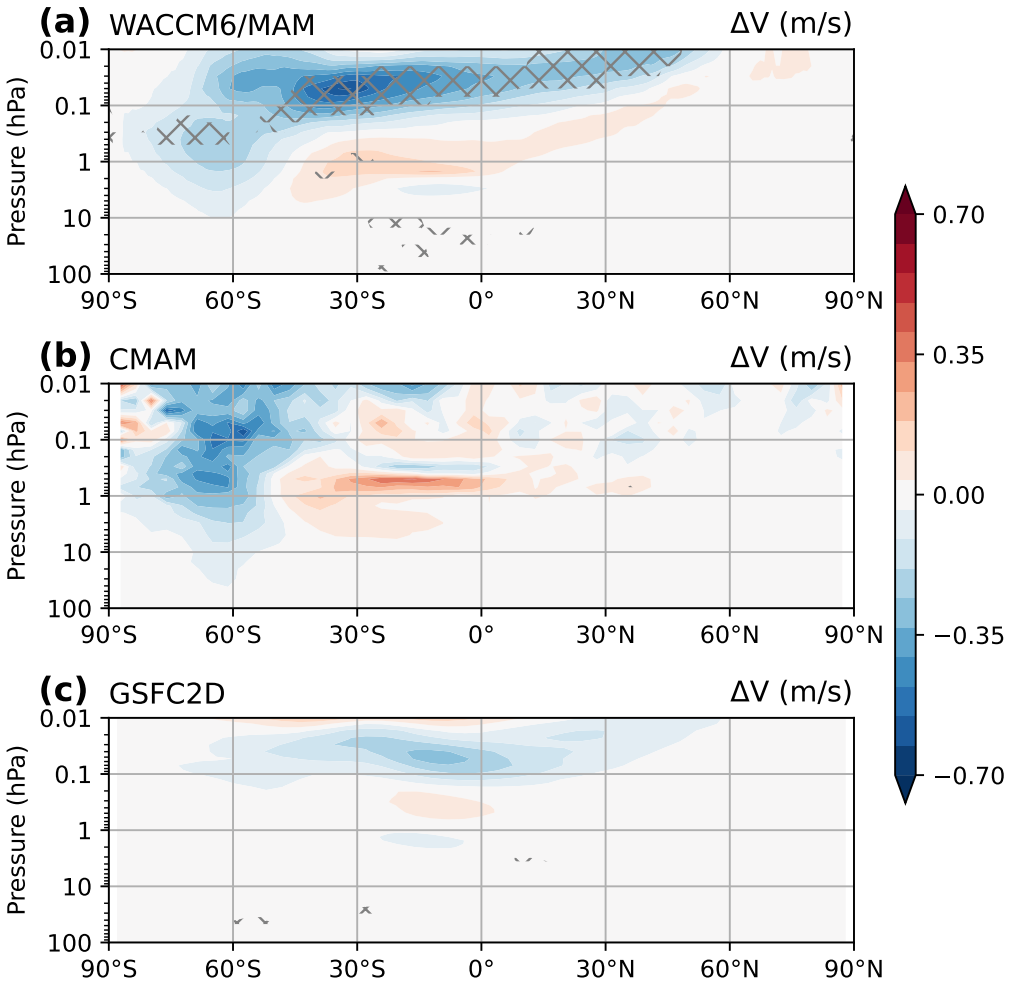

Figure S3.40: *Same as figure S3.39, but showing meridional wind differences between the volcanic and control simulations.*

S3.6 Simulated effects on total column ozone and halogen repartitioning in the Southern Hemisphere lower stratosphere

This section is based on: Bednarz et al. (2025).

Bednarz, E. M., Aquila, V., Butler, A. H., Colarco, P., Fleming, E., Østerstrøm, F. F., Plummer, D., Quaglia, I., Randel, W., Santee, M. L., Sekiya, T., Tilmes, S., Wang, X., Watanabe, S., Yu, W., Zhang, J., Zhu, Y., and Zhuo, Z.: Multi-model assessment of impacts of the 2022 Hunga eruption on stratospheric ozone and its chemical and dynamical drivers, *EGUsphere [preprint]*, https://doi.org/10.5194/egusphere-2025-4609, 2025.

This section presents the modelled effects of the 2022 Hunga eruption on total column ozone and the partitioning of halogen species in the Southern Hemisphere (SH) lower stratosphere. The results are based on a coordinated multi-model analysis using GEOSCCM, MIROC-CHASER, and WACCM-MAM simulations, encompassing both free-running and specified-dynamics experiments. The experiments assess the combined and individual effects of sulfur dioxide (SO_2) and water vapour (H_2O) injections, as well as their direct chemical and radiative–dynamical impacts.

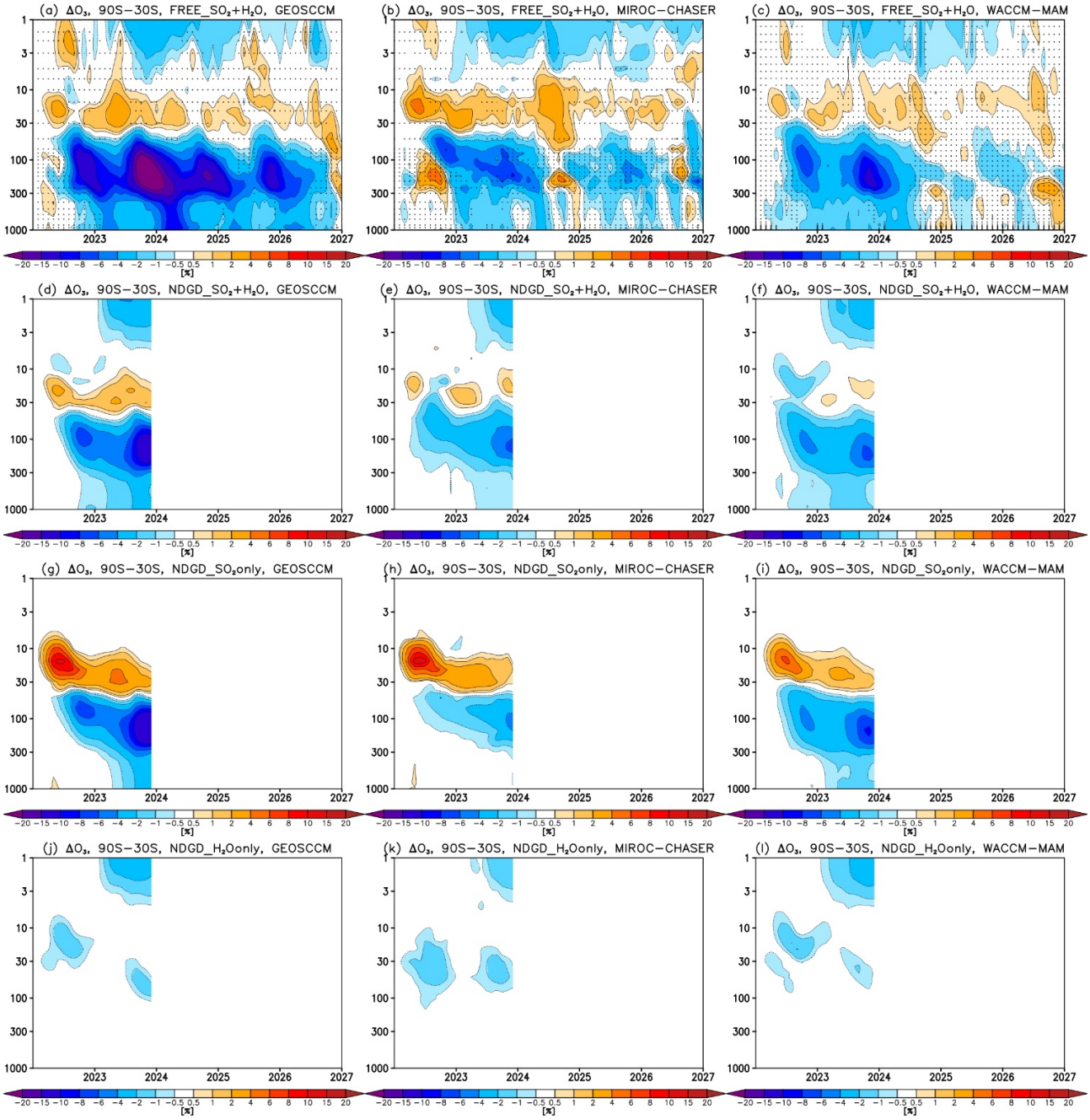

Figure S3.41: *Hunga-induced changes in SH extratropical (90°S–30°S) ozone mixing ratios, calculated as the differences (perturbed minus control) between simulations with and without Hunga forcing. Results are shown for GEOSCCM (a,d,g,j), MIROC-CHASER (b,e,h,k), and WACCM-MAM (c,f,i,l), with ensemble-mean responses displayed in all cases. (a–c) Free-running experiments including injection of both 0.5 Tg of SO_2 and ~150 Tg of H_2O (FREE_SO_2+H_2O). Stippling marks regions where the response in ozone is not statistically significant. (d–f) Specified-dynamics experiments with nudged meteorological fields (MERRA-2) including both SO_2 and H_2O injections (NDGD_SO_2+H_2O). Since the meteorology is identical for perturbed and control runs, these quantify direct chemical effects only. (g–i) Experiments with SO_2-only injections (NDGD_SO_2ONLY); (j–l) experiments with H_2O-only injections (NDGD_H_2OONLY). The bottom two rows isolate the effects of aerosol and water vapour perturbations from Hunga.*

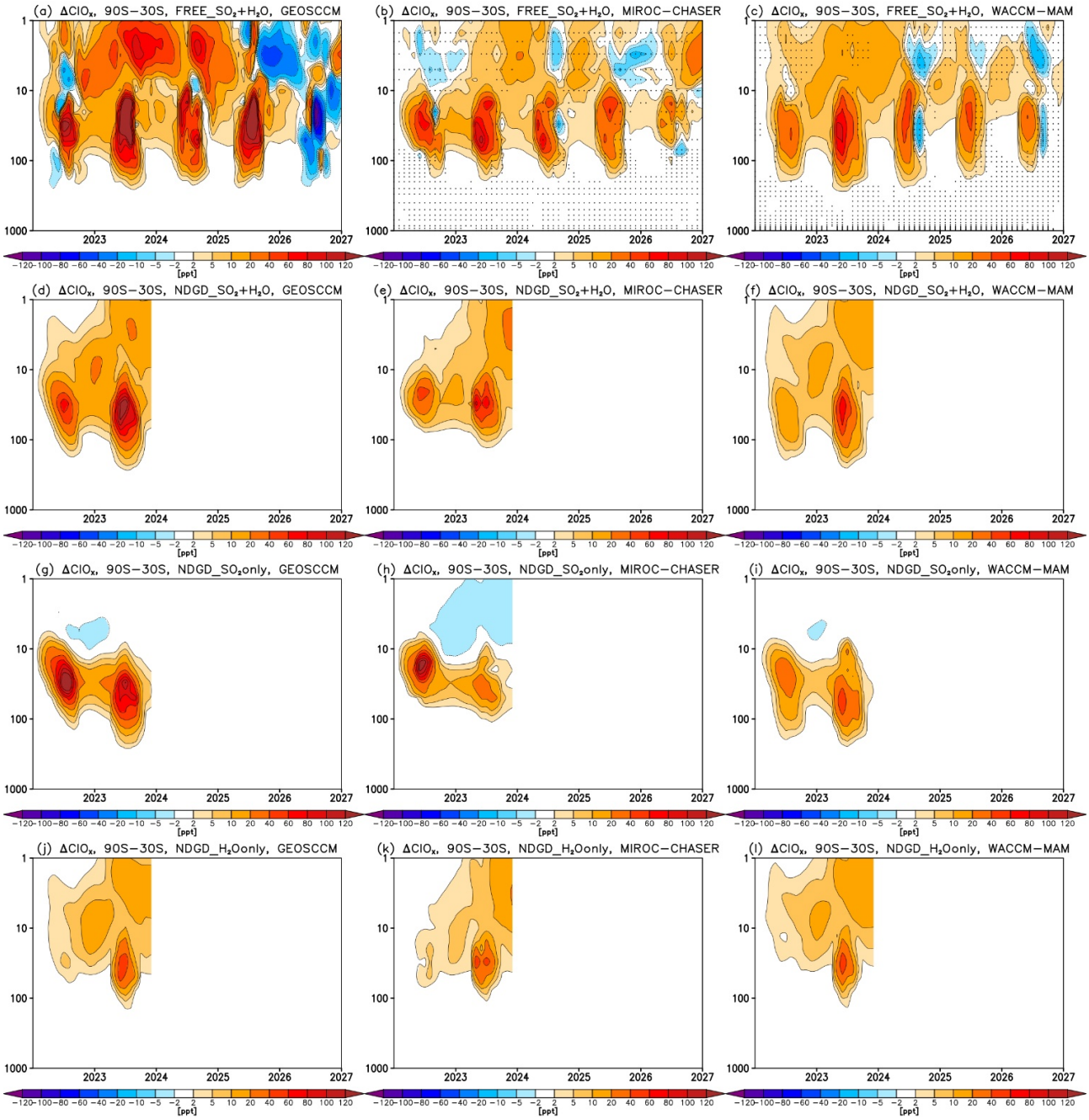

Figure S3.42: *As in Figure S3.41, but showing changes in ClO_x (Cl + ClO + 2 × ClOOCl + HOCl + OClO + 2 × Cl_2) mixing ratios.*

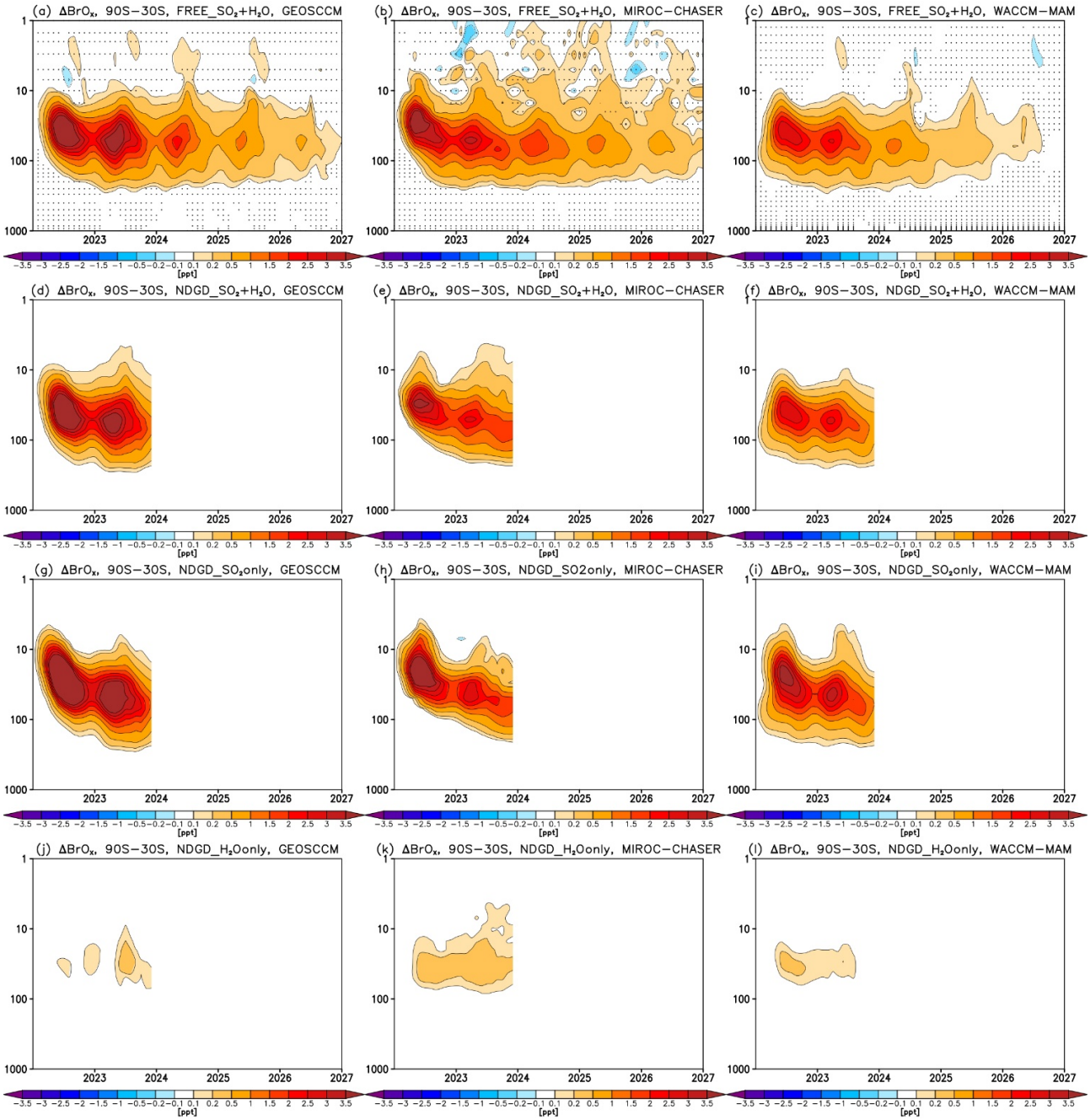

Figure S3.43: *As in Figure S3.41, but showing changes in BrO_x (Br + BrO + BrCl + HOBr) mixing ratios.*

References

Bednarz, E. M., A. H. Butler, X. Wang, Z. Zhuo, W. Yu, G. Stenchikov, M. Toohey and Y. Zhu (2026). 'Indirect climate impacts of the Hunga eruption'. *Atmos. Chem. Phys.*, 26, pp. 197–215. DOI: 10.5194/acp-26-197-2026.

Bednarz, E. M., V. Aquila, A. H. Butler, P. Colarco, E. Fleming, F. F. Østerstrøm, D. Plummer, I. Quaglia, W. Randel, M. L. Santee et al. (2025). 'Multi-model assessment of impacts of the 2022 Hunga eruption on stratospheric ozone and its chemical and dynamical drivers'. *EGUsphere [preprint]*, 2025, pp. 1–24. DOI: 10.5194/egusphere-2025-4609.

Butchart, N. (2014). 'The Brewer-Dobson circulation'. *Rev. Geophys.*, 52, pp. 157–184. DOI: 10.1002/2013rg000448.

Carr, J. L., Á. Horváth, D. L. Wu and M. D. Friberg (2022). 'Stereo Plume Height and Motion Retrievals for the Record-Setting Hunga Tonga-Hunga Ha'apai Eruption of 15 January 2022'. *Geophys. Res. Lett.*, 49, e2022GL098131. DOI: 10.1029/2022gl098131.

Clyne, M., O. B. Toon, T. Sukhodolov, G. W. Mann, S. Dhomse, S. Tilmes, Y. Zhu, P. R. Colarco, K. Tsigaridis, T. Nagashima et al. (2024). 'Tonga-MIP: The Hunga Tonga-Hunga Ha'apai Volcano Model Intercomparison Project'. In M. Clyne (Ed.), *Modeling the role of volcanoes in the climate system* (Publication No. 31487034), https://www.proquest.com/dissertations-theses/modeling-role-volcanoes-climate-system/docview/3100397790/se-2. PhD thesis. University of Colorado at Boulder.

Evan, S., J. Brioude, K. H. Rosenlof, R.-S. Gao, R. W. Portmann, Y. Zhu, R. Volkamer, C. F. Lee, J.-M. Metzger, K. Lamy et al. (2023). 'Rapid ozone depletion after humidification of the stratosphere by the Hunga Tonga eruption'. *Science*, 382, eadg2551. DOI: 10.1126/science.adg2551.

Fleming, E. L., P. A. Newman, Q. Liang and L. D. Oman (2024). 'Stratospheric Temperature and Ozone Impacts of the Hunga Tonga-Hunga Ha'apai Water Vapor Injection'. *J. Geophys. Res.*, 129, e2023JD039298. DOI: 10.1029/2023jd039298.

Manney, G. L., M. L. Santee, A. Lambert, L. F. Millán, K. Minschwaner, F. Werner, Z. D. Lawrence, W. G. Read, N. J. Livesey and T. Wang (2023). 'Siege in the Southern Stratosphere: Hunga Tonga-Hunga Ha'apai Water Vapor Excluded From the 2022 Antarctic Polar Vortex'. *Geophys. Res. Lett.*, 50. DOI: 10.1029/2023gl103855.

Millán, L., W. G. Read, M. L. Santee, A. Lambert, G. L. Manney, J. L. Neu, M. C. Pitts, F. Werner, N. J. Livesey and M. J. Schwartz (2024). 'The Evolution of the Hunga Hydration in a Moistening Stratosphere'. *Geophys. Res. Lett.*, 51, e2024GL110841. DOI: 10.1029/2024gl110841.

Millán, L., M. L. Santee, A. Lambert, N. J. Livesey, F. Werner, M. J. Schwartz, H. C. Pumphrey, G. L. Manney, Y. Wang, H. Su et al. (2022). 'The Hunga Tonga-Hunga Ha'apai Hydration of the Stratosphere'. *Geophys. Res. Lett.*, 49, e2022GL099381. DOI: 10.1029/2022gl099381.

Niemeier, U., S. Wallis, C. Timmreck, T. van Pham and C. von Savigny (2023). 'How the Hunga Tonga—Hunga Ha'apai Water Vapor Cloud Impacts Its Transport Through the Stratosphere: Dynamical and Radiative Effects'. *Geophys. Res. Lett.*, 50, e2023GL106482. DOI: 10.1029/2023gl106482.

Quaglia, I., D. Visioni, E. M. Bednarz, Y. Zhu, G. Stenchikov, V. Aquila, C.-C. Liu, G. W. Mann, Y. Peng, T. Sekiya et al. (2025). 'Multi-model analysis of the radiative impacts of the 2022 Hunga eruption indicates a significant cooling contribution from the volcanic plume'. *EGUsphere [preprint]*, 2025, pp. 1–35. DOI: 10.5194/egusphere-2025-3769.

Randel, W. J., X. Wang, J. Starr, R. R. Garcia and D. Kinnison (2024). 'Long-Term Temperature Impacts of the Hunga Volcanic Eruption in the Stratosphere and Above'. *Geophys. Res. Lett.*, 51. DOI: 10.1029/2024gl111500.

Santee, M. L., A. Lambert, L. Froidevaux, G. L. Manney, M. J. Schwartz, L. F. Millán, N. J. Livesey, W. G. Read, F. Werner and R. A. Fuller (2023). 'Strong Evidence of Heterogeneous Processing on Stratospheric Sulfate Aerosol in the Extrapolar Southern Hemisphere Following the 2022 Hunga Tonga-Hunga Ha'apai Eruption'. *J. Geophys. Res.*, 128, e2023JD039169. DOI: 10.1029/2023jd039169.

Schoeberl, M. R., Y. Wang, G. Taha, D. J. Zawada, R. Ueyama and A. Dessler (2024). 'Evolution of the Climate Forcing During the Two Years After the Hunga Tonga-Hunga Ha'apai Eruption'. *J. Geophys. Res.*, 129, e2024JD041296. DOI: 10.1029/2024jd041296.

Taha, G., R. Loughman, P. R. Colarco, T. Zhu, L. W. Thomason and G. Jaross (2022). 'Tracking the 2022 Hunga Tonga-Hunga Ha'apai Aerosol Cloud in the Upper and Middle Stratosphere Using Space-Based Observations'. *Geophys. Res. Lett.*, 49, e2022GL100091. DOI: 10.1029/2022gl100091.

Wang, X., W. Randel, Y. Zhu, S. Tilmes, J. Starr, W. Yu, R. Garcia, O. B. Toon, M. Park, D. Kinnison et al. (2023). 'Stratospheric Climate Anomalies and Ozone Loss Caused by the Hunga Tonga-Hunga Ha'apai Volcanic Eruption'. *J. Geophys. Res.*, 128, e2023JD039480. DOI: 10.1029/2023jd039480.

Wilmouth, D. M., F. F. Østerstrøm, J. B. Smith, J. G. Anderson and R. J. Salawitch (2023). 'Impact of the Hunga Tonga volcanic eruption on stratospheric composition'. *Proc. Natl. Acad. Sci.*, 120, e2301994120. DOI: 10.1073/pnas.2301994120.

Zhang, J., D. Kinnison, Y. Zhu, X. Wang, S. Tilmes, K. Dube and W. Randel (2024). 'Chemistry Contribution to Stratospheric Ozone Depletion After the Unprecedented Water-Rich Hunga Tonga Eruption'. *Geophys. Res. Lett.*, 51, e2023GL105762. DOI: 10.1029/2023gl105762.

Zhou, X., S. S. Dhomse, W. Feng, G. Mann, S. Heddell, H. Pumphrey, B. J. Kerridge, B. Latter, R. Siddans, L. Ventress et al. (2024). 'Antarctic Vortex Dehydration in 2023 as a Substantial Removal Pathway for Hunga Tonga-Hunga Ha'apai Water Vapor'. *Geophys. Res. Lett.*, 51, e2023GL107630. DOI: 10.1029/2023gl107630.

Zhu, Y., H. Akiyoshi, V. Aquila, E. Asher, E. M. Bednarz, S. Bekki, C. Brühl, A. H. Butler, P. Case, S. Chabrillat et al. (2025). 'Hunga Tonga–Hunga Ha'apai Volcano Impact Model Observation Comparison (HTHH-MOC) project: experiment protocol and model descriptions'. *Geosci. Model Dev.*, 18, pp. 5487–5512. DOI: 10.5194/gmd-18-5487-2025.

Zhu, Y., C. G. Bardeen, S. Tilmes, M. J. Mills, X. Wang, V. L. Harvey, G. Taha, D. Kinnison, R. W. Portmann, P. Yu et al. (2022). 'Perturbations in stratospheric aerosol evolution due to the water-rich plume of the 2022 Hunga-Tonga eruption'. *Commun. Earth Environ.*, 3, 248. DOI: 10.1038/s43247-022-00580-w.

Zhu, Y., R. W. Portmann, D. Kinnison, O. B. Toon, L. Millán, J. Zhang, H. Vömel, S. Tilmes, C. G. Bardeen, X. Wang et al. (2023). 'Stratospheric ozone depletion inside the volcanic plume shortly after the 2022 Hunga Tonga eruption'. *Atmos. Chem. Phys.*, 23, pp. 13355–13367. DOI: 10.5194/acp-23-13355-2023.

Zhuo, Z., X. Wang, Y. Zhu, W. Yu, E. M. Bednarz, E. Fleming, P. R. Colarco, S. Watanabe, D. Plummer, G. Stenchikov et al. (2025). 'Comparing multimodel ensemble simulations with observations and decadal projections of upper atmospheric variations following the Hunga eruption'. *Atmos. Chem. Phys.*, 25, pp. 13161–13176. DOI: 10.5194/acp-25-13161-2025.

S4 Other chapter supplementaries

Authors (Section S4.1) Xinyue Wang
Lawrence Coy

Authors (Section S4.2) Freja F. Østerstrøm
Michelle L. Santee

Contributing authors (Section S4.1) Masatomo Fujiwara
Pu Lin
Alison Ming
Feng Li
Ewa Bednarz
Zhihong Zhuo
Kirstin Krüger

Contributing authors (Section S4.2) Martyn P. Chipperfield
Stephanie Evan
Dan Smale
Krzysztof Wargan
David M. Wilmouth
Ingo Wohltmann

S4.1 Stratospheric anomalies following the Hunga eruption for Chapter 4

This section provides additional figures on stratospheric anomalies following the Hunga eruption that were not included in Chapter 4.

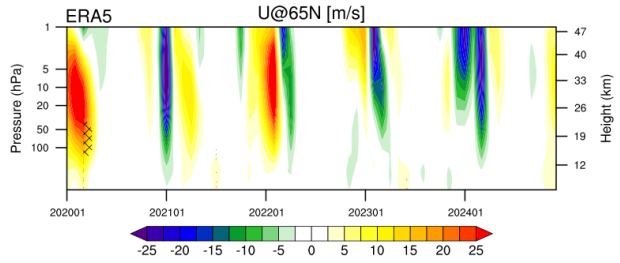

Figure S4.1: *Time series of Northern Hemisphere zonal mean zonal wind anomalies at 65°N [m/s] from ERA5, with the 2005–2021 mean removed. Hatched regions indicate anomalies that fall outside two standard deviations of internal variability.*

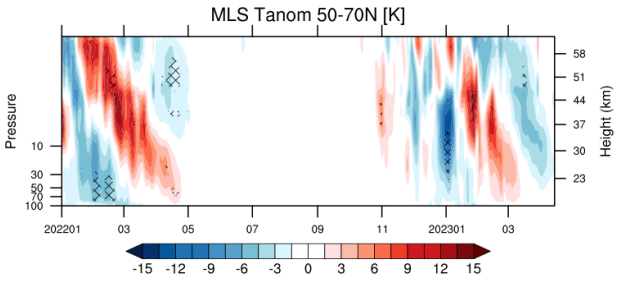

Figure S4.2: *Time series of Northern Hemisphere temperature anomalies averaged over 50°-70°N [K] from MLS, with the 2005–2021 mean removed. Hatched regions indicate anomalies that are outside the range of all variability during 2005-2021.*

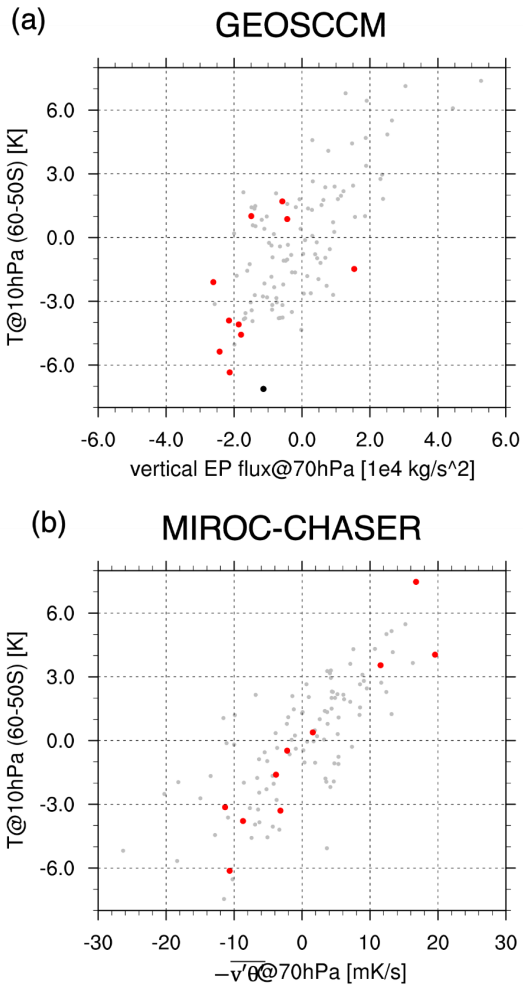

Figure S4.3: *Relationship between July–August average temperatures at 10 hPa and wave activity at 70 hPa over 55°S–65°S. Red dots show the differences between Hunga-forced and control simulations for July–August 2022, based on 10 ensemble members from (a) GEOSCCM and (b) MIROC-CHASER. Gray dots represent deviations from the control ensemble mean for July–August averages across 2022–2031 (10 ensemble members × 10 years for each model). The black dot in (a) marks the July–August 2022 value from ERA5. Note that in (b), is used as a proxy for wave activity, as it is positively correlated with upward EP flux.*

S4.2 Models used in Chapter 5 but not included in HTHH-MOC or Tonga-MIP

S4.2.1 ATLAS

Alfred Wegener InsTitute LAgrangian Chemistry/Transport System.

ATLAS is a global Lagrangian 3-D chemical transport model (Wohltmann and Rex, 2009; Wohltmann et al., 2010; Wohltmann et al., 2017). The model includes a comprehensive gas-phase stratospheric chemistry module, heterogeneous chemistry on polar stratospheric clouds (PSCs), a particle-based Lagrangian denitrification module, and a dehydration parameterisation. In addition to the binary background aerosol, the model simulates three types of PSCs, that is, supercooled ternary solutions (STS), clouds composed of solid nitric acid trihydrate (NAT) particles, and ice particles. Model runs are driven by meteorological data from the European Centre for Medium-range Weather Forecasts (ECMWF) ERA5 reanalysis (provided on a 1.125° × 1.125° horizontal grid, 3 hr temporal resolution, and 137 model levels; Hersbach et al., 2017; Hersbach et al., 2020). The horizontal resolution is ~150 km. The vertical range of the model domain is 13–50 km (~350–1900 K potential temperature). The simulations for the Antarctic winter 2023 referred to in this report (Chapter 5) are based on a reference model run initialised with MLS data from 1 May 2023 and a sensitivity run that uses exactly the same setup, with the exception of the initialisation of MLS water vapour, which is taken from the preceding year on 1 May 2022 (i.e., without the effect of Hunga on water vapour).

S4.2.2 SOCOL-AERv2-Volc

SOCOL = modeling tools for studies of SOlar Climate Ozone Links, AER = 2-D aerosol model, Volc = heat flux, mixed-layer ocean, and SSP implementation.

SOCOL-AERv2 is a fully coupled 3-D global aerosol-chemistry-climate model. Version 2 is a coupling of SOCOLv3 (Stenke et al., 2013) and the AER 2-D sectional aerosol model (Weisenstein et al., 1997; Weisenstein et al., 2007). The SOCOLv3 model is based on the general circulation model European Centre/Hamburg 5 (ECHAM5; Roeckner et al., 2003; Giorgetta et al., 2006) and the chemistry model MEZON focused on stratospheric chemistry (Rozanov et al., 1999; Egorova et al., 2003). The spatial and temporal resolution is variable; the version of the model presented in this report (Chapter 5) has T42 spectral Gaussian grid resolution (2.8° × 2.8° at the equator) and 39 hybrid sigma-pressure levels spanning the surface to 0.01 hPa (~80 km). The model version (Volc) included in the discussion in Chapter 5 (Wilmouth et al., 2023), described by Østerstrøm et al. (2023), is based on Feinberg et al. (2019) and references therein, with the following two main modifications: (1) The chemical boundary conditions were integrated with those of the Shared Socioeconomic Pathways (SSP) scenarios, and (2) heat fluxes needed to implement an interactive mixed-layer ocean in the model were generated from a 10-member perturbed initial conditions model ensemble running from 2015 to 2100 following model spin-up of 20 years at 2015 conditions. Sea surface temperatures and sea ice thickness used in the ensemble were set to MIROC6 values obtained from the CMIP6 database (Tatebe et al., 2019). The ensemble simulations included in Wilmouth et al. (2023) were initialised from spun-up atmospheric states and include large ensembles of 30 model members in both a background ensemble simulation and a volcanic perturbation ensemble simulation injecting both SO_2 and H_2O at the time of the Hunga eruption. The climatology used in both model scenarios is SSP370 and has the quasi-biennial oscillation (QBO) forced at 2000/2001 conditions.

S4.2.3 TOMCAT

University of Leeds 3-D chemical transport model.

TOMCAT is a global off-line chemical transport model (e.g. Chipperfield, 1999; Chipperfield, 2006). The resolution is variable; the simulations presented here (Chapter 5, and in, e.g., Zhou et al., 2024) used a horizontal resolution of 2.8° × 2.8° (T42 Gaussian grid) and 32 hybrid sigma-pressure levels from the surface to ~60 km. The simulations were forced with ERA5 meteorology (Hersbach et al., 2020), and the vertical motion was diagnosed within the model from the ERA5 divergence. The model has a detailed gas-phase stratospheric chemistry scheme of source gases, reservoirs, and radical species of the major chemical families. The model has a simplified aerosol and PSC scheme for the simulation of heterogeneous chemistry based on the assumption of thermodynamic equilibrium between PSC particles, including liquid aerosol, solid nitric acid trihydrate, and/or solid ice particles (Grooß et al., 2018), and the gas phase (e.g. Feng et al., 2011; Feng et al., 2021). The global abundance of binary liquid aerosols is constrained by reading files of latitude-height monthly mean aerosol surface area density. The model simulations are spun up from a control simulation which started in

1955 constrained by global mean surface observations of source gases (World Meteorological Organization (WMO), 2022). The distribution of all chemical tracers, including long-lived source gases, is thus determined by the model chemistry and transport.

For studies of future evolution, the CTM is run with repeating meteorology. Zhou et al. (2024) simulated the impact of Hunga through 2030 by using repeating winds and temperatures from 2022. While this allows the model to simulate long-term trends in composition, it removes any year-to-year dynamical variability and means that polar ozone loss, for example, is calculated for the same vortex conditions every year.

References

Chipperfield, M. P. (1999). 'Multiannual simulations with a three-dimensional chemical transport model'. *J. Geophys. Res.*, 104, pp. 1781–1805. DOI: 10.1029/98jd02597.

Chipperfield, M. P. (2006). 'New version of the TOMCAT/SLIMCAT off-line chemical transport model: Intercomparison of stratospheric tracer experiments'. *Q. J. R. Meteorol. Soc.*, 132, pp. 1179–1203. DOI: 10.1256/qj.05.51.

Egorova, T., E. Rozanov, V. Zubov and I. Karol (2003). 'Model for investigating ozone trends (MEZON)'. *Izv. Atmos. Ocean. Phys.*, 39, pp. 277–292.

Feinberg, A., T. Sukhodolov, B.-P. Luo, E. Rozanov, L. H. E. Winkel, T. Peter and A. Stenke (2019). 'Improved tropospheric and stratospheric sulfur cycle in the aerosol–chemistry–climate model SOCOL-AERv2'. *Geosci. Model Dev.*, 12, pp. 3863–3887. DOI: 10.5194/gmd-12-3863-2019.

Feng, W., M. P. Chipperfield, S. Davies, G. W. Mann, K. S. Carslaw, S. Dhomse, L. Harvey, C. Randall and M. L. Santee (2011). 'Modelling the effect of denitrification on polar ozone depletion for Arctic winter 2004/2005'. *Atmos. Chem. Phys.*, 11, pp. 6559–6573. DOI: 10.5194/acp-11-6559-2011.

Feng, W., S. S. Dhomse, C. Arosio, M. Weber, J. P. Burrows, M. L. Santee and M. P. Chipperfield (2021). 'Arctic Ozone Depletion in 2019/20: Roles of Chemistry, Dynamics and the Montreal Protocol'. *Geophys. Res. Lett.*, 48, e2020GL091911. DOI: 10.1029/2020gl091911.

Giorgetta, M. A., E. Manzini, E. Roeckner, M. Esch and L. Bengtsson (2006). 'Climatology and Forcing of the Quasi-Biennial Oscillation in the MAECHAM5 Model'. *J. Climate*, 19, pp. 3882–3901. DOI: 10.1175/jcli3830.1.

Grooß, J.-U., R. Müller, R. Spang, I. Tritscher, T. Wegner, M. P. Chipperfield, W. Feng, D. E. Kinnison and S. Madronich (2018). 'On the discrepancy of HCl processing in the core of the wintertime polar vortices'. *Atmos. Chem. Phys.*, 18, pp. 8647–8666. DOI: 10.5194/acp-18-8647-2018.

Hersbach, H., B. Bell, P. Berrisford, S. Hirahara, A. Horányi, J. Muñoz-Sabater, J. Nicolas, C. Peubey, R. Radu, D. Schepers et al. (2020). 'The ERA5 global reanalysis'. *Q. J. R. Meteorol. Soc.*, 146, pp. 1999–2049. DOI: 10.1002/qj.3803.

Hersbach, H., B. Bell, P. Berrisford, S. Hirahara, A. Horányi, J. Muñoz-Sabater and J.-N. Thépaut (2017). *Complete ERA5 from 1940: Fifth generation of ECMWF atmospheric reanalyses of the global climate [Dataset]*. Copernicus Climate Change Service (C3S) Data Store (CDS). Last access: 16 September 2024. DOI: 10.24381/cds.143582cf.

Østerstrøm, F. F., J. E. Klobas, R. P. Kennedy, A. Cadoux and D. M. Wilmouth (2023). 'Sensitivity of stratospheric ozone to the latitude, season, and halogen content of a contemporary explosive volcanic eruption'. *Sci. Rep.*, 13, 6457. DOI: 10.1038/s41598-023-32574-9.

Roeckner, E., G. Bäuml, L. Bonaventura, R. Brokopf, M. Esch, M. Giorgetta, S. Hagemann, I. Kirchner, L. Kornblueh, E. Manzini et al. (2003). *The atmospheric general circulation model ECHAM 5. PART I: Model description.* Technical Report 349. https://pure.mpg.de/rest/items/item_995269_2/component/file_995268/content. Last access: 16 September 2024. Hamburg: Max-Planck-Institut für Meteorologie.

Rozanov, E. V., V. A. Zubov, M. E. Schlesinger, F. Yang and N. G. Andronova (1999). 'The UIUC three-dimensional stratospheric chemical transport model: Description and evaluation of the simulated source gases and ozone'. *J. Geophys. Res.*, 104, pp. 11755–11781. DOI: 10.1029/1999jd900138.

Stenke, A., M. Schraner, E. Rozanov, T. Egorova, B. Luo and T. Peter (2013). 'The SOCOL version 3.0 chemistry–climate model: description, evaluation, and implications from an advanced transport algorithm'. *Geosci. Model Dev.*, 6, pp. 1407–1427. DOI: 10.5194/gmd-6-1407-2013.

Tatebe, H., T. Ogura, T. Nitta, Y. Komuro, K. Ogochi, T. Takemura, K. Sudo, M. Sekiguchi, M. Abe, F. Saito et al. (2019). 'Description and basic evaluation of simulated mean state, internal variability, and climate sensitivity in MIROC6'. *Geosci. Model Dev.*, 12, pp. 2727–2765. DOI: 10.5194/gmd-12-2727-2019.

Weisenstein, D. K., J. E. Penner, M. Herzog and X. Liu (2007). 'Global 2-D intercomparison of sectional and modal aerosol modules'. *Atmos. Chem. Phys.*, 7, pp. 2339–2355. DOI: 10.5194/acp-7-2339-2007.

Weisenstein, D. K., G. K. Yue, M. K. W. Ko, N.-D. Sze, J. M. Rodriguez and C. J. Scott (1997). 'A two-dimensional model of sulfur species and aerosols'. *J. Geophys. Res.*, 102, pp. 13019–13035. DOI: 10.1029/97jd00901.

Wilmouth, D. M., F. F. Østerstrøm, J. B. Smith, J. G. Anderson and R. J. Salawitch (2023). 'Impact of the Hunga Tonga volcanic eruption on stratospheric composition'. *Proc. Natl. Acad. Sci.*, 120, e2301994120. DOI: 10.1073/pnas.2301994120.

Wohltmann, I., R. Lehmann and M. Rex (2010). 'The Lagrangian chemistry and transport model ATLAS: simulation and validation of stratospheric chemistry and ozone loss in the winter 1999/2000'. *Geosci. Model Dev.*, 3, pp. 585–601. DOI: 10.5194/gmd-3-585-2010.

Wohltmann, I. and M. Rex (2009). 'The Lagrangian chemistry and transport model ATLAS: validation of advective transport and mixing'. *Geosci. Model Dev.*, 2, pp. 153–173. DOI: 10.5194/gmd-2-153-2009.

Wohltmann, I., R. Lehmann and M. Rex (2017). 'A quantitative analysis of the reactions involved in stratospheric ozone depletion in the polar vortex core'. *Atmos. Chem. Phys.*, 17, pp. 10535–10563. DOI: 10.5194/acp-17-10535-2017.

World Meteorological Organization (WMO) (2022). *Scientific Assessment of Ozone Depletion: 2022*. Tech. rep. GAW Report No. 278. Geneva, Switzerland.

Zhou, X., S. S. Dhomse, W. Feng, G. Mann, S. Heddell, H. Pumphrey, B. J. Kerridge, B. Latter, R. Siddans, L. Ventress et al. (2024). 'Antarctic Vortex Dehydration in 2023 as a Substantial Removal Pathway for Hunga Tonga-Hunga Ha'apai Water Vapor'. *Geophys. Res. Lett.*, 51, e2023GL107630. DOI: 10.1029/2023gl107630.

S5 Hunga Tonga-Hunga Ha'apai Volcano Model Intercomparison Project (Tonga-MIP): Experiment Protocol, Model Descriptions, and Result Preview

Authors Margot Clyne
Owen B. Toon

Contributing authors Timofei Sukhodolov
Graham Mann
Sandip Dhomse
Simone Tilmes
Yunqian Zhu
Peter R. Colarco
Kostas Tsigaridis
Tatsuya Nagashima
Takashi Sekiya
Kengo Sudo
Shingo Watanabe
Slimane Bekki
Lola Falletti
Nicolas Lebas
Marion Marchand

This section is based on: Clyne et al. (2024).

Clyne, M., O.B. Toon, T. Sukhodolov, G.W. Mann, S. Dhomse, S. Tilmes, Y. Zhu, P.R. Colarco, K. Tsigaridis, T. Nagashima, T. Sekiya, K. Sudo, and S. Watanabe, 2024: Tonga-MIP: The Hunga Tonga-Hunga Ha'apai Volcano Model Intercomparison Project. In M. Clyne (Ed.), *Modeling the role of volcanoes in the climate system* (Publication No. 31487034, Doctoral dissertation, University of Colorado at Boulder). Publicly Available Content Database. https://www.proquest.com/dissertations-theses/modeling-role-volcanoes-climate-system/docview/3100397790/se-2

Preface

Two major modeling efforts arose following the Hunga eruption. The first, designed for model-to-model comparison with the goal of identifying model differences and their causes, was Tonga-MIP. The second, designed to facilitate model-to-measurement comparison with the goal of predicting climate impacts from the eruption, was the Hunga Tonga-Hunga Ha'apai Model Observations Comparison (HTHH-MOC, Supplementary S1). Here, Supplementary S5 has been compiled to provide a brief overview of Tonga-MIP's experimental protocol and participating models, and to indicate where Tonga-MIP and HTHH-MOC differ in their design.

S5.1 Experiment protocol and model descriptions

Tonga-MIP uses a coordinated experimental protocol that requires all participating models to inject specified amounts of volcanic material at the same time in the same location, and over the same duration. Participating models are not allowed to tune their injection parameters for desired results. This is in contrast to the HTHH-MOC design, where models are given guidelines as to how to inject the material into the stratosphere, but asked to tune their injection parameters so that benchmarks comparing to observations in the early months after the eruption would be met – a requirement to accommodate HTHH-MOC's differing needs. In Tonga-MIP, daily average model outputs from January 1st, 2022 through April 30th, 2022 are used to analyze the microphysical evolution of the volcanic cloud. Hunga's massive water injection plays a role in the chemical lifetime of the SO_2 and subsequent stratospheric aerosol effective radius, composition, mass burden, extinction, and optical depth.

To ease prediction of the longer term climate response, the HTHH-MOC experiments inject the volcanic material at altitudes matching observations of the plume after its initial rapid descent. In order to retain the observed 150 Tg of water perturbation in the stratosphere, participating models had to inject unrealistic quantities of water or spread the water injection over a larger area or over a longer duration to accommodate for the lower water saturation vapor pressure at the HTHH-MOC experiments' target altitudes, where temperatures are lower than at slightly higher altitudes. However, when water injections are made at the higher altitudes observed by the Hunga plume, the water is retained in the stratosphere without falling out immediately as ice. The input values for Tonga-MIP's experimental protocol were selected for accurate representation of the observed injection of the volcanic material, whilst remaining obtainable for all models to comply with under the differing constraints of their grid and temporal resolutions. The fuller justification for Tonga-MIP's experimental protocol and explanations of its finer details remain unchanged, and so we refer the reader to Clyne et al. (2024).

Table S5.1 lists the Tonga-MIP experiments. Table S5.2 lists the participating models and references for the configurations used in Tonga-MIP. Table S5.3 lists the stratospheric aerosol and chemistry packages used in each Tonga-MIP model. Table S5.4 lists the requested outputs from participating models to allow consistent analysis via a MIP postprocessing software package for volcanoes (Clyne, 2024).

S5.2 Result preview

Tonga-MIP has enabled identification of modeling decisions regarding size distribution scheme, stratospheric chemistry, aerosol morphology, physical constants, and algorithm solving that impact aerosol microphysics and are causing underlying differences in simulated stratospheric aerosols. Consequences of differences in some of these fundamentals were made more visible under the extreme conditions of the Hunga event. The importance of continuing educated model developments cannot be understated. If science and policy decisions related to solar radiation modification are to be well informed, some of these intermodel differences will need to be resolved. While the preliminary results of Tonga-MIP can be found in Clyne et al. (2024), the analysis still needs to undergo peer review and additional model runs have since been added. Improved analysis is planned for publication in a peer reviewed journal and has been joined by additional coauthors S. Bekki, N. Lebas, M. Marchand, L. Falletti, and J.R. Pierce.

Table S5.1: *(Reprinted from Clyne et al., 2024). Tonga-MIP experiments. There is also a control run without the volcano. Eruption duration: 6 hours starting at 0400 UTC January 15th. Horizontal area: [22°S, 14°S], [182°E, 186°E]. SO_2 mass injected: 0.5 Tg.*

Exp. Name	LowAlt	LowAltH_2O	HighAlt	HighAltH_2O	LowAltH_2O Free Running	HighAltH_2O Free Running
Altitude SO_2	25–30 km	25–30 km	30–35 km	30–35 km	25–30 km	30–35 km
H_2O Mass injected	X	150 Tg	X	150 Tg	150 Tg	150 Tg
Altitude H_2O	X	25–30 km	X	30–35 km	25–30 km	30–35 km
Nudging	Specified Dynamics	Specified Dynamics	Specified Dynamics	Specified Dynamics	Free Running	Free Running

Table S5.2: *Participating models and references for the configurations used in Tonga-MIP (adapted from Clyne et al., 2024).*

Model	Horizontal resolution (lat × lon)	Model top (levels)	Specified dynamics source	Reference paper
CESM2-WACCM6-MAM4	0.95° × 1.25°	4.5×10^{-6} hPa (70)	GEOS5	Tilmes et al. (2023)
CESM2-WACCM6-CARMA	0.95° × 1.25°	4.5×10^{-6} hPa (70)	GEOS5	Tilmes et al. (2023)
GA4 UM-UKCA	1.25° × 1.875°	85 km (85)	ERA5	Dhomse et al. (2020)
SOCOLv4	1.9° × 1.9°	0.01 hPa (47)	ERA5	Sukhodolov et al. (2021)
MIROC ES2H	2.8° × 2.8°	0.004 hPa (81)	MERRA-2	Tatebe et al. (2019) and Kawamiya et al. (2020)
GEOS-V GOCART GMI[a]	Cubed sphere 90×90×6 (1°)	0.01 hPa (72)	MERRA-2 / GEOS-FP	Nielsen et al. (2017)
IPSLCM7[b] LMDZ-STRATAER-REPROBUS	1.3° × 2.5°	0.03 hPa (79)	ERA5	—

[a]) GEOS-V has comprehensive microphysics when configured with CARMA (Case et al., 2023), but not when configured with GOCART.

[b]) IPSLCM7 is a new development since the CMIP6 version of the IPSL-CM6A-LR climate model described in Boucher et al. (2020). The IPSLCM7 version still uses the atmospheric general circulation model LMDZ (Hourdin et al., 2020), now version 6.2, and couples with stratospheric aerosol chemistry and microphysics modules STRATAER and REPROBUS (see Table S V.3).

Table S5.3: *Overview of stratospheric aerosol and chemistry packages used in each Tonga-MIP model (adapted from Clyne et al., 2024).*

Model	Aerosol size distribution	Aerosol package	Reference	Chemistry package	Reference
CESM2-WACCM6-MAM4	modal	MAM4	Liu et al., 2016	WACCM6	Gettelman et al. (2019)
CESM2-WACCM6-CARMA	sectional	CARMA	Tilmes et al. (2023)	WACCM6	Gettelman et al. (2019)
GA4 UM-UKCA	modal	GLOMAPv8.2	Mann et al. (2010)	StratTrop	Archibald et al. (2020)
SOCOLv4	sectional	AER	Sukhodolov et al. (2021)	MEZON	Egorova et al. (2003)
MIROC ES2H	modal	SPRINTARS6.0	Sekiya et al. (2016)[a]	CHASER4.0	Sudo and Akimoto (2007) and Sudo et al. (2002)
GEOS-V GOCART GMI	bulk	GOCART	Colarco et al., 2010	GMI	Duncan et al. (2007)
IPSLCM7	sectional	STRATAER[b]	—	REPROBUS	Marchand et al., 2012
LMDZ-STRATAER-REPROBUS					

[a]) The Spectral Radiation Transport Model for Aerosol Species (SPRINTARS; Takemura et al., 2000; Takemura et al., 2002; Takemura et al., 2005; Takemura et al., 2009) is developed for modal size distribution in Sekiya et al. (2016).

[b]) STRATAER is an improved version of the Sectional Stratospheric Sulfate Aerosol module (S3A; Kleinschmitt et al., 2017) used in IPSL-CM6A-LR, and is still under development.

Table S5.4: *Requested outputs from participating models to allow consistent analysis via the Tonga-MIP postprocessing package for volcanoes (Clyne, 2024). All data are provided clearly labeled with units included in the metadata. Units related by powers of 10 are acceptable. Variables marked with an asterisk (*) in the help description are not required if unavailable.*

Short name	Long name	Units	Dimensions	Help description
Dimensions				
lev	Vertical gridbox level pressure	hPa	[lev]	
ilev	Pressure at grid level interface	hPa	[ilev] = [lev] + 1	* not required if unavailable
lat	Latitude	degrees north	[lat]	
lon	Longitude	degrees east	[lon]	
time	Time dimension	days since run start	[time]	e.g., "days since 2022-01-01 00:00:00"
Variables				
date	Date corresponding to time dimension	YYYYMMDD or YYYY-MM-DD	[time]	
AREA	Horizontal area of grid box	m^2	[time,lat,lon]	Only need one instance in time
MASS	Mass of grid box	kg	[time,lev,lat,lon]	* Can be substituted with density (DENS) if MASS unavailable
TROP_P	Tropopause pressure	Pa	[time,lat,lon]	
TROP_Z	Tropopause altitude	m	[time,lat,lon]	
T	Temperature	K	[time,lev,lat,lon]	
PBLH	Planetary Boundary Layer height	m	[time,lat,lon]	
PS	Surface pressure	Pa	[time,lat,lon]	
Z3	Geopotential height	m	[time,lev,lat,lon]	* not required if unavailable
OH	OH mixing ratio	mol/mol	[time,lev,lat,lon]	
O_3	Ozone mixing ratio	mol/mol	[time,lev,lat,lon]	
SO	SO mixing ratio	mol/mol or kg/kg	[time,lev,lat,lon]	Dry mixing ratio; * not required if unavailable
SO_2	Sulfur dioxide mixing ratio	mol/mol or kg/kg	[time,lev,lat,lon]	Dry mixing ratio
SO_3	SO_3 mixing ratio	mol/mol or kg/kg	[time,lev,lat,lon]	Dry mixing ratio; * not required if unavailable
H_2SO_4	Sulfuric acid mixing ratio	mol/mol or kg/kg	[time,lev,lat,lon]	Dry mixing ratio
SO_4	Sulfate aerosol dry mixing ratio	kg/kg or mol/mol	[time,lev,lat,lon]	If multiple modes, provide each with description
WTPER	H_2SO_4 weight percent	%	[time,lev,lat,lon]	Weight percent in wet sulfate aerosol (H_2O–H_2SO_4)
SO_2_CHML	SO_2 chemical loss rate	$/cm^3/s$	[time,lev,lat,lon]	* not required if unavailable, but preferred
EXTINCTUV	Aerosol extinction 350 nm	1/m or 1/km	[time,lev,lat,lon]	
EXTINCT	Aerosol extinction 550 nm	1/m or 1/km	[time,lev,lat,lon]	
EXTINCTNIR	Aerosol extinction 1020 nm	1/m or 1/km	[time,lev,lat,lon]	
SAD_AERO	Aerosol surface area density	cm^2/cm^3 or $\mu m^2/cm^3$ or $\mu m^2/\mu m^3$	[time,lev,lat,lon]	

Table S5.4 (continued)

Short name	Long name	Units	Dimensions	Help description
REFF_AERO	Aerosol effective radius (wet)	cm or μm	[time,lev,lat,lon]	
dgnumwet	Aerosol mode wet diameter (each mode)	m	[time,lev,lat,lon]	Provide for each mode if modal model
num_ax	Mode number mixing ratio	1/kg	[time,lev,lat,lon]	Provide for each mode if modal model
AODUV	Aerosol optical depth 350 nm	none	[time,lat,lon]	Total column
AODUVst	Stratospheric AOD 350 nm	none	[time,lat,lon]	Column from tropopause to TOA; * not required if unavailable
AODVIS	Aerosol optical depth 550 nm	none	[time,lat,lon]	Total column; * not required if unavailable
AODVISst	Stratospheric AOD 550 nm	none	[time,lat,lon]	Column from tropopause to TOA; * not required if unavailable
AODNIR	Aerosol optical depth 1020 nm	none	[time,lat,lon]	Total column; * not required if unavailable
AODNIRst	Stratospheric AOD 1020 nm	none	[time,lat,lon]	Column from tropopause to TOA; * not required if unavailable
H_2O	Water vapor mixing ratio	mol/mol	[time,lev,lat,lon]	
FLDS	Downwelling longwave flux at surface	W/m^2	[time,lat,lon]	* not required if unavailable
FLNS	Net longwave flux at surface	W/m^2	[time,lat,lon]	* not required if unavailable
FLNR	Net longwave flux at tropopause	W/m^2	[time,lat,lon]	* not required if unavailable
FLNT	Net longwave flux at top of model	W/m^2	[time,lat,lon]	* not required if unavailable
FLUT	Upwelling longwave flux at top of model	W/m^2	[time,lat,lon]	* not required if unavailable
FSDS	Downwelling solar flux at surface	W/m^2	[time,lat,lon]	* not required if unavailable
FSNS	Net solar flux at surface	W/m^2	[time,lat,lon]	* not required if unavailable
FSNR	Net solar flux at tropopause	W/m^2	[time,lat,lon]	* not required if unavailable
SOLIN	Solar insolation (TOA downwelling)	W/m^2	[time,lat,lon]	* not required if unavailable
FSNT	Net solar flux at top of model	W/m^2	[time,lat,lon]	* not required if unavailable
FSUTOA	Upwelling solar flux at top of model	W/m^2	[time,lat,lon]	* not required if unavailable

References

Archibald, A. T., F. M. O'Connor, N. L. Abraham, S. Archer-Nicholls, M. P. Chipperfield, M. Dalvi, G. A. Folberth, F. Dennison, S. S. Dhomse, P. T. Griffiths et al. (2020). 'Description and evaluation of the UKCA stratosphere–troposphere chemistry scheme (StratTrop vn 1.0) implemented in UKESM1'. *Geosci. Model Dev.*, 13, pp. 1223–1266. DOI: 10.5194/gmd-13-1223-2020.

Boucher, O., J. Servonnat, A. L. Albright, O. Aumont, Y. Balkanski, V. Bastrikov, S. Bekki, R. Bonnet, S. Bony, L. Bopp et al. (2020). 'Presentation and evaluation of the IPSL-CM6A-LR climate model'. *J. Adv. Model. Earth Syst.*, 12, e2019MS002010. DOI: 10.1029/2019MS002010.

Case, P., P. R. Colarco, O. B. Toon, V. Aquila and C. A. Keller (2023). 'Interactive stratospheric aerosol microphysics-chemistry simulations of the 1991 Pinatubo volcanic aerosols with newly coupled sectional aerosol and stratosphere-troposphere chemistry modules in the NASA GEOS Chemistry-Climate Model (CCM)'. *J. Adv. Model. Earth Syst.*, 15, e2022MS003147. DOI: 10.1029/2022MS003147.

Clyne, M. (2024). *MIP postprocessing software package for volcanoes*. https://github.com/maclyne/postprocessing.

Clyne, M., O. B. Toon, T. Sukhodolov, G. W. Mann, S. Dhomse, S. Tilmes, Y. Zhu, P. R. Colarco, K. Tsigaridis, T. Nagashima et al. (2024). 'Tonga-MIP: The Hunga Tonga-Hunga Ha'apai Volcano Model Intercomparison Project'. In M. Clyne (Ed.), *Modeling the role of volcanoes in the climate system* (Publication No. 31487034), https://www.proquest.com/dissertations-theses/modeling-role-volcanoes-climate-system/docview/3100397790/se-2. PhD thesis. University of Colorado at Boulder.

Colarco, P. R., A. da Silva, M. Chin and T. Diehl (2010). 'On-line simulations of global aerosol distributions in the NASA GEOS-4 model and comparisons to satellite and ground-based aerosol optical depth'. *J. Geophys. Res.*, 115, D14207. DOI: 10.1029/2009JD012820.

Dhomse, S. S., G. W. Mann, J. C. Antuña Marrero, S. E. Shallcross, M. P. Chipperfield, K. S. Carslaw, L. Marshall, N. L. Abraham and C. E. Johnson (2020). 'Evaluating the simulated radiative forcings, aerosol properties, and stratospheric warmings from the 1963 Mt Agung, 1982 El Chichón, and 1991 Mt Pinatubo volcanic aerosol clouds'. *Atmos. Chem. Phys.*, 20, pp. 13627–13654. DOI: 10.5194/acp-20-13627-2020.

Duncan, B. N., J. A. Logan, I. Bey, I. A. Megretskaia, R. M. Yantosca, P. C. Novelli, N. B. Jones and C. P. Rinsland (2007). 'Global budget of CO, 1988–1997: Source estimates and validation with a global model'. *J. Geophys. Res.*, 112, D22301. DOI: 10.1029/2007JD008459.

Egorova, T., E. Rozanov, V. Zubov and I. Karol (2003). 'Model for investigating ozone trends (MEZON)'. *Izv. Atmos. Ocean. Phys.*, 39, pp. 277–292.

Gettelman, A., M. J. Mills, D. E. Kinnison, R. R. Garcia, A. K. Smith, D. R. Marsh, S. Tilmes, F. Vitt, C. G. Bardeen, J. McInerny et al. (2019). 'The Whole Atmosphere Community Climate Model Version 6 (WACCM6)'. *J. Geophys. Res.*, 124, pp. 12380–12403. DOI: 10.1029/2019JD030943.

Hourdin, F., C. Rio, J.-Y. Grandpeix, J.-B. Madeleine, F. Cheruy, N. Rochetin, A. Jam, I. Musat, A. Idelkadi, L. Fairhead et al. (2020). 'LMDZ6A: The atmospheric component of the IPSL climate model with improved and better tuned physics'. *J. Adv. Model. Earth Syst.*, 12, e2019MS001892. DOI: 10.1029/2019MS001892.

Kawamiya, M., T. Hajima, K. Tachiiri, S. Watanabe and T. Yokohata (2020). 'Two decades of Earth system modeling with an emphasis on Model for Interdisciplinary Research on Climate (MIROC)'. *Prog. Earth Planet. Sci.*, 7, 64. DOI: 10.1186/s40645-020-00369-5.

Kleinschmitt, C., O. Boucher, S. Bekki, F. Lott and U. Platt (2017). 'The Sectional Stratospheric Sulfate Aerosol module (S3A-v1) within the LMDZ general circulation model: description and evaluation against stratospheric aerosol observations'. *Geosci. Model Dev.*, 10, pp. 3359–3378. DOI: 10.5194/gmd-10-3359-2017.

Liu, X., P.-L. Ma, H. Wang, S. Tilmes, B. Singh, R. C. Easter, S. J. Ghan and P. J. Rasch (2016). 'Description and evaluation of a new four-mode version of the Modal Aerosol Module (MAM4) within version 5.3 of the Community Atmosphere Model'. *Geosci. Model Dev.*, 9, pp. 505–522. DOI: 10.5194/gmd-9-505-2016.

Mann, G. W., K. S. Carslaw, D. V. Spracklen, D. A. Ridley, P. T. Manktelow, M. P. Chipperfield, S. J. Pickering and C. E. Johnson (2010). 'Description and evaluation of GLOMAP-mode: a modal global aerosol microphysics model for the UKCA composition-climate model'. *Geosci. Model Dev.*, 3, pp. 519–551. DOI: 10.5194/gmd-3-519-2010.

Marchand, M., P. Keckhut, S. Lefebvre, C. Claud, D. Cugnet, A. Hauchecorne, F. Lefévre, M.-P. Le-

febvre, J. Jumelet, F. Lott et al. (2012). 'Dynamical amplification of the stratospheric solar response simulated with the Chemistry-Climate Model LMDz-Reprobus'. *J. Atmos. Solar-Terr. Phys.*, 75–76, pp. 147–160. DOI: 10.1016/j.jastp.2011.11.008.

Nielsen, J. E., S. Pawson, A. Molod, B. Auer, A. M. da Silva, A. R. Douglass, B. Duncan, Q. Liang, M. Manyin, L. D. Oman et al. (2017). 'Chemical mechanisms and their applications in the Goddard Earth Observing System (GEOS) earth system model'. *J. Adv. Model. Earth Syst.*, 9, pp. 3019–3044. DOI: 10.1002/2017MS001011.

Sekiya, T., K. Sudo and T. Nagai (2016). 'Evolution of stratospheric sulfate aerosol from the 1991 Pinatubo eruption: Roles of aerosol microphysical processes'. *J. Geophys. Res.*, 121, pp. 2911–2938. DOI: 10.1002/2015JD024313.

Sudo, K. and H. Akimoto (2007). 'Global source attribution of tropospheric ozone: Long-range transport from various source regions'. *J. Geophys. Res.*, 112, D12302. DOI: 10.1029/2006JD007992.

Sudo, K., M. Takahashi, J. Kurokawa and H. Akimoto (2002). 'CHASER: A global chemical model of the troposphere 1. Model description'. *J. Geophys. Res.*, 107, 4339. DOI: 10.1029/2001JD001113.

Sukhodolov, T., T. Egorova, A. Stenke, W. T. Ball, C. Brodowsky, G. Chiodo, A. Feinberg, M. Friedel, A. Karagodin-Doyennel, T. Peter et al. (2021). 'Atmosphere ocean aerosol chemistry climate model SOCOLv4.0: description and evaluation'. *Geosci. Model Dev.*, 14, pp. 5525–5560. DOI: 10.5194/gmd-14-5525-2021.

Takemura, T., M. Egashira, K. Matsuzawa, H. Ichijo, R. O'ishi and A. Abe-Ouchi (2009). 'A simulation of the global distribution and radiative forcing of soil dust aerosols at the Last Glacial Maximum'. *Atmos. Chem. Phys.*, 9, pp. 3061–3073. DOI: 10.5194/acp-9-3061-2009.

Takemura, T., T. Nakajima, O. Dubovik, B. N. Holben and S. Kinne (2002). 'Single-scattering albedo and radiative forcing of various aerosol species with a global three-dimensional model'. *J. Climate*, 15, pp. 333–352. DOI: 10.1175/1520-0442(2002)015<0333:ssaarf>2.0.co;2.

Takemura, T., T. Nozawa, S. Emori, T. Y. Nakajima and T. Nakajima (2005). 'Simulation of climate response to aerosol direct and indirect effects with aerosol transport-radiation model'. *J. Geophys. Res.*, 110, D02202. DOI: 10.1029/2004JD005029.

Takemura, T., H. Okamoto, Y. Maruyama, A. Numaguti, A. Higurashi and T. Nakajima (2000). 'Global three-dimensional simulation of aerosol optical thickness distribution of various origins'. *J. Geophys. Res.*, 105, pp. 17853–17873. DOI: 10.1029/2000JD900265.

Tatebe, H., T. Ogura, T. Nitta, Y. Komuro, K. Ogochi, T. Takemura, K. Sudo, M. Sekiguchi, M. Abe, F. Saito et al. (2019). 'Description and basic evaluation of simulated mean state, internal variability, and climate sensitivity in MIROC6'. *Geosci. Model Dev.*, 12, pp. 2727–2765. DOI: 10.5194/gmd-12-2727-2019.

Tilmes, S., M. J. Mills, Y. Zhu, C. G. Bardeen, F. Vitt, P. Yu, D. Fillmore, X. Liu, B. Toon and T. Deshler (2023). 'Description and performance of a sectional aerosol microphysical model in the Community Earth System Model (CESM2)'. *Geosci. Model Dev.*, 16, pp. 6087–6125. DOI: 10.5194/gmd-16-6087-2023.

Overall references

Aa, E., S.-R. Zhang, P. J. Erickson, J. Vierinen, A. J. Coster, L. P. Goncharenko, A. Spicher and W. Rideout (2022a). 'Significant Ionospheric Hole and Equatorial Plasma Bubbles After the 2022 Tonga Volcano Eruption'. *Space Weather*, 20, e2022SW003101. DOI: 10.1029/2022SW003101.

Aa, E., S.-R. Zhang, W. Wang, P. J. Erickson, L. Qian, R. Eastes, B. J. Harding, T. J. Immel, D. K. Karan, R. E. Daniell et al. (2022b). 'Pronounced Suppression and X-Pattern Merging of Equatorial Ionization Anomalies After the 2022 Tonga Volcano Eruption'. *J. Geophys. Res.*, 127, e2022JA030527. DOI: 10.1029/2022ja030527.

Abbott, D. and J. L. Rubenstone (2024). 'The abundance of submarine volcanism in arcs'. *Volcanica*, 7, pp. 447–459. DOI: 10.30909/vol.07.02.447459.

Abdelkader, M., G. Stenchikov, A. Pozzer, H. Tost and J. Lelieveld (2023). 'The effect of ash, water vapor, and heterogeneous chemistry on the evolution of a Pinatubo-size volcanic cloud'. *Atmos. Chem. Phys.*, 23, pp. 471–500. DOI: 10.5194/acp-23-471-2023.

Adriani, A., P. Massoli, G. Di Donfrancesco, F. Cairo, M. L. Moriconi and M. Snels (2004). 'Climatology of polar stratospheric clouds based on lidar observations from 1993 to 2001 over McMurdo Station, Antarctica'. *J. Geophys. Res.*, 109. DOI: 10.1029/2004jd004800.

Akiyoshi, H., M. Kadowaki, Y. Yamashita and T. Nagatomo (2023). 'Dependence of column ozone on future ODSs and GHGs in the variability of 500-ensemble members'. *Sci. Rep.*, 13, 320. DOI: 10.1038/s41598-023-27635-y.

Akiyoshi, H., T. Nakamura, T. Miyasaka, M. Shiotani and M. Suzuki (2016). 'A nudged chemistry-climate model simulation of chemical constituent distribution at northern high-latitude stratosphere observed by SMILES and MLS during the 2009/2010 stratospheric sudden warming'. *J. Geophys. Res.*, 121, pp. 1361–1380. DOI: 10.1002/2015JD023334.

Andersson, S. M., B. G. Martinsson, J. P. Vernier, J. Friberg, C. A. Brenninkmeijer, M. Hermann and A. Zahn (2015). 'Significant radiative impact of volcanic aerosol in the lowermost Stratosphere'. *Nat. Commun.*, 6, 7692. DOI: 10.1038/ncomms8692.

Andres, R. J. and A. D. Kasgnoc (1998). 'A time-averaged inventory of subaerial volcanic sulfur emissions'. *J. Geophys. Res.*, 103, pp. 25251–25261. DOI: 10.1029/98JD02091.

Andrews, D. G., C. B. Leovy and J. R. Holton (2016). *Middle Atmosphere Dynamics*. Vol. 40. Academic Press.

Andrews, T., C. J. Smith, G. Myhre, P. M. Forster, R. Chadwick and D. Ackerley (2021). 'Effective Radiative Forcing in a GCM With Fixed Surface Temperatures'. *J. Geophys. Res.*, 126, e2020JD033880. DOI: 10.1029/2020jd033880.

Ansmann, A., H. Baars, A. Chudnovsky, I. Mattis, I. Veselovskii, M. Haarig, P. Seifert, R. Engelmann and U. Wandinger (2018). 'Extreme levels of Canadian wildfire smoke in the stratosphere over central Europe on 21–22 August 2017'. *Atmos. Chem. Phys.*, 18, pp. 11831–11845. DOI: 10.5194/acp-18-11831-2018.

Anstey, J. A., S. M. Osprey, J. Alexander, M. P. Baldwin, N. Butchart, L. Gray, Y. Kawatani, P. A. Newman and J. H. Richter (2022). 'Impacts, processes and projections of the quasi-biennial oscillation'. *Nature Rev. Earth Environ.*, 3, pp. 588–603. DOI: 10.1038/s43017-022-00323-7.

Antuña-Marrero, J.-C., G. W. Mann, J. Barnes, A. Rodríguez-Vega, S. Shallcross, S. S. Dhomse, G. Fiocco and G. W. Grams (2021). 'Recovery of the first ever multi-year lidar dataset of the stratospheric aerosol layer, from Lexington, MA, and Fairbanks, AK, January 1964 to July 1965'. *Earth Syst. Sci. Data*, 13, pp. 4407–4423. DOI: 10.5194/essd-13-4407-2021.

Appenzeller, C., J. R. Holton and K. H. Rosenlof (1996). 'Seasonal variation of mass transport across the tropopause'. *J. Geophys. Res.*, 101, pp. 15071–15078. DOI: 10.1029/96JD00821.

Aquila, V., L. D. Oman, R. Stolarski, A. R. Douglass and P. A. Newman (2013). 'The Response of Ozone and Nitrogen Dioxide to the Eruption of Mt. Pinatubo at Southern and Northern Midlatitudes'. *J. Atmos. Sci.*, 70, pp. 894–900. DOI: 10.1175/jas-d-12-0143.1.

Archibald, A. T., F. M. O'Connor, N. L. Abraham, S. Archer-Nicholls, M. P. Chipperfield, M. Dalvi, G. A. Folberth, F. Dennison, S. S. Dhomse, P. T. Griffiths et

al. (2020). 'Description and evaluation of the UKCA stratosphere–troposphere chemistry scheme (StratTrop vn 1.0) implemented in UKESM1'. *Geosci. Model Dev.*, 13, pp. 1223–1266. DOI: 10.5194/gmd-13-1223-2020.

Aryal, S., Q. Gan, J. S. Evans, F. I. Laskar, D. K. Karan, X. Cai, K. R. Greer, W. Wang, W. E. McClintock and R. W. Eastes (2023). 'Tongan Volcanic Eruption Induced Global-Scale Thermospheric Changes Observed by the GOLD Mission'. *Geophys. Res. Lett.*, 50, e2023GL103158. DOI: 10.1029/2023gl103158.

Asher, E., A. Baron, P. Yu, M. Todt, P. Smale, B. Liley, R. Querel, T. Sakai, I. Morino, Y. Jin et al. (2024). 'Balloon Baseline Stratospheric Aerosol Profiles (B2SAP)—Perturbations in the Southern Hemisphere, 2019–2022'. *J. Geophys. Res.*, 129, e2024JD041581. DOI: 10.1029/2024jd041581.

Asher, E., M. Todt, K. Rosenlof, T. Thornberry, R.-S. Gao, G. Taha, P. Walter, S. Alvarez, J. Flynn, S. M. Davis et al. (2023). 'Unexpectedly rapid aerosol formation in the Hunga Tonga plume'. *Proc. Natl. Acad. Sci.*, 120, e2219547120. DOI: 10.1073/pnas.2219547120.

Astafyeva, E., B. Maletckii, T. D. Mikesell, E. Munaibari, M. Ravanelli, P. Coisson, F. Manta and L. Rolland (2022). 'The 15 January 2022 Hunga Tonga Eruption History as Inferred From Ionospheric Observations'. *Geophys. Res. Lett.*, 49, e2022GL098827. DOI: 10.1029/2022GL098827.

Babu, S. R. and N.-H. Lin (2023). 'Extreme Heights of 15 January 2022 Tonga Volcanic Plume and Its Initial Evolution Inferred from COSMIC-2 RO Measurements'. *Atmosphere*, 14, 121. DOI: 10.3390/atmos14010121.

Bacmeister, J. T., M. R. Schoeberl, M. E. Summers, J. E. Rosenfield and X. Zhu (1995). 'Descent of long-lived trace gases in the winter polar vortex'. *J. Geophys. Res.*, 100, pp. 11669–11684. DOI: 10.1029/94JD02958.

Bacmeister, J. T., M. J. Suarez and F. R. Robertson (2006). 'Rain reevaporation, boundary layer–convection interactions, and Pacific rainfall patterns in an AGCM'. *J. Atmos. Sci.*, 63, pp. 3383–3403. DOI: 10.1175/jas3791.1.

Baldwin, M. P. and T. J. Dunkerton (2001). 'Stratospheric harbingers of anomalous weather regimes'. *Science*, 294, pp. 581–584. DOI: 10.1126/science.1063315.

Baldwin, M. P., L. J. Gray, T. J. Dunkerton, K. Hamilton, P. H. Haynes, W. J. Randel, J. Holton, M. J. Alexander, I. Hirota and T. Horinouchi (2001). 'The quasi-biennial oscillation'. *Rev. Geophys.*, 39, pp. 179–229. DOI: 10.1029/1999rg000073.

Banerjee, A., G. Chiodo, M. Previdi, M. Ponater, A. J. Conley and L. M. Polvani (2019). 'Stratospheric water vapor: an important climate feedback'. *Clim. Dynam.*, 53, pp. 1697–1710. DOI: 10.1007/s00382-019-04721-4.

Banzon, V., R. Reynolds and N. C. for Atmospheric Research Staff (Eds.) (2022). *The Climate Data Guide: SST data: NOAA High-resolution (0.25×0.25) Blended Analysis of Daily SST and Ice, OISSTv2.* https://climatedataguide.ucar.edu/climate-data/sst-data-noaa-high-resolution-025x025-blended-analysis-daily-sst-and-ice-oisstv2. Last access: 4 February 2025.

Baran, A. J. and J. S. Foot (1994). 'New application of the operational sounder HIRS in determining a climatology of sulphuric acid aerosol from the Pinatubo eruption'. *J. Geophys. Res.*, 99, pp. 25673–25679. DOI: 10.1029/94JD02044.

Baray, J.-L., Y. Courcoux, P. Keckhut, T. Portafaix, P. Tulet, J.-P. Cammas, A. Hauchecorne, S. Godin Beekmann, M. De Mazière, C. Hermans et al. (2013). 'Maïdo observatory: a new high-altitude station facility at Reunion Island (21° S, 55° E) for long-term atmospheric remote sensing and in situ measurements'. *Atmos. Meas. Tech.*, 6, pp. 2865–2877. DOI: 10.5194/amt-6-2865-2013.

Baray, J.-L., J. Leveau, J. Porteneuve, G. Ancellet, P. Keckhut, F. Posny and S. Baldy (1999). 'Description and evaluation of a tropospheric ozone lidar implemented on an existing lidar in the southern subtropics'. *Appl. Optics*, 38, 6808. DOI: 10.1364/ao.38.006808.

Barnes, J. E. and D. J. Hofmann (1997). 'Lidar measurements of stratospheric aerosol over Mauna Loa Observatory'. *Geophys. Res. Lett.*, 24, pp. 1923–1926. DOI: 10.1029/97GL01943.

Baron, A., P. Chazette, S. Khaykin, G. Payen, N. Marquestaut, N. Bègue and V. Duflot (2023). 'Early Evolution of the Stratospheric Aerosol Plume Following the 2022 Hunga Tonga-Hunga Ha'apai Eruption: Lidar Observations From Reunion (21°S, 55°E)'. *Geophys. Res. Lett.*, 50, e2022GL101751. DOI: 10.1029/2022gl101751.

Bednarz, E. M., A. H. Butler, X. Wang, Z. Zhuo, W. Yu, G. Stenchikov, M. Toohey and Y. Zhu (2026). 'Indirect climate impacts of the Hunga eruption'. *Atmos. Chem. Phys.*, 26, pp. 197–215. DOI: 10.5194/acp-26-197-2026.

Bednarz, E. M., V. Aquila, A. H. Butler, P. Colarco, E. Fleming, F. F. Østerstrøm, D. Plummer, I. Quaglia, W. Randel, M. L. Santee et al. (2025). 'Multi-model assessment of impacts of the 2022 Hunga eruption on stratospheric ozone and its chemical and dynamical drivers'. *EGUsphere [preprint]*, 2025, pp. 1–24. DOI: 10.5194/egusphere-2025-4609.

Bègue, N., D. Vignelles, G. Berthet, T. Portafaix, G. Payen, F. Jégou, H. Benchérif, J. Jumelet, J.-P. Vernier, T. Lurton et al. (2017). 'Long-range transport of stratospheric aerosols in the Southern Hemisphere following the 2015 Calbuco eruption'. *Atmos. Chem. Phys.*, 17, pp. 15019–15036. DOI: 10.5194/acp-17-15019-2017.

Beinart, R. A., S. M. Arellano, M. Chaknova, J. Meagher, A. J. Davies, J. Lopresti, E. J. Cowell, M. Betters, T. M. Ladd, C. Q. Plowman et al. (2024). 'Deep seafloor hydrothermal vent communities buried by volcanic ash from the 2022 Hunga eruption'. *Commun. Earth Environ.*, 5, 254. DOI: 10.1038/s43247-024-01411-w.

Bellouin, N., G. W. Mann, M. T. Woodhouse, C. Johnson, K. S. Carslaw and M. Dalvi (2013). 'Impact of the modal aerosol scheme GLOMAP-mode on aerosol forcing in the Hadley Centre Global Environmental Model'. *Atmos. Chem. Phys.*, 13, pp. 3027–3044. DOI: 10.5194/acp-13-3027-2013.

Bernath, P. F., C. T. McElroy, M. C. Abrams, C. D. Boone, M. Butler, C. Camy-Peyret, M. Carleer, C. Clerbaux, P.-F. Coheur, R. Colin et al. (2005). 'Atmospheric Chemistry Experiment (ACE): Mission overview'. *Geophys. Res. Lett.*, 32, L15S01. DOI: 10.1029/2005GL022386.

Bernath, P. (2017). 'The Atmospheric Chemistry Experiment (ACE)'. *J. Quant. Spectrosc. Radiat. Transfer*, 186, pp. 3–16. DOI: 10.1016/j.jqsrt.2016.04.006.

Bernhard, G. H., V. E. Fioletov, J.-U. Grooß, I. Ialongo, B. Johnson, K. Lakkala, G. L. Manney, R. Müller and T. Svendby (2023). 'Ozone and UV radiation [in "State of the Climate in 2022"]'. *Bull. Amer. Meteor. Soc.*, 104, S308–S310. DOI: 10.1175/BAMS-D-23-0079.1.

Bluth, G. J., W. I. Rose, I. E. Sprod and A. J. Krueger (1997). 'Stratospheric Loading of Sulfur From Explosive Volcanic Eruptions'. *J. Geol.*, 105, pp. 671–684. DOI: 10.1086/515972.

Bluth, G. J. S., S. D. Doiron, C. C. Schnetzler, A. J. Krueger and L. S. Walter (1992). 'Global tracking of the SO_2 clouds from the June, 1991 Mount Pinatubo eruptions'. *Geophys. Res. Lett.*, 19, pp. 151–154. DOI: 10.1029/91GL02792.

Bohnenstiehl, D. R., R. P. Dziak, H. Matsumoto and T.-K. Lau (2013). 'Underwater acoustic records from the March 2009 eruption of Hunga Ha'apai–Hunga Tonga volcano in the Kingdom of Tonga'. *J. Volcanol. Geotherm. Res.*, 249, pp. 12–24. DOI: 10.1016/j.jvolgeores.2012.08.014.

Boichu, M., R. Grandin, L. Blarel, B. Torres, Y. Derimian, P. Goloub, C. Brogniez, I. Chiapello, O. Dubovik, T. Mathurin et al. (2023). 'Growth and Global Persistence of Stratospheric Sulfate Aerosols From the 2022 Hunga Tonga–Hunga Ha'apai Volcanic Eruption'. *J. Geophys. Res.*, 128, e2023JD039010. DOI: 10.1029/2023JD039010.

Bond, A. and R. S. J. Sparks (1976). 'The Minoan eruption of Santorini, Greece'. *J. Geol. Soc.*, 132, pp. 1–16. DOI: 10.1144/gsjgs.132.1.0001.

Boone, C. D., P. F. Bernath and M. Lecours (2023). 'Version 5 retrievals for ACE-FTS and ACE-imagers'. *J. Quant. Spectrosc. Radiat. Transfer*, 310, 108749. DOI: 10.1016/j.jqsrt.2023.108749.

Boone, C. D., P. F. Bernath, A. Pastorek and M. Lecours (2024). 'Sulfate aerosol properties derived from combining coincident ACE-FTS and SAGE III/ISS measurements'. *J. Quant. Spectrosc. Radiat. Transfer*, 312, 108815. DOI: 10.1016/j.jqsrt.2023.108815.

Bór, J., T. Bozóki, G. Sátori, E. Williams, S. A. Behnke, M. J. Rycroft, A. Buzás, H. G. Silva, M. Kubicki, R. Said et al. (2023). 'Responses of the AC/DC Global Electric Circuit to Volcanic Electrical Activity in the Hunga Tonga-Hunga Ha'apai Eruption on 15 January 2022'. *J. Geophys. Res.*, 128, e2022JD038238. DOI: 10.1029/2022JD038238.

Borrero, J. C., S. J. Cronin, F. H. Latu'ila, P. Tukuafu, N. Heni, A. M. Tupou, T. Kula, O. Fa'anunu, C. Bosserelle, E. Lane et al. (2023). 'Tsunami Runup and Inundation in Tonga from the January 2022 Eruption of Hunga Volcano'. *Pure Appl. Geophys.*, 180, pp. 1–22. DOI: 10.1007/s00024-022-03215-5.

Boucher, O., J. Servonnat, A. L. Albright, O. Aumont, Y. Balkanski, V. Bastrikov, S. Bekki, R. Bonnet, S. Bony, L. Bopp et al. (2020). 'Presentation and evaluation of the IPSL-CM6A-LR climate model'. *J. Adv. Model. Earth Syst.*, 12, e2019MS002010. DOI: 10.1029/2019MS002010.

Bourassa, A. E., D. A. Degenstein, R. L. Gattinger and E. J. Llewellyn (2007). 'Stratospheric aerosol retrieval with optical spectrograph and infrared imaging system limb scatter measurements'. *J. Geo-*

phys. Res., 112, D10217. DOI: 10.1029/2006JD008079.

Bourassa, A. E., D. J. Zawada, L. A. Rieger, T. W. Warnock, M. Toohey and D. A. Degenstein (2023). 'Tomographic retrievals of Hunga Tonga-Hunga Ha'apai volcanic aerosol'. *Geophys. Res. Lett.*, 50, e2022GL101978. DOI: 10.1029/2022GL101978.

Brandl, P. A., F. Schmid, N. Augustin, I. Grevemeyer, R. J. Arculus, C. W. Devey, S. Petersen, M. Stewart, H. Kopp and M. D. Hannington (2020). 'The 6–8 Aug 2019 eruption of 'Volcano F' in the Tofua Arc, Tonga'. *J. Volcanol. Geotherm. Res.*, 390, 106695. DOI: 10.1016/j.jvolgeores.2019.106695.

Brasseur, G. P. and S. Solomon (2005). *Aeronomy of the middle atmosphere*. Dordrecht, The Netherlands: Springer.

Brenna, M., S. J. Cronin, I. E. M. Smith, A. Pontesilli, M. Tost, S. Barker, S. Tonga'onevai, T. Kula and R. Vaiomounga (2022). 'Post-caldera volcanism reveals shallow priming of an intra-ocean arc andesitic caldera: Hunga volcano, Tonga, SW Pacific'. *Lithos*, 412-413, 106614. DOI: 10.1016/j.lithos.2022.106614.

Bretherton, C. S. and S. Park (2009). 'A new moist turbulence parameterization in the Community Atmosphere Model'. *J. Climate*, 22, pp. 3422–3448. DOI: 10.1175/2008jcli2556.1.

Brodowsky, C., T. Sukhodolov, A. Feinberg, M. Höpfner, T. Peter, A. Stenke and E. Rozanov (2021). 'Modeling the sulfate aerosol evolution after recent moderate volcanic activity, 2008–2012'. *J. Geophys. Res.*, 126, e2021JD035472. DOI: 10.1029/2021JD035472.

Brown, R. J., C. Bonadonna and A. J. Durant (2012). 'A review of volcanic ash aggregation'. *Phys. Chem. Earth*, 45–46, pp. 65–78. DOI: 10.1016/j.pce.2011.11.001.

Bruckert, J., S. Chopra, R. Siddans, C. Wedler and G. A. Hoshyaripour (2025). 'Aerosol dynamic processes in the Hunga plume in January 2022: does water vapor accelerate aerosol aging?' *Atmos. Chem. Phys.*, 25, pp. 9859–9884. DOI: 10.5194/acp-25-9859-2025.

Bruehl, C., J. Lelieveld, J. Schallock and L. A. Rieger (2023). 'Chemistry Climate Model Studies on the Effect of the Hunga Tonga Eruption on Stratospheric Ozone in Mid and High Latitudes in 2022'. *AGU Fall Meeting Abstracts*. Vol. 2023. 2235. https://ui.adsabs.harvard.edu/abs/2023AGUFM.A21B2235B, A21B–2235.

Brühl, C. (2025). *SO_2 emission for EMAC MPIC model*. Zenodo. DOI: 10.5281/zenodo.14962925.

Bryan, S. E., A. Cook, J. P. Evans, P. W. Colls, M. G. Wells, M. G. Lawrence, J. S. Jell, A. Greig and R. Leslie (2004). 'Pumice rafting and faunal dispersion during 2001–2002 in the Southwest Pacific: record of a dacitic submarine explosive eruption from Tonga'. *Earth Planet. Sci. Lett.*, 227, pp. 135–154. DOI: 10.1016/j.epsl.2004.08.009.

Butchart, N. (2014). 'The Brewer-Dobson circulation'. *Rev. Geophys.*, 52, pp. 157–184. DOI: 10.1002/2013rg000448.

Cahalan, R. and J. Dufek (2021). 'Explosive submarine eruptions: The role of condensable gas jets in underwater eruptions'. *J. Geophys. Res.*, 126, e2020JB020969. DOI: 10.1029/2020JB020969.

Cantner, K., S. Carey and P. Nomikou (2014). 'Integrated volcanologic and petrologic analysis of the 1650 AD eruption of Kolumbo submarine volcano, Greece'. *J. Volcanol. Geotherm. Res.*, 269, pp. 28–43. DOI: 10.1016/j.jvolgeores.2013.10.004.

Carey, R., S. A. Soule, M. Manga, J. D. L. White, J. McPhie, R. Wysoczanski, M. Jutzeler, K. Tani, D. Yoerger, D. Fornari et al. (2018). 'The largest deep-ocean silicic volcanic eruption of the past century'. *Sci. Adv.*, 4, e1701121. DOI: 10.1126/sciadv.1701121.

Carey, S. and H. Sigurdsson (1986). 'The 1982 eruptions of El Chichon volcano, Mexico (2): Observations and numerical modelling of tephra-fall distribution'. *Bull. Volcanol.*, 48, pp. 127–141. DOI: 10.1007/BF01046547.

Carey, S., H. Sigurdsson, C. Mandeville and S. Bronto (1996). 'Pyroclastic flows and surges over water: an example from the 1883 Krakatau eruption'. *Bull. Volcanol.*, 57, pp. 493–511. DOI: 10.1007/BF00304435.

Carn, S., V. Fioletov, C. McLinden, C. Li and N. A. Krotkov (2017). 'A decade of global volcanic SO_2 emissions measured from space'. *Sci. Rep.*, 7, 44095. DOI: 10.1038/srep44095.

Carn, S. A., L. Clarisse and A. J. Prata (2016). 'Multi-decadal satellite measurements of global volcanic degassing'. *J. Volcanol. Geotherm. Res.*, 311, pp. 99–134. DOI: 10.1016/j.jvolgeores.2016.01.002.

Carn, S. A., N. A. Krotkov, B. L. Fisher and C. Li (2022). 'Out of the blue: volcanic SO_2 emissions during the 2021-2022 Hunga Tonga-Hunga Ha'apai eruptions'. *Front. Earth Sci.*, 13. DOI: 10.3389/feart.2022.976962.

Carn, S. (2024). *Multi-Satellite Volcanic Sulfur Dioxide L4 Long-Term Global Database V4*. Goddard Earth Science Data and Information Services Center (GES DISC), Greenbelt, MD, USA. Last access: 20 March 2025. DOI: 10.5067/MEASURES/SO2/DATA405.

Carn, S. A., P. A. Newman, V. Aquila, H. Gonnermann and J. Dufek (2021). 'Anticipating climate impacts of major volcanic eruptions'. *Eos*, 102. DOI: 10.1029/2021EO162730.

Carr, J. L., Á. Horváth, D. L. Wu and M. D. Friberg (2022). 'Stereo Plume Height and Motion Retrievals for the Record-Setting Hunga Tonga-Hunga Ha'apai Eruption of 15 January 2022'. *Geophys. Res. Lett.*, 49, e2022GL098131. DOI: 10.1029/2022gl098131.

Carslaw, K. S., B. Luo and T. Peter (1995). 'An analytic expression for the composition of aqueous HNO_3–H_2SO_4 stratospheric aerosols including gas phase removal of HNO_3'. *Geophys. Res. Lett.*, 22, pp. 1877–1880. DOI: 10.1029/95GL01668.

Carslaw, K. S., B. P. Luo, S. L. Clegg, T. Peter, P. Brimblecombe and P. J. Crutzen (1994). 'Stratospheric aerosol growth and HNO3 gas phase depletion from coupled HNO3 and water uptake by liquid particles'. *Geophys. Res. Lett.*, 21, pp. 2479–2482. DOI: 10.1029/94gl02799.

Carter, B. A., R. Pradipta, T. Dao, J. L. Currie, S. Choy, P. Wilkinson et al. (2023). 'The ionospheric effects of the 2022 Hunga Tonga volcano eruption and the associated impacts on GPS precise point positioning across the Australian region'. *Space Weather*, 21, e2023SW003476. DOI: 10.1029/2023SW003476.

Carvajal, M., I. Sepúlveda, A. Gubler and R. Garreaud (2022). 'Worldwide signature of the 2022 Tonga volcanic tsunami'. *Geophys. Res. Lett.*, 49, e2022GL098153. DOI: 10.1029/2022gl098153.

Cas, R. A. F. and J. M. Simmons (2018). 'Why deep-water eruptions are so different from subaerial eruptions'. *Front. Earth Sci.*, 6, 198. DOI: 10.3389/feart.2018.00198.

Case, P., P. R. Colarco, O. B. Toon, V. Aquila and C. A. Keller (2023). 'Interactive stratospheric aerosol microphysics-chemistry simulations of the 1991 Pinatubo volcanic aerosols with newly coupled sectional aerosol and stratosphere-troposphere chemistry modules in the NASA GEOS Chemistry-Climate Model (CCM)'. *J. Adv. Model. Earth Syst.*, 15, e2022MS003147. DOI: 10.1029/2022MS003147.

Chaknova, M., T. Giachetti, J. Paredes-Mariño, A. Soule, A. R. Van Eaton, R. Beinart, M. Crundwell, S. J. Cronin, M. Jutzeler, K. E. Fauria et al. (2025). 'How did westward volcaniclastic deposits accumulate in the deep sea following the January 2022 eruption of Hunga volcano?' *Geochem. Geophys. Geosyst.*, 26, e2024GC011629. DOI: 10.1029/2024GC011629.

Charlesworth, E., F. Plöger, T. Birner, R. Baikhadzhaev, M. Abalos, N. L. Abraham and M. Riese (2023). 'Stratospheric water vapor affecting atmospheric circulation'. *Nat. Commun.*, 14, 3925. DOI: s41467-023-39559-2.

Chau, J. L., F. L. Poblet, H.-L. Liu, A. Liu, N. Gulbrandsen, C. Jacobi, R. R. Rodriguez, D. Scipion and M. Tsutsumi (2024). 'Mesosphere and lower thermosphere wind perturbations due to the 2022 Hunga Tonga–Hunga Ha'apai eruption as observed by multistatic specular meteor radars'. *Radio Sci.*, 59. DOI: 10.1029/2024RS008013.

Chen, P., M. Xiong, R. Wang, Y. Yao, F. Tang, H. Chen and L. Qiu (2023). 'On the ionospheric disturbances in New Zealand and Australia following the eruption of the Hunga Tonga-Hunga Ha'apai volcano on 15 January 2022'. *Geoph. Monog. Series.*, 21, e2022SW003294. DOI: 10.1029/2022SW003294.

Chen, Z., P. K. Bhartia, R. Loughman, P. Colarco and M. DeLand (2018). 'Improvement of stratospheric aerosol extinction retrieval from OMPS/LP using a new aerosol model'. *Atmos. Meas. Tech.*, 11, pp. 6495–6509. DOI: 10.5194/amt-11-6495-2018.

Chiou, E. W., L. W. Thomason and W. P. Chu (2006). 'Variability of Stratospheric Water Vapor Inferred from SAGE II, HALOE, and Boulder (Colorado) Balloon Measurements'. *J. Climate*, 19, pp. 4121–4133. DOI: 10.1175/JCLI3841.1.

Chipperfield, M. P. (1999). 'Multiannual simulations with a three-dimensional chemical transport model'. *J. Geophys. Res.*, 104, pp. 1781–1805. DOI: 10.1029/98jd02597.

Chipperfield, M. P. (2006). 'New version of the TOMCAT/SLIMCAT off-line chemical transport model: Intercomparison of stratospheric tracer experiments'. *Q. J. R. Meteorol. Soc.*, 132, pp. 1179–1203. DOI: 10.1256/qj.05.51.

Choi, J. M., C. C. H. Lin, P. K. Rajesh et al. (2023). 'Giant ionospheric density hole near the 2022 Hunga–Tonga volcanic eruption: Multi-point satellite observations'. *Earth Planets Space*, 75, 184. DOI: 10.1186/s40623-023-01933-1.

Clare, M. A., I. A. Yeo, S. Watson, R. Wysoczanski, S. Seabrook, K. Mackay, J. E. Hunt, E. Lane, P. J. Talling, E. Pope et al. (2023). 'Fast and destructive density currents created by ocean-entering vol-

canic eruptions'. *Science*, 381, pp. 1085–1092. DOI: 10.1126/science.adi3038.

Clerbaux, C., A. Boynard, L. Clarisse, M. George, J. Hadji-Lazaro, H. Herbin, D. Hurtmans, M. Pommier, A. Razavi, S. Turquety et al. (2009). 'Monitoring of atmospheric composition using the thermal infrared IASI/MetOp sounder'. *Atmos. Chem. Phys.*, 9, pp. 6041–6054. DOI: 10.5194/acp-9-6041-2009.

Clyne, M. (2024). *MIP postprocessing software package for volcanoes*. https://github.com/maclyne/postprocessing.

Clyne, M., O. B. Toon, T. Sukhodolov, G. W. Mann, S. Dhomse, S. Tilmes, Y. Zhu, P. R. Colarco, K. Tsigaridis, T. Nagashima et al. (2024). 'Tonga-MIP: The Hunga Tonga-Hunga Ha'apai Volcano Model Intercomparison Project'. In M. Clyne (Ed.), *Modeling the role of volcanoes in the climate system* (Publication No. 31487034), https://www.proquest.com/dissertations-theses/modeling-role-volcanoes-climate-system/docview/3100397790/se-2. PhD thesis. University of Colorado at Boulder.

Colarco, P. R., A. da Silva, M. Chin and T. Diehl (2010). 'On-line simulations of global aerosol distributions in the NASA GEOS-4 model and comparisons to satellite and ground-based aerosol optical depth'. *J. Geophys. Res.*, 115, D14207. DOI: 10.1029/2009JD012820.

Collins, W. J., N. Bellouin, M. Doutriaux-Boucher, N. Gedney, P. Halloran, T. Hinton, J. Hughes, C. D. Jones, M. Joshi, S. Liddicoat et al. (2011). 'Development and evaluation of an Earth-System model – HadGEM2'. *Geosci. Model Dev.*, 4, pp. 1051–1075. DOI: 10.5194/gmd-4-1051-2011.

Collow, A. B., P. R. Colarco, A. M. da Silva, V. Buchard, H. Bian, M. Chin, S. Das, R. Govindaraju, D. Kim and V. Aquila (2024). 'Benchmarking GOCART-2G in the Goddard Earth Observing System (GEOS)'. *Geosci. Model Dev.*, 17, pp. 1443–1468. DOI: 10.5194/gmd-17-1443-2024.

Colombier, M., B. Scheu, F. B. Wadsworth, S. Cronin, J. Vasseur, K. J. Dobson, K.-U. Hess, M. Tost, T. I. Yilmaz, C. Cimarelli et al. (2018). 'Vesiculation and quenching during Surtseyan eruptions at Hunga Tonga-Hunga Ha'apai Volcano, Tonga'. *J. Geophys Res.*, 123, pp. 3762–3779. DOI: 10.1029/2017JB015357.

Colombier, M., I. A. Ukstins, S. Tegtmeier, B. Scheu, S. J. Cronin, S. Thivet, J. Paredes-Mariño, C. Cimarelli, K.-U. Hess, T. Kula et al. (2023). 'Atmosphere injection of sea salts during large explosive submarine volcanic eruptions'. *Sci. Rep.*, 13, 14435. DOI: 10.1038/s41598-023-41639-8.

Coy, L., P. Newman, K. Wargan, G. Partyka, S. Strahan and S. Pawson (2022). 'Stratospheric Circulation Changes Associated with the Hunga Tonga-Hunga Ha'apai Eruption'. *Geophys. Res. Lett.*, 49, e2022GL100982. DOI: 10.1029/2022GL100982.

Cronin, J. F. (1971). 'Recent volcanism and the stratosphere'. *Science*, 172, pp. 847–849. DOI: 10.1126/science.172.3985.847.

Cronin, S., M. Brenna, I. Smith, S. Barker, M. Tost, M. Ford, S. Tonga'onevai, T. Kula and R. Vaiomounga (2017). 'New volcanic island unveils explosive past'. *Eos*, 98. DOI: 10.1029/2017EO076589.

Cummins, D. P., V. Guemas, C. J. Cox, M. R. Gallagher and M. D. Shupe (2023). 'Surface Turbulent Fluxes From the MOSAiC Campaign Predicted by Machine Learning'. *Geophys. Res. Lett.*, 50, e2023GL105698. DOI: 10.1029/2023GL105698.

Currie, J. L., B. A. Carter, T. Dao and M. Terkildsen (2021). 'The importance of counting: A new index to correctly quantify Equatorial Plasma Bubble occurrence in COSMIC Radio Occultation data'. *J. Geophys. Res.*, 126, e2021JA029539. DOI: 10.1029/2021JA029539.

Damadeo, R. P., J. M. Zawodny, L. W. Thomason and N. Iyer (2013). 'SAGE v7.0 algorithm: Application to SAGE II'. *Atmos. Meas. Tech.*, 6, pp. 3539–3561. DOI: 10.5194/amt-6-3539-2013.

Damany-Pearce, L., B. Johnson, A. Wells, M. Osborne, J. Allan, C. Belcher, A. Jones and J. Haywood (2022). 'Australian wildfires cause the largest stratospheric warming since Pinatubo and extend the lifetime of the Antarctic ozone hole'. *Sci. Rep.*, 12, 12665. DOI: 10.1038/s41598-022-15794-3.

Dartevelle, S., G. G. J. Ernst, J. Stix and A. Bernard (2002). 'Origin of the Mount Pinatubo climactic eruption cloud: Implications for volcanic hazards and atmospheric impacts'. *Geology*, 30, pp. 663–666. DOI: 10.1130/0091-7613(2002)030<0663:ootmpc>2.0.co;2.

Das, S., P. R. Colarco, L. D. Oman, G. Taha and O. Torres (2021). 'The long-term transport and radiative impacts of the 2017 British Columbia pyrocumulonimbus smoke aerosols in the stratosphere'. *Atmos. Chem. Phys.*, 21, pp. 12069–12090. DOI: 10.5194/acp-21-12069-2021.

Davis, N. A., P. Callaghan, I. R. Simpson and S. Tilmes (2022). 'Specified dynamics scheme impacts on wave-mean flow dynamics, convection, and tracer transport in CESM2 (WACCM6)'. *Atmos. Chem.*

Phys., 22, pp. 197–214. DOI: 10.5194/acp-22-197-2022.

Davis, S. M., R. Damadeo, D. Flittner, K. H. Rosenlof, M. Park, W. J. Randel et al. (2021). 'Validation of SAGE III/ISS solar water vapor data with correlative satellite and balloon-borne measurements'. *J. Geophys. Res.*, 125, e2020JD033803. DOI: 10.1029/2020JD033803.

Davis, S. M., K. H. Rosenlof, B. Hassler, D. F. Hurst, W. G. Read, H. Vömel, H. Selkirk, M. Fujiwara and R. Damadeo (2016). 'The Stratospheric Water and Ozone Satellite Homogenized (SWOOSH) database:a long-term database for climate studies'. *Earth Syst. Sci. Data*, 8, pp. 461–490. DOI: 10.5194/essd-8-461-2016.

Degenstein, D. A., E. J. Llewellyn and N. D. Lloyd (2003). 'Volume emission rate tomography from a satellite platform'. *Appl. Optics*, 42, pp. 1441–1450. DOI: 10.1364/AO.42.001441.

DeLand, M. T. and M. R. Schoeberl (2025). 'Polar Stratospheric Cloud Observations From the OMPS Limb Profiler'. *J. Geophys. Res.*, 130, e2024JD042632. DOI: 10.1029/2024jd042632.

Delgado, F., J. Kubanek, K. Anderson, P. Lundgren and M. Pritchard (2019). 'Physicochemical models of effusive rhyolitic eruptions constrained with InSAR and DEM data: A case study of the 2011-2012 Cordón Caulle eruption'. *Earth Planet. Sci. Lett.*, 524, 115736. DOI: 10.1016/j.epsl.2019.115736.

Deligne, N. I. and H. Sigurdsson (2015). 'Global Rates of Volcanism and Volcanic Episodes'. *Encyclopedia of Volcanoes, 2nd Ed.* Pp. 265–272. DOI: 10.1016/B978-0-12-385938-9.00014-6.

Delos Reyes, P. J., M. A. V. Bornas, D. Dominey-Howes, A. C. Pidlaoan, C. R. Magill and R. U. Solidum, Jr. (2018). 'A synthesis and review of historical eruptions at Taal Volcano, Southern Luzon, Philippines'. *Earth Sci. Rev.*, 177, pp. 565–588. DOI: 10.1016/j.Earscirev.2017.11.014.

Delworth, T. L., A. J. Broccoli, A. Rosati, R. J. Stouffer, V. Balaji, J. A. Beesley, W. F. Cooke, K. W. Dixon, J. Dunne, K. A. Dunne et al. (2006). 'GFDL's CM2 global coupled climate models. Part I: Formulation and simulation characteristics'. *J. Climate*, 19, pp. 643–674. DOI: 10.1175/JCLI3629.1.

Dennison, F., J. Keeble, O. Morgenstern, G. Zeng, N. L. Abraham and X. Yang (2019). 'Improvements to stratospheric chemistry scheme in the UM-UKCA (v10.7) model: solar cycle and heterogeneous reactions'. *Geosci. Model Dev.*, 12, pp. 1227–1239. DOI: 10.5194/gmd-12-1227-2019.

Dennison, F. W., A. J. McDonald and O. Morgenstern (2015). 'The effect of ozone depletion on the Southern Annular Mode and stratosphere–troposphere coupling'. *J. Geophys. Res.*, 120, pp. 6305–6312. DOI: 10.1002/2014JD023009.

Deplus, C., S. Bonvalot, D. Dahrin, M. Diament, H. Harjono and J. Dubois (1995). 'Inner structure of the Krakatau volcanic complex (Indonesia) from gravity and bathymetry data'. *J. Volcanol. Geotherm. Res.*, 64, pp. 23–52. DOI: 10.1016/0377-0273(94)00038-i.

Deshler, T. (2008). 'A review of global stratospheric aerosol: Measurements, importance, life cycle and local stratospheric aerosol'. *Atmos. Res.*, 90, pp. 223–232. DOI: 10.1016/j.atmosres.2008.03.016.

Deshler, T., M. E. Hervig, D. J. Hofmann, J. M. Rosen and J. B. Liley (2003). 'Thirty years of in situ stratospheric aerosol size distribution measurements from Laramie, Wyoming (41°N), using balloon-borne instruments'. *J. Geophys. Res.*, 108. DOI: 10.1029/2002JD002514.

Deshler, T., B. Luo, M. Kovilakam, T. Peter and L. E. Kalnajs (2019). 'Retrieval of aerosol size distributions from in situ particle counter measurements: Instrument counting efficiency and comparisons with satellite measurements'. *J. Geophys. Res.*, 124, pp. 5058–5087. DOI: 10.1029/2018JD029558.

Deshler, T., B. J. Johnson and W. R. Rozier (1994). 'Changes in the Character of Polar Stratospheric Clouds Over Antarctica in 1992 Due to the Pinatubo Volcanic Aerosol'. *Geophys. Res. Lett.*, 21, pp. 273–276. DOI: 10.1029/94GL00072.

Deshler, T., L. E. Kalnajs, M. Norgren, Y. Zhu and J. Zhang (2024). 'In Situ Aerosol Size Spectra Measurements in the Austral Polar Vortex Before and After the Hunga Tonga-Hunga Ha'apai Volcanic Eruption'. *Geophys. Res. Lett.*, 51, e2024GL111388. DOI: 10.1029/2024gl111388.

Dessler, A. E., M. R. Schoeberl, T. Wang, S. Davis and K. H. Rosenlof (2013). 'Stratospheric water vapor feedback'. *Proc. Natl. Acad. Sci.*, 110, pp. 18087–18091. DOI: 10.1073/pnas.1310344110.

Dhomse, S. S., K. M. Emmerson, G. W. Mann, N. Bellouin, K. S. Carslaw, M. P. Chipperfield, R. Hommel, N. L. Abraham, P. Telford, P. Braesicke et al. (2014). 'Aerosol microphysics simulations of the Mt. Pinatubo eruption with the UM-UKCA composition-climate model'. *Atmos. Chem. Phys.*, 14, pp. 11221–11246. DOI: 10.5194/acp-14-11221-2014.

Dhomse, S. S., G. W. Mann, J. C. Antuña Marrero, S. E. Shallcross, M. P. Chipperfield, K. S. Carslaw, L. Marshall, N. L. Abraham and C. E. Johnson (2020). 'Evaluating the simulated radiative forcings, aerosol properties, and stratospheric warmings from the 1963 Mt Agung, 1982 El Chichón, and 1991 Mt Pinatubo volcanic aerosol clouds'. *Atmos. Chem. Phys.*, 20, pp. 13627–13654. DOI: 10.5194/acp-20-13627-2020.

Diallo, M., M. Riese, T. Birner, P. Konopka, R. Müller, M. I. Hegglin, M. L. Santee, M. Baldwin, B. Legras and F. Ploeger (2018). 'Response of stratospheric water vapor and ozone to the unusual timing of El Niño and the QBO disruption in 2015–2016'. *Atmos. Chem. Phys.*, 18, pp. 13055–13073. DOI: 10.5194/acp-18-13055-2018.

Donner, S., A. Steinberg, J. Lehr, C. Pilger, P. Hupe, P. Gaebler, J. O. Ross, E. P. S. Eibl, S. Heimann, D. Rebscher et al. (2023). 'The January 2022 Hunga Volcano explosive eruption from the multitechnological perspective of CTBT monitoring'. *Geophys. J. Int.*, 235, pp. 48–73. DOI: 10.1093/gji/ggad204.

Druckenmiller, M. L., R. L. Thoman, T. A. Moon, L. M. Andreassen, T. J. Ballinger, L. T. Berner, G. H. Bernhard, U. S. Bhatt, S. Bigalke, J. W. Bjerke et al. (2024). 'The Arctic'. *Bull. Am. Meteorol. Soc.*, 105, S277–S330. DOI: 10.1175/bams-d-24-0101.1.

Druitt, T., S. Kutterolf, T. A. Ronge, C. Hübscher, P. Nomikou, J. Preine, R. Gertisser, J. Karstens, J. Keller, O. Koukousioura et al. (2024). 'Giant offshore pumice deposit records a shallow submarine explosive eruption of ancestral Santorini'. *Commun. Earth Environ.*, 5, 24. DOI: 10.1038/s43247-023-01171-z.

Dubovik, O. and M. D. King (2000). 'A flexible inversion algorithm for retrieval of aerosol optical properties from Sun and sky radiance measurements'. *J. Geophys. Res.*, 105, pp. 20673–20696. DOI: 10.1029/2000JD900282.

Dubovik, O., A. Sinyuk, T. Lapyonok, B. N. Holben, M. Mishchenko, P. Yang, T. F. Eck, H. Volten, O. Muñoz, B. Veihelmann et al. (2006). 'Application of spheroid models to account for aerosol particle nonsphericity in remote sensing of desert dust'. *J. Geophys. Res.*, 111. DOI: 10.1029/2005JD006619.

Duchamp, C., F. Wrana, B. Legras, P. Sellitto, R. Belhadji and C. von Savigny (2023). 'Observation of the aerosol plume from the 2022 Hunga Tonga–Hunga Ha'apai eruption with SAGE III/ISS'. *Geophys. Res. Lett.*, 50, e2023GL105076. DOI: 10.1029/2023GL105076.

Duncan, B. N., J. A. Logan, I. Bey, I. A. Megretskaia, R. M. Yantosca, P. C. Novelli, N. B. Jones and C. P. Rinsland (2007). 'Global budget of CO, 1988–1997: Source estimates and validation with a global model'. *J. Geophys. Res.*, 112, D22301. DOI: 10.1029/2007JD008459.

Dunkerton, T. J. and D. P. Delisi (1986). 'Evolution of potential vorticity in the winter stratosphere of January–February 1979'. *J. Geophys. Res.*, 91, pp. 1199–1208. DOI: 10.1029/JD091iD01p01199.

Dutton, E. and J. DeLuisi (1983). 'Spectral extinction of direct solar radiation by the El Chichón cloud during December 1982'. *Geophys. Res. Lett.*, 10, pp. 1013–1016. DOI: 10.1029/GL010i011p01013.

Dutton, E. G. and J. R. Christy (1992). 'Solar radiative forcing at selected locations and evidence for global lower tropospheric cooling following the eruptions of El Chichón and Pinatubo'. *Geophys. Res. Lett.*, 19, pp. 2313–2316. DOI: 10.1029/92GL02495.

Dutton, E. G., P. Reddy, S. Ryan and J. J. DeLuisi (1994). 'Features and effects of aerosol optical depth observed at Mauna Loa, Hawaii: 1982–1992'. *J. Geophys. Res.*, 99, pp. 8295–8306. DOI: 10.1029/93JD03520.

Eck, T. F., B. N. Holben, J. S. Reid, O. Dubovik, A. Smirnov, N. T. O'Neill, I. Slutsker and S. Kinne (1999). 'Wavelength dependence of the optical depth of biomass burning, urban, and desert dust aerosols'. *J. Geophys. Res.*, 104, pp. 31333–31349. DOI: 10.1029/1999JD900923.

Egorova, T., E. Rozanov, V. Zubov and I. Karol (2003). 'Model for investigating ozone trends (MEZON)'. *Izv. Atmos. Ocean. Phys.*, 39, pp. 277–292.

Embley, R., Y. Tamura, S. Merle, T. Sato, O. Ishizuka, W. Chadwick, D. Wiens, P. Shore and R. Stern (2014). 'Eruption of South Sarigan seamount, Northern Mariana Islands: Insights into hazards from submarine volcanic eruptions'. *Oceanography*, 27, pp. 24–31. DOI: 10.5670/oceanog.2014.37.

Emmons, L. K., S. Walters, P. G. Hess, J.-F. Lamarque, G. G. Pfister, D. Fillmore, C. Granier, A. Guenther, D. Kinnison, T. Laepple et al. (2010). 'Description and evaluation of the Model for Ozone and Related chemical Tracers, version 4 (MOZART-4)'. *Geosci. Model Dev.*, 3, pp. 43–67. DOI: 10.5194/gmd-3-43-2010.

English, J. M., O. B. Toon, M. J. Mills and F. Yu (2011). 'Microphysical simulations of new particle formation in the upper troposphere and lower strato-

sphere'. *Atmos. Chem. Phys.*, 11, pp. 9303–9322. DOI: 10.5194/acp-11-9303-2011.

English, J. M., O. B. Toon and M. J. Mills (2013). 'Microphysical simulations of large volcanic eruptions: Pinatubo and Toba'. *J. Geophys. Res.*, 118, pp. 1880–1895. DOI: 10.1002/jgrd.50196.

Ern, M., L. Hoffmann, S. Rhode and P. Preusse (2022). 'The mesoscale gravity wave response to the 2022 Tonga volcanic eruption: AIRS and MLS satellite observations and source backtracing'. *Geophys. Res. Lett.*, 49, e2022GL098626. DOI: 10.1029/2022GL098626.

Errera, Q., S. Chabrillat, Y. Christophe, J. Debosscher, D. Hubert, W. Lahoz, M. L. Santee, M. Shiotani, S. Skachko, T. von Clarmann et al. (2019). 'Technical note: Reanalysis of Aura MLS chemical observations'. *Atmos. Chem. Phys.*, 19, pp. 13647–13679. DOI: 10.5194/acp-19-13647-2019.

Eskes, H., A. Tsikerdekis, M. Ades, M. Alexe, A. C. Benedictow, Y. Bennouna, L. Blake, I. Bouarar, S. Chabrillat, R. Engelen et al. (2024). 'Technical note: Evaluation of the Copernicus Atmosphere Monitoring Service Cy48R1 upgrade of June 2023'. *Atmos. Chem. Phys.*, 24, pp. 9475–9514. DOI: 10.5194/acp-24-9475-2024.

Evan, S., J. Brioude, K. H. Rosenlof, R.-S. Gao, R. W. Portmann, Y. Zhu, R. Volkamer, C. F. Lee, J.-M. Metzger, K. Lamy et al. (2023). 'Rapid ozone depletion after humidification of the stratosphere by the Hunga Tonga eruption'. *Science*, 382, eadg2551. DOI: 10.1126/science.adg2551.

Eyring, V., S. Bony, G. A. Meehl, C. A. Senior, B. Stevens, R. J. Stouffer and K. E. Taylor (2016). 'Overview of the Coupled Model Intercomparison Project Phase 6 (CMIP6) experimental design and organization'. *Geosci. Model Dev.*, 9, pp. 1937–1958. DOI: 10.5194/gmd-9-1937-2016.

Eyring, V., I. Cionni, G. E. Bodeker, A. J. Charlton-Perez, D. E. Kinnison, J. F. Scinocca, D. W. Waugh, H. Akiyoshi, S. Bekki, M. P. Chipperfield et al. (2010). 'Multi-model assessment of stratospheric ozone return dates and ozone recovery in CCMVal-2 models'. *Atmos. Chem. Phys.*, 10, pp. 9451–9472. DOI: 10.5194/acp-10-9451-2010.

Eyring, V., N. R. P. Harris, M. Rex, T. G. Shepherd, D. W. Fahey, G. T. Amanatidis, J. Austin, M. P. Chipperfield, M. Dameris, P. M. D. F. Forster et al. (2005). 'A Strategy for Process-Oriented Validation of Coupled Chemistry–Climate Models'. *Bull. Am. Meteorol. Soc.*, 86, pp. 1117–1134. DOI: 10.1175/bams-86-8-1117.

Eyring, V., J.-F. Lamarque, P. Hess, F. Arfeuille, K. Bowman, M. P. Chipperfield, B. Duncan, A. Fiore, A. Gettelman, M. A. Giorgetta et al. (2013). *Overview of the IGAC/SPARC Chemistry-Climate Model Initiative (CCMI) Community Simulations in Support of Upcoming Ozone and Climate Assessments*. http://www.aparc-climate.org/wp-content/uploads/2017/12/SPARCnewsletter_No40_Jan2013_web.pdf. SPARC Newsletter No. 40, Last access: 21 August 2025.

Fahey, D. W., S. R. Kawa, E. L. Woodbridge, P. Tin, J. C. Wilson, H. H. Jonsson, J. E. Dye, D. Baumgardner, S. Borrmann, D. W. Toohey et al. (1993). 'In situ measurements constraining the role of sulphate aerosols in mid-latitude ozone depletion'. *Nature*, 363, pp. 509–514. DOI: 10.1038/363509a0.

Fahey, D. W., K. K. Kelly, S. R. Kawa, A. F. Tuck, M. Loewenstein, K. R. Chan and L. E. Heidt (1990). 'Observations of denitrification and dehydration in the winter polar stratospheres'. *Nature*, 344, pp. 321–324. DOI: 10.1038/344321a0.

Fauria, K. E., M. Jutzeler, T. Mittal, A. K. Gupta, L. J. Kelly, J. Rausch, R. Bennartz, B. Delbridge and L. Retailleau (2023). 'Simultaneous creation of a large vapor plume and pumice raft by a shallow submarine eruption'. *Earth Planet. Sci. Lett.*, 609, 118076. DOI: 10.1016/j.epsl.2023.118076.

Feinberg, A., T. Sukhodolov, B.-P. Luo, E. Rozanov, L. H. E. Winkel, T. Peter and A. Stenke (2019). 'Improved tropospheric and stratospheric sulfur cycle in the aerosol–chemistry–climate model SOCOL-AERv2'. *Geosci. Model Dev.*, 12, pp. 3863–3887. DOI: 10.5194/gmd-12-3863-2019.

Fels, S. B., J. D. Mahlman, M. D. Schwarzkopf and R. W. Sinclair (1980). 'Stratospheric sensitivity to perturbations in ozone and carbon dioxide: Radiative and dynamical response'. *J. Atmos. Sci.*, 37, pp. 2265–2297. DOI: 10.1175/1520-0469(1980)037%3C2265:SSTPIO%3E2.0.CO;2.

Feng, W., M. P. Chipperfield, S. Davies, G. W. Mann, K. S. Carslaw, S. Dhomse, L. Harvey, C. Randall and M. L. Santee (2011). 'Modelling the effect of denitrification on polar ozone depletion for Arctic winter 2004/2005'. *Atmos. Chem. Phys.*, 11, pp. 6559–6573. DOI: 10.5194/acp-11-6559-2011.

Feng, W., S. S. Dhomse, C. Arosio, M. Weber, J. P. Burrows, M. L. Santee and M. P. Chipperfield (2021). 'Arctic Ozone Depletion in 2019/20: Roles of Chemistry, Dynamics and the Montreal Protocol'. *Geophys. Res. Lett.*, 48, e2020GL091911. DOI: 10.1029/2020gl091911.

Feofilov, A. G., A. A. Kutepov, W. D. Pesnell, R. A. Goldberg, B. T. Marshall, L. L. Gordley and J. M. I. Russell (2009). 'Daytime SABER/TIMED observations of water vapor in the mesosphere: Retrieval approach and first results'. *Atmos. Chem. Phys.*, 9, pp. 8139–8158. DOI: 10.5194/acp-9-8139-2009.

Figueiredo, C. A. O. B., S. L. Vadas, E. Becker, C. M. Wrasse, H. Takahashi, P. K. Nyassor and D. Barros (2023). 'Secondary gravity waves from the Tonga volcano eruption: Observation and modeling over New Zealand and Australia'. *J. Geophys. Res.*, 128, e2023JA031476. DOI: 10.1029/2023JA031476.

Fioletov, V., C. A. McLinden, D. Griffin, I. Abboud, N. Krotkov, P. J. T. Leonard, C. Li, J. Joiner, N. Theys and S. Carn (2022). *Multi-Satellite Air Quality Sulfur Dioxide (SO_2) Database Long-Term L4 Global V2*. Ed. by P. Leonard. Greenbelt, MD, USA: Goddard Earth Science Data and Information Services Center (GES DISC). DOI: 10.5067/MEASURES/SO2/DATA406.

Fleming, E. L., P. A. Newman, Q. Liang and J. S. Daniel (2020). 'The Impact of Continuing CFC-11 Emissions on Stratospheric Ozone'. *J. Geophys. Res.*, 125, e2019JD031849. DOI: 10.1029/2019jd031849.

Fleming, E. L., P. A. Newman, Q. Liang and L. D. Oman (2024). 'Stratospheric Temperature and Ozone Impacts of the Hunga Tonga-Hunga Ha'apai Water Vapor Injection'. *J. Geophys. Res.*, 129, e2023JD039298. DOI: 10.1029/2023jd039298.

Flemming, J., V. Huijnen, J. Arteta, P. Bechtold, A. Beljaars, A.-M. Blechschmidt, M. Diamantakis, R. J. Engelen, A. Gaudel, A. Inness et al. (2015). 'Tropospheric chemistry in the Integrated Forecasting System of ECMWF'. *Geosci. Model Dev.*, 8, pp. 975–1003. DOI: 10.5194/gmd-8-975-2015.

Fomichev, V. I., C. Fu, J. de Grandpré, S. R. Beagley, V. P. Ogibalov and J. C. McConnell (2004). 'Model thermal response to minor radiative energy sources and sinks in the middle atmosphere'. *J. Geophys. Res.*, 109, D19107. DOI: 10.1029/2004JD004892.

Forster, P. M., V. I. Fomichev, E. Rozanov, C. Cagnazzo, A. I. Jonsson, U. Langematz and K. Shibata (2011). 'Evaluation of radiation scheme performance within chemistry climate models'. *J. Geophys. Res.*, 116, D10302. DOI: 10.1029/2010JD015361.

Forster, P. M., T. Richardson, A. C. Maycock, C. J. Smith, B. H. Samset, G. Myhre and M. Schulz (2016). 'Recommendations for diagnosing effective radiative forcing from climate models for CMIP6'. *J. Geophys. Res.*, 121, pp. 12460–12475. DOI: 10.1002/2016JD025320.

Forster, P. M. D. and K. P. Shine (1999). 'Stratospheric water vapour changes as a possible contributor to observed stratospheric cooling'. *Geophys. Res. Lett.*, 26, pp. 3309–3312. DOI: 10.1029/1999GL010487.

Forster, P. M. D. F. and K. P. Shine (2002). 'Assessing the climate impact of trends in stratospheric water vapor'. *Geophys. Res. Lett.*, 29. DOI: 10.1029/2001GL013909.

Friberg, J., B. Martinsson, S. Andersson and O. Sandvik (2018). 'Volcanic impact on the climate – the stratospheric aerosol load in the period 2006–2015'. *Atmos. Chem. Phys.*, 18, pp. 11149–11169. DOI: 10.5194/acp-18-11149-2018.

Frith, S. M., N. A. Kramarova, R. S. Stolarski, R. D. McPeters, P. K. Bhartia and G. J. Labow (2014). 'Recent changes in total column ozone based on the SBUV Version 8.6 Merged Ozone Data Set'. *J. Geophys. Res.*, 119, pp. 9735–9751. DOI: 10.1002/2014jd021889.

Frith, S. M., R. S. Stolarski, N. A. Kramarova and R. D. McPeters (2017). 'Estimating uncertainties in the SBUV Version 8.6 merged profile ozone data set'. *Atmos. Chem. Phys.*, 17, pp. 14695–14707. DOI: 10.5194/acp-17-14695-2017.

Fromm, M., D. T. Lindsey, R. Servranckx, G. Yue, T. Trickl, R. Sica, P. Doucet and S. Godin-Beekmann (2010). 'The untold story of pyrocumulonimbus'. *Bull. Am. Meteorol. Soc.*, 91, pp. 1193–1209. DOI: 10.1175/2010bams3004.1.

Fueglistaler, S., Y. S. Liu, T. J. Flannaghan, P. H. Haynes, D. P. Dee, W. J. Read and P. F. Bernath (2013). 'The relation between atmospheric humidity and temperature trends for stratospheric water'. *J. Geophys. Res.*, 118, pp. 1052–1074. DOI: 10.1002/jgrd.50157.

Fujiwara, M., J. S. Wright, G. L. Manney, L. J. Gray, J. Anstey, T. Birner, S. Davis, E. P. Gerber, V. L. Harvey, M. I. Hegglin et al. (2017). 'Introduction to the SPARC Reanalysis Intercomparison Project (S-RIP) and overview of the reanalysis systems'. *Atmos. Chem. Phys.*, 17, pp. 1417–1452. DOI: 10.5194/acp-17-1417-2017.

Gao, R. S., H. Telg, R. J. McLaughlin, S. J. Ciciora, L. A. Watts, M. S. Richardson, J. P. Schwarz, A. E. Perring, T. D. Thornberry, A. W. Rollins et al. (2016). 'A lightweight, high-sensitivity particle spectrometer for PM2.5 aerosol measurements'. *Aerosol Sci. Technol.*, 50, pp. 88–99. DOI: 10.1080/02786826.2015.1131809.

Garcia, R. R., A. K. Smith, D. E. Kinnison, Á. de la Cámara and D. J. Murphy (2017). 'Modification of

the Gravity Wave Parameterization in the Whole Atmosphere Community Climate Model: Motivation and Results'. *J. Atmos. Sci.*, 74, pp. 275–291. DOI: 10.1175/JAS-D-16-0104.1.

Garrett, C. J. R. (1969). 'Atmospheric edge waves'. *Q. J. R. Meteorol. Soc.*, 95, pp. 731–753. DOI: 10.1002/qj.49709540607.

Garvin, J. B., D. A. Slayback, V. Ferrini, J. Frawley, C. Giguere, G. R. Asrar and K. Andersen (2018). 'Monitoring and modeling the rapid evolution of Earth's newest volcanic island: Hunga Tonga Hunga Ha'apai (Tonga) using high spatial resolution satellite observations'. *Geophys. Res. Lett.*, 45, pp. 3445–3452. DOI: 10.1002/2017GL076621.

Gasque, L. C., Y.-J. Wu, B. J. Harding, T. J. Immel and C. C. Triplett (2022). 'Rapid volcanic modification of the E-region dynamo: ICON's first glimpse of the Tonga eruption'. *Geophys. Res. Lett.*, 49, e2022GL100825. DOI: 10.1029/2022GL100825.

Gates, W. L., J. S. Boyle, C. Covey, C. G. Dease, C. M. Doutriaux, R. S. Drach, M. Fiorino, P. J. Gleckler, J. J. Hnilo, S. M. Marlais et al. (1999). 'An Overview of the Results of the Atmospheric Model Intercomparison Project (AMIP I)'. *Bull. Am. Meteorol. Soc.*, 80, pp. 29–55. DOI: 10.1175/1520-0477(1999)080<0029:aootro>2.0.co;2.

Gelaro, R., W. McCarty, M. J. Suárez, R. Todling, A. Molod, L. Takacs, C. A. Randles, A. Darmenov, M. G. Bosilovich and R. Reichle (2017). 'The Modern-Era Retrospective Analysis for Research and Applications, Version 2 (MERRA-2)'. *J. Climate*, 30, pp. 5419–5454. DOI: 10.1175/jcli-d-16-0758.1.

Gerlach, T. M., H. R. Westrich and R. B. Symonds (1996). 'Preeruption Vapor in Magma of the Climactic Mount Pinatubo Eruption: Source of the Giant Stratospheric Sulfur Dioxide Cloud'. *Fire and Mud: Eruptions and Lahars of Mount Pinatubo, Philippines*. Ed. by C. Newhall and R. Punongbayan. University of Washington Press, Seattle, USA.

Gettelman, A., M. J. Mills, D. E. Kinnison, R. R. Garcia, A. K. Smith, D. R. Marsh, S. Tilmes, F. Vitt, C. G. Bardeen, J. McInerny et al. (2019). 'The Whole Atmosphere Community Climate Model Version 6 (WACCM6)'. *J. Geophys. Res.*, 124, pp. 12380–12403. DOI: 10.1029/2019JD030943.

Gidden, M. J., K. Riahi, S. J. Smith, S. Fujimori, G. Luderer, E. Kriegler, D. P. van Vuuren, M. van den Berg, L. Feng, D. Klein et al. (2019). 'Global emissions pathways under different socioeconomic scenarios for use in CMIP6: a dataset of harmonized emissions trajectories through the end of the century'. *Geosci. Model Dev.*, 12, pp. 1443–1475. DOI: 10.5194/gmd-12-1443-2019.

Giorgetta, M. A., E. Manzini, E. Roeckner, M. Esch and L. Bengtsson (2006). 'Climatology and Forcing of the Quasi-Biennial Oscillation in the MAECHAM5 Model'. *J. Climate*, 19, pp. 3882–3901. DOI: 10.1175/jcli3830.1.

Glaze, L. S., S. M. Baloga and L. Wilson (1997). 'Transport of atmospheric water vapor by volcanic eruption columns'. *J. Geophys. Res.*, 102, pp. 6099–6108. DOI: 10.1029/96JD03125.

Global Volcanism Program (2009). *Report on Hunga Tonga-Hunga Ha'apai (Tonga) (Venzke, E. A., and Wunderman, R., eds.)* Bulletin of the Global Volcanism Network, 34:2. Smithsonian Institution. DOI: 10.5479/si.GVP.BGVN200902-243040.

Global Volcanism Program (2022a). *Report on Hunga Tonga-Hunga Ha'apai (Tonga) (Bennis, K. L., and Venzke, E., eds.)* Bulletin of the Global Volcanism Network, 47:3. Smithsonian Institution. DOI: 10.5479/si.GVP.BGVN202203-243040.

Global Volcanism Program (2022b). *Report on Hunga Tonga-Hunga Ha'apai (Tonga) (Crafford, A. E., and Venzke, E., eds.)* Bulletin of the Global Volcanism Network, 47:2. Smithsonian Institution. DOI: 10.5479/si.GVP.BGVN202202-243040.

Global Volcanism Program (2024). *Volcanoes of the World (v. 5.2.8; 6 May 2025).* Distributed by Smithsonian Institution, compiled by Venzke, E. DOI: 10.5479/si.GVP.VOTW5-2024.5.2.

Godin-Beekmann, S., N. Azouz, V. F. Sofieva, D. Hubert, I. Petropavlovskikh, P. Effertz, G. Ancellet, D. A. Degenstein, D. Zawada, L. Froidevaux et al. (2022). 'Updated trends of the stratospheric ozone vertical distribution in the 60°S–60°N latitude range based on the LOTUS regression model'. *Atmos. Chem. Phys.*, 22, pp. 11657–11673. DOI: 10.5194/acp-22-11657-2022.

Graf, H., J. Perlwitz and I. Kirchner (1994). 'Northern Hemisphere tropospheric mid-latitude circulation after violent volcanic eruptions'. *Contrib. Atmos. Phys. (also Beitr. Phys. Atmosph.)*, 67, pp. 3–13.

Green, D. N., L. G. Evers, D. Fee, R. S. Matoza, M. Snellen, P. Smets and D. Simons (2013). 'Hydroacoustic, infrasonic and seismic monitoring of the submarine eruptive activity and sub-aerial plume generation at South Sarigan, May 2010'. *J. Volcanol. Geotherm. Res.*, 257, pp. 31–43. DOI: 10.1016/j.jvolgeores.2013.03.006.

Grell, G. A. and S. R. Freitas (2014). 'A scale and aerosol aware stochastic convective parameterization

for weather and air quality modeling'. *Atmos. Chem. Phys.*, 14, pp. 5233–5250. DOI: 10.5194/acp-14-5233-2014.

Grooß, J.-U., R. Müller, R. Spang, I. Tritscher, T. Wegner, M. P. Chipperfield, W. Feng, D. E. Kinnison and S. Madronich (2018). 'On the discrepancy of HCl processing in the core of the wintertime polar vortices'. *Atmos. Chem. Phys.*, 18, pp. 8647–8666. DOI: 10.5194/acp-18-8647-2018.

Guerra, M., C. Cesaroni, M. Ravanelli and L. Spogli (2024). 'Travelling ionospheric disturbances detection: A statistical study of detrending techniques, induced period error and near real-time observables'. *J. Space Weather Space Clim.*, 14. DOI: 10.1051/swsc/2024017.

Guo, S., G. J. Bluth, W. I. Rose, I. M. Watson and A. J. Prata (2004a). 'Re-evaluation of SO_2 release of the 15 June 1991 Pinatubo eruption using ultraviolet and infrared satellite sensors'. *Geochem. Geophys. Geosyst.*, 5, Q04001. DOI: 10.1029/2003GC000654.

Guo, S., W. I. Rose, G. J. Bluth and I. M. Watson (2004b). 'Particles in the great Pinatubo volcanic cloud of June 1991: The role of ice'. *Geochem. Geophys. Geosyst.*, 5, Q05003. DOI: 10.1029/2003GC000655.

Gupta, A. K., R. Bennartz, K. E. Fauria and T. Mittal (2022). 'Eruption chronology of the December 2021 to January 2022 Hunga Tonga-Hunga Ha'apai eruption sequence'. *Commun. Earth Environ.*, 3, 314. DOI: 10.1038/s43247-022-00606-3.

Gupta, A. K., T. Mittal, K. E. Fauria, R. Bennartz and J. F. Kok (2025). 'The January 2022 Hunga eruption cooled the Southern Hemisphere in 2022 and 2023'. *Commun. Earth Environ.*, 6, 240. DOI: 10.1038/s43247-025-02181-9.

Hamill, P., E. J. Jensen, P. B. Russell and J. J. Bauman (1997). 'The life cycle of stratospheric aerosol particles'. *Bull. Am. Meteorol. Soc.*, 7, pp. 1395–1410. DOI: 10.1175/1520-0477(1997)078<1395:tlcosa>2.0.co;2.

Han, S.-C., S. McClusky, T. D. Mikesell, L. Rolland, E. Okal and C. Benson (2023). 'CubeSat GPS observation of traveling ionospheric disturbances after the 2022 Hunga–Tonga Hunga–Ha'apai volcanic eruption and its potential use for tsunami warning'. *Earth Space Sci.*, 10, e2022EA002586. DOI: 10.1029/2022EA002586.

Hansen, J. (2002). 'Climate forcing in Goddard Institute for Space Studies SI2000 simulations'. *J. Geophys. Res.*, 107, 4347. DOI: 10.1029/2001jd001143.

Hansen, J., M. Sato, R. Ruedy, L. Nazarenko, A. Lacis, G. Schmidt, G. Russell, I. Aleinov, M. Bauer and S. Bauer (2005). 'Efficacy of climate forcings'. *J. Geophys. Res.*, 110, D18104. DOI: 10.1029/2005jd005776.

Harding, B. J., Y.-J. J. Wu, P. Alken, Y. Yamazaki, C. C. Triplett, T. J. Immel, L. C. Gasque, S. B. Mende and C. Xiong (2022). 'Impacts of the January 2022 Tonga volcanic eruption on the ionospheric dynamo: ICON–MIGHTI and Swarm observations of extreme neutral winds and currents'. *Geophys. Res. Lett.*, 49, e2022GL098577. DOI: 10.1029/2022GL098577.

He, J., E. Astafyeva, X. Yue, F. Ding and B. Maletckii (2023). 'The giant ionospheric depletion on 15 January 2022 around the Hunga Tonga–Hunga Ha'apai volcanic eruption'. *J. Geophys. Res.*, 128, e2022JA030984. DOI: 10.1029/2022JA030984.

He, R. and Y. Huang (2025). 'Muted radiative feedback of stratospheric water vapor found in a multimodel assessment'. *J. Geophys. Res.*, 130, e2025JD043676. DOI: 10.1029/2025jd043676.

Henley, R. W., C. E. J. de Ronde, R. J. Arculus, G. Hughes, T.-S. Pham, A. S. Casas, V. Titov and S. L. Walker (2024). 'The 15 January 2022 Hunga (Tonga) eruption: A gas-driven climactic explosion'. *J. Volcanol. Geotherm. Res.*, 451, 108077. DOI: 10.1016/j.jvolgeores.2024.108077.

Hersbach, H., B. Bell, P. Berrisford, S. Hirahara, A. Horányi, J. Muñoz-Sabater, J. Nicolas, C. Peubey, R. Radu, D. Schepers et al. (2020). 'The ERA5 global reanalysis'. *Q. J. R. Meteorol. Soc.*, 146, pp. 1999–2049. DOI: 10.1002/qj.3803.

Hersbach, H., B. Bell, P. Berrisford, S. Hirahara, A. Horányi, J. Muñoz-Sabater, J. Nicolas and J.-N. Thépaut (2017). *Complete ERA5 from 1940: Fifth generation of ECMWF atmospheric reanalyses of the global climate [Dataset].* Copernicus Climate Change Service (C3S) Data Store (CDS). Last access: 16 September 2024. DOI: 10.24381/cds.143582cf.

Hitchcock, P., T. G. Shepherd and S. Yoden (2010). 'On the approximation of local and linear radiative damping in the middle atmosphere'. *J. Atmos. Sci.*, 67, pp. 2070–2085. DOI: 10.1175/2009jas3286.1.

Holasek, R. E., S. Self and A. W. Woods (1996). 'Satellite observations and interpretation of the 1991 Mount Pinatubo eruption plumes'. *J. Geophys. Res.*, 101, pp. 27635–27655. DOI: 10.1029/96JB01179.

Holben, B. N., T. F. Eck, I. Slutsker, D. Tanré, J. P. Buis, A. Setzer, E. Vermote, J. A. Reagan, Y. J. Kaufman, T. Nakajima et al. (1998). 'AERONET—A Federated Instrument Network and Data Archive for Aerosol

Characterization'. *Remote Sens. Environ.*, 66, pp. 1–16. DOI: 10.1016/S0034-4257(98)00031-5.

Holben, B. N., A. Setzer, T. F. Eck, A. Pereira and I. Slutsker (1996). 'Effect of dry-season biomass burning on Amazon basin aerosol concentrations and optical properties, 1992–1994'. *J. Geophys. Res.*, 101, pp. 19465–19481. DOI: 10.1029/96JD01114.

Holton, J. R., P. H. Haynes, M. E. McIntyre, A. R. Douglass, R. B. Rood and L. Pfister (1995). 'Stratosphere-troposphere exchange'. *Rev. Geophys.*, 33, pp. 403–439. DOI: 10.1029/95rg02097.

Höpfner, M., C. D. Boone, B. Funke, N. Glatthor, U. Grabowski, A. Günther, S. Kellmann, M. Kiefer, A. Linden, S. Lossow et al. (2015). 'Sulfur dioxide (SO_2) from MIPAS in the upper troposphere and lower stratosphere 2002–2012'. *Atmos. Chem. Phys.*, 15, pp. 7017–7037. DOI: 10.5194/acp-15-7017-2015.

Horváth, Á., J. L. Carr, D. L. Wu, J. Bruckert, G. A. Hoshyaripour and S. A. Buehler (2022). 'Measurement report: Plume heights of the April 2021 La Soufrière eruptions from GOES-17 side views and GOES-16–MODIS stereo views'. *Atmos. Chem. Phys.*, 22, pp. 12311–12330. DOI: 10.5194/acp-22-12311-2022.

Horváth, Á., S. L. Vadas, C. C. Stephan and S. A. Buehler (2024). 'One-Minute Resolution GOES-R Observations of Lamb and Gravity Waves Triggered by the Hunga Tonga-Hunga Ha'apai Eruptions on 15 January 2022'. *J. Geophys. Res.*, 129, e2023JD039329. DOI: 10.1029/2023JD039329.

Houghton, B., J. White and A. Van Eaton (2015). 'Phreatomagmatic and Related Eruption Styles'. *Encyclopedia of Volcanoes, 2nd Ed.* Pp. 537–552. DOI: 10.1016/B978-0-12-385938-9.00030-4.

Hourdin, F., C. Rio, J.-Y. Grandpeix, J.-B. Madeleine, F. Cheruy, N. Rochetin, A. Jam, I. Musat, A. Idelkadi, L. Fairhead et al. (2020). 'LMDZ6A: The atmospheric component of the IPSL climate model with improved and better tuned physics'. *J. Adv. Model. Earth Syst.*, 12, e2019MS001892. DOI: 10.1029/2019MS001892.

Hourdin, F., I. Musat, S. Bony, P. Braconnot, F. Codron, J.-L. Dufresne, L. Fairhead, M.-A. Filiberti, P. Friedlingstein, J.-Y. Grandpeix et al. (2006). 'The LMDZ4 general circulation model: climate performance and sensitivity to parametrized physics with emphasis on tropical convection'. *Clim. Dynam.*, 27, pp. 787–813. DOI: 10.1007/s00382-006-0158-0.

Huang, Y., Y. Wang and H. Huang (2020). 'Stratospheric water vapor feedback disclosed by a locking experiment'. *Geophys. Res. Lett.*, 47, e2020GL087987. DOI: 10.1029/2020gl087987.

Huba, J. D., E. Becker and S. L. Vadas (2023). 'Simulation study of the 15 January 2022 Tonga event: Development of super equatorial plasma bubbles'. *Geophys. Res. Lett.*, 50, e2022GL101185. DOI: 10.1029/2022GL101185.

Huijnen, V., J. Flemming, S. Chabrillat, Q. Errera, Y. Christophe, A.-M. Blechschmidt, A. Richter and H. Eskes (2016). 'C-IFS-CB05-BASCOE: stratospheric chemistry in the Integrated Forecasting System of ECMWF'. *Geosci. Model Dev.*, 9, pp. 3071–3091. DOI: 10.5194/gmd-9-3071-2016.

Hurrell, J. W., M. M. Holland, P. R. Gent, S. Ghan, J. E. Kay, P. J. Kushner, J.-F. Lamarque, W. G. Large, D. Lawrence, K. Lindsay et al. (2013). 'The community Earth system model: A framework for collaborative research'. *Bull. Am. Meteorol. Soc.*, 94, pp. 1339–1360. DOI: 10.1175/BAMS-D-12-00121.1.

Hurst, D. F., S. J. Oltmans, H. Vömel, K. H. Rosenlof, S. M. Davis, E. A. Ray, E. G. Hall and A. F. Jordan (2011). 'Stratospheric water vapor trends over Boulder, Colorado: Analysis of the 30 year Boulder record'. *J. Geophys. Res.*, 116, D02306. DOI: 10.1029/2010JD015065.

Hurst, D. F., W. G. Read, H. Vömel, H. B. Selkirk, K. H. Rosenlof, S. M. Davis, E. G. Hall, A. F. Jordan and S. J. Oltmans (2016). 'Recent divergences in stratospheric water vapor measurements by frost point hygrometers and the Aura Microwave Limb Sounder'. *Atmos. Meas. Tech.*, 9, pp. 4447–4457. DOI: 10.5194/amt-9-4447-2016.

Iacono, M. J., J. S. Delamere, E. J. Mlawer, M. W. Shephard, S. A. Clough and W. D. Collins (2008). 'Radiative forcing by long-lived greenhouse gases: Calculations with the AER radiative transfer models'. *J. Geophys. Res.*, 113, D13103. DOI: 10.1029/2008JD009944.

Inchin, P. A., A. Bhatt, S. A. Cummer, S. D. Eckermann, B. J. Harding, D. D. Kuhl, J. Ma, J. J. Makela, R. Sabatini and J. B. Snively (2023). 'Multilayer evolution of acoustic-gravity waves and ionospheric disturbances over the United States after the 2022 Hunga Tonga volcano eruption'. *AGU Adv.*, 4, e2023AV000870. DOI: 10.1029/2023AV000870.

International Seismological Centre (2022). *On-line Bulletin.* DOI: 10.31905/D808B830.

Ivy, D. J., S. Solomon, N. Calvo and D. W. Thompson (2017). 'Observed connections of Arctic stratospheric ozone extremes to Northern Hemisphere

surface climate'. *Environ. Res. Lett.*, 12, 024004. DOI: 10.1088/1748-9326/aa57a4.

Jäger, H. and T. Deshler (2002). 'Lidar backscatter to extinction, mass and area conversions for stratospheric aerosols based on midlatitude balloonborne size distribution measurements'. *Geophys. Res. Lett.*, 29. DOI: 10.1029/2002gl015609.

Jarvis, P. A., T. G. Caldwell, C. Noble, Y. Ogawa and C. Vagasky (2024). 'Volcanic lightning reveals umbrella cloud dynamics of the 15 January 2022 Hunga volcano eruption, Tonga'. *B. Volcanol.*, 86, 54. DOI: 10.1007/s00445-024-01739-3.

Jégou, F., G. Berthet, C. Brogniez, J.-B. Renard, P. François, J. M. Haywood, A. Jones, Q. Bourgeois, T. Lurton, F. Auriol et al. (2013). 'Stratospheric aerosols from the Sarychev volcano eruption in the 2009 Arctic summer'. *Atmos. Chem. Phys.*, 13, pp. 6533–6552. DOI: 10.5194/acp-13-6533-2013.

Jenkins, S., C. Smith, M. Allen and R. Grainger (2023). 'Tonga eruption increases chance of temporary surface temperature anomaly above 1.5° C'. *Nat. Clim. Change*, 13, pp. 127–129. DOI: 10.1038/s41558-022-01568-2.

Jöckel, P., A. Kerkweg, A. Pozzer, R. Sander, H. Tost, H. Riede, A. Baumgaertner, S. Gromov and B. Kern (2010). 'Development cycle 2 of the Modular Earth Submodel System (MESSy2)'. *Geosci. Model Dev.*, 3, pp. 717–752. DOI: 10.5194/gmd-3-717-2010.

Johnson, J., G. Taha, R. Loughman, T. Zhu and M. DeLand (2025). *README Document for the Suomi-NPP OMPS LP L2 AER Daily Product, Collection 2.5, Version 2.5*. Tech. rep. https://disc.gsfc.nasa.gov/, Last access: 14 August 2025. Greenbelt, MD, USA: NASA GES DISC.

Jones, A. C., J. M. Haywood, A. Jones and V. Aquila (2016). 'Sensitivity of volcanic aerosol dispersion to meteorological conditions: a Pinatubo case study'. *J. Geophys. Res.*, 121, pp. 6892–6908. DOI: 10.1002/2016JD025001.

Jonsson, A. I., J. de Grandpré, V. I. Fomichev, J. C. McConnell and S. R. Beagley (2004). 'Doubled CO2-induced cooling in the middle atmosphere: Photochemical analysis of the ozone radiative feedback'. *J. Geophys. Res.*, 109, D24103. DOI: 10.1029/2004JD005093.

Jörimann, A., T. Sukhodolov, B. Luo, G. Chiodo, G. Mann and T. Peter (2025). 'REtrieval Method for optical and physical Aerosol Properties in the stratosphere (REMAPv1)'. *Geosci. Model Dev.*, 18, pp. 6023–6041. DOI: 10.5194/gmd-18-6023-2025.

Jörimann, A. (2025). *REMAP-GloSSAC-2023*. Zenodo. DOI: 10.5281/zenodo.14961868.

Joshi, M. M. and G. S. Jones (2009). 'The climatic effects of the direct injection of water vapour into the stratosphere by large volcanic eruptions'. *Atmos. Chem. Phys.*, 9, pp. 6109–6118. DOI: 10.5194/acp-9-6109-2009.

Joshi, M. M. and K. P. Shine (2003). 'A GCM Study of Volcanic Eruptions as a Cause of Increased Stratospheric Water Vapor'. *J. Climate*, 16, pp. 3525–3534. DOI: 10.1175/1520-0442(2003)016<3525:AGSOVE>2.0.CO;2.

Jucker, M., C. Lucas and D. Dutta (2024). 'Long-term climate impacts of large stratospheric water vapor perturbations'. *J. Climate*, 37, pp. 4507–4521. DOI: 10.1175/JCLI-D-23-0437.1.

Junge, C. E., C. W. Chagnon and J. E. Manson (1961). 'Stratospheric aerosols'. *J. Atmos. Sci.*, 18, pp. 81–108. DOI: 10.1175/1520-0469(1961)018<0081:sa>2.0.co;2.

Jutzeler, M., R. Marsh, R. J. Carey, J. D. L. White, P. J. Talling and L. Karlstrom (2014). 'On the fate of pumice rafts formed during the 2012 Havre submarine eruption'. *Nat. Commun.*, 5, 3660. DOI: 10.1038/ncomms4660.

Kablick, G. P. I., D. R. Allen, M. D. Fromm and G. E. Nedoluha (2020). 'Australian pyroCb smoke generates synoptic-scale stratospheric anticyclones'. *Geophys. Res. Lett.*, 47, e2020GL088101. DOI: 10.1029/2020GL088101.

Kahn, R. A. and B. J. Gaitley (2015). 'An analysis of global aerosol type as retrieved by MISR'. *J. Geophys. Res.*, 120, pp. 4248–4281. DOI: 10.1002/2015JD023322.

Kahn, R. A., B. J. Gaitley, M. J. Garay, D. J. Diner, T. F. Eck, A. Smirnov and B. N. Holben (2010). 'Multiangle Imaging Spectroradiometer global aerosol product assessment by comparison with the Aerosol Robotic Network'. *J. Geophys. Res.*, 115, D23209. DOI: 10.1029/2010JD014601.

Kahn, R. A., B. J. Gaitley, J. V. Martonchik, D. J. Diner, K. A. Crean and B. N. Holben (2005). 'Multiangle Imaging Spectroradiometer (MISR) global aerosol optical depth validation based on two years of coincident AERONET observations'. *J. Geophys. Res.*, 110, D10S04. DOI: 10.1029/2004JD004706.

Kahn, R. A., J. A. Limbacher, K. T. Junghenn Noyes, V. J. B. Flower, L. M. Zamora and K. F. McKee (2024). 'Evolving Particles in the 2022 Hunga Tonga—Hunga Ha'apai Volcano Eruption Plume'.

J. Geophys. Res., 129, e2023JD039963. DOI: 10.1029/2023JD039963.

Kalnajs, L. E. and T. Deshler (2024). 'The Stratospheric Total Aerosol Counter (STAC): Instrument description and first results'. *J. Atmos. Ocean. Tech.*, 41, pp. 635–650. DOI: 10.1175/JTECH-D-23-0072.1.

Kalnajs, L. E. and T. Deshler (2022). 'A New Instrument for Balloon-Borne In Situ Aerosol Size Distribution Measurements, the Continuation of a 50 Year Record of Stratospheric Aerosols Measurements'. *J. Geophys. Res.*, 127, e2022JD037485. DOI: 10.1029/2022JD037485.

Kar, J., K.-P. Lee, M. A. Vaughan, J. L. Tackett, C. R. Trepte, D. M. Winker, P. L. Lucker and B. J. Getzewich (2019). 'CALIPSO level 3 stratospheric aerosol profile product: version 1.00 algorithm description and initial assessment'. *Atmos. Meas. Tech.*, 12, pp. 6173–6191. DOI: 10.5194/amt-12-6173-2019.

Kawamiya, M., T. Hajima, K. Tachiiri, S. Watanabe and T. Yokohata (2020). 'Two decades of Earth system modeling with an emphasis on Model for Interdisciplinary Research on Climate (MIROC)'. *Prog. Earth Planet. Sci.*, 7, 64. DOI: 10.1186/s40645-020-00369-5.

Kelly, K. K., A. F. Tuck, D. M. Murphy, M. H. Proffitt, D. W. Fahey, R. L. Jones, D. S. McKenna, M. Loewenstein, J. R. Podolske, S. E. Strahan et al. (1989). 'Dehydration in the lower Antarctic stratosphere during late winter and early spring, 1987'. *J. Geophys. Res.*, 94, pp. 11317–11357. DOI: 10.1029/jd094id09p11317.

Kelly, L. J., K. E. Fauria, M. Manga, S. J. Cronin, F. H. Latu'ila, J. Paredes-Mariño, T. Mittal and R. Bennartz (2024). 'Airfall volume of the 15 January 2022 eruption of Hunga volcano estimated from ocean color changes'. *Bull. Volcanol.*, 86, 59. DOI: 10.1007/s00445-024-01744-6.

Khaykin, S., G. Taha, T. Leblanc, T. Sakai, I. Morino, B. Liley and S. Godin-Beekmann (2024). 'Stratospheric aerosols [in "State of the Climate in 2022"]'. *Bull. Am. Meteorol. Soc.*, 105, S96–S98. DOI: 10.1175/BAMS-D-24-0116.1.

Khaykin, S. M., S. Godin-Beekmann, P. Keckhut, A. Hauchecorne, J. Jumelet, J.-P. Vernier, A. Bourassa, D. A. Degenstein, L. A. Rieger, C. Bingen et al. (2017). 'Variability and evolution of the midlatitude stratospheric aerosol budget from 22 years of ground-based lidar and satellite observations'. *Atmos. Chem. Phys.*, 17, pp. 1829–1845. DOI: 10.5194/acp-17-1829-2017.

Khaykin, S. M., S. Godin-Beekmann, A. Hauchecorne, J. Pelon, F. Ravetta and P. Keckhut (2018). 'Stratospheric smoke with unprecedentedly high backscatter observed by lidars above southern France'. *Geophys. Res. Lett.*, 45, pp. 1639–1646. DOI: 10.1002/2017GL076763.

Khaykin, S., B. Legras, S. Bucci, P. Sellitto, L. Isaksen, F. Tencé, S. Bekki, A. Bourassa, L. Rieger, D. Zawada et al. (2020). 'The 2019/20 Australian wildfires generated a persistent smoke-charged vortex rising up to 35 km altitude'. *Commun. Earth Environ.*, 1, 22. DOI: 10.1038/s43247-020-00022-5.

Khaykin, S., A. Podglajen, F. Ploeger, J.-U. Grooß, F. Tence, S. Bekki, K. Khlopenkov, K. Bedka, L. Rieger, A. Baron et al. (2022). 'Global perturbation of stratospheric water and aerosol burden by Hunga eruption'. *Commun. Earth Environ.*, 3, 316. DOI: 10.1038/s43247-022-00652-x.

Kim, M.-H., A. H. Omar, J. L. Tackett, M. A. Vaughan, D. M. Winker, C. R. Trepte, Y. Hu, Z. Liu, L. R. Poole, M. C. Pitts et al. (2018). 'The CALIPSO version 4 automated aerosol classification and lidar ratio selection algorithm'. *Atmos. Meas. Tech.*, 11, pp. 6107–6135. DOI: 10.5194/amt-11-6107-2018.

King, M. D., D. M. Byrne, B. M. Herman and J. A. Reagan (1978). 'Aerosol Size Distributions Obtained by Inversions of Spectral Optical Depth Measurements'. *J. Atmos. Sci.*, 35, pp. 2153–2167. DOI: 10.1175/1520-0469(1978)035<2153:ASDOBI>2.0.CO;2.

Kinne, S., U. Lohmann, J. Feichter, M. Schulz, C. Timmreck, S. Ghan, R. Easter, M. Chin, P. Ginoux, T. Takemura et al. (2003). 'Monthly averages of aerosol properties: A global comparison among models, satellite data, and AERONET ground data'. *J. Geophys. Res.*, 108, 4634. DOI: 10.1029/2001JD001253.

Kinnison, D. E., K. E. Grant, P. S. Connell, D. A. Rotman and D. J. Wuebbles (1994). 'The chemical and radiative effects of the Mount Pinatubo eruption'. *J. Geophys. Res.*, 99, pp. 25705–25731. DOI: 10.1029/94jd02318.

Kleinschmitt, C., O. Boucher, S. Bekki, F. Lott and U. Platt (2017). 'The Sectional Stratospheric Sulfate Aerosol module (S3A-v1) within the LMDZ general circulation model: description and evaluation against stratospheric aerosol observations'. *Geosci. Model Dev.*, 10, pp. 3359–3378. DOI: 10.5194/gmd-10-3359-2017.

Klenzing, J., K. Zawdie, E. Astafyeva, A. Belehaki, M. Burleigh, A. G. Burrell, C. A. O. B. Figueiredo, N. A. Frissell, W. Fu, D. Hickey et al. (2025). 'Resolving

the generation mechanisms and electrodynamical effects of medium-scale traveling ionospheric disturbances (MSTIDs)'. *Front. Astron. Space Sci.*, 12, 1539821. DOI: 10.3389/fspas.2025.1539821.

Kloss, C., G. Berthet, P. Sellitto, F. Ploeger, G. Taha, M. Tidiga, M. Eremenko, A. Bossolasco, F. Jégou, J.-B. Renard et al. (2021). 'Stratospheric aerosol layer perturbation caused by the 2019 Raikoke and Ulawun eruptions and their radiative forcing'. *Atmos. Chem. Phys.*, 21, pp. 535–560. DOI: 10.5194/acp-21-535-2021.

Kloss, C., P. Sellitto, B. Legras, J.-P. Vernier, F. Jégou, M. Venkat Ratnam, B. Suneel Kumar, B. Lakshmi Madhavan and G. Berthet (2020). 'Impact of the 2018 Ambae eruption on the global stratospheric aerosol layer and climate'. *J. Geophys. Res.*, 125, e2020JD032410. DOI: 10.1029/2020JD032410.

Kloss, C., P. Sellitto, J.-B. Renard, A. Baron, N. Bègue, B. Legras, G. Berthet, E. Briaud, E. Carboni, C. Duchamp et al. (2022). 'Aerosol characterization of the stratospheric plume from the volcanic eruption at Hunga Tonga 15 January 2022'. *Geophys. Res. Lett.*, 49, e2022GL099394. DOI: 10.1029/2022GL099394.

Knafelc, J., S. E. Bryan, M. W. M. Jones, D. Gust, G. Mallmann, H. E. Cathey, A. J. Berry, E. C. Ferré and D. L. Howard (2022). 'Havre 2012 pink pumice is evidence of a short-lived, deep-sea, magnetite nanolite-driven explosive eruption'. *Commun. Earth Environ.*, 3, 19. DOI: 10.1038/s43247-022-00355-3.

Knepp, T. N., M. Kovilakam, L. Thomason and S. J. Miller (2024). 'Characterization of stratospheric particle size distribution uncertainties using SAGE II and SAGE III/ISS extinction spectra'. *Atmos. Meas. Tech.*, 17, pp. 2025–2054. DOI: 10.5194/amt-17-2025-2024.

Knutson, T. R., T. L. Delworth, K. W. Dixon, I. M. Held, J. Lu, V. Ramaswamy, M. D. Schwarzkopf, G. Stenchikov and R. J. Stouffer (2006). 'Assessment of twentieth-century regional surface temperature trends using the GFDL CM2 coupled models'. *J. Climate*, 19, pp. 1624–1651. DOI: 10.1175/jcli3709.1.

Kobayashi, S., Y. Ota, Y. Harada, A. Ebita, M. Moriya, H. Onoda, K. Onogi, H. Kamahori, C. Kobayashi and H. Endo (2015). 'The JRA-55 reanalysis: General specifications and basic characteristics'. *J. Meteorol. Soc. Japan. Ser. II*, 93, pp. 5–48. DOI: 10.2151/jmsj.2015-001.

Kodera, K. (1994). 'Influence of volcanic eruptions on the troposphere through stratospheric dynamical processes in the Northern Hemisphere winter'. *J. Geophys. Res.*, 99, pp. 1273–1282. DOI: 10.1029/93JD02731.

Kohl, M., C. Brühl, J. Schallock, H. Tost, P. Jöckel, A. Jost, S. Beirle, M. Höpfner and A. Pozzer (2025). 'New submodel for emissions from Explosive Volcanic ERuptions (EVER v1.1) within the Modular Earth Submodel System (MESSy, version 2.55.1)'. *Geosci. Model Dev.*, 18, pp. 3985–4007. DOI: 10.5194/gmd-18-3985-2025.

Kosaka, Y., S. Kobayashi, Y. Harada, C. Kobayashi, H. Naoe, K. Yoshimoto, M. Harada, N. Goto, J. Chiba and K. Miyaoka (2024). 'The JRA-3Q reanalysis'. *J. Meteorol. Soc. Japan. Ser. II*, 102, pp. 49–109. DOI: 10.2151/jmsj.2024-004.

Kovilakam, M., L. Thomason and T. Knepp (2023). 'SAGE III/ISS aerosol/cloud categorization and its impact on GloSSAC'. *Atmos. Meas. Tech.*, 16, pp. 2709–2731. DOI: 10.5194/amt-16-2709-2023.

Kovilakam, M., L. W. Thomason, N. Ernest, L. Rieger, A. Bourassa and L. Millán (2020). 'The Global Space-based Stratospheric Aerosol Climatology (version 2.0): 1979–2018'. *Earth Syst. Sci. Data*, 12, pp. 2607–2634. DOI: 10.5194/essd-12-2607-2020.

Kovilakam, M., L. W. Thomason, M. Verkerk, T. Aubry and T. N. Knepp (2025). 'OMPS-LP aerosol extinction coefficients and their applicability in GloSSAC'. *Atmos. Chem. Phys.*, 25, pp. 535–553. DOI: 10.5194/acp-25-535-2025.

Kraft, T., O. K. A. Ling, T. Toledo, B. Scheu, S. C. Stähler, J. Clinton and S. Stange (2023). 'An Antipodal Seismic and (Infra)acoustic View from Central Europe on the 15 January 2022 Hunga–Tonga–Hunga–Ha'apai Eruption'. *Seismol. Res. Lett.*, DOI: 10.1785/0220220254.

Kramarova, N. A., P. A. Newman, L. R. Lait, B. Johnson, M. Pitts, M. L. Santee, I. Petropavlovskikh, L. Coy and J. De Laat (2024). '2023 Antarctic ozone hole [in "State of the Climate in 2023"]'. *Bull. Amer. Meteor. Soc.*, 105, S358–S361. DOI: 10.1175/BAMS-D-24-0099.1.

Kratzmann, D. J., S. Carey, R. Scasso and J.-A. Naranjo (2009). 'Compositional variations and magma mixing in the 1991 eruptions of Hudson volcano, Chile'. *Bull. Volcanol.*, 71, pp. 419–439. DOI: 10.1007/s00445-008-0234-x.

Kremser, S., L. W. Thomason, M. Von Hobe, M. Hermann, T. Deshler, C. Timmreck, M. Toohey, A. Stenke, J. P. Schwarz, R. Weigel et al. (2016). 'Stratospheric aerosol-Observations, processes, and impact on climate: Stratospheric Aerosol'. *Rev. Geo-*

phys., 54, pp. 278–335. DOI: 10.1002/2015RG000511.

Kroll, C. A., S. Dacie, A. Azoulay, H. Schmidt and C. Timmreck (2021). 'The impact of volcanic eruptions of different magnitude on stratospheric water vapor in the tropics'. *Atmos. Chem. Phys.*, 21, pp. 6565–6591. DOI: 10.5194/acp-21-6565-2021.

Kroll, C. A. and A. Schmidt (2024). 'Indirect stratospheric moisture increase after a Pinatubo-magnitude eruption can be comparable to direct increase after 2022 Hunga'. *Commun. Earth Environ.*, 5, 497. DOI: 10.1038/s43247-024-01651-w.

Kuchar, A., T. Sukhodolov, G. Chiodo, A. Jörimann, J. Kult-Herdin, E. Rozanov and H. H. Rieder (2025). 'Modulation of the northern polar vortex by the Hunga Tonga–Hunga Ha'apai eruption and the associated surface response'. *Atmos. Chem. Phys.*, 25, pp. 3623–3634. DOI: 10.5194/acp-25-3623-2025.

Kuhlbrodt, T., C. G. Jones, A. Sellar, D. Storkey, E. Blockley, M. Stringer, R. Hill, T. Graham, J. Ridley, A. Blaker et al. (2018). 'The Low–Resolution Version of HadGEM3 GC3.1: Development and Evaluation for Global Climate'. *J. Adv. Model. Earth Syst.*, 10, pp. 2865–2888. DOI: 10.1029/2018MS001370.

Labitzke, K. and M. P. McCormick (1992). 'Stratospheric temperature increases due to Pinatubo aerosols'. *Geophys. Res. Lett.*, 19, pp. 207–210. DOI: 10.1029/91gl02940.

Lacis, A., J. Hansen and M. Sato (1992). 'Climate forcing by stratospheric aerosols'. *Geophys. Res. Lett.*, 19, pp. 1607–1610. DOI: 10.1029/92gl01620.

Lamarque, J.-F., L. K. Emmons, P. G. Hess, D. E. Kinnison, S. Tilmes, F. Vitt, C. L. Heald, E. A. Holland, P. H. Lauritzen, J. Neu et al. (2012). 'CAM-chem: description and evaluation of interactive atmospheric chemistry in the Community Earth System Model'. *Geosci. Model Dev.*, 5, pp. 369–411. DOI: 10.5194/gmd-5-369-2012.

Lamb, H. (1881). 'On the vibrations of an elastic sphere'. *Proc. Lond. Math. Soc.*, s1-13, pp. 189–212. DOI: 10.1112/plms/s1-13.1.189.

Lambert, A., R. G. Grainger, J. J. Remedios, C. D. Rodgers, M. Corney and F. W. Taylor (1993). 'Measurements of the evolution of the Mt. Pinatubo aerosol cloud by ISAMS'. *Geophys. Res. Lett.*, 20, pp. 1287–1290. DOI: 10.1029/93gl00827.

Landerer, F. W., F. M. Flechtner, H. Save, F. H. Webb, T. Bandikova, W. I. Bertiger, S. V. Bettadpur, S. H. Byun, C. Dahle, H. Dobslaw et al. (2020). 'Extending the global mass change data record: GRACE Follow-On instrument and science data performance'. *Geophys. Res. Lett.*, 47, e2020GL088306. DOI: 10.1029/2020GL088306.

Landulfo, E., F. S. Lopes, J. C. Antuña, R. Arredondo and G. Taha (2022a). *Monitoring stratospheric aerosols in South America with ground-based lidar*. https://homepages.see.leeds.ac.uk/~amtgwm/SSirC_Landulfo_ForShareOffUnivLeedsSEEpage.pdf. May 2022 SSiRC workshop presentation.

Landulfo, E., F. S. Lopes, J.-P. Vernier, J. C. Antuña and the LALINET team (2022b). *VolRes and the BRAVO field campaign*. https://homepages.see.leeds.ac.uk/~amtgwm/SSirC_BRAVO_Landulfo_ForShareOffSEEpage.pdf. May 2022 SSiRC workshop presentation.

Larson, E. J. and R. W. Portmann (2016). 'A temporal kernel method to compute effective radiative forcing in CMIP5 transient simulations'. *J. Climate*, 29, pp. 1497–1509. DOI: 10.1175/jcli-d-15-0577.1.

Lawrence, B. N., V. Bennett, J. Churchill, M. Juckes, P. Kershaw, P. Oliver, M. Pritchard and A. Stephens (2012). *The JASMIN super-data-cluster*. arXiv preprint. DOI: 10.48550/arXiv.1204.3553.

Lawrence, Z. D., G. L. Manney and K. Wargan (2018). 'Reanalysis intercomparisons of stratospheric polar processing diagnostics'. *Atmos. Chem. Phys.*, 18, pp. 13547–13579. DOI: 10.5194/acp-18-13547-2018.

Le, G., G. Liu, E. Yizengaw and C. R. Englert (2022). 'Intense equatorial electrojet and counter electrojet caused by the 15 January 2022 Tonga volcanic eruption: Space- and ground-based observations'. *Geophys. Res. Lett.*, 49, e2022GL099002. DOI: 10.1029/2022GL099002.

Le Mével, H., C. A. Miller, M. Ribó, S. Cronin and T. Kula (2023). 'The magmatic system under Hunga volcano before and after the 15 January 2022 eruption'. *Sci. Adv.*, 9. DOI: 10.1126/sciadv.adh3156.

Lecours, M., C. D. Boone and P. F. Bernath (2024). 'Antarctic Polar Stratospheric Cloud Analysis of ACE-FTS Data From 2005 to 2023'. *J. Geophys. Res.*, 129, e2024JD040990. DOI: 10.1029/2024jd040990.

Lee, S., G. L. Manney and A. H. Butler (2024a). 'The 2023 Major Sudden Stratospheric Warming [in "State of the Climate in 2023"]'. *Bull. Am. Meteorol. Soc.*, 105, S288–S289. DOI: 10.1175/BAMS-D-24-0101.1.

Lee, S. H., A. H. Butler and G. L. Manney (2024b). 'Two major sudden stratospheric warmings during winter 2023/2024'. *Weather*, 80, pp. 45–53. DOI: 10.1002/wea.7656.

Lee, Y.-K., N. Hindley, C. Grassotti and Q. Liu (2023). 'The Hunga Tonga–Hunga Ha'apai volcanic eruption as seen in satellite microwave observations and MiRS temperature retrievals'. *Geophys. Res. Lett.*, 50, e2023GL106439. DOI: 10.1029/2023GL106439.

Leeuw, J. de, A. Schmidt, C. S. Witham, N. Theys, I. A. Taylor, R. G. Grainger, R. J. Pope, J. Haywood, M. Osborne and N. I. Kristiansen (2021). 'The 2019 Raikoke volcanic eruption – Part 1: Dispersion model simulations and satellite retrievals of volcanic sulfur dioxide'. *Atmos. Chem. Phys.*, 21, pp. 10851–10879. DOI: 10.5194/acp-21-10851-2021.

Lefèvre, F., G. P. Brasseur, I. Folkins, A. K. Smith and P. Simon (1994). 'Chemistry of the 1991–1992 stratospheric winter: Three-dimensional model simulations'. *J. Geophys. Res.*, 99, pp. 8183–8195. DOI: 10.1029/93JD03476.

Lefèvre, F., F. Figarol, K. S. Carslaw and T. Peter (1998). 'The 1997 Arctic Ozone depletion quantified from three-dimensional model simulations'. *Geophys. Res. Lett.*, 25, pp. 2425–2428. DOI: 10.1029/98GL51812.

LeGrande, A., K. Tsigaridis and S. Bauer (2016). 'Role of atmospheric chemistry in the climate impacts of stratospheric volcanic injections'. *Nat. Geosci.*, pp. 652–655. DOI: 10.1038/ngeo2771.

Legras, B. (2025). 'Hunga eruption on 15 January 2022: was there a precursor plume one hour before the eruption?' EarthArXiV manuscript. DOI: 10.31223/X5DT8F.

Legras, B., C. Duchamp, P. Sellitto, A. Podglajen, E. Carboni, R. Siddans, J.-U. Grooß, S. Khaykin and F. Ploeger (2022). 'The evolution and dynamics of the Hunga Tonga–Hunga Ha'apai sulfate aerosol plume in the stratosphere'. *Atmos. Chem. Phys.*, 22, pp. 14957–14970. DOI: 10.5194/acp-22-14957-2022.

Leslie, R. C. (1885). 'Sky glows'. *Nature*, 32, 245. DOI: 10.1038/032245a0.

Lestrelin, H., B. Legras, A. Podglajen and M. Salihoglu (2021). 'Smoke-charged vortices in the stratosphere generated by wildfires and their behaviour in both hemispheres: comparing Australia 2020 to Canada 2017'. *Atmos. Chem. Phys.*, 21, pp. 7113–7134. DOI: 10.5194/acp-21-7113-2021.

Li, C., N. A. Krotkov, S. A. Carn, Y. Zhang, R. J. D. Spurr and J. Joiner (2017). 'New-generation NASA Aura Ozone Monitoring Instrument volcanic SO_2 dataset: Algorithm description, initial results, and continuation with the Suomi-NPP Ozone Mapping and Profiler Suite'. *Atmos. Meas. Tech.*, 10, pp. 445–458. DOI: 10.5194/amt-10-445-2017.

Li, C., Y. Peng, E. Asher, A. A. Baron, M. Todt, T. D. Thornberry, S. Evan, J. Brioude, P. Smale, R. Querel et al. (2024). 'Microphysical Simulation of the 2022 Hunga Volcano Eruption Using a Sectional Aerosol Model'. *Geophys. Res. Lett.*, 51, e2024GL108522. DOI: 10.1029/2024GL108522.

Li, F. and P. Newman (2020). 'Stratospheric water vapor feedback and its climate impacts in the coupled atmosphere–ocean Goddard Earth Observing System Chemistry-Climate Model'. *Clim. Dynam.*, 55, pp. 1585–1595. DOI: 10.1007/s00382-020-05348-6.

Li, Q., Y. Qian, Y. Luo, L. Cao, H. Zhou, T. Yang, F. Si and W. Liu (2023a). 'Diffusion Height and Order of Sulfur Dioxide and Bromine Monoxide Plumes from the Hunga Tonga–Hunga Ha'apai Volcanic Eruption'. *Remote Sens.*, 15, 1534. DOI: 10.3390/rs15061534.

Li, R., J. Lei, J. Kusche, T. Dang, F. Huang, X. Luan, S.-R. Zhang, M. Yan, Z. Yang, F. Liu et al. (2023b). 'Large-scale disturbances in the upper thermosphere induced by the 2022 Tonga volcanic eruption'. *Geophys. Res. Lett.*, 50, e2022GL102265. DOI: 10.1029/2022GL102265.

Li, X., F. Ding, X. Yue, T. Mao, B. Xiong and Q. Song (2023c). 'Multiwave structure of traveling ionospheric disturbances excited by the Tonga volcanic eruptions observed by a dense GNSS network in China'. *Space Weather*, 21, e2022SW003210. DOI: 10.1029/2022SW003210.

Li, Y., C. Pedersen, J. Dykema, J.-P. Vernier, S. Vattioni, A. K. Pandit, A. Stenke, E. Asher, T. Thornberry, M. A. Todt et al. (2023d). 'In situ measurements of perturbations to stratospheric aerosol and modeled ozone and radiative impacts following the 2021 La Soufrière eruption'. *Atmos. Chem. Phys.*, 23, pp. 15351–15364. DOI: 10.5194/acp-23-15351-2023.

Limbacher, J. A., R. A. Kahn and J. Lee (2022). 'The new MISR research aerosol retrieval algorithm: A multi-angle, multi-spectral, bounded-variable least-squares retrieval of aerosol particle properties over both land and water'. *Atmos. Meas. Tech.*, 15, pp. 6865–6887. DOI: 10.5194/amt-15-6865-2022.

Lin, J.-T., P. K. Rajesh, C. C. H. Lin, M.-Y. Chou, J.-Y. Liu, J. Yue, T.-Y. Hsiao, H.-F. Tsai, H.-M. Chao and M.-M. Kung (2022). 'Rapid conjugate appearance of the giant ionospheric Lamb wave signatures in the northern hemisphere after Hunga Tonga volcano

eruptions'. *Geophys. Res. Lett.*, 49, e2022GL098222. DOI: 10.1029/2022GL098222.

Lin, S. J. and R. B. Rood (1996). 'Multidimensional flux-form semi-Lagrangian transport schemes'. *Mon. Weather Rev.*, 124, pp. 2046–2070. DOI: 10.1175/1520-0493(1996)124<2046:MFFSLT>2.0.CO;2.

Liu, C. H., J. Klostermeyer, K. C. Yeh, T. B. Jones, T. Robinson, O. Holt, R. Leitinger, T. Ogawa, K. Sinno, S. Kato et al. (1982). 'Global dynamic responses of the atmosphere to the eruption of Mount St. Helens on May 18, 1980'. *J. Geophys. Res.*, 87, pp. 6281–6290. DOI: 10.1029/JA087iA08p06281.

Liu, H.-L., W. Wang, J. D. Huba, P. H. Lauritzen and F. Vitt (2023). 'Atmospheric and ionospheric responses to the Hunga–Tonga volcano eruption simulated by WACCM-X'. *Geophys. Res. Lett.*, 50, e2023GL103682. DOI: 10.1029/2023GL103682.

Liu, X., R. C. Easter, S. J. Ghan, R. Zaveri, P. Rasch, X. Shi, J.-F. Lamarque, A. Gettelman, H. Morrison, F. Vitt et al. (2012). 'Toward a minimal representation of aerosols in climate models: description and evaluation in the Community Atmosphere Model CAM5'. *Geosci. Model Dev.*, 5, pp. 709–739. DOI: 10.5194/gmd-5-709-2012.

Liu, X., P.-L. Ma, H. Wang, S. Tilmes, B. Singh, R. C. Easter, S. J. Ghan and P. J. Rasch (2016). 'Description and evaluation of a new four-mode version of the Modal Aerosol Module (MAM4) within version 5.3 of the Community Atmosphere Model'. *Geosci. Model Dev.*, 9, pp. 505–522. DOI: 10.5194/gmd-9-505-2016.

Liu, X., J. Xu, J. Yue and M. Kogure (2022). 'Strong gravity waves associated with the Tonga volcano eruption revealed by SABER observations'. *Geophys. Res. Lett.*, 49, e2022GL098339. DOI: 10.1029/2022GL098339.

Livesey, N. J., W. G. Read, P. A. Wagner, L. Froidevaux, A. Lambert, G. L. Manney et al. (2020). *EOS MLS Version 4.2x Level 2 and 3 data quality and description document*. Technical Report JPL-D33509 Rev. E. https://mls.jpl.nasa.gov/data/v4-2_data_quality_document.pdf. Jet Propulsion Laboratory, California Institute of Technology.

Livesey, N. J., W. G. Read, P. A. Wagner, L. Froidevaux, M. L. Santee, M. J. Schwartz et al. (2022). *EOS MLS Version 5.0x Level 2 and 3 data quality and description document*. Technical Report JPL-D105336 Rev. B. https://mls.jpl.nasa.gov/data/v5-0_data_quality_document.pdf. Jet Propulsion Laboratory, California Institute of Technology.

Livesey, N. J., W. G. Read, L. Froidevaux, A. Lambert, M. L. Santee, M. J. Schwartz, L. F. Millán, R. F. Jarnot, P. A. Wagner, D. F. Hurst et al. (2021). 'Investigation and amelioration of long-term instrumental drifts in water vapor and nitrous oxide measurements from the Aura Microwave Limb Sounder (MLS) and their implications for studies of variability and trends'. *Atmos. Chem. Phys.*, 21, pp. 15409–15430. DOI: 10.5194/acp-21-15409-2021.

Lock, A. P., A. R. Brown, M. R. Bush, G. M. Martin and R. N. B. Smith (2000). 'A new boundary layer mixing scheme. Part I: Scheme description and single-column model tests'. *Mon. Weather Rev.*, 128, pp. 3187–3199. DOI: 10.1175/1520-0493(2000)128<3187:anblms>2.0.co;2.

Lopez, T., L. Clarisse, H. Schwaiger, A. Van Eaton, M. Loewen, D. Fee, J. Lyons, K. Wallace, C. Searcy, A. Wech et al. (2020). 'Constraints on eruption processes and event masses for the 2016–2017 eruption of Bogoslof volcano, Alaska, through evaluation of IASI satellite SO_2 masses and complementary datasets'. *Bull. Volcanol.*, 82, 17. DOI: 10.1007/s00445-019-1348-z.

Loughman, R. P., P. K. Bhartia, Z. Chen, P. Xu, E. Nyaku and G. Taha (2018). 'The Ozone Mapping and Profiler Suite (OMPS) Limb Profiler Version 1 aerosol extinction retrieval algorithm: Theoretical basis'. *Atmos. Meas. Tech.*, 11, pp. 2633–2651. DOI: 10.5194/amt-11-2633-2018.

Lu, J., S. Lou, X. Huang, L. Xue, K. Ding, T. Liu, Y. Ma, W. Wang and A. Ding (2023). 'Stratospheric aerosol and ozone responses to the Hunga Tonga-Hunga Ha'apai volcanic eruption'. *Geophys. Res. Lett.*, 50, e2022GL102315. DOI: 10.1029/2022GL102315.

Luo, B. (2016). *Stratospheric aerosol data for use in CMIP6 models*. ftp://iacftp.ethz.ch/pub_read/luo/CMIP6/Readme_Data_Description.pdf.

Luo, B. (2017). *SAGE-3λ v4: Stratospheric aerosol data for use in CMIP6 models*. ETH Zurich. DOI: 10.3929/ethz-b-000715155.

Lurton, T., Y. Balkanski, V. Bastrikov, S. Bekki, L. Bopp, P. Braconnot, P. Brockmann, P. Cadule, C. Contoux, A. Cozic et al. (2020). 'Implementation of the CMIP6 forcing data in the IPSL-CM6A-LR model'. *J. Adv. Model. Earth Syst.*, 12, e2019MS001940. DOI: 10.1029/2019MS001940.

Lynett, P., M. McCann, Z. Zhou, W. Renteria, J. Borrero, D. Greer, O. Fa'anunu, C. Bosserelle, B. Jaffe, S. La Selle et al. (2022). 'Diverse tsunamigenesis triggered by the Hunga Tonga-Hunga Ha'apai erup-

tion'. *Nature*, 609, pp. 728–733. DOI: 10.1038/s41586-022-05170-6.

Lyons, J. J., M. M. Haney, D. Fee, A. G. Wech and C. F. Waythomas (2019). 'Infrasound from giant bubbles during explosive submarine eruptions'. *Nat. Geosci.*, 12, pp. 952–958. DOI: 10.1038/s41561-019-0461-0.

Madden-Nadeau, A. L., M. Cassidy, D. M. Pyle, T. A. Mather, S. F. L. Watt, S. L. Engwell, M. Abdurrachman, M. E. M. Nurshal, D. R. Tappin and T. Ismail (2021). 'The magmatic and eruptive evolution of the 1883 caldera-forming eruption of Krakatau: Integrating field- to crystal-scale observations'. *J. Volcanol. Geotherm. Res.*, 411, 107176. DOI: 10.1016/j.jvolgeores.2021.107176.

Maeno, F., T. Kaneko, M. Ichihara, Y. J. Suzuki, A. Yasuda, K. Nishida and T. Ohminato (2022). 'Seawater-magma interactions sustained the high column during the 2021 phreatomagmatic eruption of Fukutoku-Oka-no-Ba'. *Commun. Earth Environ.*, 3, 260. DOI: 10.1038/s43247-022-00594-4.

Maletckii, B. and E. Astafyeva (2022). 'Near-real-time analysis of the ionospheric response to the 15 January 2022 Hunga Tonga–Hunga Ha'apai volcanic eruption'. *J. Geophys. Res.*, 127, e2022JA030735. DOI: 10.1029/2022JA030735.

Malinina, E., A. Rozanov, U. Niemeier, S. Wallis, C. Arosio, F. Wrana, C. Timmreck, C. von Savigny and J. P. Burrows (2021). 'Changes in stratospheric aerosol extinction coefficient after the 2018 Ambae eruption as seen by OMPS-LP and MAECHAM5-HAM'. *Atmos. Chem. Phys.*, 21, pp. 14871–14891. DOI: 10.5194/acp-21-14871-2021.

Mandeville, C. W., S. Carey and H. Sigurdsson (1996a). 'Magma mixing, fractional crystallization and volatile degassing during the 1883 eruption of Krakatau volcano, Indonesia'. *J. Volcanol. Geotherm. Res.*, 74, pp. 243–274. DOI: 10.1016/s0377-0273(96)00060-1.

Mandeville, C. W., S. Carey and H. Sigurdsson (1996b). 'Sedimentology of the Krakatau 1883 submarine pyroclastic deposits'. *Bull. Volcanol.*, 57, pp. 512–529. DOI: 10.1007/BF00304436.

Mandeville, C. W., S. Carey, H. Sigurdsson and J. King (1994). 'Paleomagnetic evidence for high-temperature emplacement of the 1883 subaqueous pyroclastic flows from Krakatau Volcano, Indonesia'. *J. Geophys. Res.*, 99, pp. 9487–9504. DOI: 10.1029/94JB00239.

Manga, M., K. E. Fauria, C. Lin, S. J. Mitchell, M. P. Jones, C. E. Conway, W. Degruyter, B. Hosseini, R. Carey, R. Cahalan et al. (2018). 'The pumice raft-forming 2012 Havre submarine eruption was effusive'. *Earth Planet. Sci. Lett.*, 489, pp. 49–58. DOI: 10.1016/j.epsl.2018.02.025.

Mann, G. W., K. S. Carslaw, D. A. Ridley, D. V. Spracklen, K. J. Pringle, J. Merikanto, H. Korhonen, J. P. Schwarz, L. A. Lee, P. T. Manktelow et al. (2012). 'Intercomparison of modal and sectional aerosol microphysics representations within the same 3-D global chemical transport model'. *Atmos. Chem. Phys.*, 12, pp. 4449–4476. DOI: 10.5194/acp-12-4449-2012.

Mann, G. W., K. S. Carslaw, D. V. Spracklen, D. A. Ridley, P. T. Manktelow, M. P. Chipperfield, S. J. Pickering and C. E. Johnson (2010). 'Description and evaluation of GLOMAP-mode: a modal global aerosol microphysics model for the UKCA composition-climate model'. *Geosci. Model Dev.*, 3, pp. 519–551. DOI: 10.5194/gmd-3-519-2010.

Manney, G. L., R. W. Zurek, M. E. Gelman, A. J. Miller and R. Nagatani (1994). 'The anomalous Arctic lower stratospheric polar vortex of 1992–1993'. *Geophys. Res. Lett.*, 21, pp. 2405–2408. DOI: 10.1029/94gl02368.

Manney, G. L., M. L. Santee, A. Lambert, L. F. Millán, K. Minschwaner, F. Werner, Z. D. Lawrence, W. G. Read, N. J. Livesey and T. Wang (2023). 'Siege in the Southern Stratosphere: Hunga Tonga-Hunga Ha'apai Water Vapor Excluded From the 2022 Antarctic Polar Vortex'. *Geophys. Res. Lett.*, 50. DOI: 10.1029/2023gl103855.

Marchand, M., P. Keckhut, S. Lefebvre, C. Claud, D. Cugnet, A. Hauchecorne, F. Lefévre, M.-P. Lefebvre, J. Jumelet, F. Lott et al. (2012). 'Dynamical amplification of the stratospheric solar response simulated with the Chemistry-Climate Model LMDz-Reprobus'. *J. Atmos. Solar-Terr. Phys.*, 75–76, pp. 147–160. DOI: 10.1016/j.jastp.2011.11.008.

Marshall, L. R., E. C. Maters, A. Schmidt, C. Timmreck, A. Robock and M. Toohey (2022). 'Volcanic effects on climate: recent advances and future avenues'. *B. Volcanol.*, 84, 54. DOI: 10.1007/s00445-022-01559-3.

Marshall, L. R., C. J. Smith, P. M. Forster, T. J. Aubry, T. Andrews and A. Schmidt (2020). 'Large Variations in Volcanic Aerosol Forcing Efficiency Due to Eruption Source Parameters and Rapid Adjustments'. *Geophys. Res. Lett.*, 47, e2020GL090241. DOI: 10.1029/2020GL090241.

Martineau, P., J. S. Wright, N. Zhu and M. Fujiwara (2018). 'Zonal-mean data set of global atmospheric reanalyses on pressure levels'. *Earth Syst. Sci. Data*, 10, pp. 1925–1941. DOI: 10.5194/essd-10-1925-2018.

Mastin, L. G., M. Guffanti, R. Servranckx, P. Webley, S. Barsotti, K. Dean, A. Durant, J. W. Ewert, A. Neri, W. I. Rose et al. (2009). 'A multidisciplinary effort to assign realistic source parameters to models of volcanic ash-cloud transport and dispersion during eruptions'. *J. Volcanol. Geotherm. Res.*, 186, pp. 10–21. DOI: 10.1016/j.jvolgeores.2009.01.008.

Mastin, L. G. and J. B. Witter (2000). 'The hazards of eruptions through lakes and seawater'. *J. Volcanol. Geotherm. Res.*, 97, pp. 195–214. DOI: 10.1016/s0377-0273(99)00174-2.

Mastin, L. G., A. R. Van Eaton and S. J. Cronin (2024). 'Did steam boost the height and growth rate of the giant Hunga eruption plume?' *Bull. Volcanol.*, 86, 64. DOI: 10.1007/s00445-024-01749-1.

Matoza, R. S., D. Fee, J. D. Assink, A. M. Iezzi, D. N. Green, K. Kim, L. Toney, T. Lecocq, S. Krishnamoorthy, J.-M. Lalande et al. (2022). 'Atmospheric waves and global seismoacoustic observations of the January 2022 Hunga eruption, Tonga'. *Science*, 377, pp. 95–100. DOI: 10.1126/science.abo7063.

Maycock, A. C. and K. P. Shine (2012). 'Stratospheric water vapor and climate: Sensitivity to the representation in radiation codes'. *J. Geophys. Res.*, 117, D13102. DOI: 10.1029/2012JD017484.

Maycock, A. C., M. M. Joshi, K. P. Shine and A. A. Scaife (2013). 'The Circulation Response to Idealized Changes in Stratospheric Water Vapor'. *J. Climate*, 26, pp. 545–561. DOI: 10.1175/JCLI-D-12-00155.1.

Millán, L., W. G. Read, M. L. Santee, A. Lambert, G. L. Manney, J. L. Neu, M. C. Pitts, F. Werner, N. J. Livesey and M. J. Schwartz (2024). 'The Evolution of the Hunga Hydration in a Moistening Stratosphere'. *Geophys. Res. Lett.*, 51, e2024GL110841. DOI: 10.1029/2024gl110841.

Millán, L., M. L. Santee, A. Lambert, N. J. Livesey, F. Werner, M. J. Schwartz, H. C. Pumphrey, G. L. Manney, Y. Wang, H. Su et al. (2022). 'The Hunga Tonga-Hunga Ha'apai Hydration of the Stratosphere'. *Geophys. Res. Lett.*, 49, e2022GL099381. DOI: 10.1029/2022gl099381.

Miller, S. D., W. C. Straka, J. Yue, S. M. Smith, M. J. Alexander, L. Hoffmann, M. Setvák and P. T. Partain (2015). 'Upper atmospheric gravity wave details revealed in nightglow satellite imagery'. *Proc. Natl. Acad. Sci. U.S.A.*, 112, E6728–E6735. DOI: 10.1073/pnas.1508084112.

Mills, M. J., J. H. Richter, S. Tilmes, B. Kravitz, D. G. Mac-Martin, A. A. Glanville, J. J. Tribbia, J.-F. Lamarque, F. Vitt, A. Schmidt et al. (2017). 'Radiative and chemical response to interactive stratospheric sulfate aerosols in fully coupled CESM1(WACCM)'. *J. Geophys. Res.*, 122, pp. 13061–13078. DOI: 10.1002/2017JD027006.

Mills, M. J., A. Schmidt, R. Easter, S. Solomon, D. E. Kinnison, S. J. Ghan et al. (2016). 'Global volcanic aerosol properties derived from emissions, 1990–2014, using CESM1 (WACCM)'. *J. Geophys. Res.*, 121, pp. 2332–2348. DOI: 10.1002/2015jd024290.

Mills, M. J., O. B. Toon, V. Vaida, P. E. Hintze, H. G. Kjaergaard, D. P. Schofield and T. W. Robinson (2005). 'Photolysis of sulfuric acid vapor by visible light as a source of the polar stratospheric CN layer'. *J. Geophys. Res.*, 110, D08201. DOI: 10.1029/2004JD005519.

Minnis, P., E. F. Harrison, L. L. Stowe, G. G. Gibson, F. M. Denn, D. R. Doelling and W. L. J. Smith (1993). 'Radiative climate forcing by the Mt. Pinatubo eruption'. *Science*, 259, pp. 1411–1415. DOI: 10.1126/science.259.5100.1411.

Miyoshi, Y. and H. Shinagawa (2023). 'Upward propagation of gravity waves and ionospheric perturbations triggered by the 2022 Hunga–Tonga volcanic eruption'. *Earth Planets Space*, 75, 68. DOI: 10.1186/s40623-023-01827-2.

Molod, A., L. Takacs, M. Suarez and J. Bacmeister (2015). 'Development of the GEOS-5 atmospheric general circulation model: evolution from MERRA to MERRA2'. *Geosci. Model Dev.*, 8, pp. 1339–1356. DOI: 10.5194/gmd-8-1339-2015.

Morgenstern, O., P. Braesicke, F. M. O'Connor, A. C. Bushell, C. E. Johnson, S. M. Osprey and J. A. Pyle (2009). 'Evaluation of the new UKCA climate-composition model – Part 1: The stratosphere'. *Geosci. Model Dev.*, 2, pp. 43–57. DOI: 10.5194/gmd-2-43-2009.

Morgenstern, O., M. I. Hegglin, E. Rozanov, F. M. O'Connor, N. L. Abraham, H. Akiyoshi, A. T. Archibald, S. Bekki, N. Butchart, M. P. Chipperfield et al. (2017). 'Review of the global models used within phase 1 of the Chemistry–Climate Model Initiative (CCMI)'. *Geosci. Model Dev.*, 10, pp. 639–671. DOI: 10.5194/gmd-10-639-2017.

Mulcahy, J. P., C. Jones, A. Sellar, B. Johnson, I. A. Boutle, A. Jones, T. Andrews, S. T. Rumbold, J.

Mollard, N. Bellouin et al. (2018). 'Improved Aerosol Processes and Effective Radiative Forcing in HadGEM3 and UKESM1'. *J. Adv. Model. Earth Syst.*, 10, pp. 2786–2805. DOI: 10.1029/2018MS001464.

Mulcahy, J. P., C. Johnson, C. G. Jones, A. C. Povey, C. E. Scott, A. Sellar, S. T. Turnock, M. T. Woodhouse, N. L. Abraham, M. B. Andrews et al. (2020). 'Description and evaluation of aerosol in UKESM1 and HadGEM3-GC3.1 CMIP6 historical simulations'. *Geosci. Model Dev.*, 13, pp. 6383–6423. DOI: 10.5194/gmd-13-6383-2020.

Mulcahy, J. P., C. G. Jones, S. T. Rumbold, T. Kuhlbrodt, A. J. Dittus, E. W. Blockley, A. Yool, J. Walton, C. Hardacre, T. Andrews et al. (2023). 'UKESM1.1: development and evaluation of an updated configuration of the UK Earth System Model'. *Geosci. Model Dev.*, 16, pp. 1569–1600. DOI: 10.5194/gmd-16-1569-2023.

Murcray, D. G., F. J. Murcray, D. B. Barker and H. J. Mastenbrook (1981). 'Changes in stratospheric water vapor associated with the Mount St. Helens eruption'. *Science*, 211, pp. 823–824. DOI: 10.1126/science.211.4484.823.

Murphy, D. M., K. D. Froyd, I. Bourgeois, C. A. Brock, A. Kupc, J. Peischl, G. P. Schill, C. R. Thompson, C. J. Williamson and P. Yu (2021). 'Radiative and chemical implications of the size and composition of aerosol particles in the existing or modified global stratosphere'. *Atmos. Chem. Phys.*, 21, pp. 8915–8932. DOI: 10.5194/acp-21-8915-2021.

Muser, L. O., G. A. Hoshyaripour, J. Bruckert, Á. Horváth, E. Malinina, S. Wallis, F. J. Prata, A. Rozanov, C. von Savigny, H. Vogel et al. (2020). 'Particle aging and aerosol–radiation interaction affect volcanic plume dispersion: evidence from the Raikoke 2019 eruption'. *Atmos. Chem. Phys.*, 20, pp. 15015–15036. DOI: 10.5194/acp-20-15015-2020.

Muthers, S., F. Arfeuille, C. C. Raible and E. Rozanov (2015). 'The impacts of volcanic aerosol on stratospheric ozone and the Northern Hemisphere polar vortex: separating radiative-dynamical changes from direct effects due to enhanced aerosol heterogeneous chemistry'. *Atmos. Chem. Phys.*, 15, pp. 11461–11476. DOI: 10.5194/acp-15-11461-2015.

Nagai, T., B. Liley, T. Sakai, T. Shibata and O. Uchino (2010). 'Post-Pinatubo Evolution and Subsequent Trend of the Stratospheric Aerosol Layer Observed by Mid-Latitude Lidars in Both Hemispheres'. *Scientific Online Letters on the Atmosphere (SOLA)*, 6, pp. 69–72. DOI: 10.2151/sola.2010-018.

NASA/LARC/SD/ASDC (2023). *Global Space-based Stratospheric Aerosol Climatology Version 2.21*. Data set. NASA Langley Atmospheric Science Data Center DAAC. DOI: 10.5067/GLOSSAC-L3-V2.21.

NASEM (2017). *Volcanic Eruptions and Their Repose, Unrest, Precursors, and Timing*. National Academies Press. DOI: 10.17226/24650.

Nassar, R., P. F. Bernath, C. D. Boone, C. Clerbaux, P. F. Coheur, G. Dufour, L. Froidevaux, E. Mahieu, J. C. McConnell, S. D. McLeod et al. (2006). 'A global inventory of stratospheric chlorine in 2004'. *J. Geophys. Res.*, 111, 2006JD007073. DOI: 10.1029/2006JD007073.

Naujokat, B. (1986). 'An update of the observed Quasi-Biennial Oscillation of the stratospheric winds over the tropics'. *J. Atmos. Sci.*, 43, pp. 1873–1877. DOI: 10.1175/1520-0469(1986)043<1873:AUOTOQ>2.0.CO;2.

Nedoluha, G. E., R. M. Bevilacqua and K. W. Hoppel (2002). 'POAM III measurements of dehydration in the Antarctic and comparisons with the Arctic'. *J. Geophys. Res.*, 107, 8290. DOI: 10.1029/2001JD001184.

Nedoluha, G. E., R. M. Gomez, I. Boyd, H. Neal, D. R. Allen and A. Lambert (2024). 'The Spread of the Hunga Tonga H2O Plume in the Middle Atmosphere Over the First Two Years Since Eruption'. *J. Geophys. Res.*, 129, e2024JD040907. DOI: 10.1029/2024jd040907.

Nedoluha, G. E., R. M. Gomez, I. Boyd, H. Neal, D. R. Allen, A. Lambert and N. J. Livesey (2023). 'Mesospheric Water Vapor in 2022'. *J. Geophys. Res.*, 128, e2023JD039196. DOI: 10.1029/2023jd039196.

Nedoluha, G. E., R. M. Gomez, I. Boyd, H. Neal, D. R. Allen, A. Parrish, B. J. Connor and D. E. Siskind (2025). 'Measurements of Stratospheric ClO From Mauna Kea: 1992–2023'. *J. Geophys. Res.*, 130, e2024JD041848. DOI: 10.1029/2024jd041848.

Neely III, R. R. and A. Schmidt (2016). *VolcanEESM: Global volcanic sulphur dioxide (SO_2) emissions database from 1850 to present*. Centre for Environmental Data Analysis. DOI: 10.5285/76ebdc0b-0eed-4f70-b89e-55e606bcd568.

Newhall, C. and S. Self (1982). 'The volcanic explosivity index (VEI) an estimate of explosive magnitude for historical volcanism'. *J. Geophys. Res.*, 87, pp. 1231–1238. DOI: 10.1029/hg002p0143.

Newman, P. A., L. R. Lait, N. A. Kramarova, L. Coy, S. M. Frith, L. D. Oman and S. S. Dhomse (2024). 'Record High March 2024 Arctic Total Column Ozone'.

Geophys. Res. Lett., 51, e2024GL110924. DOI: 10.1029/2024gl110924.

Nielsen, J. E., S. Pawson, A. Molod, B. Auer, A. M. da Silva, A. R. Douglass, B. Duncan, Q. Liang, M. Manyin, L. D. Oman et al. (2017). 'Chemical mechanisms and their applications in the Goddard Earth Observing System (GEOS) earth system model'. *J. Adv. Model. Earth Syst.*, 9, pp. 3019–3044. DOI: 10.1002/2017MS001011.

Niemeier, U., C. Timmreck, H.-F. Graf, S. Kinne, S. Rast and S. Self (2009). 'Initial fate of fine ash and sulfur from large volcanic eruptions'. *Atmos. Chem. Phys.*, 9, pp. 9043–9057. DOI: 10.5194/acp-9-9043-2009.

Niemeier, U., S. Wallis, C. Timmreck, T. van Pham and C. von Savigny (2023). 'How the Hunga Tonga—Hunga Ha'apai Water Vapor Cloud Impacts Its Transport Through the Stratosphere: Dynamical and Radiative Effects'. *Geophys. Res. Lett.*, 50, e2023GL106482. DOI: 10.1029/2023gl106482.

Norgren, M., L. E. Kalnajs and T. Deshler (2024). 'Measurements of Total Aerosol Concentration in the Stratosphere: A New Balloon-Borne Instrument and a Report on the Existing Measurement Record'. *J. Geophys. Res.*, 129, e2024JD040992. DOI: 10.1029/2024JD040992.

Novak, G. A., C. H. Fite, C. D. Holmes, P. R. Veres, J. A. Neuman, I. Faloona, J. A. Thornton, G. M. Wolfe, M. P. Vermeuel, C. M. Jernigan et al. (2021). 'Rapid cloud removal of dimethyl sulfide oxidation products limits SO_2 and cloud condensation nuclei production in the marine atmosphere'. *Proc. Natl. Acad. Sci.*, 118, e2110472118. DOI: 10.1073/pnas.2110472118.

Nowack, P., P. Ceppi, S. M. Davis, G. Chiodo, W. Ball, M. A. Diallo, B. Hassler, Y. Jia, J. Keeble and M. Joshi (2023). 'Response of stratospheric water vapour to warming constrained by satellite observations'. *Nat. Geosci.*, 16, pp. 577–583. DOI: 10.1038/s41561-023-01183-6.

O'Connor, F. M., C. E. Johnson, O. Morgenstern, N. L. Abraham, P. Braesicke, M. Dalvi, G. A. Folberth, M. G. Sanderson, P. J. Telford, A. Voulgarakis et al. (2014). 'Evaluation of the new UKCA climate-composition model – Part 2: The Troposphere'. *Geosci. Model Dev.*, 7, pp. 41–91. DOI: 10.5194/gmd-7-41-2014.

O'Neill, B. C., C. Tebaldi, D. P. van Vuuren, V. Eyring, P. Friedlingstein, G. Hurtt, R. Knutti, E. Kriegler, J.-F. Lamarque, J. Lowe et al. (2016). 'The Scenario Model Intercomparison Project (ScenarioMIP) for CMIP6'. *Geosci. Model Dev.*, 9, pp. 3461–3482. DOI: 10.5194/gmd-9-3461-2016.

O'Neill, N. T., C. Perro, A. Saha, G. Lesins, T. J. Duck, E. W. Eloranta, G. J. Nott, A. Hoffman, M. L. Karumudi, C. Ritter et al. (2012). 'Properties of Sarychev sulphate aerosols over the Arctic'. *J. Geophys. Res.*, 117, 2011JD016838. DOI: 10.1029/2011JD016838.

Ohneiser, K., A. Ansmann, B. Kaifler, A. Chudnovsky, B. Barja, D. A. Knopf, N. Kaifler, H. Baars, P. Seifert, D. Villanueva et al. (2022). 'Australian wildfire smoke in the stratosphere: the decay phase in 2020/2021 and impact on ozone depletion'. *Atmos. Chem. Phys.*, 22, pp. 7417–7442. DOI: 10.5194/acp-22-7417-2022.

Ohneiser, K., A. Ansmann, J. Witthuhn, H. Deneke, A. Chudnovsky, G. Walter and F. Senf (2023). 'Self-lofting of wildfire smoke in the troposphere and stratosphere: simulations and space lidar observations'. *Atmos. Chem. Phys.*, 23, pp. 2901–2925. DOI: 10.5194/acp-23-2901-2023.

Ohya, H., F. Tsuchiya, T. Takamura, H. Shinagawa, Y. Takahashi and A. B. Chen (2024). 'Lower ionospheric resonance caused by Pekeris wave induced by the 2022 Tonga volcanic eruption'. *Sci. Rep.*, 14, 15659. DOI: 10.1038/s41598-024-65929-x.

Oman, L., A. Robock, G. Stenchikov, T. Thordarson, D. Koch, D. Shindell and C. Gao (2006). 'Modeling the distribution of the volcanic aerosol cloud from the 1783–1784 Laki eruption'. *J. Geophys. Res.*, 111, D12209. DOI: 10.1029/2005jd006899.

Oppenheimer, C., T. P. Fischer and B. Scaillet (2014). 'Volcanic Degassing: Process and Impact'. *Treatise on Geochemistry*. Vol. 4. Elsevier, pp. 111–179. DOI: 10.1016/b978-0-08-095975-7.00304-1.

Østerstrøm, F. F., J. E. Klobas, R. P. Kennedy, A. Cadoux and D. M. Wilmouth (2023). 'Sensitivity of stratospheric ozone to the latitude, season, and halogen content of a contemporary explosive volcanic eruption'. *Sci. Rep.*, 13, 6457. DOI: 10.1038/s41598-023-32574-9.

Otsuka, S. (2022). 'Visualizing Lamb Waves From a Volcanic Eruption Using Meteorological Satellite Himawari-8'. *Geophys. Res. Lett.*, 49, e2022GL098324. DOI: 10.1029/2022GL098324.

Pacheco, E. E., J. P. Velasquez, R. Flores, L. Condori, G. Fajardo, K. Kuyeng, D. E. Scipion, M. Milla, J. F. Conte, F. L. Poblet et al. (2024). 'The impact of the Hunga Tonga–Hunga Ha'apai volcanic eruption on the Peruvian atmosphere: From the sea surface to the ionosphere'. *Earth Planets Space*, 76, 79. DOI: 10.1186/s40623-024-02022-7.

Park, M., W. J. Randel, R. P. Damadeo, D. E. Flittner, S. M. Davis, K. H. Rosenlof, N. Livesey, A. Lambert and W. Read (2021). 'Near-Global Variability of Stratospheric Water Vapor Observed by SAGE III/ISS'. *J. Geophys. Res.*, 126, e2020JD034274. DOI: 10.1029/2020JD034274.

Pausata, F. S., L. Chafik, R. Caballero and D. S. Battisti (2015). 'Impacts of high-latitude volcanic eruptions on ENSO and AMOC'. *Proc. Nat. Acad. Sci.*, 112, pp. 13784–13788. DOI: 10.1073/pnas.1509153112.

Pedatella, N. M., X. Yue and W. S. Schreiner (2015). 'An improved inversion for FORMOSAT-3/COSMIC ionosphere electron density profiles'. *J. Geophys. Res.*, 120, pp. 8942–8953. DOI: 10.1002/2015JA021704.

Perlwitz, J. and H.-F. Graf (2001). 'Troposphere-stratosphere dynamic coupling under strong and weak polar vortex conditions'. *Geophys. Res. Lett.*, 28, pp. 271–274. DOI: 10.1029/2000GL012405.

Pernter, J. (1889). 'Der Krakatau-Ausbruch und seine Folge-Erscheinungen'. *Meteorol. Z.*, 6, 457. https://homepages.see.leeds.ac.uk/~amtgwm/Pernter_1889_Pg457.pdf.

Perttu, A., J. Assink, A. R. Van Eaton, C. Caudron, C. Vagasky, J. Krippner, K. McKee, S. De Angelis, B. Perttu, B. Taisne et al. (2023). 'Remote Characterization of the 12 January 2020 Eruption of Taal Volcano, Philippines, Using Seismo-Acoustic, Volcanic Lightning, and Satellite Observations'. *Bull. Seismol. Soc. Am.*, 113, pp. 1471–1492. DOI: 10.1785/0120220223.

Peter, T. (1997). 'Microphysics and heterogeneous chemistry of polar startospheric clouds'. *Annu. Rev. Phys. Chem.*, 48, pp. 785–822. DOI: 10.1146/annurev.physchem.48.1.785.

Peuch, V.-H., R. Engelen, M. Rixen, D. Dee, J. Flemming, M. Suttie, M. Ades, A. Agusti-Panareda, C. Ananasso, E. Andersson et al. (2022). 'The Copernicus Atmosphere Monitoring Service: From Research to Operations'. *Bull. Am. Meteorol. Soc.*, 103, E2650–E2668. DOI: 10.1175/BAMS-D-21-0314.1.

Pierce, A. D. and J. W. Posey (2010). 'Theory of the Excitation and Propagation of Lamb's Atmospheric Edge Mode from Nuclear Explosions'. *Geophys. J. R. Astron. Soc.*, 26, pp. 341–368. DOI: 10.1111/j.1365-246X.1971.tb03406.x.

Pinnick, R. G. and D. J. Hofmann (1973). 'Efficiency of light-scattering aerosol particle counters'. *Appl. Optics*, 12, pp. 2593–2597. DOI: 10.1364/AO.12.002593.

Pitari, G. and E. Mancini (2002). 'Short-term climatic impact of the 1991 volcanic eruption of Mt. Pinatubo and effects on atmospheric tracers'. *Nat. Hazards Earth Syst. Sci.*, DOI: 10.5194/nhess-2-91-2002.

Pitts, M. C., L. R. Poole and R. Gonzalez (2018). 'Polar stratospheric cloud climatology based on CALIPSO spaceborne lidar measurements from 2006 to 2017'. *Atmos. Chem. Phys.*, 18, pp. 10881–10913. DOI: 10.5194/acp-18-10881-2018.

Plumb, R. A. and R. C. Bell (1982). 'A model of the quasi-biennial oscillation on an equatorial beta-plane'. *Q. J. R. Meteorol. Soc.*, 108, pp. 335–352. DOI: 10.1002/qj.49710845604.

Plumb, R. A. (1996). 'A "tropical pipe" model of stratospheric transport'. *J. Geophys. Res.*, 101, pp. 3957–3972. DOI: 10.1029/95JD03002.

Poblet, F. L., J. L. Chau, J. F. Conte, J. Vierinen, J. Suclupe, A. Liu and R. R. Rodriguez (2023). 'Extreme horizontal wind perturbations in the mesosphere and lower thermosphere over South America associated with the 2022 Hunga eruption'. *Geophys. Res. Lett.*, 50, e2023GL103809. DOI: 10.1029/2023GL103809.

Podglajen, A., A. Le Pichon, R. F. Garcia, S. Gérier, C. Millet, K. Bedka, K. Khlopenkov, S. Khaykin and A. Hertzog (2022). 'Stratospheric Balloon Observations of Infrasound Waves From the 15 January 2022 Hunga Eruption, Tonga'. *Geophys. Res. Lett.*, 49, e2022GL100833. DOI: 10.1029/2022GL100833.

Podglajen, A., B. Legras, G. Lapeyre, R. Plougonven, V. Zeitlin, V. Brémaud and P. Sellitto (2024). 'Dynamics of diabatically forced anticyclonic plumes in the stratosphere'. *Q. J. R. Meteorol. Soc.*, 150, pp. 1538–1565. DOI: 10.1002/qj.4658.

Poli, P. and N. M. Shapiro (2022). 'Rapid Characterization of Large Volcanic Eruptions: Measuring the Impulse of the Hunga Tonga Ha'apai Explosion From Teleseismic Waves'. *Geophys. Res. Lett.*, 49, e2022GL098123. DOI: 10.1029/2022GL098123.

Polvani, L. M., D. W. Waugh and R. A. Plumb (1995). 'On the Subtropical Edge of the Stratospheric Surf Zone'. *J. Atmos. Sci.*, 52, pp. 1288–1309. DOI: 10.1175/1520-0469(1995)052<1288:otseot>2.0.co;2.

Posey, J. W. and A. D. Pierce (1971). 'Estimation of Nuclear Explosion Energies from Microbarograph Records'. *Nature*, 232, pp. 253–253. DOI: 10.1038/232253a0.

Pradipta, R., B. A. Carter, J. L. Currie, S. Choy, P. Wilkinson, P. Maher and R. Marshall (2023).

'On the propagation of traveling ionospheric disturbances from the Hunga Tonga–Hunga Ha'apai volcano eruption and their possible connection with tsunami waves'. *Geophys. Res. Lett.*, 50, e2022GL101925. DOI: 10.1029/2022GL101925.

Prata, A. T., A. Folch, A. J. Prata, R. Biondi, H. Brenot, C. Cimarelli, S. Corradini, J. Lapierre and A. Costa (2020). 'Anak Krakatau triggers volcanic freezer in the upper troposphere'. *Sci. Rep.*, 10, pp. 1–13. DOI: 10.1038/s41598-020-60465-w.

Prata, A. T., R. G. Grainger, I. A. Taylor, A. C. Povey, S. R. Proud and C. A. Poulsen (2022). 'Uncertainty-bounded estimates of ash cloud properties using the ORAC algorithm: application to the 2019 Raikoke eruption'. *Atmos. Meas. Tech.*, 15, pp. 5985–6010. DOI: 10.5194/amt-15-5985-2022.

Prata, A. T., S. A. Young, S. T. Siems and M. J. Manton (2017). 'Lidar ratios of stratospheric volcanic ash and sulfate aerosols retrieved from CALIOP measurements'. *Atmos. Chem. Phys.*, 17, pp. 8599–8618. DOI: 10.5194/acp-17-8599-2017.

Prata, F., A. T. Prata, R. Tanner, R. G. Grainger, M. Borgas and T. J. Aubry (2025). 'The radial spreading of volcanic umbrella clouds deduced from satellite measurements'. *Volcanica*, 8, pp. 1–29. DOI: 10.30909/vol.08.01.0129.

Predybaylo, E., G. L. Stenchikov, A. T. Wittenberg and F. Zeng (2017). 'Impacts of a Pinatubo-Size Volcanic Eruption on ENSO'. *J. Geophys. Res.*, 122, pp. 925–947. DOI: 10.1002/2016JD025796.

Preine, J., J. Karstens, C. Hübscher, T. Druitt, S. Kutterolf, P. Nomikou, M. Manga, R. Gertisser, K. Pank, S. Beethe et al. (2024). 'Hazardous explosive eruptions of a recharging multi-cyclic island arc caldera'. *Nat. Geosci.*, 17, pp. 323–331. DOI: 10.1038/s41561-024-01392-7.

Pringle, K. J., H. Tost, S. Message, B. Steil, D. Giannadaki, A. Nenes, C. Fountoukis, P. Stier, E. Vignati and J. Lelieveld (2010). 'Description and evaluation of GMXe: a new aerosol submodel for global simulations (v1)'. *Geosci. Model Dev.*, 3, pp. 391–412. DOI: 10.5194/gmd-3-391-2010.

Proud, S. R., A. T. Prata and S. Schmauß (2022). 'The January 2022 eruption of Hunga Tonga-Hunga Ha'apai volcano reached the mesosphere'. *Science*, 378, pp. 554–557. DOI: 10.1126/science.abo4076.

Pueschel, R. F. (1996). 'Stratospheric Aerosols: Formation, Properties, Effects'. *J. Aerosol Sci.*, 27, pp. 383–402. DOI: 10.1016/0021-8502(95)00557-9.

Purkis, S. J., S. N. Ward, N. M. Fitzpatrick, J. B. Garvin, D. Slayback, S. J. Cronin, M. Palaseanu-Lovejoy and A. Dempsey (2023). 'The 2022 Hunga-Tonga megatsunami: Near-field simulation of a once-in-a-century event'. *Sci. Adv.*, 9, eadf5493. DOI: 10.1126/sciadv.adf5493.

Putman, W. M. and S.-J. Lin (2007). 'Finite-volume transport on various cubed-sphere grids'. *J. Comput. Phys.*, 227, pp. 55–78. DOI: 10.1016/j.jcp.2007.07.022.

Pyle, D. M. (2015). 'Sizes of Volcanic Eruptions'. *The Encyclopedia of Volcanoes*. Ed. by H. Sigurdsson et al. 2nd. Elsevier, pp. 257–264. DOI: 10.1016/b978-0-12-385938-9.00013-4.

Quaglia, I., V. Aquila and Z. Zhuo (2025a). *HTHHMOC zonal average H2O anomaly in June 2022 from multi-model data*. Zenodo. DOI: 10.5281/zenodo.14963276.

Quaglia, I., D. Visioni, E. M. Bednarz, Y. Zhu, G. Stenchikov, V. Aquila, C.-C. Liu, G. W. Mann, Y. Peng, T. Sekiya et al. (2025b). 'Multi-model analysis of the radiative impacts of the 2022 Hunga eruption indicates a significant cooling contribution from the volcanic plume'. *EGUsphere [preprint]*, 2025, pp. 1–35. DOI: 10.5194/egusphere-2025-3769.

Quaglia, I., C. Timmreck, U. Niemeier, D. Visioni, G. Pitari, C. Brodowsky, C. Brühl, S. S. Dhomse, H. Franke, A. Laakso et al. (2023). 'Interactive stratospheric aerosol models' response to different amounts and altitudes of SO_2 injection during the 1991 Pinatubo eruption'. *Atmos. Chem. Phys.*, 23, pp. 921–948. DOI: 10.5194/acp-23-921-2023.

Rajesh, P. K., C. C. H. Lin, J. T. Lin, C. Y. Lin, J. Y. Liu, T. Matsuo, C. Y. Huang, M. Y. Chou, J. Yue, M. Nishioka et al. (2022). 'Extreme poleward expanding super plasma bubbles over the Asia–Pacific region triggered by the Tonga volcano eruption during the recovery phase of a geomagnetic storm'. *Geophys. Res. Lett.*, 49, e2022GL099798. DOI: 10.1029/2022GL099798.

Ramaswamy, V., W. Collins, J. Haywood, J. Lean, N. Mahowald, G. Myhre and T. Storelvmo (2019). 'Radiative forcing of climate: The historical evolution of the radiative forcing concept, the forcing agents and their quantification, and applications'. *Meteor. Mon.*, 59, pp. 14.1–14.101. DOI: 10.1175/AMSMONOGRAPHS-D-19-0001.1.

Ramaswamy, V. e. a. (2006). 'Anthropogenic and natural influences in the evolution of lower stratospheric cooling'. *Science*, 311, pp. 1138–1141. DOI: 10.1126/science.1122587.

Rampino, M. R. and S. Self (1982). 'Historic Eruptions of Tambora (1815), Krakatau (1883), and Agung (1963), Their Stratospheric Aerosols, and Climatic Impact'. *Quat. Res.*, 18, pp. 127–143. DOI: 10.1016/0033-5894(82)90065-5.

Randel, W. J. and P. A. Newman (1998). 'The stratosphere in the Southern Hemisphere'. *Meteorol. South. Hemisphere*. Springer, pp. 243–282. DOI: 10.1007/978-1-935704-10-2_9.

Randel, W. J., B. R. Johnston, J. J. Braun, S. Sokolovskiy, H. Vömel, A. Podglajen and B. Legras (2023). 'Stratospheric Water Vapor from the Hunga Tonga–Hunga Ha'apai Volcanic Eruption Deduced from COSMIC-2 Radio Occultation'. *Remote Sens.*, 15, 2167, p. 2167. DOI: 10.3390/rs15082167.

Randel, W. J., A. K. Smith, F. Wu, C.-Z. Zou and H. Qian (2016). 'Stratospheric Temperature Trends over 1979–2015 Derived from Combined SSU, MLS, and SABER Satellite Observations'. *J. Climate*, 29, pp. 4843–4859. DOI: 10.1175/jcli-d-15-0629.1.

Randel, W. J., X. Wang, J. Starr, R. R. Garcia and D. Kinnison (2024). 'Long-Term Temperature Impacts of the Hunga Volcanic Eruption in the Stratosphere and Above'. *Geophys. Res. Lett.*, 51. DOI: 10.1029/2024gl111500.

Randel, W. J., F. Wu, S. J. Oltmans, K. Rosenlof and G. E. Nedoluha (2004). 'Interannual Changes of Stratospheric Water Vapor and Correlations with Tropical Tropopause Temperatures'. *J. Atmos. Res.*, 61, pp. 2133–2148. DOI: 10.1175/1520-0469(2004)061<2133:icoswv>2.0.co;2.

Ravanelli, M., E. Astafyeva, E. Munaibari, L. Rolland and T. D. Mikesell (2023). 'Ocean–ionosphere disturbances due to the 15 January 2022 Hunga Tonga–Hunga Ha'apai eruption'. *Geophys. Res. Lett.*, 50, e2022GL101465. DOI: 10.1029/2022GL101465.

Read, W. G., L. Froidevaux and J. W. Waters (1993). 'Microwave limb sounder measurement of stratospheric SO_2 from the Mt. Pinatubo Volcano'. *Geophys. Res. Lett.*, 20, pp. 1299–1302. DOI: 10.1029/93GL00831.

Reinecker, M., M. Suarez, R. Todling, J. Bacmeister, L. Takacs and H. Liu (2008). *The GEOS-5 Data Assimilation System: Documentation of Versions 5.0.1, 5.1.0.* Tech. rep. NASA Technical Report TM-2007-104606.

Reinisch, B. W. (1987). 'New Techniques in Ground-Based Ionospheric Sounding and Studies'. *Radio Sci.*, 21, pp. 331–341. DOI: 10.1029/RS021i003p00331.

Remer, L. A. and Y. J. Kaufman (2006). 'Aerosol direct radiative effect at the top of the atmosphere over cloud free ocean derived from four years of MODIS data'. *Atmos. Chem. Phys.*, 6, pp. 237–253. DOI: 10.5194/acp-6-237-2006.

Remsberg, E. E., B. T. Marshall, M. Garcia-Comas, D. Krueger, G. S. Lingenfelser, J. Martin-Torres, M. G. Mlynczak, J. M. Russell III, A. K. Smith, Y. Zhao et al. (2008). 'Assessment of the quality of the Version 1.07 temperature-versus-pressure profiles of the middle atmosphere from TIMED/SABER'. *J. Geophys. Res.*, 113. DOI: 10.1029/2008JD010013.

Rémy, S., Z. Kipling, V. Huijnen, J. Flemming, P. Nabat, M. Michou, M. Ades, R. Engelen and V.-H. Peuch (2022). 'Description and evaluation of the tropospheric aerosol scheme in the Integrated Forecasting System (IFS-AER, cycle 47R1) of ECMWF'. *Geosci. Model Dev.*, 15, pp. 4881–4912. DOI: 10.5194/gmd-15-4881-2022.

Renard, J.-B., F. Dulac, G. Berthet, T. Lurton, D. Vignelles, F. Jégou, T. Tonnelier, M. Jeannot, B. Couté, R. Akiki et al. (2016). 'LOAC: a small aerosol optical counter/sizer for ground-based and balloon measurements of the size distribution and nature of atmospheric particles – Part 1: Principle of measurements and instrument evaluation'. *Atmos. Meas. Tech.*, 9, pp. 1721–1742. DOI: 10.5194/amt-9-1721-2016.

Revell, L. E., A. Stenke, B. Luo, S. Kremser, E. Rozanov, T. Sukhodolov and T. Peter (2017). 'Impacts of Mt Pinatubo volcanic aerosol on the tropical stratosphere in chemistry–climate model simulations using CCMI and CMIP6 stratospheric aerosol data'. *Atmos. Chem. Phys.*, 17, pp. 13139–13150. DOI: 10.5194/acp-17-13139-2017.

Reynolds, R. W., N. A. Rayner, T. M. Smith, D. C. Stokes and W. Wang (2002). 'An Improved In Situ and Satellite SST Analysis for Climate'. *J. Climate*, 15, pp. 1609–1625. DOI: 10.1175/1520-0442(2002)015<1609:AIISAS>2.0.CO;2.

Rideout, W. and A. Coster (2006). 'Automated GPS processing for global total electron content data'. *GPS Solutions*, 10, pp. 219–228. DOI: 10.1007/s10291-006-0029-5.

Rieger, L. A., A. E. Bourassa and D. A. Degenstein (2014). 'Stratospheric aerosol particle size information in Odin-OSIRIS limb scatter spectra'. *Atmos. Meas. Tech.*, 7, pp. 507–522. DOI: 10.5194/amt-7-507-2014.

Rieger, L. A., W. J. Randel, A. E. Bourassa and S. Solomon (2021). 'Stratospheric temperature and

ozone anomalies associated with the 2020 Australian New Year fires'. *Geophys. Res. Lett.*, 48, e2021GL095898. DOI: 10.1029/2021gl095898.

Rieger, L. A., D. J. Zawada, A. E. Bourassa and D. A. Degenstein (2019). 'A Multiwavelength Retrieval Approach for Improved OSIRIS Aerosol Extinction Retrievals'. *J. Geophys. Res.*, 124, pp. 7286–7307. DOI: 10.1029/2018jd029897.

Riese, M., F. Ploeger, A. Rap, B. Vogel, P. Konopka, M. Dameris and P. Forster (2012). 'Impact of uncertainties in atmospheric mixing on simulated UTLS composition and related radiative effects'. *J. Geophys. Res.*, 117, D16305. DOI: 10.1029/2012JD017751.

Ringler, A. T., R. E. Anthony, R. C. Aster, T. Taira, B. R. Shiro, D. C. Wilson, S. De Angelis, C. Ebeling, M. Haney, R. S. Matoza et al. (2023). 'The global seismographic network reveals atmospherically coupled normal modes excited by the 2022 Hunga Tonga eruption'. *Geophys. J. Int.*, 232, pp. 2160–2174. DOI: 10.1093/gji/ggac284.

Robock, A., C. M. Ammann, L. Oman, D. Shindell, S. Levis and G. Stenchikov (2009). 'Did the Toba volcanic eruption of 74 ka B.P. produce widespread glaciation?' *J. Geophys. Res.*, 114, D10107. DOI: 10.1029/2008JD011652.

Robock, A. (2000). 'Volcanic eruptions and climate'. *Rev. Geophys.*, 38, pp. 191–219. DOI: 10.1029/1998RG000054.

Roeckner, E., G. Bäuml, L. Bonaventura, R. Brokopf, M. Esch, M. Giorgetta, S. Hagemann, I. Kirchner, L. Kornblueh, E. Manzini et al. (2003). *The atmospheric general circulation model ECHAM 5. PART I: Model description*. Technical Report 349. https://pure.mpg.de/rest/items/item_995269_2/component/file_995268/content. Last access: 16 September 2024. Hamburg: Max-Planck-Institut für Meteorologie.

Romeo, F., L. Mereu and S. Scollo (2025). 'Ash and Ice Aggregation in Satellite Retrieval: The 15 January 2022 Hunga Tonga-Hunga Ha'apai Hydromagmatic Eruption'. *J. Geophys. Res.*, 130, e2024JD041196. DOI: 10.1029/2024JD041196.

Rose, W. I., D. J. Delene, D. J. Schneider, G. J. S. Bluth, A. J. Krueger, I. Sprod, C. McKee, H. L. Davies and G. G. J. Ernst (1995). 'Ice in the 1994 Rabaul eruption cloud: implications for volcano hazard and atmospheric effects'. *Nature*, 375, pp. 477–479. DOI: 10.1038/375477a0.

Rosen, J. M. (1964). 'The vertical distribution of dust to 30 km'. *J. Geophys. Res.*, 69, pp. 4673–4676. DOI: 10.1029/JZ069i021p04673.

Rosen, J. M. and D. J. Hofmann (1977). 'Balloon-borne measurements of condensation nuclei'. *J. Appl. Meteorol.*, 16, pp. 56–62. DOI: 10.1175/1520-0450(1977)016<0056:BMOCN>2.0.CO;2.

Rosen, J. M., D. J. Hofmann and J. W. Harder (1988). 'Aerosol measurements in the winter/spring Antarctic stratosphere. 2. Impact on Polar Stratospheric Cloud theories'. *J. Geophys. Res.*, 93, pp. 677–686. DOI: 10.1029/JD093iD01p00677.

Rowell, C. R., A. M. Jellinek, S. Hajimirza and T. J. Aubry (2022). 'External Surface Water Influence on Explosive Eruption Dynamics, With Implications for Stratospheric Sulfur Delivery and Volcano-Climate Feedback'. *Front. Earth Sci.*, 10, 788294. DOI: 10.3389/feart.2022.788294.

Rozanov, A., C. Pohl, C. Arosio, A. Bourassa, K. Bramstedt, E. Malinina, L. Rieger and J. P. Burrows (2024). 'Retrieval of stratospheric aerosol extinction coefficients from sun-normalized Ozone Mapper and Profiler Suite Limb Profiler (OMPS-LP) measurements'. *Atmos. Meas. Tech.*, 17, pp. 6677–6695. DOI: 10.5194/amt-17-6677-2024.

Rozanov, E. V., V. A. Zubov, M. E. Schlesinger, F. Yang and N. G. Andronova (1999). 'The UIUC three-dimensional stratospheric chemical transport model: Description and evaluation of the simulated source gases and ozone'. *J. Geophys. Res.*, 104, pp. 11755–11781. DOI: 10.1029/1999jd900138.

Russell, J. M., M. G. Mlynczak, L. L. Gordley, J. Tansock and R. Esplin (1999). 'Overview of the SABER experiment and preliminary calibration results'. *SPIE Proc.*, 3756, pp. 277–288. DOI: 10.1117/12.366382.

Russell, P. B., J. M. Livingston, E. G. Dutton, R. F. Pueschel, J. A. Reagan, T. E. DeFoor and D. J. Hofmann (1993). 'Pinatubo and pre-Pinatubo optical-depth spectra: Mauna Loa measurements, comparisons, inferred particle size distributions, radiative effects, and relationship to lidar data'. *J. Geophys. Res.*, 98, pp. 22969–22985. DOI: 10.1029/93JD02308.

Russell, P. B., J. M. Livingston, R. F. Pueschel, J. J. Bauman, J. B. Pollack, S. L. Brooks, P. Hamill, L. W. Thomason, L. L. Stowe, T. Deshler et al. (1996). 'Global to microscale evolution of the Pinatubo volcanic aerosol derived from diverse measurements and analyses'. *J. Geophys. Res.*, 101, pp. 18745–18763. DOI: 10.1029/96jd01162.

Ryan, R. A., M. A. Vaughan, S. D. Rodier, J. L. Tackett, J. A. Reagan, R. A. Ferrare, J. W. Hair, J. A. Smith

and B. J. Getzewich (2024). 'Total column optical depths retrieved from CALIPSO lidar ocean surface backscatter'. *Atmos. Meas. Tech.*, 17, pp. 6517–6545. DOI: 10.5194/amt-17-6517-2024.

Sakai, T., O. Uchino, T. Nagai, B. Liley, I. Morino and T. Fujimoto (2016). 'Long-term variation of stratospheric aerosols observed with lidars over Tsukuba, Japan, from 1982 and Lauder, New Zealand, from 1992 to 2015'. *J. Geophys. Res.*, 121, pp. 10, 283–10, 293. DOI: 10.1002/2016JD025132.

Salby, M. L. (1979). 'On the Solution of the Homogeneous Vertical Structure Problem for Long-Period Oscillations'. *J. Atmos. Sci.*, 36, pp. 2350–2359. DOI: 10.1175/1520-0469(1979)036<2350:OTSOTH>2.0.CO;2.

Santee, M. L., A. Lambert, L. Froidevaux, G. L. Manney, M. J. Schwartz, L. F. Millán, N. J. Livesey, W. G. Read, F. Werner and R. A. Fuller (2023). 'Strong Evidence of Heterogeneous Processing on Stratospheric Sulfate Aerosol in the Extrapolar Southern Hemisphere Following the 2022 Hunga Tonga-Hunga Ha'apai Eruption'. *J. Geophys. Res.*, 128, e2023JD039169. DOI: 10.1029/2023jd039169.

Santee, M. L., A. Lambert, G. L. Manney, N. J. Livesey, L. Froidevaux, J. L. Neu, M. J. Schwartz, L. F. Millán, F. Werner, W. G. Read et al. (2022). 'Prolonged and Pervasive Perturbations in the Composition of the Southern Hemisphere Midlatitude Lower Stratosphere From the Australian New Year's Fires'. *Geophys. Res. Lett.*, 49, e2021GL096270. DOI: 10.1029/2021gl096270.

Santee, M. L., G. L. Manney, A. Lambert, L. F. Millán, N. J. Livesey, M. C. Pitts, L. Froidevaux, W. G. Read and R. A. Fuller (2024). 'The Influence of Stratospheric Hydration From the Hunga Eruption on Chemical Processing in the 2023 Antarctic Vortex'. *J. Geophys. Res.*, 129, e2023JD040687. DOI: 10.1029/2023jd040687.

Santer, B. D., T. M. L. Wigley, C. Doutriaux, J. S. Boyle, J. E. Hansen, P. D. Jones and K. E. Taylor (2001). 'Accounting for the effects of volcanoes and ENSO in comparisons of modeled and observed temperature trends'. *J. Geophys. Res.*, 106, pp. 28033–28059. DOI: 10.1029/2000JD000189.

Saunders, R., J. Hocking, E. Turner, P. Rayer, M. Matricardi, A. Geer et al. (2018). 'An update on the RTTOV fast radiative transfer model (currently at version 12)'. *Geosci. Model Dev.*, 11, pp. 2717–2737. DOI: 10.5194/gmd-11-2717-2018.

Savigny, C. von and C. G. Hoffmann (2020). 'Issues related to the retrieval of stratospheric-aerosol particle size information based on optical measurements'. *Atmos. Meas. Tech.*, 13, pp. 1909–1920. DOI: 10.5194/amt-13-1909-2020.

Scaillet, B., J. F. Luhr and M. R. Carroll (2003). 'Petrological and Volcanological Constraints on Volcanic Sulfur Emissions to the Atmosphere'. *Volcanism and the Earth's Atmosphere*. Vol. 139. Geophysical Monograph. American Geophysical Union, pp. 11–40. DOI: 10.1029/139GM02.

Schallock, J., C. Brühl, C. Bingen, M. Höpfner, L. Rieger and J. Lelieveld (2023). 'Reconstructing volcanic radiative forcing since 1990, using a comprehensive emission inventory and spatially resolved sulfur injections from satellite data in a chemistry-climate model'. *Atmos. Chem. Phys.*, 23, pp. 1169–1207. DOI: 10.5194/acp-23-1169-2023.

Schodlok, M. P., M. Tomczak and N. White (1997). 'Deep sections through the South Australian Basin and across the Australian-Antarctic Discordance'. *Geophys. Res. Lett.*, 24. DOI inferred from journal issue, pp. 2785–2788. DOI: 10.1029/97GL01929.

Schoeberl, M. R., M. Toohey, Y. Wang and R. Ueyama (2025). 'Stratospheric Injection Lifetimes'. *J. Geophys. Res.*, 130, e2025JD043928. DOI: 10.1029/2025jd043928.

Schoeberl, M. R., Y. Wang, G. Taha, D. J. Zawada, R. Ueyama and A. Dessler (2024). 'Evolution of the Climate Forcing During the Two Years After the Hunga Tonga-Hunga Ha'apai Eruption'. *J. Geophys. Res.*, 129, e2024JD041296. DOI: 10.1029/2024jd041296.

Schoeberl, M. R., Y. Wang, R. Ueyama, A. Dessler, G. Taha and W. Yu (2023a). 'The Estimated Climate Impact of the Hunga Tonga-Hunga Ha'apai Eruption Plume'. *Geophys. Res. Lett.*, 50, e2023GL104634. DOI: 10.1029/2023gl104634.

Schoeberl, M. R., Y. Wang, R. Ueyama, G. Taha, E. Jensen and W. Yu (2022). 'Analysis and Impact of the Hunga Tonga-Hunga Ha'apai Stratospheric Water Vapor Plume'. *Geophys. Res. Lett.*, 49, e2022GL100248. DOI: 10.1029/2022gl100248.

Schoeberl, M. R., Y. Wang, R. Ueyama, G. Taha and W. Yu (2023b). 'The Cross Equatorial Transport of the Hunga Tonga-Hunga Ha'apai Eruption Plume'. *Geophys. Res. Lett.*, 50, e2022GL102443. DOI: 10.1029/2022gl102443.

Schulz, M., C. Textor, S. Kinne, Y. Balkanski, S. Bauer, T. Berntsen, T. Berglen, O. Boucher, F. Dentener, S. Guibert et al. (2006). 'Radiative forcing by aerosols as derived from the AeroCom present-day and

pre-industrial simulations'. *Atmos. Chem. Phys.*, 6, pp. 5225–5246. DOI: 10.5194/acp-6-5225-2006.

Scinocca, J. F. (2003). 'An Accurate Spectral Non-Orographic Gravity Wave Parameterization for General Circulation Models'. *J. Atmos. Sci.*, 60, pp. 667–682. DOI: 10.1175/1520-0469(2003)060<0667:AASNGW>2.0.CO;2.

Scinocca, J. F., N. A. McFarlane, M. Lazare, J. Li and D. Plummer (2008). 'Technical Note: The CCCma third generation AGCM and its extension into the middle atmosphere'. *Atmos. Chem. Phys.*, 8, pp. 7055–7074. DOI: 10.5194/acp-8-7055-2008.

Scott, W. E. et al. (1996). 'Pyroclastic Flows of the June 15, 1991, Climactic Eruption of Mount Pinatubo'. *Fire and Mud: Eruptions and Lahars of Mount Pinatubo, Philippines*. Ed. by C. Newhall and R. Punongbayan. https://pubs.usgs.gov/pinatubo/index.html. Seattle, USA: University of Washington Press.

Seabrook, S., K. Mackay, S. J. Watson, M. A. Clare, J. E. Hunt, I. A. Yeo, E. M. Lane, M. R. Clark, R. Wysoczanski, A. A. Rowden et al. (2023). 'Volcaniclastic density currents explain widespread and diverse seafloor impacts of the 2022 Hunga Volcano eruption'. *Nat. Commun.*, 14, 7881. DOI: 10.1038/s41467-023-43607-2.

Seddon, J., A. Stephens, M. S. Mizielinski, P. L. Vidale and M. J. Roberts (2023). 'Technology to aid the analysis of large-volume multi-institute climate model output at a central analysis facility (PRIMAVERA Data Management Tool V2.10)'. *Geosci. Model Dev.*, 16, pp. 6689–6700. DOI: 10.5194/gmd-16-6689-2023.

Sekiya, T., K. Sudo and T. Nagai (2016). 'Evolution of stratospheric sulfate aerosol from the 1991 Pinatubo eruption: Roles of aerosol microphysical processes'. *J. Geophys. Res.*, 121, pp. 2911–2938. DOI: 10.1002/2015JD024313.

Self, S. (1992). 'Krakatau revisited: the course of events and interpretation of the 1883 eruption'. *GeoJournal*, 28, pp. 109–121. DOI: 10.1007/BF00177223.

Self, S. and M. R. Rampino (1981). 'The 1883 eruption of Krakatau'. *Nature*, 294, pp. 699–704. DOI: 10.1038/294699a0.

Self, S. and R. S. J. Sparks (1978). 'Characteristics of widespread pyroclastic deposits formed by the interaction of silicic magma and water'. *Bull. Volcanol.*, 41, pp. 196–212. DOI: 10.1007/bf02597223.

Sellar, A. A., C. G. Jones, J. P. Mulcahy, Y. Tang, A. Yool, A. Wiltshire, F. M. O'Connor, M. Stringer, R. Hill, J. Palmieri et al. (2019). 'UKESM1: Description and Evaluation of the U.K. Earth System Model'. *J. Adv. Model. Earth Syst.*, 11, pp. 4513–4558. DOI: 10.1029/2019MS001739.

Sellar, A. A., J. Walton, C. G. Jones, R. Wood, N. L. Abraham, M. Andrejczuk, M. B. Andrews, T. Andrews, A. T. Archibald, L. de Mora et al. (2020). 'Implementation of U.K. Earth System Models for CMIP6'. *J. Adv. Model. Earth Syst.*, 12, e2019MS001946. DOI: 10.1029/2019MS001946.

Sellitto, P., H. Guermazi, E. Carboni, R. Siddans and M. Burton (2019). 'Unified quantitative observation of coexisting volcanic sulfur dioxide and sulfate aerosols using ground-based Fourier transform infrared spectroscopy'. *Atmos. Meas. Tech.*, 12, pp. 5381–5389. DOI: 10.5194/amt-12-5381-2019.

Sellitto, P. and B. Legras (2016). 'Sensitivity of thermal infrared nadir instruments to the chemical and microphysical properties of UTLS secondary sulfate aerosols'. *Atmos. Meas. Tech.*, 9, pp. 115–132. DOI: 10.5194/amt-9-115-2016.

Sellitto, P., A. Podglajen, R. Belhadji, M. Boichu, E. Carboni, J. Cuesta, C. Duchamp, C. Kloss, R. Siddans, N. Bègue et al. (2022a). 'The unexpected radiative impact of the Hunga Tonga eruption of 15th January 2022'. *Commun. Earth Environ.*, 3, 288. DOI: 10.1038/s43247-022-00618-z.

Sellitto, P., R. Siddans, R. Belhadji, E. Carboni, B. Legras, A. Podglajen and et al. (2024). 'Observing the SO_2 and sulfate aerosol plumes from the 2022 Hunga eruption with the Infrared Atmospheric Sounding Interferometer (IASI)'. *Geophys. Res. Lett.*, 51, e2023GL105565. DOI: 10.1029/2023GL105565.

Sellitto, P., R. Belhadji, C. Kloss and B. Legras (2022b). 'Radiative impacts of the Australian bushfires 2019–2020 – Part 1: Large-scale radiative forcing'. *Atmos. Chem. Phys.*, 22, pp. 9299–9311. DOI: 10.5194/acp-22-9299-2022.

Sepúlveda, I., M. Carvajal and D. C. Agnew (2023). 'Global Winds Shape Planetary-Scale Lamb Waves'. *Geophys. Res. Lett.*, 50, e2023GL106097. DOI: 10.1029/2023GL106097.

Shaikh, M. M., R. Notarpietro and B. Nava (2014). 'The impact of spherical symmetry assumption on radio occultation data inversion in the ionosphere: An assessment study'. *Adv. Space Res.*, 53, pp. 599–608. DOI: 10.1016/j.asr.2013.10.025.

Shallcross, S. E. (2020). 'The role of volcanic ash in the global dispersion of the aerosol cloud from major tropical eruptions'. https://etheses.whiteros e.ac.uk/id/eprint/28125/1/Sarah_Shallcr

oss_PhD_thesis.pdf. PhD thesis. University of Leeds.

Sherwood, S. C., S. Bony, O. Boucher, C. Bretherton, P. M. Forster, J. M. Gregory and B. Stevens (2015). 'Adjustments in the forcing-feedback framework for understanding climate change'. *Bull. Am. Meteorol. Soc.*, 96, pp. 217–228. DOI: 10.1175/bams-d-13-00167.1.

Shinagawa, H. and Y. Miyoshi (2024). 'Simulation study of atmosphere–ionosphere variations driven by the eruption of Hunga Tonga–Hunga Ha'apai on 15 January 2022'. *Earth Planets Space*, 76, 15. DOI: 10.1186/s40623-024-01960-6.

Shinbori, A., Y. Otsuka, T. Sori, M. Nishioka, S. Perwitasari, T. Tsuda et al. (2022). 'Electromagnetic conjugacy of ionospheric disturbances after the 2022 Hunga Tonga–Hunga Ha'apai volcanic eruption as seen in GNSS–TEC and SuperDARN Hokkaido pair of radars observations'. *Earth Planets Space*, 74, 106. DOI: 10.1186/s40623-022-01665-8.

Shinbori, A., T. Sori, Y. Otsuka, M. Nishioka, S. Perwitasari, T. Tsuda et al. (2023). 'Generation of equatorial plasma bubble after the 2022 Tonga volcanic eruption'. *Sci. Rep.*, 13, 6450. DOI: 10.1038/s41598-023-33603-3.

Shindell, D. T., G. A. Schmidt, M. Mann and G. Faluvegi (2004). 'Dynamic winter climate response to large tropical volcanic eruptions since 1600'. *J. Geophys. Res.*, 109, D05104. DOI: 10.1029/2003JD004151.

Shindell, D. T., G. A. Schmidt, R. L. Miller and M. Mann (2003). 'Volcanic and solar forcing of climate change during the preindustrial era'. *J. Climate*, 16, pp. 4094–4107. DOI: 10.1175/1520-0442(2003)016<4094:vasfoc>2.0.co;2.

Sicard, M., A. Baron, M. Ranaivombola, D. Gantois, T. Millet, P. Sellitto, N. Bègue, H. Bencherif, G. Payen, N. Marquestaut et al. (2025). 'Radiative impact of the Hunga stratospheric volcanic plume: role of aerosols and water vapor over Réunion Island (21° S, 55° E)'. *Atmos. Chem. Phys.*, 25, pp. 367–381. DOI: 10.5194/acp-25-367-2025.

Siddans, R. (2019). *Water Vapour Climate Change Initiative (WV_cci) – Phase One, Deliverable 2.2; Version 1.0, 27 March 2019*. Technical Report. https://climate.esa.int/documents/1337/Water_Vapour_CCI_D2.2_ATBD_Part2-IMS_L2_product_v1.0.pdf. European Space Agency (ESA) / ECSAT.

Siddans, R. (2023). *Water Vapour Climate Change Initiative (WV_cci) – Phase Two, ATBD Part 2 – IMS L2 Product, Version 2.0, 21 November 2023*. Technical Report CCIWV.REP.005, D2.2. https://climate.esa.int/media/documents/Water_Vapour_CCI_D2.2_ATBD_Part2-IMS_L2_product_v2.0.pdf. European Space Agency (ESA) / ECSAT.

Sigl, M., M. Winstrup, J. R. McConnell, K. C. Welten, G. Plunkett, F. Ludlow, U. Büntgen, M. Caffee, N. Chellman, D. Dahl-Jensen et al. (2015). 'Timing and climate forcing of volcanic eruptions for the past 2,500 years'. *Nature*, 523, pp. 543–549. DOI: 10.1038/nature14565.

Sigurdsson, H., S. Carey, C. W. Mandeville and S. Bronto (1991). 'Pyroclastic Flows of the 1883 Krakatau Eruption'. *Eos*, 72. DOI: 10.1029/90EO00286.

Simmons, A., C. Soci, J. Nicolas, B. Bell, P. Berrisford, R. Dragani, J. Flemming, L. Haimberger, S. Healy, H. Hersbach et al. (2020). 'Global stratospheric temperature bias and other stratospheric aspects of ERA5 and ERA5.1'. *ECMWF Technical Memoranda*, DOI: 10.21957/rcxqfmg0.

Simpson, I. R., T. G. Shepherd and M. Sigmond (2011). 'Dynamics of the lower stratospheric circulation response to ENSO'. *J. Atmos. Sci.*, 68, pp. 2537–2556. DOI: 10.1175/jas-d-11-05.1.

Sioris, C. E., A. Malo, C. A. McLinden and R. D'Amours (2016). 'Direct injection of water vapor into the stratosphere by volcanic eruptions'. *Geophys. Res. Lett.*, 43, pp. 7694–7700. DOI: 10.1002/2016GL069918.

Smale, D., M. P. Chipperfield, R. Querel, G. E. Nedoluha, U. Frieß, J. Robinson, S. Nichol, S. Heddell, W. Feng, R. M. Gomez et al. (2025). 'The impact of the Hunga Tonga-Hunga Ha'apai volcanic eruption on the 2023 Antarctic Ozone hole, as observed from Arrival Heights, Antarctica'. *J. Atmos. Chem.*, 82. DOI: 10.1007/s10874-025-09478-1.

Smart, D. (2022). 'The first hour of the paroxysmal phase of the 2022 Hunga Tonga–Hunga Ha'apai volcanic eruption as seen by a geostationary meteorological satellite'. *Weather*, 77, pp. 81–82. DOI: 10.1002/wea.4173.

Smith, C. J., R. J. Kramer, G. Myhre, K. Alterskjær, W. Collins, A. Sima, O. Boucher, J.-L. Dufresne, P. Nabat and M. Michou (2020). 'Effective radiative forcing and adjustments in CMIP6 models'. *Atmos. Chem. Phys.*, 20, pp. 9591–9618. DOI: 10.5194/acp-20-9591-2020.

Solomon, S., J. S. Daniel, R. R. Neely, J.-P. Vernier, E. G. Dutton and L. W. Thomason (2011). 'The Persistently Variable "Background" Stratospheric Aerosol

Layer and Global Climate Change'. *Science*, 333, pp. 866–870. DOI: 10.1126/science.1206027.

Solomon, S. (1999). 'Stratospheric ozone depletion: A review of concepts and history'. *Rev. Geophys.*, 37, pp. 275–316. DOI: 10.1029/1999rg900008.

Solomon, S., K. Dube, K. Stone, P. Yu, D. Kinnison, O. B. Toon, S. E. Strahan, K. H. Rosenlof, R. Portmann, S. Davis et al. (2022). 'On the stratospheric chemistry of midlatitude wildfire smoke'. *Proc. Natl. Acad. Sci.*, 119, e2117325119. DOI: 10.1073/pnas.2117325119.

Solomon, S., K. H. Rosenlof, R. W. Portmann, J. S. Daniel, S. M. Davis, T. J. Sanford and G.-K. Plattner (2010). 'Contributions of Stratospheric Water Vapor to Decadal Changes in the Rate of Global Warming'. *Science*, 327, pp. 1219–1223. DOI: 10.1126/science.1182488.

Solomon, S., K. Stone, P. Yu, D. M. Murphy, D. Kinnison, A. R. Ravishankara and P. Wang (2023). 'Chlorine activation and enhanced ozone depletion induced by wildfire aerosol'. *Nature*, 615, pp. 259–264. DOI: 10.1038/s41586-022-05683-0.

Sonnemann, G. R. and M. Grygalashvyly (2005). 'Solar influence on mesospheric water vapor with impact on NLCs'. *J. Atmos. Solar-Terr. Phys.*, 67, pp. 177–190. DOI: 10.1016/j.jastp.2004.07.026.

Souza, G., J.-P. Vernier, D. Quintão, B. Biazon, F. Lopes, J. Ricardo, A. K. Pandit, R. C. Das, H. Liu, T. N. N. Knepp et al. (2025). 'Sedimentation and growth of volcanic aerosols within the Hunga plume: Insights from unique tropical in situ and satellite measurements'. *ESS Open Archive*, DOI: 10.22541/essoar.174241613.36494891/v1.

SPARC (2006). *Assessment of Stratospheric Aerosol Properties (ASAP)*. Tech. rep. SPARC Report No. 4. https://www.aparc-climate.org/publications/sparc-reports/sparc-report-no-4/. Stratosphere–troposphere Processes and their Role in Climate (SPARC) Project, WCRP.

SPARC (2010). *SPARC CCMVal Report on the Evaluation of Chemistry-Climate Models*. Tech. rep. https://www.aparc-climate.org/publications/sparc-reports/sparc-report-no-5/. SPARC Report No. 5, WCRP-30/2010, WMO/TD-No. 40.

SPARC (2022). *Reanalysis Intercomparison Project (S-RIP) Final Report*. Tech. rep. SPARC Report No. 10, WCRP-6/2021. https://www.aparc-climate.org/sparc-reports/sparc-report-no-10/. SPARC/WCRP.

Sparks, R. S. J. et al. (1997). *Volcanic Plumes (Chapter 8: Submarine volcanism and hydrovolcanism)*. John Wiley & Sons, Inc., p. 557.

Spurr, R. J. D., M. Christi, N. A. Krotkov, W.-E. Choi, S. Carn, C. Li, N. Kramarova, D. Haffner, E.-S. Yang, N. Gorkavyi et al. (2025). 'Solar Backscatter Ultraviolet (BUV) Retrievals of Mid-Stratospheric Aerosols from the 2022 Hunga Eruption'. *EGUsphere [preprint]*, 2025, pp. 1–43. DOI: 10.5194/egusphere-2025-2938.

Stankov, S. M., T. G. W. Verhulst and D. Sapundjiev (2023). 'Automatic Ionospheric Weather Monitoring With DPS-4D Ionosonde and ARTIST-5 Autoscaler: System Performance at a Mid-Latitude Observatory'. *Radio Sci.*, 58, e2022RS007628. DOI: 10.1029/2022RS007628.

Steiner, A. K., F. Ladstädter, W. J. Randel, A. C. Maycock, Q. Fu, C. Claud, H. Gleisner, L. Haimberger, S.-P. Ho and P. Keckhut (2020). 'Observed temperature changes in the troposphere and stratosphere from 1979 to 2018'. *J. Climate*, 33, pp. 8165–8194. DOI: 10.1175/jcli-d-19-0998.1.

Stenchikov, G. (2016). 'The role of volcanic activity in climate and global change'. *Climate Change: Observed Impact on Planet Earth, 2nd Edition*. Ed. by T. Letcher. Elsevier, pp. 419–448.

Stenchikov, G., T. L. Delworth, V. Ramaswamy, R. J. Stouffer, A. Wittenberg and F. Zeng (2009). 'Volcanic signals in oceans'. *J. Geophys. Res.*, 114, D16104. DOI: 10.1029/2008jd011673.

Stenchikov, G., K. Hamilton, A. Robock, V. Ramaswamy and M. D. Schwarzkopf (2004). 'Arctic Oscillation response to the 1991 Pinatubo eruption in the SKYHI GCM with a realistic quasi-biennial oscillation'. *J. Geophys. Res.*, 109, D03112. DOI: 10.1029/2003JD003699.

Stenchikov, G., K. Hamilton, R. J. Stouffer, A. Robock, V. Ramaswamy, B. Santer and H.-F. Graf (2006). 'Arctic oscillation response to volcanic eruptions in the IPCC AR4 climate models'. *J. Geophys. Res.*, 111, D07107. DOI: 10.1029/2005JD006286.

Stenchikov, G., A. Robock, V. Ramaswamy, M. D. Schwarzkopf, K. Hamilton and S. Ramachandran (2002). 'Arctic Oscillation response to the 1991 Mount Pinatubo eruption: effects of volcanic aerosols and ozone depletion'. *J. Geophys. Res.*, 107, 4803. DOI: 10.1029/2002JD002090.

Stenchikov, G., A. Ukhov and S. Osipov (2025). 'Modeling the Radiative Forcing and Atmospheric Temperature Perturbations Caused by the 2022 Hunga Vol-

cano Explosion'. *J. Geophys. Res.*, e2024JD041940. DOI: 10.1029/2024JD041940.

Stenchikov, G., A. Ukhov, S. Osipov, R. Ahmadov, G. Grell, K. Cady-Pereira, E. Mlawer and M. Iacono (2021). 'How does a Pinatubo-size volcanic cloud reach the middle stratosphere?' *J. Geophys. Res.*, 126, e2020JD033829. DOI: 10.1029/2020jd033829.

Stenchikov, G. L., I. Kirchner, A. Robock, H.-F. Graf, J. C. Antuña, R. G. Grainger, A. Lambert and L. Thomason (1998). 'Radiative forcing from the 1991 Mount Pinatubo volcanic eruption'. *J. Geophys. Res.*, 103, pp. 13837–13857. DOI: 10.1029/98jd00693.

Stenke, A., M. Schraner, E. Rozanov, T. Egorova, B. Luo and T. Peter (2013). 'The SOCOL version 3.0 chemistry–climate model: description, evaluation, and implications from an advanced transport algorithm'. *Geosci. Model Dev.*, 6, pp. 1407–1427. DOI: 10.5194/gmd-6-1407-2013.

Stephens, G. L., D. G. Vane, R. J. Boain, G. G. Mace, K. Sassen, Z. Wang, A. J. Illingworth, E. J. O'connor, W. B. Rossow, S. L. Durden et al. (2002). 'The CLOUDSAT mission and the A-train: A new Dimension of Space-Based Observations of Clouds and Precipitation'. *Bull. Am. Meteorol. Soc.*, 83, pp. 1771–1790. DOI: 10.1175/bams-83-12-1771.

Stober, G., A. Liu, A. Kozlovsky, Z. Qiao, W. Krochin, G. Shi, J. Kero, M. Tsutsumi, N. Gulbrandsen, S. Nozawa et al. (2023). 'Identifying gravity waves launched by the Hunga Tonga–Hunga Ha'apai volcanic eruption in mesosphere/lower-thermosphere winds derived from CONDOR and the Nordic Meteor Radar Cluster'. *Ann. Geophys.*, 41, pp. 197–208. DOI: 10.5194/angeo-41-197-2023.

Stober, G., S. L. Vadas, E. Becker, A. Liu, A. Kozlovsky, D. Janches, Z. Qiao, W. Krochin, G. Shi, W. Yi et al. (2024). 'Gravity waves generated by the Hunga Tonga–Hunga Ha'apai volcanic eruption and their global propagation in the mesosphere/lower thermosphere observed by meteor radars and modeled with the High-Altitude general Mechanistic Circulation Model'. *Atmos. Chem. Phys.*, 24, pp. 4851–4873. DOI: 10.5194/acp-24-4851-2024.

Stocker, M., A. K. Steiner, F. Ladstädter, U. Foelsche and W. J. Randel (2024). 'Strong persistent cooling of the stratosphere after the Hunga eruption'. *Commun. Earth Environ.*, 5, 450. DOI: 10.1038/s43247-024-01620-3.

Stone, K. A., S. Solomon, D. E. Kinnison, M. C. Pitts, L. R. Poole, M. J. Mills, A. Schmidt, R. R. Neely, D. Ivy, M. J. Schwartz et al. (2017). 'Observing the impact of Calbuco volcanic aerosols on south polar ozone depletion in 2015'. *J. Geophys. Res.*, 122, pp. 11862–11879. DOI: 10.1002/2017JD026987.

Strahan, S. E., B. N. Duncan and P. Hoor (2007). 'Observationally derived transport diagnostics for the lowermost stratosphere and their application to the GMI chemistry and transport model'. *Atmos. Chem. Phys.*, 7, pp. 2435–2445. DOI: 10.5194/acp-7-2435-2007.

Strahan, S. E., D. Smale, S. Solomon, G. Taha, M. R. Damon, S. D. Steenrod, N. Jones, B. Liley, R. Querel and J. Robinson (2022). 'Unexpected repartitioning of stratospheric inorganic chlorine after the 2020 Australian wildfires'. *Geophys. Res. Lett.*, 49, e2022GL098290. DOI: 10.1029/2022GL098290.

Sudo, K. and H. Akimoto (2007). 'Global source attribution of tropospheric ozone: Long-range transport from various source regions'. *J. Geophys. Res.*, 112, D12302. DOI: 10.1029/2006JD007992.

Sudo, K., M. Takahashi, J. Kurokawa and H. Akimoto (2002). 'CHASER: A global chemical model of the troposphere 1. Model description'. *J. Geophys. Res.*, 107, 4339. DOI: 10.1029/2001JD001113.

Sukhodolov, T., T. Egorova, A. Stenke, W. T. Ball, C. Brodowsky, G. Chiodo, A. Feinberg, M. Friedel, A. Karagodin-Doyennel, T. Peter et al. (2021). 'Atmosphere ocean aerosol chemistry climate model SOCOLv4.0: description and evaluation'. *Geosci. Model Dev.*, 14, pp. 5525–5560. DOI: 10.5194/gmd-14-5525-2021.

Swingedouw, D., J. Mignot, P. Ortega, M. Khodri, M. Menegoz, C. Cassou and V. Hanquiez (2017). 'Impact of explosive volcanic eruptions on the main climate variability modes'. *Global Planet. Change*, 150, pp. 24–45. DOI: 10.1016/j.gloplacha.2017.01.006.

Symons, G. J. et al., eds. (1888). *The Eruption of Krakatoa and Subsequent Phenomena: report of the Krakatoa committee of the Royal Society*. UK: Trübner & Company, p. 494.

Syndergaard, S., W. S. Schreiner, C. Rocken, D. C. Hunt and K. F. Dymond (2006). 'Preparing for COSMIC: Inversion and Analysis of Ionospheric Data Products'. *Atmosphere and Climate: Studies by Occultation Methods*. Ed. by U. Foelsche, G. Kirchengast and A. Steiner. Berlin, Heidelberg: Springer Berlin Heidelberg, pp. 137–146. DOI: 10.1007/3-540-34121-8_12.

Tackett, J. L., J. Kar, M. A. Vaughan, B. J. Getzewich, M.-H. Kim, J.-P. Vernier, A. H. Omar, B. E. Magill, M. C. Pitts and D. M. Winker (2023). 'The CALIPSO version 4.5 stratospheric aerosol subtyp-

ing algorithm'. *Atmos. Meas. Tech.*, 16, pp. 745–768. DOI: 10.5194/amt-16-745-2023.

Taha, G., R. Loughman, P. R. Colarco, T. Zhu, L. W. Thomason and G. Jaross (2022). 'Tracking the 2022 Hunga Tonga-Hunga Ha'apai Aerosol Cloud in the Upper and Middle Stratosphere Using Space-Based Observations'. *Geophys. Res. Lett.*, 49, e2022GL100091. DOI: 10.1029/2022gl100091.

Taha, G., R. Loughman, T. Zhu, L. Thomason, J. Kar, L. Rieger and A. Bourassa (2021). 'OMPS LP Version 2.0 multi-wavelength aerosol extinction coefficient retrieval algorithm'. *Atmos. Meas. Tech.*, 14, pp. 1015–1036. DOI: 10.5194/amt-14-1015-2021.

Takahashi, H., C. A. O. B. Figueiredo, D. Barros, C. M. Wrasse, G. A. Giongo, R. H. Honda, L. F. R. Vital, L. C. A. Resende, P. K. Nyassor, T. T. Ayorinde et al. (2023). 'Ionospheric disturbances over South America related to the Tonga volcanic eruption'. *Earth Planets Space*, 75, 92. DOI: 10.1186/s40623-023-01844-1.

Takemura, T., M. Egashira, K. Matsuzawa, H. Ichijo, R. O'ishi and A. Abe-Ouchi (2009). 'A simulation of the global distribution and radiative forcing of soil dust aerosols at the Last Glacial Maximum'. *Atmos. Chem. Phys.*, 9, pp. 3061–3073. DOI: 10.5194/acp-9-3061-2009.

Takemura, T., T. Nakajima, O. Dubovik, B. N. Holben and S. Kinne (2002). 'Single-scattering albedo and radiative forcing of various aerosol species with a global three-dimensional model'. *J. Climate*, 15, pp. 333–352. DOI: 10.1175/1520-0442(2002)015<0333:ssaarf>2.0.co;2.

Takemura, T., T. Nozawa, S. Emori, T. Y. Nakajima and T. Nakajima (2005). 'Simulation of climate response to aerosol direct and indirect effects with aerosol transport-radiation model'. *J. Geophys. Res.*, 110, D02202. DOI: 10.1029/2004JD005029.

Takemura, T., H. Okamoto, Y. Maruyama, A. Numaguti, A. Higurashi and T. Nakajima (2000). 'Global three-dimensional simulation of aerosol optical thickness distribution of various origins'. *J. Geophys. Res.*, 105, pp. 17853–17873. DOI: 10.1029/2000JD900265.

Tarasick, D. W., H. G. J. Smit, A. M. Thompson, G. A. Morris, J. C. Witte, J. Davies, W. Davies, T. Nakano, R. van Malderen, R. Stübi et al. (2021). 'Improving ECC ozonesonde data quality: Assessment of current methods and outstanding issues'. *Earth Space Sci.*, 8, e2019EA000914. DOI: 10.1029/2019EA000914.

Tatebe, H., T. Ogura, T. Nitta, Y. Komuro, K. Ogochi, T. Takemura, K. Sudo, M. Sekiguchi, M. Abe, F. Saito et al. (2019). 'Description and basic evaluation of simulated mean state, internal variability, and climate sensitivity in MIROC6'. *Geosci. Model Dev.*, 12, pp. 2727–2765. DOI: 10.5194/gmd-12-2727-2019.

Taylor, G. I. (1929). 'Waves and tides in the atmosphere'. *Proc. R. Soc. Lond. A*, 126, pp. 169–183. DOI: 10.1098/rspa.1929.0213.

Taylor, I. A., R. G. Grainger, A. T. Prata, S. R. Proud, T. A. Mather and D. M. Pyle (2023). 'A satellite chronology of plumes from the April 2021 eruption of La Soufrière, St Vincent'. *Atmos. Chem. Phys.*, 23, pp. 15209–15234. DOI: 10.5194/acp-23-15209-2023.

Telford, P., P. Braesicke, O. Morgenstern and J. Pyle (2009). 'Reassessment of causes of ozone column variability following the eruption of Mount Pinatubo using a nudged CCM'. *Atmos. Chem. Phys.*, 9, pp. 4251–4260. DOI: 10.5194/acp-9-4251-2009.

Telford, P. J., P. Braesicke, O. Morgenstern and J. A. Pyle (2008). 'Technical Note: Description and assessment of a nudged version of the new dynamics Unified Model'. *Atmos. Chem. Phys.*, 8, pp. 1701–1712. DOI: 10.5194/acp-8-1701-2008.

Tencé, F., J. Jumelet, S. Bekki, S. Khaykin, A. Sarkissian and P. Keckhut (2022). 'Australian Black Summer Smoke Observed by Lidar at the French Antarctic Station Dumont d'Urville'. *J. Geophys. Res.*, 127, e2021JD035349. DOI: 10.1029/2021JD035349.

Textor, C., H.-F. Graf, M. Herzog and J. M. Oberhuber (2003). 'Injection of gases into the stratosphere by explosive volcanic eruptions'. *J. Geophys. Res.*, 108, 2002JD002987. DOI: 10.1029/2002JD002987.

Themens, D. R., B. Reid and S. Elvidge (2022a). 'ARTIST ionogram autoscaling confidence scores: best practices'. *URSI Radio Sci. Lett.*, 4, pp. 1–5. DOI: 10.46620/22-0001.

Themens, D. R., P. T. Jayachandran, R. B. Langley, J. W. MacDougall and M. J. Nicolls (2013). 'Determining receiver biases in GPS-derived total electron content in the auroral oval and polar cap region using ionosonde measurements'. *GPS Solut.*, 17, pp. 357–369. DOI: 10.1007/s10291-012-0284-6.

Themens, D. R., C. Watson, N. Žagar, S. Vasylkevych, S. Elvidge, A. McCaffrey, P. Prikryl, B. Reid, A. Wood and P. T. Jayachandran (2022b). 'Global propagation of ionospheric disturbances associated with the 2022 Tonga volcanic eruption'. *Geophys.*

Res. Lett., 49, e2022GL098158. DOI: 10.1029/2022GL098158.

Theys, N., I. De Smedt, H. Yu, T. Danckaert, J. van Gent, C. Hörmann, T. Wagner, P. Hedelt, H. Bauer, F. Romahn et al. (2017). 'Sulfur dioxide retrievals from TROPOMI onboard Sentinel-5 Precursor: algorithm theoretical basis'. *Atmos. Meas. Tech.*, pp. 119–153. DOI: 10.5194/amt-10-119-2017.

Thomas, E. M., T. S. Stallard, H. Melin, M. N. Chowdhury, L. Moore, J. O'Donoghue, R. E. Johnson, R. Wang, K. L. Knowles, P. I. Tiranti et al. (2024). 'Auroral and Non-Auroral H3+ Ion Winds at Uranus With Keck-NIRSPEC and IRTF-iSHELL'. *Geophys. Res. Lett.*, 52, e2024GL112001. DOI: 10.1029/2024gl112001.

Thomason, L. W., S. P. Burton, B.-P. Luo and T. Peter (2008). 'SAGE II measurements of stratospheric aerosol properties at non-volcanic levels'. *Atmos. Chem. Phys.*, 8, pp. 983–995. DOI: 10.5194/acp-8-983-2008.

Thomason, L. W., N. Ernest, L. Millán, L. Rieger, A. Bourassa, J.-P. Vernier, G. Manney, B. Luo, F. Arfeuille and T. Peter (2018). 'A global space-based stratospheric aerosol climatology: 1979–2016'. *Earth Syst. Sci. Data*, 10, pp. 469–492. DOI: 10.5194/essd-10-469-2018.

Thomason, L. W., L. R. Poole and T. Deshler (1997). 'A global climatology of stratospheric aerosol surface area density deduced from Stratospheric Aerosol and Gas Experiment II measurements: 1984–1994'. *J. Geophys. Res.*, 102, pp. 8967–8976. DOI: 10.1029/96JD02962.

Thomason, L. W., M. Kovilakam, A. Schmidt, C. von Savigny, T. Knepp and L. Rieger (2021). 'Evidence for the predictability of changes in the stratospheric aerosol size following volcanic eruptions of diverse magnitudes using space-based instruments'. *Atmos. Chem. Phys.*, 21, pp. 1143–1158. DOI: 10.5194/acp-21-1143-2021.

Thompson, D. W. and J. M. Wallace (1998). 'The Arctic Oscillation signature in the wintertime geopotential height and temperature fields'. *Geophys. Res. Lett.*, 25, pp. 1297–1300. DOI: 10.1029/98GL00950.

Thompson, D. W. and J. M. Wallace (2000). 'Annular modes in the extratropical circulation. Part I: Month-to-month variability'. *J. Climate*, 13, pp. 1000–1016. DOI: 10.1175/1520-0442(2000)013<1000:amitec>2.0.co;2.

Thurin, J., C. Tape and R. Modrak (2022). 'Multi-Event Explosive Seismic Source for the 2022 Mw 6.3 Hunga Tonga Submarine Volcanic Eruption'. *The Seismic Record*, 2, pp. 217–226. DOI: 10.1785/0320220027.

Tilling, R. I., L. Topinka and D. A. Swanson, eds. (1990). *Eruptions of Mount St. Helens: Past, Present, and Future*. Denver, CO: U.S. Geological Survey. DOI: 10.3133/7000008.

Tilmes, S., M. J. Mills, Y. Zhu, C. G. Bardeen, F. Vitt, P. Yu, D. Fillmore, X. Liu, B. Toon and T. Deshler (2023). 'Description and performance of a sectional aerosol microphysical model in the Community Earth System Model (CESM2)'. *Geosci. Model Dev.*, 16, pp. 6087–6125. DOI: 10.5194/gmd-16-6087-2023.

Timmreck, C. (2012). 'Modeling the climatic effects of significant explosive volcanic eruptions'. *Wiley Interdiscip. Rev. Clim. Change*, 3, pp. 545–564. DOI: 10.1002/wcc.192.

Timmreck, C., G. W. Mann, V. Aquila, R. Hommel, L. A. Lee, A. Schmidt, C. Brühl, S. Carn, M. Chin, S. S. Dhomse et al. (2018). 'The interactive stratospheric aerosol model intercomparison project (ISA-MIP): motivation and experimental design'. *Geosci. Model Dev.*, 11, pp. 2581–2608. DOI: 10.5194/gmd-11-2581-2018.

Todt, M. A., E. Asher, E. Hall, P. Cullis, A. Jordan, K. Xiong, D. F. Hurst and T. Thornberry (2023). 'Baseline Balloon Stratospheric Aerosol Profiles (B2SAP)—Systematic Measurements of Aerosol Number Density and Size'. *J. Geophys. Res.*, 128, e2022JD038041. DOI: 10.1029/2022JD038041.

Toohey, M., Y. Jia, S. Khanal and S. Tegtmeier (2025). 'Stratospheric residence time and the lifetime of volcanic stratospheric aerosols'. *Atmos. Chem. Phys.*, 25, pp. 3821–3839. DOI: 10.5194/acp-25-3821-2025.

Toohey, M. and M. Sigl (2017). 'Volcanic stratospheric sulfur injections and aerosol optical depth from 500 BCE to 1900 CE'. *Earth Syst. Sci. Data*, 9, pp. 809–831. DOI: 10.5194/essd-9-809-2017.

Trepte, C. R. and M. H. Hitchman (1992). 'Tropical stratospheric circulation deduced from satellite aerosol data'. *Nature*, 355, pp. 626–628. DOI: 10.1038/355626a0.

Tritscher, I., M. C. Pitts, L. R. Poole, S. P. Alexander, F. Cairo, M. P. Chipperfield, J.-U. Grooß, M. Höpfner, A. Lambert, B. Luo et al. (2021). 'Polar Stratospheric Clouds: Satellite Observations, Processes, and Role in Ozone Depletion'. *Rev. Geophys.*, 59, e2020RG000702. DOI: 10.1029/2020rg000702.

Tsujino, H., S. Urakawa, H. Nakano, R. J. Small, W. M. Kim, S. G. Yeager, G. Danabasoglu, T. Suzuki, J. L.

Bamber, M. Bentsen et al. (2018). 'JRA-55 based surface dataset for driving ocean–sea-ice models (JRA55-do)'. *Ocean Model.*, 130, pp. 79–139. DOI: 10.1016/j.ocemod.2018.07.002.

Turco, R. P., R. C. Witten and O. B. Toon (1982). 'Stratospheric Aerosols: Observation and Theory'. *Rev. Geophys. Space Phys.*, 20, pp. 233–279. DOI: 10.1029/RG020i002p00233.

Ulvrova, M., R. Paris, P. Nomikou, K. Kelfoun, S. Leibrandt, D. Tappin and F. McCoy (2016). 'Source of the tsunami generated by the 1650 AD eruption of Kolumbo submarine volcano (Aegean Sea, Greece)'. *J. Volcanol. Geotherm. Res.*, 321, pp. 125–139. DOI: 10.1016/j.jvolgeores.2016.04.034.

Vadas, S. L., E. Becker, C. Figueiredo, K. Bossert, B. J. Harding and L. C. Gasque (2023a). 'Primary and secondary gravity waves and large-scale wind changes generated by the Tonga volcanic eruption on 15 January 2022: Modeling and comparison with ICON-MIGHTI winds'. *J. Geophys. Res.*, 128, e2022JA031138. DOI: 10.1029/2022JA031138.

Vadas, S. L., C. Figueiredo, E. Becker, J. D. Huba, D. R. Themens, N. P. Hindley, S. Mrak, I. Galkin and K. Bossert (2023b). 'Traveling ionospheric disturbances induced by the secondary gravity waves from the Tonga eruption on 15 January 2022: Modeling with MESORAC–HIAMCM–SAMI3 and comparison with GPS/TEC and ionosonde data'. *J. Geophys. Res.*, 128, e2023JA031408. DOI: 10.1029/2023JA031408.

Valentine, G. (1993). 'Role of magma-water interaction in very large explosive eruptions'. *International Seminar on Physics of Vapor Explosion (Proceedings)*. https://www.osti.gov/biblio/144909. Tomakomai, Hokkaido, Japan, pp. 210–216.

Van Eaton, A. R., M. Herzog, C. J. N. Wilson and J. McGregor (2012). 'Ascent dynamics of large phreatomagmatic eruption clouds: The role of microphysics'. *J. Geophys. Res.*, 117, B03203. DOI: 10.1029/2011jb008892.

Van Eaton, A. R., J. Lapierre, S. A. Behnke, C. Vagasky, C. J. Schultz, M. Pavolonis, K. Bedka and K. Khlopenkov (2023). 'Lightning Rings and Gravity Waves: Insights Into the Giant Eruption Plume From Tonga's Hunga Volcano on 15 January 2022'. *Geophys. Res. Lett.*, 50, e2022GL102341. DOI: 10.1029/2022gl102341.

Van Eaton, A. R., C. M. Smith, M. Pavolonis and R. Said (2022). 'Eruption dynamics leading to a volcanic thunderstorm—The January 2020 eruption of Taal volcano, Philippines'. *Geology*, 50, pp. 491–495. DOI: 10.1130/g49490.1.

Vaughan, G., D. P. Wareing, S. B. Jones, L. Thomas and N. Larsen (1994). 'Lidar measurements of Mt. Pinatubo aerosols at Aberystwyth from August 1991 through March 1992'. *Geophys. Res. Lett.*, 21, pp. 1315–1318. DOI: 10.1029/93gl02893.

Vaughan, R. G. and P. W. Webley (2010). 'Satellite observations of a surtseyan eruption: Hunga Ha'apai, Tonga'. *J. Volcanol. Geotherm. Res.*, 198, pp. 177–186. DOI: 10.1016/j.jvolgeores.2010.08.017.

Veefkind, J., I. Aben, K. McMullan, H. Förster, J. de Vries, G. Otter, J. Claas, H. Eskes, J. de Haan, Q. Kleipool et al. (2012). 'TROPOMI on the ESA Sentinel-5 Precursor: A GMES mission for global observations of the atmospheric composition for climate, air quality and ozone layer applications'. *Remote Sens. Env.*, 120, pp. 70–83. DOI: 10.1016/j.rse.2011.09.027.

Vehkamäki, H., M. Kulmala, I. Napari, K. E. Lehtinen, C. Timmreck, M. Noppel and A. Laaksonen (2002). 'An improved parameterization for sulfuric acid-water nucleation rates for tropospheric and stratospheric conditions'. *J. Geophys. Res.*, 107, AAC3-1–AAC3-10. DOI: 10.1029/2002JD002184.

Verbeek, R. D. M. (1884). 'The Krakatoa Eruption'. *Nature*, 30, pp. 10–15. DOI: 10.1038/030010a0.

Verbeek, R. D. M. (1885). *Krakatau*. Batavia, p. 614. DOI: 10.2307/196734.

Vergoz, J., P. Hupe, C. Listowski, A. Le Pichon, M. A. Garcés, E. Marchetti, P. Labazuy, L. Ceranna, C. Pilger, P. Gaebler et al. (2022). 'IMS observations of infrasound and acoustic-gravity waves produced by the January 2022 volcanic eruption of Hunga, Tonga: A global analysis'. *Earth Planet. Sci. Lett.*, 591, 117639. DOI: 10.1016/j.epsl.2022.117639.

Verhulst, T. G. W., D. Altadill, V. Barta, A. Belehaki, D. Burešová, C. Cesaroni et al. (2022). 'Multi-instrument detection in Europe of ionospheric disturbances caused by the 15 January 2022 eruption of the Hunga volcano'. *J. Space Weather Space Clim.*, 12, 35. DOI: 10.1051/swsc/2022032.

Vernier, H., D. Quintão, B. Biazon, E. Landulfo, G. Souza, F. J. S. Lopes, N. Rastogi, R. Meena, H. Liu, S. Fadnavis et al. (2023). 'Understanding the impact of Hunga-Tonga undersea eruption on the stratospheric aerosol population using Balloon measurements, Satellite data, and model simulations'. *EGU General Assembly 2023*. Vienna, Austria: Copernicus Meetings, EGU23–6882. DOI: 10.5194/egusphere-egu23-6882.

Vernier, H., D. Quintão, B. Biazon, E. Landulfo, G. Souza, V. A. Santos, J. S. F. Lopes, C. P. A. Mendes, A. S. J. D. Matta, K. P. Damaris et al. (2025). 'Balloon Observations Suggesting Sea Salt Injection into the Stratosphere from Hunga Tonga-Hunga Ha'apai'. DOI: 10.5194/egusphere-2025-924.

Vernier, J. P., J. P. Pommereau, A. Garnier, J. Pelon, N. Larsen, J. Nielsen, T. Christensen, F. Cairo, L. W. Thomason, T. Leblanc et al. (2009). 'Tropical stratospheric aerosol layer from CALIPSO lidar observations'. *J. Geophys. Res.*, 114, D00H10. DOI: 10.1029/2009JD011946.

Vernier, J.-P., E. Landulfo, F. S. Lopes, H. Vernier et al. (2024a). 'Long-duration balloon sampling of volcanic aerosols from the 2022 Hunga Tonga eruption'. *Geophys. Res. Lett.*, 51, e2024GL111801. DOI: 10.1029/2024GL111801.

Vernier, J.-P., C. Timmreck and S. Kremser (2022). *Atmospheric Impacts of the 2022 Hunga Tonga–Hunga Ha'apai Eruption: Summary of VolRes Discussion for the SSiRC Community*. Tech. rep. https://sparc-ssirc.org/downloads/VolRes_summary_of_the_Hunga-Vfinal.pdf. SPARC Stratospheric Sulfur and its Role in Climate (SSiRC) Initiative.

Vernier, J.-P., T. J. Aubry, C. Timmreck, A. Schmidt, L. Clarisse, F. Prata, N. Theys, A. T. Prata, G. Mann, H. Choi et al. (2024b). 'The 2019 Raikoke eruption as a testbed used by the Volcano Response group for rapid assessment of volcanic atmospheric impacts'. *Atmos. Chem. Phys.*, 24, pp. 5765–5782. DOI: 10.5194/acp-24-5765-2024.

Vernier, J.-P., T. D. Fairlie, T. Deshler, M. Natarajan, T. Knepp, K. Foster, F. G. Wienhold, K. M. Bedka, L. Thomason and C. Trepte (2016). 'In situ and space-based observations of the Kelud volcanic plume: the persistence of ash in the lower stratosphere'. *J. Geophys. Res.*, 121, pp. 11104–11118. DOI: 10.1002/2016jd025344.

Vömel, H., S. Evan and M. Tully (2022). 'Water vapor injection into the Stratosphere by Hunga Tonga-Hunga Ha'apai'. *Science*, 377, pp. 1444–1447. DOI: 10.1126/science.abq2299.

Vömel, H., S. J. Oltmans, D. J. Hofmann, T. Deshler and J. M. Rosen (1995). 'The evolution of the dehydration in the Antarctic stratospheric vortex'. *J. Geophys. Res.*, 100, pp. 13919–13926. DOI: 10.1029/95JD01000.

Walker, G. P. L. (1973). 'Explosive volcanic eruptions — a new classification scheme'. *Geol. Rundschau*, 62, pp. 431–446. DOI: 10.1007/bf01840108.

Walker, G. P. L. (1979). 'A volcanic ash generated by explosions where ignimbrite entered the sea'. *Nature*, 281, pp. 642–646. DOI: 10.1038/281642a0.

Walker, S. L. and C. E. J. de Ronde (2024). 'Ongoing activity at Hunga submarine volcano, Tonga: The case for better monitoring of submarine volcanoes worldwide'. *Geochem. Geophys. Geosyst.*, 25, e2024GC011685. DOI: 10.1029/2024GC011685.

Wallace, J. M., R. L. Panetta and J. Estberg (1993). 'Representation of the Equatorial Stratospheric Quasi-Biennial Oscillation in EOF Phase Space'. *J. Atmos. Sci.*, 50, pp. 1751–1762. DOI: 10.1175/1520-0469(1993)050<1751:ROTESQ>2.0.CO;2.

Wallis, S., M. DeLand and C. von Savigny (2025). 'Did the 2022 Hunga eruption impact the noctilucent cloud season in 2023/24 and 2024?' *Atmos. Chem. Phys.*, 25, pp. 3635–3645. DOI: 10.5194/acp-25-3635-2025.

Walsh, A., J. A. Screen, A. A. Scaife and D. M. Smith (2022). 'Non-Linear response of the extratropics to tropical climate variability'. *Geophys. Res. Lett.*, 49, e2022GL100416. DOI: 10.1029/2022GL100416.

Walters, D., A. J. Baran, I. Boutle, M. Brooks, P. Earnshaw, J. Edwards, K. Furtado, P. Hill, A. Lock, J. Manners et al. (2019). 'The Met Office Unified Model Global Atmosphere 7.0/7.1 and JULES Global Land 7.0 configurations'. *Geosci. Model Dev.*, 12, pp. 1909–1963. DOI: 10.5194/gmd-12-1909-2019.

Wang, H. J. R., R. Damadeo, D. Flittner, N. Kramarova, G. Taha, S. Davis, A. M. Thompson, S. Strahan, Y. Wang, L. Froidevaux et al. (2020). 'Validation of SAGE III/ISS Solar Occultation Ozone Products With Correlative Satellite and Ground-Based Measurements'. *J. Geophys. Res.*, 125, e2020JD032430. DOI: 10.1029/2020jd032430.

Wang, J., S. Park, J. Zeng, C. Ge, K. Yang, S. Carn, N. Krotkov and A. H. Omar (2013). 'Modeling of 2008 Kasatochi volcanic sulfate direct radiative forcing: assimilation of OMI SO 2 plume height data and comparison with MODIS and CALIOP observations'. *Atmos. Chem. Phys.*, 13, pp. 1895–1912. DOI: 10.5194/acp-13-1895-2013.

Wang, X. (2025). *MLS H2O anomaly 2022*. Zenodo. DOI: 10.5281/zenodo.14962954.

Wang, X., W. Randel, Y. Zhu, S. Tilmes, J. Starr, W. Yu, R. Garcia, O. B. Toon, M. Park, D. Kinnison et al. (2023). 'Stratospheric Climate Anomalies and Ozone Loss Caused by the Hunga Tonga-Hunga Ha'apai Volcanic Eruption'. *J. Geophys. Res.*, 128, e2023JD039480. DOI: 10.1029/2023jd039480.

Wang, Y. and Y. Huang (2024). 'Compensating atmospheric adjustments reduce the volcanic forcing from Hunga stratospheric water vapor enhancement'. *Sci. Adv.*, 10, eadl2842. DOI: 10.1126/sciadv.adl2842.

Wargan, K., G. L. Manney and N. J. Livesey (2025). 'Factors Contributing to the Unusually Low Antarctic Springtime Ozone in 2020–2023'. *J. Geophys. Res.*, 130, e2025JD043621. DOI: 10.1029/2025jd043621.

Wargan, K., B. Weir, G. L. Manney, S. E. Cohn, K. E. Knowland, P. A. Wales and N. J. Livesey (2023). 'M2-SCREAM: A Stratospheric Composition Reanalysis of Aura MLS Data With MERRA-2 Transport'. *Earth Space Sci.*, 10, e2022EA002632. DOI: 10.1029/2022ea002632.

Watanabe, S., T. Hajima, K. Sudo, T. Nagashima, T. Takemura, H. Okajima, T. Nozawa, H. Kawase, M. Abe, T. Yokohata et al. (2011). 'MIROC-ESM 2010: model description and basic results of CMIP5-20c3m experiments'. *Geosci. Model Dev.*, 4, pp. 845–872. DOI: 10.5194/gmd-4-845-2011.

Watanabe, S., K. Hamilton, T. Sakazaki and M. Nakano (2022). 'First Detection of the Pekeris Internal Global Atmospheric Resonance: Evidence from the 2022 Tonga Eruption and from Global Reanalysis Data'. *J. Atmos. Sci.*, 79, pp. 3027–3043. DOI: 10.1175/JAS-D-22-0078.1.

Waters, J. W., L. Froidevaux, R. S. Harwood, R. F. Jarnot, H. M. Pickett, W. G. Read, P. H. Siegel, R. E. Cofield, M. J. Filipiak, D. A. Flower et al. (2006). 'The Earth observing system microwave limb sounder (EOS MLS) on the aura Satellite'. *IEEE Trans. Geosci. Remote Sens.*, 44, pp. 1075–1092. DOI: 10.1109/tgrs.2006.873771.

Waugh, D. W. and L. M. Polvani (2010). 'Stratospheric polar vortices'. *The stratosphere: Dynamics, transport, and chemistry*. Ed. by L. M. Polvani, A. H. Sobel and D. W. Waugh. Vol. 190. Geophysical Monograph Series. American Geophysical Union, pp. 43–57. DOI: 10.1029/GM190.

Weber, M., W. Steinbrecht, C. Arosio, R. van der A, S. Frith, J. Anderson, L. Ciasto, M. Coldewey-Egbers, S. Davis, D. Degenstein et al. (2024). 'Stratospheric ozone [in "State of the Climate in 2023"]'. *Bull. Amer. Meteor. Soc.*, 105, S99–S100. DOI: 10.1175/BAMS-D-24-0116.1.

Wei, L., X. Pan, E. Trasatti, M. Ao, S. Liu, C. Tolomei, G. Liu and G. Ventura (2025). 'Deformation and morphological changes before the 2021–2022 explosive eruption at Hunga Tonga-Hunga Ha'apai submarine caldera revealed by satellite remote sensing'. *Bull. Volcanol.*, 87, 17. DOI: 10.1007/s00445-025-01804-5.

Weisenstein, D. K., J. E. Penner, M. Herzog and X. Liu (2007). 'Global 2-D intercomparison of sectional and modal aerosol modules'. *Atmos. Chem. Phys.*, 7, pp. 2339–2355. DOI: 10.5194/acp-7-2339-2007.

Weisenstein, D. K., G. K. Yue, M. K. W. Ko, N.-D. Sze, J. M. Rodriguez and C. J. Scott (1997). 'A two-dimensional model of sulfur species and aerosols'. *J. Geophys. Res.*, 102, pp. 13019–13035. DOI: 10.1029/97jd00901.

Wetherald, R. T. and S. Manabe (1988). 'Cloud feedback processes in a general circulation model'. *J. Atmos. Sci.*, 45, pp. 1397–1416. DOI: 10.1175/1520-0469(1988)045<1397:CFPIAG>2.0.CO;2.

Wexler, H. (1951). 'Spread of the Krakatoa volcanic dust cloud as related to the high-level circulation'. *Bull. Am. Meteorol. Soc.*, 32, pp. 48–51. DOI: 10.1175/1520-0477-32.2.48.

White, J. D. L., C. I. Schipper and K. Kano (2015). 'Submarine Explosive Eruptions'. *Encyclopedia of Volcanoes, 2nd Ed.* Pp. 553–570. DOI: 10.1016/b978-0-12-385938-9.00031-6.

Williams, J. E., V. Huijnen, I. Bouarar, M. Meziane, T. Schreurs, S. Pelletier, V. Marécal, B. Josse and J. Flemming (2022). 'Regional evaluation of the performance of the global CAMS chemical modeling system over the United States (IFS cycle 47r1)'. *Geosci. Model Dev.*, 15, pp. 4657–4687. DOI: 10.5194/gmd-15-4657-2022.

Williams, K. D., D. Copsey, E. W. Blockley, A. Bodas-Salcedo, D. Calvert, R. Comer, P. Davis, T. Graham, H. T. Hewitt, R. Hill et al. (2018). 'The Met Office Global Coupled Model 3.0 and 3.1 (GC3.0 and GC3.1) Configurations'. *J. Adv. Model. Earth Syst.*, 10, pp. 357–380. DOI: 10.1002/2017MS001115.

Wilmouth, D. M., F. F. Østerstrøm, J. B. Smith, J. G. Anderson and R. J. Salawitch (2023). 'Impact of the Hunga Tonga volcanic eruption on stratospheric composition'. *Proc. Natl. Acad. Sci.*, 120, e2301994120. DOI: 10.1073/pnas.2301994120.

Winker, D. M., W. H. Hunt and M. J. McGill (2007). 'Initial performance assessment of CALIOP'. *Geophys. Res. Lett.*, 34. DOI: 10.1029/2007gl030135.

Witze, A. (2022). 'Why the Tongan eruption will go down in the history of volcanology'. *Nature*, 602, pp. 376–378. DOI: 10.1038/d41586-022-00394-y.

Wohltmann, I., R. Lehmann and M. Rex (2010). 'The Lagrangian chemistry and transport model ATLAS: simulation and validation of stratospheric

chemistry and ozone loss in the winter 1999/2000'. *Geosci. Model Dev.*, 3, pp. 585–601. DOI: 10.5194/gmd-3-585-2010.

Wohltmann, I. and M. Rex (2009). 'The Lagrangian chemistry and transport model ATLAS: validation of advective transport and mixing'. *Geosci. Model Dev.*, 2, pp. 153–173. DOI: 10.5194/gmd-2-153-2009.

Wohltmann, I., R. Lehmann and M. Rex (2017). 'A quantitative analysis of the reactions involved in stratospheric ozone depletion in the polar vortex core'. *Atmos. Chem. Phys.*, 17, pp. 10535–10563. DOI: 10.5194/acp-17-10535-2017.

Wohltmann, I., M. L. Santee, G. L. Manney and L. F. Millán (2024). 'The Chemical Effect of Increased Water Vapor From the Hunga Tonga-Hunga Ha'apai Eruption on the Antarctic Ozone Hole'. *Geophys. Res. Lett.*, 51, e2023GL106980. DOI: 10.1029/2023gl106980.

Wood, N., A. Staniforth, A. White, T. Allen, M. Diamantakis, M. Gross, T. Melvin, C. Smith, S. Vosper, M. Zerroukat et al. (2014). 'An inherently mass-conserving semi-implicit semi-Lagrangian discretization of the deep-atmosphere global non-hydrostatic equations'. *Q. J. R. Meteorol. Soc.*, 140, pp. 1505–1520. DOI: 10.1002/qj.2235.

World Meteorological Organization (WMO) (2022). *Scientific Assessment of Ozone Depletion: 2022*. Tech. rep. GAW Report No. 278. Geneva, Switzerland.

Wrana, F., U. Niemeier, L. W. Thomason, S. Wallis and C. Von Savigny (2023). 'Stratospheric aerosol size reduction after volcanic eruptions'. *Atmos. Chem. Phys.*, 23, pp. 9725–9743. DOI: 10.5194/acp-23-9725-2023.

Wrana, F., C. von Savigny, J. Zalach and L. W. Thomason (2021). 'Retrieval of stratospheric aerosol size distribution parameters using satellite solar occultation measurements at three wavelengths'. *Atmos. Meas. Tech.*, 14, pp. 2345–2357. DOI: 10.5194/amt-14-2345-2021.

Wright, C. J. (2019). 'Quantifying the global impact of tropical cyclone-associated gravity waves using HIRDLS, MLS, SABER, and IBTrACS data'. *Q. J. R. Meteorol. Soc.*, 145, pp. 3023–3039. DOI: 10.1002/qj.3602.

Wright, C. J., N. P. Hindley, M. J. Alexander, M. Barlow, L. Hoffmann, C. N. Mitchell, F. Prata, M. Bouillon, J. Carstens, C. Clerbaux et al. (2022). 'Surface-to-space atmospheric waves from Hunga Tonga-Hunga Ha'apai eruption'. *Nature*, 609, pp. 741–746. DOI: 10.1038/s41586-022-05012-5.

Wu, H., X. Lu, W. Wang and H.-L. Liu (2023). 'Simulation of the propagation and effects of gravity waves generated by the Tonga volcano eruption in the thermosphere and ionosphere using nested-grid TIEGCM'. *J. Geophys. Res.*, 128, e2023JA031354. DOI: 10.1029/2023JA031354.

Wu, J., S. J. Cronin, M. Brenna, S.-H. Park, A. Pontesilli, I. A. Ukstins, D. Adams, J. Paredes-Mariño, K. Hamilton, M. Huebsch et al. (2025). 'Low sulfur emissions from 2022 Hunga eruption due to seawater–magma interactions'. *Nat. Geosci.*, 18, pp. 518–524. DOI: 10.1038/s41561-025-01691-7.

Xu, J., D. Li, Z. Bai, M. Tao and J. Bian (2022). 'Large Amounts of Water Vapor Were Injected into the Stratosphere by the Hunga Tonga–Hunga Ha'apai Volcano Eruption'. *Atmosphere*, 13, 912. DOI: 10.3390/atmos13060912.

Yamazaki, Y., G. Soares and J. Matzka (2022). 'Geomagnetic detection of the atmospheric acoustic resonance at 3.8 mHz during the Hunga Tonga eruption event on 15 January 2022'. *J. Geophys. Res.*, 127, e2022JA030540. DOI: 10.1029/2022JA030540.

Yeo, I. A., I. M. McIntosh, S. E. Bryan, K. Tani, M. Dunbabin, D. Metz, P. C. Collins, K. Stone and M. S. Manu (2022). 'The 2019–2020 volcanic eruption of Late'iki (Metis Shoal), Tonga'. *Sci. Rep.*, 12, 7468. DOI: 10.1038/s41598-022-11133-8.

Yeo, I. A., I. M. McIntosh, S. E. Bryan, K. Tani, M. Dunbabin, K. J. Dobson, S. J. Mitchell, P. C. Collins, M. A. Clare, H. Cathey et al. (2024). 'The 2019 pumice raft forming eruption of Volcano-F (Volcano 0403–091) and implications for hazards posed by submerged calderas'. *J. Volcanol. Geotherm. Res.*, 454, 108160. DOI: 10.1016/j.jvolgeores.2024.108160.

Yook, S., S. Solomon and X. Wang (2025). 'The impact of 2022 Hunga Tonga-Hunga Ha'apai (Hunga) eruption on stratospheric circulation and climate'. *J. Geophys. Res.*, 130, e2024JD042943. DOI: 10.1029/2024JD042943.

Yoon, S., A. Kotsakis, S. L. Alvarez, M. G. Spychala, E. Klovenski, P. Walter, G. Morris, E. Corrales, A. Alan, J. A. Diaz et al. (2022). 'Development and testing of a novel sulfur dioxide sonde'. *Atmos. Meas. Tech.*, 15, pp. 4373–4384. DOI: 10.5194/amt-15-4373-2022.

Young, S. A. and M. A. Vaughan (2009). 'The Retrieval of Profiles of Particulate Extinction from Cloud-Aerosol Lidar Infrared Pathfinder Satellite Observations (CALIPSO) Data: Algorithm Description'. *J. Atmos. Ocean. Tech.*, 26, pp. 1105–1119. DOI: 10.1175/2008JTECHA1221.1.

Young, S. A., M. A. Vaughan, R. E. Kuehn and D. M. Winker (2013). 'The Retrieval of Profiles of Particulate Extinction from Cloud–Aerosol Lidar and Infrared Pathfinder Satellite Observations (CALIPSO) Data: Uncertainty and Error Sensitivity Analyses'. *J. Atmos. Ocean. Tech.*, 30, pp. 395–428. DOI: 10.1175/jtech-d-12-00046.1.

Yu, P., R. W. Portmann, Y. Peng, C.-C. Liu, Y. Zhu, E. Asher, Z. Bai, Y. Lu, J. Bian, M. Mills et al. (2023a). 'Radiative Forcing From the 2014–2022 Volcanic and Wildfire Injections'. *Geophys. Res. Lett.*, 50, e2023GL103791. DOI: 10.1029/2023GL103791.

Yu, P., O. B. Toon, C. G. Bardeen, M. J. Mills, T. Fan, J. M. English and R. R. Neely (2015). 'Evaluations of tropospheric aerosol properties simulated by the Community Earth System Model with a sectional aerosol microphysics scheme'. *J. Adv. Model. Earth Syst.*, 7, pp. 865–914. DOI: 10.1002/2014MS000421.

Yu, P., S. M. Davis, O. B. Toon, R. W. Portmann, C. G. Bardeen, J. E. Barnes, H. Telg, C. Maloney and K. H. Rosenlof (2021). 'Persistent stratospheric warming due to 2019–2020 Australian wildfire smoke'. *Geophys. Res. Lett.*, 48, e2021GL092609. DOI: 10.1029/2021GL092609.

Yu, P., O. B. Toon, C. G. Bardeen, Y. Zhu, K. H. Rosenlof, R. W. Portmann, T. D. Thornberry, R.-S. Gao, S. M. Davis, E. T. Wolf et al. (2019). 'Black carbon lofts wildfire smoke high into the stratosphere to form a persistent plume'. *Science*, 365, pp. 587–590. DOI: 10.1126/science.aax1748.

Yu, Q. and Y. Huang (2023a). 'A Dissection of the Inter-Model Spread of the Aerosol Direct Radiative Effect in CMIP6 Models'. *Geophys. Res. Lett.*, 50, e2023GL105112. DOI: 10.1029/2023GL105112.

Yu, Q. and Y. Huang (2023b). 'Distributions and Trends of the Aerosol Direct Radiative Effect in the 21st Century: Aerosol and Environmental Contributions'. *J. Geophys. Res.*, 128. DOI: 10.1029/2022JD037716.

Yu, Q. and Y. Huang (2024). 'Quantifying the Direct Radiative Effect of Stratospheric Aerosols Using Radiative Kernels'. *ESS Open Archive*, DOI: 10.22541/essoar.172374105.56686934/v1.

Yu, W., R. Garcia, J. Yue, A. Smith, X. Wang, W. Randel, Z. Qiao, Y. Zhu, V. L. Harvey, S. Tilmes et al. (2023b). 'Mesospheric temperature and circulation response to the Hunga Tonga-Hunga-Ha'apai volcanic eruption'. *J. Geophys. Res.*, 128, e2023JD039636. DOI: 10.1029/2023JD039636.

Yue, J., S. D. Miller, W. C. I. Straka, Y.-J. Noh, M.-Y. Chou, R. Kahn and V. Flower (2022). 'La Soufriere volcanic eruptions launched gravity waves into space'. *Geophys. Res. Lett.*, 49, e2022GL097952. DOI: 10.1029/2022GL097952.

Yulaeva, E., J. R. Holton and J. M. Wallace (1994). 'On the cause of the annual cycle in tropical lower-stratospheric temperatures'. *J. Atmos. Sci.*, 51, pp. 169–174. DOI: 10.1175/1520-0469(1994)051<0169:otcota>2.0.co;2.

Zawada, D. J., L. A. Rieger, A. E. Bourassa and D. A. Degenstein (2018). 'Tomographic retrievals of ozone with the OMPS Limb Profiler: algorithm description and preliminary results'. *Atmos. Meas. Tech.*, 11, pp. 2375–2393. DOI: 10.5194/amt-11-2375-2018.

Zettergren, M. D., J. B. Snively, A. Komjathy and O. P. Verkhoglyadova (2017). 'Nonlinear ionospheric responses to large-amplitude infrasonic–acoustic waves generated by undersea earthquakes'. *J. Geophys. Res.*, 122, pp. 2272–2291. DOI: 10.1002/2016JA023159.

Zhang, C., C. Hu, S. Shang, F. E. Müller-Karger, Y. Li, M. Dai, B. Huang, X. Ning and H. Hong (2006). 'Bridging between SeaWiFS and MODIS for continuity of chlorophyll-a concentration assessments off Southeastern China'. *Remote Sens. Environ.*, 102, pp. 250–263. DOI: 10.1016/j.rse.2006.02.015.

Zhang, H., F. Wang, J. Li, Y. Duan, C. Zhu and J. He (2022). 'Potential Impact of Tonga Volcano Eruption on Global Mean Surface Air Temperature'. *J. Meteorol. Res.*, 36, pp. 1–5. DOI: 10.1007/s13351-022-2013-6.

Zhang, J., D. Kinnison, Y. Zhu, X. Wang, S. Tilmes, K. Dube and W. Randel (2024a). 'Chemistry Contribution to Stratospheric Ozone Depletion After the Unprecedented Water-Rich Hunga Tonga Eruption'. *Geophys. Res. Lett.*, 51, e2023GL105762. DOI: 10.1029/2023gl105762.

Zhang, J., P. Wang, D. Kinnison, S. Solomon, J. Guan, K. Stone and Y. Zhu (2024b). 'Stratospheric Chlorine Processing After the Unprecedented Hunga Tonga Eruption'. *Geophys. Res. Lett.*, 51, e2024GL108649. DOI: 10.1029/2024gl108649.

Zhou, L., B. Yan, N. Sun, J. Huang, Q. Liu, C. Grassotti, Y.-K. Lee, W. Straka, J. Niu, A. Huff et al. (2023). 'Observed Atmospheric Features for the 2022 Hunga Tonga Volcanic Eruption from Joint Polar Satellite System Science Data Products'. *Atmosphere*, 14, 263, p. 263. DOI: 10.3390/atmos14020263.

Zhou, X., Q. Chen, W. Feng, S. Heddell, S. S. Dhomse, G. Mann, H. C. Pumphrey, L. Millán, M. L. Santee and M. P. Chipperfield (2025). 'When will the stratospheric water vapour return to pre-Hunga level?'

Commun. Earth Environ., submitted, manuscript COMMSENV-25-4119-T.

Zhou, X., S. S. Dhomse, W. Feng, G. Mann, S. Heddell, H. Pumphrey, B. J. Kerridge, B. Latter, R. Siddans, L. Ventress et al. (2024). 'Antarctic Vortex Dehydration in 2023 as a Substantial Removal Pathway for Hunga Tonga-Hunga Ha'apai Water Vapor'. *Geophys. Res. Lett.*, 51, e2023GL107630. DOI: 10.1029/2023gl107630.

Zhu, Y., H. Akiyoshi, V. Aquila, E. Asher, E. M. Bednarz, S. Bekki, C. Brühl, A. H. Butler, P. Case, S. Chabrillat et al. (2025). 'Hunga Tonga–Hunga Ha'apai Volcano Impact Model Observation Comparison (HTHH-MOC) project: experiment protocol and model descriptions'. *Geosci. Model Dev.*, 18, pp. 5487–5512. DOI: 10.5194/gmd-18-5487-2025.

Zhu, Y., C. G. Bardeen, S. Tilmes, M. J. Mills, X. Wang, V. L. Harvey, G. Taha, D. Kinnison, R. W. Portmann, P. Yu et al. (2022). 'Perturbations in stratospheric aerosol evolution due to the water-rich plume of the 2022 Hunga-Tonga eruption'. *Commun. Earth Environ.*, 3, 248. DOI: 10.1038/s43247-022-00580-w.

Zhu, Y., R. W. Portmann, D. Kinnison, O. B. Toon, L. Millán, J. Zhang, H. Vömel, S. Tilmes, C. G. Bardeen, X. Wang et al. (2023). 'Stratospheric ozone depletion inside the volcanic plume shortly after the 2022 Hunga Tonga eruption'. *Atmos. Chem. Phys.*, 23, pp. 13355–13367. DOI: 10.5194/acp-23-13355-2023.

Zhu, Y., O. B. Toon, E. J. Jensen, C. G. Bardeen, M. J. Mills, M. A. Tolbert, P. Yu and S. Woods (2020). 'Persisting volcanic ash particles impact stratospheric SO2 lifetime and aerosol optical properties'. *Nat. Commun.*, 11, 4526. DOI: 10.1038/s41467-020-18352-5.

Zhu, Y., O. B. Toon, D. Kinnison, V. L. Harvey, M. J. Mills, C. G. Bardeen, M. Pitts, N. Bègue, J.-B. Renard, G. Berthet et al. (2018). 'Stratospheric aerosols, polar stratospheric clouds, and polar ozone depletion after the Mount Calbuco eruption in 2015'. *J. Geophys. Res.*, 123, pp. 12308–12331. DOI: 10.1029/2018JD028974.

Zhuo, Z., X. Wang, Y. Zhu, W. Yu, E. M. Bednarz, E. Fleming, P. R. Colarco, S. Watanabe, D. Plummer, G. Stenchikov et al. (2025). 'Comparing multimodel ensemble simulations with observations and decadal projections of upper atmospheric variations following the Hunga eruption'. *Atmos. Chem. Phys.*, 25, pp. 13161–13176. DOI: 10.5194/acp-25-13161-2025.

Zi, Y., Z. Long, J. Sheng, G. Lu, W. Perrie and Z. Xiao (2025). 'The Sudden Stratospheric Warming Events in the Antarctic in 2024'. *Geophys. Res. Lett.*, 52, e2025GL115257. DOI: 10.1029/2025gl115257.

Zielinski, G. A. (1995). 'Stratospheric loading and optical depth estimates of explosive volcanism over the last 2100 years derived from the Greenland Ice Sheet Project 2 ice core'. *J. Geophys. Res.*, 100, pp. 20937–20955. DOI: 10.1029/95jd01751.

Zimanowski, B., R. Büttner, P. Dellino, J. D. L. White and K. H. Wohletz (2015). 'Magma-Water Interaction and Phreatomagmatic Fragmentation'. *Encyclopedia of Volcanoes, 2nd Ed.* Pp. 473–484. DOI: 10.1016/B978-0-12-385938-9.00026-2.

Zou, C.-Z. and H. Qian (2016). 'Stratospheric Temperature Climate Data Record from Merged SSU and AMSU-A Observations'. *J. Atmos. Ocean. Tech.*, 33, pp. 1967–1984. DOI: 10.1175/JTECH-D-16-0018.1.

Zou, C.-Z., H. Qian, W. Wang, L. Wang and C. Long (2014). 'Recalibration and merging of SSU observations for stratospheric temperature trend studies'. *J. Geophys. Res.*, 119, pp. 13, 180–13, 205. DOI: 10.1002/2014JD021603.